

NDOR Sponsoring Agency Contract No. DPS-STWD (118)

PHASE I EVALUATION OF SELECTED CONCRETE MATERIAL IN LS-DYNA

Submitted by

Bradley J. Winkelbauer
Graduate Research Assistant

Ronald K. Faller, Ph.D., P.E.
Research Associate Professor
MwRSF Director

Robert W. Bielenberg, M.S.C.E., E.I.T.
Research Associate Engineer

Scott K. Rosenbaugh, M.S.C.E., E.I.T.
Research Associate Engineer

John D. Reid, Ph.D.
Professor

Jennifer D. Schmidt, Ph.D., P.E.
Research Associate Professor

MIDWEST ROADSIDE SAFETY FACILITY

Nebraska Transportation Center
University of Nebraska-Lincoln
130 Whittier Research Center
2200 Vine Street
Lincoln, Nebraska 68583-0853
(402) 472-0965

Submitted to

NEBRASKA DEPARTMENT OF ROADS
1500 Nebraska Highway 2
Lincoln, NE 68502

FEDERAL HIGHWAY ADMINISTRATION
Nebraska Division
100 Centennial Mall – Room 220
Lincoln, NE 68508

MwRSF Research Report No. TRP-03-330-16

April 29, 2016

TECHNICAL REPORT DOCUMENTATION PAGE

1. Report No. TRP-03-330-16	2.	3. Recipient's Accession No.	
4. Title and Subtitle Phase I Evaluation of Selected Concrete Material in LS-DYNA		5. Report Date April 29, 2016	
7. Author(s) Winkelbauer, B.J., Faller, R.K., Bielenberg, R.W., Rosenbaugh, S.K., Reid, J.D., and Schmidt, J.D.,		8. Performing Organization Report No. TRP-03-330-16	
9. Performing Organization Name and Address Midwest Roadside Safety Facility (MwRSF) Nebraska Transportation Center University of Nebraska-Lincoln 130 Whittier Research Center 2200 Vine Street Lincoln, Nebraska 68583-0853		10. Project/Task/Work Unit No.	
12. Sponsoring Organization Name and Address Nebraska Department of Roads 1500 Nebraska Highway 2 Lincoln, NE 68502 Federal Highway Administration – Nebraska Division 100 Centennial Mall North – Room 220 Lincoln, NE 68508		11. Contract © or Grant (G) No. NDOR DPS-STWD (118)	
13. Type of Report and Period Covered Final Report 2013-2016		14. Sponsoring Agency Code	
15. Supplementary Notes Prepared in cooperation with U.S. Department of Transportation, Federal Highway Administration.			
16. Abstract <p>Numerous roadside safety systems are configured with reinforced concrete materials, such as bridge railings, median barriers, and roadside parapets. The analysis and design of these structures may involve impact simulation with finite element software, like LS-DYNA, which includes multiple concrete material models. This Phase I study investigated the viability and performance of existing concrete material models to simulate unreinforced components subjected to common loading conditions, such as compression, tension, shear, and bending. For this study, five material models were evaluated – CSCM, K&C, RHT, Winfrith, and CDPM.</p> <p>Initially, single-element simulations were conducted in order to gain a basic understanding of material model performance. Next, small components with multiple elements were simulated to evaluate different loading conditions. Physical test data was obtained from several external experimental testing programs with unreinforced concrete in three basic load cases - compression, tension, and shear. The CSCM and K&C concrete material models provided adequate simulation results when compared to the experimental test results. Experimental tests with unreinforced concrete were conducted to obtain more results to compare with simulations. Concrete cylinder compression tests, dog-bone specimen tension tests, and four-point bend tests which created either flexure or shear failures were conducted. The CSCM and K&C material models showed promise in predicting peak forces and damage patterns in simulations of the experimental tests. Further investigation is recommended for the five selected concrete material models when used in combination with steel reinforcement.</p>			
17. Document Analysis/Descriptors Concrete Fracture, Failure Criterion, Dynamic Loading Conditions, Strain-Energy Density, Stress Concentration, LS-DYNA		18. Availability Statement No restrictions. Document available from: National Technical Information Services, Springfield, Virginia 22161	
19. Security Class (this report) Unclassified	20. Security Class (this page) Unclassified	21. No. of Pages 485	22. Price

DISCLAIMER STATEMENT

This report was completed with funding from the Federal Highway Administration, U.S. Department of Transportation. The contents of this report reflect the views and opinions of the authors who are responsible for the facts and the accuracy of the data presented herein. The contents do not necessarily reflect the official views or policies of the Nebraska Department of Roads nor the Federal Highway Administration, U.S. Department of Transportation. This report does not constitute a standard, specification, regulation, product endorsement, or an endorsement of manufacturers.

UNCERTAINTY OF MEASUREMENT STATEMENT

The Midwest Roadside Safety Facility (MwRSF) has determined the uncertainty of measurements for several parameters involved in standard full-scale crash testing and non-standard testing of roadside safety features. Information regarding the uncertainty of measurements for critical parameters is available upon request by the sponsor and the Federal Highway Administration. Test nos. CFC-1 through CFC-7, CFT-1 through CFT-6, and CFS-1 through CFS-6 were non-certified component tests conducted for research and development purposes only and are outside the scope of the MwRSF's A2LA Accreditation.

ACKNOWLEDGEMENTS

The authors wish to acknowledge several sources that made a contribution to this project: (1) The Nebraska Department of Roads and the Federal Highway Administration for sponsoring this project; and (2) MwRSF personnel for constructing the systems and conducting the component tests.

Acknowledgement is also given to the following individuals who made a contribution to the completion of this research project.

Midwest Roadside Safety Facility

J.C. Holloway, M.S.C.E., E.I.T., Test Site Manager
K.A. Lechtenberg, M.S.M.E., E.I.T., Research Associate Engineer
C.S. Stolle, Ph.D., Research Assistant Professor
A.T. Russell, B.S.B.A., Shop Manager
K.L. Krenk, B.S.M.A., Maintenance Mechanic
S.M. Tighe, Laboratory Mechanic
D.S. Charroin, Laboratory Mechanic
M.A. Rasmussen, Laboratory Mechanic
E.W. Krier, Laboratory Mechanic
Undergraduate and Graduate Research Assistants

Nebraska Department of Roads

Phil TenHulzen, P.E., Design Standards Engineer
Jim Knott, P.E., State Roadway Design Engineer
Jodi Gibson, Research Coordinator

Federal Highway Administration

John Perry, P.E., Nebraska Division Office
Danny Briggs, Nebraska Division Office

TABLE OF CONTENTS

TECHNICAL REPORT DOCUMENTATION PAGE	i
DISCLAIMER STATEMENT	ii
UNCERTAINTY OF MEASUREMENT STATEMENT	ii
ACKNOWLEDGEMENTS	iii
TABLE OF CONTENTS	iv
LIST OF FIGURES	x
LIST OF TABLES	xix
CHAPTER 1 INTRODUCTION	1
1.1 Background	1
1.2 Research Objectives	2
1.3 Research Scope	2
CHAPTER 2 LITERATURE REVIEW	4
2.1 Concrete Fracture	4
2.1.1 Compression	6
2.1.2 Tension	9
2.2 Concrete Constitutive Modeling	12
2.2.1 Empirical and Elastic Models	14
2.2.2 Linear-Elastic Models	14
2.2.3 Non-linear-Elastic Models	15
2.2.4 Plasticity Models	15
2.2.5 Plasticity and Damage Mechanics Models	16
2.2.6 Varying-Level Models	16
2.2.7 Single- and Double-Parameter Models	17
2.2.8 Continuum Damage Mechanics Models	18
2.2.9 Damage Models	18
2.3 Special Considerations	20
2.3.1 Mesh Independence	20
2.3.2 Nonlocal Modeling	21
2.3.3 Dynamic Loading Conditions	21
2.4 FEA Concrete Modeling Codes	22
2.5 Standard Concrete Component Testing Methods	24
2.5.1 Compression	24
2.5.2 Tension	25
2.5.3 Flexure	25
2.6 Relevant Laboratory Testing of Plain Concrete	26
2.7 Fracture Energy	32
2.8 Strain Rate Effects	38

CHAPTER 3 LS-DYNA CONCRETE MATERIAL MODELS.....	41
3.1 Introduction.....	41
3.2 CSCM Model.....	42
3.3 Concrete Damage (K&C) Model.....	45
3.4 RHT Model.....	48
3.5 Winfrith Model.....	51
3.6 CDPM Model.....	52
3.7 Concrete Model Use in Practice.....	55
CHAPTER 4 SINGLE ELEMENT SIMULATION.....	63
4.1 Introduction.....	63
4.2 Compression Simulations and Results.....	64
4.2.1 Baseline Condition (Unconfined).....	66
4.2.2 Constraint Condition (Confined).....	70
4.3 Tension Simulations and Results.....	73
4.3.1 Baseline Condition (Unconfined).....	74
4.3.2 Constraint Condition (Confined).....	78
4.4 Shear Simulations and Results.....	80
4.5 Discussion of Results.....	84
4.5.1 CSCM Model.....	85
4.5.2 K&C Model.....	86
4.5.3 RHT Model.....	86
4.5.4 Winfrith Model.....	86
4.5.5 CDPM Model.....	87
4.5.6 Summary.....	87
CHAPTER 5 COMPRESSION SIMULATIONS ON EXTERNAL COMPONENT TESTS.....	89
5.1 Introduction.....	89
5.2 Simulation Data Evaluation Process.....	90
5.3 CSCM Model – Simulation Results.....	95
5.3.1 Element Type.....	95
5.3.2 Rigid Wall-Cylinder Friction.....	97
5.3.3 Mesh.....	98
5.3.4 ERODE, repow, and recov.....	100
5.3.5 Fracture Energy.....	101
5.3.6 Hourglass Controls.....	103
5.3.7 Final Selection.....	104
5.3.8 Model Instabilities.....	105
5.4 K&C Model – Simulation Results.....	107
5.4.1 Element Type.....	108
5.4.2 Rigid Wall-Cylinder Friction.....	109
5.4.3 Mesh.....	110
5.4.4 Compressive Damage Scaling Factor.....	111
5.4.5 Strain Rate Effects.....	113
5.5 RHT Model – Simulation Results.....	117
5.5.1 Element Type.....	117

5.5.2 Friction.....	119
5.5.3 Mesh.....	120
5.6 Winfrith Model – Simulation Results.....	120
5.6.1 Friction.....	121
5.6.2 Mesh.....	122
5.6.3 Hourglass Energy.....	123
5.6.4 Strain Rate Effects	125
5.6.5 Fracture Energy.....	126
5.7 CDPM Model – Simulation Results	127
5.8 Discussion	128
CHAPTER 6 TENSION SIMULATIONS ON EXTERNAL COMPONENT TESTS ..	131
6.1 Introduction.....	131
6.2 Simulation Data Evaluation Process.....	132
6.3 CSCM Model – Simulation Results.....	134
6.3.1 Element Type.....	135
6.3.2 Mesh.....	136
6.3.3 Fracture Energy.....	138
6.3.4 ERODE, recov, and repow.....	139
6.4 K&C Model – Simulation Results	140
6.4.1 Element Type.....	140
6.4.2 Mesh.....	142
6.4.3 Compressive Damage Scaling Factor	143
6.4.4 Strain Rate Effects	144
6.5 RHT Model – Simulation Results.....	147
6.5.1 Element Type.....	147
6.5.2 Mesh.....	148
6.6 Winfrith Model – Simulation Results.....	149
6.7 CDPM Model – Simulation Results	150
6.8 Discussion	150
CHAPTER 7 SHEAR SIMULATIONS ON EXTERNAL COMPONENT TESTS	153
7.1 Introduction.....	153
7.2 Simulation Data Evaluation Process.....	155
7.3 CSCM Model – Simulation Results.....	157
7.3.1 Element Type.....	157
7.3.2 Mesh.....	158
7.3.3 ERODE, recov, and repow.....	160
7.4 K&C Model – Simulation Results	160
7.4.1 Element Type.....	161
7.4.2 Mesh.....	162
7.4.3 Compressive Damage Scaling Factor	163
7.5 RHT Model – Simulation Results.....	164
7.5.1 Element Type.....	164
7.5.2 Mesh.....	165
7.6 Winfrith Model – Simulation Results.....	166
7.7 CDPM Model – Simulation Results	167

7.8 Discussion	168
CHAPTER 8 RECOMMENDATIONS FOR FURTHER ANALYSIS	169
8.1 Selection of Material Models	169
CHAPTER 9 COMPONENT TESTING CONDITIONS – INTERNAL	173
9.1 Purpose	173
9.2 Scope	173
9.3 Concrete Test Specimens – Preparation	173
9.4 Cylinder Compression Testing	177
9.5 Dogbone Tension Testing	179
9.6 Beam Flexure and Shear Testing	187
9.7 Additional Instrumentation	188
CHAPTER 10 COMPRESSION TESTING (CFC-1 THROUGH CFC-7)	196
10.1 Test No. CFC-1	197
10.2 Test No. CFC-2	200
10.3 Test No. CFC-3	203
10.4 Test No. CFC-4	206
10.5 Test No. CFC-5	209
10.6 Test No. CFC-6	212
10.7 Test No. CFC-7	215
10.8 Discussion	218
CHAPTER 11 TENSION TESTING (CFT-1 THROUGH CFT-6)	221
11.1 Test No. CFT-1	223
11.2 Test No. CFT-2	226
11.3 Test No. CFT-3	229
11.4 Test No. CFT-4	232
11.5 Test No. CFT-5	235
11.6 Test No. CFT-6	238
11.7 Discussion	241
CHAPTER 12 BEAM TESTING – FLEXURE AND SHEAR (CFS-1 THROUGH CFS-6)	244
12.1 Introduction	244
12.2 Test Data Evaluation Process	245
12.3 Test No. CFS-1 [Support Span – 18 in. (457 mm)]	252
12.4 Test No. CFS-2 [Support Span – 12 in. (305 mm)]	270
12.5 Test No. CFS-3 [Support Span – 10 in. (254 mm)]	287
12.6 Test No. CFS-4 [Support Span – 11 in. (279 mm)]	304
12.7 Test No. CFS-5 [Support Span – 10 in. (254 mm)]	323
12.8 Test No. CFS-6 [Support Span – 9 in. (229 mm)]	340
12.9 Discussion	356
CHAPTER 13 SIMULATION OF INTERNAL CONCRETE CYLINDER TESTS	359
13.1 Introduction	359

13.2 Simulation Data Evaluation Process	360
13.3 CSCM Model – Simulation Results.....	363
13.3.1 Mesh.....	363
13.3.2 ERODE, recov, and repow.....	366
13.4 K&C Model – Simulation Results	369
13.4.1 Mesh.....	370
13.5 Discussion.....	371
CHAPTER 14 SIMULATION OF INTERNAL CONCRETE DOGBONE TESTS	373
14.1 Introduction.....	373
14.2 Simulation Data Evaluation Process.....	374
14.3 CSCM Model – Simulation Results.....	376
14.3.1 Mesh.....	376
14.3.2 ERODE, recov, and repow.....	378
14.4 K&C Model – Simulation Results	381
14.4.1 Mesh.....	381
14.4.2 Compressive Damage Scaling Factor	383
14.5 Discussion.....	384
CHAPTER 15 SIMULATIONS OF INTERNAL CONCRETE BEAM TESTS.....	386
15.1 Introduction.....	386
15.2 Simulation Data Evaluation Process.....	387
15.3 CSCM Model Investigation and Evaluation	388
15.3.1 9-in. (229-mm) Support Span	388
15.3.2 10-in. (254-mm) Support Span	392
15.3.3 11-in. (279-mm) Support Span	395
15.3.4 12-in. (305-mm) Support Span	399
15.3.5 18-in. (457-mm) Support Span	402
15.4 K&C Model Investigation and Evaluation	405
15.4.1 9-in. (229-mm) Support Span	405
15.4.2 10-in. (254-mm) Support Span	408
15.4.3 11-in. (279-mm) Support Span	411
15.4.4 12-in. (305-mm) Support Span	414
15.4.5 18-in. (457-mm) Support Span	417
15.5 Discussion.....	420
CHAPTER 16 SUMMARY, CONCLUSIONS, AND RECOMMENDATIONS	424
16.1 Summary and Conclusions	424
16.2 Recommendations.....	432
CHAPTER 17 REFERENCES	436
CHAPTER 18 APPENDICES	442
Appendix A. Material Model Card Inputs.....	443
Appendix B. Instrumentation Specification Sheets.....	446
Appendix C. True Axial Stress-Engineering Axial Strain for Test Nos. CFC-1 through CFC-7	452

Appendix D. String Potentiometer Data for CFS Testing457
Appendix E. Results from Alternate Beam Simulations for CSCM Model474

LIST OF FIGURES

Figure 1. Longitudinal Cracks in Concrete due to Applied Load [3]	5
Figure 2. Four-Point Bending Test Loading Apparatus [28]	26
Figure 3. Test Setup for Study by Zhang, et al. [29]	27
Figure 4. Test Setup for Study by Kim and Taha [30].....	28
Figure 5. Test Setup for Study by Yan and Lin [31]	29
Figure 6. Test Setup for Study by Graybeal and Baby [32].....	30
Figure 7. Test Setup for Study by Kim, El-Tawil, and Naaman [33]	31
Figure 8. Test Setup for Study by Zhen-hai and Xiu-qin [34].....	32
Figure 9. Failure Surface and Cap Shape of CSCM Model [51]	43
Figure 10. Plot of Three Failure Surfaces for RHT Model [55]	49
Figure 11. Elliptical Cap Function at High Pressure	50
Figure 12. Evolution of Yield Surface During Hardening [58]	53
Figure 13. Damage Contours of Cylinders Simulated by APTEK [51]	56
Figure 14. Damage in Parapet Simulation after Impact Loading [59].....	57
Figure 15. Comparison of Axial Stress vs. Axial Strain Data for K&C Simulations [60].....	58
Figure 16. Experimental and Simulation Damage Contours for RHT Model [55]	60
Figure 17. Single Element Model Overview	63
Figure 18. Baseline (Unconfined) and Constraint (Confined) Conditions for Compression and Tension.....	65
Figure 19. Simulation Images for Baseline Condition, Compression	67
Figure 20. True Stress-Strain Plot for Compression Loading, Baseline Condition.....	70
Figure 21. Simulation Images for Constraint Condition, Compression (elform 2)	71
Figure 22. True Stress-Strain Plot for Compression Loading, Constraint Condition.....	73
Figure 23. Simulation Images for Baseline Condition, Tension (elform 2)	75
Figure 24. True Stress-Strain Plot for Tension Loading, Baseline Condition	77
Figure 25. True Stress-Strain Plot for Tension Loading, Constraint Condition	80
Figure 26. Angled Constraint Conditions for Shear	81
Figure 27. Simulation Images for Angled Condition, Shear (elform 2)	82
Figure 28. True Stress-Strain Plot for Shear Loading, Angled Condition.....	84
Figure 29. Compression Stress-Strain Test Results [42]	89
Figure 30. Overview of External Compression Simulation.....	91
Figure 31. Mesh Sizes for Compression Cylinders	92
Figure 32. Compression Stress-Strain for Elform Simulation, CSCM Model	96
Figure 33. Compression Fracture Pattern of Element Type Cylinders, CSCM Model	97
Figure 34. Compression Damage Pattern for Friction Simulation, CSCM Model.....	98
Figure 35. Compression Stress-Strain Plot for Mesh Simulation, CSCM Model	99
Figure 36. Compression Damage Contours for Mesh Simulation (¾-in. [19-mm] mesh), CSCM Model	100
Figure 37. Compression Stress-Strain for ERODE Simulation, CSCM Model	101
Figure 38. Compression Stress-Strain for Fracture Energy Simulation, CSCM Model	102
Figure 39. Compression Stress-Strain for Decreased Fracture Energy Simulation, CSCM Model.....	103

Figure 40. Compression Stress-Strain for HG6 Fracture Energy Simulation, CSCM Model	104
Figure 41. Compression Damage Profiles for Final Combination, CSCM Model	105
Figure 42. Compression Part Deletion with HG6 Fracture Energy Simulation, CSCM Model	106
Figure 43. Compression Damage Profiles for ERODE Simulation, CSCM Model	107
Figure 44. Compression Stress-Strain for Elform Simulation, K&C Model	108
Figure 45. Compression Stress-Strain for Friction Simulation, K&C Model	110
Figure 46. Compression Stress-Strain for Mesh Simulation, K&C Model	110
Figure 47. Compression Stress-Strain for B ₁ Simulation, K&C Model	112
Figure 48. Compression Behavior of Cylinders in B ₁ Simulation, K&C Model	113
Figure 49. Compression Stress-Strain for LCRATE Simulation, K&C Model	115
Figure 50. Compression Stress-Strain for 1.0 LCRATE Simulation, K&C Model	116
Figure 51. Compression Stress-Strain Plot for Full LCRATE Simulation, K&C Model	117
Figure 52. Compression Stress-Strain for Elform Simulation, RHT Model	118
Figure 53. Compression Stress-Strain for Friction Simulation, RHT Model	119
Figure 54. Compression Hourglass Energy for Mesh Simulation, RHT Model	120
Figure 55. Compression Hourglass Energy for Friction Simulation, Winfrith Model	121
Figure 56. Compression Stress-Strain for Friction Simulation, Winfrith Model	122
Figure 57. Compression Hourglass Energy for Mesh Simulation, Winfrith Model	123
Figure 58. Compression Dilation of Cylinders for Mesh Simulation, Winfrith Model	124
Figure 59. Compression Hourglass Energy with HG4, Winfrith Model	125
Figure 60. Compression Stress-Strain with Rate Effects Off, Winfrith Model	126
Figure 61. Compression Stress-Strain for Fracture Energy Simulation, Winfrith Model	127
Figure 62. Tension Stress-Deformation Test Results [67]	132
Figure 63. Overview of External Tension Simulation	133
Figure 64. Tension Stress-Deformation for Elform Simulation, CSCM Model	135
Figure 65. Tension Fracture Pattern of Specimens, CSCM Model	136
Figure 66. Tension Stress-Deformation for Mesh Simulation, CSCM Model	137
Figure 67. Tension Stress-Deformation for Additional Mesh Simulation, CSCM Model	138
Figure 68. Tension Stress-Deformation for Fracture Energy Simulation, CSCM Model	139
Figure 69. Tension Stress-Deformation for Element Type, K&C Model	141
Figure 70. Tension Damage Contours for Element Type Simulation, K&C Model	141
Figure 71. Tension Stress-Deformation for Refined Mesh, K&C Model	142
Figure 72. Tension Stress-Deformation for Compressive Damage Scaling Factor, K&C Model	143
Figure 73. Tension Stress-Deformation for Base Strain Rate Effects, K&C Model	146
Figure 74. Tension Stress-Deformation for Varying Strain Rates, K&C Model	147
Figure 75. Tension Stress-Deformation for Element Type, RHT Model	148
Figure 76. Tension Stress-Deformation for Finer Mesh, RHT Model	149
Figure 77. Shear Box Testing Specimen [68]	153
Figure 78. Shear Stress-Deformation Test Results [68]	154

Figure 79. Overview of External Shear Simulation.....	156
Figure 80. Shear Stress-Deformation for Element Type Simulation, CSCM Model	158
Figure 81. Shear Damage Contours for Element Type Simulation, CSCM Model.....	158
Figure 82. Shear Stress-Deformation for Mesh Simulation, CSCM Model.....	159
Figure 83. Shear Damage Contours for Mesh Simulation, CSCM Model	160
Figure 84. Shear Stress-Deformation for Element Type, K&C Model	162
Figure 85. Shear Stress-Deformation for Mesh Simulation, K&C Model	163
Figure 86. Shear Stress-Deformation for Element Type, RHT Model	164
Figure 87. Shear Damage Contours for Element Type Simulation, RHT Model.....	165
Figure 88. Shear Stress-Deformation for Mesh Simulation, RHT Model	166
Figure 89. Shear Hourglass Energy Plots with HG4, Winfrith Model	167
Figure 90. Shear Stress-Deformation for Mesh Simulation, Winfrith Model	167
Figure 91. Metal Molds for Tension, Flexure, and Shear Concrete Specimens	174
Figure 92. Concrete Mixing for Internal Testing Program	176
Figure 93. Specimens in Moisture Curing Room	177
Figure 94. Cylinder Specimens for Test Nos. CFC-1 through CFC-7.....	178
Figure 95. Dogbone Specimens for Test Nos. CFT-1 through CFT-6	180
Figure 96. Direct Tension Test Jig, System Setup.....	182
Figure 97. Direct Tension Test Jig, Permanent Jig Components.....	183
Figure 98. Direct Tension Test Jig, Temporary Jig Components	184
Figure 99. Direct Tension Test Jib, Bill of Materials	185
Figure 100. Beam Specimens for Test Nos. CFS-1 through CFS-6	187
Figure 101. Typical GoPro Digital Video Camera Setup	190
Figure 102. Instrumentation Layout	193
Figure 103. Data Acquisition Setup for Beam Testing.....	195
Figure 104. Pre-Test Photographs, Test Nos. CFC-1 through CFC-7	197
Figure 105. Stress-Strain History, Test No. CFC-1	198
Figure 106. Post-Test Photographs, Test No. CFC-1	199
Figure 107. Stress-Strain History, Test No. CFC-2.....	201
Figure 108. Post-Test Photographs, Test No. CFC-2	202
Figure 109. Stress-Strain History, Test No. CFC-3	204
Figure 110. Post-Test Photographs, Test No. CFC-3	205
Figure 111. Stress-Strain History, Test No. CFC-4.....	207
Figure 112. Post-Test Photographs, Test No. CFC-4	208
Figure 113. Stress-Strain History, Test No. CFC-5.....	210
Figure 114. Post-Test Photographs, Test No. CFC-5	211
Figure 115. Stress-Strain History, Test No. CFC-6.....	213
Figure 116. Post-Test Photographs, Test No. CFC-6	214
Figure 117. Stress-Strain History, Test No. CFC-7.....	216
Figure 118. Post-Test Photographs, Test No. CFC-7	217
Figure 119. Stress-Strain Histories, Test Nos. CFC-1 through CFC-7.....	219
Figure 120. Pre-Test Photographs, Test Nos. CFT-1 through CFT-6	222
Figure 121. Stress-Time History, Test No. CFT-1	224
Figure 122. Post-Test Photographs, Test No. CFT-1.....	225
Figure 123. Stress-Time History, Test No. CFT-2	227
Figure 124. Post-Test Photographs, Test No. CFT-2.....	228

Figure 125. Stress-Time History, Test No. CFT-3	230
Figure 126. Post-Test Photographs, Test No. CFT-3.....	231
Figure 127. Stress-Time History, Test No. CFT-4	233
Figure 128. Post-Test Photographs, Test No. CFT-4.....	234
Figure 129. Stress-Time History, Test No. CFT-5	236
Figure 130. Post-Test Photographs, Test No. CFT-5.....	237
Figure 131. Stress-Time History, Test No. CFT-6	239
Figure 132. Post-Test Photographs, Test No. CFT-6.....	240
Figure 133. Stress-Time Histories, Test No. CFT-1 through CFT-6.....	241
Figure 134. Post-Test Photographs, Test Nos. CFT-1 through CFT-6.....	242
Figure 135. Four-Point Bending Test Setup	246
Figure 136. Test Setup for Test No. CFS-1 [18-in. (457-mm) Span].....	252
Figure 137. Load vs. Time, Test No. CFS-1 [18-in. (457-mm) Span]	253
Figure 138. Post-Test Damage, Test No. CFS-1 [18-in. (457-mm) Span]	254
Figure 139. Additional Post-Test Damage, Test No. CFS-1 [18-in. (457-mm) Span]....	255
Figure 140. Normal Strains for Top, Side, and Bottom Gauges, Test No. CFS-1 [18-in. (457-mm) Span].....	258
Figure 141. Vertical Distance versus Normal Strain, Test No. CFS-1 [18-in. (457-mm) Span].....	258
Figure 142. Estimated Midspan Normal Stresses from Bottom Strain Gauges and MTS Load Data, Test No. CFS-1 [18-in. (457-mm) Span]	259
Figure 143. Estimated Midspan Normal Stresses from Top Strain Gauges and MTS Load Data, Test No. CFS-1 [18-in. (457-mm) Span]	260
Figure 144. Extracted Strain Plots for Rosette Strain Gauges 1 and 2, Test No. CFS-1 [18-in. (457-mm) Span]	265
Figure 145. Extracted Strain Plots for Rosette Strain Gauges 3 and 4, Test No. CFS-1 [18-in. (457-mm) Span]	266
Figure 146. Principal Strains for Test No. CFS-1 [18-in. (457-mm) Span]	268
Figure 147. Principal Angles for Test No. CFS-1 [18-in. (457-mm) Span]	269
Figure 148. Test Setup for Test No. CFS-2 [12-in. (305-mm) Span].....	270
Figure 149. Load vs. Time, Test No. CFS-2 [12-in. (305-mm) Span]	271
Figure 150. Post-Test Damage, Test No. CFS-2 [12-in. (305-mm) Span]	272
Figure 151. Additional Post-Test Damage, Test No. CFS-2 [12-in. (305-mm) Span]....	273
Figure 152. Normal Strains for Top, Side, and Bottom Gauges, Test No. CFS-2 [12-in. (305-mm) Span].....	276
Figure 153. Vertical Distance versus Normal Strain, Test No. CFS-2 [12-in. (305-mm) Span].....	276
Figure 154. Estimated Midspan Normal Stresses from Bottom Strain Gauges and MTS Load Data, Test No. CFS-2 [12-in. (305-mm) Span]	277
Figure 155. Estimated Midspan Normal Stresses from Top Strain Gauges and MTS Load Data, Test No. CFS-2 [12-in. (305-mm) Span]	278
Figure 156. Extracted Strain Plots for Rosette Strain Gauges 1 and 2, Test No. CFS-2 [12-in. (305-mm) Span]	283
Figure 157. Extracted Strain Plots for Rosette Strain Gauges 3 and 4, Test No. CFS-2 [12-in. (305-mm) Span]	284

Figure 158. Principal Strains and Angles for Test No. CFS-2 [12-in. (305-mm) Span]286

Figure 159. Test Setup for Test No. CFS-3 [10-in. (254-mm) Span].....287

Figure 160. Load vs. Time, Test No. CFS-3 [10-in. (254-mm) Span]288

Figure 161. Post-Test Damage, Test No. CFS-3 [10-in. (254-mm) Span]289

Figure 162. Additional Post-Test Damage, Test No. CFS-3 [10-in. (254-mm) Span]....290

Figure 163. Normal Strains for Top, Side, and Bottom Gauges, Test No. CFS-3 [10-in. (254-mm) Span].....293

Figure 164. Vertical Distance versus Normal Strain, Test No. CFS-3 [10-in. (254-mm) Span].....293

Figure 165. Estimated Midspan Normal Stresses from Bottom Strain Gauges and MTS Load Data, Test No. CFS-3 [10-in. (254-mm) Span]294

Figure 166. Estimated Midspan Normal Stresses from Top Strain Gauges and MTS Load Data, Test No. CFS-3 [10-in. (254-mm) Span]295

Figure 167. Extracted Strain Plots for Rosette Strain Gauges 1 and 2, Test No. CFS-3 [10-in. (254-mm) Span]300

Figure 168. Extracted Strain Plots for Rosette Strain Gauges 3 and 4, Test No. CFS-3 [10-in. (254-mm) Span]301

Figure 169. Principal Strains and Angles for Test No. CFS-3 [10-in. (254-mm) Span]303

Figure 170. Test Setup for Test No. CFS-4 [11-in. (279-mm) Span]304

Figure 171. Load vs. Time, Test No. CFS-4 [11-in. (279-mm) Span]305

Figure 172. Post-Test Damage, Test No. CFS-4 [11-in. (279-mm) Span]306

Figure 173. Additional Post-Test Damage, Test No. CFS-4 [11-in. (279-mm) Span]....307

Figure 174. Normal Strains for Top, Side, and Bottom Gauges, Test No. CFS-4 [11-in. (279-mm) Span].....310

Figure 175. Vertical Distance versus Normal Strain, Test No. CFS-4 [11-in. (279-mm) Span].....310

Figure 176. Estimated Midspan Normal Stresses from Bottom Strain Gauges and MTS Load Data, Test No. CFS-4 [11-in. (279-mm) Span]311

Figure 177. Estimated Midspan Normal Stresses from Top Strain Gauges and MTS Load Data, Test No. CFS-4 [11-in. (279-mm) Span]312

Figure 178. Extracted Strain Plots for Rosette Strain Gauges 1 and 2, Test No. CFS-4 [10-in. (254-mm) Span]317

Figure 179. Extracted Strain Plots for Rosette Strain Gauges 3 and 4, Test No. CFS-4 [11-in. (279-mm) Span]318

Figure 180. Extracted Strain Plots for Rosette Strain Gauges 3 and 4 with Alternative Scale, Test No. CFS-4 [11-in. (279-mm) Span]319

Figure 181. Principal Strains for Gauges 1 and 3, Test No. CFS-4 [10-in. (254-mm) Span]321

Figure 182. Principal Angles for Test No. CFS-4 [11-in. (279-mm) Span]322

Figure 183. Test Setup for Test No. CFS-5 [10-in. (254-mm) Span].....323

Figure 184. Load vs. Time, Test No. CFS-5 [10-in. (254-mm) Span]324

Figure 185. Post-Test Damage, Test No. CFS-5 [10-in. (254-mm) Span]325

Figure 186. Additional Post-Test Damage, Test No. CFS-5 [10-in. (254-mm) Span]....326

Figure 187. Normal Strains for Top, Side, and Bottom Gauges, Test No. CFS-5 [10-in. (254-mm) Span].....	329
Figure 188. Vertical Distance versus Normal Strain, Test No. CFS-5 [10-in. (254-mm) Span].....	329
Figure 189. Estimated Midspan Normal Stresses from Bottom Strain Gauges and MTS Load Data, Test No. CFS-5 [10-in. (254-mm) Span].....	330
Figure 190. Estimated Midspan Normal Stresses from Top Strain Gauges and MTS Load Data, Test No. CFS-5 [10-in. (254-mm) Span]	331
Figure 191. Extracted Strain Plots for Rosette Strain Gauges 1 and 2, Test No. CFS-5 [10-in. (254-mm) Span]	335
Figure 192. Extracted Strain Plots for Rosette Strain Gauges 3 and 4, Test No. CFS-5 [10-in. (254-mm) Span]	336
Figure 193. Principal Strains for Gauges 2 and 4, Test No. CFS-5 [10-in. (254-mm) Span]	338
Figure 194. Principal Angles for Test No. CFS-5 [10-in. (254-mm) Span]	339
Figure 195. Test Setup for Test No. CFS-6 [9-in. (229-mm) Span].....	340
Figure 196. Load vs. Time, Test No. CFS-6 [9-in. (229-mm) Span]	341
Figure 197. Post-Test Damage, Test No. CFS-6 [9-in. (229-mm) Span]	342
Figure 198. Additional Post-Test Damage, Test No. CFS-6 [9-in. (229-mm) Span]	343
Figure 199. Normal Strains for Top, Side, and Bottom Gauges, Test No. CFS-6 [9-in. (229-mm) Span].....	346
Figure 200. Vertical Distance versus Normal Strain, Test No. CFS-6 [9-in. (229-mm) Span].....	346
Figure 201. Estimated Midspan Normal Stresses from Bottom Strain Gauges and MTS Load Data, Test No. CFS-6 [9-in. (229-mm) Span].....	347
Figure 202. Estimated Midspan Normal Stresses from Top Strain Gauges and MTS Load Data, Test No. CFS-6 [9-in. (229-mm) Span]	348
Figure 203. Extracted Strain Plots for Rosette Strain Gauges 1 and 2, Test No. CFS-6 [9-in. (229-mm) Span]	352
Figure 204. Extracted Strain Plots for Rosette Strain Gauges 3 and 4, Test No. CFS-6 [9-in. (229-mm) Span]	353
Figure 205. Principal Strains and Angles for Test No. CFS-6 [9-in. (229-mm) Span]	355
Figure 206. Vertical Distance versus Normal Strain, All CFS Tests.....	356
Figure 207. Shear Load-Time Histories, All CFS Tests.....	358
Figure 208. Overview of Internal Compression Simulation.....	360
Figure 209. Mesh Sizes for Compression Cylinders	362
Figure 210. Compression Test Stress-Strain Behavior, Compression (Average of 7 Tests).....	363
Figure 211. Compression Damage Contours for Mesh-Size Simulation, CSCM Model	364
Figure 212. Compression Stress-Strain Behavior for Mesh-Size Variation, CSCM Model	365
Figure 213. Compression Stress-Time Behavior for Mesh Size Variation, CSCM Model	366
Figure 214. Compression Stress-Time Behavior for ERODE, recov, and repow Variations, CSCM Model	368

Figure 215. Compression Damage Contours for ERODE Simulation, CSCM Model....369
Figure 216. Compression Damage Contours for Mesh-Size Simulation, K&C Model...370
Figure 217. Compression Stress-Time Behavior for Mesh-Size Simulation, K&C
Model371
Figure 218. Overview of Internal Tension Simulation374
Figure 219. Mesh Sizes for Tension Dogbones375
Figure 220. Tension Damage Contours of Mesh-Size Simulation, CSCM Model.....377
Figure 221. Tension Stress-Strain Behavior for Mesh-Size Variation, CSCM Model....378
Figure 222. Tension Stress-Strain Behavior for ERODE, recov, and repow
Variations, CSCM Model380
Figure 223. Tension Damage Contours for Mesh-Size Simulation, K&C Model.....382
Figure 224. Tension Stress-Strain Behavior for Mesh-Size Simulation, K&C Model....383
Figure 225. Tension Stress-Strain Behavior and Damage Contours for B₁
Simulation, K&C Model.....384
Figure 226. Overview of Internal Flexure and Shear Simulation.....387
Figure 227. Damage Pattern for 9-in. (229-mm) Span at 130 ms, CSCM Model390
Figure 228. Force Comparison for 9-in. (229-mm) Span, CSCM Model.....391
Figure 229. Energy Comparison for 9-in. (229-mm) Span, CSCM Model391
Figure 230. Damage Pattern for 10-in. (254-mm) Span at 100 ms, CSCM Model393
Figure 231. Force Comparison for 10-in. (254-mm) Span, CSCM Model.....394
Figure 232. Energy Comparison for 10-in. (254-mm) Span, CSCM Model394
Figure 233. Damage Pattern for 11-in. (279-mm) Span at 100 ms, CSCM Model397
Figure 234. Force Comparison for 11-in. (279-mm) Span, CSCM Model.....398
Figure 235. Energy Comparison for 11-in. (279-mm) Span, CSCM Model398
Figure 236. Damage Pattern for 12-in. (305-mm) Span at 100 ms, CSCM Model400
Figure 237. Force Comparison for 12-in. (305-mm) Span, CSCM Model.....401
Figure 238. Energy Comparison for 12-in. (305-mm) Span, CSCM Model401
Figure 239. Damage Pattern for 18-in. (457-mm) Span at 100 ms, CSCM Model403
Figure 240. Force Comparison for 18-in. (457-mm) Span, CSCM Model.....404
Figure 241. Energy Comparison for 18-in. (457-mm) Span, CSCM Model404
Figure 242. Damage Pattern for 9-in. (229-mm) Span at 50 ms, K&C Model406
Figure 243. Force Comparison for 9-in. (229-mm) Span, K&C Model407
Figure 244. Energy Comparison for 9-in. (229-mm) Span, K&C Model.....408
Figure 245. Damage Pattern for 10-in. (254-mm) Span at 50 ms, K&C Model409
Figure 246. Force Comparison for 10-in. (254-mm) Span, K&C Model410
Figure 247. Energy Comparison for 10-in. (254-mm) Span, K&C Model.....411
Figure 248. Damage Pattern for 11-in. (279-mm) Span at 50 ms, K&C Model412
Figure 249. Force Comparison for 11-in. (279-mm) Span, K&C Model413
Figure 250. Energy Comparison for 11-in. (279-mm) Span, K&C Model.....414
Figure 251. Damage Pattern for 12-in. (305-mm) Span at 50 ms, K&C Model415
Figure 252. Force Comparison for 12-in. (305-mm) Span, K&C Model416
Figure 253. Energy Comparison for 12-in. (305-mm) Span, K&C Model.....417
Figure 254. Damage Pattern for 18-in. (457-mm) Span at 50 ms, K&C Model418
Figure 255. Force Comparison for 18-in. (457-mm) Span, K&C Model419
Figure 256. Energy Comparison for 18-in. (457-mm) Span, K&C Model.....420
Figure A-1. Material Model Input Card for CSCM Model444

Figure A-2. Material Model Input Card for K&C Model	444
Figure A-3. Material Model Input Card for RHT Model.....	444
Figure A-4. Material Model Input Card for Winfrith Model.....	445
Figure A-5. Material Model Input Card for CDPM Model	445
Figure B-1. Specifications for Linear Strain Gauges.....	447
Figure B-2. Specifications for Rosette Strain Gauges	448
Figure B-3. Specification for String Potentiometer, ID #43445	449
Figure B-4. Specification for String Potentiometer, ID #43446.....	450
Figure B-5. Specification for String Potentiometer, ID #43447	451
Figure C-1. Stress-Strain History, Test No. CFC-1	453
Figure C-2. Stress-Strain History, Test No. CFC-2	453
Figure C-3. Stress-Strain History, Test No. CFC-3	454
Figure C-4. Stress-Strain History, Test No. CFC-4.....	454
Figure C-5. Stress-Strain History, Test No. CFC-5.....	455
Figure C-6. Stress-Strain History, Test No. CFC-6.....	455
Figure C-7. Stress-Strain History, Test No. CFC-7	456
Figure D-1. String Potentiometer Summary for Gauge A, Test No. CFS-1	458
Figure D-2. String Potentiometer Summary for Gauge B, Test No. CFS-1	459
Figure D-3. String Potentiometer Summary for Gauge C, Test No. CFS-1	460
Figure D-4. String Potentiometer Summary for Gauge A, Test No. CFS-2.....	461
Figure D-5. String Potentiometer Summary for Gauge B, Test No. CFS-2.....	462
Figure D-6. String Potentiometer Summary for Gauge C, Test No. CFS-2	463
Figure D-7. String Potentiometer Summary for Gauge A, Test No. CFS-3	464
Figure D-8. String Potentiometer Summary for Gauge B, Test No. CFS-3	465
Figure D-9. String Potentiometer Summary for Gauge C, Test No. CFS-3	466
Figure D-10. String Potentiometer Summary for Gauge A, Test No. CFS-4.....	467
Figure D-11. String Potentiometer Summary for Gauge B, Test No. CFS-4	468
Figure D-12. String Potentiometer Summary for Gauge C, Test No. CFS-4.....	469
Figure D-13. String Potentiometer Summary for Gauge A, Test No. CFS-5.....	470
Figure D-14. String Potentiometer Summary for Gauge B, Test No. CFS-5	471
Figure D-15. String Potentiometer Summary for Gauge C, Test No. CFS-5	472
Figure D-16. String Potentiometer Summary for Gauge B, Test No. CFS-6.....	473
Figure E-1. Damage Pattern for 9-in. (229-mm) Span at 140 ms, CSCM Model (Alternate).....	475
Figure E-2. Force Comparison for 9-in. (229-mm) Span, CSCM Model (Alternate)	476
Figure E-3. Energy Comparison for 9-in. (229-mm) Span, CSCM Model (Alternate)...	476
Figure E-4. Damage Pattern for 10-in. (254-mm) Span at 120 ms, CSCM Model (Alternate).....	477
Figure E-5. Force Comparison for 10-in. (254-mm) Span, CSCM Model (Alternate) ...	478
Figure E-6. Energy Comparison for 10-in. (254-mm) Span, CSCM Model (Alternate).....	478
Figure E-7. Damage Pattern for 11-in. (279-mm) Span at 100 ms, CSCM Model (Alternate).....	479
Figure E-8. Force Comparison for 11-in. (279-mm) Span, CSCM Model (Alternate) ...	480
Figure E-9. Energy Comparison for 11-in. (279-mm) Span, CSCM Model (Alternate).....	480

Figure E-10. Damage Pattern for 12-in. (305-mm) Span at 100 ms, CSCM Model
(Alternate).....481

Figure E-11. Force Comparison for 12-in. (305-mm) Span, CSCM Model
(Alternate).....482

Figure E-12. Energy Comparison for 12-in. (305-mm) Span, CSCM Model
(Alternate).....482

Figure E-13. Damage Pattern for 18-in. (457-mm) Span at 100 ms, CSCM Model
(Alternate).....483

Figure E-14. Force Comparison for 18-in. (457-mm) Span, CSCM Model
(Alternate).....484

Figure E-15. Energy Comparison for 18-in. (457-mm) Span, CSCM Model
(Alternate).....484

LIST OF TABLES

Table 1. LS-DYNA Concrete Material Model Evaluation	42
Table 2. Material Card Inputs	64
Table 3. Results for Compression Loading, Baseline Condition.....	68
Table 4. Results for Compression Loading, Constraint Condition.....	72
Table 5. Results for Tension Loading, Baseline Condition	76
Table 6. Results for Tension Loading, Constraint Condition	79
Table 7. Results for Shear Loading, Angled Condition.....	83
Table 8. Simulation Run Times	85
Table 9. Material Model Input Changes for Simulation	94
Table 10. DIF Factors for K&C Model - 6,585 psi (45.4 MPa) and 4,450 psi (31.0 MPa) Concrete	114
Table 11. DIF Values for K&C Model – (a) 6,585 psi (45.4 MPa) and (b) 6,367 psi (43.9 MPa)	145
Table 12. Concrete Mix Proportions for Internal Testing Program.....	175
Table 13. Cylinder Testing Matrix for Test Nos. CFC-1 through CFC-7	179
Table 14. Dogbone Testing Matrix for Test Nos. CFT-1 through CFT-6.....	186
Table 15. Beam Testing Matrix for Test Nos. CFS-1 through CFS-6.....	188
Table 16. Rosette Locations for Beam Tests	194
Table 17. Test Data Sheet, Test No. CFC-1	198
Table 18. Test Data Sheet, Test No. CFC-2	200
Table 19. Test Data Sheet, Test No. CFC-3	203
Table 20. Test Data Sheet, Test No. CFC-4	206
Table 21. Test Data Sheet, Test No. CFC-5	209
Table 22. Test Data Sheet, Test No. CFC-6	212
Table 23. Test Data Sheet, Test No. CFC-7	215
Table 24. Summary of Peak Engineering Stress for Test Nos. CFC-1 through CFC- 7.....	219
Table 25. Summary of Moduli of Elasticity for Test Nos. CFC-1 through CFC-7	220
Table 26. Test Data Sheet, Test No. CFT-1	223
Table 27. Test Data Sheet, Test No. CFT-2.....	226
Table 28. Test Data Sheet, Test No. CFT-3.....	229
Table 29. Test Data Sheet, Test No. CFT-4.....	232
Table 30. Test Data Sheet, Test No. CFT-5.....	235
Table 31. Test Data Sheet, Test No. CFT-6.....	238
Table 32. Summary of Dogbone Compression Tests	243
Table 33. Normal Strain and Stress Distribution for Horizontal Gauges, Test No. CFS-1	256
Table 34. Summary of Stress and Strains for Rosette Gauges, Test No. CFS-1	267
Table 35. Normal Strain and Stress Distribution for Horizontal Gauges, Test No. CFS-2	274
Table 36. Summary of Stress and Strains for Rosette Gauges, Test No. CFS-2	285
Table 37. Normal Strain and Stress Distribution for Horizontal Gauges, Test No. CFS-3	291
Table 38. Summary of Stress and Strains for Rosette Gauges, Test No. CFS-3	302

Table 39. Normal Strain and Stress Distribution for Horizontal Gauges, Test No.
CFS-4308

Table 40. Summary of Stress and Strains for Rosette Gauges, Test No. CFS-4320

Table 41. Normal Strain and Stress Distribution for Horizontal Gauges, Test No.
CFS-5327

Table 42. Summary of Stress and Strains for Rosette Gauges, Test No. CFS-5337

Table 43. Normal Strain and Stress Distribution for Horizontal Gauges, Test No.
CFS-6344

Table 44. Summary of Stress and Strains for Rosette Gauges, Test No. CFS-6354

Table 45. Summary of Principal Angles, All CFS Tests358

Table 46. Summary of CSCM and K&C Material Model Behavior421

CHAPTER 1 INTRODUCTION

1.1 Background

Currently, concrete modeling with finite element analysis software is used in many applications. Specifically in roadside safety applications, it is important to be able to analyze and design reinforced concrete structures (e.g., concrete barriers mounted on bridge decks or road slabs) to withstand design limit conditions, contain and redirect impacting vehicles, and anticipate damage. Concrete modeling in roadside safety applications can include the study of portable temporary concrete barriers as well as solid median barriers, among others.

Past modeling practices within the roadside safety community have often assigned a rigid definition that does not allow for the analysis of stresses and strains throughout the part for prediction of concrete fracture. Over the last several decades, the use of concrete material models has become prevalent as opposed to the use of a rigid definition. However, research is still needed to select appropriate concrete material models for both plain and reinforced applications under various load scenarios. Concrete is a heterogeneous material and requires advanced modeling to predict the onset of cracking. Using accurate properties in concrete material models in lieu of rigid definition will allow for improved analysis and design methods that incorporate stress, deformation, and cracking.

There are numerous concrete material models for studying and investigating impact loading with available finite element analysis software, such as LS-DYNA, ANSYS, and Abaqus. However, some of these concrete material models have not been extensively used in roadside safety applications. As such, a multi-phase investigation and

evaluation was desired to help guide selection and use for plain and reinforced concrete applications. This analysis would include single element and component test simulations, which have been previously completed for some concrete material models. However, a full comparative analysis has not been performed for single element, component, and system simulations, which include static and dynamic investigations, plain and reinforced concrete, multiple failure modes, and numerous concrete material models. Upon completion of a multi-phase study, enhanced guidance for selecting concrete material models for use in a particular modeling effort will be provided. Further, the study may identify needs for creating a blueprint for a new concrete material model. The end result is to develop improved guidance and/or methodologies for the analysis of concrete structures within the roadside safety community.

1.2 Research Objectives

The objective of this Phase I study was to investigate and evaluate several current concrete material models that are available in LS-DYNA and determine their accuracy in predicting failure modes for plain concrete in different loading conditions. This material model investigation was performed by comparing simulated tests to physical tests performed by other researchers as well as those performed in the Midwest Roadside Safety Facility (MwRSF) at the University of Nebraska-Lincoln structures laboratory. Single-element and component-level simulations were completed to understand model behavior and provide guidance for the Phase II study.

1.3 Research Scope

To fully understand the topic of concrete fracture, an initial background study was completed. This literature review included concrete constitutive modeling, applicable

ASTM standards, previous laboratory testing, limited LS-DYNA concrete modeling efforts in roadside safety and other applications, and studies focused on fracture energy and strain rate effects. A thorough literature review was also completed on five material models that were specifically investigated in this research study. Single-element simulations were completed using these five material models and three different loading cases: compression; tension; and shear. The performance of the selected concrete material models was explored by changing parameters within each model.

Following this study and using knowledge gained from the single-element investigation, one experiment that was found in the literature was selected for continued investigation with each of the three major load cases. Each test setup was replicated in LS-DYNA, and the material properties from the testing were implemented directly into the pertinent material model. Initial simulations were run for each test scenario and from there, material model parameters were changed in order to investigate their effect on behavior as well as to improve simulation results to correlate with the physical test results obtained from the literature.

The final component of this research report was an internal testing program. Concrete was batched, cast in molds, and tested using MTS testing equipment. Cylinder, dogbone, and beam specimens were created to examine compression, tension, and flexure/shear load cases, respectively. The physical test setups were again replicated in LS-DYNA, and simulations were completed. Material model parameters were varied to find a good correlation with physical tests. The test curves were again compared to the simulation curves. Conclusions and recommendations were provided about each material model.

CHAPTER 2 LITERATURE REVIEW

2.1 Concrete Fracture

Concrete is a heterogeneous material, which makes the prediction of failure extremely challenging. Since concrete is often made of different parts (i.e., coarse aggregate, sand, cement, and water) and is not uniform, different failure behaviors can occur under the same loading conditions. Its mechanical behavior is therefore non-linear in all loading conditions. The mechanical behavior can be affected by properties such as water to cement ratio, shape and size of aggregate, and type of cement [1]. The majority of failure occurs at the cement-aggregate interface. The cement does not expand under increased loading, but it does contribute to the non-linear response. Given that the aggregate is a granular material, it can contribute to the dilation behavior and can undergo extensive plastic flow [2]. If the bond between the aggregate and cement is broken, the behavior of the material changes significantly. As such, the load resistance and stiffness of the material will decrease drastically as the concrete continues to exhibit damage.

The cement-aggregate interface is the focus of concrete fracture analysis. Plain concrete is known to be weak in tension, and these tension forces cause failure locally. The predominant failure in concrete is generally accepted to be due to tension alone or tension in combination with shear forces [3]. These tensile stresses appear near the aggregate and eventually cause longitudinal cracking, as shown in Figure 1. Mortar cracks may also occur in the material, but this region is not considered the weak point of the material.

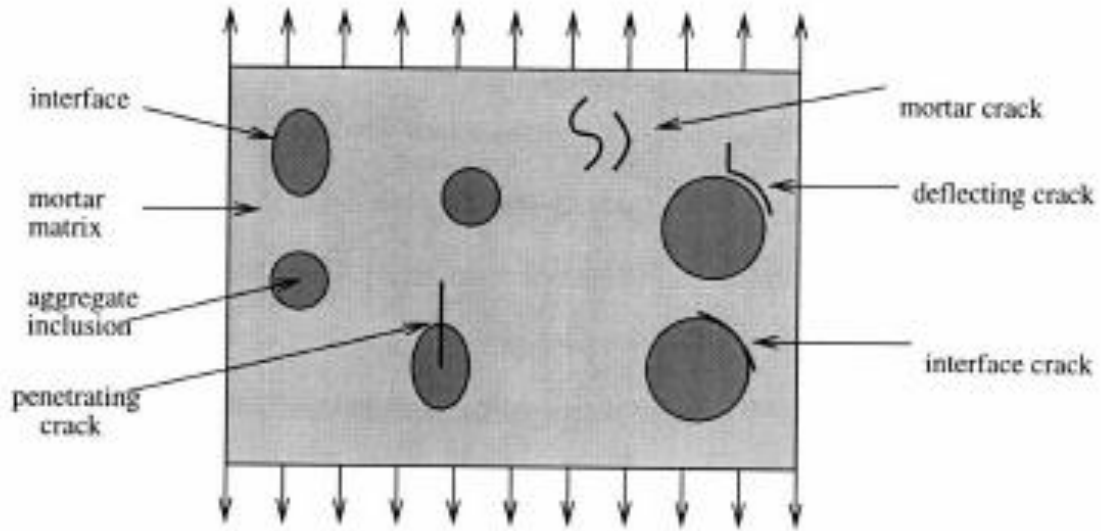


Figure 1. Longitudinal Cracks in Concrete due to Applied Load [3]

At a microscopic level, the path along which the cracking occurs is based largely on the size of the aggregate in the concrete. In normal strength concrete, the cracks will propagate around the aggregate, but in high strength concrete, the cracks usually extend through the individual aggregate particles [4].

There are two major phases of concrete fracture. The first major stage is the appearance of narrow areas of increased strain and deformation, known as microcracks. After microcracks begin to form, they link together and form macrocracks, the second major stage of failure. When a crack opens, the material begins to soften and lose strength at that location. If load is released or reversed and the crack is able to close, hardening will occur. These cracks typically lead to a brittle state, with the degree of brittleness being influenced by compressive stresses, unconfined concrete strength, volumetric expansion, and concrete softening [5]. Softening is a major focus of concrete failure, which can be defined as load resistant capacity after peak and localized strain [6].

Although these descriptions of failure are generic for all loading cases, there are differences in concrete behavior is different for compression and tension. In both load cases, the material exhibits strain-softening behavior when concrete is loaded beyond peak. The local deformations that occur under both loading conditions make prediction of stress-strain behavior very difficult. The unrecoverable deformation, in the form of open cracks, is what leads to plasticity in the material and eventual failure. This plasticity and softening behavior is more pronounced in compression than tension [7]. Damage, in the form of cracking, will typically occur at higher strains for compression than it will for tension, largely due to the difference in strength and stiffness degradation. When tension stresses are present in concrete, the likelihood of cracks opening is increased, which will lead to lower peak capacities and stresses. The compressive stresses generally arrest cracks that are formed by tensile stresses.

Compression and tension are two major loading cases that have been investigated in laboratory testing for concrete. Concrete is significantly stronger in compression than tension, and this behavior has been widely studied for over 100 years. Unfortunately, there is no ASTM standard for uniaxial tension testing for concrete. The uniaxial compression cylinder test (ASTM C39) is a very common laboratory test for determining the strength of plain concrete. When concrete fractures in uniaxial compression, the strains are transmitted by the Poisson effect and are perpendicular to the direction of loading [8].

2.1.1 Compression

In compression loading, three major stages can be observed for continuously loaded concrete. The first stage of loading occurs when the applied load on the concrete

ranges from 0 to 30% of the maximum compressive stress of the given concrete type [1]. During this loading stage, the behavior of the concrete is elastic. The stress-strain curve of the material will essentially be linear during this stage of loading, following Hooke's Law. The modulus of elasticity during this stage is constant due to the linear-elastic behavior. Before the load begins to increase significantly, cracks are uniformly distributed, and a limited damage zone begins to form around each crack. The cracks present at this stage may be microcracks that were initially in the material before loading or cracks that have begun to form under initial loading. Regardless of their origin, the microcracks are present at this stage and will eventually grow in the next loading stage. This first stage is quasi-brittle, and there is no realistic expectation of failure under compression load.

The second stage of compressive loading occurs when the stress reaches 30 to 75% of the peak compressive stress [1]. At this stage, bonds begin to break between the cement and aggregate, and some of the microcracks that began to form in the previous loading stage grow. Near the end of this loading stage, these microcracks will bridge and eventually become macrocracks in the final loading stage. Although cracks are forming, the propagation is stable in this loading stage, and instability will only start to occur when stresses are closer to 75% of peak compressive stress. The non-linear response of concrete starts to show near the end of this stage. The larger cracks that are forming during this stage are parallel to the axis of loading [2]. The bond cracks begin to develop and will eventually lead to catastrophic failure for normal strength concrete. The larger cracks form as microcracks and propagate and join up along the shortest path, not necessarily the path of least resistance.

The final loading stage is 75% of the peak compressive stress and beyond, including post-peak softening behavior [1]. The mortar starts to crack and crush and the cement-aggregate interface slips. The failure occurs when bond cracks join and form a fracture zone. The failure cracks will continue to open up parallel to the loading direction, often resulting in failure planes forming at approximately 45 degree angles. A combination of crack opening and crack sliding at the micro-level causes further crack opening [9]. The stiffness degradation continues as the damage increases post-peak. The non-linearity becomes the most evident at this loading stage. In general, the stress-strain curve begins to bend sharply until the peak stress is reached, after being linear before this point [10]. The behavior drastically decreases after this point as softening is occurring. The volume dilation increases significantly at the tail end of this stage before softening begins. Dilation refers to the expansion of the concrete at the lateral pressure increases.

Softening is a phenomenon that initiates after the peak compressive stress of concrete is reached. The stress-strain response after peak depends on many external factors, such as test equipment, test procedure, sample dimensions, and stiffness of the machine [11]. These factors all indicate that softening is difficult to precisely quantify. It is known that the Poisson's ratio increases beyond the elastic value and the inelastic behavior of concrete is fully exposed. Specifically, the Poisson's ratio generally remains constant up to a stress level of 80%, at which point the ratio increases suddenly due to dilation [10], as the transverse strain is increasing faster than the longitudinal strain. With dependence on specimen geometry, the size effect generally controls over material properties for softening.

2.1.2 Tension

Concrete behavior in uniaxial tension is similar to uniaxial compression in some regards, but there are differences in the behavior that need to be noted. Tensile strength is generally assumed to be an order of magnitude lower than the compressive strength [10], but the compressive strength has also been defined as 10 to 20 times as large as the tensile strength [1]. The modulus of elasticity in tension is similar to that observed for compression loading. This results in stress-strain curves for tension loading being similar to compression loading. The limit of elasticity remains valid to about 60 to 80 percent of the ultimate tensile strength [11]. Strain localization also occurs for this load case.

The low tensile strength is due to reduced strength of the cement-aggregate interface, defined as the weak link in concrete. The unstable crack propagation phase occurs much sooner in tension than in compression, and the tension failure process is much more brittle than observed for concrete loaded in compression. The sequence of cracking therefore occurs more rapidly, with the cracks forming perpendicular to the loading when the tensile capacity is exceeded.

The stages of concrete behavior under tension loading are somewhat similar to those of compression. In the first stage, the applied loads range between 0 to 30% of peak tensile stress [1]. At this point, the concrete has linear behavior and behaves elastically. For the second stage, the applied load ranges between 30 to 80% of peak tensile stress when the cracks begin to initiate and propagate but are generally isolated and not spreading. As the load increases, some microcracking starts to reduce the stiffness of the material. The microcracks remain unchanged with a stress less than 80% of peak stress. The final stage is above 80% peak tensile stress when the cracks propagate to form large

cracks and flaws begin to link. Strain localization only appears after the 80% mark is reached. Major cracks continue to grow until failure is reached. Softening is much less of a factor in concrete subjected to tension loading.

Concrete fracture is heterogeneous and not centered at a discrete point, but instead the fracture is distributed over a “zone” that has substantial size. The concept of a fracture process zone (FPZ) can be used to describe the micro level concrete behavior under load. The size of the fracture process zone may be as large as the whole cross section or as small as a single cement-aggregate interface. Within this zone, strains are increasing while the remainder of the concrete area outside the zone unloads; since, stress is concentrated at the crack. Typically in high strength concrete, which is more brittle than normal strength concrete, the fracture process zone is smaller than observed in normal strength concrete [12]. The material inside the fracture zone behaves inelastically and softens, but the material outside behaves linear-elastically and remains undamaged. The non-linear behavior inside the fracture process zone is characterized by two parameters: the effective length of the fracture process zone and the fracture energy, G_F [12]. Both of these parameters are size-dependent and indicate that the size effect is present in concrete. The second of the two determinants, fracture energy, will be discussed later.

Ultimately, microcracking is the failure mechanism for concrete through the formation of a web which eventually becomes macrocracks, which damages the concrete beyond its limit. Prior to any load being placed on a concrete specimen, microcracks can already be present, caused by shrinkage and thermal expansion in the cement paste [1]. These early-age microcracks are pre-existing and a contributing factor in the low tensile strength of concrete. These cracks before loading have also been attributed to the

following material properties: aggregate/cement stiffness ratio; type of cement-aggregate bond; and percentage of voids in the sample [3]. Before the larger cracks can even form under load, pre-existing damage is typically invisible.

Once load is applied on the concrete, additional microcracks form as the bond cracks between cement and aggregate. Microcracks can also be present separately in the cement and aggregate. These types of microcracks form due to loss of cohesion between the mortar and aggregate, frictional slip at the interface between the cement and aggregate, and crushing of the cement [1]. These cracks grow in the fracture process zone and contribute to the inelasticity of the material. These cracks eventually join with each other and ultimately cause the failure of the material.

There are three commonly accepted modes of concrete failure: Modes I; II; and III. Mode I refers to failure under tension load where the stresses are perpendicular to the crack surface, while Modes II and III are characterized by shear failure caused by stresses acting in the same plane as the crack surface [13]. Mode I is the most common and is easy to achieve through laboratory testing. It is described by the relationship between the normal stress at the crack and the opening of the crack. A crack is characteristic of Mode I when the crack opening dominates over crack sliding [9]. If the opposite were true, the cracks would propagate perpendicular to the direction of loading.

Different levels of confinement can also change the failure patterns of concrete. It is generally assumed that as confinement increases, so does the strength and ductility of concrete. Adding pressure in a third direction will affect the behavior of the cement-aggregate interface, and the pores within the concrete since dilation is delayed. When high levels of confinement are present, the cracks develop through the aggregate, the

pores collapse, and the failure mode transforms from brittle to ductile [5]. Softening will still be present in low confinement levels, but once the confinement increases past a certain level the softening will cease to exist and hardening will occur post-peak.

2.2 Concrete Constitutive Modeling

For many years, concrete behavior has been modeled by researchers. The general consensus is that concrete is very difficult to model due to the complicated fracture process and heterogeneity of the material. It is commonly used as a structural material, but there is much to be learned about its behavior under loading. In the first attempts to simulate concrete, many of the constitutive models were simple, phenomenological and not based directly on engineering mechanics. Along these lines, simple models were developed for the different components of concrete, such as cement and aggregate. Once these individual models acted together, the complex behavior of concrete could be simulated. In these models, the concrete is generally assumed to be linear, and the microstructure of the material is not considered. This selection prevents the onset of microcracking from ever occurring; therefore, the prediction of fracture is not possible.

Concrete becomes especially difficult to model when different loading conditions are applied to the material. A model should be able to accurately depict the behavior of concrete over a broad range of applications and be able to replicate results of experimental tests. However, this depiction is quite challenging to achieve, due to various effects such as anisotropic elastic degradation, nonassociated plastic flow, and unstable post-failure behavior [2]. One of the main goals of concrete modeling is to better understand and predict crack formation, propagation, and specimen fracture under common applied loading conditions. From there, complexity can be added to account for

specific loading cases or experimental setups. Concrete responds differently under different conditions, such as compression and tension loading; therefore, special treatment is required.

Most of the concrete material models currently in place are based on two major theories: damage mechanics and elastoplasticity. In general, these two theories are coupled together using various equations within the material model, because the progressive failure of the material depends heavily on its mechanics. Important considerations for developing a constitutive model include evolution of failure surface, representing material damage under basic loading conditions, incorporating softening, dilatation of the material, and representation of shear response [7]. Many of the models described herein consider these major emphases.

Over the years, many researchers have made varying contributions to the area of concrete constitutive modeling, such as creating entire models or just a specific failure surface. Many of the modeling feats were created for a specific purpose, such as high loading rates or high temperature loading. These models are useful, and portions of these specific models are applicable to concrete modeling as a whole. Some common theories include: plasticity; continuum damage mechanics; fracture mechanics; elastic-damage; and combined plasticity and damage mechanics [14]. These theories have led to many different types of models, including empirical, linear and non-linear elastic, plasticity based, fracturing and damage mechanics, and macro/micro mechanics. All of these models are described in detail below.

2.2.1 Empirical and Elastic Models

The first two types of models are the simplest forms. Empirical models are based solely on experimental data and rely on curve fitting to develop constitutive laws. This type of model is used infrequently when modeling concrete. The next type of model is elastic, both linear and non-linear. There are many models that seek to model concrete solely on an elasticity basis. Despite the fact that concrete has non-linear plastic behavior post-peak, an elastic approach is simpler. The development of parameters and equations can be very complex, and elasticity makes this process simpler. An elastic assumption makes the material model more generalized, but constitutive equations are very limited. Specifically, using only elastic behavior results in models being limited to path-independent reversible processes [15]. Cracks can be assumed to occur in certain areas of the material, but the crack formulation cannot be modeled using only elasticity.

2.2.2 Linear-Elastic Models

Some of the equations used in elastic concrete models rely on Hooke's Law and a constant Poisson's ratio to make many calculations. The concrete is treated as linear elastic until the ultimate strength is reached, and then failure occurs. Given that the failure stress for concrete in tension is generally low, a linear-elastic model is well suited. Elastic models are inadequate in complex loading conditions and when excessive, non-linear behavior is encountered. The major flaw in this type of material model is that the specimen will return to its original shape; since plastic deformations cannot occur. Linear-elastic models are simply not robust enough to capture the mechanical behavior of concrete at high loading rates.

2.2.3 Non-linear-Elastic Models

Some non-linear behavior can be modeled using the basic elastic approach. There are two major approaches for non-linear modeling: secant and tangential formulations [11]. The secant formulation is based on total stress-strain and the tangential on incremental stress-strain. The secant method is more common, and it is an extension of the linear-elastic model, meaning it is load dependent. This type of formulation is generally only used with monotonically-loaded concrete samples.

Some failure criterion can be added for elastic models. The ultimate strength surface is utilized in this instance. For these models, failure can only be defined as the ultimate load capacity of concrete, representing the boundary of the work-hardening region [11]. Many different yield and failure surfaces can be implemented, with failure criteria ranging from models with one parameter to those with five or more.

2.2.4 Plasticity Models

An improvement over the elasticity models is adding plasticity to the constitutive model. Hooke's law and elastic behavior are still present in these models, but plastic behavior is added in the form of failure criteria and softening laws. The addition of plasticity also allows for microcracks to form and be unrecoverable. The components of a plasticity model are: an initial yielding surface defining the stress level at which plastic deformation begins; a hardening rule defining the yield surface evolution; and a flow rule which gives an incremental plastic stress-strain relation [11]. A flow rule is used to determine the amount of plastic deformation in concrete. In this model, the total strain is the sum of the individual elastic and plastic strains.

2.2.5 Plasticity and Damage Mechanics Models

Plasticity alone cannot model the microcracking phenomenon. Stiffness degradation, or softening, can only be modeled by combining plasticity and damage mechanics by using both a damage and plasticity surface [8]. This degradation is a very difficult process, which has been accomplished in different ways by various researchers. Nguyen looked at modeling these two surfaces coincidentally to allow consistency in the constitutive equations and efficiency [1]. Surfaces can be separated as well, one defined by the flow rule and the other defined by fracturing theory. The flow rule is the necessary kinematic assumption postulated for plastic deformation or plastic flow, giving the ratio or relative magnitudes of the components of the plastic strain tensor [11]. The rules essentially determine the direction of plastic flow.

Compared to the elastic models, the unique aspect of this group of models is the plasticity yield surface. This surface typically includes pressure sensitivity, load-path sensitivity, non-associated flow rule, and hardening/softening work [11]. If a point lies within the elastic region of the yield surface, no plastic strains will develop. Inelastic volume change will take place in the form of contraction at the beginning of yield. However, continual plastic deformation will occur once the point moves to the boundary with the plastic strain region. This non-linear volume change is exactly what occurs in the concrete material once 75 to 90% of ultimate stress is reached [11]. Then, dilation will occur, and the shape of the yield surface will change.

2.2.6 Varying-Level Models

The next set of constitutive models is the varying levels of models: macroscopic; mesomechanic; and microplane. The macroscopic model looks at the material in a wider

scope. Due to its scope, a major disadvantage of this type of model is that some of the behavior at the mesoscopic or microscopic level cannot be displayed. Macroscopic models generally include features such as a non-regular array of particles representing the largest aggregates, a homogeneous matrix of cement and some small aggregates, and interfaces between the cement and aggregate [11]. The mesomechanic model provides analysis in between macro and micro levels and is able to better demonstrate behavior. Finally, the microplane models use aspects of the macroscopic model to represent the mechanics of the microstructure. These models typically use vectors, despite it still being very complex and computationally robust. These models interact and allow for analysis and different levels.

2.2.7 Single- and Double-Parameter Models

Another set of models consist of varying numbers of parameters. The single-parameter models are the simplest and are used for pressure-independent materials. These models use the von Mises or Tresca type failure surface. Typically, these models are not accurate enough for concrete due to the use of only one parameter. Further, only compression loading conditions are considered.

Some examples of two parameter models are the Drucker-Prager and Mohr-Coulomb failure surfaces. These failure surfaces will be discussed in more detail following the damage models. These two parameter models with straight lines in the surfaces are inadequate for concrete failure surfaces, especially in high compression regions [11]. More refined models with three or more parameters provide better validation for experimental testing.

2.2.8 Continuum Damage Mechanics Models

A major set of models are the continuum damage mechanics models, primarily used for tension loading. In these models, the softening is modeled by defining the relationship between stresses and effective strain [11]. However, it has been proven that continuum damage mechanics is inadequate for predicting softening. A simplified method is to set the tensile strength of concrete equal to the elastic limit, but this selection does not solve the issue with softening. The issue comes with strain localization in the fracture process zone, but mesh dependency exists because the zone is very narrow. Strain localization results from heterogeneous deformation, commonly exhibited as a narrow band of high strain. This local damage is represented using internal damage variables. Three types of continuum damage mechanics and fracturing models are cohesive crack models, softening continuum models with partial regularization, and softening continuum models with full regularization.

2.2.9 Damage Models

Other damage models that have been created by researchers, include smeared crack, fixed crack, multiple fixed crack, and rotating crack models [1]. Many different models have been created for special circumstances, such as for high temperature loading resulting in spalling [16], fully-graded aggregate mass concrete [17], and simple beam cracking [18]. A damage model can be tailored to a specific experimental setup or loading condition and must be used with caution. Typically, damage models are not accurate with concrete loaded both in compression and tension.

The smeared crack model is a generic method of modeling cracks in concrete. The smeared crack method is more appropriate when overall behavior is of concern; it is

similar to a macroscopic model. For the term “smeared crack approach” stiffness is lost at an element, the element remains in position, and it loses the ability to carry any load. Therefore, the crack is not displayed explicitly in the material. As a result, mesh size is very important, and the damage is highly mesh-dependent.

There are two major surfaces that are used in most constitutive models: the yield and failure surfaces. One example yield surface corresponds to the Haigh-Westergaard stress space. In this surface, the stress tensor has six independent components [11]. This type of yield surface is very common in plasticity-based models and also used in conjunction with failure surfaces. The yield stress is a function of this Haigh-Westergaard stress space. Other examples of yield surfaces are the Tresca and von Mises yield criteria. These are extremely common for metals but can also be used for a pressure-independent material, such as concrete. A tensile cutoff is added to these criteria to allow for the pressure-independence of concrete. The yield surface is a constantly adapting surface based on the change in stress. Once stress increases, the yield surface responds accordingly, and elastic and plastic deformations occur. A new yield surface is often created after plastic deformation begins. The surface will continue to inflate until the failure surface is reached. The yield surface can take many different shapes, with the teardrop being a common shape [19]. A cap surface is often added to the yield surface in order to cap the open shape of the yield surface and more accurately reflect the behavior of concrete.

Failure surfaces are a major part of the constitutive modeling process. Concrete can be described by a failure surface with curved meridians [11]. This surface changes in shape similar to the yield surface but generally transforms from a triangular shape to a

bulged shape as compressive forces increase. Different failure criteria exist as well, ranging from one parameter to more than five parameters. The two most common failure surfaces are the Mohr-Coulomb and the Drucker-Prager. A third common surface is the William-Warnke failure surface. There are various other surfaces, which are typically specialized for a specific geometry or loading condition.

The Mohr-Coulomb surface is a modified version of the Tresca criterion. Its basic assumption is that the maximum shear stress is the only decisive measure of failure, and this shear stress is a function of the normal stress [7]. The criterion has a discontinuity in the surface which makes it only a moderate fit for the response of concrete, as observed in experimental testing. The Drucker-Prager surface is a modified version of the von Mises criterion, and its shape is a circular cone. The behavior of the failure surface is defined by the hardening rule, and it generally is used for multi-axial loading [7]. The Drucker-Prager criterion is known to overestimate the compressive or tensile strength of concrete.

2.3 Special Considerations

2.3.1 Mesh Independence

Mesh independence is a feat that many modelers have attempted to accomplish when it comes to modeling any material. It is especially useful when attempting to model concrete using finite element analysis. It does become very challenging because strain localization is present in the material, which must be considered when mesh sizes are both small and large. One study was able to determine that the characteristic length is found to be about 0.2 in. (5 mm) for concrete [20]. In this study, the strain localization was captured by a continuous approach and macrocracks by a discontinuous one.

Mesh independence is highly desired as mesh size can affect crack propagation in concrete modeling. In regions where the fracture is expected to occur, the mesh size needs to be very fine to capture the failure behavior. But if there is no indication of where failure will occur, the entire mesh would need to be extremely fine. Making this mesh size more fine will also affect the size of the fracture process zone. The strain localization is the reason for the mesh sensitivity during softening and homogenization has been used to remove this sensitivity [6]. Softening behavior can be shown in a mesh independent model, but the true heterogeneity of concrete is lost with large elements.

2.3.2 Nonlocal Modeling

Nonlocal modeling has also been used to investigate concrete failure patterns. In nonlocal modeling, the focus is on the relationship between the internal length of the model and the width of the fracture process zone [21]. The unique aspect of the nonlocal model is that it includes a spatial relation (i.e., scale) in the constitutive equations, which does not appear in other models that have been covered. The model parameters are the controlling factor in the interaction of material points [21]. They add complexity to the model, but it does allow for automatic calibration of the parameters. Nonlocal modeling has not been as popular for concrete materials due to its complexity.

2.3.3 Dynamic Loading Conditions

Real world, dynamic laboratory testing of concrete is less common than static testing because there are not many experimental tests that involve such high loading rates. Concrete is often dynamically loaded in the real world but given the lack of laboratory testing, there are not many models that have been created to support it. One such study did investigate the dynamic behavior of concrete by modifying the William-

Warnke surface [22]. Another constitutive model has been created to accommodate dynamic loading, specifically impact and impulse loading [10]. Microcracks in the model are tracked using a continuum damage parameter and the constitutive equations are based on a strain energy function. Neither of these models has been validated with robust experimental data.

2.4 FEA Concrete Modeling Codes

LS-DYNA is a non-linear, 3D finite element analysis software that includes concrete material models, is robust, has dynamic capabilities, and has the ability to perform numerous calculations with the constitutive equations. LS-DYNA has been used in the roadside safety community for modeling impacts events into concrete roadside safety systems, such as barriers and bridge rails. However, other programs, such as Abaqus, do have some use when it comes to modeling concrete fracture. Abaqus is a finite element analysis software for a variety of industrial engineering applications.

Abaqus has been used to simulate a wide variety of different loading conditions and specimens. One study looked at creating a user-defined material model (UMAT) in Abaqus based on a specific constitutive model [14]. Creating a UMAT means that all material behavior is defined by code written by the researcher. Double-edge notched specimens using a coupled plasticity damage model were simulated with one UMAT. Another UMAT, based on a microplane model, was created to simulate mixed-mode fracture [13].

Most of the concrete models in Abaqus are plasticity models and based on incremental theory, where the total strain is made up of the elastic and plastic strains. These models usually have the following characteristics: a yield surface; flow rule; and

hardening/softening behavior [11]. There are two major concrete material models available in Abaqus: the Concrete Damaged Plasticity Model and the Brittle Cracking Model.

The Concrete Damaged Plasticity Model is intended for cyclic loading or dynamic loading. The model features cracking in tension and crushing in compression, with different yield strengths and stiffness degradations in each of the two loading conditions. In the model, elastic behavior is followed until the failure stress is reached, after which point microcracks are represented macroscopically with softening and strain localization [11]. Its behavior is also sensitive to the strain rate of the model. The following tests are needed to generate all required parameters for this model: uniaxial compression; uniaxial tension; biaxial failure; and triaxial test [23]. Elements in this model cannot be deleted, because no failure criterion exists in the model, one of the major drawbacks of this particular model. Excessive dilation may occur due to the lack of element deletion, but dilation can be avoided by using adaptive meshing techniques.

The second model available in Abaqus is the Brittle Cracking Model. This model was created mostly to be used with tension loading. Its major strength is displaying tensile cracking in the concrete. The model's major drawback is that it is linear elastic, thus there is no plasticity and has little application in other loading conditions besides tension. It is most accurate when brittle behavior dominates so that the linear elastic assumption for compression is adequate [24]. It does have element deletion capability using a brittle failure criterion, which is very useful to avoid excessive dilation.

Two other software programs have been utilized and their results have been limitedly published. The first analysis program is Co.Dri which focuses on the

mechanical modeling of concrete and produces interactive graphics [11]. It was used by researchers in conjunction with Abaqus to simulate the behavior of plain concrete. The second is Atena, a commercial software package that was used to model unnotched and notched specimens simulated in three point bend tests [25].

2.5 Standard Concrete Component Testing Methods

There are several standards for laboratory testing of concrete samples. Three of these standards have been selected for the basis of in-house component testing portion of this research study. The standard for compression testing of concrete, ASTM C39 [26], is very common and is directly applicable to the in-house testing program. There is no standard for direct tension testing of concrete. There is a standard for splitting test for tension strength, but this standard was not desirable for this research effort. Instead, a different ASTM standard, ASTM D2936 [27], was adapted for use for the direct tension testing. Similar to tension, there is no directly applicable standard for shear testing of concrete. The test method for flexural strength of concrete, ASTM C78 [28], was adapted for use in the flexure and shear component testing program.

2.5.1 Compression

The standard concrete compression test, ASTM C39, consists of loading cylinders in compression. Cylinders should be sawed or ground to meet tolerances on its ends if they are not plane. The specimens must be capped, with all cylinder diameters within 2% of each other. Common cylinder sizes use 4-in. (102-mm) or 6-in. (152-mm) diameters and lengths of 8 in. (203 mm) or 12 in. (305 mm), respectively. The test method requires a loading rate of 35 ± 7 psi/s (0.25 ± 0.05 MPa/s) during the second half of the loading phase. A higher loading rate is allowed through the initial portion of the test, but the

specimen must be loaded continuously throughout the test. Load must remain on the specimen until the resistance has dropped below 95% of the peak load. The C39 standard also has equations used for calculations as well as a schematic for different types of common failures. This test provides a compressive strength of concrete. Additional results require advanced instrumentation.

2.5.2 Tension

The test method for direct tensile strength, ASTM D2936, is specifically for rock core specimens. Cylinder are tested with the ends of the rock core sample are cut and the ends cemented to metal caps, using no more than a $\frac{1}{16}$ -in. (1.5-mm) layer of cement. No special care is needed to smooth or plane the ends of the specimens and the water content of the sample should be monitored and remain at appropriate levels for the testing conditions. It is necessary to ensure that the caps are aligned with the axis of the specimen. The tensile load must be applied continuously throughout the test, at a constant rate that would result in a failure in not less than five and not greater than 15 minutes. This test provides a tensile strength of concrete.

2.5.3 Flexure

ASTM C78 is used to obtain flexural strength of concrete. A four-point bending apparatus is used in conjunction with a test machine in order to obtain the correct loading pattern. The loads must be applied perpendicular to the specimen, and the supports must be wider than the specimen. An example schematic of the loading apparatus from the standard is shown in Figure 2. The testing specimen is a rectangular beam with a cross-section of 4 in. x 4 in. (102 mm x 102 mm) or 6 in. x 6 in. (152 mm x 152 mm). The unsupported span is three times greater than the height of the beam, and the beam length

is the unsupported span length plus 1 in. (25 mm) of overhang on both ends. A continuous load rate is applied until rupture occurs.

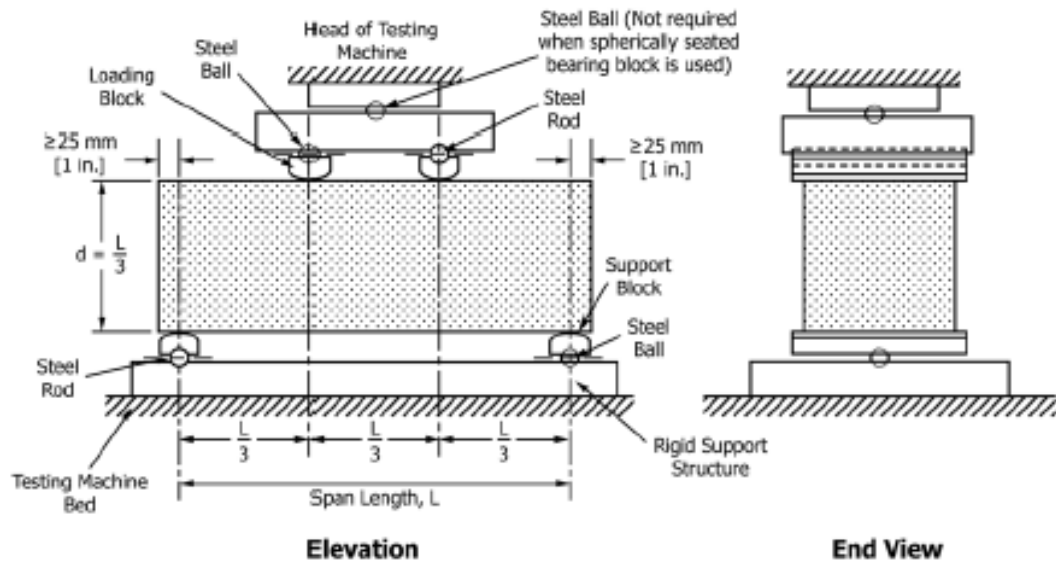


Figure 2. Four-Point Bending Test Loading Apparatus [28]

2.6 Relevant Laboratory Testing of Plain Concrete

Aside from the ASTM standard-based testing for compression, tension, and shear, researchers have developed alternative test methods for concrete. Currently, no standard test methods exist for evaluating concrete in direct tension and direct shear. Direct shear testing is often very difficult to achieve, although one study will be highlighted and discussed later. Tension testing has been performed by many researchers and has proved to be quite difficult. Some of the following test methods involve specimens with fiber reinforcement instead of plain concrete, but the purpose is the evaluation of the test method and specimen geometry. A literature review of direct tension methods was completed to develop a test method for the in-house laboratory testing to follow.

Zhang, et al. loaded a 4.3-in. (109-mm) cylinder in direct tension and monitored the damage level within the cylinder using Coda Wave Interferometry (CWI), a non-

destructive testing analysis method [29]. The specimens were fitted with two rings that were attached to the concrete cylinders using three screws. The rings were then used to fasten the specimen to the frame on one end and glued to the frame on the other end. Three LVDT units were used to track small displacements in the cylinders and then strain was calculated. The test setup is shown in Figure 3. Sensors on the cylinder face captured velocity and were used in the CWI analysis method. An initial compressive force was applied to the specimen in order to improve the cohesion with the glued end. This method was unique, and worked well, but it would require the gluing of concrete directly to the test frame.

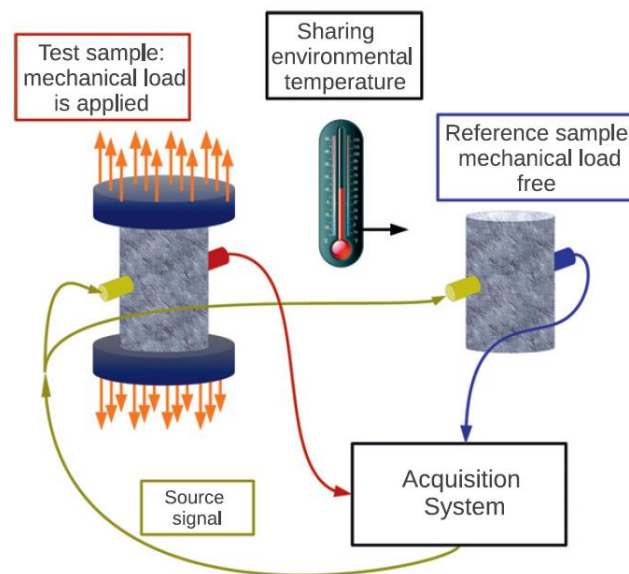


Figure 3. Test Setup for Study by Zhang, et al. [29]

An additional study was conducted on cylinders by Kim and Taha to observe the behavior of concrete cylinders in direct tension [30]. A 4-in. (102-mm) cylinder was attached to double steel plates on each end with epoxy to create a uniform loading area on the cylinder, as shown in Figure 4. Eight bolts connected the two plates together which were attached to the load frame. The tension load was applied through ball bearings to

allow for free rotation and reduce bending or torsional stresses. The specimen geometry was not ideal, because the fracture location is difficult to predict in a constant cross-section. One benefit of this test method was that secondary stresses that come as a result of uneven loading were avoided, which is often seen in gripping or epoxy methods.

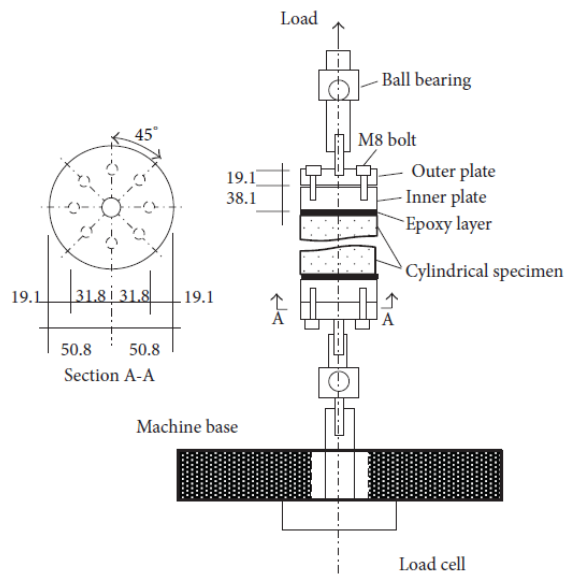


Figure 4. Test Setup for Study by Kim and Taha [30]

Yan and Lin investigated the dynamic properties of concrete specimens in direct tension [31]. A displacement-controlled MTS machine loaded the dogbone-shaped specimens in direct tension, as shown in Figure 5. Strain gauges measured strain, and two pairs of LVDTs measured the displacement once cracks started to form. The dogbone shape was preferred, because it provided an indication of where failure would likely occur and allowed for a better estimate of placement for instrumentation. Both ends of the specimens were attached to steel plates using epoxy, and the plates were then fixed to the heads of the testing machine using bolts. Different strain rates were tested, and the conclusion was that the fracture surfaces were created through the cement-aggregate interfaces instead of around them.

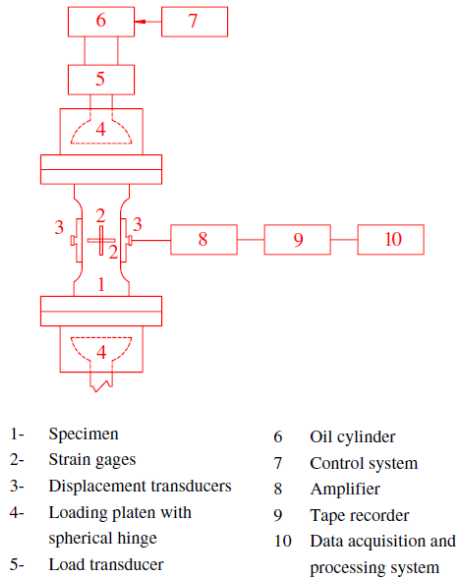


Figure 5. Test Setup for Study by Yan and Lin [31]

Most of the test methods in this literature review follow one of two basic methods for affixing the specimen to the testing machine: epoxy or grips. This testing looked at gripping flat concrete plates using wedge grips [32]. Gluing was intentionally avoided, because it can cause localized stresses if it is not applied correctly. However, grips may induce bending stresses in the plate specimen. In order to prevent localized and bending stresses, free rotation was allowed at the top of the specimen along with tapered aluminum plates that were placed along each end of the specimen on both sides, as shown in Figure 6. The researchers found that the grip plates had reduced levels of localized stress in the specimen, relative to levels that would be present with an epoxy application or nothing in place. Specifically, the stress at the grip plate was within 20% of the stress at the center of the specimen with the plates and 60% without the plates [32]. Although this method requires extra attention to ensure additional stresses did not occur, the gripping setup worked adequately.

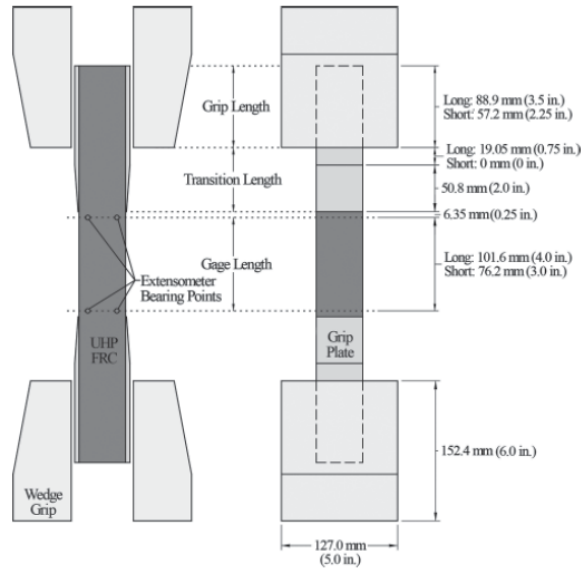


Figure 6. Test Setup for Study by Graybeal and Baby [32]

A study on high performance fiber reinforced concrete was completed in order to define rate-dependent tensile behavior of the material [33]. Fiber reinforcement matrices were placed throughout the specimen and additional reinforcement, steel wire mesh, was added to the ends of the specimens. This mesh was a safeguard to prevent failure of the specimen outside of the gauge length. The 21 in. (533 mm) long dogbone specimens were loaded near their 5 in. x 1 in. (127 mm x 25 mm) ends and pulled in tension, as shown in Figure 7. LVDTs were not used in this testing program because they could not adequately capture data for a 0.7 in./s (18 mm/s) loading rate. Instead, markers were attached to the specimen at different locations to track displacements using high-speed video cameras. The necessary extra reinforcement and the location of load application indicates this method is less reliable.

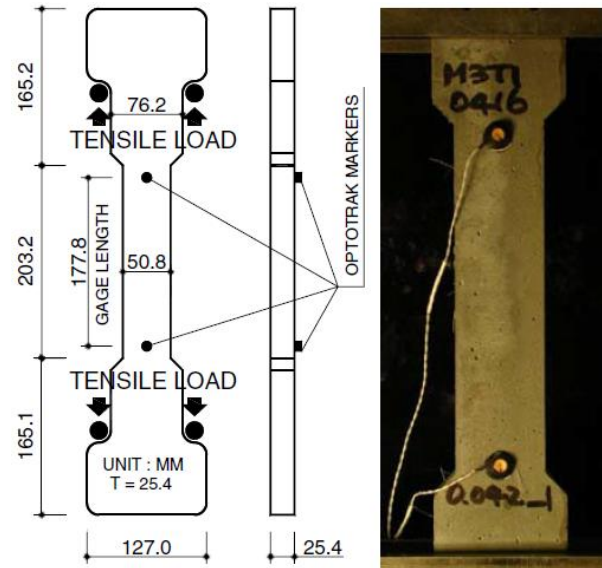


Figure 7. Test Setup for Study by Kim, El-Tawil, and Naaman [33]

Zhen-hai and Xiu-qin predicted the ascending and descending portions of the stress-strain curves using experimental testing [34]. Dogbone-shaped specimens were placed in a stiff frame and loaded in direct tension using a custom jig. Transducers captured data for load and deformation during the test. Strain gauges measured strain in the longitudinal and transverse directions. The loading jig had steel plates, a beam on the top and bottom, and bars on the sides of the specimen as shown in Figure 8. The specimen itself was epoxied to the steel plate which was connected to the load frame. Cracks were monitored closely using the naked eye.

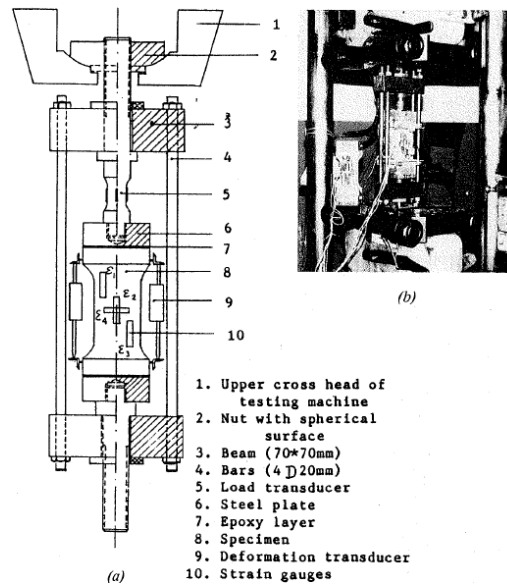


Figure 8. Test Setup for Study by Zhen-hai and Xiu-qin [34]

2.7 Fracture Energy

Fracture energy principles are used to determine behavior of the material after peak stress is reached. Fracture energy levels can be measured by completing certain laboratory testing and can be implemented in most constitutive models. Fracture energy is important to replicate softening. Fracture energy is defined as the average energy required for the creation of a stress-free unit fracture surface and represents a global evaluation of fracture toughness [35]. It is typically measured as the area under the stress-deformation test curve after peak strength is achieved. It has also been defined as the average dissipated energy per unit crack surface area [12] or the energy required to break a notched three point bend specimen into two pieces [36]. The fracture energy is assumed to be constant throughout the cross section of the material.

Experimental testing can determine fracture energy values. The stress-deformation curve after peak is determined from indirect tension tests or three point bend tests. It can also be calculated from the energy required for a crack to grow into a

complete separation in the bend test. Determining fracture energy from a direct tension test can be difficult because there is no standardized test. Other test methods, such as edge-notched tensile specimens and eccentric compression specimens, have shown to return similar fracture energies as the bend tests [37]. Other attempted test methods include shear testing and punching slab strength. A stiff, closed-loop test machine with displacement control is important to obtain proper values.

Experimental testing is not exact and is not a perfect depiction of fracture energy levels. There have been some disagreements regarding its exact measurement. It is widely accepted that the area under the stress-deformation plot after peak is used, some studies have included the full area under the stress-deformation curve [38]. Fracture energies can be affected by external sources, such as loading rate and testing frame stiffness [35]. Overestimations of the fracture energy can occur from errors in measurement and difficulties that come with measuring small deflections during the test.

Fracture energies can also be calculated using a variety of different models. The three major models are the size effect model (SEM), the two-parameter model (TPM), and the work-of-fracture model (WFM) [35]. The fracture energy values calculated from these models are used to calibrate other numerical models. Technically, the initial energy is found from the SEM and TPM, while the total fracture energy uses WFM. According to an analysis of all models, the fracture energy values were found to be level or larger than values calculated based on theoretical equations [39].

The SEM focuses on the size effect phenomenon by accounting for specimens of different geometries. It includes the energy concept, equivalent elastic crack model, and two size-independent fracture parameters [40]. The model calculates the fracture energy

using the strength of specimens with similar geometrical proportions but with different sizes. This relationship is used in combination with the size effect law and the energy of interest is the area under the initial crack-stress opening curve [39].

For the TPM, stress and crack displacement are the focal point. Specifically, fracture of concrete is characterized by critical stress intensity factor and the critical crack tip opening displacement [39]. This displacement can be measure by loading notched specimens and gathering data near the notch. The two parameters referred to in the name of the model are the two size-independent fracture parameters that are used in the model.

The WFM allows for the simplest testing procedure and is the most commonly used method. Using this method, the total fracture energy is defined as the ratio between the total energy and the concrete fracture area [41]. This method requires a notched three-point beam test, and the method assumes that the fracture energy is affected by the specimen size, but it is not of critical importance. The fracture energy values calculated from this model are higher on average than for the other two models.

This size effect discussed refers to the difference in fracture energy when the concrete properties are the same but the geometry is different. A function called the characteristic length can also be used to develop a relation between the fracture energy and the specimen geometry. The size effect has been hard to determine, given its effect has only been mild and there are no clear trends that have been discovered. Fracture energy must be accurate for all specimen lengths, as the definition of the concept specifies an infinitely large specimen.

Many different studies have been completed regarding the size effect of concrete and the associated fracture energy, with varying results. The assumption of a constant

fracture energy and crack surface area will result in larger crack density when the length of specimen is shorter. One study found that the stiffness, strength, and local fracture energy had little influence on the specimen height [42]. The peak was not any more influenced than the compressive strength when size effect was considered. Another study indicated that the dependence of the fracture energy on the size of the specimen is attributable to rate effects and slight variations in loading rate between tests [43]. Both of these studies showed that structure size does not have a significant effect on the calculated fracture energy.

However, other studies have shown that the size effect is at least of some concern when calculating fracture energy values. In one study, a four times larger beam resulted in a 35 percent increase in fracture energy for lower strength concrete and a 59 percent increase for higher strength concrete [35]. These results show that higher strength concrete will exhibit higher size effects, but the increase is only moderate. It is hard to determine what an acceptable increase would be, but the instance in this test only seems moderate. Other studies have indicated that fracture energy depends on specimen size and geometry and confirmed that it increases with increases in size [39]. An increase should be expected; since, the fracture process zone will be larger for larger specimens, and the size effect will be more obvious when plasticity is reached.

There are three major properties that affect the fracture energy of concrete: aggregate size; compressive strength; and load rate. Aggregate size has the most drastic effect on fracture energy. In general, higher fracture energy values were found for larger aggregate size for normal strength concrete than smaller aggregate size [35]. The fracture energy only increased slightly when the volume fraction of aggregate was increased in a

specimen. Specifically, when the aggregate size was doubled from 0.3 in. (8 mm) to 0.6 in. (16 mm), the fracture energy increased by 25 percent [35]. The larger aggregate size also resulted in rougher fracture surfaces, which may be another indication of why fracture energy values were higher. A 4.2 times increase in aggregate size was required to reach 100 percent increase in fracture energy [35]. The use of rounded aggregate resulted in higher fracture energies than specimens with angular aggregate [39]. In addition to size and shape, a stronger aggregate will also increase the fracture energy.

Concrete compressive strength is another material property that has an effect on the fracture energy of a given specimen. Based on the relationship of stronger aggregates and higher levels of fracture energy, it should be expected that increased compressive strength will result in increased fracture energy. One such study confirmed this trend; fracture energy was 35 percent higher in high strength concrete than that for normal concrete [38]. There also were increases in the fracture energy when curing time was increased to 28 days, which coincidentally resulted in higher strength. As the compressive strength increased, the energy stored in the material at peak strength increased, while the ability of the material to dissipate energy remained constant, resulting in more brittle failure [44]. The fracture toughness of concrete increases as well, but not at the same rate as the fracture energy-compressive strength relation.

There is also a direct relationship between the loading rate and the fracture energy of concrete. Fracture energy only increases slightly under quasi-static loading conditions but increases drastically when dynamically loaded [4]. Some possible explanations for this behavior include inertia and geometry of the specimen. Also, the fracture process zone extends at a greater rate when the loading rate increases. Specifically, the fracture

energy increased by approximately 50 percent when the loading rate was increased, up until about 0.04 in./s (1 mm/s), at which point the fracture energy increased more rapidly [4].

Notched specimens are very common when determining fracture energy through experimental testing. The crack mouth opening displacement (CMOD) can be directly used to calculate fracture energy [38]. CMOD measures require a lot of precision, because small deflection measurements are being taken at an area where damage is occurring. There may be deviations in the CMOD values, because the crack path is not necessarily a straight line and the CMOD is not measured directly at the crack opening, but nearby [38]. This study found that the CMOD could in fact be used as a replacement for standard displacement. Based on these findings, it is assumed that the energy dissipated at the crack is the same as the fracture energy. The use of CMOD may be more difficult when determining when to cut off data for the curve.

In order for a parameter to be considered a material property, that parameter must not change when adjustments are made to the geometry of a structure. The material property must also have repeatability and be consistent across multiple tests. Based on the results of the studies mentioned, it appears that fracture energy is size-independent. Therefore, it can be considered a material property of concrete. This independence relies on controlled experimental tests. The size effect law does have an effect on fracture energy, but it is not enough of an effect to warrant fracture energy not being considered a material property of concrete.

2.8 Strain Rate Effects

When concrete is loaded at high strain rates, the concrete strength typically increases. At these high strain rates, the concrete has increased opposition to imposed stresses and therefore becomes stronger. Strain rate effects on concrete are generally accepted to be higher in tension than in compression [45]. Strain rate effects are important both in modeling and design. Concrete fracture mainly depends on loading type, loading velocity, and moisture level, making it a rate-dependent material [20]. Most of all, the rate dependence of concrete is due to microcracking and the rate at which it occurs.

The increase in strength can be explained by the following phenomenon: increase in strength is due to both material strain rate effect and inertial confinement effect [46]. When high strain rates are present, an increase in strength occurs due to inertial resistance of the material as it cracks; two changes come as a result [47]. The specimen will be forced to crack through greater resistance paths in the cement-aggregate interface, because there is not enough time to find a weaker path. The cracks are therefore sporadic and do not link up as smoothly as under normal strain rates, meaning more cracking will be needed for failure to occur.

The term given to represent the strain rate effect is the dynamic increase factor (DIF). This DIF gives the increase factor by which the concrete strength is multiplied for a given strain rate. It is defined as the ratio of the dynamic strength to the quasi-static strength in compression [48]. The DIF is based on a semi-log or log-log scale. The DIF increases by 50% when the strain rate varies from 10^{-5} to 10^1 s^{-1} , with a sharp rise in DIF values coming when a 10^2 s^{-1} strain rate occurs [48]. An increase of 80% was seen when

the strain rate increased from static at 10^{-6} s^{-1} to 10 s^{-1} [22]. The DIF can be implemented directly in constitutive modeling.

The concept of DIF and strain rate effects can be confirmed by many different test methods. Some of these include Split-Hopkinson bar, drop-hammer, servo-hydraulic loading, and explosive tests [48]. Lateral confinement can be added in certain tests, further enhancing the compressive strength of concrete. Some uncertainties are associated with testing and validating DIFs. Uncertainties arise from DIF results coming from different testing techniques and the specimen size effect [48] and the increased magnitudes in strength being a result of concrete quality, aggregate, age, curing and moisture conditions, instead of strain rate effects [22]. These are all valid concerns, but DIFs have been proven realistic.

The test data coming from various researchers solidifies the use of DIFs in constitutive modeling. Transition points between low strain rate sensitivity and high strain rate sensitivity have been reported at a range of 63.1 s^{-1} [48] to 200 s^{-1} [46]. Strain rate effects not only increase the strength of concrete but also the stiffness, while the brittleness decreases. In one study, the DIF values were found to be 1.33, 1.24, and 1.17 for strain rates of 3 s^{-1} , 0.3 s^{-1} , and 0.1 s^{-1} , respectively [22]. Several studies have shown that smaller strain rates tended to under-predict the DIF, while larger strain rates over-predicted the DIF value, for both compression and tension.

Strain rate effects can be added to constitutive concrete models or material models, but they must be validated to ensure they are working properly. Some researchers have assumed the DIF to be the rate effect and thus incorrectly predicted the value used in simulations and numerical models. With an incorrect value, this typically

led to the overprediction of concrete strength [48]. Dynamic strength enhancement relates to lateral confinement and not strain rate effects.

CHAPTER 3 LS-DYNA CONCRETE MATERIAL MODELS

3.1 Introduction

There are many concrete material models available in LS-DYNA version 7.1.1. In order to select a small group of models for analysis, selection criteria were developed to identify qualifying models. Ideally, a preferred model would have minimal material input, rate-dependent behavior, and the ability to track concrete damage. Minimal material input typically includes automatic parameter generation, which makes the model more user-friendly. Rate-dependent behavior was important in order to account for rate effects that would occur in dynamic loading conditions. Rate-dependent behavior would not be necessary for quasi-static component tests, but it would be important in more dynamic impact analyses. Damage tracking was another benefit that would be desired. This feature should highlight the behavior of concrete in all load cases as well as accumulate damage under different loading conditions.

With these criteria in mind, selections were made from the list of available concrete material models in LS-DYNA, as shown in Table 1. After consideration of all the models available and their capabilities, five models were chosen for further analysis: CSCM; K&C; RHT; Winfrith; and CDPM. Only the CSCM, K&C, and RHT models had minimal input, rate dependency, and damage tracking, with the other two models having minimal input and rate dependency, but not damage tracking. Background research on these models was performed before any simulations were attempted. The material model input cards for each model are found in Appendix A.

Table 1. LS-DYNA Concrete Material Model Evaluation

<i>MATERIAL MODEL</i>	<i>MAT_ID</i>	<i>MINIMAL INPUT</i>	<i>RATE DEPENDENT</i>	<i>DAMAGE TRACKING</i>
Soil and Foam Model	*MAT_005	No	No	No
Psuedo-Tensor	*MAT_016	Yes	No	No
Oriented Crack	*MAT_017	No	No	No
Geological Cap	*MAT_025	No	No	No
Concrete Damage	*MAT_072	Yes	Yes	No
Concrete Damage Rel3 (K&C)	*MAT_072R3	Yes	Yes	Yes
Brittle Damage	*MAT_096	No	No	No
Soil Concrete	*MAT_078	No	No	No
Winfrith Concrete	*MAT_084	Yes	Yes	No
Johnson Holmquist Concrete	*MAT_111	No	Yes	No
Schwer Murray Cap	*MAT_145	No	No	Yes
CSCM Concrete	*MAT_159	Yes	Yes	Yes
RHT	*MAT_272	Yes	Yes	Yes
Concrete Damage Plastic Model (CDPM)	*MAT_273	Yes	Yes	No

3.2 CSCM Model

The CSCM model was developed by APTEK, Inc. in the 1990s and was intended to be used for roadside safety analyses [49]. It is a continuous surface cap model, as shown in Figure 9. There are two different input versions of the material model, one of which allows for parameter generation based on a limited number of inputs. The other input version requires specific data of all material model parameters. The parameter generation option (*MAT_CSCM_CONCRETE) only requires data for the concrete compressive strength and maximum aggregate size, which makes this material model much more user-friendly.

There is a smooth and continuous intersection between the shear surface of the model and the hardening cap, as shown in Figure 9. The model combines the shear surface and hardening cap using a multiplicative formulation, which allows for the continuous and smooth intersection. The shear surface is plotted as shear strength versus pressure. The cap is specifically used to model plastic volume change, and its motion determines the shape of the pressure-volumetric strain curves. Without the presence of a

cap, the model would be perfectly plastic. Since the cap simulates plastic volume change, it will expand to simulate plastic volume compaction and contract to simulate plastic volume expansion. The specific motion of the cap is determined by the hardening rule [50]:

Equation 1.
$$\varepsilon_v^p = W(1 - \exp^{-D_1(X-X_0)-D_2(X-X_0)^2})$$

where ε_v^p is the plastic volumetric strain, W is the maximum plastic volumetric strain, X_0 is the initial location of the cap, X is the current position of the cap, and D_1 and D_2 are model input parameters.

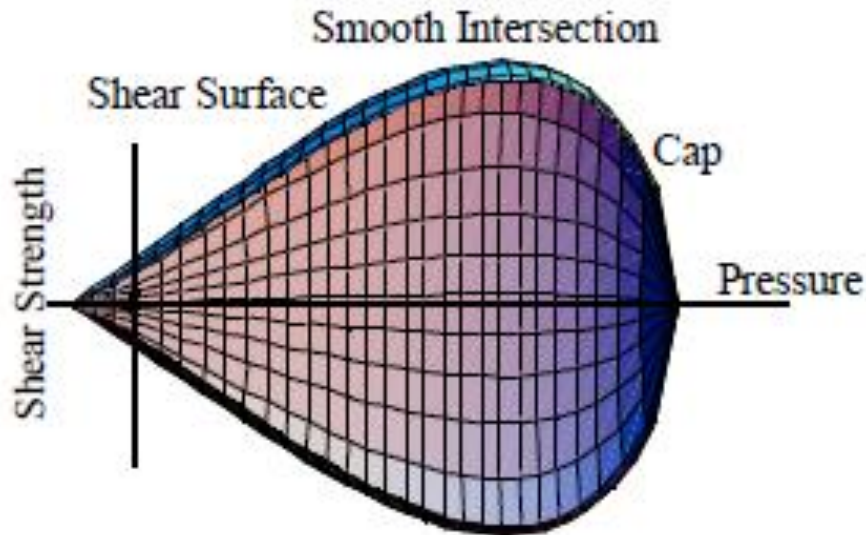


Figure 9. Failure Surface and Cap Shape of CSCM Model [51]

The yield surface of the model uses three different stress invariants, making it an isotropic model. The yield stresses are defined by this three-dimensional yield surface. Formulations in previous concrete material models only used two stress invariants. The strength of concrete, $F_f(J_1)$ is modeled by the shear surface [50]:

Equation 2.
$$F_f(J_1) = \alpha - \lambda \exp^{-\beta J_1} + \theta J_1$$

where α , β , λ , and θ are curve fit parameters from triaxial compression tests on plain concrete cylinders and J_1 is the first invariant of the stress tensor. Many of the other constitutive equations used in the material model can be obtained in the Comite europeen du beton (CEB) model code [52].

The CSCM model also has the ability to track damage as it accumulates in the simulation. The damage is a rather simple formulation and accounts for both strain softening and modulus reduction and is rather simple [50]:

Equation 3.
$$\sigma^d = (1 - D)\sigma^{vp}$$

where σ^d is the damage tensor, D is the damage parameter and σ^{vp} is a stress tensor, updated using a viscoplastic algorithm. The CSCM model handles damage using a strain-based energy approach, such that when the energy exceeds a predetermined threshold, damage will start to accumulate. One of the major benefits of this model is that brittle and ductile damage are considered separately. Brittle damage will accumulate in the model when the pressure is tensile, and ductile damage accumulates when the pressure is compressive.

Damage initiates at peak strength on the shear surface and can range from 0 to 1 for no damage to complete damage, respectively. The maximum increment that the damage parameter can increase in one time step is 0.1, which helps to avoid excessive damage. As the damage parameter reaches 1, an element loses all strength and stiffness, and the element will erode. Due to this erosion, dilation will not occur. The ERODE parameter can also be used in order to determine when erosion will occur. When the default value of 1.0 is used, an element erodes when $D > 0.99$ and the maximum principal strain is greater than a user-supplied input value.

The CSCM model uses fracture energy in order to regulate mesh size sensitivity, thus the concrete material model will maintain constant fracture energy regardless of element size. The CSCM model was developed specifically for a mesh size of 0.79-1.0 in. (20-25 mm). However, this mesh size is not required in order to use the model. For this particular model, the fracture energy, G_f , is defined as the area under the stress-displacement curve after peak strength is reached. The fracture energy is calculated based on the compressive, tensile, and shear fracture energy values. Two different equations are used for the calculation of the fracture energy, depending on if the pressure is compressive or tensile.

The CSCM model, like all five models under consideration, is rate dependent. The strength of the concrete material increases with increasing strain rate. Rate effects are used on the surfaces of the model and applied to the fracture energy. A modified Duvaut-Lions formulation is applied to the yield surface [53]. Viscoplastic rate effects are used in the model. At each time step, the viscoplastic algorithm sets the viscoplastic stress with rate effects, σ^{vp} . The interpolation is made between the elastic trial stress, σ^T , and the stress without rate effects, σ^p [50]:

Equation 4.
$$\sigma^{vp} = (1 - \gamma)\sigma^T + \gamma\sigma^p$$

where $\gamma = \frac{\Delta t/\eta}{1+\Delta t/\eta}$, η is the effective fluidity coefficient, and Δt is the time step. Due to the model predicting high rate effects at dynamic strain rates, an overstress limit is in place to ensure that the rate effects do not reach substantial levels.

3.3 Concrete Damage (K&C) Model

The Concrete Damage Models, also referred to as the Karagozian & Case (K&C) model, was designed to be used to analyze buried, steel-reinforced concrete structures

subjected to impulsive loadings [50]. This initial model, *MAT_072, is similar to the Pseudo-TENSOR model, *MAT_016. Improvements have been made to form the most current version, Release III, *MAT_072R3. Currently, the model has parameter generation capability, and is not mesh dependent. For the K&C model, only the unconfined concrete compression strength of the concrete and its density are required in order to use the model. Among the many Release III improvements was a change to the input format of the material model, which made it reliable for use in blast and impact analyses.

The K&C model is a three-invariant model which uses three shear failure surfaces and includes damage contours and strain rate effects. It uses an equation-of-state to detail the relationship between pressure and volumetric strain. This equation can either be provided by the user or automatically generated. The three independent strength surfaces are the yield surface, limit surface, and residual surface. The initial yield surface either hardens to reach the limit surface or softens to reach the residual surface. Any of the surfaces can be formulated as [49]:

Equation 5.
$$F_i(p) = a_{0i} + \frac{p}{a_{1i} + a_{2i}p}$$

where $F_i(p)$ is the surface definition, the a parameters are calibrated from test data, and p is pressure. The failure surface is interpolated between the maximum strength surface and either the yield strength surface or the residual strength surface using the following equation [49]:

Equation 6.
$$F(I_1, J_2, J_3) = \begin{cases} r(J_3) [\eta(\lambda) (F_m(p) - F_y(p)) + F_y(p)] & \lambda \leq \lambda_{max} \\ r(J_3) [\eta(\lambda) (F_m(p) - F_r(p)) + F_r(p)] & \lambda > \lambda_{max} \end{cases}$$

where λ is the modified effective plastic strain or the internal damage parameter, λ_{max} is the maximum modified effective plastic strain, η is a user-defined damage function, F_m , F_y , and F_r are the surfaces, p is pressure, and $r(J_3)$ is a scale factor in the form of the Willam-Warnke equation. The Willam-Warnke function is used to describe the cross-section of the surface. The failure surface starts at the yield surface. As the λ parameter increases to λ_{max} , it reaches the maximum strength surface.

Damage is also a feature of the K&C model, although damage is different in tension and compression. Once the yield surface is first reached, the stress state will change based on the following [53]:

Equation 7.
$$\Delta\sigma = \eta(\Delta\sigma_m - \Delta\sigma_y) + \Delta\sigma_y$$

where η is a user-defined damage function indicating the location of the current yield surface relative to the limit surface, $\Delta\sigma_m$ is the limit surface, and $\Delta\sigma_y$ is the yield surface. Damage initially starts at zero and will increase to unity, at which point softening will start to occur. The damage, η , will decrease during softening and can be used to interpolate between the limit and residual surfaces [53]:

Equation 8.
$$\Delta\sigma = \eta(\Delta\sigma_m - \Delta\sigma_r) + \Delta\sigma_r$$

where $\Delta\sigma_r$ is the residual surface. The effective plastic strain parameter will initially be zero when damage is zero, but it will increase during softening as the damage parameter decreases. Dilation will occur in this material model because the model is not capable of erosion.

The K&C model is also rate-dependent and uses a strain-rate enhancement factor to scale the strength surface and fracture energy when dynamic load rates are present. This factor is also called the dynamic increase factor (DIF), which varies based on the

strain rate. Separate DIF values are calculated for tension and compression load cases. Rate effects account for both moisture in the initial stages of loading and inertia effects at high load rates. The DIF is multiplied by the strength surface in order to create a new limit surface at the same stress level. DIF values can be calculated from literature for compression [52]:

Equation 9.
$$DIF = \begin{cases} (\dot{\epsilon}_c/\dot{\epsilon}_{co})^{1.026\alpha} & \text{for } |\dot{\epsilon}_c| \leq 30 \text{ s}^{-1} \\ \gamma_c(\dot{\epsilon}_c/\dot{\epsilon}_{co})^{1/3} & \text{for } |\dot{\epsilon}_c| > 30 \text{ s}^{-1} \end{cases}$$

and tension [54]:

Equation 10.
$$DIF = \begin{cases} (\dot{\epsilon}_t/\dot{\epsilon}_{to})^\delta & \text{for } |\dot{\epsilon}_t| \leq 1 \text{ s}^{-1} \\ \beta_t(\dot{\epsilon}_t/\dot{\epsilon}_{to})^{1/3} & \text{for } |\dot{\epsilon}_t| > 1 \text{ s}^{-1} \end{cases}$$

where $\dot{\epsilon}_c$ and $\dot{\epsilon}_t$ are the strain rates, $\dot{\epsilon}_{co} = -30 * 10^{-6} \text{ s}^{-1}$, $\dot{\epsilon}_{to} = 10^{-6} \text{ s}^{-1}$, $\alpha = \frac{1}{5+9(f'_c/1450 \text{ psi})}$, $\delta = \frac{1}{1+8(f'_c/1450 \text{ psi})}$, $\log \gamma_c = 6.156\alpha - 2$, $\log \beta_t = 6\delta - 2$, and f'_c is the compressive strength of concrete. DIF values should be calculated for a variety of strain rates ranging between $3 * 10^{-6} \text{ s}^{-1}$ and 300 s^{-1} to generate a table of strain rate vs. DIF values for use in the material model.

3.4 RHT Model

The RHT model uses damage mechanics and was originally created as a macro-model to analyze fracture of rock under impulsive and impact conditions. The model has automatic generation for parameters and only requires the input of the concrete compressive strength. The model has a default value of 5,076 psi (35 MPa) for the compressive strength concrete and interpolates between that value and the maximum value of 20,305 psi (140 MPa) in order to calculate other material parameters.

Similar to the CSCM and K&C models, the RHT model uses three strength surfaces in the material model: the initial elastic yield surface; the failure surface; and the residual friction surface [55], graphically shown in Figure 10.

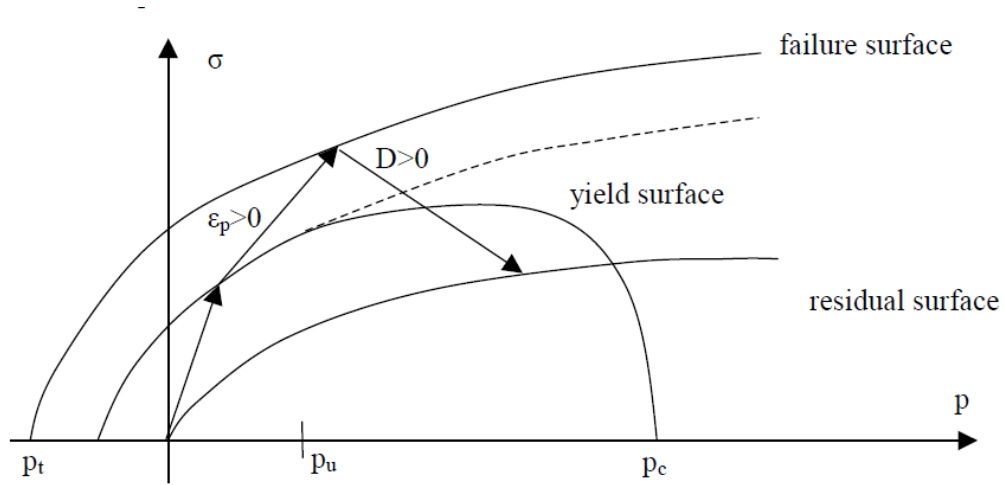


Figure 10. Plot of Three Failure Surfaces for RHT Model [55]

The model is in an elastic state until the initial yield surface is reached, at which point plastic strains begin to develop. The strength surfaces, $F(I_1)$, are expressed as follows [53]:

Equation 11.
$$F(I_1) = \frac{a_1}{\sqrt{3}} \left[\frac{I_1}{3} - r_f p_{spall} \right]^{a_2}$$

where a_1 and a_2 are the initial slope of the failure surface and pressure dependence of failure surface, respectively, I_1 is the first stress tensor, p_{spall} is the spall strength, and r_f is the rate factor, defined as [53]:

Equation 12.
$$r_f = \begin{cases} (\dot{\epsilon}/\dot{\epsilon}_0)^\alpha & : p > f'_c, \text{ with } \dot{\epsilon}_0 = 30 * 10^{-6} \text{ s}^{-1} \\ (\dot{\epsilon}/\dot{\epsilon}_0)^\beta & : p < f'_c, \text{ with } \dot{\epsilon}_0 = 3 * 10^{-6} \text{ s}^{-1} \end{cases}$$

where α and β are material constants and p is pressure. The RHT model is unique in that it has an elliptical cap function, F_{cap} , that closes when high pressure is present, as shown in Figure 11.

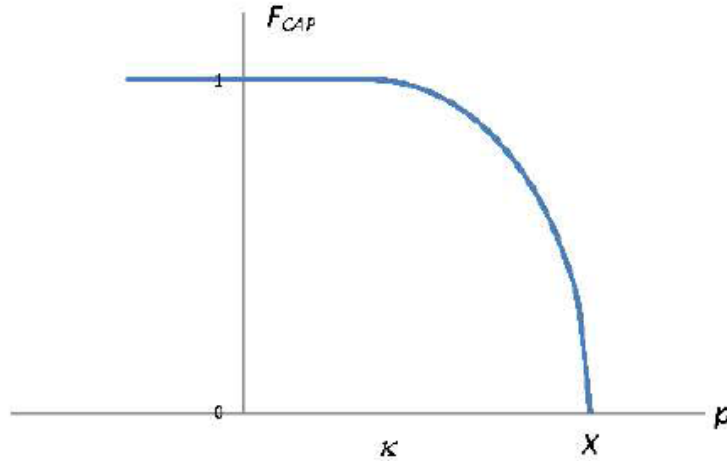


Figure 11. Elliptical Cap Function at High Pressure

Damage tracking is also a capability of this model. When the failure surface is reached, damage starts to evolve as plastic strain increases. The failure surface is interpolated between the limit and residual surfaces and shifted from the initial surface to a damage surface. The damage factor D is used to determine the location of the surface and is defined as [53]:

Equation 13.
$$D = \sum \frac{\Delta \varepsilon^p}{\varepsilon^f}$$

where $\Delta \varepsilon^p$ is the accumulated plastic strain and ε^f is the failure strain, defined as [53]:

Equation 14.
$$\varepsilon^f = D_1 \left(\frac{p}{f'_c} - \frac{p_{spall}}{f'_c} \right)^{D_2}$$

where D_1 and D_2 are user input material constants and f'_c is the concrete compressive strength. A failure strain can also be set by the user and be used to delete elements once a threshold is reached. Dilation will not occur in this material model.

Rate effects are also in place in the RHT model for tension loading. They include a DIF factor obtained from the CEB-FIB model code [52]:

Equation 15.
$$DIF = \begin{cases} (\dot{\varepsilon}/\dot{\varepsilon}_s)^{1.016\delta_s} & \text{for } \dot{\varepsilon} \leq 30 \text{ s}^{-1} \\ \beta_s(\dot{\varepsilon}/\dot{\varepsilon}_s)^{1/3} & \text{for } \dot{\varepsilon} > 30 \text{ s}^{-1} \end{cases}$$

where $\dot{\epsilon}$ is the strain rate between 10^{-6} to 160 s^{-1} , $\dot{\epsilon}_s = 3 * 10^{-6} \text{ s}^{-1}$, $\delta_s = \frac{1}{10+6f'_c/1450 \text{ psi}}$, and $\beta_s = 10^{7.112\delta_s-2.33}$. Rate effects are only applied for tension loading as the majority of the damage, such as cracking and spalling, occurs during tension loads. The fracture energy is scaled, similar to the K&C model.

3.5 Winfrith Model

The Winfrith model was developed in the 1980s, and the initial focus was on reinforced concrete structures that experience impact loadings [49]. The model includes an option to place smeared reinforcement directly in the material model, something not offered by any of the other four models. It is a basic plasticity model that uses three stress invariants, which are mainly called upon when triaxial compression and extension are loading conditions [56]. It also includes strain softening for concrete in tension and supports mesh regularization using either cracking opening width or fracture energy. Strain rate effects can either be included or omitted in the material input.

The Winfrith model requires slightly more input than other material models and only has a limited automatic generation capability. Although there are more inputs, most of the values can be solved using known empirical equations. The model is based on the four parameter model that was developed by Ottosen [57]:

Equation 16.
$$Y(I_1, J_2, J_3) = aJ_2 + \lambda\sqrt{J_2} + bI_1 - 1$$

where
$$\lambda = \begin{cases} k_1 \cos \left[\frac{1}{3} \cos^{-1}(k_2 \cos(3\theta)) \right] & \cos(3\theta) \geq 0 \\ k_1 \cos \left[\frac{\pi}{3} - \frac{1}{3} \cos^{-1}(-k_2 \cos(3\theta)) \right] & \cos(3\theta) \leq 0 \end{cases}, \quad \cos(3\theta) = \frac{3\sqrt{3}}{2} \frac{J_3}{J_2^{3/2}},$$

and the four parameters (a , b , k_1 , and k_2) are functions of the ratio of tensile strength to compression strength and are determined from a variety of tests, including: uniaxial compression, uniaxial tension, biaxial compression, and triaxial compression.

The Winfrith model also has a cap in the model, often called a “flat cap”. Its name comes from the linear strain-based relationship between pressure and volume. The model allows for the input of a user-defined volumetric strain vs. pressure curve in order to define this behavior. The input can also be omitted, and the model will generate a pressure-volume relationship based on other inputs. Although the predefined, automatic option is preferred, the model allows up to eight pairs of data to be used. The model does not have element erosion, but is not capable of dilation.

The strain rate enhancement factors in the Winfrith model are based on recommendations made in the CEB-FIB code, similar to those used for the K&C model. These rates can either be turned on or off in the Winfrith model. Low strain-rate factors are those for which the strain rate ($\dot{\epsilon}$) is less than 30 s^{-1} , while high strain rate factors are those for strain rates greater than 30 s^{-1} [56]. The Winfrith model does not use a modified factor for tension as used in the K&C model. Instead, it uses the original equations in the CEB-FIB model code. These factors are applied directly to the surface of the model. A factor can also be applied to the specified Young’s modulus, E_E , and the enhancement factor is the average of the tensile ($\dot{\epsilon}_{0T}$) and compressive ($\dot{\epsilon}_{0C}$) rate enhancements [56]:

Equation 17.

$$E_E = 0.5 \left[\left(\frac{\dot{\epsilon}}{\dot{\epsilon}_{0T}} \right)^{0.016} + \left(\frac{\dot{\epsilon}}{\dot{\epsilon}_{0C}} \right)^{0.026} \right]$$

3.6 CDPM Model

The CDPM model is a damage plastic concrete model that is used in dynamic loading simulations [58]. The focus of the material model is to accurately depict failure of the concrete structure when dynamic loading conditions are present. The CDPM model is based on effective stress plasticity and the damage aspect of the model is based on both plastic and elastic strain measurements [50]. The required input for the model is

significantly more complicated than the previous four material models. Other models have an automatic generation capability, while the CDPM model relies on default values. These default values are taken from experimental testing and may not be applicable for every loading condition or type of concrete. If the default values are not satisfactory, constitutive equations for calculating the parameters are provided, although these are quite complicated.

The shape of the yield surface in the CDPM model is based on two separate hardening laws, as shown in Figure 12. This yield surface is described by the Haigh-Westergaard coordinates, which are based on the volumetric effective stress, the norm of the deviatoric effective stress, and the Lode angle [50]. A hardening variable is controlled by the hardening laws and is used to control the size and shape of the yield surface and overall elastic portion of the model. The hardening variable will increase as the structure is loaded and has a maximum of 1, at which point the yield surface will become the failure surface.

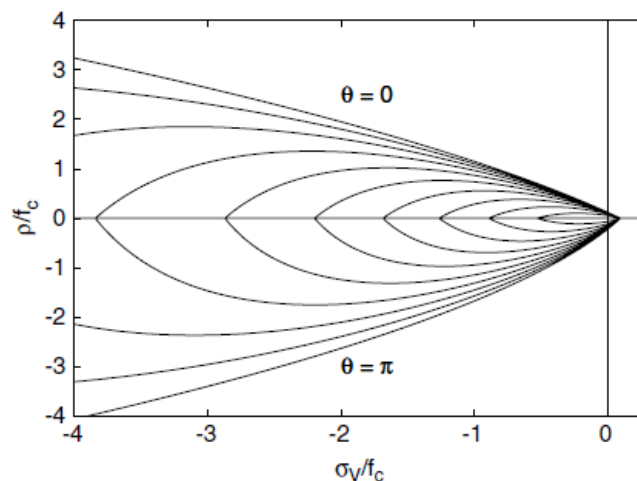


Figure 12. Evolution of Yield Surface During Hardening [58]

Damage in the model, based on an isotropic scalar formulation, begins to form when a threshold value for stress is surpassed. The damage portion of the model is based on plastic strain and uses a damage loading function, the damage law, and is influenced by the loading and unloading conditions [58]. Softening is controlled by the input parameters of the model. The damage is linked directly to the changes in the plastic strain, which is unlike some concrete material models where damage is based on total strain and represents pure damage. Damage can be shown in the output of the model for either tension or compression as the model has separate damage functions for each. There is no erosion capability for this model.

Since concrete is a rate-dependent material, strain-rate effects are considered in this model. The strain-rate enhancement factors in the CDPM model have some resemblance to formulations from the CEB-FIB model code that have also been seen in the K&C and Winfrith models. When the loading rate is increased, the tensile and compressive strengths are likewise increased due to these factors, with greater increase in tension than compression. The rate dependency is included in the model by scaling both the equivalent strain rate and the inelastic strain. For tension [50]:

Equation 18.
$$\alpha_{rt} = \left\{ \begin{array}{ll} 1 & \text{for } \dot{\epsilon}_{max} < 30 * 10^{-6} s^{-1} \\ \left(\frac{\dot{\epsilon}_{max}}{\dot{\epsilon}_{t0}}\right)^{\delta_t} & \text{for } 30 * 10^{-6} < \dot{\epsilon}_{max} < 1 s^{-1} \\ \beta_t \left(\frac{\dot{\epsilon}_{max}}{\dot{\epsilon}_{t0}}\right)^{\frac{1}{3}} & \text{for } \dot{\epsilon}_{max} > 1 s^{-1} \end{array} \right\}$$

where α_{rt} is the tensile rate parameter, $\dot{\epsilon}_{max}$ is the maximum strain rate, $\delta_t = \frac{1}{1+8f_c/f_{c0}}$,

$\beta_t = e^{6\delta_t-2}$, and $\dot{\epsilon}_{t0} = 1 * 10^{-6} s^{-1}$. For compression [50]:

Equation 19.
$$\alpha_{rc} = \left\{ \begin{array}{ll} 1 & \text{for } |\dot{\epsilon}_{min}| < 30 * 10^{-6} \text{ s}^{-1} \\ \left(\frac{|\dot{\epsilon}_{min}|}{\dot{\epsilon}_{c0}} \right)^{1.026\delta_c} & \text{for } 30 * 10^{-6} < |\dot{\epsilon}_{min}| < 1 \text{ s}^{-1} \\ \beta_c \left(\frac{|\dot{\epsilon}_{min}|}{\dot{\epsilon}_{c0}} \right)^{\frac{1}{3}} & \text{for } |\dot{\epsilon}_{min}| > 30 \text{ s}^{-1} \end{array} \right\}$$

where α_{rc} is the compressive rate parameter, $\dot{\epsilon}_{min}$ is the minimum strain rate, $\delta_c = \frac{1}{5+9f_c/f_{c0}}$, $\beta_t = e^{6.156\delta_c-2}$, and $\dot{\epsilon}_{c0} = 30 * 10^{-6} \text{ s}^{-1}$. The f_{c0} parameter for both tension and compression is a default value of 10.

3.7 Concrete Model Use in Practice

With an understanding of the background of each of the models and their basic equations, it is also important to understand how these five LS-DYNA material models have been previously used by researchers. All of the material models have been used to varying degrees for concrete research, development, and testing efforts. A review of these efforts can provide insight for this study by understanding the prior successes and failures to validate the models. This review will be helpful as initial expectations can be obtained regarding the use of models.

The CSCM model was created by APTEK, Inc., where one of its creators, Dr. Yvonne Murray performed a theory and evaluation study of the model [51] to investigate its capabilities. In this study, a wide variety of simulations were completed, including single element, drop tower test, and bogie vehicle impact test simulations. The simulations used various loading conditions, including compression, tension, and shear. The single element and simple component simulation results were compared to expected values and damage patterns based on theoretical knowledge. It was found that the model was performing well, and the peaks and damage contours were consistent with expected results, as shown in Figure 13.

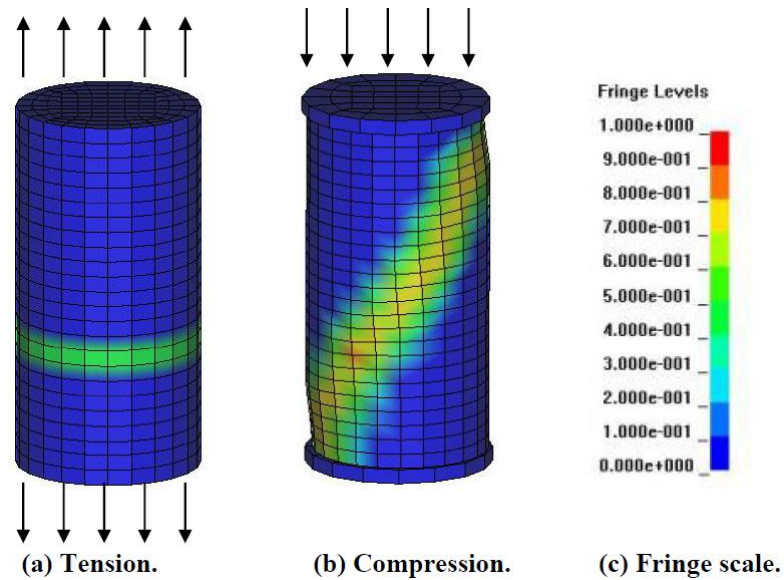


Figure 13. Damage Contours of Cylinders Simulated by APTEK [51]

In the drop tower simulations, the failure and response modes of the over-reinforced beams and under-reinforced beams were replicated. Additionally in the over-reinforced beam tests, an accelerometer was attached to the beams, and the velocity and displacement histories taken from physical tests matched those observed in the simulations fairly well. Displacement history comparisons were also made between results obtained from both low- and high-velocity bogie vehicle impact tests and representative simulations. Some differences were observed between the test and simulation curves after the rebound phase of the beam, in which the vehicle rebounded more during the simulation than observed in the test. In all, the material model was successfully used to simulate basic testing, and the simulation and test results matched well.

Another study by Abu-Odeh further investigated the use of the CSCM model for dynamic impact loading scenarios on roadside safety barriers [59]. For this study, two variations of the T4 reinforced concrete bridge railing were impacted with a pendulum in

both physical tests and simulations. The velocity-time and damage histories were compared between tests and simulations. Steel reinforcement was added to the concrete beams using the *CONSTRAINED_LAGRANGE_IN_SOLID option in LS-DYNA. The velocity-time histories were found to have reasonable agreement, although they were certainly not exact. The damage profile was found to be somewhat consistent, and elements were deleted where cracking occurred on the physical test beams, as shown in Figure 14.

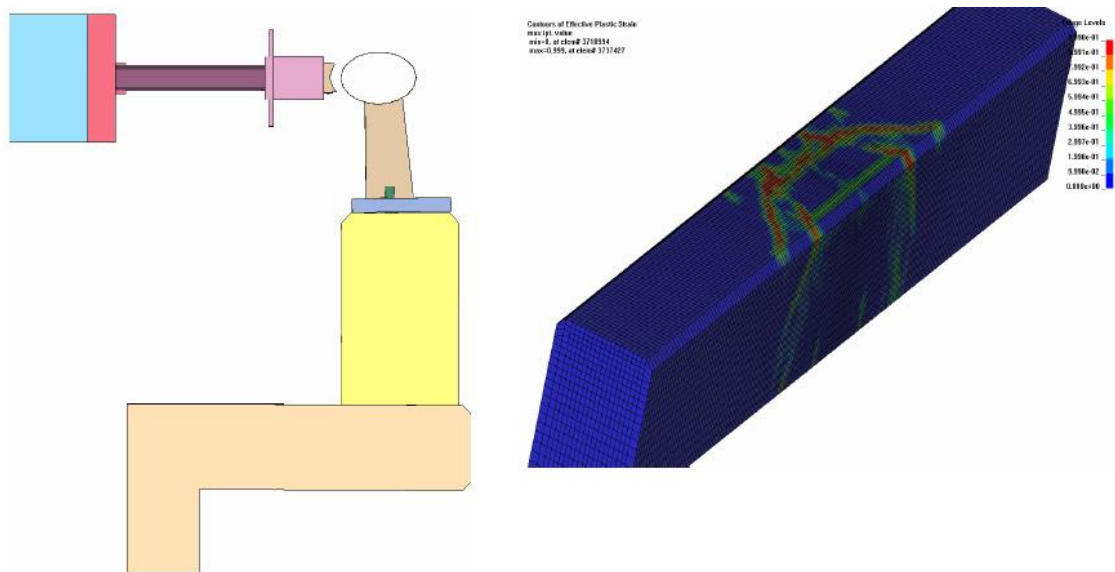


Figure 14. Damage in Parapet Simulation after Impact Loading [59]

A major conclusion was that the simulations provided a good benchmark for evaluating strength, sensitivity, and usability of the concrete material model. The study indicated that the material model may be a viable option for future use, but this test was very controlled compared to many loading conditions observed in full-scale crash tests on barrier systems. However, the model did perform well under design variations, as there were different damage contours for the two different T4 bridge rails that were simulated. Although this simulation effort was focused on reinforced concrete specimens and not

plain concrete specimens, the results were still deemed useful for the evaluation of the CSCM model.

The K&C model has also been analyzed by various researchers for different types of simulations. Schwer performed a study [60] on ‘standard’ concrete where theoretical calculations were compared with LS-DYNA simulation results when using the K&C model. The study specifically investigated the default, automatic generation capability of the K&C model and its ability to match physical test data. The single-element simulations were validated with uniaxial strain, compression, and tensile test data. For the uniaxial tension tests, the simulated stress-strain curve was slightly higher than the physical test curves, but it was within a reasonable range, as shown in Figure 15. The material model compared very well with the test data when only the most minimal information was inputted into the model. The study suggested that if more precise laboratory data was available, it could be used to refine the default parameters to better match true test data. With more precise data, the material model could provide even more accurate results.

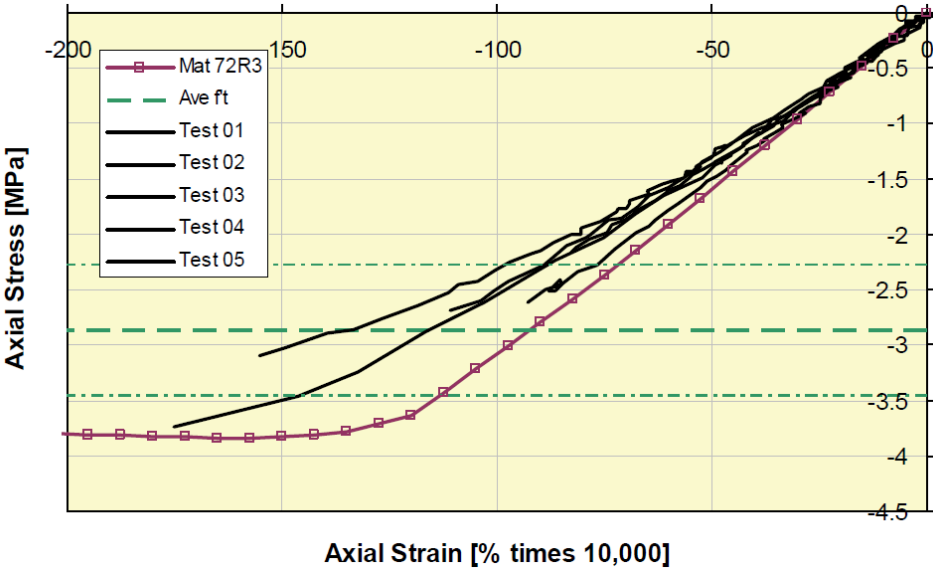


Figure 15. Comparison of Axial Stress vs. Axial Strain Data for K&C Simulations [60]

A more complete evaluation of the K&C material model was performed by the company who created the model, Karagozian & Case [61]. Simulation results were compared with physical tests for various scenarios, such as blast on reinforced concrete specimens, triaxial compression and uniaxial tension tests, beam tests, and aircraft impact tests. Many of the model parameters were also evaluated using a variety of component tests. In many cases, the concrete material model was able to capture the behavior of plain and reinforced concrete under complicated geometries and loading conditions. Despite the general success of the model, recommended improvements to the model include: a load-unload-reload methodology, addition of non-isotropic cracking, and addressing uncertainties related to the shear-dilatancy parameter. In terms of regularization features, several recommendations were made, including: resolve the lack of objectivity associated with tensile softening; provide a study for selection of B_1 parameter; improved regularization with differing element sizes; and remove the influence of aggregate size on model parameters and softening. Although recommendations were suggested in this study, it is important to understand that the model still provided accurate results.

For the RHT model, Borrvall and Riedel completed a study to analyze this material model under blast conditions [55]. A model was constructed to resemble a reinforced concrete plate that was subjected to a blast detonation approximately 3.9 in. (100 mm) away from the plate. Only 0.1% of the total area of the part was reinforcement, so the beam was mostly plain concrete. The major points of comparison were the damage contour of the beam and pressure-time history of the center of the concrete block, as shown in Figure 16.

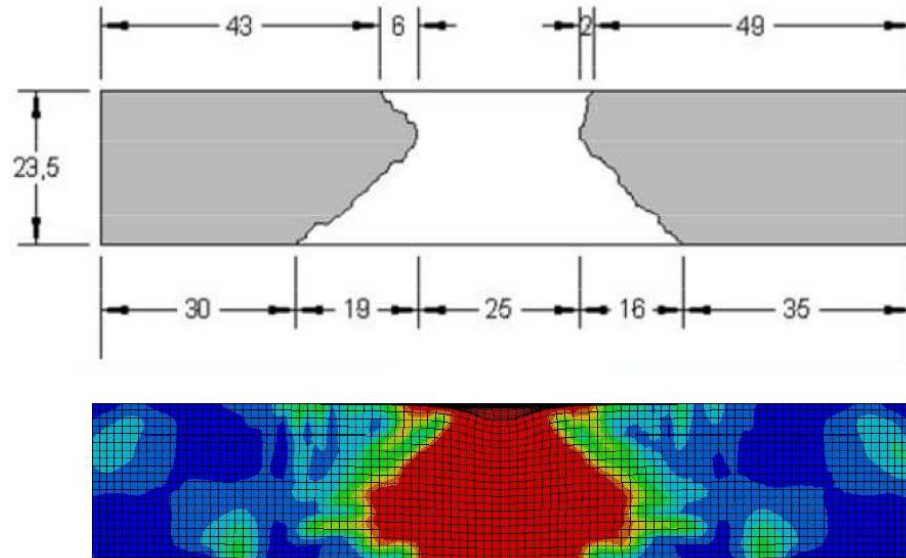


Figure 16. Experimental and Simulation Damage Contours for RHT Model [55]

For the damage comparison, the model performed well, and the damage profile of the simulated beam was similar to the damaged test beam. For the pressure-time history, the peak pressure of the test was not reached by the simulation, but it was still within an acceptable range. The study concluded that the compression behavior of the RHT material model was adequate, but there were some shortcomings related to tension softening. These shortcomings limited the ability of the model to correctly map spalling and other damage; because, tensile properties are directly related to the correct prediction of damage. Other recommendations for the model included a more general strain rate treatment.

For the Winfrith model, Schwer conducted a study [56] to test single elements and basic components under various loading conditions. These results were analyzed, and conclusions were made. However, the material model was not verified against experimental data. Unit cubes and non-uniformly meshed cylinders were tested under the following loading conditions: hydrostatic compression; unconfined compression; and

uniaxial tension. The major results that were analyzed included pressure vs. volume strain, stress vs. strain, displacement vs. time, and strain vs. time. The ability for the model to display crack planes and carry compression load after tension failure was also evaluated. The compression and tension failure strengths were confirmed in this study. The crack planes were developed in the simulations, but there was no strain softening after the compression damage started to accumulate. Although the crack planes did appear, they did not appear in all elements indicating mesh sensitivity; they were also inconsistent between simulations with similar loading conditions. The study also recommended additional investigation into strain softening regularization, as some issues were apparent in the non-uniformly meshed cylinders.

Although reinforced concrete is not a part of this specific concrete fracture study, the Winfrith model is unique in that it allows for the placement of reinforcement directly in the material model input. For this reason, further investigation of this particular material model was completed. For the Winfrith model, Schwer conducted a study to investigate the use of smeared reinforcement in concrete modeling [62]. The purpose of this study was to investigate the performance of reinforced concrete slabs under severe blast loading. A maximum pressure of 49.3 psi (0.3 MPa) and a maximum impulse of 1,015 psi-ms (7.0 MPa-ms) were applied to the specimens, and the center displacement was plotted against time. In an initial simulation and comparison with a physical test curve, the simulated displacements were much higher than the physical test results. Additional simulations were performed with mesh refinement in order to create a much better match. The refined mesh size did improve the simulation results, decreasing the center displacement values. However, they still over-predicted the experimental results.

Since the CDPM model was released in May 2014 for use with LS-DYNA, no published studies have been completed using the material model at this time. Some initial numerical simulations have been completed, but none include finite element simulation.

CHAPTER 4 SINGLE ELEMENT SIMULATION

4.1 Introduction

The five selected concrete materials were simulated with single element models under simple loading conditions: compression, tension, and shear. Single-element simulations have short run times and are helpful to better understand material model behavior at their most basic level. LS-DYNA version 7.1.1 finite element software was used to complete the single element simulations. Each model had time units in milliseconds (ms), length in millimeters (mm), mass in kilograms (kg), force in kilonewtons (kN), stress in gigapascals (GPa), and energy in kilojoules (kJ). Once results were obtained from the simulations, they were compared between different material models.

Five solid single elements were run in the same simulation, each representing one of the five material models. Each element was 25 mm x 25 mm x 25 mm (1.0 in. x 1.0 in. x 1.0 in.) and each designated with a different color: red (CSCM), blue (K&C), green (RHT), yellow (Winfrith), and brown (CDPM), as shown in Figure 17.

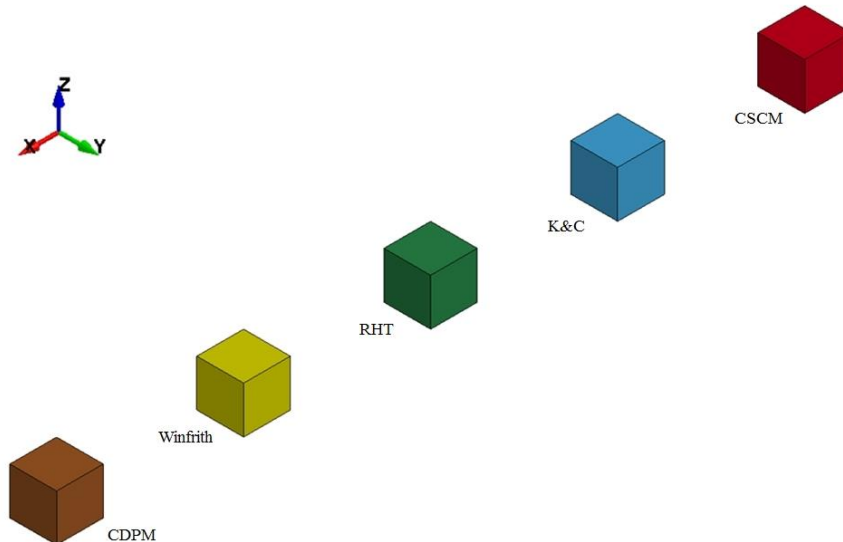


Figure 17. Single Element Model Overview

The five different material models had the same basic inputs, as shown in Table 2. Each model had different input requirements, but these default inputs were used for each of the five different material models. Optional material card inputs were not changed at this stage in order to isolate the basic material model behavior. Further experimentation with variation of the material model inputs was completed during later simulations of concrete component tests. The automatic generation capabilities were used for the CSCM and K&C models, requiring significantly less inputs. At this stage of the simulation investigation, strain rate effects were turned off for all simulations. Two different solid element formulations (elform) were used in the single element tests: elform 1 and elform 2. Elform 1 is a single-point integration element, while elform 2 is a fully-integrated element.

Table 2. Material Card Inputs

<i>Parameter</i>	<i>Units</i>	<i>Value</i>
Density	<i>kg/mm³ (lb/in.³)</i>	2.402E-06 (0.0868)
Compressive Strength	<i>GPa (psi)</i>	0.035 (5076)
Tensile Strength	<i>GPa (psi)</i>	0.00314 (455)
Maximum Aggregate Size	<i>mm (in.)</i>	19 (0.75)
Poisson's Ratio	-	0.19
Young's Modulus	<i>GPa (psi)</i>	28 (4,061,057)

4.2 Compression Simulations and Results

For the compression load case, a prescribed velocity based on a smoothly varying displacement curve was applied in the negative z-direction to the top four nodes of the element. According to this prescribed curve, the elements deflected a total of 0.5 mm (0.02 in.) over the course of 30 ms. This deflection was specified in order to incite failure. The smooth curve also incorporated a 0.25 ms rise and fall time period in order for the

load to ramp up and drop off. For the compression load case, two constraint conditions were applied to the elements using BOUNDARY_SPC. The baseline condition included a different set of constraints at each node, representing an unconfined element. The constraint condition represented a confined element. These specific constraints cases, as shown in Figure 18, have blue arrows representing the directions in which the nodes are free to translate. There were no rotational constraints on the nodes.

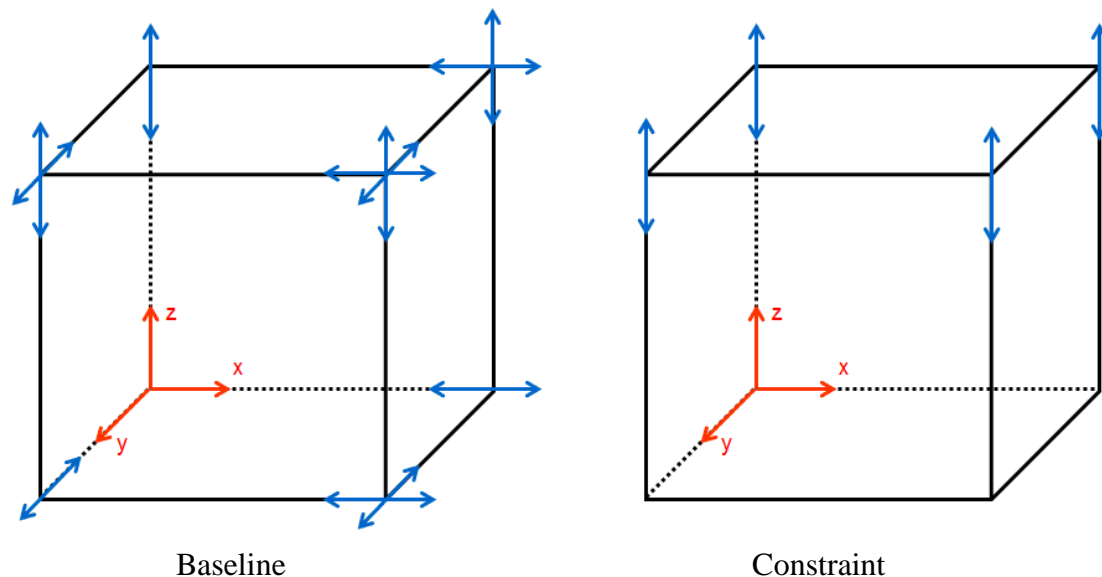


Figure 18. Baseline (Unconfined) and Constraint (Confined) Conditions for Compression and Tension

For all load cases, the following major results were evaluated: stress-strain relationships for true stresses and strains; true stress in the z-direction; change in volume at the peak stress; percent change in the total volume; force in the z-direction; the maximum damage value for the element; and whether or not the element failed and/or eroded. Failure is defined as the element no longer being able to transfer load and the damage threshold being reached, and erosion is defined as when the element is deleted from the simulation. These results, as well as simulation images at the beginning and end of the run at 30 ms, were presented compression load and the two constraint conditions.

In order to affirm that the simulation was behaving as expected the maximum stresses were compared with the input value for concrete compressive stress. Additionally, failure should occur due to the displacement in the simulation.

4.2.1 Baseline Condition (Unconfined)

For the compression load case, the simulation images at the beginning and end of the simulation (30 ms) are shown in Figure 19 for elform 2 with the baseline (unconfined) condition. Due to the compression loading, the single elements expanded in both x- and y-directions, with the K&C element showing excessive amounts of expansion. The CSCM element deleted at 3.5 ms. The elements in the elform 1 simulation behaved similarly, without the element deletion for the CSCM element.

The results for the baseline condition of the compression loading case were consistent between element types, as shown in Table 3. The tabulated values shown for Z-stress, Z-force, and damage were the maximums for the simulation. The maximum change in volume was taken at the peak stress and not at the end of the simulation as the elements continued to expand after peak. Results were not included for the Winfrith model for elform 2 in all simulations; since, the Winfrith model is not compatible with this element type. The maximum stresses for the CSCM, K&C, Winfrith, and CDPM models were similar and near the compressive strength input for the models, 0.035 GPa (5,076 psi).

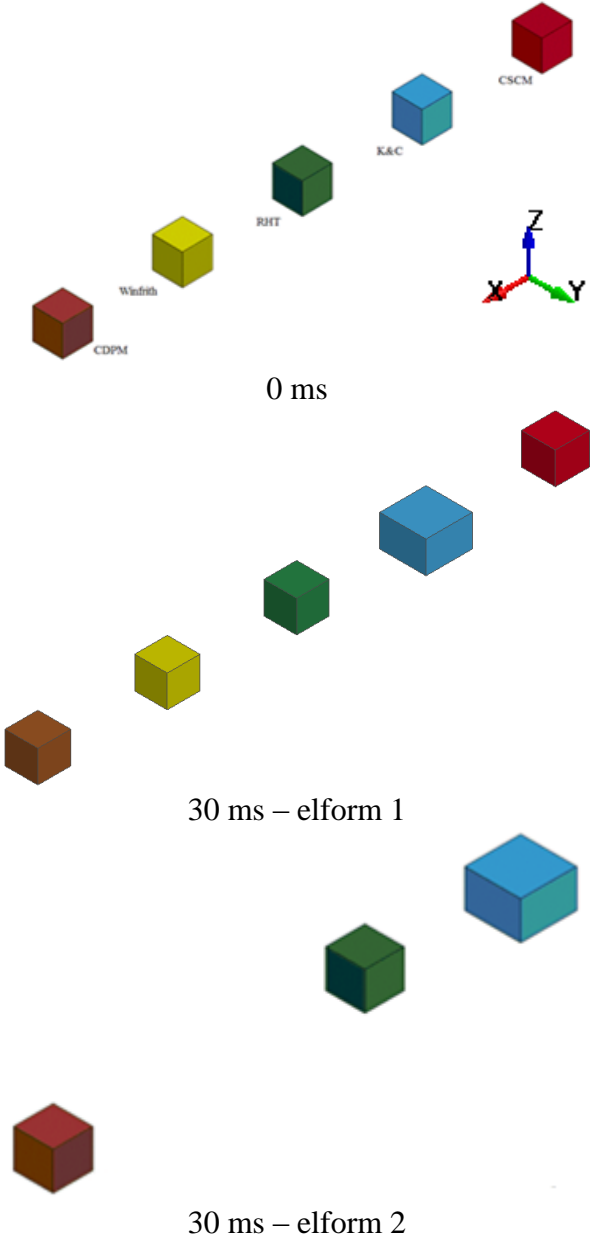


Figure 19. Simulation Images for Baseline Condition, Compression

The volume changes were all small and decreasing, aside from the CDPM model which increased in volume at the peak stress time. All volume values varied for the different element types. The sign of the volume change was misleading, because the value was taken at the peak force (i.e., at the beginning of the simulation). At this point, there was a slight decrease in the volume before it started to increase and continued to do so through the end of the simulation.

The maximum damage threshold for the CSCM and K&C models were 0.99 and 2.0, respectively. After this threshold, the elements no longer resisted deformations and did not transfer load. As shown in Figure 19, the CSCM element eroded with elform 2, but it did not erode with elform 1. This behavior is opposite of the tabular results, because the maximum damage is higher for elform 1 at 0.981, while the elform 2 simulation only reaches 0.202. The lower damage threshold seen in the elform 2 simulation was due to the high confining pressure provided by the constraint condition. The K&C element failed but did not erode, because the material model does not have the erosion capability.

Table 3. Results for Compression Loading, Baseline Condition

ELFORM 1	Z-Stress (True)	ΔVolume at Peak	Volume % Diff.	Force (Z-Force)	Damage	Failure, Erosion?
	<i>GPa</i>	<i>mm³</i>	<i>%</i>	<i>kN</i>	-	-
CSCM	0.0359	-8.8	-0.056	22.49	0.981	N/N
K&C	0.0351	-4.3	-0.028	21.96	2.000	Y/N
RHT	0.0480	-8.5	-0.054	30.07	×	N/N
Winfrith	0.0354	-12.2	-0.078	22.53	×	N/N
CDPM	0.0357	16.2	0.104	22.67	×	N/N

ELFORM 2	Z-Stress (True)	ΔVolume at Peak	Volume % Diff.	Force (Z-Force)	Damage	Failure, Erosion?
	<i>GPa</i>	<i>mm³</i>	<i>%</i>	<i>kN</i>	-	-
CSCM	0.0358	-12.6	-0.080	22.42	0.202	Y/Y
K&C	0.0351	-5.3	-0.034	21.95	2.000	Y/N
RHT	0.0480	-8.5	-0.054	30.07	×	N/N
Winfrith	×	×	×	×	×	×
CDPM	0.0351	-3.1	-0.020	22.30	×	N/N

The curves for the true stress-true strain relationship were fairly similar between elforms 1 and 2, as shown in Figure 20. The curves were identical for the K&C model and nearly matched for the RHT and CDPM models. There were, however, notable differences in the CSCM curves for the different element formulations. The CSCM curve for elform 2 did reach the same peak stress of 0.0358 GPa (5192 psi) as the elform 1 curve, but it quickly dropped off and the element eroded. The CSCM curve for elform 1 decreased to nearly zero by the end of the simulation, but it did not erode. The failure and time to fail the element were the only major difference in the CSCM curves between element types.

All curves, except for the RHT model, peaked at similar stress, corresponding to the maximum concrete compressive stress value of 0.035 GPa (5076 psi) from Table 2. The CSCM and K&C models peaked at 0.0358 GPa (5192 psi) and 0.0351 GPa (5091 psi), respectively, and started to decline, indicating the elements reached failure. The K&C curve fell off quickly, while the CSCM curve carried on longer for elform 2, and subsequently eroded. The CSCM model failed and eroded at 15 ms, and the K&C model failed at approximately 6 ms. After reaching peak stresses of 0.0354 GPa (5134 psi) and 0.0357 GPa (5178 psi), respectively, the Winfrith and CDPM models exhibited plasticity and remained at a constant stress. After reaching its peak of 0.048 GPa (6962 psi), RHT model stresses decreased until reaching approximately 0.015 mm/mm strain and then continued at a constant stress of approximately 0.0217 GPa (3147 psi).

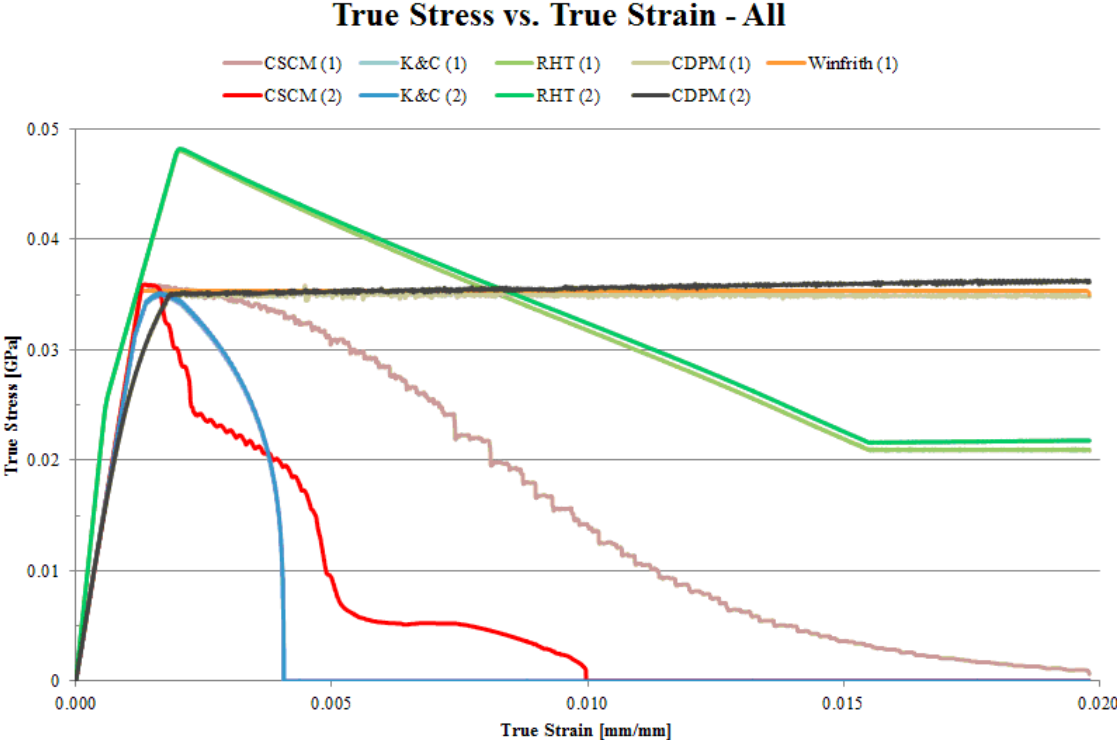


Figure 20. True Stress-Strain Plot for Compression Loading, Baseline Condition

4.2.2 Constraint Condition (Confined)

The constraint condition provided very different results, because the element was unable to expand in the x- and y-directions, as shown in Figure 21. The elements only displaced in the z-direction. No elements failed or eroded in this simulation. The confinement of the element resulted in significantly larger stresses due to the inability of the element to expand in the x- and y-directions.

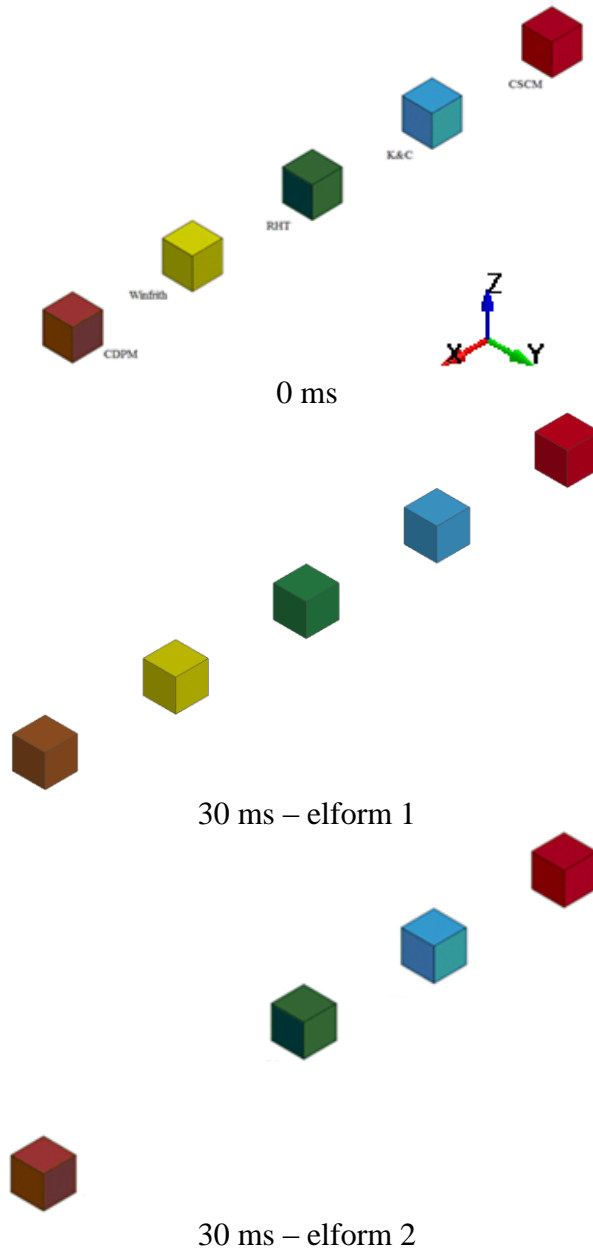


Figure 21. Simulation Images for Constraint Condition, Compression (elform 2)

The results for the constraint condition, as shown in Table 4, were consistent between element types, as found for the baseline condition. Volume change was not tabulated for the constraint condition as nodes only had free motion in the z-direction. Therefore, the cross-sectional area of the elements did not change in the xy-plane. The maximum stresses were larger and more varied than observed for the baseline condition.

Specifically, the maximum stresses were an order of magnitude higher than the 0.035 GPa input value. The forces were also significantly higher than those observed for the baseline condition. Damage values were zero for the CSCM model, and the 0.298 maximum value for the K&C model was well below the damage threshold. Even when the simulation time was extended, the damage values remained the same. With such high forces and stresses, it was surprising that none of the elements failed or eroded. The only discrepancy between element types for stress was with the CDPM model.

Table 4. Results for Compression Loading, Constraint Condition

ELFORM 1	Z-Stress (True)	Force (Z-Force)	Damage	Failure, Erosion?
	<i>GPa</i>	<i>kN</i>	-	-
CSCM	0.278	173.75	×	N/N
K&C	0.224	140.06	0.298	N/N
RHT	0.312	194.73	×	N/N
Winfrith	0.159	99.13	×	N/N
CDPM	0.204	127.92	×	N/N

ELFORM 2	Z-Stress (True)	Force (Z-Force)	Damage	Failure, Erosion?
	<i>GPa</i>	<i>kN</i>	-	-
CSCM	0.278	173.75	×	N/N
K&C	0.224	140.06	0.298	N/N
RHT	0.312	194.73	×	N/N
Winfrith	×	×	×	×
CDPM	0.201	125.83	×	N/N

The curves for elforms 1 and 2 within a specific material model were identical for the CSCM, K&C, and RHT models, as shown in Figure 22. There was a slight difference in the elform 1 and 2 curves for the CDPM material model; however, it was very small and did not affect the results of the simulation.

None of the curves reached a distinct peak or yield point as observed during the baseline condition investigation. Instead, they continually increased throughout the

simulation, and their maximum stresses were at the end of the simulation. The curves were mostly linear, but all had different slopes. All five curves followed the same general path through 0.005 mm/mm strain but started to divert from there. The RHT model recorded the largest stresses.

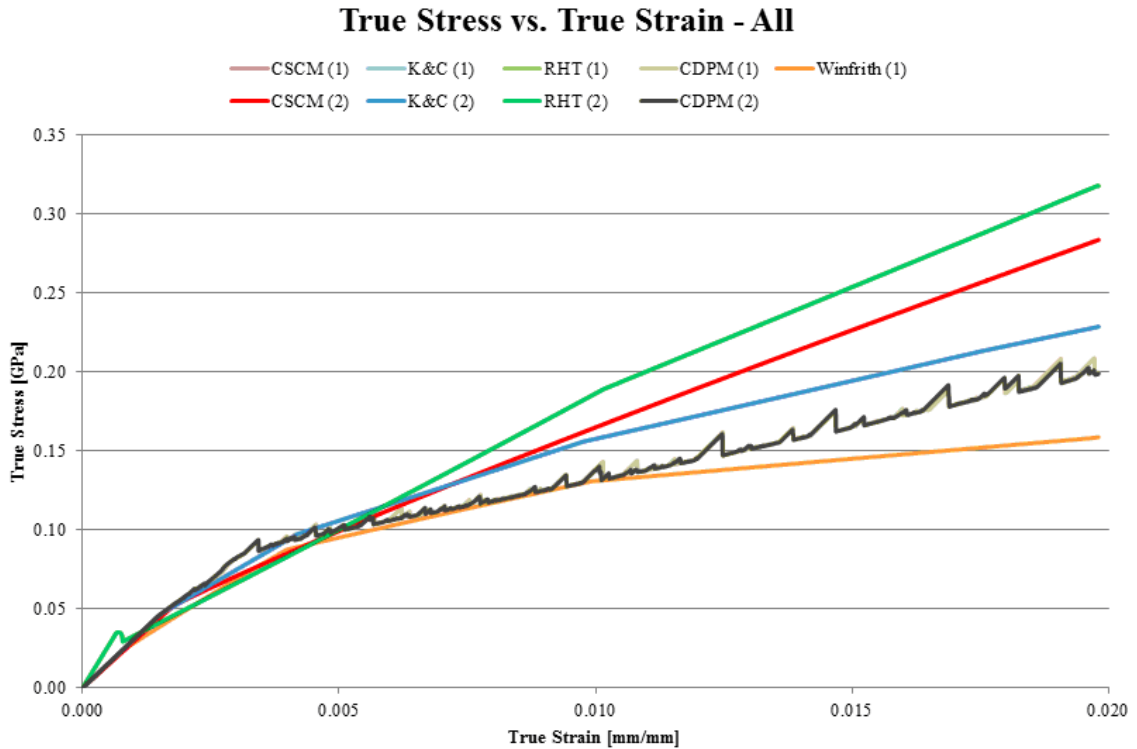


Figure 22. True Stress-Strain Plot for Compression Loading, Constraint Condition

All material models experienced unrealistic, high forces. Therefore, overconstraining solid concrete elements is not recommended as none of the material models were realistic.

4.3 Tension Simulations and Results

For the tension load case, a prescribed velocity was applied in the positive z-direction at the top four nodes, using the same displacement curve as with the compression load case in order to incite failure. The same element types and constraint

conditions were used as well. The parameters that were compared were also the same as used for the compression load case. It was expected that the true stress in the elements should match the input tensile strength of the concrete and the elements should fail.

4.3.1 Baseline Condition (Unconfined)

For the tension load case, the elform 2 simulation images at the beginning and after 30 ms of the simulation are shown in Figure 23. Due to the tensile loading, the single elements contracted in both x- and y-directions, with less volume change than the compression load case. In the elform 2 simulation, the CSCM element eroded at 8.0 ms, and the CDPM element eroded at 30.0 ms. In the elform 1 simulation with baseline condition, the CSCM element eroded at 8.0 ms.

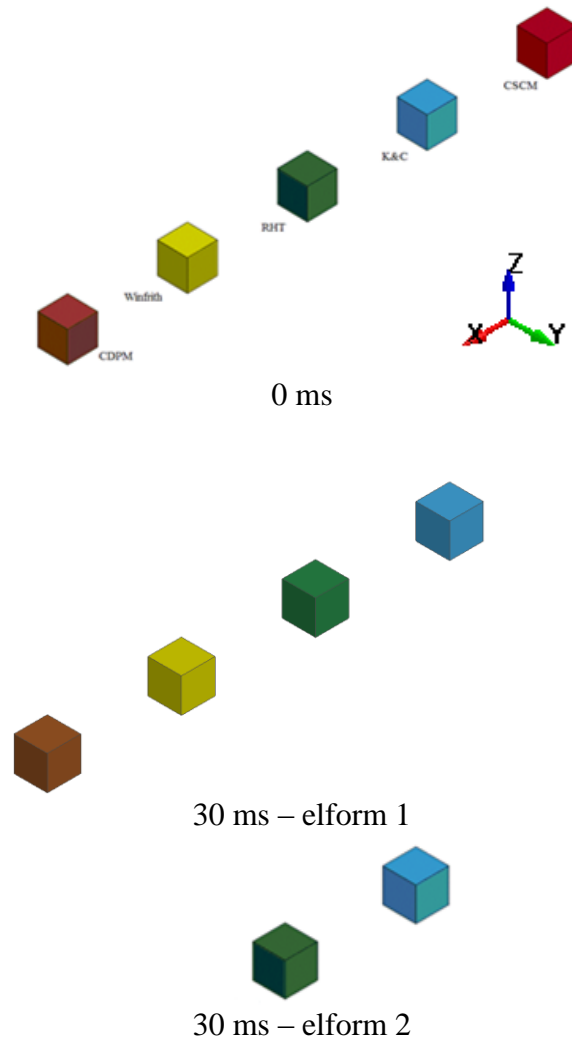


Figure 23. Simulation Images for Baseline Condition, Tension (elform 2)

The results for the baseline condition, as shown in Table 5, varied between element types. During this simulation, the plastic solver did not immediately converge for the CDPM model. Therefore, the CDPM values in Table 5 were carefully considered due to this warning in the simulation. The maximum stresses for the K&C and CDPM models were similar and near the expected tensile strength, 0.00314 GPa (455 psi). The expected tensile strength was found assuming a range from 9 to 15% of the compressive strength [63]. The maximum tensile stress for the CSCM model was near this limit, while the

RHT and Winfrith model results were much larger. The RHT model had the largest change in volume, and all models had small volume decreases. The decrease in volume was expected for the tension load case. The CSCM elements in both simulations eroded due to the elements reaching the damage threshold.

Table 5. Results for Tension Loading, Baseline Condition

ELFORM 1	Z-Stress (True)	ΔVolume at Peak	Volume % Diff.	Force (Z-Force)	Damage	Failure, Erosion?
	<i>GPa</i>	<i>mm³</i>	<i>%</i>	<i>kN</i>	-	-
CSCM	0.00273	-2.2	-0.014	1.72	0.990	Y/Y
K&C	0.00314	-3.3	-0.021	1.97	1.986	Y/N
RHT	0.00490	-5.4	-0.034	3.08	×	Y/N
Winfrith	0.00525	-3.9	-0.025	3.39	×	Y/N
CDPM	0.00314	-2.7	-0.017	1.96	×	Y/N

ELFORM 2	Z-Stress (True)	ΔVolume at Peak	Volume % Diff.	Force (Z-Force)	Damage	Failure, Erosion?
	<i>GPa</i>	<i>mm³</i>	<i>%</i>	<i>kN</i>	-	-
CSCM	0.00273	-2.2	-0.014	1.71	0.990	Y/Y
K&C	0.00314	-3.3	-0.021	1.97	1.983	Y/N
RHT	0.00491	-5.4	-0.034	3.07	×	Y/N
Winfrith	×	×	×	×	×	×
CDPM	0.00314	-2.7	-0.017	1.96	×	Y/Y

The true stress-true strain curves for the CSCM and K&C models were identical between element formulations, as shown in Figure 24. The RHT curves were fairly similar, with both element types having “noisy” data instead of a smooth curve. The elform 1 simulation for the RHT model had more “noise” at the beginning of the simulation than observed for the elform 2 curve. Aside from that, there were minor differences in the RHT curve. There were significant differences in the CDPM curve. The curves were identical through the first 5 ms, but differed from that point forward. The elform 1 CDPM element failed at 22.6 ms, while the elform 2 CDPM element failed at 11.7 ms. The values between element types were nearly identical for all five material models.

Similar to the compression baseline condition, the CSCM, K&C, and CDPM curves all peaked around 0.00314 GPa (455 psi). The RHT curve peaked at a higher value, 0.00490 GPa (711 psi), than those three models, also similar to the compression baseline condition. However, the Winfrith curve peaked at a higher stress value than the other four models, at 0.00525 GPa (761 psi). For these loading and constraint conditions, all five models failed before the end of the simulation. Despite the CSCM model failing for both element types, it only eroded in the elform 1 simulation. The CDPM model for elform 2 eroded at 23.0 ms, yet the curve was no longer transferring load at 11.7 ms; erosion was inconsistent with failure. Based on the comparisons between the input tensile stress and the simulation stresses, the forces were realistic.

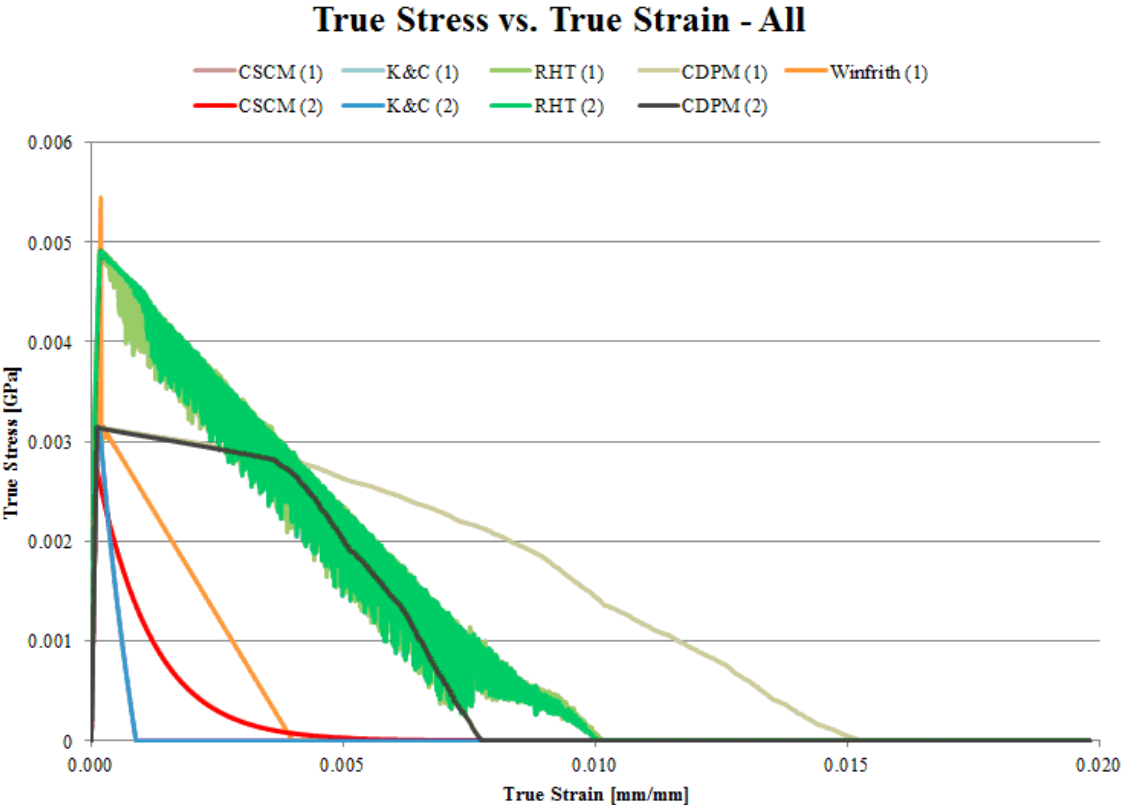


Figure 24. True Stress-Strain Plot for Tension Loading, Baseline Condition

4.3.2 Constraint Condition (Confined)

The constraint condition provided similar nodal displacements to those observed for the compression constraint condition, where the elements only displaced in the z-direction. The CSCM elements eroded in both simulations, as observed in the baseline condition.

During this simulation, the CDPM model's plastic solver did not immediately converge for elform 1 and never converged for elform 2. Therefore, the elform 2 simulation was re-run without the CDPM model. The CDPM values were considered for elform 1 and were not included for elform 2, as shown in Table 6. The stresses for the K&C and CDPM models were closest to the 0.00314 GPa (455 psi) expected value for all models. The CSCM value was slightly lower than the input, and the RHT and Winfrith values were higher than the input. The damage value for the CSCM model was 0.990, the highest value recorded among all simulations, yet the element did not erode during the simulation. The values for elform 1 and elform 2 were identical for stress, force, and damage. Both element types also had the same failure and erosion trends.

Table 6. Results for Tension Loading, Constraint Condition

ELFORM 1	Z-Stress (True)	Force (Z-Force)	Damage	Failure, Erosion?
	<i>GPa</i>	<i>kN</i>	-	-
CSCM	0.00277	1.73	0.990	Y/Y
K&C	0.00314	1.97	1.994	Y/N
RHT	0.00419	2.63	×	Y/N
Winfrith	0.00634	4.09	×	N/N
CDPM	0.00315	1.97	×	Y/N

ELFORM 2	Z-Stress (True)	Force (Z-Force)	Damage	Failure, Erosion?
	<i>GPa</i>	<i>kN</i>	-	-
CSCM	0.00277	1.73	0.990	Y/Y
K&C	0.00314	1.97	1.994	Y/N
RHT	0.00419	2.63	×	Y/N
Winfrith	×	×	×	×
CDPM	×	×	×	×

In terms of the two element types for the constraint condition, there were no differences in the curves for the tension loading condition, as shown in Figure 25. This finding was somewhat expected due to the matching results provided in Table 6.

Similar to the tension baseline condition, the Winfrith model had the highest peak stress at 0.00634 GPa (916 psi). The RHT model had the next highest peak stress at 0.00419 GPa (608 psi), but it was not as high as the baseline condition of 0.00490 GPa (711 psi). The CSCM, K&C, and CDPM curves continued to peak near the same true stress of 0.00314 GPa (455 psi). The plastic portion of the Winfrith curve started immediately after reaching its peak, and the model did not fail. The other four models did fail; however, the CDPM model failed at the very end of the simulation. The CSCM model failed near zero at 10.2 ms, but it never eroded, a trend that has been seen in previous simulations. Similar to the baseline condition, there were simulation stresses that were near the input tensile stress, thus those forces were realistic.

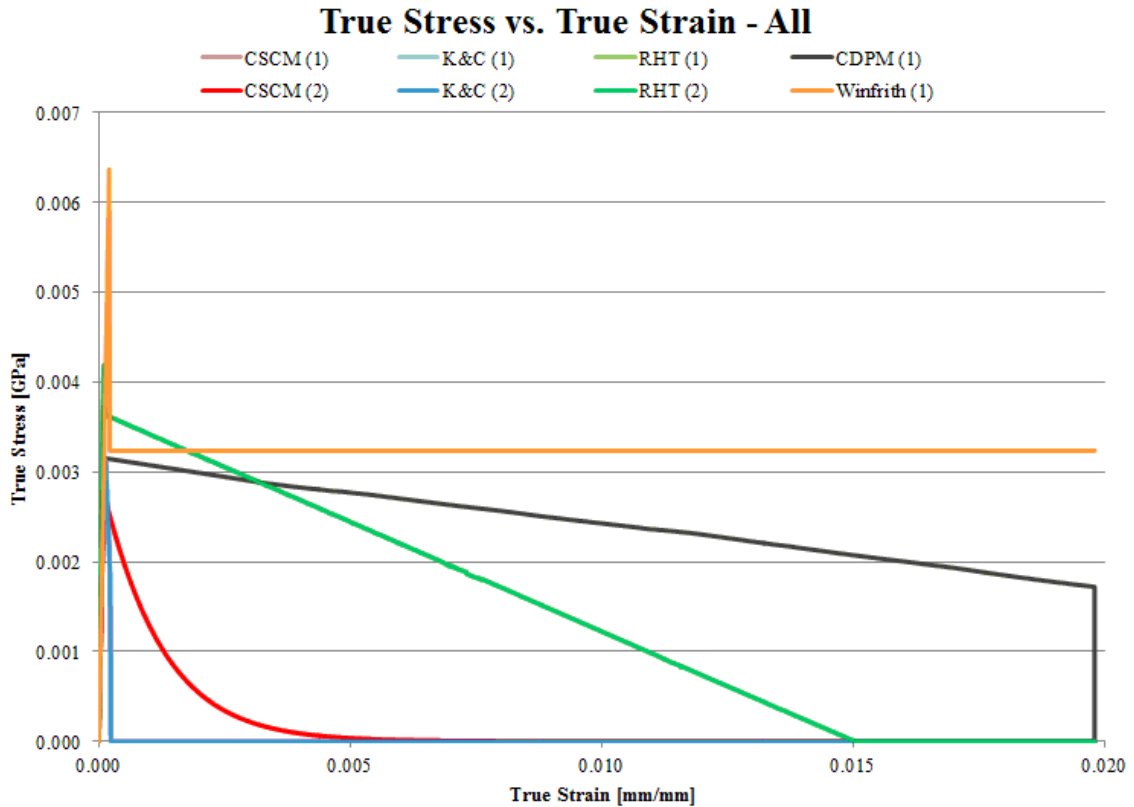


Figure 25. True Stress-Strain Plot for Tension Loading, Constraint Condition

4.4 Shear Simulations and Results

A shear load was applied at two of the top nodes at a 45 degree angle, directed in the x- and z-directions. The same prescribed velocity as the compression loading, using the same smooth curve method, was used for the shear loading case, resulting in a displacement of 0.5 mm (0.02 in.). It was again expected that the elements would fail. This case required a unique set of constraints due to the different loading and element behavior. Development of the pure shear loading was not straight forward; therefore, many constraint iterations were attempted. In the final case, all nodes were free to move, except for the two nodes opposite the load on the bottom of the element, as shown in Figure 26. The orange arrows in this rendering indicate the direction of the applied velocity. This constraint condition will allowed the element to deflect in a way that most

accurately represented pure shear. The stress values in the simulations were expected to match the shear strength input for concrete, 0.0063 GPa (914 psi), based on a known ratio of approximately 18% [63] of the compressive strength. Element failure was expected as well.

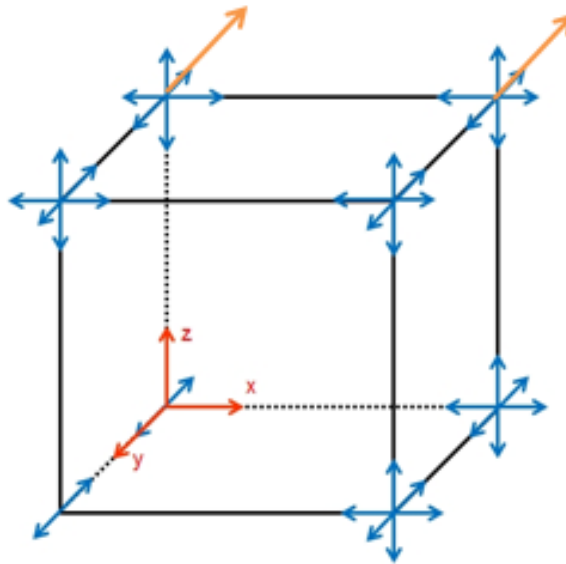


Figure 26. Angled Constraint Conditions for Shear

For the shear load case, the following major results were analyzed: stress-strain relationships for true stresses and strains; peak true shear stress; change in volume at the peak stress; percent difference in the volume change; the sum of the constraint forces in the x- or z-direction; the maximum damage value for the element; and whether or not the element failed or eroded. The shear strength was expected to be approximately 18% of the compressive strength, or 0.0063 GPa (914 psi) [18].

For the shear load case, the elform 2 simulation images at the beginning and after 30 ms of the simulation are shown in Figure 27 for the angled condition. Due to the general lack of constraints, the single elements expanded in all three directions. The CSCM element eroded in the elform 1 and elform 2 simulations at 10.9 ms.

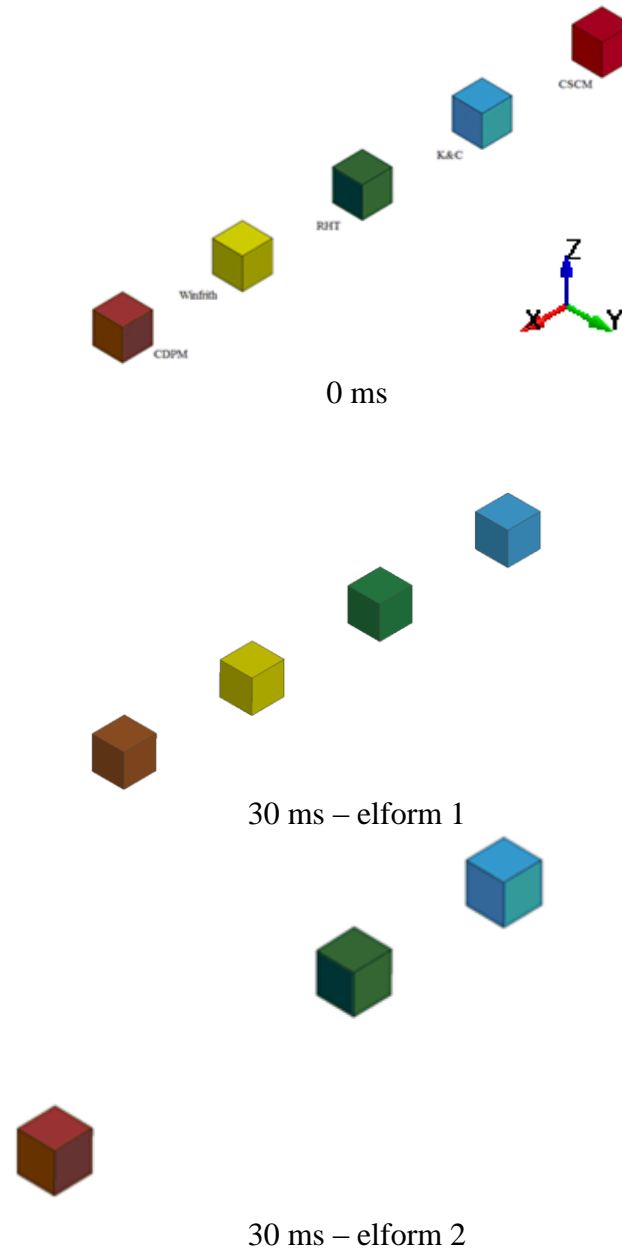


Figure 27. Simulation Images for Angled Condition, Shear (elform 2)

During this simulation, the CDPM model's plastic solver did not immediately converge for elform 1 and never converged for elform 2. Therefore, the CDPM element was omitted from further elform 2 simulations. The CDPM results were considered for elform 1 and were not included for elform 2, as shown in Table 7. None of the maximum stresses for the five models were near the expected shear strength for concrete, 0.0063

GPa (914 psi). The closest stress was 0.00265 GPa (384 psi), as obtained from the Winfrith model. The volume changes were small, with the RHT model having the highest changes at 0.126% and 0.295% for the elform 1 and elform 2 simulations, respectively. The damage value for the CSCM element, 0.990, was lower than previous damage values for this model that did not erode. However, the CSCM elements eroded for both simulations.

Table 7. Results for Shear Loading, Angled Condition

ELFORM 1	ZX-Stress (True)	ΔVolume at Peak	Volume % Diff.	Constraint Forces	Damage	Failure, Erosion?
	<i>GPa</i>	<i>mm³</i>	<i>%</i>	<i>kN</i>	-	-
CSCM	0.00137	1.5	0.010	0.86	0.990	Y/Y
K&C	0.00158	2.7	0.017	0.98	1.970	Y/N
RHT	0.00247	19.7	0.126	1.24	×	Y/N
Winfrith	0.00265	1.1	0.007	1.67	×	Y/N
CDPM	0.00157	0.5	0.003	0.98	×	Y/N

ELFORM 2	ZX-Stress (True)	ΔVolume at Peak	Volume % Diff.	Constraint Forces	Damage	Failure, Erosion?
	<i>GPa</i>	<i>mm³</i>	<i>%</i>	<i>kN</i>	-	-
CSCM	0.00137	1.2	0.008	0.86	0.990	Y/Y
K&C	0.00157	3.0	0.019	0.98	1.971	Y/N
RHT	0.00250	46.1	0.295	1.29	×	Y/N
Winfrith	×	×	×	×	×	×
CDPM	×	×	×	×	×	×

The CSCM and K&C true stress-true strain curves were identical for both element types, as shown in Figure 28. The only differences between the element types came in the RHT model. The curves were similar through 0.005 mm/mm strain, but then they diverged. The stress for the elform 1 element decreased until the end of the simulation and then failed. Conversely, the elform 2 curve quickly dropped off after its peak stress of 0.0025 GPa (363 psi) and failed at approximately 18 ms. The data for this model was “noisy”, as has been noted during the previous simulations.

Following the trend seen in previous simulations, the CSCM, K&C, and CDPM models all peaked near the same stress of 0.00157 GPa (228 psi). The RHT model had a

slightly higher peak stress of 0.00247 GPa (358 psi), and the Winfrith model had the highest peak stress of 0.00265 GPa (384 psi). All models failed during the simulation, at varying times. The RHT and CDPM models slowly lost the ability to transfer load and failed near the end of the simulation. The peak stresses were much lower than the expected values and therefore the forces were also low.

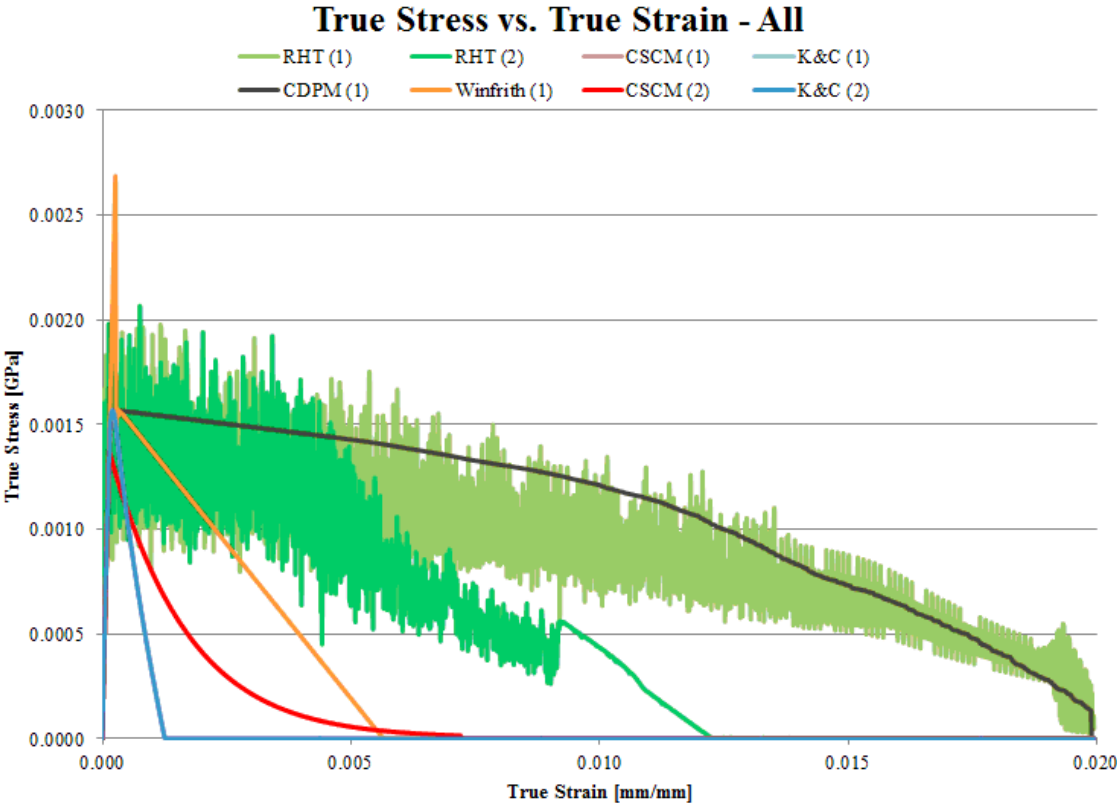


Figure 28. True Stress-Strain Plot for Shear Loading, Angled Condition

4.5 Discussion of Results

Single-element simulations were completed on five concrete material models for the different loading, constraint, and element type conditions. For the compression and tension loading conditions, there were two different constraint conditions and two different element types. For the shear loading condition, there was only one constraint condition and two different element types. Varying run times were present for the

simulations which were run on the UNL supercomputer, Tusker, Opetron 6272 2.1 GHz processors on 1 CPU, as shown in Table 8. The simulations with the higher run times were those in which the CDPM plastic solver did not converge. Note that tracking the run time was more helpful when larger-scale models were later evaluated.

Table 8. Simulation Run Times

<i>Loading</i>	<i>Constraints</i>	<i>Element Type</i>	<i>Run Time (MM:SS)</i>
Compression	Baseline	elform 1	00:11
		elform 2	00:12
	Constraint	elform 1	00:11
		elform 2	00:13
Tension	Baseline	elform 1	07:10
		elform 2	180:14
	Constraint	elform 1	00:35
		elform 2	00:14
Shear	Angled	elform 1	06:02
		elform 2	00:13

4.5.1 CSCM Model

The CSCM model constantly provided results near the expected values. The maximum stresses were generally near the expected values for the compression and tension loading cases. The elements failed in most of the simulations shortly after the peak was reached. The significant issue with the model was the erosion capability. For the tension and shear simulations, the damage value was near the threshold limit (1.0) and sometimes eroded at 0.990, but not always. It did, however, erode at lower damage values (0.990). This finding revealed an undesirable trend for an otherwise efficient material model. This result was further examined during the component testing efforts.

4.5.2 K&C Model

The K&C model performed the best in the compression and tension loading cases. The maximum stresses were similar with the model inputs, especially for the tension case when it was an exact match. Aside from the compression constraint case, the K&C element failed for each simulation. Although this material model does not have erosion capability, the elements did not transfer load shortly after the peak stress was reached. The only oddity with the model was observed with the excessive expansion that occurred in the compression load case with elform 2. The element continued to expand, even after the element had failed. This behavior should be addressed with an erosion capability.

4.5.3 RHT Model

The RHT model had consistent problems throughout all simulations. For compression, the RHT stresses and forces were much higher than the expected stress of 0.035 GPa (5076 psi). For tension, the RHT stresses of 0.00490 GPa (711 psi) were much higher than the expected stress of 0.00314 GPa (455 psi). The most obvious issue with this model came with the general shape of the stress-strain curves. For the tension and shear load cases, the curves had a lot of “noise” in the data, causing the curve to oscillate back and forth. In addition, significant energy occurred after the peak stress was reached, which was not expected for a brittle material, such as concrete. The noise in the stress-strain curve was an issue that was further evaluated during the component testing effort.

4.5.4 Winfrith Model

Although it did not fail, the Winfrith model performed well in the baseline compression case, and the maximum stress nearly matched the input stress for the model. For tension, the Winfrith stress of 0.00525 GPa (761 psi) was much higher than the

expected stress of 0.00314 GPa (455 psi). The Winfrith model was specifically tailored for compression, and the model did not perform well in tension. In addition, the model only worked for elform 1, which may become an issue in a larger component or full-scale system model if a different element type were needed. This evidence indicates that the Winfrith model may not be sufficiently robust and accurate enough for plain, unreinforced-concrete applications.

4.5.5 CDPM Model

The CDPM model nearly reached the target stresses of 0.035 GPa (5076 psi) and 0.00314 GPa (455 psi) for compression and tension but not for shear. Failure of the CDPM elements generally occurred at the end of the simulation and in a gradual manner. However, the CDPM model had problems like stability and convergence of the model. The simulations with the larger run times in Table 8 had problems with convergence of the plastic solver within LS-DYNA. This finding only occurred for the CDPM elements; therefore, those results should be carefully considered. The constrained tension and shear simulations were unable to complete due to the plastic solver not converging. For these simulations, results for the CDPM model were not obtained. This problem was seen in both tension and shear loading for both element types and all constraint cases. This issue incited a lack of confidence in this model to provide adequate results while using reasonable CPU time. This trend was further explored when component test simulations were completed.

4.5.6 Summary

The single-element simulations were helpful for understanding concrete behavior in five material models at the most basic level. The models were tested with a variety of

loading cases, constraint conditions, and element types. The compression and tension simulations were successful in that the CSCM, K&C and CDPM models provided maximum stresses that matched the input values of the simulation. However, the shear case was not perfected and may not provide results representative of the pure shear case. The results and trends of the compression and tension simulations were helpful in evaluating the effectiveness for the material models to simulate concrete behavior. This information was essential, but additional simulations were deemed necessary in order to further understand and investigate concrete behavior with the five material models.

CHAPTER 5 COMPRESSION SIMULATIONS ON EXTERNAL COMPONENT TESTS

5.1 Introduction

In addition to the single-element simulations, component simulations were completed in order to further evaluate the concrete material models. The first loading case for the component simulations was compression. To validate the performance of each of the five material models, external test data was desired while an internal component testing program had yet to be completed. Specifically, a search was performed to locate tests involving a concrete cylinder loaded in compression where adequate stress and strain data was acquired and reported. The cylinder was loaded until 10% of peak load was reached. A stress-strain test curve was obtained from a study by Lee and Willam [42] that focused on the pre- and post-peak response phenomena when concrete cylinders were loaded, unloaded, and reloaded in uniaxial compression, as shown in Figure 29. The area under the physical test curve was 7.00×10^{-2} k/in. (1.23×10^{-2} kN/mm).

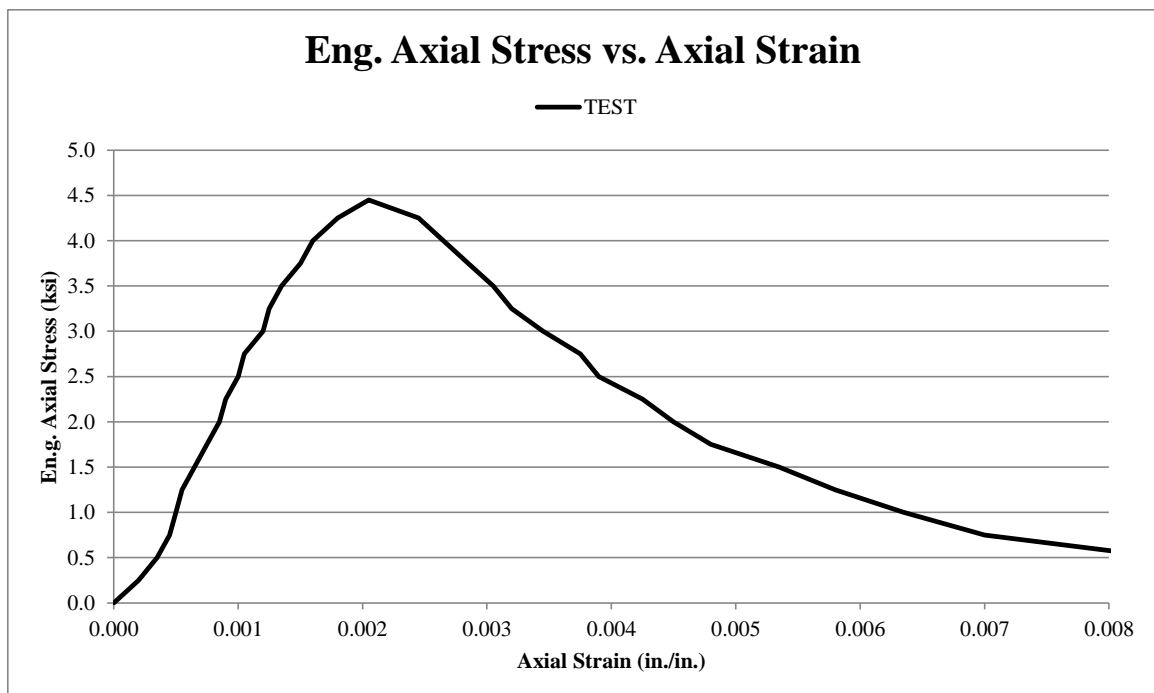


Figure 29. Compression Stress-Strain Test Results [42]

The study included three different test specimen sizes, and a 5.4-in. (137-mm) height and 3.0-in. (76-mm) diameter cylinder was used for simulation effort. The maximum aggregate size of the cylinders was $\frac{3}{8}$ in. (9.5 mm), and the concrete had a compressive strength of 4.5 ksi (30.7 MPa). The cylinders were loaded using a fixed loading plate at a deformation rate of 1.7×10^{-5} in./s (4.2×10^{-4} mm/s) with rubber pads placed between the cylinder and loading plates. The axial force was measured with a load cell, and engineering axial stress was calculated using the force and original cross-sectional area. In the experiment, axial strains were taken from readings of two axial LVDTs.

5.2 Simulation Data Evaluation Process

A displacement rate analysis was completed for each of the five material models to determine the simulation loading rate. The test displacement rate was much slower than recommended for use in explicit LS-DYNA analyses. A linear displacement function was assumed. Potential displacement rates ranged from 4.5 in./s (114.3 mm/s) to 4.5×10^{-3} in./s (0.11 mm/s), and the goal was to find convergence in the stress-strain curves. Once convergence was reached, this displacement rate would be considered optimum. For all material models, the convergence was found to be 5,000 ms.

The intent of the cylinder simulations was to compare the simulation results from each of the five material models to the acquired test results obtained from the external source. The cylinders in the model had a 5.4-in. (137-mm) height and 3.0-in. (76-mm) diameter. A *RIGIDWALL_PLANAR was in place under the cylinders and fixed. A *RIGIDWALL_GEOMETRIC was displaced in the z-axis down onto the tops of the cylinders. The displacement rate was increased linearly until the end of the simulation.

Cross-sections were placed through the center of the cylinders in order to measure forces for use in computing stresses. An overview of the model is shown in Figure 30.

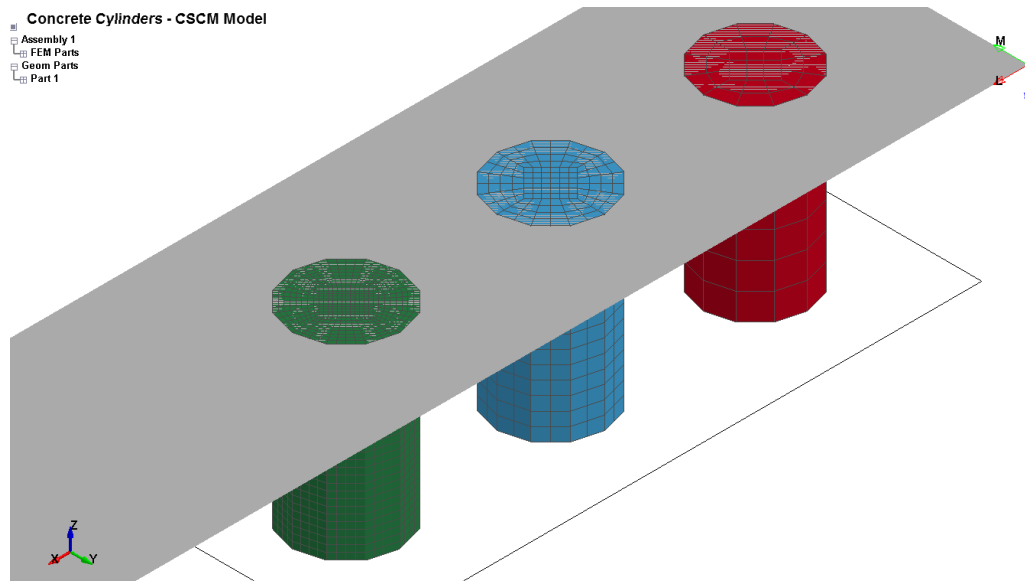


Figure 30. Overview of External Compression Simulation

Variations were made to the model as well as to the default material inputs in order to find a combination that best matched the published test curve, as shown in Figure 29. Multiple cylinders were used in the same simulation to directly compare variations in the model and material input parameters. The model variations included: mesh size; friction between the loading plate and the cylinder; and element type. Three different mesh sizes were evaluated: $\frac{3}{4}$ -in. (19-mm); $\frac{3}{8}$ -in. (9.5-mm); and $\frac{3}{16}$ -in. (4.8-mm). Although each of the three sizes was different, they all had the same mesh pattern (i.e., the outer diameter was configured with 12 linear chord segments rather than a different chord for each outer element), as shown in Figure 31. The friction variations included: no friction between the rigid wall and cylinder; a friction coefficient of 0.105; and the cylinder fully fixed to the rigid wall. The 0.105 friction coefficient corresponded to an average test value which involved rubber pads between loading plates and a cylinder

[64]. Two different element types were considered: elform 1 (a single-point integration element) and elform 2 (a fully-integrated element). Additionally, if unreasonable hourglass energy was present, attempts were made to control it by changing the default hourglass control to types 4, 5, and 6 using *HOURGLASS.

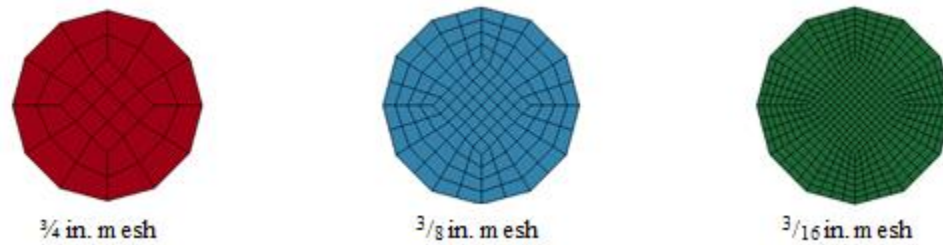


Figure 31. Mesh Sizes for Compression Cylinders

Material input parameter variations were different for each material model, as shown in Table 9. For the CSCM model, variations included compressive, tensile, and shear fracture energies (G_{fc} , G_{ft} , and G_{fs}), ERODE, repow, and recov. Fracture energy is defined in the CSCM User's Manual [51] as the area under the stress-displacement curve after peak strength. The first step in evaluating the fracture energy parameter was to review the ratios between the compressive, tensile, and shear fracture energies. Ratios between the shear and tensile fracture energies (G_{fs}/G_{ft}) and compressive and tensile fracture energies (G_{fc}/G_{ft}) were suggested by Murray [51]: $\frac{G_{fs}}{G_{ft}} = 0.5$ and $\frac{G_{fc}}{G_{ft}} = 50$. The default ratio for the material model is $\frac{G_{fs}}{G_{ft}} = 1$ and $\frac{G_{fc}}{G_{ft}} = 100$. The ERODE parameter defines deformation of the element when both the damage threshold of 0.99 and the maximum principal strains are exceeded. For these simulations, the ERODE parameter was varied between 1.0 and 1.1. The next parameter that was varied was repow, the power for the equation defining fracture energy with rate effects. For these simulations,

the repow parameter was varied between 0 and 1. Finally, the recov parameter, which defines the recovery modulus in compression, was evaluated. This parameter was varied between 0 and 1, as well as 10 and 11. When set between 0 and 1, the recovery was based on the sign of the pressure invariant only. When set between 10 and 11, recovery was based on the sign of the pressure invariant and volumetric strain.

For the K&C model, the compressive damage scaling factor, B_1 , and rate effects using the LCRATE parameter were changed. The compressive damage scaling factor is a basic parameter of the material model that adjusts for element size and its default value is 1.6. The parameter was varied among three different ranges: 0-1; 1-2; and 2-3. The second material input parameter that was investigated included strain rate effects using the LCRATE parameter. The model can either have strain rate effects turned on or off. When the strain rate effects are turned on in the K&C model, an associated dynamic increase factor (DIF) is used, which is based on the strain rate of the model. A set of strain rate vs. enhancement factor values are inputted into the K&C material model as a load curve.

For the RHT model, the relative shear strength and relative tensile strength parameters could be varied, but were not for any simulations. Potential variations for the Winfrith model included changes to the f_e parameter representing fracture energy and crack width as well as the pressure vs. volume relationship.

Finally, parameters that could be changed in the CDPM included the hardening parameter and the tensile strength threshold value. However, varying these parameters resulted in errors in the simulations and therefore the only variations made in these material model simulations were the element type, friction, and mesh size.

Table 9. Material Model Input Changes for Simulation

CSCM		K&C		RHT		Winfrith		CDPM	
Parameter	Inputs	Parameter	Inputs	Parameter	Inputs	Parameter	Inputs	Parameter	Inputs
G _{fs}	0.5G _{ft}	B ₁ (comp. damage scale factor)	0.0	N/A	fe (fracture energy)	0.00	N/A		
	G _{ft}		0.2			0.01			
G _{fc}	50 G _{ft}		0.4			0.10			
	100 G _{ft}		0.6			0.025			
ERODE	1.000		0.8			0.050			
	1.025		1.0			0.075			
	1.050		1.2			0.25			
	1.075		1.4			0.50			
	1.100		1.6			0.75			
repow	0.0		1.8						
	0.5		2.0						
	1.0		2.2						
recov	0.0		2.4						
	0.5		2.6						
	1.0		2.8						
	10.0		3.0						
	10.5	rate effects off							
	11.0	LCRATE	for 31 MPa concrete						
		for 45.4 MPa concrete							

Once the different variations were made to the model and material input parameters, the simulation results were compared to the external physical test data. Trends in the stress-strain curves and damage profiles were also tracked. The stress-strain curves were compared between the simulations and physical test. Engineering stress from the simulation was computed from the cross-section force divided by the original cross-sectional area. The axial strain was found as the axial displacement divided by the height of the cylinder. The simulated stress and strain results were plotted along against the physical test results. The second evaluation of the material models involved the animation of the compressed cylinder, including element deletion pattern (only available in CSCM model) and cylinder damage profile (only available in the CSCM and K&C models).

5.3 CSCM Model – Simulation Results

All simulations using the CSCM model required 2 to 3 hours to complete. The initial simulations with the CSCM model varied element type, friction, and mesh. Later, material input variations included the ERODE, repow, and recov parameters.

5.3.1 Element Type

Two element types, elform 1 and 2, were evaluated with a friction of 0.105 and a $\frac{3}{8}$ -in. (9.5-mm) mesh size. For this effort, a significant difference in performance was observed between the two element types. Although no major hourglass energy were observed with either element type, low internal energy levels occurred in the elform 2 cylinder. The modulus of elasticity for both the simulation and test matched well through the majority of the elastic range, but started to diverge near peak stress. The stress-strain curves differed by element formulation, as shown in Figure 32. The peak strengths for both element types were only slightly higher than observed in the test, but it occurred at a lower strain than observed in the test. Once the peak strength was reached for the elform 1 simulation, the stress continued at nearly the same level over the course of the simulation. The elform 2 simulation had immediate softening after reaching peak stress, but it had a more rapid softening than observed in the test.

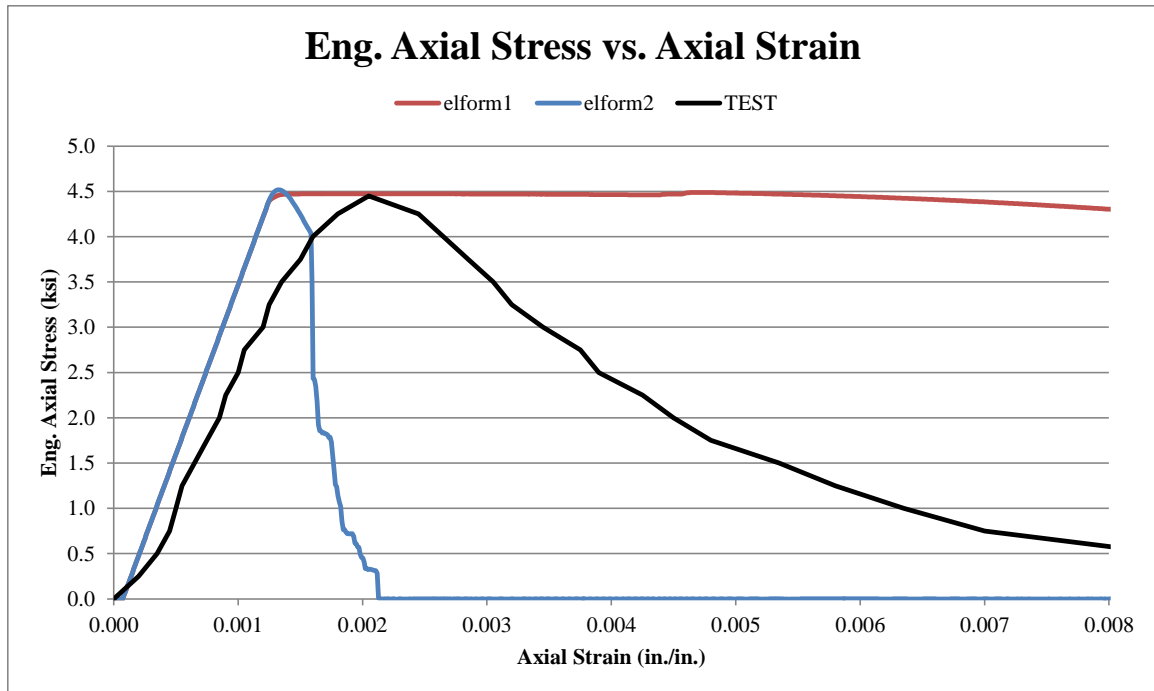


Figure 32. Compression Stress-Strain for Elform Simulation, CSCM Model

In the animation of the simulation, the elform 2 cylinder sheared at approximately a 45-degree angle near peak stress and broke into two major pieces, as shown in Figure 33. The cylinder fractured despite the highest damage value in the model only reached 0.77, far below the 1.0 threshold. This irregularity indicates the damage formulation was not accurate for elform 2 using the selected input parameters and model configuration. It was determined that elform 1 would be the best element type for this material model, because it provided a more stable behavior despite not having softening. Additionally, this material model was primarily developed for used with elform 1, as recommended in the material model user's manual [65]. Elform 1 was used for the remainder of the simulations.

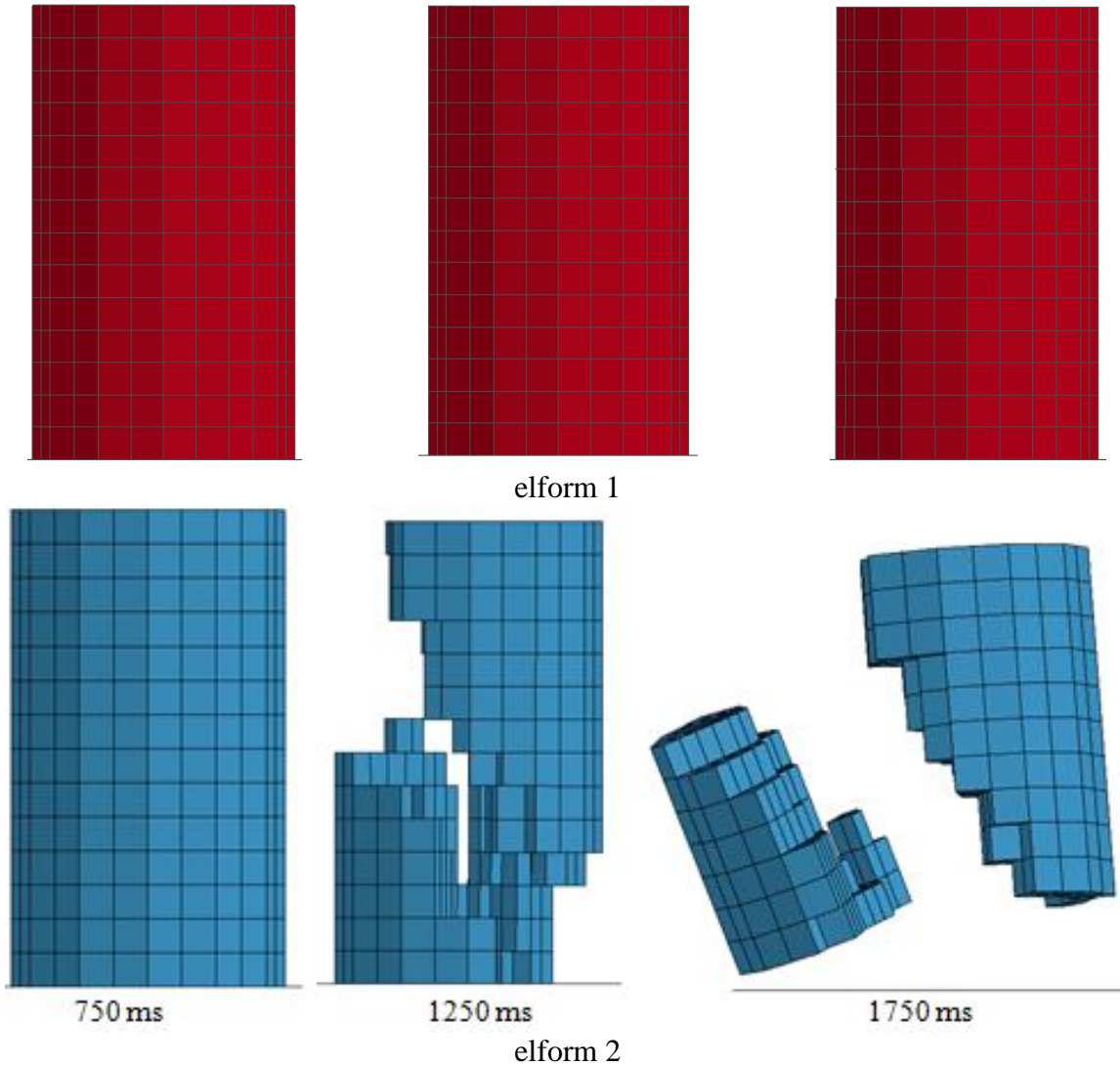


Figure 33. Compression Fracture Pattern of Element Type Cylinders, CSCM Model

5.3.2 Rigid Wall-Cylinder Friction

For the friction simulation effort, hourglass energies were minimal, and there was a slight difference between the modulus of elasticity observed in the test and simulations. The ‘no friction’ and ‘0.105 friction’ between the rigid wall and cylinder cases were very similar and closely matched the elform 1 stress-strain results shown in Figure 32. The ‘fully-fixed friction’ case resulted in a slightly higher peak strength and a slightly lower stress during softening as compared to the other two friction cases. The ‘fully fixed

friction' condition was ruled out, because it was deemed unrealistic since cylinder testing allows for some movement at the compression interfaces. Since there should be some friction between the cylinder and loading plates, the 'no friction' case was ruled out. No elements deleted in this simulation effort, but the elements did appear to become unstable during softening, as shown in Figure 34. This behavior was not only limited to the CSCM material model. The highest damage values were discovered in the 'fully fixed friction' cylinder. There were also differences in the physical deformation behavior. The '0.105 friction' value was used moving forward.

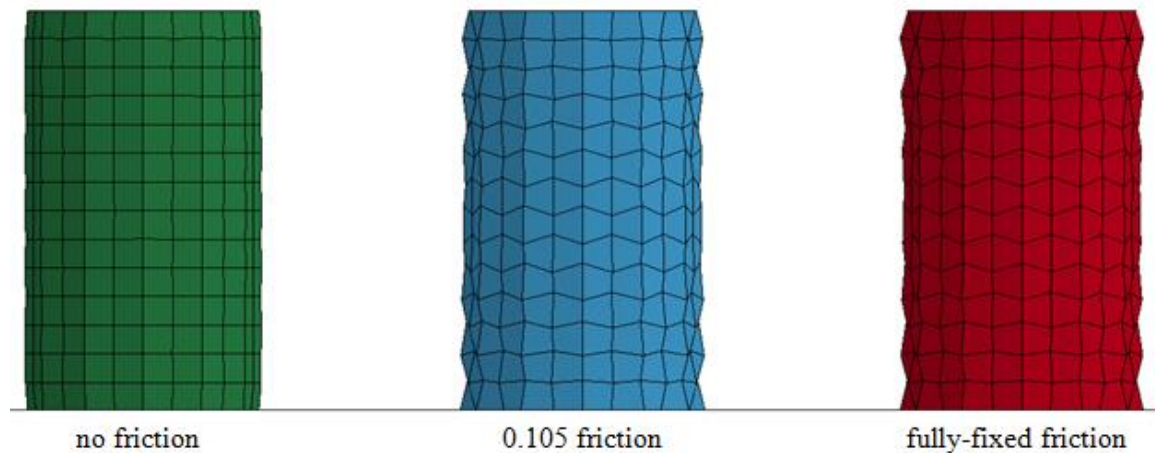


Figure 34. Compression Damage Pattern for Friction Simulation, CSCM Model

5.3.3 Mesh

The simulation effort also investigated the use of $\frac{3}{4}$ -in. (19-mm), $\frac{3}{8}$ -in. (9.5-mm), and $\frac{3}{16}$ -in. (4.8-mm) mesh sizes, as shown in Figure 31. Smaller mesh sizes were not investigated due to concerns for excessive simulation run times and being impractical for use in modeling large concrete structure subjected to impact loading. In the mesh simulation study, there were no hourglass issues, although the modulus of elasticity observed in the simulations, 2531 ksi (17.4 GPa) was greater than in the test modulus, 2171 ksi (15.0 GPa). Each of the three mesh sizes revealed different stress-strain

behavior, which is odd given the fracture energy should remain constant regardless of mesh size. For the $\frac{3}{16}$ -in. (4.8-mm) mesh, the stress peaked at 4.55 ksi (31.7 MPa) and continued at the same level until the end of the simulation, as shown in Figure 35. There was a slight decrease in stress after peak was reached with the $\frac{3}{8}$ -in. (9.5-mm) mesh, similar to the stress-strain behavior using elform 1 in the element type simulation effort. The “jump” in stress for both the $\frac{3}{4}$ -in. (19-mm) and $\frac{3}{8}$ -in. (9.5-mm) mesh sizes was unique to this simulation effort and did not appear in other simulations.

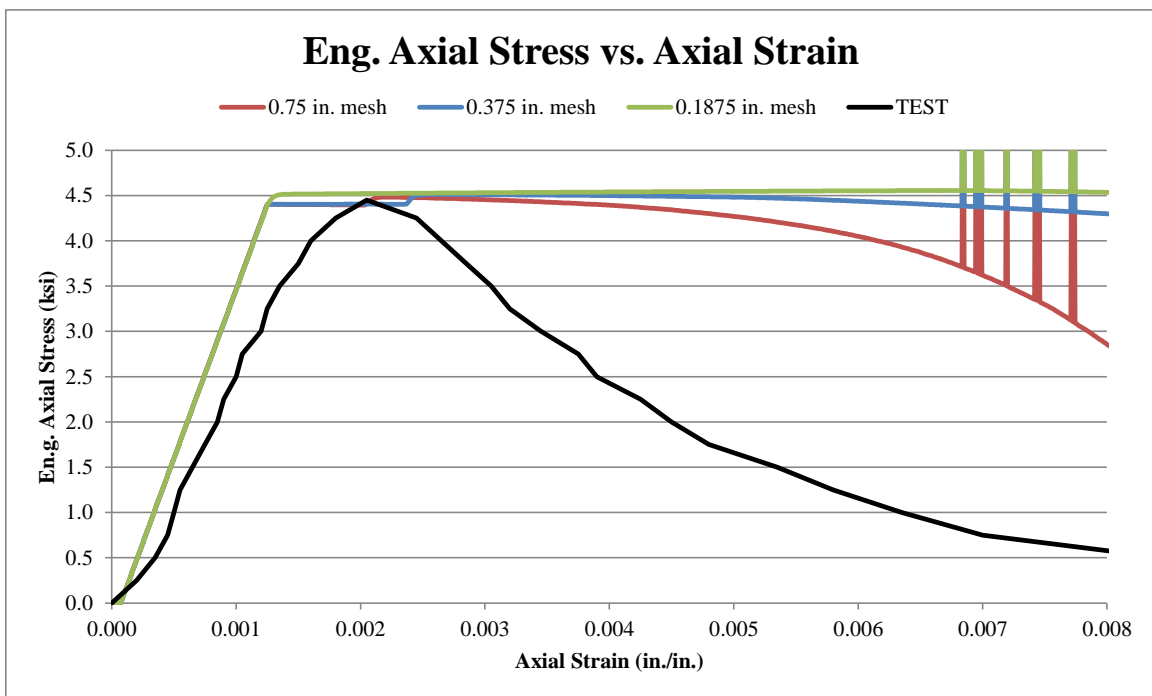


Figure 35. Compression Stress-Strain Plot for Mesh Simulation, CSCM Model

The stress-strain behavior for a $\frac{3}{4}$ -in. (19-mm) mesh size had the most softening among the three different mesh sizes. The stress in this cylinder decreased from 4.6 ksi (31.7 MPa) to 2.9 ksi (20 MPa) by the end of the simulation at 5000 ms. The compressed cylinder animation revealed high damage with the $\frac{3}{4}$ -in. (19-mm) mesh, as shown in Figure 36. It was determined that the $\frac{3}{16}$ -in. (4.8-mm) mesh size was deemed to be too

fine and resulted in a run time of 8.5 hours, as compared to the previous run times of 2 to 3 hours. The 3/4-in. (19-mm) mesh was too coarse; the effect of two elements failing resulted in a significantly different stress-strain curve and damage profile. Therefore, the 3/8-in. (9.5-mm) mesh was selected as optimum for all CSCM simulations using the current input parameters and model configuration.

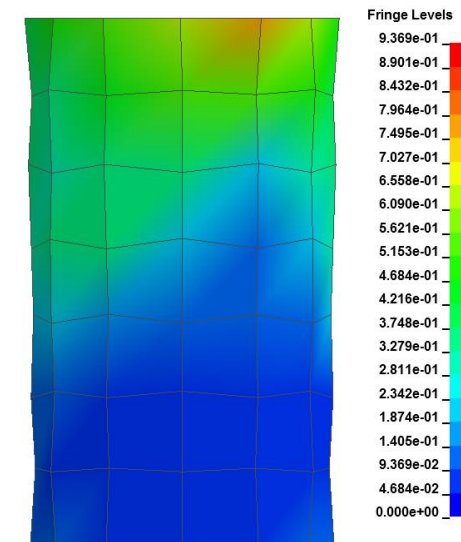


Figure 36. Compression Damage Contours for Mesh Simulation (3/4-in. [19-mm] mesh), CSCM Model

5.3.4 ERODE, repow, and recov

After completion of the initial simulations which investigated element type, friction, and mesh size, changes were made to the material input parameters in order to track trends and attempt to better match the simulation and physical test results. The first three changes were made to the ERODE, repow, and recov parameters.

Ultimately, there was not much difference in simulation results when the ERODE, repow, and recov values were varied as shown in Figure 37 for the ERODE parameter. The repow and recov had similar results. As observed in some initial simulations, there was not much softening after the peak stress of 4.6 ksi (31.7 MPa) was reached.

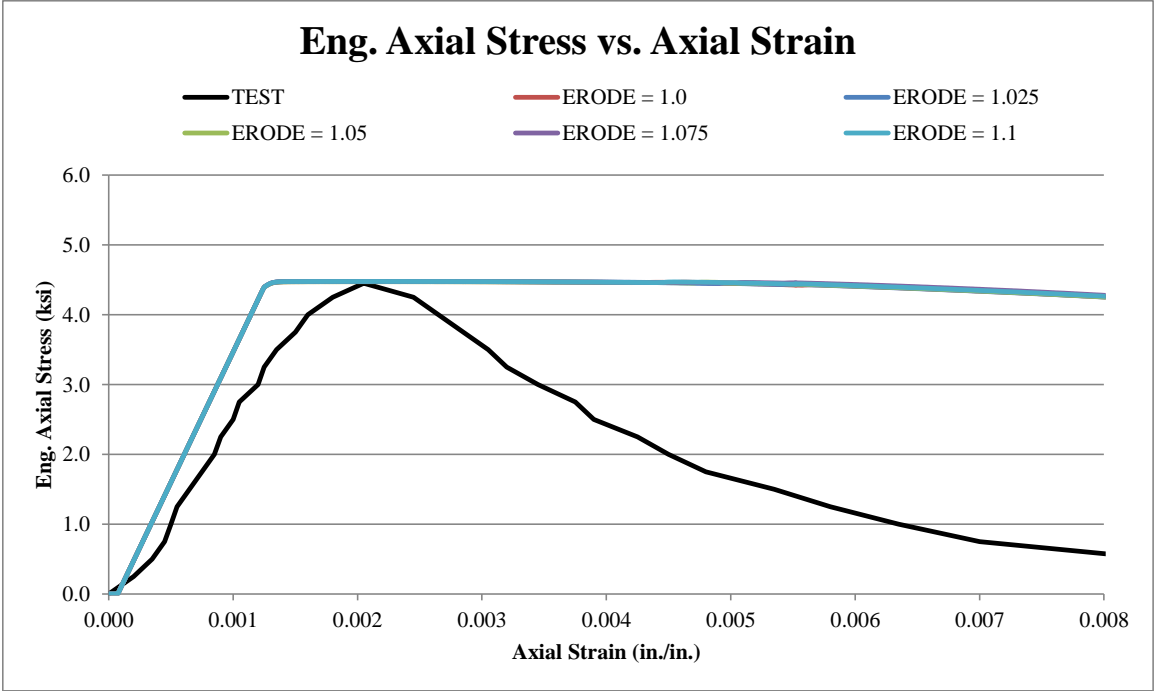


Figure 37. Compression Stress-Strain for ERODE Simulation, CSCM Model

5.3.5 Fracture Energy

The shear-tensile fracture energy and compressive-tensile fracture energy were simulated separately, as a combination of the two ratios, and using the default case. More softening occurred when $G_{fc} = 50G_{ft}$, as shown in Figure 38. This finding may have occurred as the major loading condition was compression, and the shear and tension fracture energies appeared to be unaffected. Although some softening occurred, additional softening may occur with a change in the fracture energies.

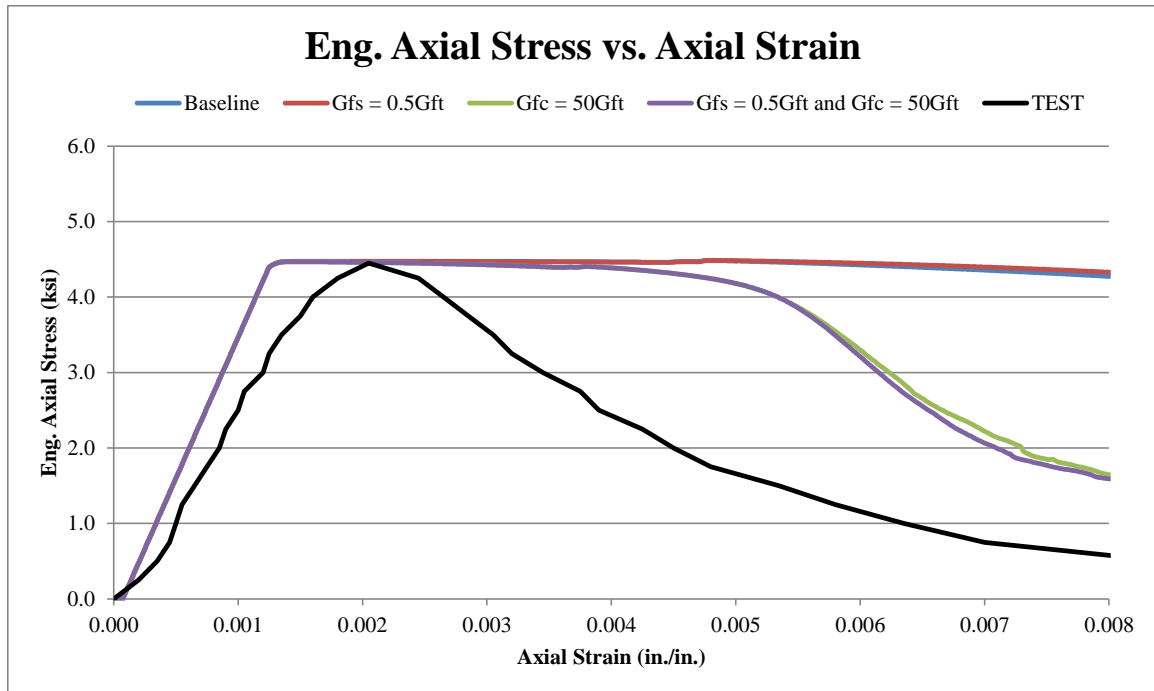


Figure 38. Compression Stress-Strain for Fracture Energy Simulation, CSCM Model

The compressive fracture energy, G_{fc} , was arbitrarily decreased from the default value [3.27×10^{-2} k/in. (5.73×10^{-3} kN/mm)] with the hope of producing more post-peak softening. The compressive fracture energy was decreased iteratively from 3.27×10^{-2} k/in. (5.73×10^{-3} kN/mm) to 5.56×10^{-3} k/in. (9.74×10^{-4} kN/mm), as shown in Figure 39. The behavior in the stress-strain curves confirms that as the compressive fracture energy is lowered, the softening will initiate at lower strains. These fracture energies were arbitrary choices and were not calculated using the fracture energy definition. The area under the physical test curve, 7.00×10^{-2} k/in. (1.23×10^{-2} kN/mm), was larger than the arbitrary values that were simulated. Therefore, the test had less softening, which was confirmed in the simulations. Therefore, the default fracture energy values were deemed unreliable and provided a poor estimation of softening behavior.

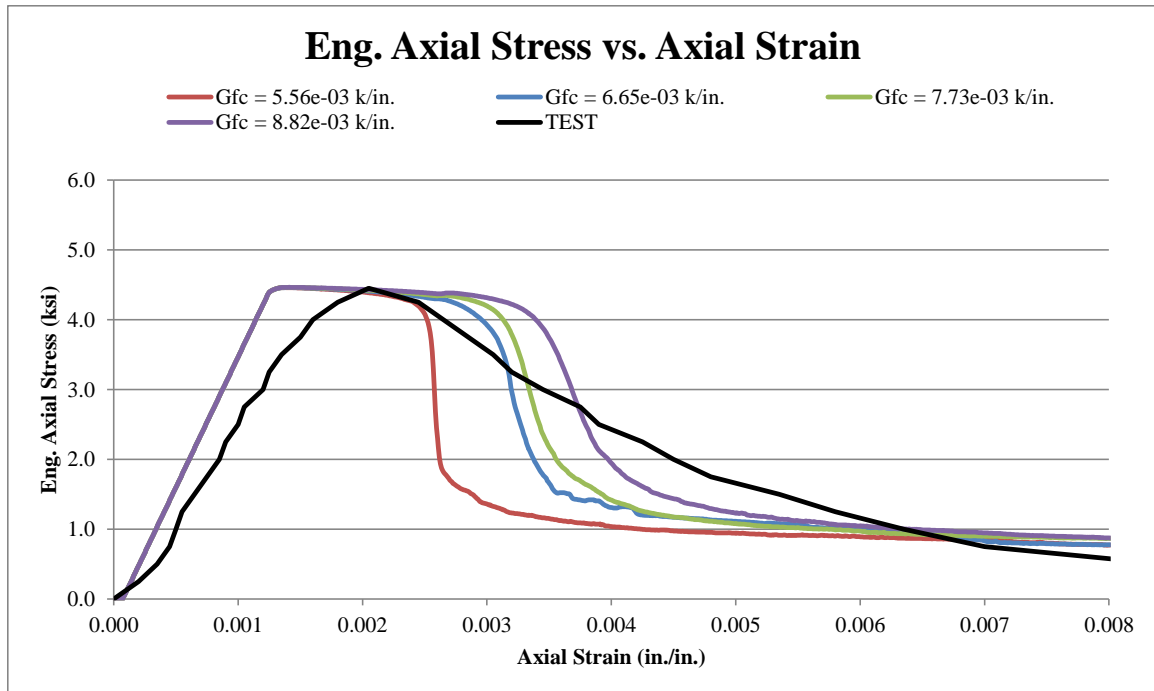


Figure 39. Compression Stress-Strain for Decreased Fracture Energy Simulation, CSCM Model

5.3.6 Hourglass Controls

Despite the positive influence of decreasing the compressive fracture energies, hourglass energies increased when the compressive fracture energy was altered. In an attempt to decrease hourglass energy, different hourglass control types were evaluated, specifically types 4, 5, and 6. Hourglass control types 4 and 5 are stiffness formulations for solids, while type 6 is an assumed strain stiffness formulation. These specific controls were chosen because they are stiffness controls for solids. The goal was to decrease hourglass energies without significantly affecting the stress-strain behavior and failure patterns. All hourglass control types nearly eliminated the high hourglass energies, but they did affect the stress-strain results. The simulation peak stresses were now at 4.5 ksi (31.0 MPa) which is above the physical test result, due to the elimination of hourglass energy. However, there was limited differences between the stress-strain behavior for the

three hourglass control types. Some minute differences in cylinder failure patterns were observed with different hourglass control types.

5.3.7 Final Selection

Since there was not much variability between the hourglass control types, future simulations with the CSCM model used hourglass control type 6 (HG6), which was commonly used in the CSCM Evaluation Manual [66]. Due to the hourglass control increasing the stress-strain results, new fracture energy values were needed. An iterative process was again used to determine the optimum fracture energies. Multiple iterations were completed before the best compressive fracture energy, G_{fc} , was found, 4.48×10^{-3} k/in. (7.85×10^{-4} kN/mm). As shown in Figure 40, the stress-strain behavior with these fracture energies was very close to the physical test result. The modulus of elasticity for the simulation and test curves did not match, as observed in previous simulations.

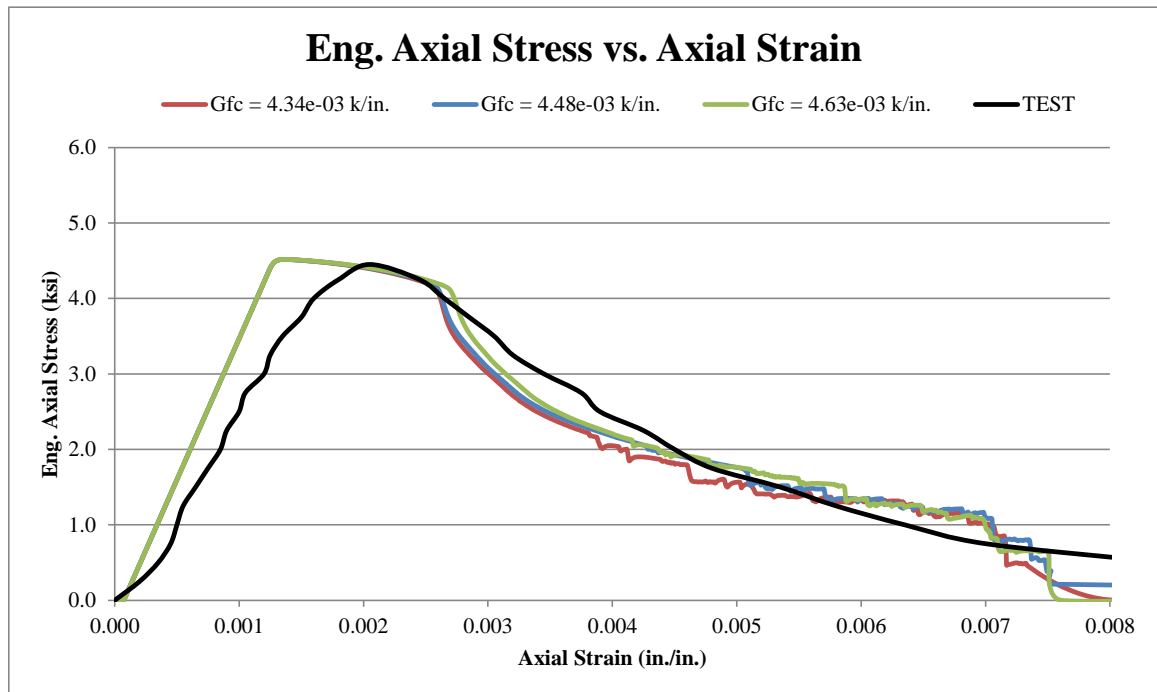


Figure 40. Compression Stress-Strain for HG6 Fracture Energy Simulation, CSCM Model

In the damage profiles, the 45-degree shear plane across the cylinder, as shown in Figure 41, evolved throughout the simulation run. Near the end of the simulation at 5000 ms, the cylinder eroded completely, which was not expected based on the damage profile of the cylinder.

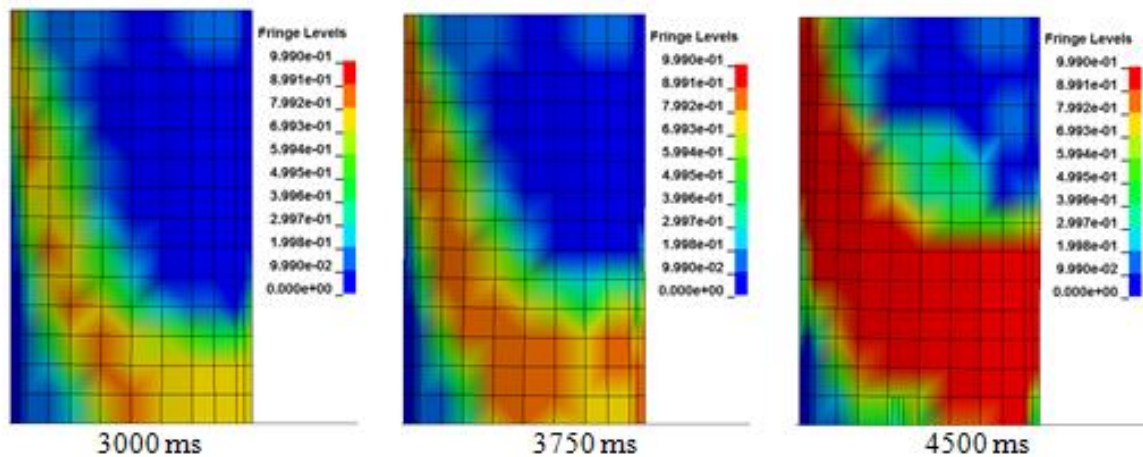


Figure 41. Compression Damage Profiles for Final Combination, CSCM Model

5.3.8 Model Instabilities

The first of the two major model instabilities was excessive element deletion, as shown in Figure 42. This deletion tendency occurred between compressive fracture energies of 5.34×10^{-3} k/in. (9.35×10^{-4} kN/mm) and 3.05×10^{-3} k/in. (5.35×10^{-4} kN/mm). Concrete cylinders simulated with compressive fracture energies outside of this range remained stable. Excessive deletion did not occur prior to using hourglass energy controls with decreased fracture energies. Instabilities sometimes occurred even when the stress-strain behavior matched well. Thus, these fracture energies provided a good representation for the validation effort. The cylinders did not delete when certain parameters were used in conjunction with the new fracture energy values. These parameters included an ERODE value of 1.0 and recov values of 1.0, 10.0, 10.5, and 11.0.

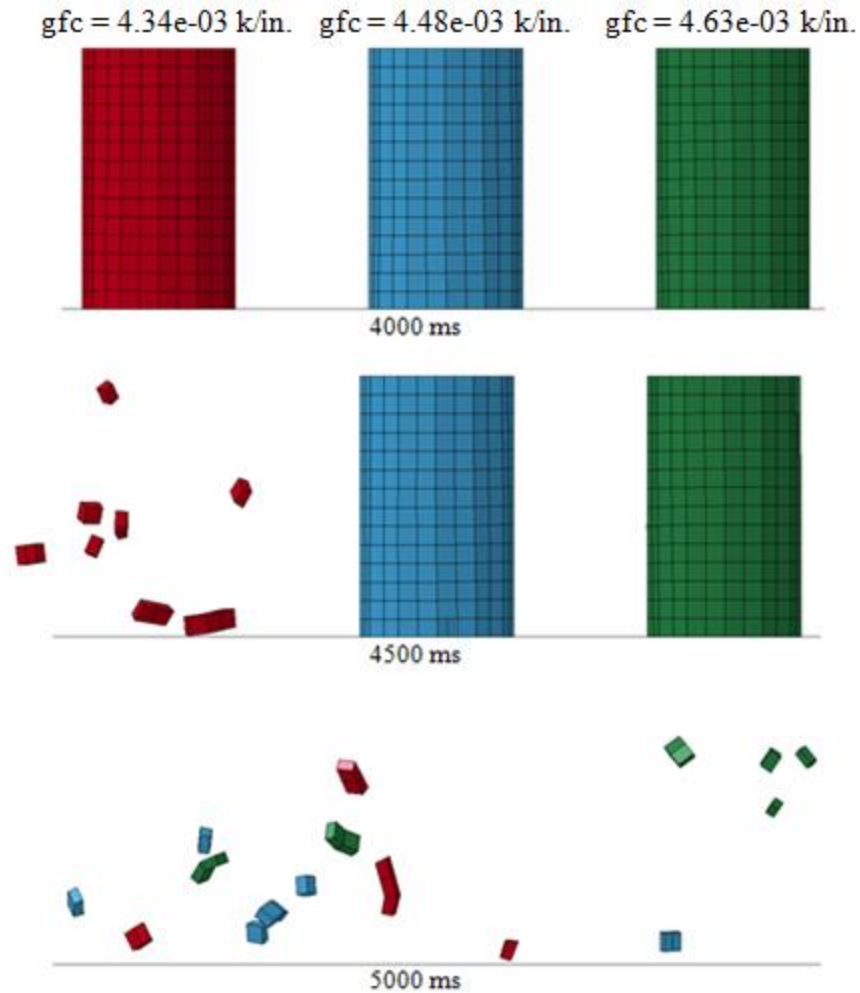


Figure 42. Compression Part Deletion with HG6 Fracture Energy Simulation, CSCM Model

The second instability occurred when parameters such as ERODE, repow, and recov changed within the material input deck. It was noted in previous simulations that cylinders with the same material properties were not producing identical stress-strain curves, as would be expected. To investigate this finding, simulations were set up with multiple cylinders having the exact same material properties in the same model for ERODE, repow, and recov. In the fringe plots at time 900 ms depicted in Figure 43, all five cylinders had the same ERODE value, 1.0, yet different damage profiles. They did have the same 45 degree shear planes. The stress-strain curves also did not match,

although the curves were the same until near the end of the simulation at 5000 ms. This behavior was important to note and was re-evaluated when a larger model was simulated using this material model.

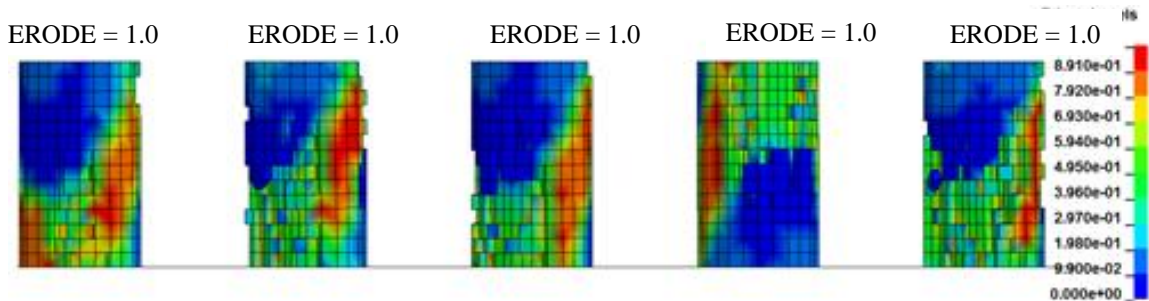


Figure 43. Compression Damage Profiles for ERODE Simulation, CSCM Model

In order to try to resolve these instability issues, a new mesh was created for the cylinders. The outside edges of the cylinders were smoothed slightly to eliminate potential stress concentrations that may develop at sharp corners in the original mesh pattern. This new mesh pattern was used in additional fracture energy simulation iterations as well as in a new mesh simulation effort. The new mesh did not show any significant differences in the stress-strain behavior and animations of the simulations. Therefore, the previous mesh pattern was maintained and considered acceptable.

5.4 K&C Model – Simulation Results

The initial simulations with the K&C model included element type, friction, and mesh size investigations. None of these simulations had major hourglass energy issues that required additional attention. Additional material input parameters were evaluated, including the compressive damage scaling factor and strain rate effects using the LCRATE parameter.

5.4.1 Element Type

When the two different element types were investigated, differences in model performance was observed. Both element types had similar behavior through peak stress of 4.4 ksi (30.3 MPa), but after peak stress was reached, the stress-strain behavior with elform 1 curve softened more than observed with elform 2, as shown in Figure 44. This trend was contrary to the element type behavior found with the CSCM model. The peak strength in both simulations matched well with the physical test result of 4.5 ksi (31.0 MPa). The modulus of elasticity for each of the two simulations was 2676 ksi (18.5 GPa), but it was greater than the modulus of elasticity of 2171 ksi (15.0 GPa) observed in the physical test. There was not much softening observed for elform 2 as the stress at the end of the simulation was approximately 3.5 ksi (24.1 MPa).

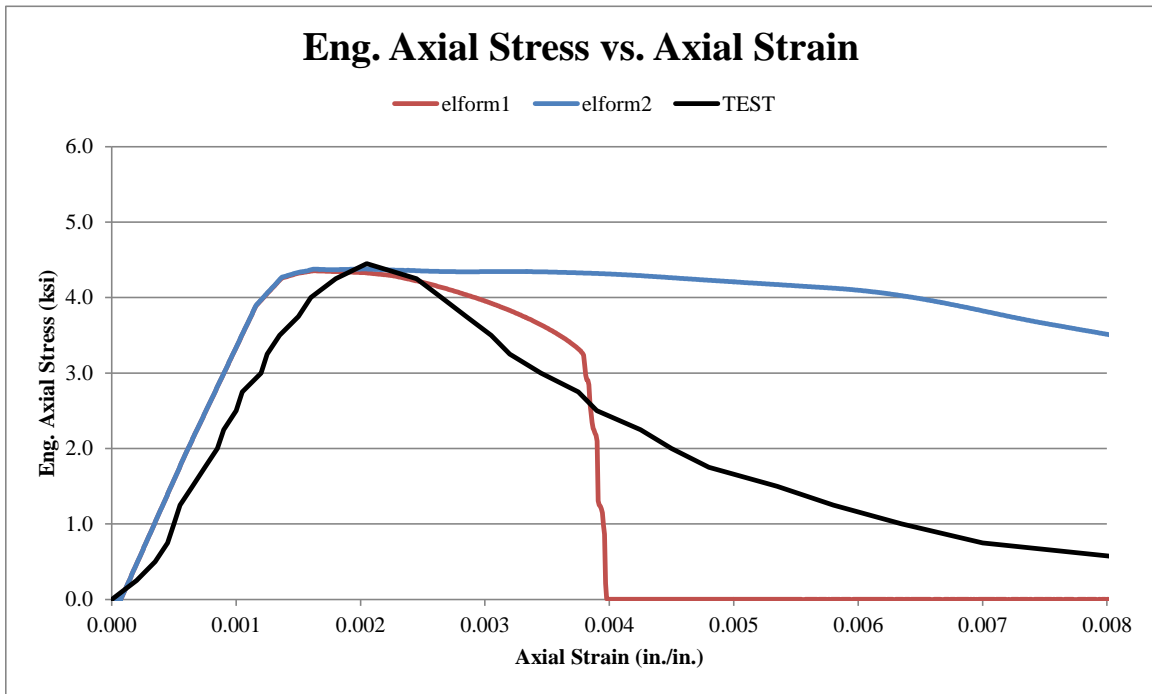


Figure 44. Compression Stress-Strain for Elform Simulation, K&C Model

In terms of animation, there was no significant deformation in the cylinders, with some deformation occurring near the top of the cylinder. Although the stress-strain behavior did drop to zero for the elform 1 simulation, the cylinder did not delete; since element deletion is not a capability in this material model. Due to the presence of softening, elform 1 was preferred.

5.4.2 Rigid Wall-Cylinder Friction

In the friction simulation, the modulus of elasticity for the physical test was 2171 ksi (15.0 GPa) and in the simulations was 2692 ksi (18.6 GPa) did not match well in the elastic region. When examining at the stress-strain results, the ‘no friction’ and ‘0.105 friction’ cases were nearly the same, with only a minor difference when the force dropped to zero, as shown in Figure 45. The ‘fully-fixed friction’ cylinder had the highest stresses among the three friction cases. Additionally, the peak strength of the ‘fully-fixed friction’ cylinder was 4.7 ksi (32.4 MPa), which was higher than observed in the other simulations and the physical test. For this reason, the 0.105 friction case was preferred.

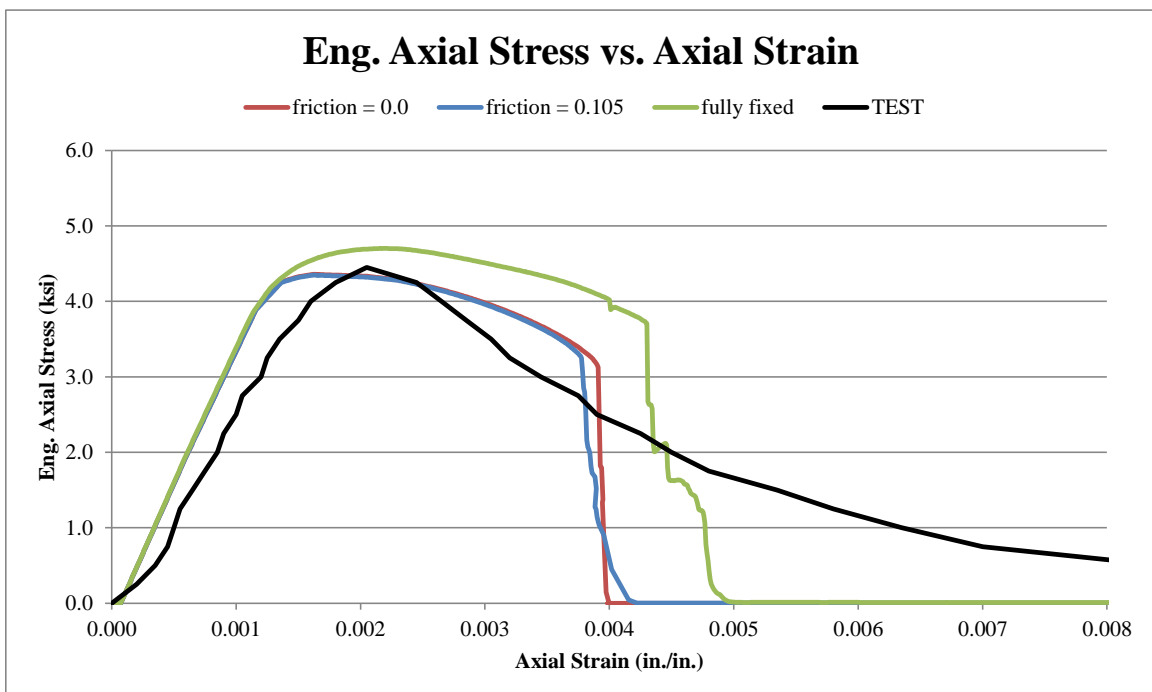


Figure 45. Compression Stress-Strain for Friction Simulation, K&C Model

In the animation of the cylinders, the ‘no friction’ and ‘0.105 friction’ cylinders had deformations near the top of the cylinders. The ‘fully-fixed friction’ cylinder revealed that most of its deformation occurred near the middle of the cylinder.

5.4.3 Mesh

In the mesh-size simulations, the same difference in the modulus of elasticity was observed between the simulation and physical test results. In the stress-strain curves, all mesh sizes behaved in a similar way and were similar to the ‘0.105 friction’ case shown in Figure 45. The peak strengths of 4.4 ksi (30.3 MPa) were near the physical test peak stress of 4.5 ksi (31.0 MPa) and the simulated stress dropped rapidly to zero after some softening had occurred, as seen in Figure 46.

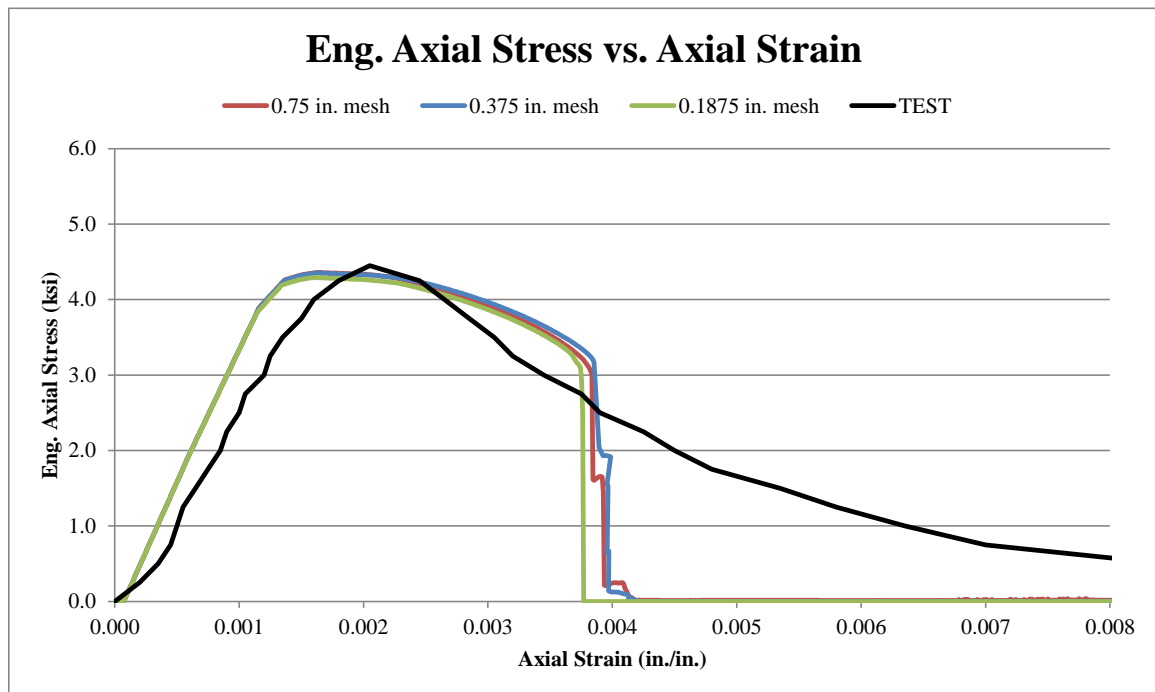


Figure 46. Compression Stress-Strain for Mesh Simulation, K&C Model

Since there were no noticeable differences in the stress-strain curves, the cylinder animation was the deciding factor. The $\frac{3}{16}$ -in. (4.8-mm) mesh size resulted in larger deflection than the other mesh sizes. At the end of the simulation, bulging occurred at the top and bottom of the cylinder to the point when the cylinder had an hourglass shape. Coincidentally, hourglass energy was 143% of the internal energy in the finest mesh at failure, potentially ruling it out as a mesh size for this material model. The $\frac{3}{4}$ -in. (19-mm) mesh again had too few elements through the cross-section to show exact deformations, so the $\frac{3}{8}$ -in. (9.5-mm) mesh was preferred at this time.

5.4.4 Compressive Damage Scaling Factor

After the initial simulations were complete, two material input parameters were investigated to better understand their effect on simulation results. The first parameter was the compressive damage scaling factor, B_1 . The default value for this parameter is 1.6. A range of 1.0 to 2.0 was analyzed for this parameter, as shown in Figure 47. None of the simulated stress-strain curves matched the physical test result very well, but they all had peak stresses near the physical test peak stress. As the B_1 value increased, the slope of the softening region became more flat and softened at higher strains.

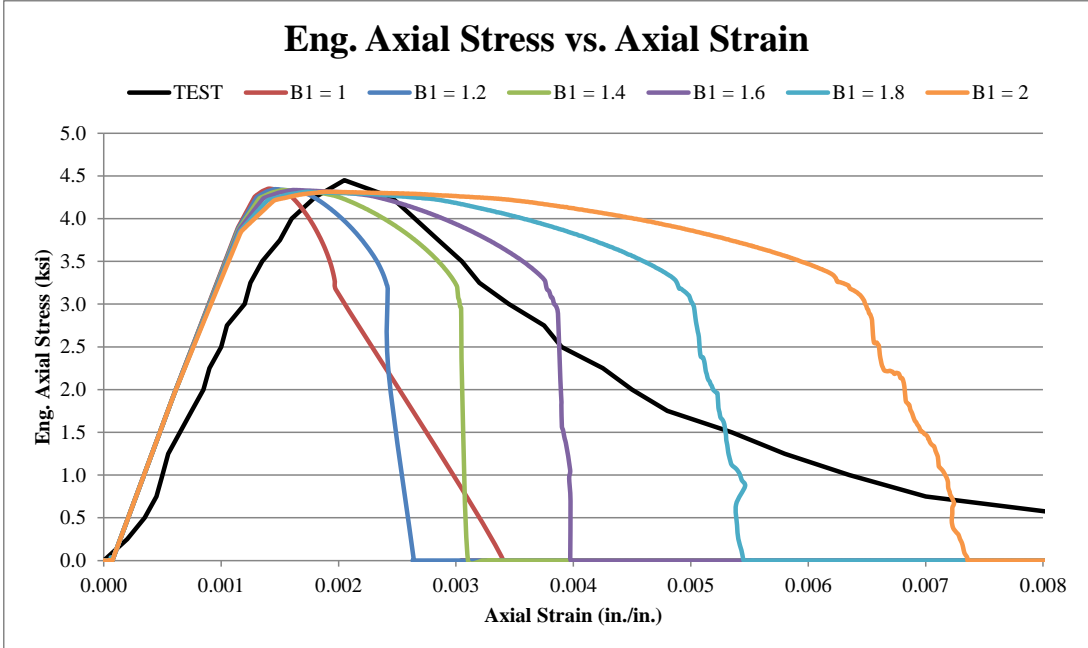


Figure 47. Compression Stress-Strain for B₁ Simulation, K&C Model

In the animation of the cylinders, the B₁ = 1.0 cylinder slid outside the plane of loading during the course of the simulation, as shown in Figure 48. The 1.2 and 1.4 cylinders slid as well and had the largest deformation near the top of the cylinder. All cylinders experienced bulging near their tops. Based on the stress-strain and physical behavior of the simulated cylinders, the default compressive damage scaling factor of 1.6 was preferred. Ranges from 0.0 to 1.0 and 2.0 to 3.0 were also simulated, but these parameter values had poor stress-strain and physical behavior.

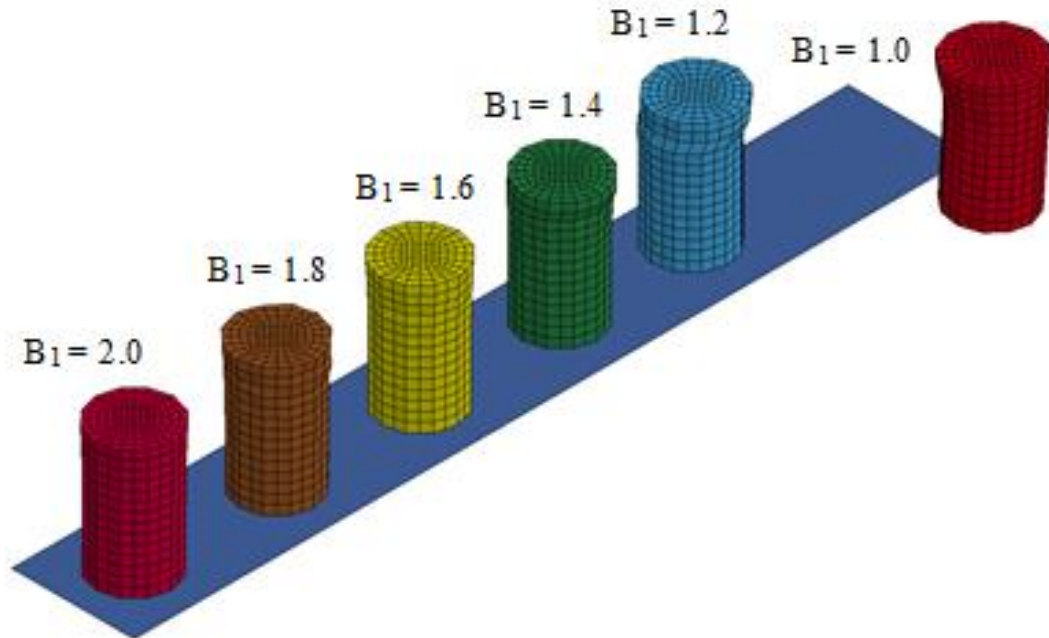


Figure 48. Compression Behavior of Cylinders in B_1 Simulation, K&C Model

5.4.5 Strain Rate Effects

A default set of strain rates and DIFs was provided in the LS-DYNA User's Manual [50] for a 6,585 psi (45.4 MPa) concrete compressive strength. These default values were then used to verify that the equations used to compute the compression [52] and tension [54] DIFs were correct. In this material model, tension strain rates are negative and compression strain rates are positive. Once this verification was completed, DIF values were computed for the test compression strength, 4,450 psi (31.0 MPa), as shown in Table 10. The strain rate for the simulation was $1.7 \times 10^{-6} \text{ ms}^{-1}$, as listed in the table.

Table 10. DIF Factors for K&C Model - 6,585 psi (45.4 MPa) and 4,450 psi (31.0 MPa) Concrete

Strain Rate	Enhancement	Strain Rate	Enhancement
<i>1/ms</i>	-	<i>1/ms</i>	-
-3.0E-01	9.69	-3.0E-01	11.44
-1.0E-01	6.72	-1.0E-01	7.93
-3.0E-02	4.50	-3.0E-02	5.31
-1.0E-02	3.12	-1.0E-02	3.68
-3.0E-03	2.09	-3.0E-03	2.46
-1.0E-03	1.46	-1.0E-03	1.72
-1.0E-04	1.37	-1.0E-04	1.57
-1.0E-05	1.28	-1.0E-05	1.44
-1.7E-06	1.22	-1.7E-06	1.34
-1.0E-06	1.21	-1.0E-06	1.31
-1.0E-07	1.13	-1.0E-07	1.20
-1.0E-08	1.06	-1.0E-08	1.09
0.0E+00	1.00	0.0E+00	1.00
3.0E-08	1.00	3.0E-08	1.00
1.0E-07	1.03	1.0E-07	1.04
1.0E-06	1.08	1.0E-06	1.12
1.7E-06	1.09	1.7E-06	1.13
1.0E-05	1.14	1.0E-05	1.20
1.0E-04	1.20	1.0E-04	1.29
1.0E-03	1.26	1.0E-03	1.38
3.0E-03	1.29	3.0E-03	1.43
1.0E-02	1.33	1.0E-02	1.49
3.0E-02	1.36	3.0E-02	1.54
1.0E-01	2.03	1.0E-01	2.30
3.0E-01	2.93	3.0E-01	3.31

A default set of values for 6,585 psi (45.4 MPa) concrete was used as a point of comparison to ensure correct DIF values were being calculated for the 4,450 psi (31.0 MPa) concrete. Once a set of values was developed for the test compression strength, a simulation was completed with the default 6,585 psi (45.4 MPa) concrete, strain rate effects turned off with 4,450 psi (31.0 MPa) concrete, and the 4,450 psi (31.0 MPa) concrete. In this initial simulation, the compression portion (i.e., positive strain rates) of the curve was defined using the LCRATE parameter. The calculated DIF was 1.09 and the test DIF was 1.13, as shown in Table 10 for the $1.7 \times 10^{-6} \text{ ms}^{-1}$ strain rate. Based on the stress-strain curves in Figure 49, the peak stresses were magnified for the 6,585 psi

(45.4 MPa) and 4,450 psi (31.0 MPa) concrete by 1.15 and 1.35, respectively. Since there were significant differences between the calculated DIF and the enhancement seen in Figure 49, the strain rate effects were not behaving as expected. Also, the DIFs affected the stress-strain behavior too much, because the peak stresses for both the 6,585 psi (45.4 MPa) and 4,450 psi (31.0 MPa) concrete were too large. Based on Figure 49, the best results were obtained with a compressive strength of 4,450 psi (31.0 MPa) and with the strain rate effects were off.

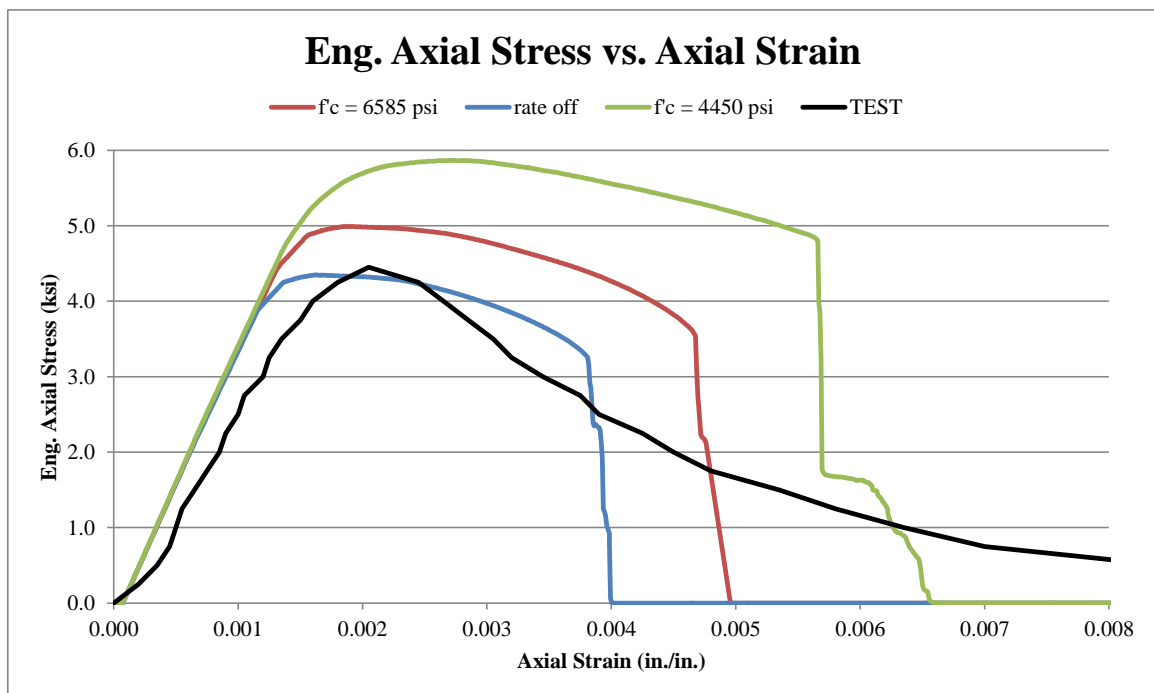


Figure 49. Compression Stress-Strain for LCRATE Simulation, K&C Model

In order to further understand strain rate effects, additional simulation iterations were completed. In another iteration, the strain rate enhancement factors from Table 10 were all set to 1.0, while using the compression side only and both the compression and tension sides of the strain rate factors. This investigation should have resulted in simulations with the 4,450 psi (31.0 MPa) concrete matching the behavior with rate

effects turned off. With inclusion of the tension-side strain rate factors, different results occurred as the stresses were larger than with the rate effects turned off and compression-only rate effects, as shown in Figure 50. Specifically, there was an 8% increase in peak stress when the tension-side rate effects were added. This effect was not well understood as tension should not occur in the model.

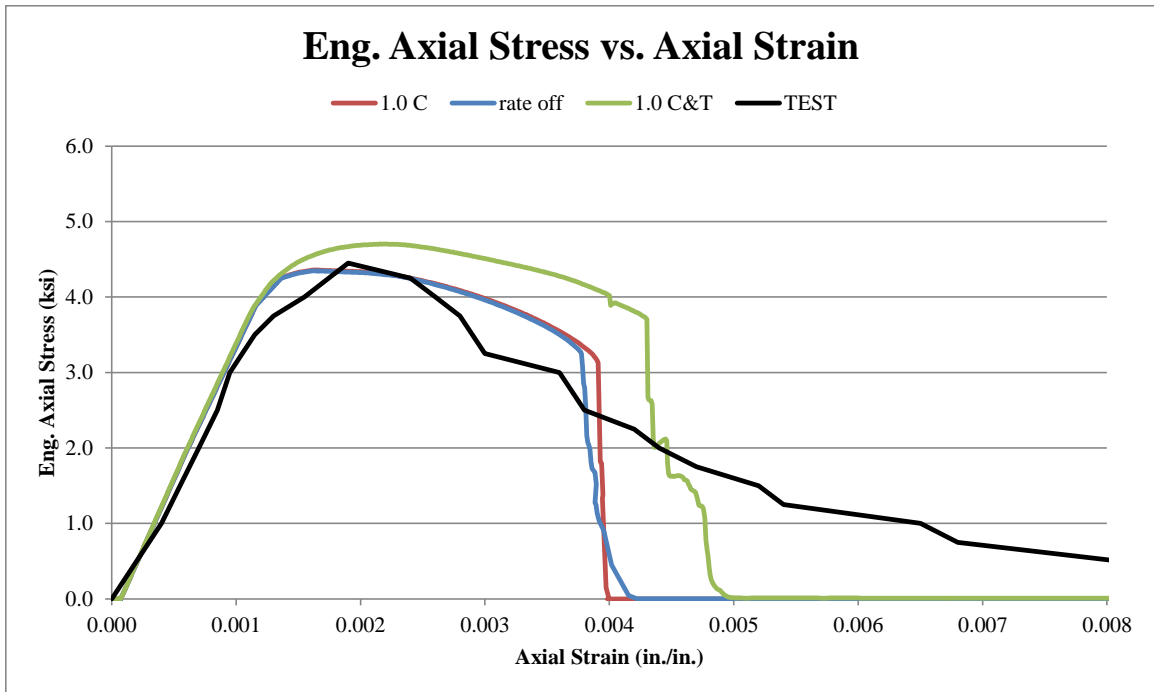


Figure 50. Compression Stress-Strain for 1.0 LCRATE Simulation, K&C Model

The final iteration examined using the full compression and tension strain-rate factors for the strain rate vs. enhancement relationship for both the 6,585 psi (45.4 MPa) and 4,450 psi (31.0 MPa) concrete cylinders. The results, as shown in Figure 51, matched well with the first iteration in Figure 49. This finding was strange when considering that the addition of the tension side of the strain rate factors resulted in a stress increase shown in Figure 50. However, a match of stress-strain between the compression only and compression and tension was desired. Although the strain rate effects defined to be turned

off for this simulation based on their accurate match of the physical test results, it was important to understand their effect for future simulations.

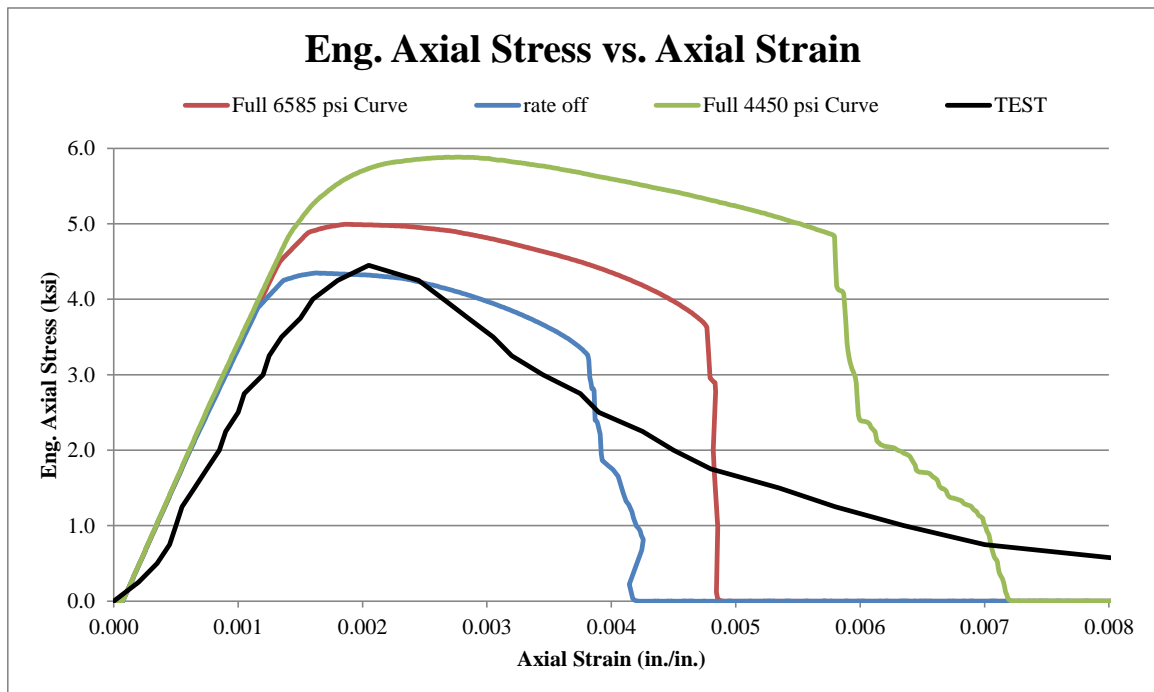


Figure 51. Compression Stress-Strain Plot for Full LCRATE Simulation, K&C Model

5.5 RHT Model – Simulation Results

The initial simulations for the RHT model included an analysis of element type, friction, and mesh size. No variations to material input parameter were made due to the poor performance observed in the initial simulations and excessive CPU time.

5.5.1 Element Type

When element types elform 1 and elform 2 were evaluated, the CPU time required to complete the simulations was 19 hours, which is much longer than observed with the other material models that were simulated up to this point. This result was especially concerning; since, this model contained a relatively low number of elements when compared to potential simulations on large-scale structures. There were no hourglass

energy issues with this particular simulation effort using the RHT material model. The modulus of elasticity observed in the physical test was 2171 ksi (15.0 GPa) and was 3002 ksi (20.7 GPa) in simulations. Also of note, there was a bend in the elastic portion of the curve, which created two different moduli before peak. The stress-strain curves for elform 1 and elform 2 were above the physical test curve, with peak strengths of approximately 5.0 ksi (34.5 MPa), as shown in Figure 52. The stress-strain behavior with elform 1 and elform 2 were nearly identical, thus indicating that the element type did not matter for this material model and selected model configuration. Softening occurred with both element types, but the softening was too gradual and did not match well with the physical test result. Elform 1 was used for the mesh and friction simulations.

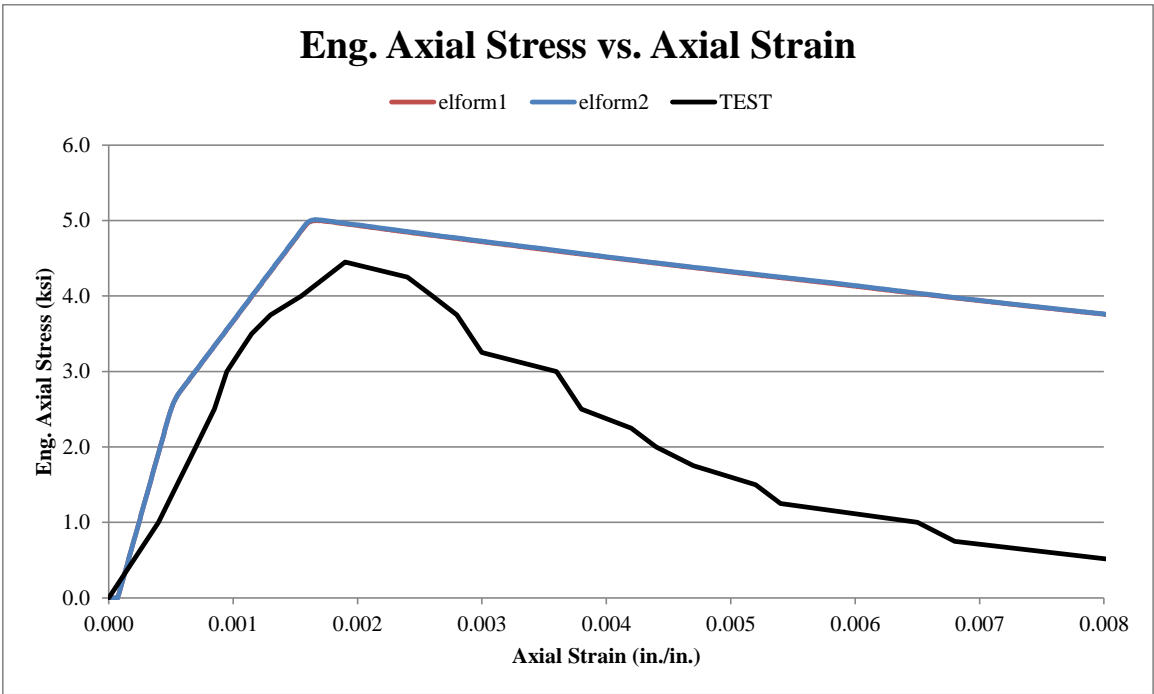


Figure 52. Compression Stress-Strain for Elform Simulation, RHT Model

In the animation of the simulation, typical cylinder deflection and bulging near its top occurred.

5.5.2 Friction

For the friction simulation investigation, the required CPU time for the simulations exceeded 9 hours for three cylinders. The hourglass energies were noticeable, but they were not high enough to be of concern, as much as 14.5% for the finest mesh at failure. The moduli of elasticity observed in the physical test and simulations did not match and had a similar bend in the elastic region as before. As shown in Figure 53, the stress-strain behavior had the same general shape as observed in the element type investigation, with a peak stress of 5.0 ksi (34.5 MPa) in the simulations, and the entire simulated stress-strain curve above the physical test stress. In this simulation, the ‘fully-fixed friction’ cylinder did not have as high of a peak stress as no friction and 0.105 friction and had slightly higher stresses as the softening occurred. Cylinder deformation was similar to the elform simulations.

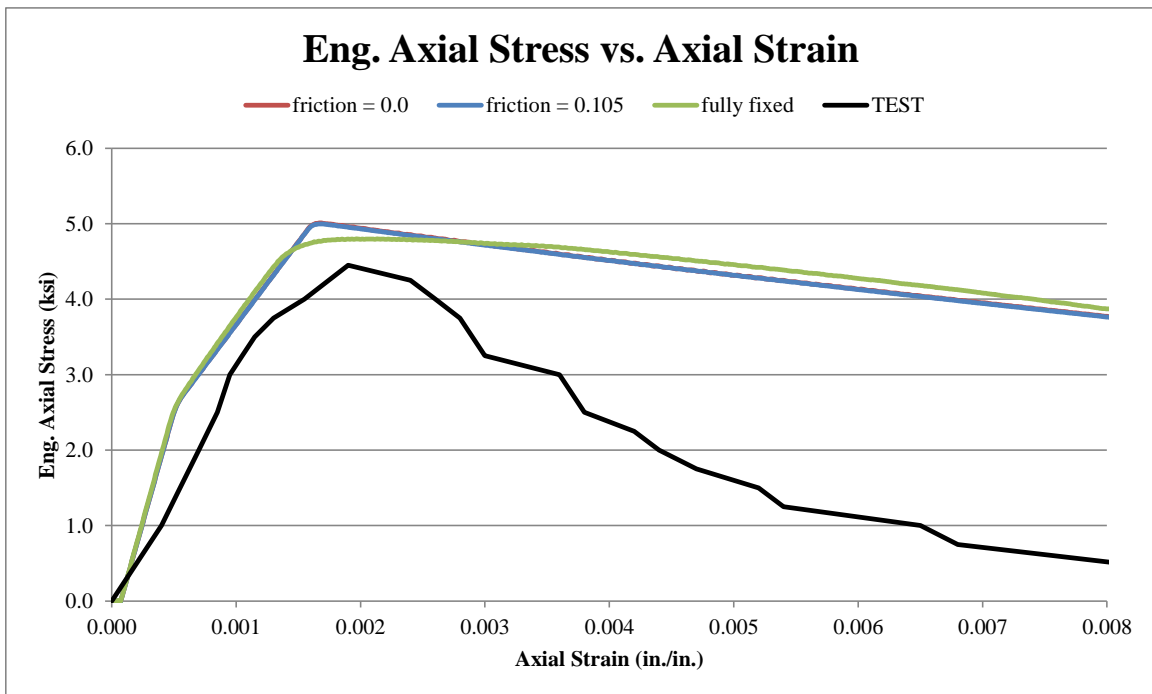


Figure 53. Compression Stress-Strain for Friction Simulation, RHT Model

5.5.3 Mesh

For the mesh-size simulations, the three-cylinder model required more than 36 hours to complete. There were energy issues with the finest mesh size in the simulation, as the hourglass energy was very large and the internal energies were negative, as shown in Figure 54. There were no hourglass issues with the two coarser mesh sizes.

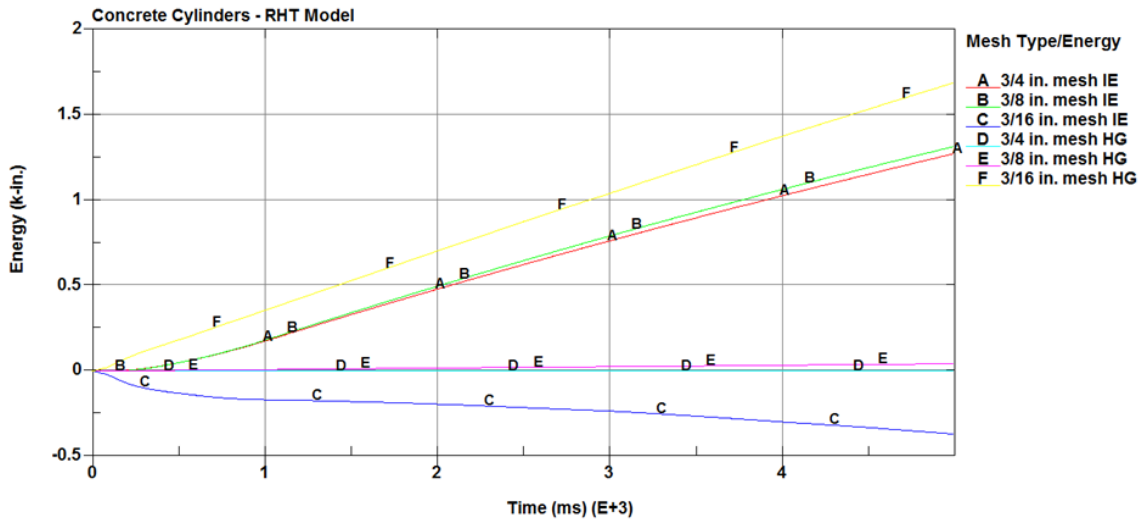


Figure 54. Compression Hourglass Energy for Mesh Simulation, RHT Model

The initial moduli of elasticity were not the same in the physical test and simulations, as before. The stress-strain behavior for this simulation was nearly identical to that observed with the elform simulations shown in Figure 52. There were some minute differences in the stress-strain curves for each mesh size, but the differences were inconsequential. The deflections in the animation were similar to those observed in the element type and mesh simulations. Due to the excessive run times in all three simulations, further investigation was not pursued into changing material input parameters.

5.6 Winfrith Model – Simulation Results

The first simulations with the Winfrith model included the basic model changes for mesh and friction. This material model only allows for the use of elform 1; therefore,

an element type simulation effort was not completed. An investigation of hourglass energy controls, strain rate effects, and fracture energy was completed.

5.6.1 Friction

In the friction simulation effort, there were significant hourglass energy levels in all three friction types, as shown in Figure 55. The hourglass energy for the ‘no friction’ case was an order of magnitude larger than any other energy. Hourglass energy control measures needed to be investigated, at least for the friction simulation.

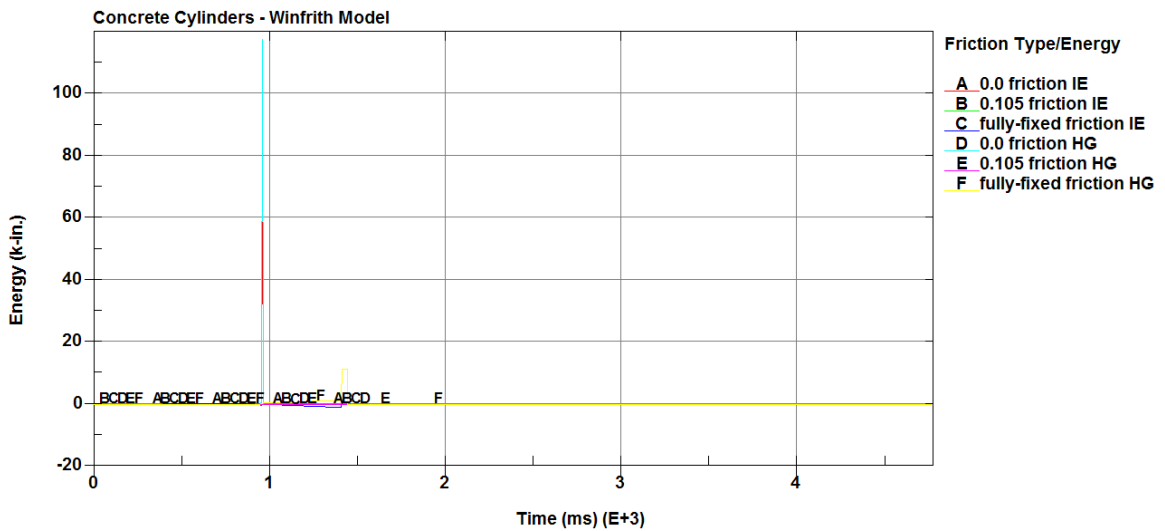


Figure 55. Compression Hourglass Energy for Friction Simulation, Winfrith Model

The stress-strain behavior for all friction values were quite different than observed in the test curve. This particular model does not have an element deletion capability. After the peak stress was reached, the stress dropped to zero. The peak stresses were much higher in the simulations than observed in the physical test, reaching as high as 5.0 ksi (34.5 MPa) for the fully-fixed friction cylinder and slightly lower for the other two cylinders, as shown in Figure 56. Stress-strain for the no friction and fully-fixed cases did not soften after peak stress was reached at low strain before deleting.

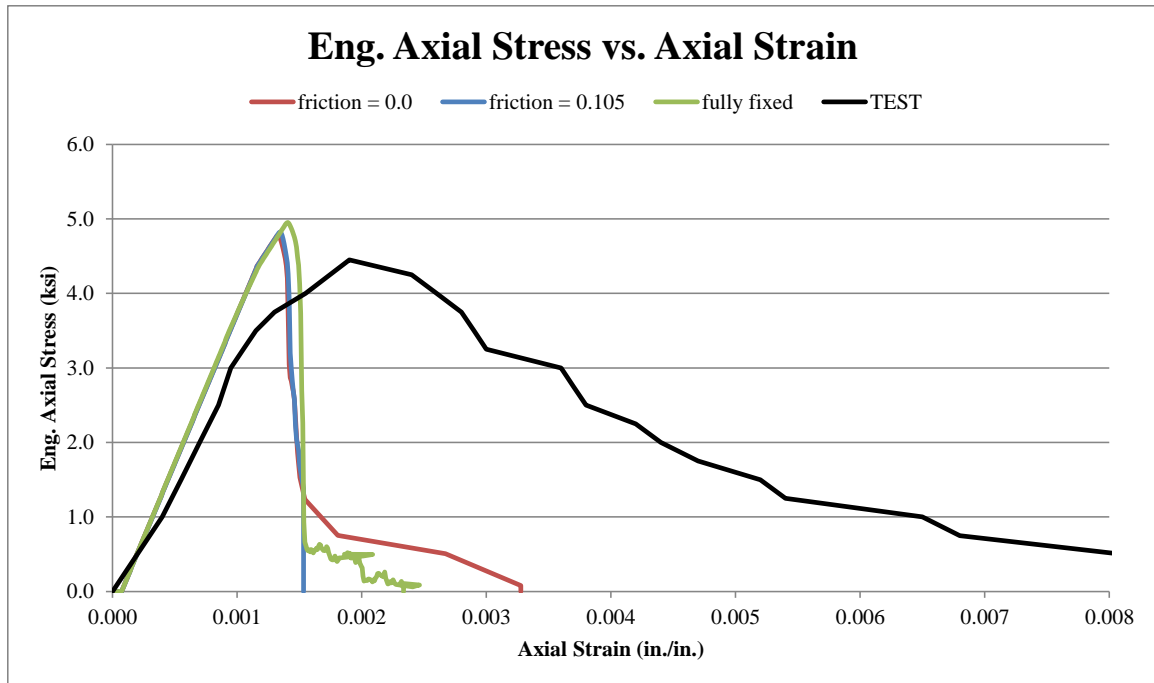


Figure 56. Compression Stress-Strain for Friction Simulation, Winfrith Model

Before the end of the simulation, all three cylinders completely deleted. This material model does not have the ability to delete elements, thus the entire part deleting indicated the material model erred out. In the animation, the fully-fixed cylinder was last to delete, but it did so right after the other two cylinders.

5.6.2 Mesh

In the mesh simulation effort, only 1000 ms of the 5000 ms were completed when the simulations ended. In these simulations, the internal energies curves dropped below zero near the end of the simulation at 875 ms and at the same point. The hourglass energies rapidly increased and became greater than internal energies. Prior to this energy reversal, the hourglass energies were zero, as shown in Figure 57. This trend did not show up in the friction simulation, highlighting some of the inconsistencies of this material model.

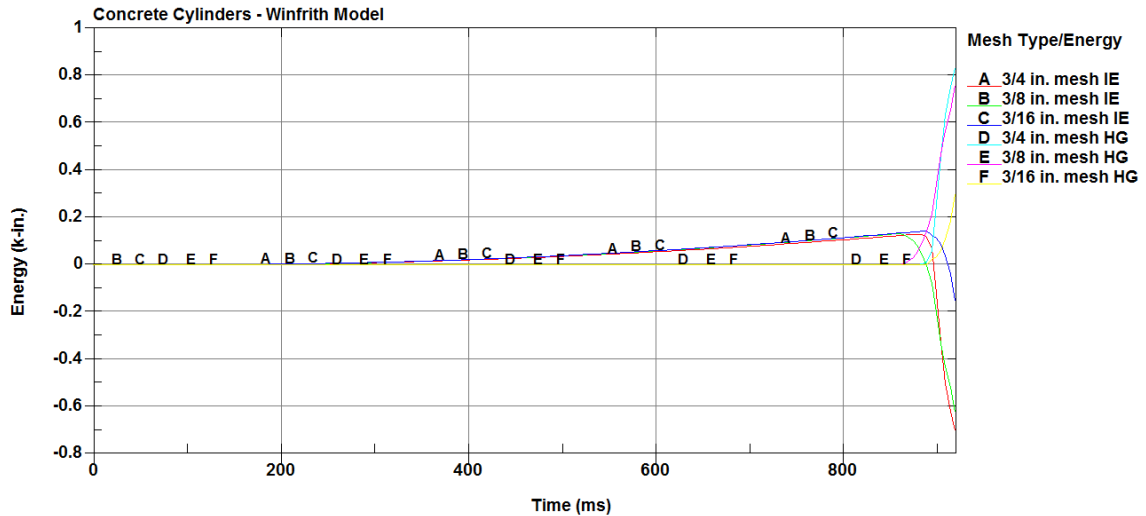


Figure 57. Compression Hourglass Energy for Mesh Simulation, Winfrith Model

The stress-strain behavior followed the same general tendencies as those observed in the friction simulations shown in Figure 56. The peak stresses were higher than observed in the physical test and the stresses dropped off immediately after peak was reached. Not much could be gathered from the animations; since, only 1000 ms completed in the model. It was not possible to determine if any of the cylinders deformed during the course of the animation.

5.6.3 Hourglass Energy

In order to alleviate some of the high hourglass energies seen in the friction and mesh simulations for this material model, different hourglass controls were tested. Hourglass control types 4, 5, and 6 were tested using *HOURLASS, all with $qm = 0.05$. Although type 6 had been used reliably for the CSCM model, it did not alleviate the hourglass issues for the Winfrith model. In the friction simulation with type 6, hourglass energies were still present and in some cases extreme. In the mesh simulation with type 6, only 11 of the 22 plot states were completed. In the animation of the mesh simulation, there was dilation of the cylinders in addition to high hourglass energy levels, as shown

in Figure 58. Hourglass control type 5 performed better than type 6, but there were still high hourglass energies in the friction and mesh simulations, specifically in the fully-fixed friction cylinder and the finest mesh cylinder.

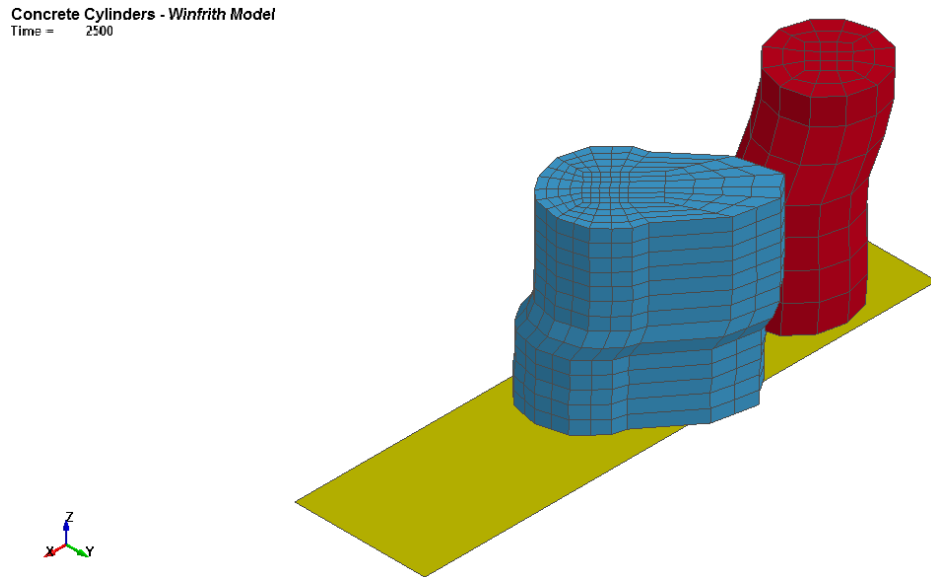


Figure 58. Compression Dilation of Cylinders for Mesh Simulation, Winfrith Model

Hourglass control type 4 proved to be the best hourglass control type. It did not alter the shape of the stress-strain curves and reduced hourglass energy levels to more acceptable levels, as shown in Figure 59 for the friction and mesh simulations, respectively. All plot states were completed, and all three cylinders deleted completely, indicating an error. The hourglass energies were 27% of the internal energy, and this issue was checked when rate effects were turned off.

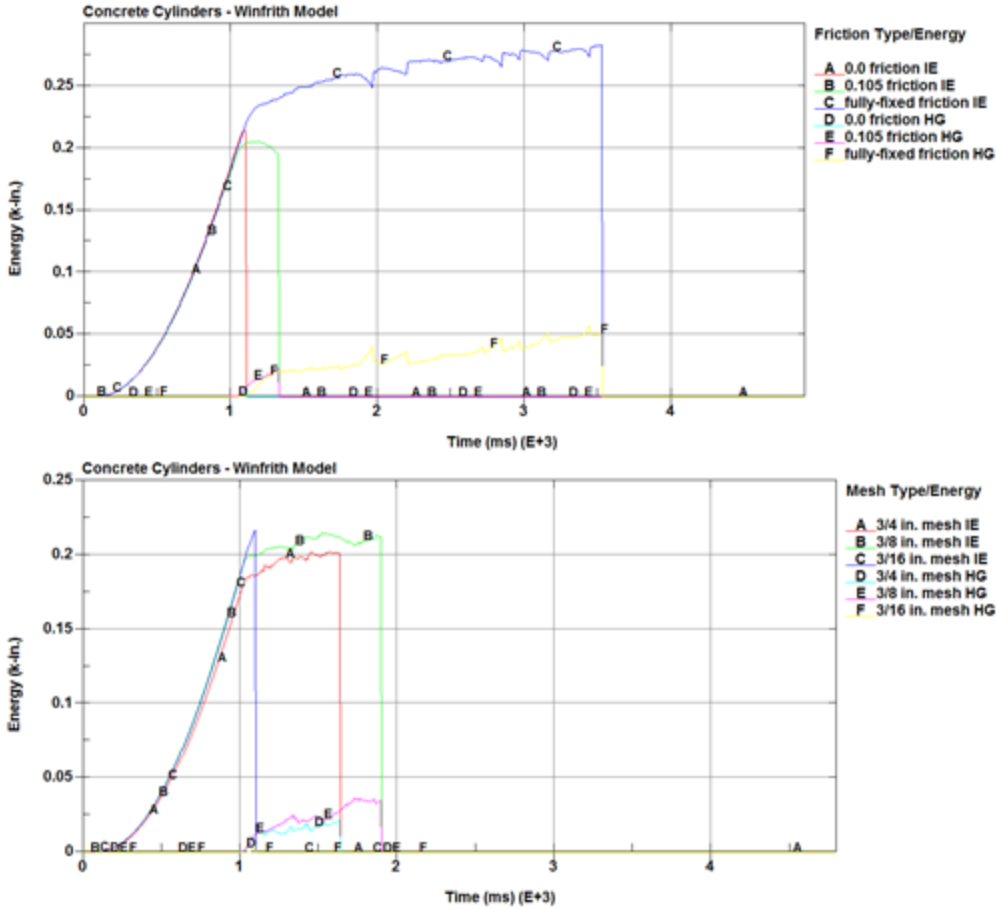


Figure 59. Compression Hourglass Energy with HG4, Winfrith Model

5.6.4 Strain Rate Effects

Turning the rate effects off by setting rate = 1 made a significant difference in the results. Not only did it reduce the hourglass energies in the friction simulation, but the peak strength also decreased to 4.3 ksi (29.7 MPa) to match the physical test result of 4.5 ksi (31.0 MPa) more closely, as seen in Figure 60. All three cylinders in the friction simulation still deleted before the end of the simulation, and the stresses dropped right to zero after peak was reached, which is expected with no compression softening capability in this model.

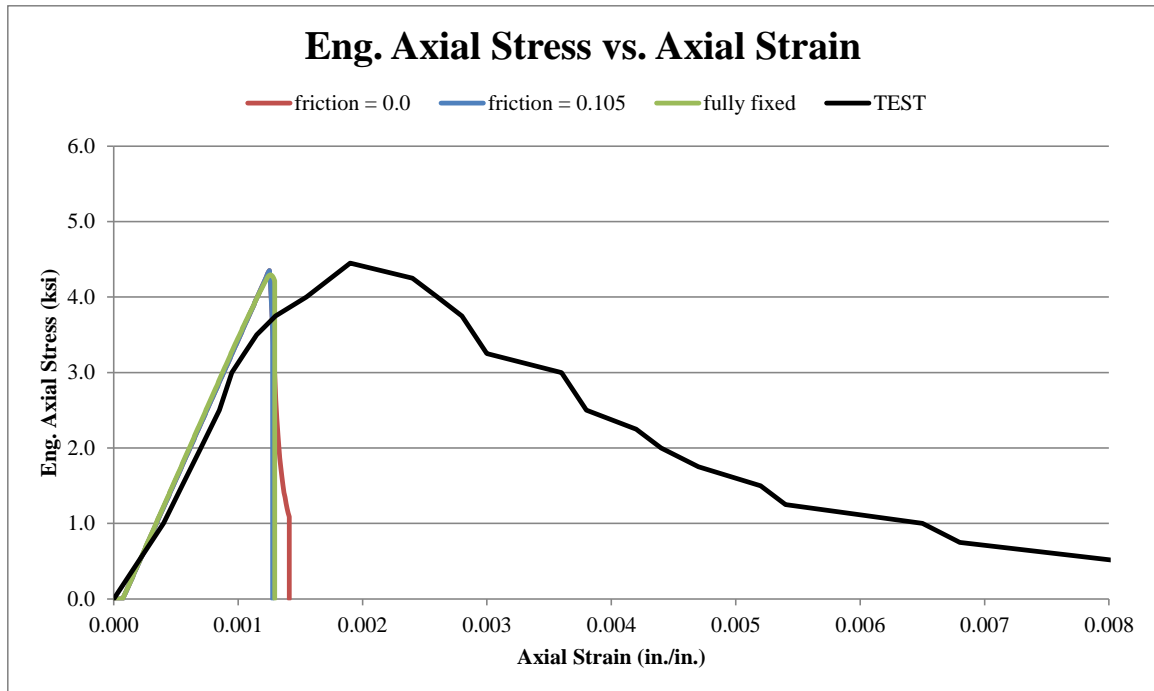


Figure 60. Compression Stress-Strain with Rate Effects Off, Winfrith Model

5.6.5 Fracture Energy

Since there were no major differences between the varied friction and mesh values, changes in the material input parameters were made assuming a 0.105 friction value and a $\frac{3}{8}$ -in. (9.5-mm) mesh as used in other models. Since the pressure vs. volume relation was automatically generated by the model, the only material input parameter that was investigated was the fracture energy (fe) value. These simulations were completed with the rate effects off using rate = 1 and hourglass control type 4 in place. Three different simulation iterations were completed with three different fe used in each iteration: (1) 0, 0.1, and 0.01; (2) 0.025, 0.050, and 0.075; and (3) 0.25, 0.50, and 0.75. The stress-strain results for the first iteration are shown in Figure 61. The third iteration produced high hourglass energies that were 17% of the internal energy; therefore, those values were not considered. The stress-strain behavior for the remaining six fe values

were all similar. Therefore, the final conclusion for the fe parameter was to use $fe = 0$ as the input.

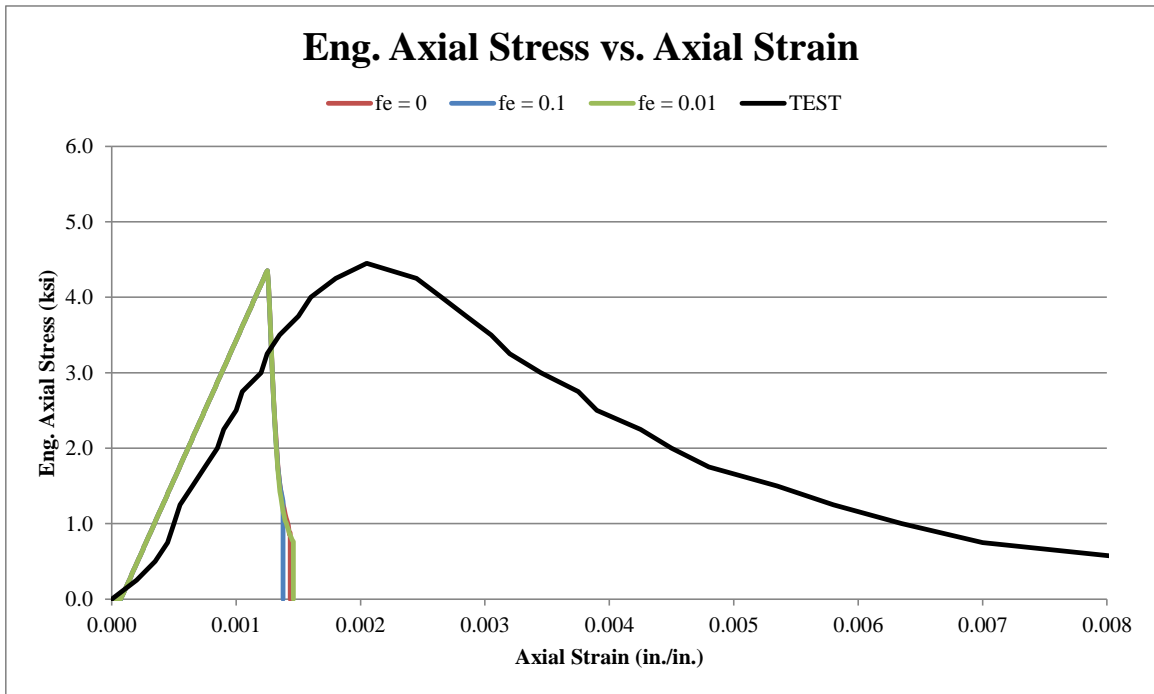


Figure 61. Compression Stress-Strain for Fracture Energy Simulation, Winfrith Model

5.7 CDPM Model – Simulation Results

For the element type and friction simulations, only 750 ms out of 5000 ms completed in 24 hours of CPU time, which is excessive for 5544 elements. This simulation time is too CPU-expensive to be considered an effective material model for the cylinder compression simulations. In addition, the plastic solver did not converge for one element in the mesh simulation; therefore, only 500 ms out of 5000 ms completed. There was also an error in the Jacobian matrix slot in the simulation. Due to the complications with the basic model, changes to the material input parameters were not considered.

5.8 Discussion

Based on the results of all simulations with the five different material models, there was not one material model that was completely flawless. Two of the models (RHT and CDPM) were not realistic for use because of excessive run times for simple models. The other three material models (CSCM, K&C, and Winfrith) provided adequate results and were not as CPU expensive. Excessive hourglass energies that occurred could be controlled using various hourglass controls. None of the moduli of elasticity in the simulations matched the physical test results. Since many of the simulations had similar moduli of elasticity, the strain values in the physical test may not have been gathered accurately. The simulated stress-strain results only matched well in the CSCM model, as changes were made to the material input to develop a good match. Finally, the animation of the cylinders was most accurate for the CSCM model, as elements were deleted and the damage profile was very clear and realistic.

Overall, the CSCM model performed the best out of the five. It provided accurate stress-strain behavior once an arbitrary compressive fracture energy was found to match the physical test results. Although this fracture energy did not match the calculated value using the material model's default equations, it created softening in the curve. Specifically, as the fracture energy decreased, more softening occurred. Hourglass control type 6 did well to eliminate most hourglass energy for this model. Although it was difficult to confirm whether or not the observed element erosion and the damage profile were similar to the physical test results, they appeared realistic based on theoretical damage patterns. The ability to display damage values and erode elements was a major advantage of this model and set it apart from the other material models that were

evaluated. The ability to change multiple parameters that directly affected the stress-strain results was especially helpful. However, a change in mesh size should not result in different behavior because the fracture energy should remain constant despite element size. It was assumed in all remaining simulations that the mesh sensitivity characteristic of the model was not performing as expected.

The K&C model performed moderately well, with lesser correlation than CSCM between the simulated and physical test stress-strain results. The major drawback of this model was the inability for elements to erode, but erosion can be added separately if needed. Also, the strain rate effects appeared to not work as defined. The stress-strain results did not match well with the test results, because the softening behavior in the simulations was more severe. The simulation results had a very steep slope after the peak stress was reached. The K&C model would require additional investigation into compression softening behavior in order to make the model more accurate. In addition, it also would have been helpful to have element deletion capability in this model, so as to better depict progressive cylinder damage. This effect could have been accomplished by using a damage function that calculates damage for compression and tension separately, instead of together. The damage threshold is 2.0 instead of 1.0 for this reason.

The Winfrith model performed well in terms of matching the peak strength of the physical test. The model does not have compression softening capability, so the softening in the test was not replicated in the simulations. The only parameter that could have been changed was a fracture energy parameter, but varying it did not result in much difference in stress-strain. This model also did not have element deletion capability, yet cylinder

deleted due to error in the simulation. With the limited capabilities of the Winfrith model, it still performed reasonably well.

As mentioned previously, the RHT and CDPM models were ruled unacceptable for the compression loading case, because excessive simulation run time was required for the models. In the case of the RHT model, simulations required as long as 36 hours to complete. For the CDPM model, only 500 ms of 5000 ms were completed in 24 hours, and none of the models completed within 60 hours of run time. It was difficult to have confidence in a material model that required long run times to simulate small models with 5544 elements, especially when the goal is to simulate large-scale structures subjected to impact loading and that may have 10 to 1,000 times as many elements.

CHAPTER 6 TENSION SIMULATIONS ON EXTERNAL COMPONENT TESTS

6.1 Introduction

The second loading case for the component simulations was tension. External data was acquired to investigate the material models further. Many different test specimen shapes were considered for direct tension. In the end, a flat concrete plate was chosen. Gopalaratnam determined the axial stress-displacement for a flat concrete plate in direct tension and focused on the softening response [67]. In the study, a 3-in. x ¾-in. x 12-in. (76-mm x 19-mm x 305-mm) flat plate specimen was gripped by the testing apparatus using aluminum and steel wedges at both ends of the specimen. The wedges were attached to a universal joint, which was connected directly to the testing apparatus. The maximum aggregate size in the specimens was ¾ in. (10 mm), and the concrete had a compressive strength of 6,364 psi (43.9 MPa). The tensile strength of concrete was found to be 565 psi (3.9 MPa), as shown in Figure 62. The specimens were loaded using a tension-compression load cell at a monotonically increasing strain at a rate of 1 µ-strain/s and did fracture. The axial force was measured with this load cell and engineering axial stress was calculated based on this force divided by the original cross-sectional area. The strain data was measured by two LVDTs placed within the gauge length. Some specimens in the study were notched, but an unnotched specimen was chosen for the simulation effort, and only the ¾-in. (83-mm) gauge length was simulated as opposed to the entire part.

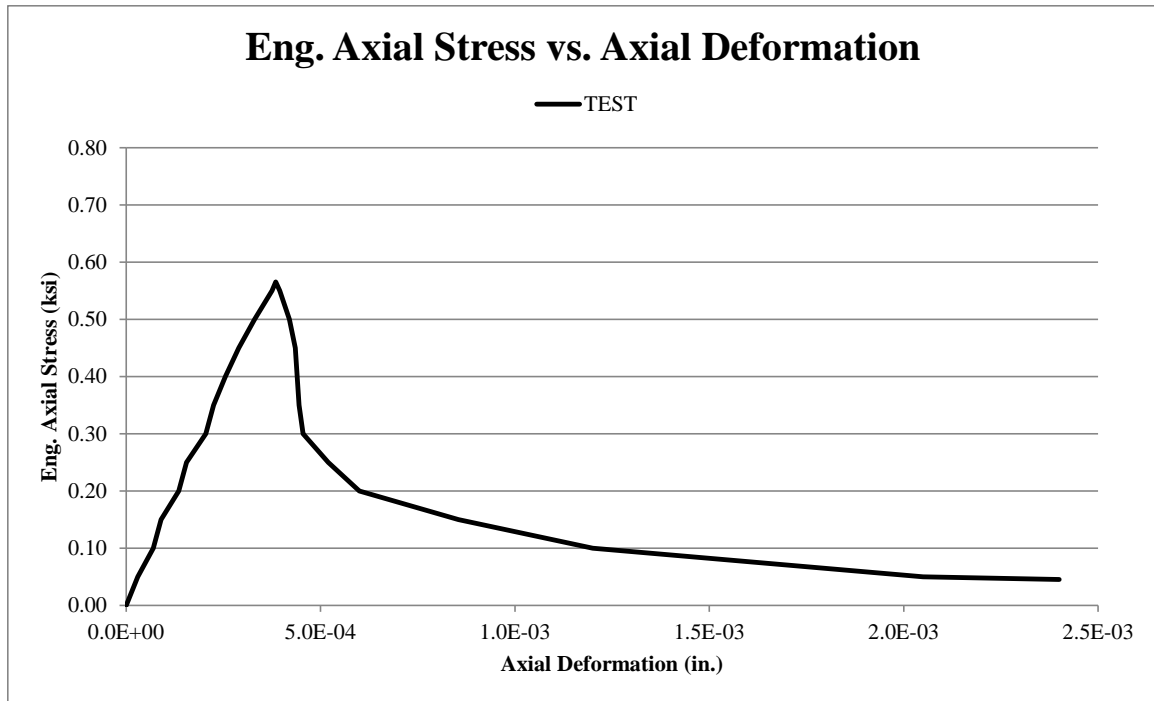


Figure 62. Tension Stress-Deformation Test Results [67]

6.2 Simulation Data Evaluation Process

As with the compression study, an initial loading rate analysis was completed for each of the five models given that the displacement rate of the test was disadvantageous for use in explicit LS-DYNA analyses. Potential displacement rates ranged from 0.55 in./s (14 mm/s) to 1.1×10^{-4} in./s (2.8×10^{-3} mm/s). The goal was to find convergence in the stress-strain behavior at a reasonable displacement rate. Convergence was reached for all material models at 500 ms for a rate of 0.011 in./s (0.28 mm/s), and this time was considered optimum.

The intent of the plate simulations was to compare the simulation results from each of the five material models to the acquired test results obtained from the external source. The plate in the model was 3 in. x $\frac{3}{4}$ in. x 12 in. (76 mm x 19 mm x 305 mm). A *BOUNDARY_PRESCRIBED_MOTION was applied to the top nodes of the cylinder to

allow for movement in the z-axis. A *BOUNDARY_SPC definition was given to the bottom nodes in order to hold them in place. The displacement rate was increased linearly until the end of the simulation. Cross-sections were placed through the center of the plates in order to measure forces for use in computing stresses. An overview of the model is shown in Figure 63.

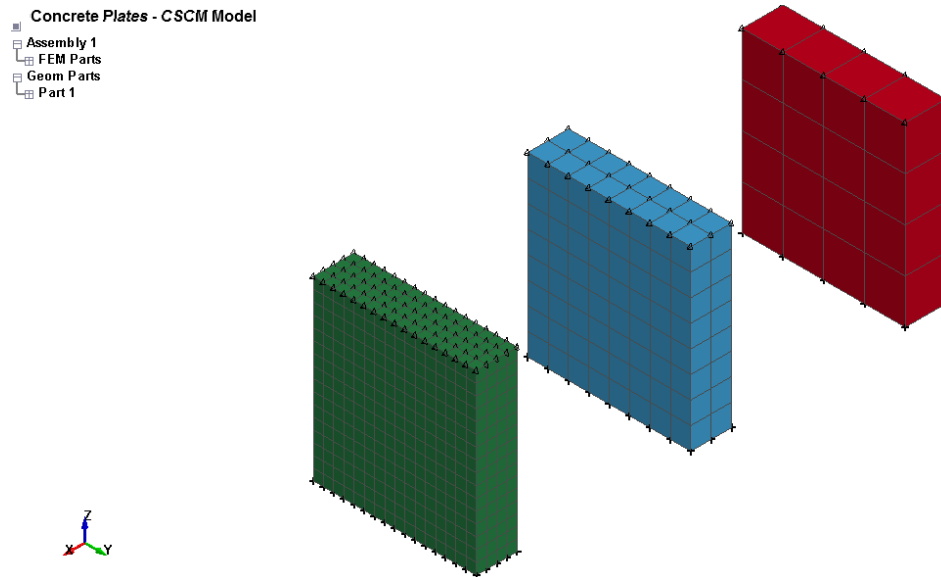


Figure 63. Overview of External Tension Simulation

Variations were again made to the model and default material input parameters in order to find a combination that best matched the physical test results. Basic model changes included different mesh sizes and two different element types, as was evaluated for compression. Individual mesh sizes of $\frac{3}{4}$ in. (19 mm), $\frac{3}{8}$ in. (10 mm), and $\frac{3}{16}$ in. (5 mm) were evaluated with each material model in order to determine the optimal mesh size. Element types 1 and 2 were checked as well for the CSCM, K&C, RHT, and CDPM material models. The Winfrith model is not compatible with element type 2, so an element type simulation was not completed for this material model. Hourglass energy control types with *HOURGLASS were used for all material models in the initial

simulations due to high hourglass energies, relative to the internal energy. Additional simulations were completed to vary some of the material model input parameters. For the CSCM model, the following material model input parameters were evaluated: fracture energy; ERODE; recov; and repow. For the K&C model, the compressive damage scaling factor and strain rate effects were evaluated. No material model input parameters were evaluated for the other three models.

Once these simulations were completed, the simulation results were compared to the external physical test data, as shown in Figure 62 [67]. The stress-deformation results were compared between the simulations and test. Engineering stress from the simulation was computed as the cross-section force divided by the original cross-sectional area. The simulated stress and deformations were plotted along with the physical test results. The damage profile of the specimens was also considered when evaluating model performance, where applicable.

6.3 CSCM Model – Simulation Results

The initial simulations for the CSCM model included variations in element type and mesh size. Based on the high hourglass energies in the initial compression models, different hourglass energy controls were applied. Hourglass energy control type 7 was found to be incompatible with this material model. After testing HG4, HG5, and HG9 and not getting enough of a reduction, HG6 was found to decrease the hourglass energies and it was used going forward. The mesh size and element type simulation investigations were followed by these material input variations: ERODE; repow; and recov.

6.3.1 Element Type

For both element types, the peak stress was 435 psi (3.0 MPa) which was lower than the physical test peak stress of 565 psi (3.9 MPa), as shown in Figure 64. The initial mesh size was $\frac{3}{4}$ in. (19 mm). The difference in the two responses was in post-peak behaviors with the stress higher in elform 2 versus elform 1 during the softening. The modulus of elasticity was 4147 ksi (28.6 GPa) in the simulation and 4710 ksi (32.5 GPa) in the physical test. The simulated softening behavior did not match well with the physical test results. In the test, a peak stress was reached, the stress decreased immediately and then gradually decreased through the rest of the test. For the simulations, stresses gradually decreased after peak through the end of the simulation.

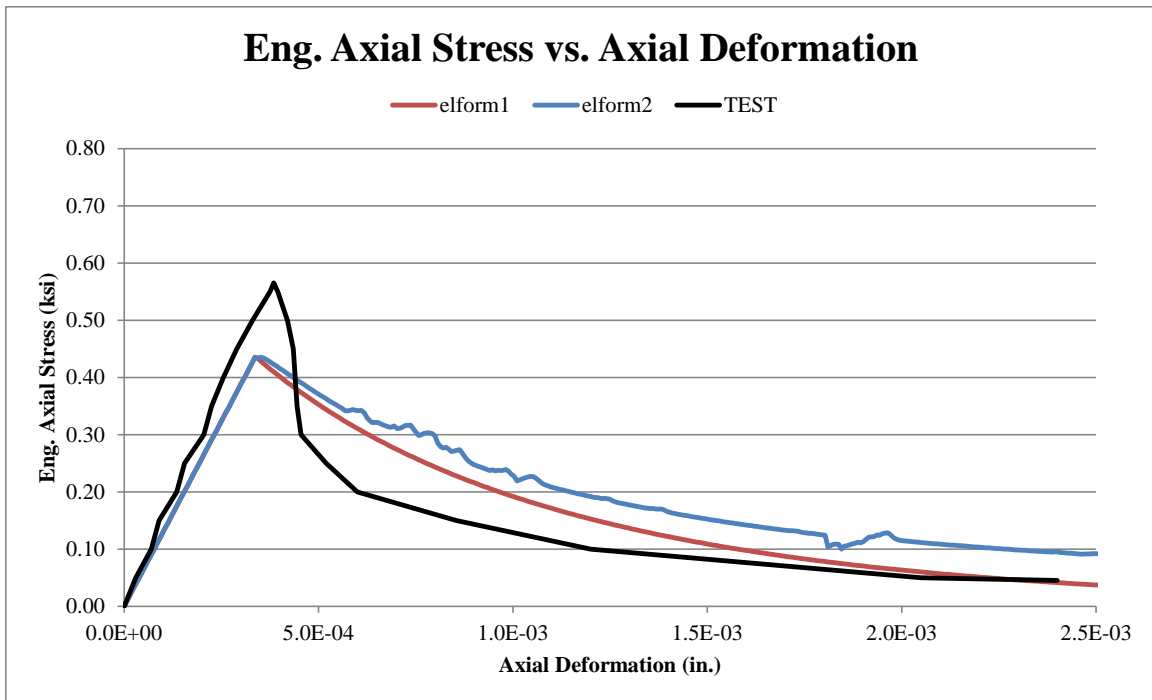


Figure 64. Tension Stress-Deformation for Elform Simulation, CSCM Model

Damage for both parts formed in bands near the bottom of each specimen. The damage resulted in element deletion patterns, as shown in Figure 65. The elform 1 part

(red) had a clean break near the bottom of the part, which would be expected given it is the gauge length of the specimen. Damage started to form in the same location on the elform 2 specimen (blue), but elements were deleted along the edge of the part, and the deletion pattern was atypical for a uniaxial tension test. Elform 1 was used in the following simulations.

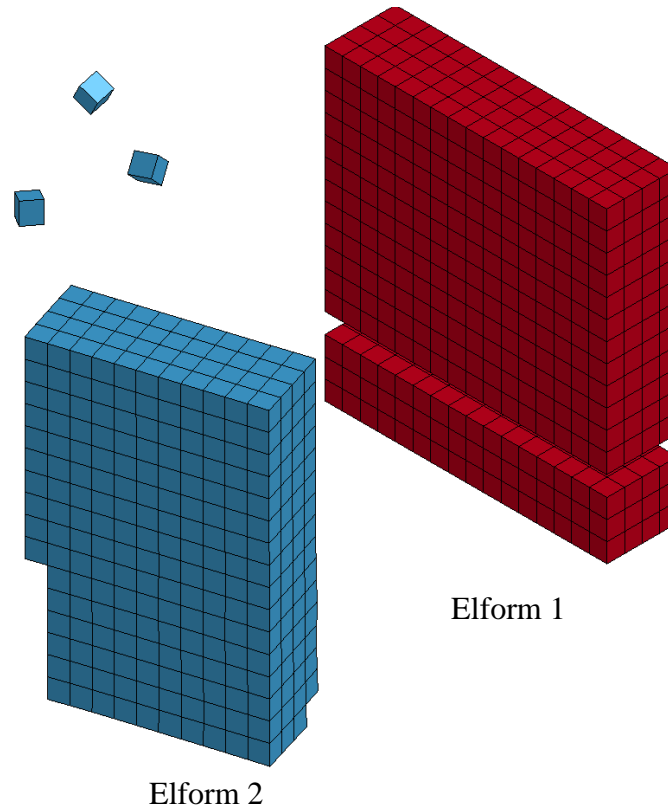


Figure 65. Tension Fracture Pattern of Specimens, CSCM Model

6.3.2 Mesh

A mesh simulation effort was then carried out for the three initial mesh sizes. Results similar to those obtained for the element type simulation effort were found, the modulus of elasticity and peak stress values for the simulations were lower than observed in the test, as shown in Figure 66. The softening behavior was similar for the $\frac{3}{4}$ -in. (19-mm) and $\frac{3}{8}$ -in. (10-mm) mesh sizes. However, the $\frac{3}{16}$ -in. (5-mm) mesh resulted in a

similar peak, but it remained constant longer before softening. This behavior was not seen in previous simulations; therefore, an additional mesh size was evaluated, $3/32$ in. (2 mm). The plates failed near the middle of the part, as was seen in the previous elform 1 simulation.

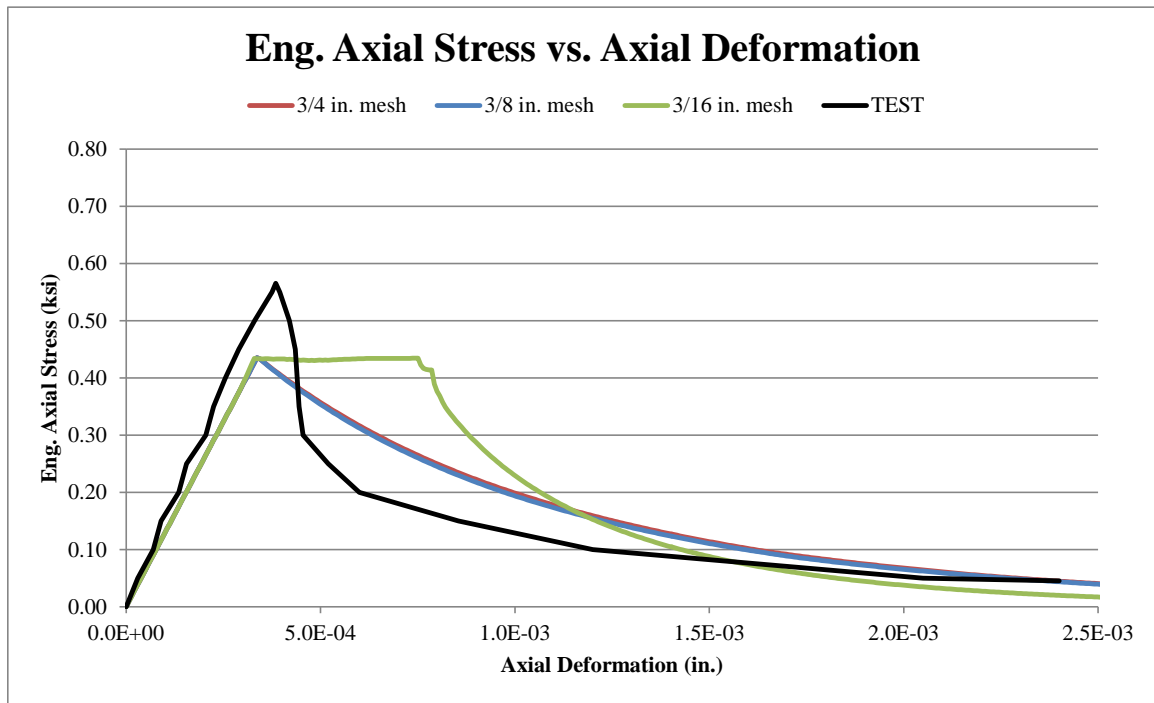


Figure 66. Tension Stress-Deformation for Mesh Simulation, CSCM Model

Additional concerns arose when this finer mesh simulation was completed. As shown in Figure 67, neither the $3/16$ -in. (5-mm) or $3/32$ -in. (3-mm) mesh curves repeated the behavior shown in Figure 66. This problem with consistency between simulations was previously seen with this material model in the compression simulation investigation. In this additional simulation, the same trends regarding peak stress, modulus, and softening behavior were occurring. The peak stress of 0.44 ksi (3.0 MPa) and modulus of elasticity of 4190 ksi (28.9 GPa) were less than those observed in the physical test, and the post-peak behavior did not match the test results. More simulations were run with

three parts having the exact dimensions and properties for the $\frac{3}{8}$ -in. (10-mm) and $\frac{3}{16}$ -in. (5-mm) mesh sizes, but different stress-deformation results occurred. Despite all the issues surrounding this mesh simulation, the $\frac{3}{16}$ -in. (5-mm) mesh size was used going forward.

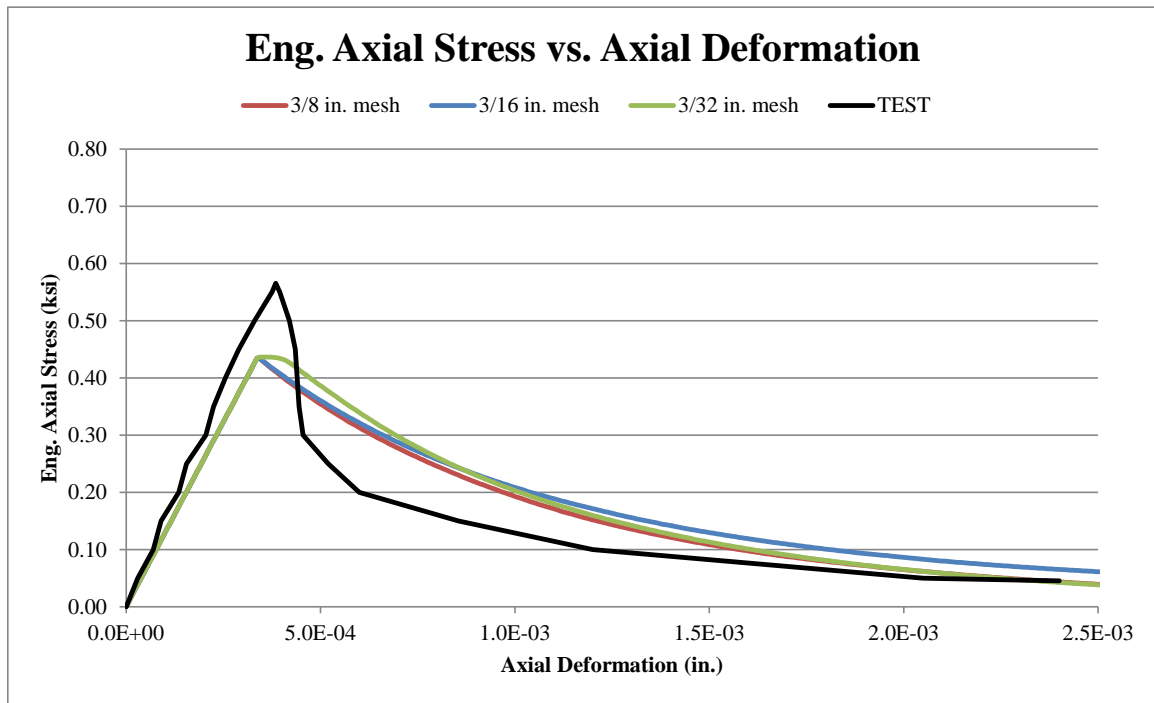


Figure 67. Tension Stress-Deformation for Additional Mesh Simulation, CSCM Model

6.3.3 Fracture Energy

Different fracture energies were evaluated for G_{ft} in order to determine if a revised fracture energy would result in a better match between the simulations and physical test. The other fracture energy inputs, G_{fc} and G_{fs} , were changed based on the G_{ft} value. The tensile default value was found by running an initial simulation with automatic parameter generation in place. In the simulation results, the tensile fracture energy, G_{ft} , was calculated as 4.23×10^{-4} k/in. (7.41×10^{-5} kN/mm), but it returned a peak stress of 0.44 ksi (3.0 MPa). Iterative simulations indicated that the ideal value for G_{ft} was

between 3.09×10^{-4} k/in. (5.41×10^{-5} kN/mm) and 2.33×10^{-4} k/in. (4.08×10^{-5} kN/mm). Simulations with fracture energies within this range as well as the calculated fracture energy are shown in Figure 68. Element did erode near the cross-section of the parts. The simulation trends did not seem logical as the highest fracture energy resulted in the second highest stresses during softening. It was expected that as the fracture energy decreased, so would stress. Fracture occurred near the center of the specimen for the largest of the fracture energies.

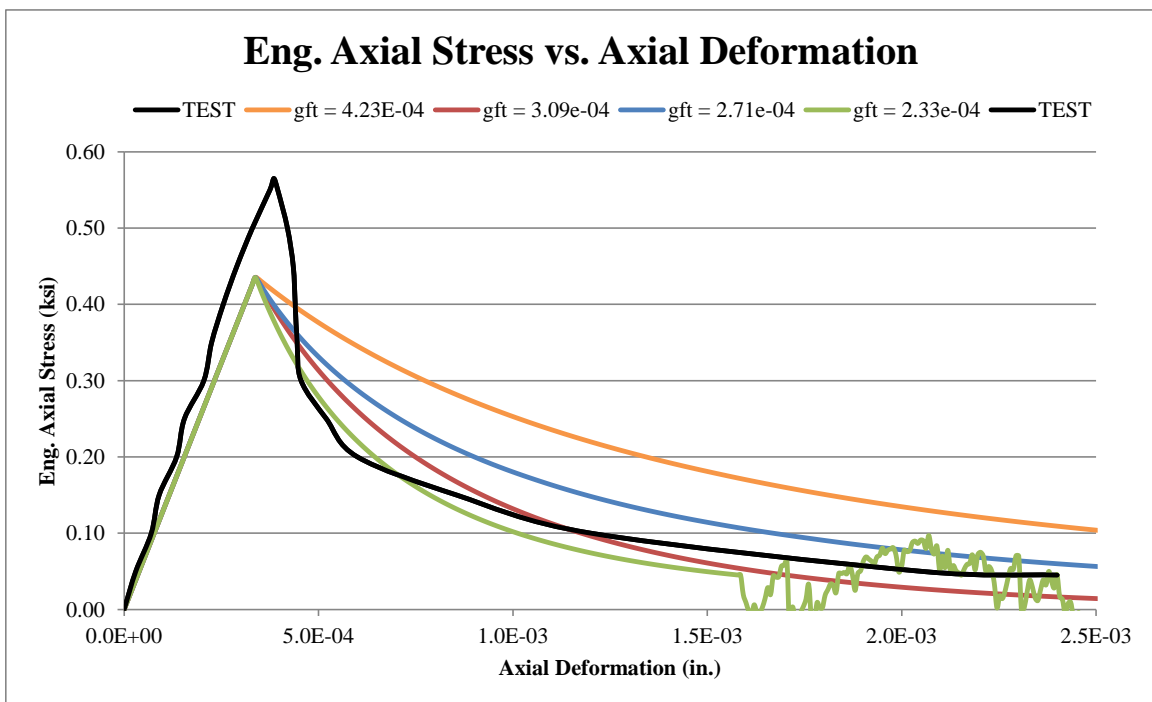


Figure 68. Tension Stress-Deformation for Fracture Energy Simulation, CSCM Model

6.3.4 ERODE, recov, and repow

After the initial simulations were completed for element type and mesh size, changes were made to the material input parameters, specifically ERODE, repow, and recov. The parameters were varied in the same way used for the compression simulations. Ultimately, there was not much difference between the ERODE, repow, and recov results

when values were varied. Since peak stress and softening did not change, it was assumed that these parameters were not affecting stress-strain behavior. There were no distinct trends in the stress-deformation behavior and element deletion did not occur for all parameter values. It was determined that the default values for each of the input parameters would be adequate.

6.4 K&C Model – Simulation Results

The initial simulations for the K&C model included variations in element type and mesh size. Based on the high hourglass energies observed in the initial models, different hourglass energy controls were attempted. Hourglass energy control type 9 was found to be incompatible with the material model. After testing the remaining control types, HG4 was found to decrease the hourglass energies the most and was used going forward. The mesh size and element type investigations were followed by variations in the material input parameters for the compressive damage scaling factor and the strain rate effects.

6.4.1 Element Type

For the element type simulations, the results for elform 1 and elform 2 were nearly identical. The peak stress of 0.51 ksi (3.5 MPa) was similar to the peak stress of 0.57 ksi (3.9 MPa) in the physical test, as shown in Figure 69. The modulus of elasticity for the simulations was 4206 ksi (29.0 GPa) which was slightly lower than 4710 ksi (32.5 GPa) observed in the physical test. The stress-deformation behavior largely was linear nearly to peak. Little softening occurred after peak in this simulation, and the stress dropped to zero, which represented failure of the specimens. The use of different element types resulted in damage accumulations in two different areas of the part. The elform 1

part had damage occurring in a band near the top of the part, and the elform 2 part had a similar band near the bottom of the part, as shown in Figure 70. This finding was the only difference between the element types. However, elform 1 was chosen due to its use with this material model in other simulations.

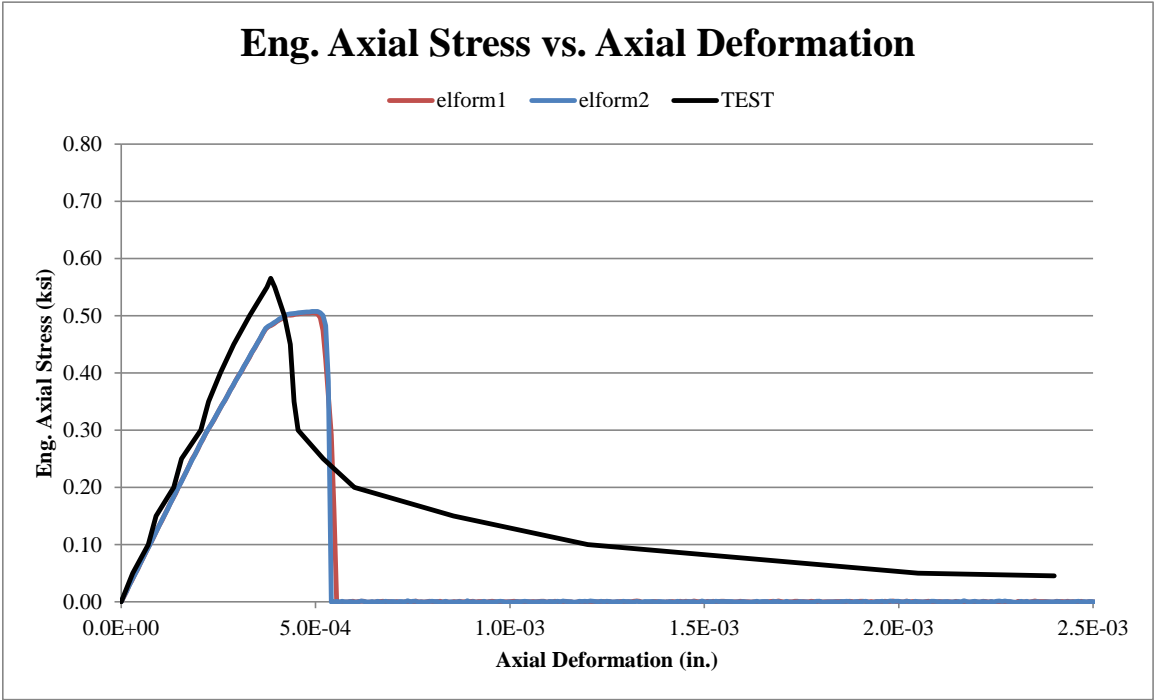


Figure 69. Tension Stress-Deformation for Element Type, K&C Model

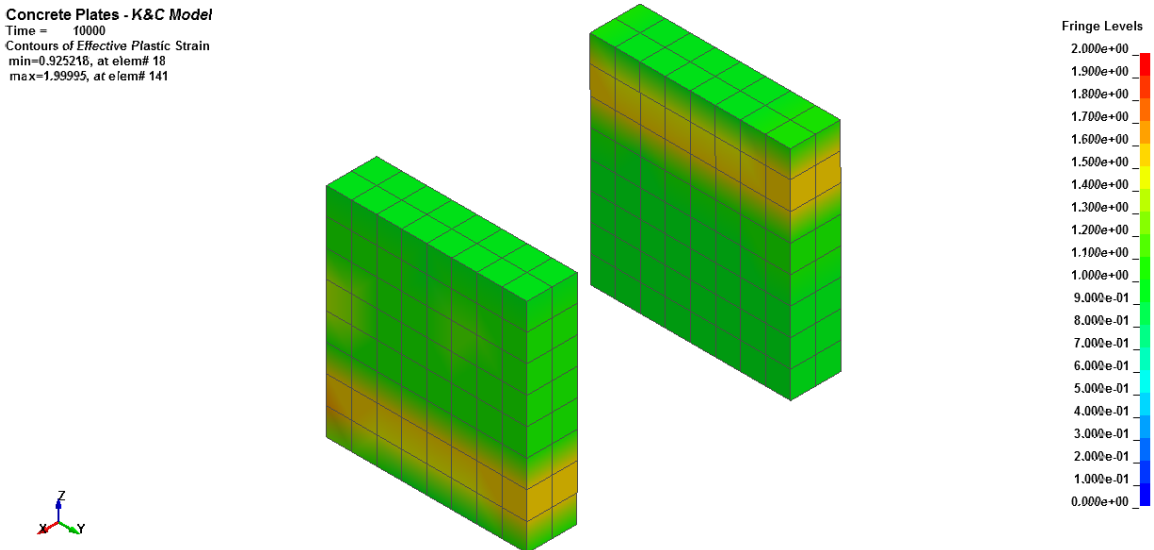


Figure 70. Tension Damage Contours for Element Type Simulation, K&C Model

6.4.2 Mesh

Two different mesh investigations were completed to determine if a closer match could be made between the simulation and test results. In the initial simulation, the finest mesh size of $\frac{3}{16}$ in. (5 mm) was explored, and it resulted in peak stresses at slightly higher deformations than observed in the physical test. As mesh size decreased, the deformation closer matched the test results. An additional simulation was completed to evaluate a $\frac{3}{32}$ -in. (2-mm) mesh size, as shown in Figure 71. Although the associated peak deformation was decreasing with smaller meshes, the peak stress decreased between the $\frac{3}{16}$ -in. (5-mm) and $\frac{3}{32}$ -in. (2-mm) mesh sizes. No softening occurred in the simulations, a trend that was also seen in the element type simulations. Damage accrued near the top of the specimens. Due to these results, the $\frac{3}{16}$ -in. (5-mm) mesh was used for the other material model input parameter simulations.

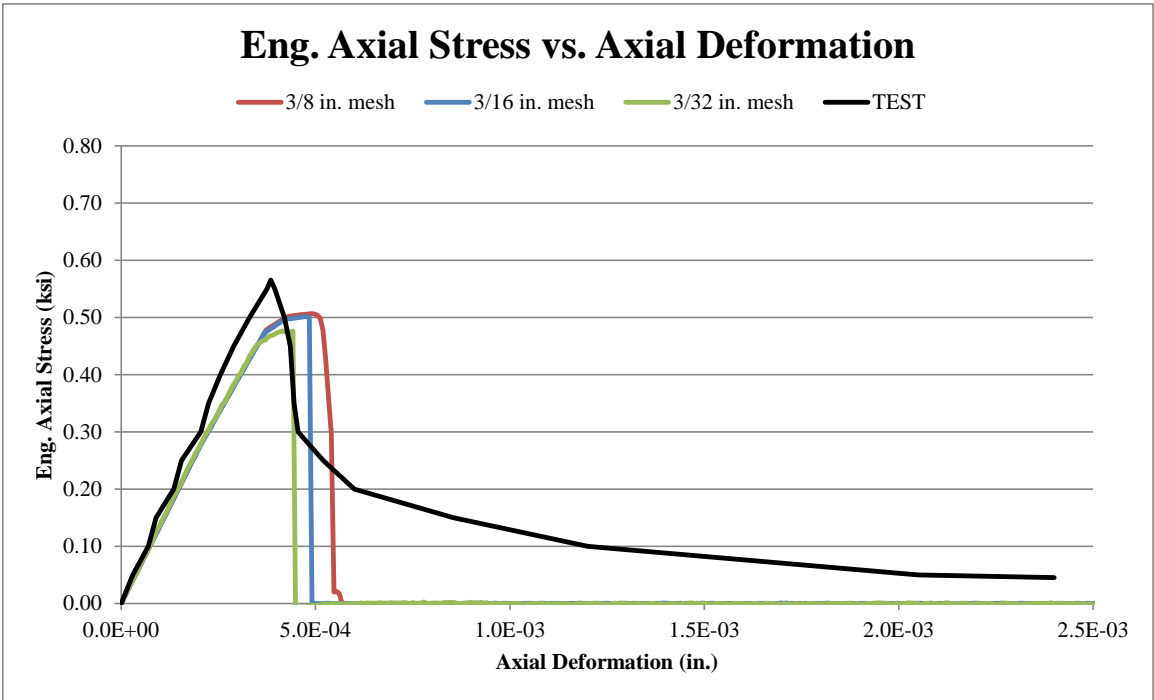


Figure 71. Tension Stress-Deformation for Refined Mesh, K&C Model

6.4.3 Compressive Damage Scaling Factor

The first of the two material model input parameter investigations involved the compressive damage scaling factor. Three different parameter ranges were explored: 0-1; 1-2; and 2-3. The model default value is 1.6. There was not much difference in simulation results for any of the compressive damage scaling factor values, as shown in Figure 72. Peak stresses were similar, most occurring at the same deformation. They all had the same general trends seen previously. The modulus of elasticity was lower than observed in the physical test. The plot shown in Figure 72 is for the 1-2 range, but the remaining two simulations yielded similar results. Damage accrued near the top of the specimen for all simulated parameter values. Due to the limited differences, the default value was used going forward.

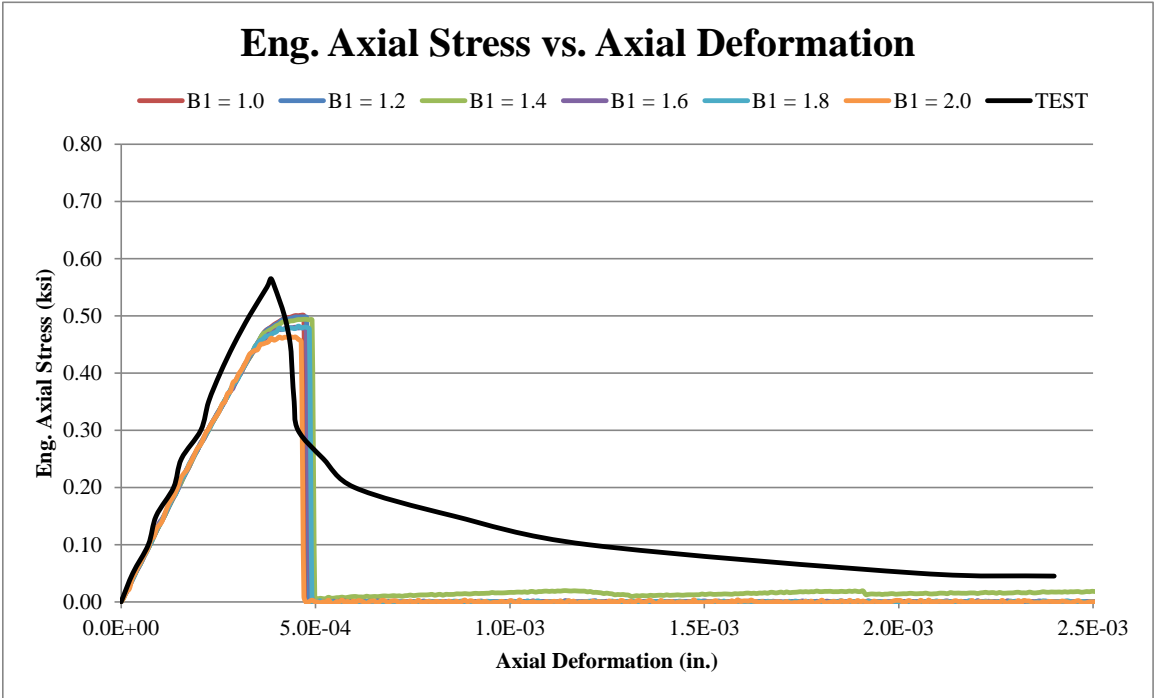


Figure 72. Tension Stress-Deformation for Compressive Damage Scaling Factor, K&C Model

6.4.4 Strain Rate Effects

The other material input parameter was the strain rate effects using the LCRATE parameter. The model can either have strain rate effects turned on or off. Dynamic increase factors were again calculated for both the default set, using a 6,585 psi (45.4 MPa) concrete compressive strength and a 6,367 psi (43.9 MPa) concrete compressive strength (physical test). These strengths and DIF values are shown in Table 11. The strain rate for the simulation was 2.2×10^{-7} 1/ms and theoretical enhancement values were 1.16 for both types of concrete.

Table 11. DIF Values for K&C Model – (a) 6,585 psi (45.4 MPa) and (b) 6,367 psi (43.9 MPa)

Strain Rate	Enhancement	Strain Rate	Enhancement
<i>1/ms</i>	-	<i>1/ms</i>	-
-3.0E-01	9.69	-3.0E-01	9.81
-1.0E-01	6.72	-1.0E-01	6.80
-3.0E-02	4.50	-3.0E-02	4.55
-1.0E-02	3.12	-1.0E-02	3.16
-3.0E-03	2.09	-3.0E-03	2.11
-1.0E-03	1.46	-1.0E-03	1.47
-1.0E-04	1.37	-1.0E-04	1.38
-1.0E-05	1.28	-1.0E-05	1.30
-1.0E-06	1.21	-1.0E-06	1.21
-2.2E-07	1.16	-2.2E-07	1.16
-1.0E-07	1.13	-1.0E-07	1.14
-1.0E-08	1.06	-1.0E-08	1.07
0.0E+00	1.00	0.0E+00	1.00
3.0E-08	1.00	3.0E-08	1.00
1.0E-07	1.03	1.0E-07	1.03
2.2E-07	1.05	2.2E-07	1.05
1.0E-06	1.08	1.0E-06	1.08
1.0E-05	1.14	1.0E-05	1.14
1.0E-04	1.20	1.0E-04	1.21
1.0E-03	1.26	1.0E-03	1.27
3.0E-03	1.29	3.0E-03	1.30
1.0E-02	1.33	1.0E-02	1.34
3.0E-02	1.36	3.0E-02	1.38
1.0E-01	2.03	1.0E-01	2.05
3.0E-01	2.93	3.0E-01	2.96

(a)

(b)

An initial simulation was completed to examine both concrete strengths with strain rate effects turned on, which were then compared to results with strain rate effects turned off using the 6,367 psi (43.9 MPa) strength. When strain rates effects were turned on, the stresses were enhanced by 36.3 and 41.3 percent, more than the 1.16 factor, as shown in Figure 73. This finding indicates that the strain rate effects were not working as defined, a trend that was seen in the simulations for the compression testing effort.

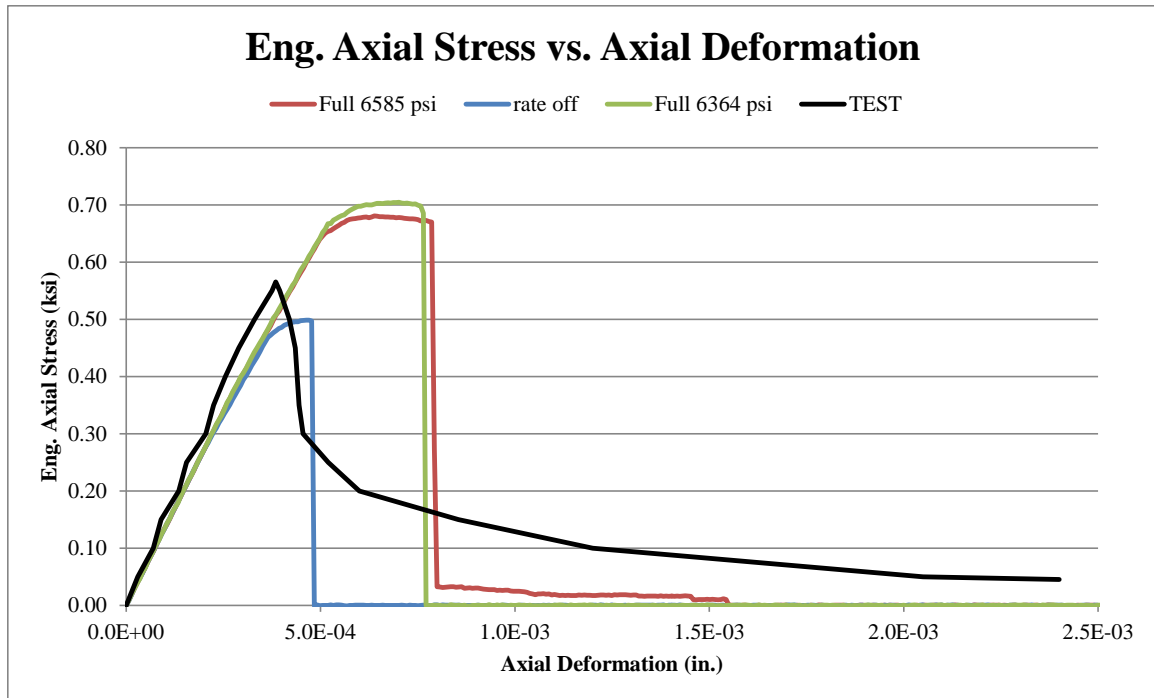


Figure 73. Tension Stress-Deformation for Base Strain Rate Effects, K&C Model

Additional investigations were completed to analyze the strain rate effects, similar to what was performed for the compression testing effort. When the rate effects were set to 1.0, they matched the ‘strain rate effects off’ behavior exactly. A comparison of strain rate effects on stress-deformation behavior was also completed, as shown in Figure 74. The 1.0×10^{-5} 1/ms and 1.0×10^{-6} 1/ms strain rates should result in enhancements of 28 and 21 percent, respectively. Instead, these two strain rates resulted in enhancements of 67.7 percent and 42.1 percent, respectively. This finding indicates that the simulation strain rate was not the problem, but there is an issue with how the strain rate effects are treated as a whole.

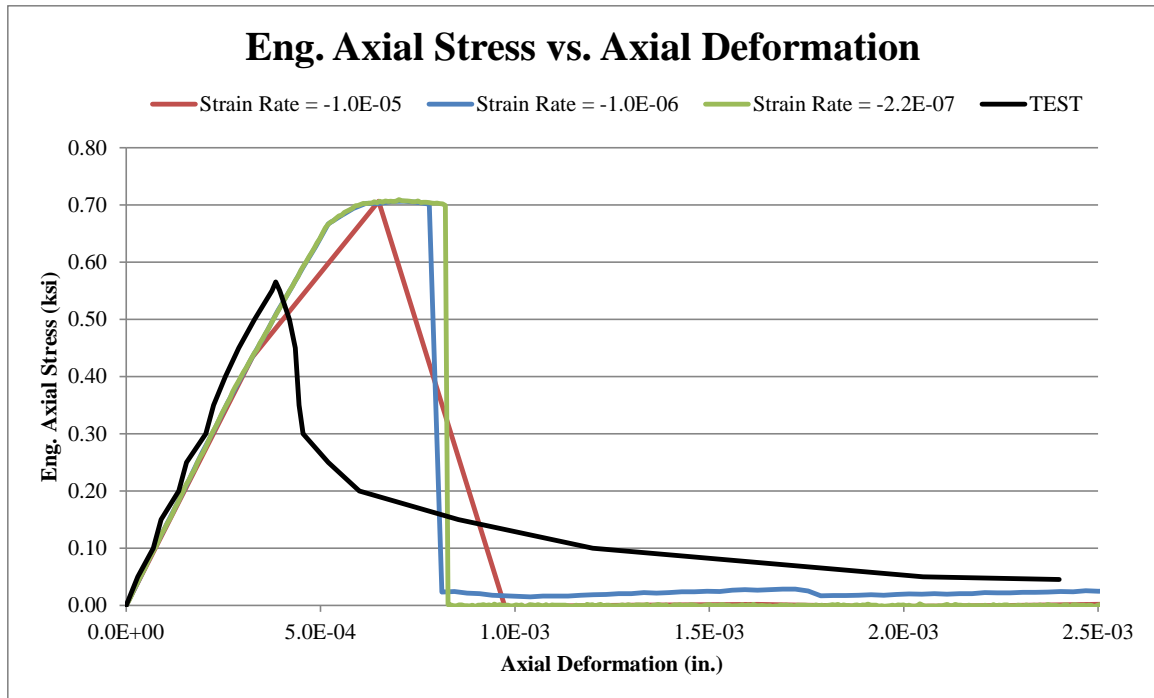


Figure 74 Tension Stress-Deformation for Varying Strain Rates, K&C Model

6.5 RHT Model – Simulation Results

The initial simulations for the RHT model included variations in element type and mesh size. Different hourglass energy control types were evaluated to limit initial hourglass energies, but HG6, HG7, and HG9 were found to be incompatible with this material model. After testing the remaining control types, HG5 was found to decrease the hourglass energies more than the other attempts and was used going forward. No material model input parameters were investigated.

6.5.1 Element Type

Similar to the compression testing effort, the simulation and test results did not match well. The simulation stress-deformation behavior have much higher stresses, and the average simulated peak stress, 0.7 ksi (4.8 MPa), was much higher than the physical test peak stress of 0.6 ksi (4.1 MPa), as shown in Figure 75. Softening did not occur

immediately after peak, as it did in the physical test. Instead, a nearly constant stress was maintained for a significant deformation before finally falling off near the end of the simulation. The modulus of elasticity was 6061 ksi (41.8 GPa) in the simulation, which was larger than the test result of 4710 ksi (32.5 GPa). There was also a bend in the elastic response that resulted in two distinct slopes through the pre-peak region. Overall, the simulated responses were identical through most of the simulation, with no noticeable differences in the damage accumulation. Elform 1 was chosen moving forward due to its softening occurring earlier and its use in previous simulations with this material model. Damage accrued near the bottom of the specimens.

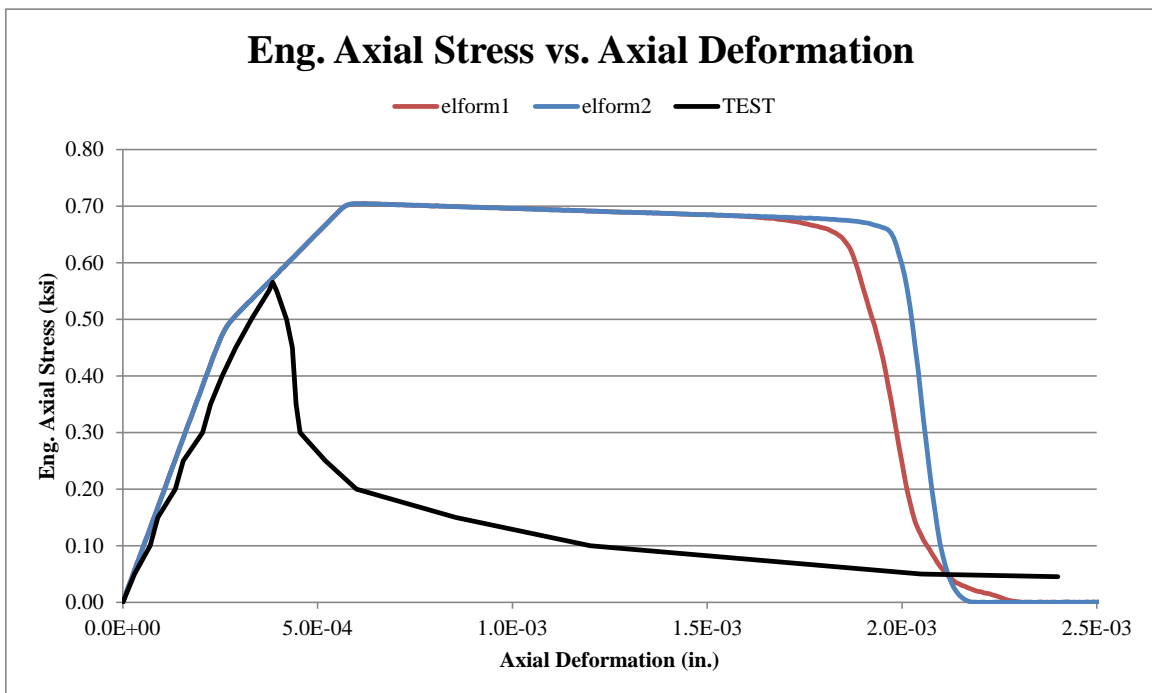


Figure 75. Tension Stress-Deformation for Element Type, RHT Model

6.5.2 Mesh

The mesh size simulations had some similar trends that were discovered in the element type simulations. The simulated stress-deformation behavior had a higher peak

stress of 0.7 ksi (4.8 GPa) in the simulations than observed in the physical test at 4710 ksi (32.5 GPa), with softening occurring after a constant stress was maintained. The modulus of elasticity was 6054 ksi (41.7 GPa) and two distinct slopes were formed in the pre-peak region. The following mesh sizes were evaluated: $\frac{3}{4}$ in. (19 mm); $\frac{3}{8}$ in. (10 mm); $\frac{3}{16}$ in. (5 mm); and $\frac{3}{32}$ in. (2 mm). Since softening was occurring at large deformations and a trend was showing that finer meshes began softening at lower deformation values, a $\frac{3}{32}$ -in. (2-mm) mesh size was investigated. This mesh size did soften the behavior earlier than observed in the other mesh sizes, but it still resulted in deformations greater than the test, as shown in Figure 76.

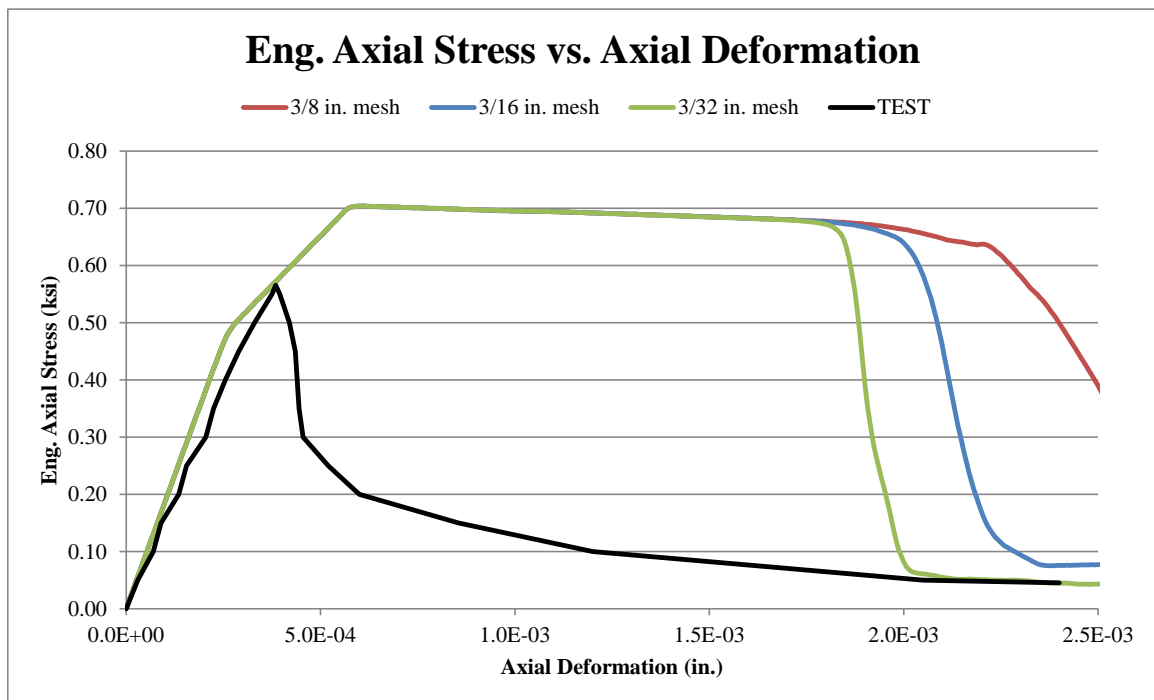


Figure 76. Tension Stress-Deformation for Finer Mesh, RHT Model

6.6 Winfrith Model – Simulation Results

The simulations using the Winfrith model did not complete in the tension simulations, using both the default hourglass energy control or different types of

hourglass control. There were nodes with out-of-range velocities in the simulation that caused termination errors before finishing. Less than 2500 ms of 10,000 ms were completed for each of the simulations that were attempted. Based on this performance, no results could be obtained using this material model in tension. Therefore, the Winfrith model in tension was unstable and no conclusions could be made about input parameters.

6.7 CDPM Model – Simulation Results

As with the previous set of simulations for the compression load case, the CDPM model failed to complete any simulations due to errors. In fact and in all simulations, less than 1000 ms of 10,000 ms were completed in 24 hours of computing time. There are bigger issues with this material model, and it cannot be trusted to provide useful results for this study.

6.8 Discussion

After completing the tension simulations, it was clear that issues remain with all of the material models. Some of the same issues seen in the compression simulation investigation were repeated, while new problems arose for other material models. This finding reiterates the fact that no model is flawless, but there are parts of each model that are useful. In the compression simulations, the modulus of elasticity was generally higher than the observed in test for the CSCM and K&C models. However, these models underestimated the modulus of elasticity in the tension simulations. In the RHT simulations, the modulus of elasticity was higher than observed in the physical test in compression and tension. An increase in percent error for the tensile stresses may have occurred as some of the material models assume tension strength as a specific percentage of the concrete compressive strength. If the assumed compression to tension strength

ratio was not replicated in the physical test, the peak stresses between the simulation and test results will likely not match, which may have occurred with the CSCM and RHT models. Specifically, these models generate a tensile strength. The CSCM and K&C peak stresses were lower than the physical test result, with the RHT peak stress significantly higher.

The issue with the plastic solver for the CDPM model continued, and no results were obtained from this model. The Winfrith model experienced a new issue as there were nodes with out-of-range velocities, not allowing results to be obtained. The model erred out before completion, and no data could be extracted from the simulation. Finer mesh sizes and different hourglass controls were attempted, but these changes still did not solve the issue of nodes with out-of-range velocities. The geometry of the part was not complicated, thus making the presence of nodes with out-of-range velocities even stranger.

The CSCM model did not perform as well in the tension load case as it did in the compression load case. The simulation peak stresses of 0.44 ksi (3.0 MPa) were below the physical test peaks stresses of 0.57 ksi (3.9 MPa); the simulation modulus of elasticity of 4197 ksi (28.9 GPa) was below the physical test modulus of 4710 ksi (32.5 GPa). There was an issue with the results being repeatable between simulations. The stress-deformation behavior with the $\frac{3}{16}$ -in. (5-mm) mesh size in the initial simulations did not match the results obtained in the secondary, refined mesh size simulation effort and is quite concerning. This problem was seen in the compression simulations, but with using the additional material model input parameters such as ERODE, repow, and recov. The stress-deformation behavior of the curves was less of a match in tension, as there was a

gradual decrease in stress after peak instead of an initial drop-off in stress followed by a gradual decline.

The K&C performed the best of the five models in the tension simulations. The peak stresses of 0.51 ksi (3.5 MPa) were much closer to the physical test peak of 0.57 ksi (3.9 MPa), likely due to the fact that the tensile strength was inputted directly into the material input deck. The post-peak softening behavior in the physical test was not replicated in the K&C simulations. Instead, the simulated stresses dropped immediately to zero after peak was reached. Although this finding is probably a more realistic expectation for a tension failure, it is a result of the model having inadequate softening capability. This behavior was also demonstrated in the compression simulations. Further strain rate effects did not behave as defined. Additional investigations were performed to determine the exact problem in both tension and compression simulations.

Finally, the RHT model overestimated both the modulus of elasticity and the peak stress. The simulation peak stresses of 0.70 ksi (4.8 MPa) were larger than the physical test peak stresses of 0.57 ksi (3.9 MPa); the simulation modulus of elasticity of 6055 ksi (41.8 GPa) was larger than the physical test modulus of 4710 ksi (32.5 GPa). This behavior was seen in the compression simulation efforts and continued in the tension load case. This behavior needs to be monitored in the shear simulations to determine if this model is adequate for future simulations. No changes to the material model input parameters can be made; since, there are none available, and automatic parameter generation was relied upon.

CHAPTER 7 SHEAR SIMULATIONS ON EXTERNAL COMPONENT TESTS

7.1 Introduction

The third and final loading case for the initial simulation investigation was shear. External component testing data was acquired for use in the validation of the five selected material models. Shear testing of unreinforced concrete is not very common, and limited research studies were available for use in this study. One particular study by Wong involved a rectangular specimen placed in a shear box [68], as shown in Figure 77.

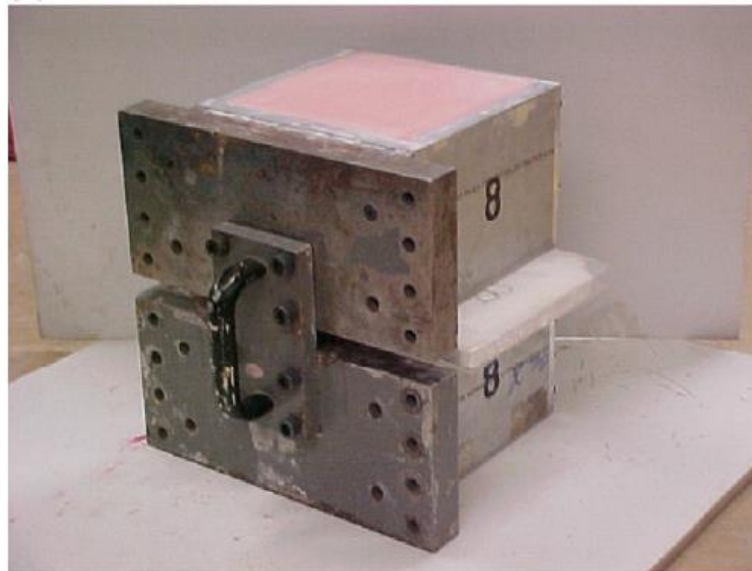


Figure 77. Shear Box Testing Specimen [68]

A shear stress versus horizontal displacement was prepared from the study information and used for comparison with future simulation results, as shown in Figure 78. Specifically, a 5.5-in. x 5.5-in. x 11.8-in. (140-mm x 140-mm x 300-mm) specimen was placed within a shear box, separated into two halves. Each half of the metal shear box was 7.9-in. x 7.9-in. x 5.5-in. (200-mm x 200-mm x 140-mm) with a thickness of $\frac{7}{8}$ in. (20 mm). Grout was used to fill the space between the specimen edge and the inside of the metal box. The maximum aggregate size of the specimens was assumed to be $\frac{3}{8}$ in.

(10 mm) since it was unknown, and the concrete had a compressive strength of 5,802 psi (40.0 MPa). In this study, the specimens were loaded using an MTS Direct Shear Test System in which normal (vertical) load and shear forces were applied. In the following simulations, a normal force of 0.87 ksi (6.0 MPa) was applied. The shearing force was applied to the specimen based on a rate of 0.002 in./min (0.05 mm/min).

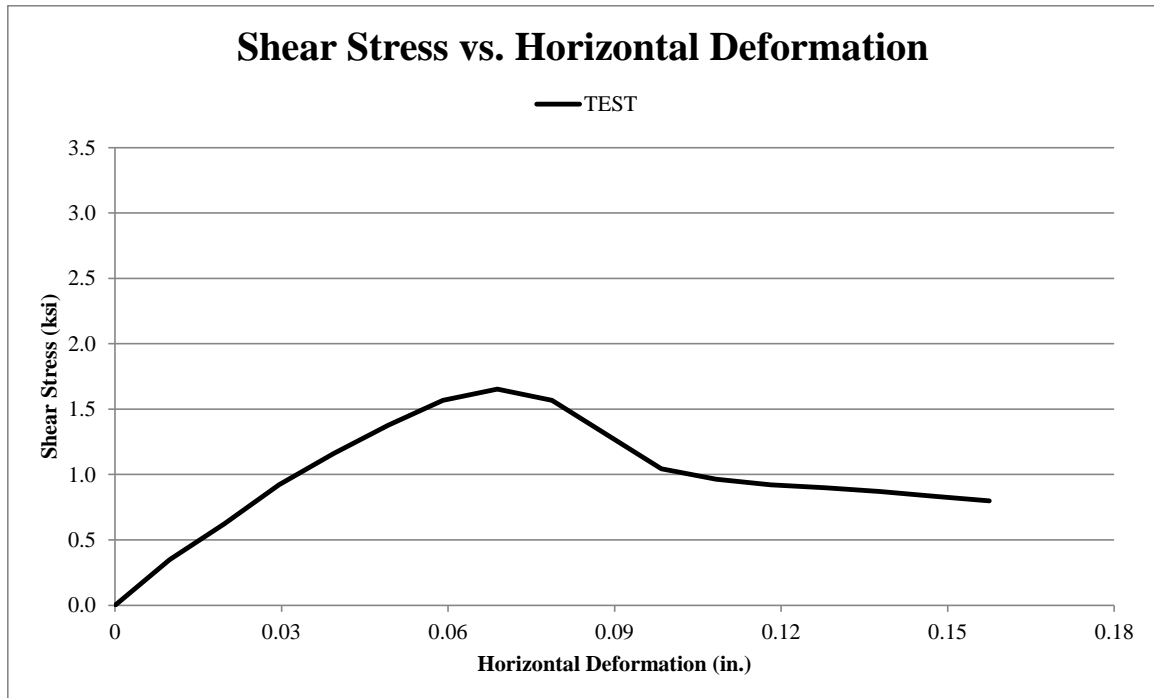


Figure 78. Shear Stress-Deformation Test Results [68]

Despite the completion of the three experimental tests and a novel testing approach, the shear tests may not have had accurate data. As shown in Figure 78, the peak stress in the experiment occurred at a horizontal displacement of 0.07 in. (1.8 mm), which is much higher than for the compression and tension experimental tests previously evaluated. These peak deformations were 0.01 in. (0.3 mm) and 0.0004 in. (0.01 mm), respectively. Based on the relationship between the three load cases, it would be expected that the shear peak deformation be nearer to that of the tension test. The discrepancy may

have either come from improper documentation of test data or compliance within the testing equipment. Therefore, only the peak stress values will be used when comparing the simulation curves to the test curves. Since the softening behavior of the model was not considered, material model input changes were simulated, but only peak stress values were compared.

7.2 Simulation Data Evaluation Process

An initial loading rate analysis was completed with the LS-DYNA software for each of the five models. Potential displacement rates ranged from 15.8 in./s (400 mm/s) to 0.02 in./s (0.4 mm/s), and the goal was to find convergence in the stress-strain behavior at a reasonable displacement rate. Convergence was reached for all material models at 0.32 in./s (8 mm/s), which was considered optimum.

The intent of the shear simulations was to compare the simulation results from each of the five material models to the acquired test results obtained from the external source. The concrete section in the model was 5.5 in. x 5.5 in. x 12 in. (140 mm x 140 mm x 305 mm). A layer of grout, given an elastic definition was placed between the concrete specimen and the steel box components. A rigid definition was assigned to the shear box pieces. A *RIGIDWALL_PLANAR was placed below the shear box and concrete components. The top sections of the shear box were assigned a *BOUNDARY_PRESCRIBED_MOTION definition in the x-direction. The displacement rate was increased linearly until the end of the simulation. A *LOAD_NODE definition was assigned to the top nodes of the setup in order to simulation the normal force on the specimen. Cross-sections were placed through the

center of the concrete specimens in order to measure forces for use in computing stresses. An overview of the model is shown in Figure 79.

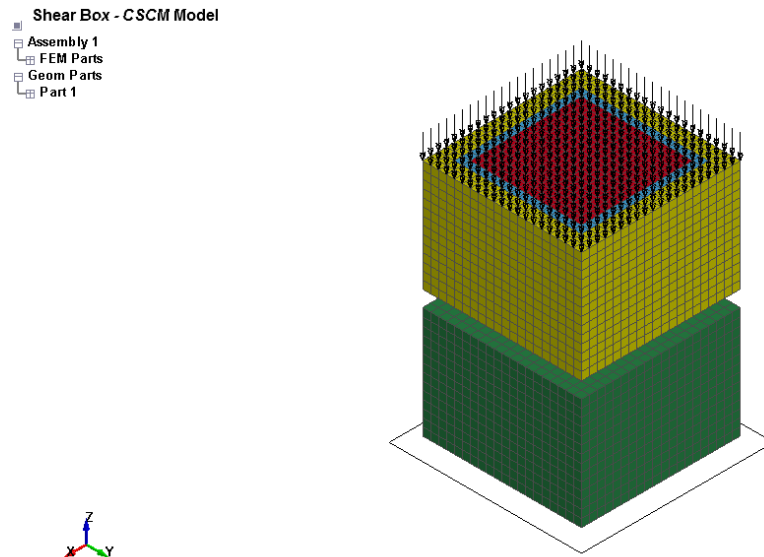


Figure 79. Overview of External Shear Simulation

Two material model parameters were investigated, different mesh sizes and two element types. Individual mesh sizes of $\frac{3}{8}$ in. (10 mm) and $\frac{3}{16}$ in. (5 mm) were explored for each material model in order to determine the optimal mesh size. Element types elform 1 and elform 2 were examined for the CSCM, K&C, RHT, and CDPM material models. The Winfrith model is not compatible with elform 2, so an element type simulation was not completed. Hourglass energy control types were used as needed, specifically when the hourglass energies were larger than 20% of the internal energy.

Once these simulations completed, the results were compared to the test results [68]. Stress-deformation results were used to validate the simulation findings. Engineering stress from the simulation was computed as the cross-section force divided by the original cross-sectional area. The simulation stresses and deformations were plotted against the physical test results. Again, the peak stress was primarily used for the

validation effort; since, softening was not considered due to perceived inaccuracies in the deformation measurements.

7.3 CSCM Model – Simulation Results

The initial simulations for the CSCM model included variations in element type and mesh size. In this effort, no hourglass energy issues occurred. Thus, the mesh size and element type investigations were performed followed by simulations with the ERODE, repow, and recov parameters.

7.3.1 Element Type

The simulated stress-deformation behavior had limited similarities to the physical test result. For the two simulations, only minor differences were observed between the elform 1 and elform 2 element types, largely after peak stress was reached, as shown in Figure 80. The peak stress observed with elform 2 was lower. The average peak stress for the two was 2.2 ksi (15.2 MPa), which is higher than the physical test peak stress of 1.7 ksi (11.7 MPa). A significant number of elements deleted through the cross section of the elform 2 part as compared to the elform 1 part, as shown in Figure 81. However, there still was some element deletion in the elform 1 part. Based on its previous performance, elform 1 was used moving forward. A $\frac{3}{8}$ -in. (10 mm) mesh size was used for this initial simulation.

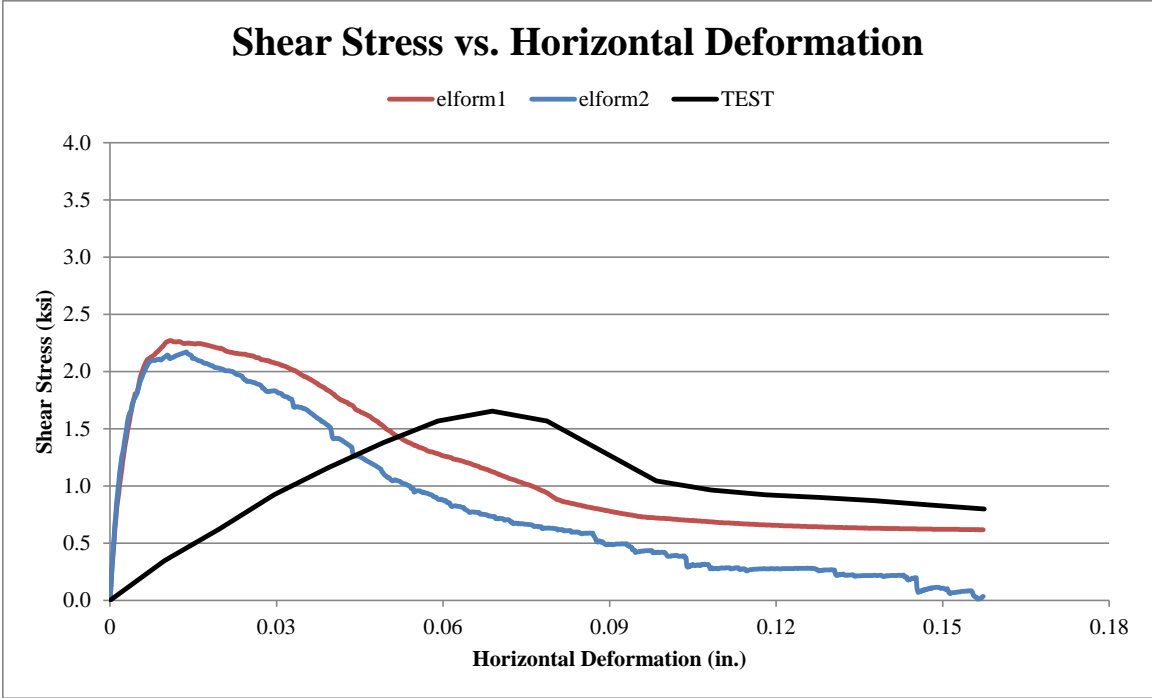


Figure 80. Shear Stress-Deformation for Element Type Simulation, CSCM Model

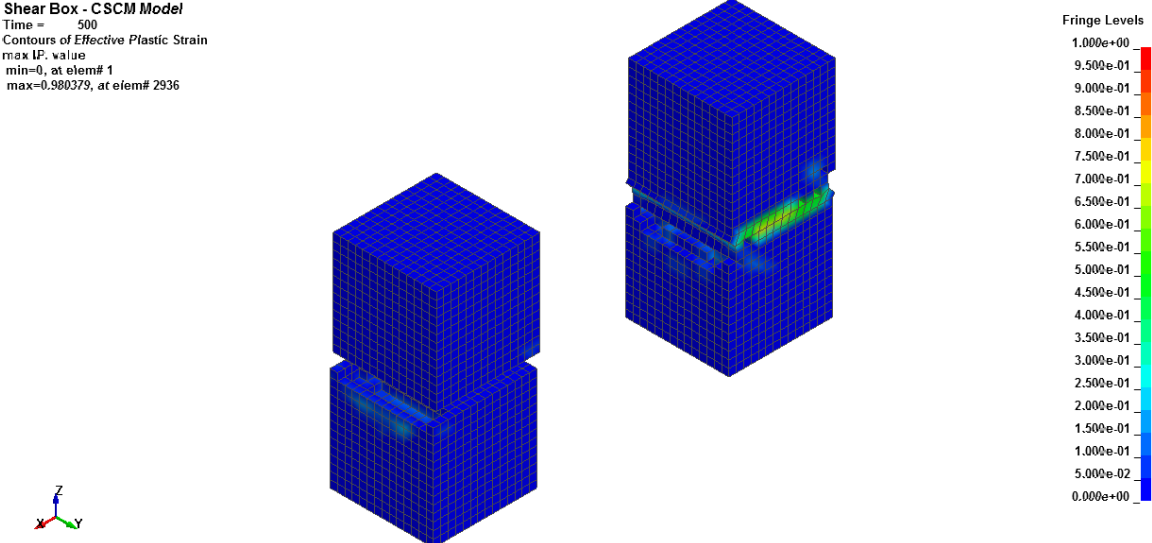


Figure 81. Shear Damage Contours for Element Type Simulation, CSCM Model

7.3.2 Mesh

Two mesh sizes were investigated: a 3/8-in. (10-mm) and 3/16-in. (5-mm) mesh size for all simulated parts. Failure was not achieved for either mesh size. Significant

differences were found in the stress deformation results, as shown in Figure 82. The finer mesh size had a peak stress of 3.1 ksi (21.4 MPa), a drop, and then a secondary peak of 2.5 ksi (17.2 MPa) after initial softening occurred. The coarser mesh size had a peak stress of 2.3 ksi (15.9 MPa) and then gradual softening. The finer mesh size resulted in less element deletion as compared to the coarser mesh size, as shown in Figure 83. Due to its stress-deformation behavior, the coarser mesh size was deemed the better option going forward.

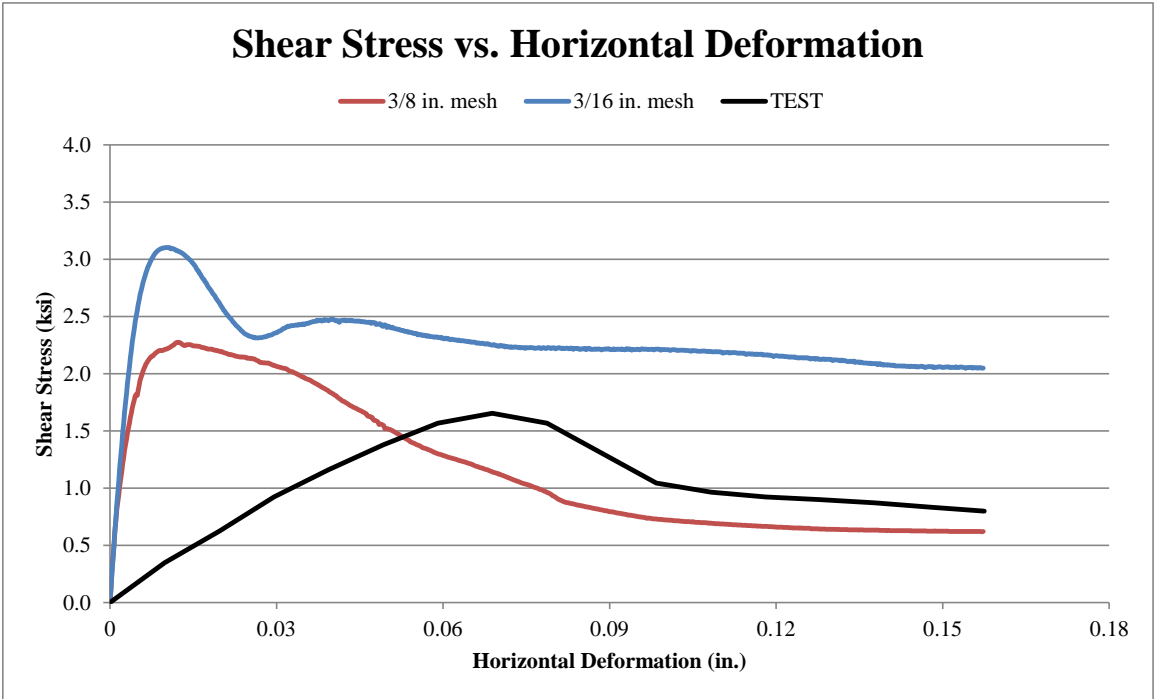


Figure 82. Shear Stress-Deformation for Mesh Simulation, CSCM Model

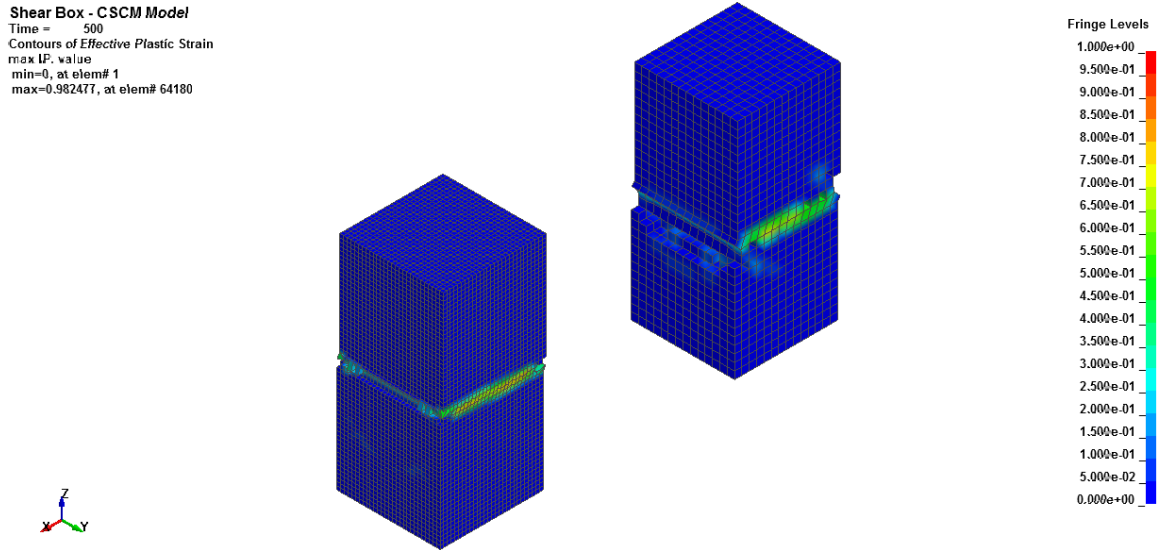


Figure 83. Shear Damage Contours for Mesh Simulation, CSCM Model

7.3.3 ERODE, recov, and repow

After the initial simulations for element type and mesh size were completed, changes were made to the ERODE, repow, and recov input parameters. These parameters were varied in the same manner as used in previous simulations. Ultimately, there was not much difference in results when the ERODE, repow, and recov values were varied. The average peak stresses for all simulations using three inputs were 2.3 ksi (15.9 MPa). The largest difference in simulation results occurred with the repow parameter. Although small, noticeable gaps occurred in the stress-deformation behavior for this parameter, which decreased as repow was decreased. However, it was determined that the default values for each of the inputs would be adequate.

7.4 K&C Model – Simulation Results

The initial simulations for the K&C model included variations in element type and mesh size. There were no hourglass energy concerns for the shear simulation effort. The mesh size and element type investigation were followed by material input parameter

variations for the compressive damage scaling factor. Strain rate effects were examined in previous simulations, but it was not considered for shear loading. Only strain rate effects are included in the material model for compression and tension.

7.4.1 Element Type

The peak stresses for this material model were much closer to the physical test results than those observed in the CSCM simulations. Failure occurred for elform 2, but not elform 1. As shown in Figure 84, the average peak stress was 1.6 ksi (11.0 MPa), as compared to 1.7 ksi (11.7 MPa) for the physical test peak stress. The same general behavior was seen in the simulations as a peak stress was reached with some steep decline in stress, followed by a more gradual decrease. It seems as though the general shape and trend of the simulated stress-deformation behavior would be similar to the physical test results had the deformation scale been shifted to the left for physical testing only. The elform 2 part deleted before the end of the simulation due to shooting nodes in the specimen portion of the part. Therefore, elform 1 was considered for use in future simulations. Elform 1 also had a peak stress closer to the physical test, so it was preferred anyway.

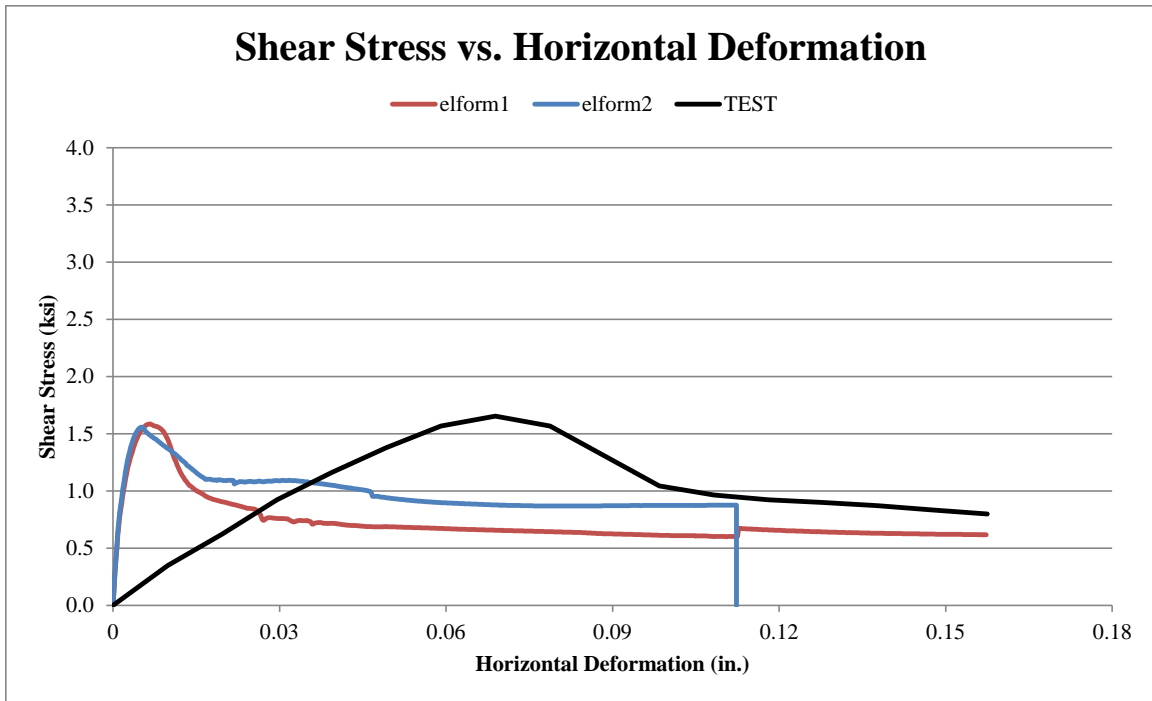


Figure 84. Shear Stress-Deformation for Element Type, K&C Model

7.4.2 Mesh

Similar to the CSCM simulation effort, shear stresses increased significantly when a finer mesh size was used. The K&C model reached a peak stress of 3.3 ksi (22.8 MPa), as shown in Figure 85. The coarser $\frac{3}{8}$ -in. (10-mm) mesh size had a more accurate peak stress and was used going forward.

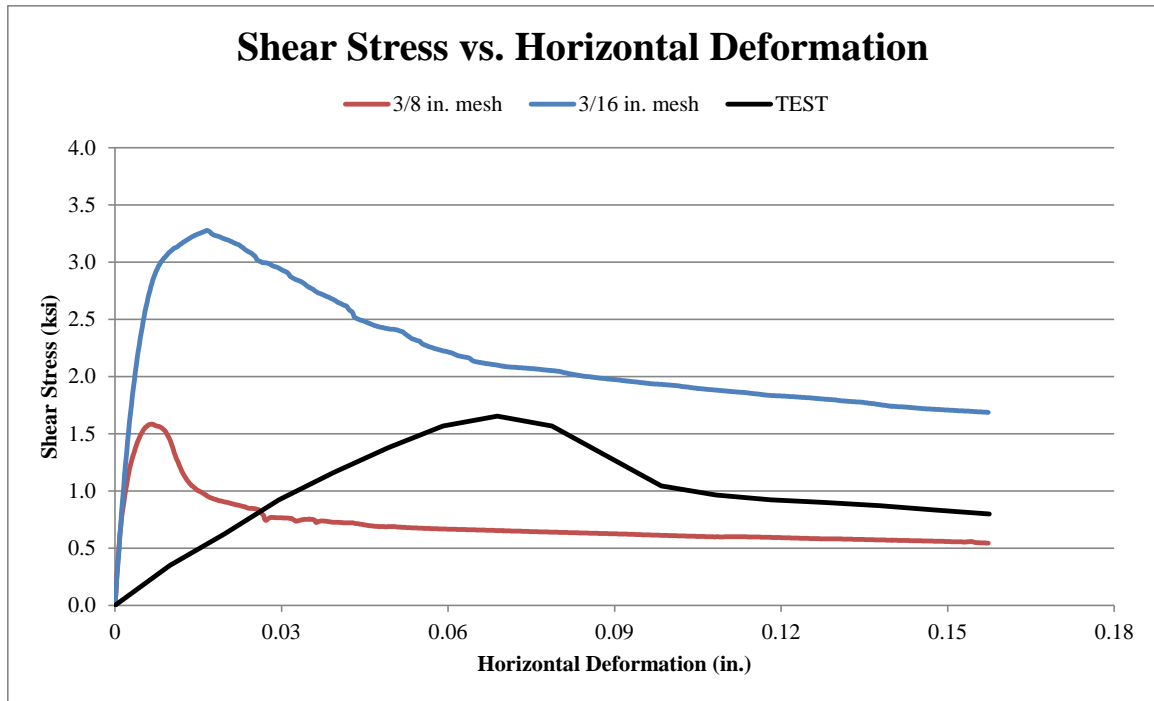


Figure 85. Shear Stress-Deformation for Mesh Simulation, K&C Model

7.4.3 Compressive Damage Scaling Factor

Similar to previous simulations, there were three ranges of values for the compressive damage scaling factor: 1 to 2; 0 to 1; and 2 to 3, split up in increments of 0.2, with the default being 1.6. For the 1 to 2 range, as the compressive damage scaling factor decreased, the peak stresses decreased as well. The peak stress for this range of 1 to 2 was 1.5 ksi (10.3 MPa) to 1.6 ksi (11.0 MPa). For the 0 to 1 range, the peak stress varied from 1.2 ksi (8.3 MPa) to 1.6 ksi (11.0 MPa). For the 2 to 3 range, the peak stress varied from 1.6 ksi (11.0 MPa) to 1.7 ksi (11.7 MPa). The deformation and damage also decreased with a decreasing compressive damage scaling factor.

7.5 RHT Model – Simulation Results

The initial simulations for the RHT model included variations in element type and mesh size. No material model input parameters were investigated. No hourglass issues were encountered in these two simulation investigations.

7.5.1 Element Type

There was not much difference in results between the two element types used in this simulation in terms of peak stress and general behavior. Neither element type resulted in failure. As shown in Figure 86, the stress for elform 2 was 1.8 ksi (12.4 MPa), which was slightly higher than the physical test peak stress of 1.7 ksi (11.7 MPa). Both element types had similar trends in deflection behavior, as shown in Figure 87. The internal energy did decrease for the elform 2 part halfway through the simulation and continued to do so through the end of the simulation. Thus, elform 1 was used going forward.

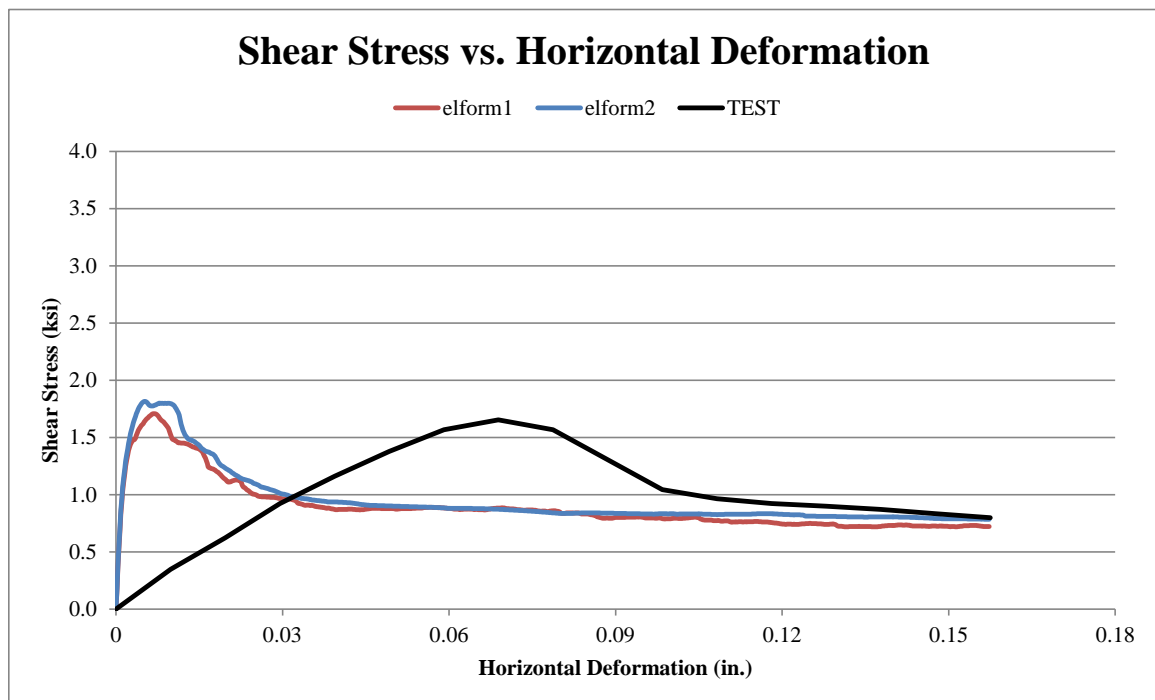


Figure 86. Shear Stress-Deformation for Element Type, RHT Model

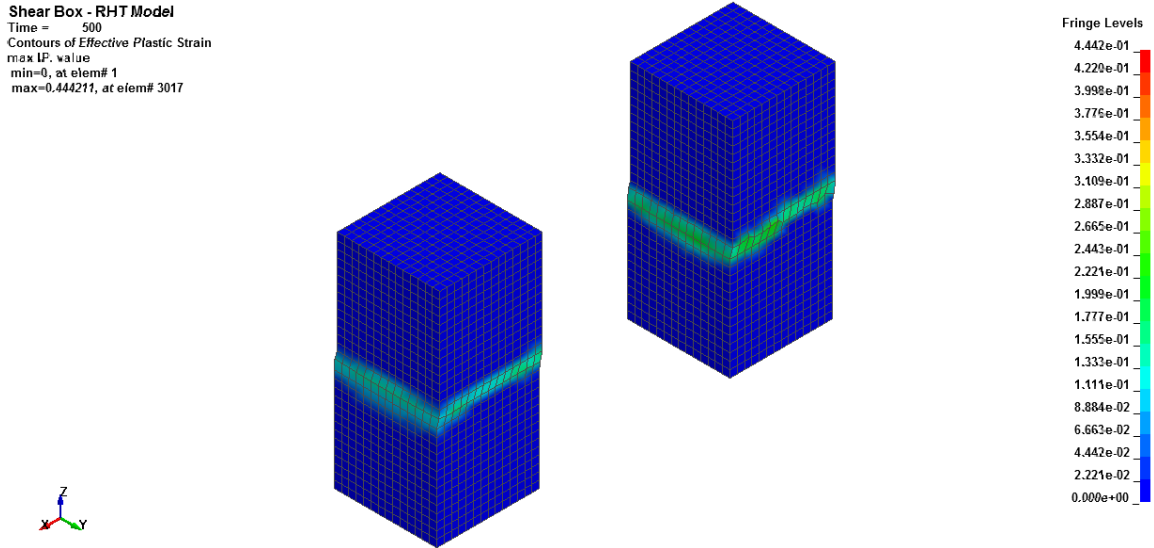


Figure 87. Shear Damage Contours for Element Type Simulation, RHT Model

7.5.2 Mesh

As seen with previous mesh size investigations under shear loading, larger stresses occurred for the finer $\frac{3}{16}$ -in. (5-mm) mesh, reaching 3.1 ksi (21.4 MPa), as shown in Figure 88. The $\frac{3}{8}$ -in. (10-mm) mesh had a peak stress of 1.7 ksi (11.7 MPa). Higher damage was observed in the finer mesh model, which extended to a larger area of the part. This damage also resulted in more element warping as deletion is not a feature of the model. Similar to previous mesh size investigations, the internal energy was also higher for the finer mesh. Thus, the $\frac{3}{8}$ -in. (10-mm) mesh was preferred.

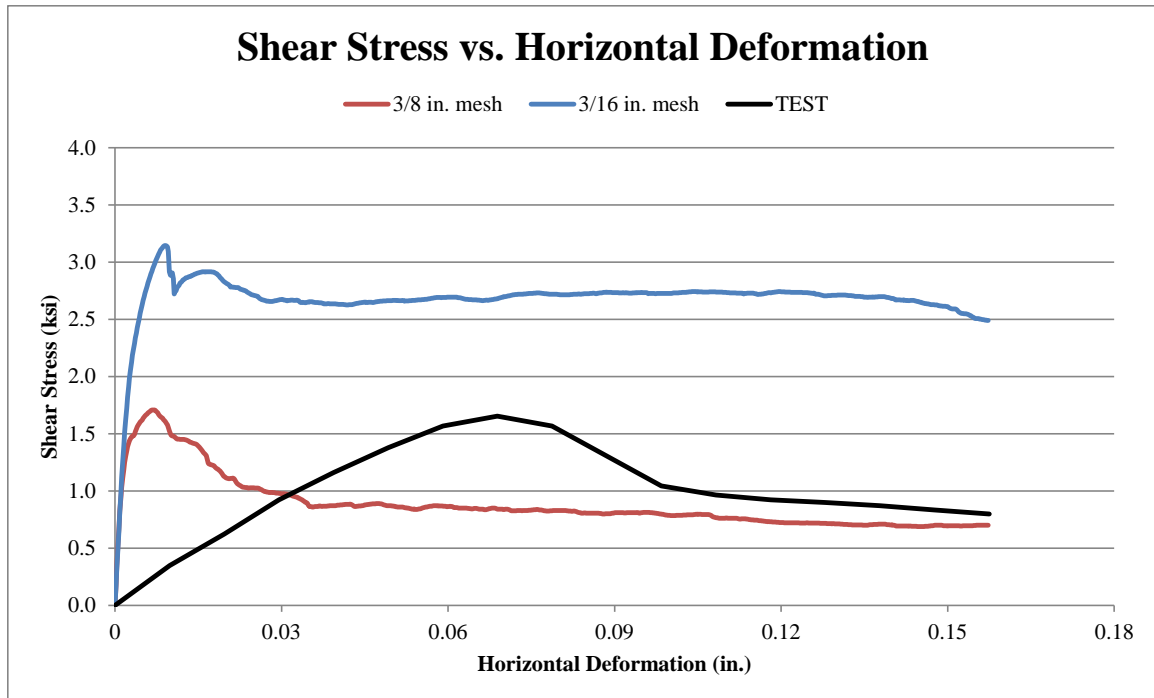


Figure 88. Shear Stress-Deformation for Mesh Simulation, RHT Model

7.6 Winfrith Model – Simulation Results

An initial attempt at a mesh size investigation using the Winfrith material model erred out before completing, after only 75 ms out of 500 ms. It was thought that this may be due to hourglass energy issues with the simulation, thus the full complement of hourglass control types were evaluated. HG4 was the only hourglass control type for which a simulation completed 500 ms. However, hourglass energies were 18% of the internal energies, as shown in Figure 89. Although control of the hourglass energy was attempted, no solution could be found. Similar to the tension loading case, no useable results were obtained with this material model and this loading case, although the peak stress comparisons were reasonable, as shown in Figure 90.

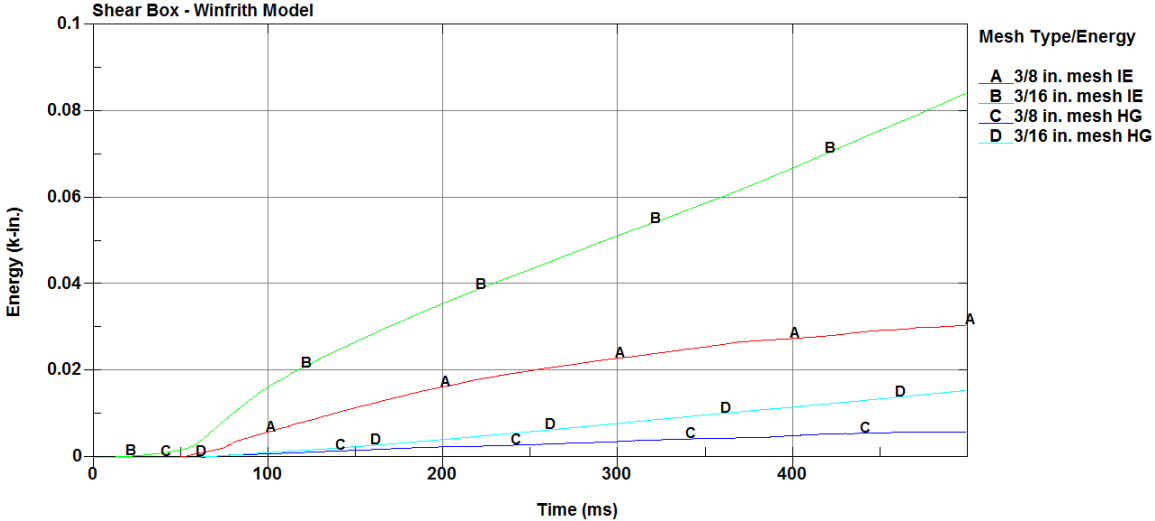


Figure 89. Shear Hourglass Energy Plots with HG4, Winfrith Model

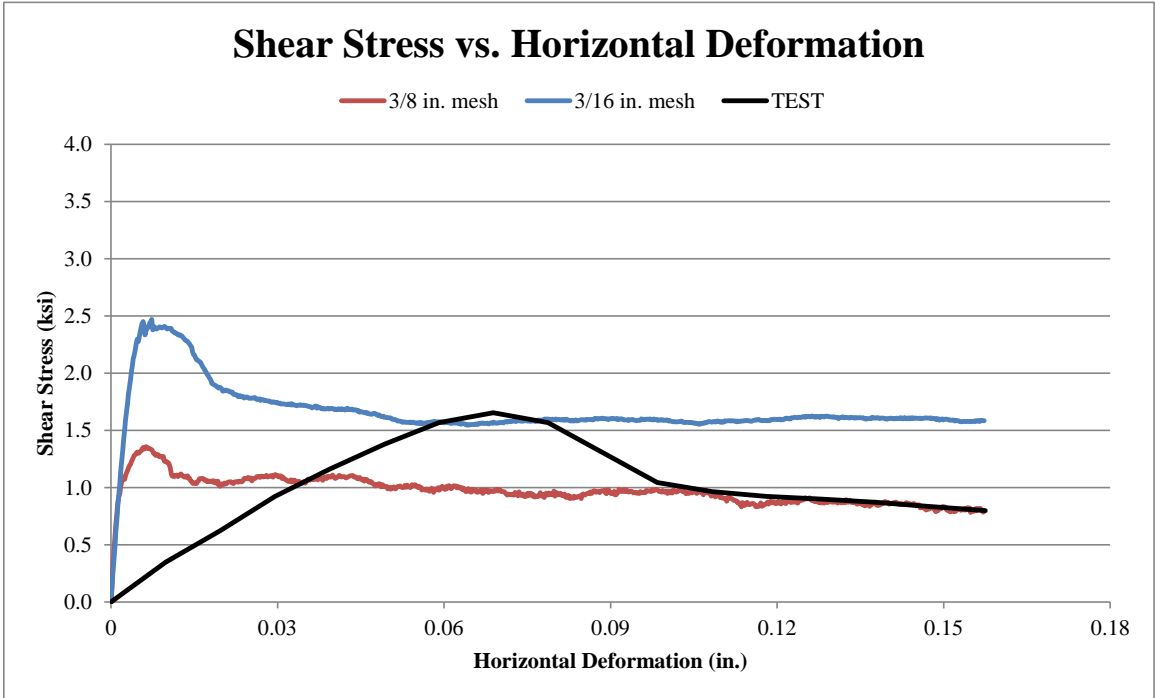


Figure 90. Shear Stress-Deformation for Mesh Simulation, Winfrith Model

7.7 CDPM Model – Simulation Results

As with previous simulations, the CDPM model failed to complete any simulations. In all simulations, 50 ms or less were completed in a 24 hour span. There are

bigger issues with this material model, and it cannot be trusted to provide useful results for this study.

7.8 Discussion

Three material models (CSCM, K&C, and RHT) adequately predicted the physical test peak stress during the shear simulations. The simulated stress-deformation behavior did not match, and there was uncertainty about the deformation values in the physical testing results. If the test results were accurate, then none of the models were able to represent shear deformation behavior. There were some outliers in the mesh size simulations as a finer mesh size resulted in significantly higher stresses. The K&C and RHT models provided the closest match to the physical test peak stress, with the CSCM model peak stress higher than observed in the physical test. The RHT model performed best in this load case, as it had previously been unreliable for both compression and tension load cases

The other two material models, Winfrith and CDPM, had issues running and could not provide any useful results. The plastic solver caused problems for the CDPM model. For the Winfrith model, initial models were erring out before completion, so hourglass energy controls were attempted. Only one of those control types resulted in a completed simulation; however, hourglass energies were higher than desired.

CHAPTER 8 RECOMMENDATIONS FOR FURTHER ANALYSIS

8.1 Selection of Material Models

Previously, two LS-DYNA simulation efforts were performed – one on single-element modeling and another directed toward component modeling of external laboratory tests. From these efforts, it was clear that further investigation was required, so more test data with different test setups was deemed necessary to further evaluate the selected material models. Furthermore, in-house testing would allow for more accurate and specialized data collection using similar load cases to those simulated in past analyses. In order to create a more efficient simulation plan after the in-house testing, the material models were reviewed to determine if all five models would be included in the continued simulation investigations.

The CSCM model performed consistently well during the single element and external component simulations. For the compression and tension single element simulations, the peak stresses were similar to expected values, although not the closest among all five models. In the external component simulations, the CSCM model performed well across all three load cases. Within the compression simulations, the CSCM model performed better than the other four models. The CSCM model predicted peak stresses with 1.1% of the physical test. Despite these benefits, it was discovered in the external component simulations that the model does have some issues regarding selected input parameters. Namely, identical simulations did not produce repeatable results. Simulations were run with the exact same loading, geometry, and material properties for all parts in the model, yet the results were often different. Some randomness in results should be expected, but the propensity for occurrence was

concerning. Despite these issues, the model does have some benefits that others do not, including the ability to erode elements directly in the model and its softening behavior. Although there were some inconsistencies in the model, it generally provided good results and had unique features.

The K&C model also performed well across all simulations. In the single element modeling, it provided the closest matches for peak stresses for the compression and tension loading cases. The material model performed poorly in shear. In the external component simulations, it also performed well, having the closest match for peak stresses between the simulation and physical test results for the tension and shear load cases. In all component simulations, there was not much softening after peak stress, especially in the tension simulations. This finding is a drawback of the material model, as no material model input parameters were found to affect softening. Additionally, there is no element deletion capability; this makes it difficult to show when specific elements fail, unless the damage profile is carefully monitored. Finally, the strain rate effects were not found to work as expected, oftentimes overestimating the dynamic increase factor that should be used for a specific strain rate. Despite some of these shortcomings, the material model handled all three load cases reasonably well both in single element and component testing simulations.

The RHT model was inconsistent throughout all simulations. In the single element simulations, the RHT model always overpredicted stresses by approximately 56% and the response or behavior was different than observed with the other material models. The trend continued in the external component simulations as the material model overpredicted the peak stresses for both compression and tension by approximately 14%. Its

results were seen as an outlier in those simulations as they greatly differed from physical test data. However, the RHT model accurately predicted peak strength in the shear component simulations. Despite this finding, the RHT model still did not perform well in the single element shear simulations or for the other two load cases. The material model has some benefits, such as damage tracking, but its inability to perform well for basic behaviors is concerning.

The Winfrith model was inadequate across most load cases in the single element and external component simulations. The material model performed well in the compression load case, but it failed to provide any useable results in the tension and shear load cases for the external component simulations. Specifically in the external component simulation effort for tension, the material model erred out due to out-of-range velocities in the simulation. This finding is a major concern when considering its use in future applications. In addition to its initial poor performance, the material model lacks some of the key capabilities that are preferred, such as element deletion and damage tracking.

Finally, the CDPM model performed poorly across all simulations. Results were obtained in the single element simulations but not for the external component simulations due to excessive run times. In the single element simulations, the model predicted peak stresses near the expected value for all load cases, but not as close as predicted for some of the other models. For the shear single element simulations, the plastic solver within the material model did not converge which resulted in incomplete simulations or long run times. This problem continued in the external component simulations, except no results were obtained for any of the three load cases. This instability in the material model indicates its inability to be used for component-level simulations.

After comparing and evaluating all material models, it was determined that the CSCM and K&C models would be further investigated during the internal component testing phase.

CHAPTER 9 COMPONENT TESTING CONDITIONS – INTERNAL

9.1 Purpose

Additional, in-house component testing was performed to acquire specific and robust data to furthering knowledge regarding concrete fracture as well as support the investigation and validation of five concrete material models. Four different loading tests were performed and later simulated, including compression, tension, flexure, and shear. This in-house testing helped to ensure that more robust data was available using advanced instrumentation as compared to data obtained in the literature and used in the three external analyses. Additionally, high-speed video and high-resolution photographs were used to document the tests and support validation efforts.

9.2 Scope

For the internal testing program, 19 total tests were completed across three different load cases. Seven concrete cylinder compression tests were completed along with six direct tension tests and six four-point bending tests to investigate flexure and shear. The major data that was acquired from these tests included applied force, component displacement, and strain. The damage patterns were documented and evaluated using test video and photographs.

9.3 Concrete Test Specimens – Preparation

A major part of the testing plan was selecting specimen types for the testing for each load case. The external studies provided a mix of ASTM standard component testing and unique component testing. For the compression load case, 4-in. (102-mm) diameter x 8-in. (203-mm) long concrete cylinders were selected using molds that were readily available and applicable to ASTM C39. For the tension specimens, a dogbone-shape

geometry was chosen. The dogbone tensile specimens measured 4 in. x 4 in. (102 mm x 102 mm) square on the ends and were 12 in. (305 mm) long. The specimen necked to a 4-in. x 3-in. (102-mm x 76-mm) cross-section in the critical region. This specimen type was commonly used in steel tension testing as the necked geometry allows for easier prediction of the failure region. This specimen type has also been used in various concrete testing programs by other researchers. Molds for this specimen geometry were custom fabricated; since, there is no standard tension dogbone-shaped specimen for concrete. For the flexure and shear load cases, four-point beam bending tests were performed on rectangular 6-in. x 6-in. x 22-in. (152-mm x 152-mm x 559-mm) concrete beams. Molds for these beams were commercially produced and conformed to ASTM C78 standard. Since all component test specimens were to be fabricated from the same concrete batch, 23 different molds were ordered: 11 cylinder molds; 6 tension specimen molds; and 6 beam specimen molds. The tension, flexure, and shear specimen molds are shown in Figure 91.



Figure 91. Metal Molds for Tension, Flexure, and Shear Concrete Specimens

Once the specimen geometries were configured and the molds were acquired, the concrete mix was selected. Based on the capacity of the two MTS load test frames that were available, the design compression strength of the concrete was selected as 6,000 psi (41.4 MPa) with an absolute maximum strength of 7,500 psi (51.7 MPa). With the assistance of Concrete Industries Inc. in Lincoln, Nebraska, a 6,000 psi (41.4 MPa) nominal mix design was created using the proportions shown in Table 12. Air entrainment was not used in the mix design, and the maximum size for the fine aggregate was $\frac{3}{8}$ in. (10 mm). In order to get enough concrete for the full complement of test specimens, the required batch size was 5.0 ft³ (0.14 m³).

Table 12. Concrete Mix Proportions for Internal Testing Program

Cementitious Materials	SSD	Unit Weight (lb/ft ³)	Actual Batched Proportions	
			Weight (lb)	Volume (ft ³)
ASTM C150 Portland Cement Type	3.15	196.6	130.6	0.66
Aggregates				
Fine Aggregate (Sand)	2.62	163.5	551.1	3.37
Water				
Batched Water	1.00	62.4	48.9	0.78
Air				
3.5% Air Content (non-entrained)	-	-	-	0.18

The concrete was batched at the general lab testing facility at Concrete Industries Inc. using a 9 ft³ (0.25 m³) circulating mixer, as shown in Figure 92. The mixing was completed outdoors with the assistance of MwRSF technicians. The molds were assembled with form oil placed on the inside of the molds to allow for easier specimen

separation after the concrete cured. Once the concrete was mixed, it was placed into the concrete molds. Tamping rods were used to consolidate the concrete, and hammers were used to vibrate the concrete to ensure that the molds were properly filled.



Figure 92. Concrete Mixing for Internal Testing Program

Once the molds were filled, they were squared off on the top and moved to the moisture curing room at the general test lab. The specimens remained in the molds, and plastic sheeting was placed over them to lock-in some of the internal moisture, as shown in Figure 93. Following an initial curing period of 96 hours, the specimens were removed from the molds and placed on the curing racks in the moisture room. The moisture room was a vital resource, because it allowed for uniform curing of the specimens under conditions explained in the ASTM C39 standard. The specimens were removed from the moisture curing room 28 days after fabrication.



Figure 93. Specimens in Moisture Curing Room

9.4 Cylinder Compression Testing

The concrete cylinder compression tests were designed to match ASTM C39 [26]. The cylinders had a diameter of 4 in. (102 mm) and a height of 8 in. (203 mm), as shown in Figure 94.

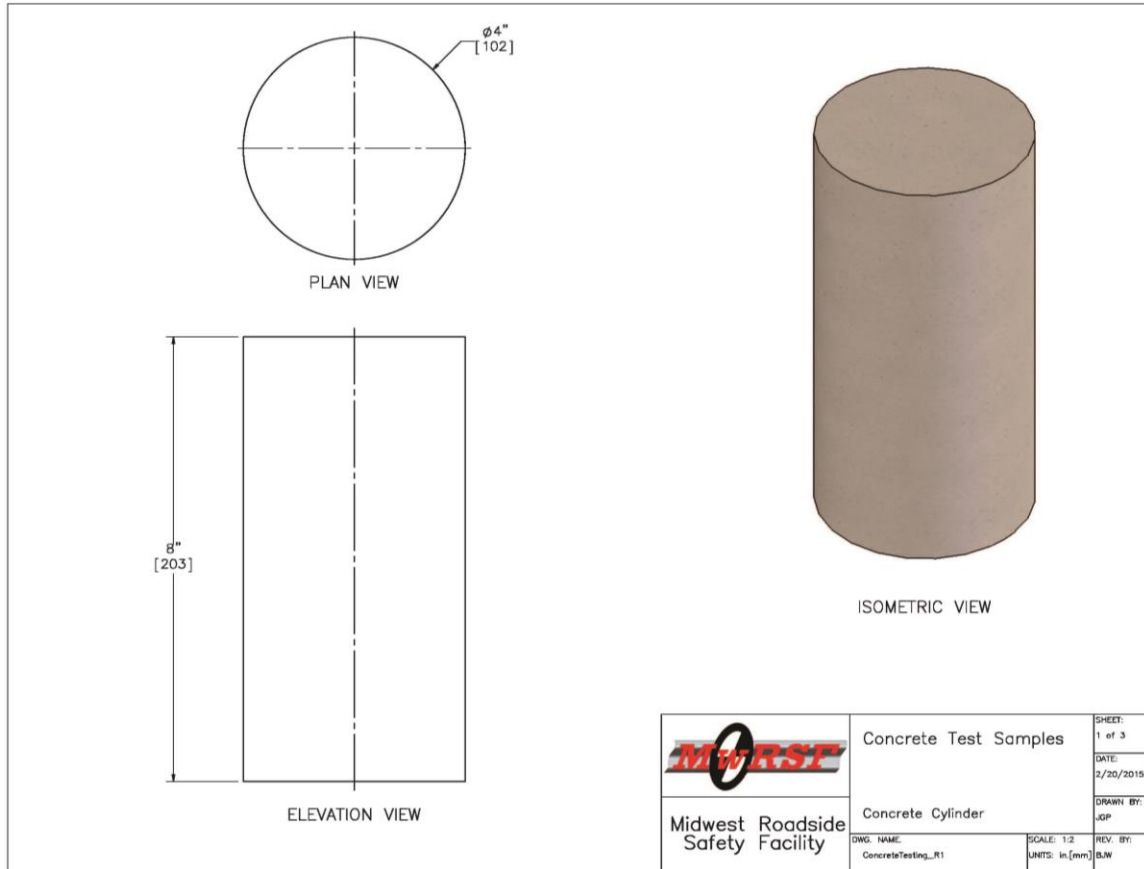


Figure 94. Cylinder Specimens for Test Nos. CFC-1 through CFC-7

The testing was completed using the MTS Criterion Model 64.106 machine, which has a load capacity of 220 kips (1,000 kN). In the tests, a concrete cylinder was capped using steel caps with rubber pads. The cylinder was placed between the upper and lower loading plates of the testing apparatus. The bottom plate was fixed, and the upper loading plate compressed the cylinder at a uniform loading rate. The machine loaded each cylinder at a displacement rate equal to a rate of 35 psi/s (0.25 MPa/s), per the ASTM standard. A higher rate (10x) was used in the first half of the load application in order to reach a suitable pressure in a reasonable amount of time. The pressure was continually applied to the cylinder until softening and failure occurred. The test was stopped once the

peak load was reduced to 5% of peak. The testing matrix for the cylinder testing is shown in Table 13.

Table 13. Cylinder Testing Matrix for Test Nos. CFC-1 through CFC-7

<i>Load Case</i>	<i># of Tests</i>	<i>Test Designation</i>	<i>ASTM Standard</i>	<i>Nominal Dimensions</i>
Compression	7	CFC-1	ASTM C39	4" x 8"
		CFC-2		
		CFC-3		
		CFC-4		
		CFC-5		
		CFC-6		
		CFC-7		

The major data points that were taken from these tests were force, strain, and displacement. A circumferential gauge was used to capture cylinder dilation as it was compressed. The load cell on the testing machine was used to capture force data. The laser extensometer was also used to capture small displacements and compute strain.

9.5 Dogbone Tension Testing

There is no ASTM standard for direct tension testing of concrete specimens, but a similar test exists for rock core specimens, ASTM D2936 [27]. The tension test method for the internal testing program was based on this standard as well as other published experiments within the literature. The dogbone tensile specimens measured 4 in. x 4 in. (102 mm x 102 mm) square on the ends and were 12 in. (305 mm) long. The specimen necked to a 4-in. x 3-in. (102-mm x 76-mm) cross-section in the middle region. Dimensions for the specimens are shown in Figure 95.

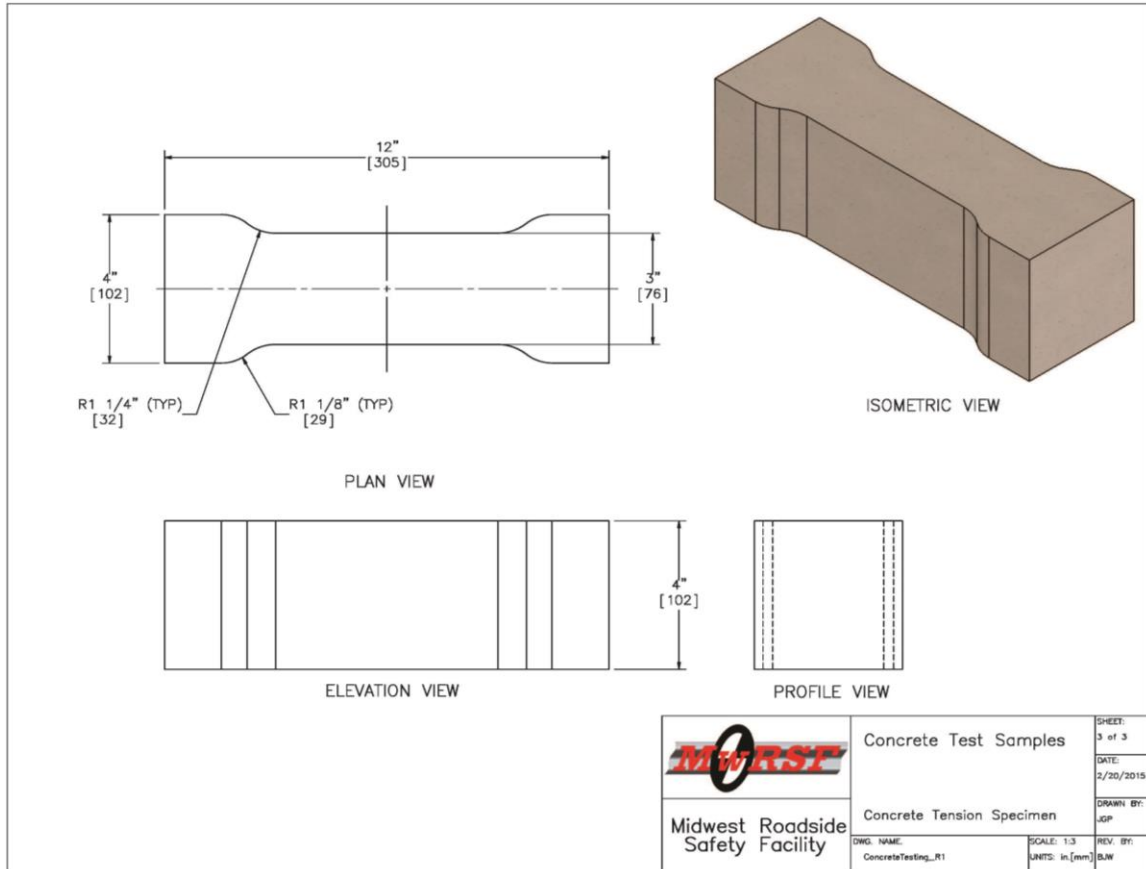
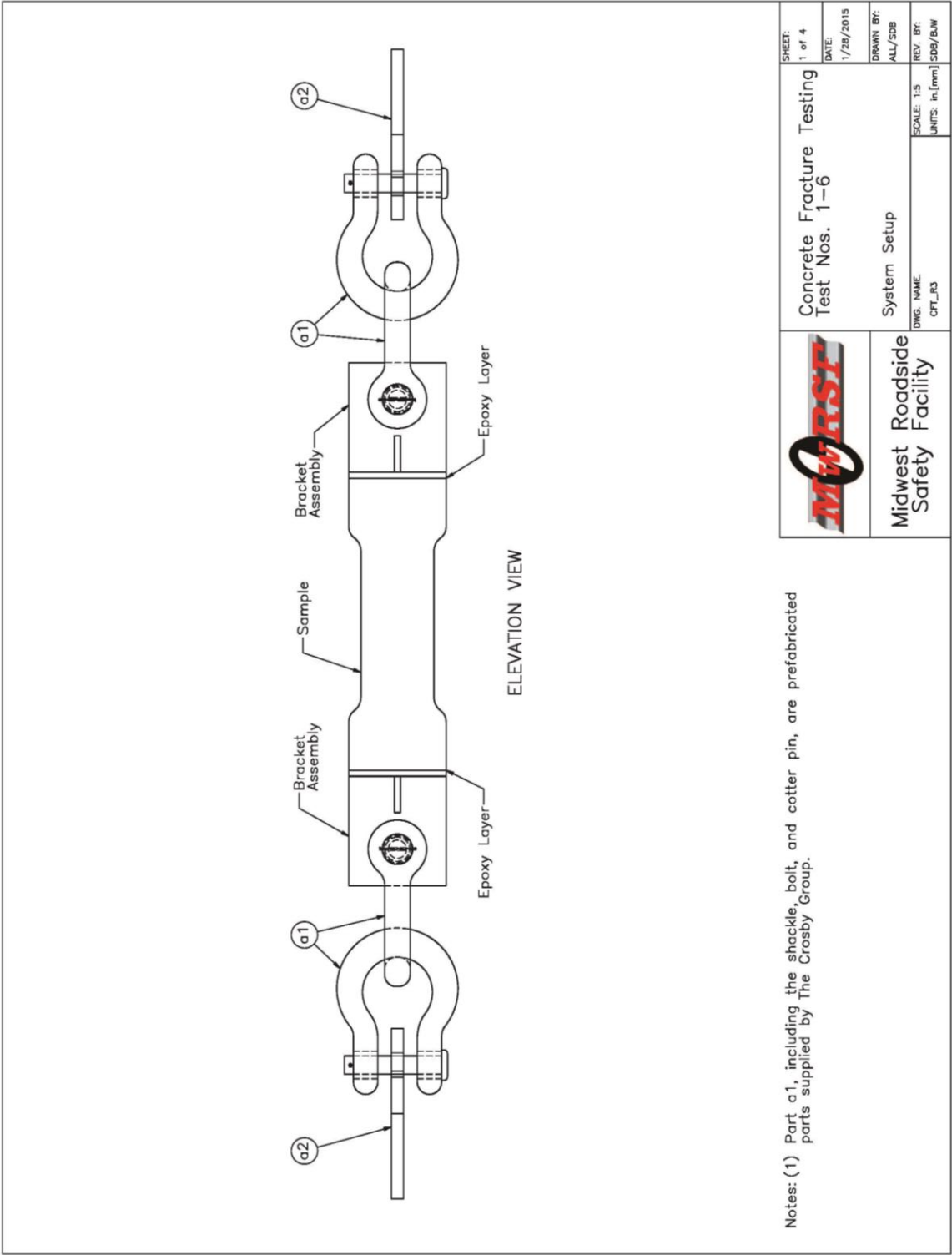



Figure 95. Dogbone Specimens for Test Nos. CFT-1 through CFT-6

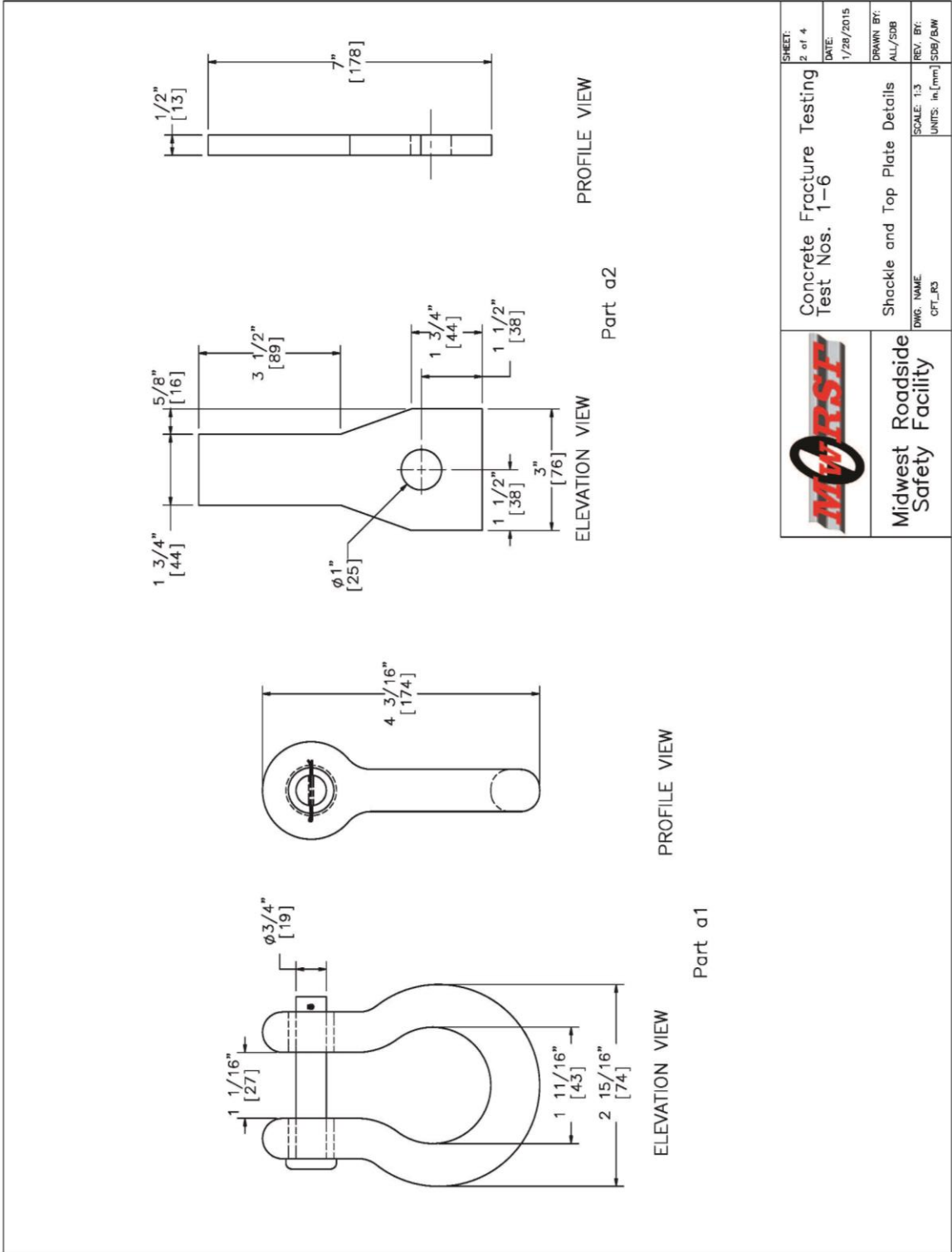
The testing was conducted using the MTS Landmark Servohydraulic Test System. This testing apparatus has a load capacity of 22 kips (100 kN). Prior to testing, a test jig was designed to accommodate the direct tension testing, as shown in Figures 96 through 99. There are two different components to the test jig, the permanent and temporary parts. The permanent portion makes use of steel plate and shackles to connect to the testing apparatus on one end and the temporary part of the jig on the other end. The jig is gripped using the wedge grips (part no. GF647002) that were previously attached to the machine. The hydraulic wedges gripped the 1/2-in. (13-mm) thick top plate and ensured that the specimen was aligned correctly. Two 5/8-in. (16-mm) shackles were used in opposite orientations in order to allow for rotational freedom in two directions. The temporary

bracket assembly was connected to the specimen using an epoxy adhesive layer having a required minimum bond strength of 1,000 psi (6.9 MPa). The specimen was roughed with a wire brush before a thin layer of Hilti HIT-RE epoxy was placed between the bracket assembly and the end of the specimen.



Notes: (1) Part a1, including the shackle, bolt, and cotter pin, are prefabricated parts supplied by The Crosby Group.

	Concrete Fracture Testing Test Nos. 1-6	SHEET: 1 of 4
	System Setup	DATE: 1/28/2015
Midwest Roadside Safety Facility	DWG. NAME: CRT_R3	DRAWN BY: ALL/SDB
	SCALE: 1:5 UNITS: in. (mm)	REV. BY: SDB/BLW




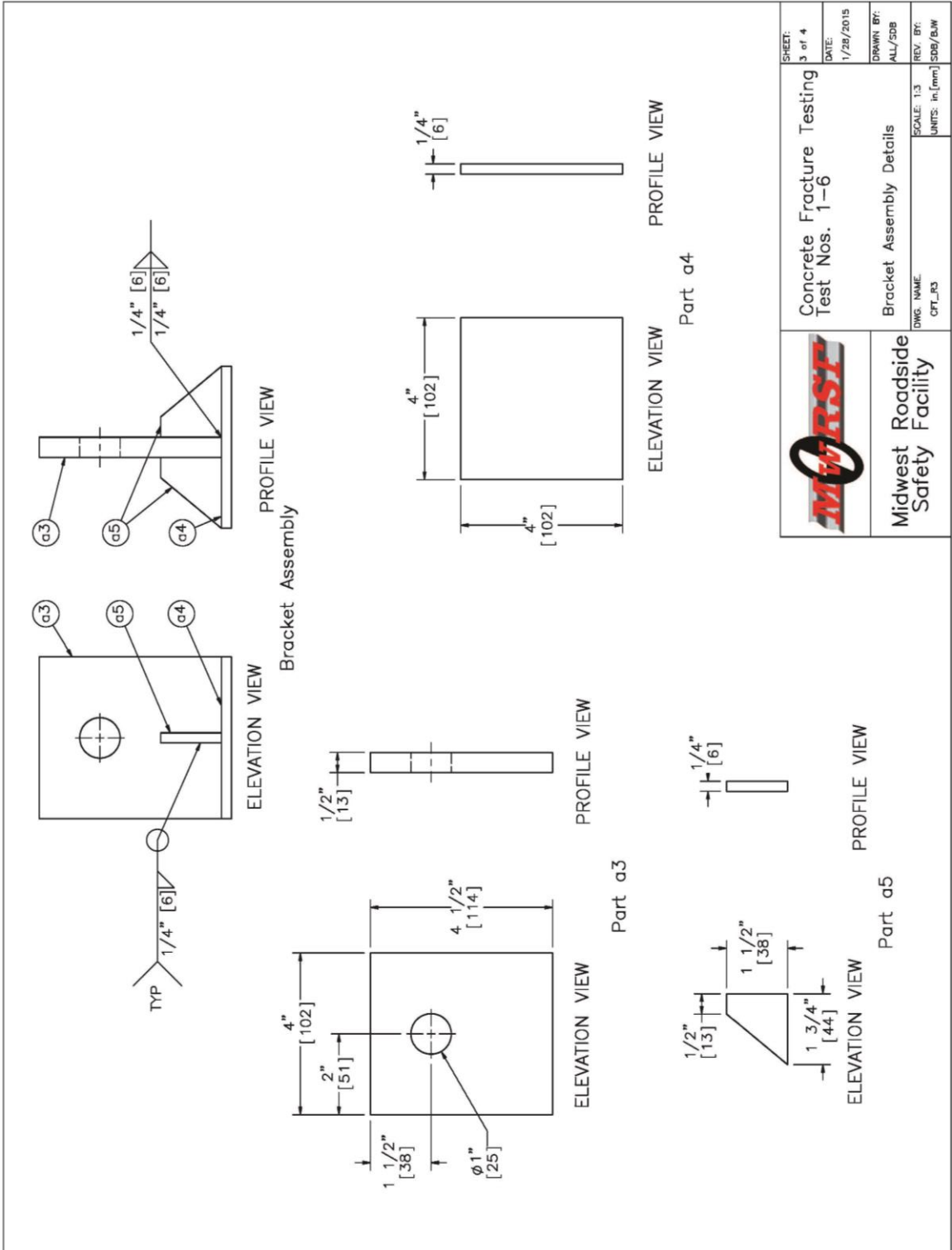
	Concrete Fracture Testing Test Nos. 1-6	SHEET: 2 of 4
	Shackle and Top Plate Details	DATE: 1/28/2015
Midwest Roadside Safety Facility	DWG. NAME: CFT_R3	DRAWN BY: ALL/SDB
	SCALE: 1:3 UNITS: in, [mm]	REV. BY: SDB/BAW

Figure 97. Direct Tension Test Jig, Permanent Jig Components





	Concrete Fracture Testing Test Nos. 1-6	SHEET: 3 of 4
	Bracket Assembly Details	DATE: 1/28/2015
Midwest Roadside Safety Facility	DWG. NAME: CFT_R3	DRAWN BY: ALL/SDB
	SCALE: 1:3 UNITS: in, [mm]	REV. BY: SDB/BAW

Figure 98. Direct Tension Test Jig, Temporary Jig Components

Item No.	QTY.	Description	Material Spec	Hardware Guide
a1	4	5/8" [16] Crosby G-213 Round Pin Shackle	Hot Dipped Galvanized Steel	-
a2	2	7"x3"x1/2" [178x76x13] Steel Plate	A572 Gr. 50 Steel	-
a3	2	4 1/2"x4"x1/2" [114x102x13] Steel Plate	A572 Gr. 50 Steel	-
a4	2	4"x4"x1/4" [102x102x6] Steel Plate	A572 Gr. 50 Steel	-
a5	4	1 1/2"x1 3/4"x1/4" [38x44x6] Steel Gusset	A572 Gr. 50 Steel	-
a6	-	Epoxy	Structural Grade Epoxy Minimum Bond Strength = 1,000psi [6.9MPa]	-

Figure 99. Direct Tension Test Jib, Bill of Materials

	Concrete Fracture Testing Test Nos. 1-6	SHEET: 4 of 4
	Bill of Materials	DATE: 1/28/2015
DWG. NAME: CFT_R3	SCALE: 1:2 UNITS: In. (mm)	DRAWN BY: ALL/SDB
		REV. BY: SDB/BW

The specimen was connected to the temporary bracket assembly using the epoxy adhesive. After the epoxy adhesive had cured and reached its bond strength, the bracket assembly was connected to the permanent portion of test jig and gripped by the testing apparatus. Hydraulic pressure was applied to the grips to assure that the specimen was properly aligned in the testing machine. In conformance with the ASTM standard, the actuator moved at a constant displacement rate so that the specimen would fail somewhere within a time range of 5 to 15 minutes. According to this standard, the failure should occur near the capped ends, but with the dogbone geometry, it should occur in the necked region.

The testing matrix for the tension tests is shown in Table 14. As with the compression tests, the desired data output was force, strain, and displacement. A laser extensometer was used across the necked region of the specimen. This technology tracked displacement of reflective tape, which could in turn be used to calculate axial strain between prescribed points (i.e., gauge length). The load cell on the testing apparatus captured the force readings.

Table 14. Dogbone Testing Matrix for Test Nos. CFT-1 through CFT-6

<i>Load Case</i>	<i># of Tests</i>	<i>Test Designation</i>	<i>ASTM Standard</i>	<i>Nominal Dimensions</i>
Tension	6	CFT-1	Modified ASTM D2936	4" x 4" x 12" (End) 4" x 3" x 12" (Neck)
		CFT-2		
		CFT-3		
		CFT-4		
		CFT-5		
		CFT-6		

9.6 Beam Flexure and Shear Testing

The flexure and shear tests were partially designed to match ASTM C78 for four-point bending tests, except that the support span would be decreased over the test series in order to investigate flexure and shear failure modes. The test specimens were 6-in. x 6-in. x 22-in. (152-mm x 152-mm x 559-mm) concrete beams, as shown in Figure 100.

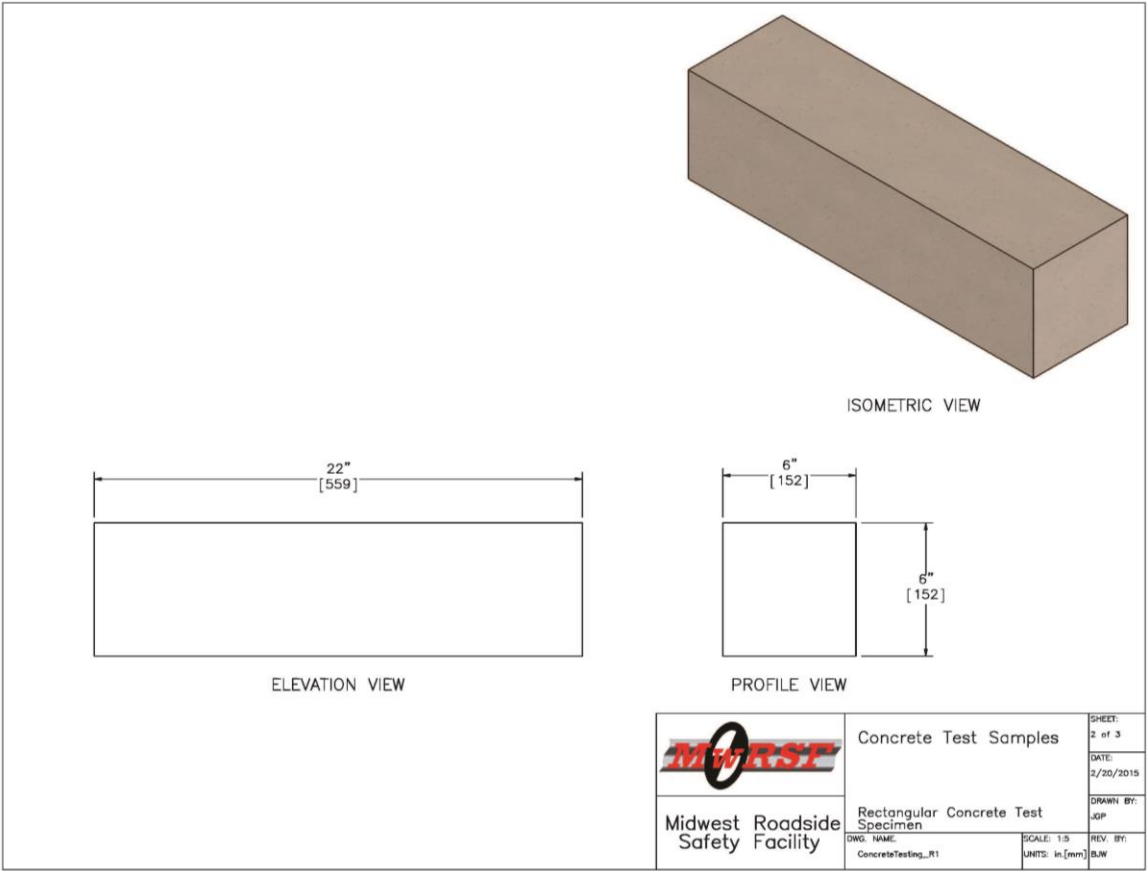


Figure 100. Beam Specimens for Test Nos. CFS-1 through CFS-6

The testing was performed on the MTS Criterion Model 64.106 machine, which has a load capacity of 220 kips (1,000 kN). The Series 60 (StH) Bend Fixture System was attached to the testing apparatus, and the beam was placed on the lower flexural fixture, model no. F-JZH305A1. In order to investigate the transition between failure modes/locations, a deviation from the ASTM standard was made to the support span. The

standard specifies that the bottom supports be placed at a distance $3d$ away from each other, where d is a beam depth of 6 in. (152 mm). For an unreinforced beam and an 18-in. (457-mm) span, the failure plane would likely occur near the vertical centerline of the beam between upper rollers due to flexure, and no shear failure would occur. For subsequent tests, the lower supports were moved closer to each other in order to obtain a different mode near the supports, such as tension or shear failure versus flexural failure. Note that the span distance could only range from 9 in. (229 mm) to 18 in. (457 mm) due to the configuration and limits of the lower flexural fixture.

The major data that was acquired from these beam tests included force, strain, and displacement. Strain gauges, both linear and 0-45-90 degree rosettes, were used to capture surface strains on the concrete beams. String potentiometers were used to track vertical displacement of the beam at its midspan and upper roller loading points. The load cell on the machine was used to capture force data. The testing matrix for the beam testing program is shown in Table 15.

Table 15. Beam Testing Matrix for Test Nos. CFS-1 through CFS-6

<i>Load Case</i>	<i># of Tests</i>	<i>Test Designation</i>	<i>ASTM Standard</i>	<i>Nominal Dimensions</i>
Flexure and Shear	6	CFS-1	Modified ASTM C78	6" x 6" x 22"
		CFS-2		
		CFS-3		
		CFS-4		
		CFS-5		
		CFS-6		

9.7 Additional Instrumentation

A MTS Series LX 500 Laser Extensometer was used to track displacements during the compression and tension tests. This laser extensometer has a resolution of

0.0001 in. (0.001 mm) with measurements updated 100 times per second. For tests nos. CFC-1 through CFC-7, the laser was placed 15 in. (381 mm) away from the front face of the cylinders. Two pieces of reflective tape were placed between 1.1 to 1.6 in. (28 to 41 mm) apart on the specimen. A 5-in. (127-mm) full-scale range was used for the laser, and the measurements were averaged over 8 scans. For test nos. CFT-1 through CFT-6, the laser was placed 12 in. (305 mm) away from the specimen. A 4-in. (102-mm) spacing was used between the two pieces of reflective tape, a 5-in. (127-mm) full-scale range was used with the laser, and 512 scans were averaged.

A circumferential gauge was used on all compression tests. This gauge is made up of two components, a mechanical extensometer and a chain attachment kit. The chain was wrapped around each of the cylinders, and both ends of the chain were attached to the arms of the extensometer. The circumferential gauge was removed when the load reached 75% of its expected peak to protect the extensometer from damage when the specimen failed. The gauge readings were used to calculate the change in area of the cross-sectional area as well as circumferential strain. The extensometer model and serial numbers were 632.12E-20 and 10421161, respectively. The extensometer had a 1-in. (25-mm) gauge length and a ½-in. (13-mm) travel length. It had a 6-V excitation voltage and a 250-ohm resistance.

An additional mechanical extensometer, model no. 634.25E-24, was used on test no. CFT-5 in order to measure axial displacements. In prior tension tests, there were inconsistencies with the laser extensometer due to minute changes in displacement. The serial number for the mechanical extensometer was 10416009B, and it had a 2-in. (51-

mm) gauge length and 1-in. (25-mm) travel length. The extensometer had a 6-V excitation voltage and a 350-ohm resistance.

One GoPro digital video camera was used to document each compression and tension test. A second GoPro camera was used for beam testing. The GoPro video cameras had a frame rate of 120 frames per second and were placed laterally from the test specimens. The high-speed videos were edited using ImageExpress MotionPlus software and RedLake MotionScope software. A Nikon EOS 30D digital still camera was also used to document pre- and post-test conditions for all tests. Typical placement of the GoPro digital video camera was near the laser extensometer for compression and tension tests, as shown in Figure 101. For the beam flexure and shear tests, one GoPro was placed on either side of the beam and perpendicular to the linear strain gauges.



Figure 101. Typical GoPro Digital Video Camera Setup

In the beam testing program, strain was an important data point for the tests. The specifications for all instrumentation used in the beam tests are provided in Appendix B. To capture the strains, different types of gauges were used. Two types of strain gauges were purchased from HBM, Inc. Linear strain gauges had a longer measuring grid to capture normal strains between the upper rollers. One linear gauge was placed on the top of the beam, one placed on the bottom, and three placed on the front face of the beam at specified heights. Rosette strain gauges were used to capture strains near the horizontal centerline of the beam and between the load and support points. The rosettes were configured with three separate gauges at a 0-45-90 degree orientation. Four rosette gauges were placed at the horizontal centerline of the beam, two on the front side of the front and two on the back side. All gauges were 120 ohm resistance, required a 2-V excitation, and had 2 wires. A gain of 1,000 was used on test no. CFS-1, but a gain of 2,500 was used on test nos. CFS-2 through CFS-6. Data was sampled at a rate of 10 Hz, and the gauges were zeroed prior to testing. All gauges were attached to the concrete beams using protocol, specified by the manufacturer.

The third type of instrumentation included miniature string potentiometers to capture vertical beam deflection. These devices were from Firstmark Inc. and had a maximum stretch of 1.5 in. (38 mm). Three of these devices were placed under the beam with one at the center midspan and two directly under the load points. In test no. CFS-6, the outer two string potentiometers were removed due to clearance issues. The string pots required an excitation of 5 V and a gain of 1 was used. These devices sampled data at 10 Hz. They were not zeroed prior to testing, but instead the voltage difference was calculated. Two bent washers were adhered to the bottom of the beam at the midspan and

3 in. (76 mm) on either side of the midspan. A cotter pin was placed between the pair of washers and the loop of the string surrounded the cotter pin. The string potentiometers were stretched at the beginning of the test, and the strings were intended to decrease in length as the beam displaced downward.

A layout of the strain gauges and string potentiometers is shown in Figure 102. The linear strain gauges are labeled D to H, the rosette gauges are labeled 1 to 4, with A, B, and C components, and the string potentiometers are labeled A to C.

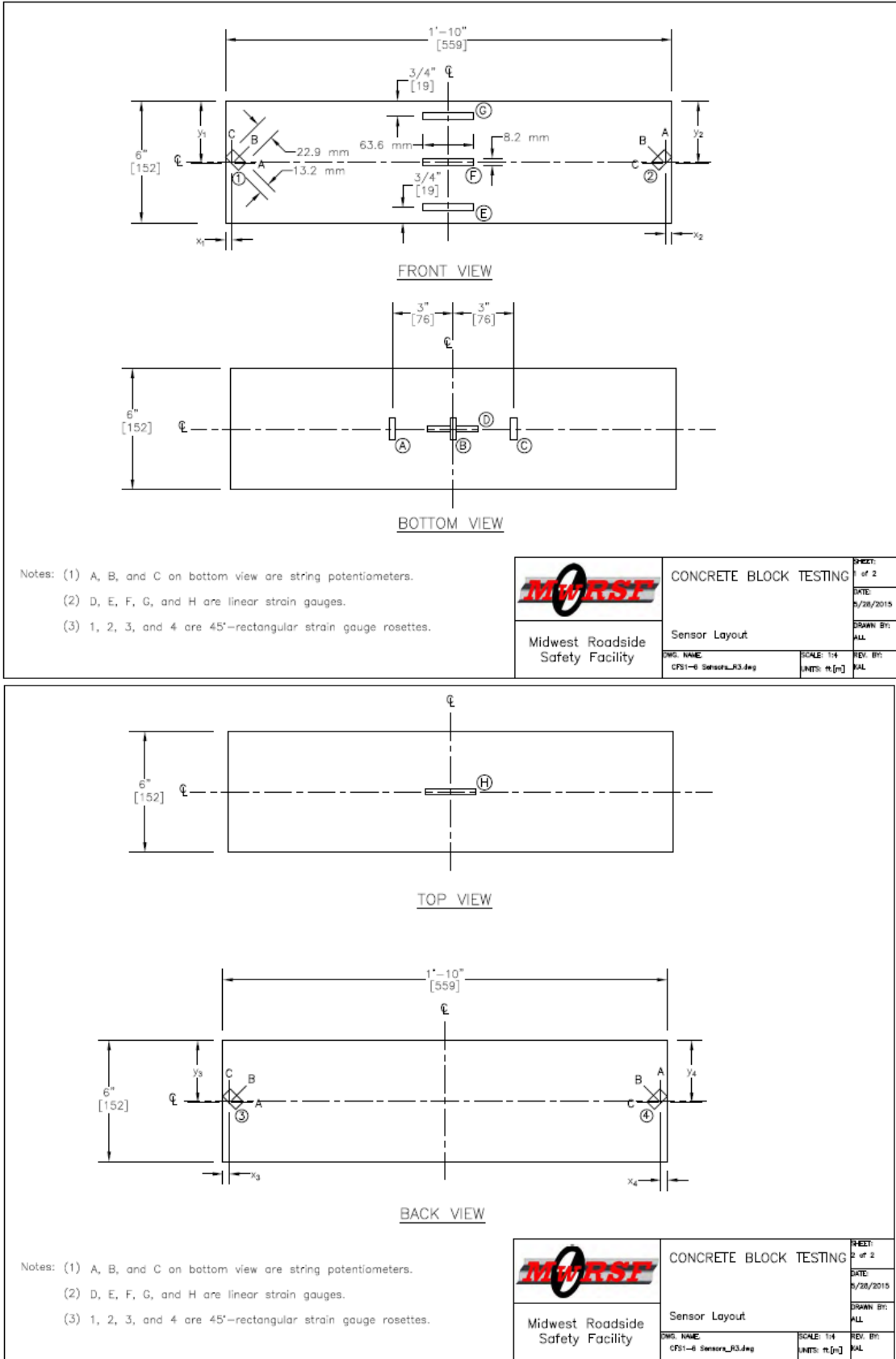


Figure 102. Instrumentation Layout

The specific locations of the rosettes are outlined in Table 16. The x and y distances are the distances from the edges of the beam. The y distance was constant at the horizontal centerline of the beam, 3 in. (76 mm). An example schematic of the loading apparatus from the standard is shown in Figure 2.

Table 16. Rosette Locations for Beam Tests

Test No.	Rosette No.	x	y
CFS-1	1-4	5.0"	3.0"
CFS-2	1-4	6.5"	3.0"
CFS-3	1-4	7.0"	3.0"
CFS-4	1-4	6.75"	3.0"
CFS-5	1-4	7.0"	3.0"
CFS-6	1-4	7.25"	3.0"

The strain and string potentiometer data was captured on a data acquisition system separate from the MTS testing machine and the MTS controller. This additional system was used to increase the available channels as the MTS machine and control system provided 8 total channels. Based on the instrumentation needs described above, 20 data channels were required and supported by two separate Vishay racks with 10 channels on each rack. These Vishay units served as the signal conditioners as well as voltage sources for the different instrumentation. A trigger pulse was set up to be recorded on the Vishay and MTS data acquisition systems in order to sync the data and recorded on different systems to the same time scale. All linear and rosette strain gauges were balanced and zeroed using the Vishay signal conditioners for each data channel which had its own input voltage and gain settings. The Vishay system setup is shown in Figure 103. The units allowed for voltage and gain settings to be changed directly with knobs on the front

of the unit. Additionally, a voltmeter could be used to check the voltage in the channel and ensure it was zeroed before testing began.

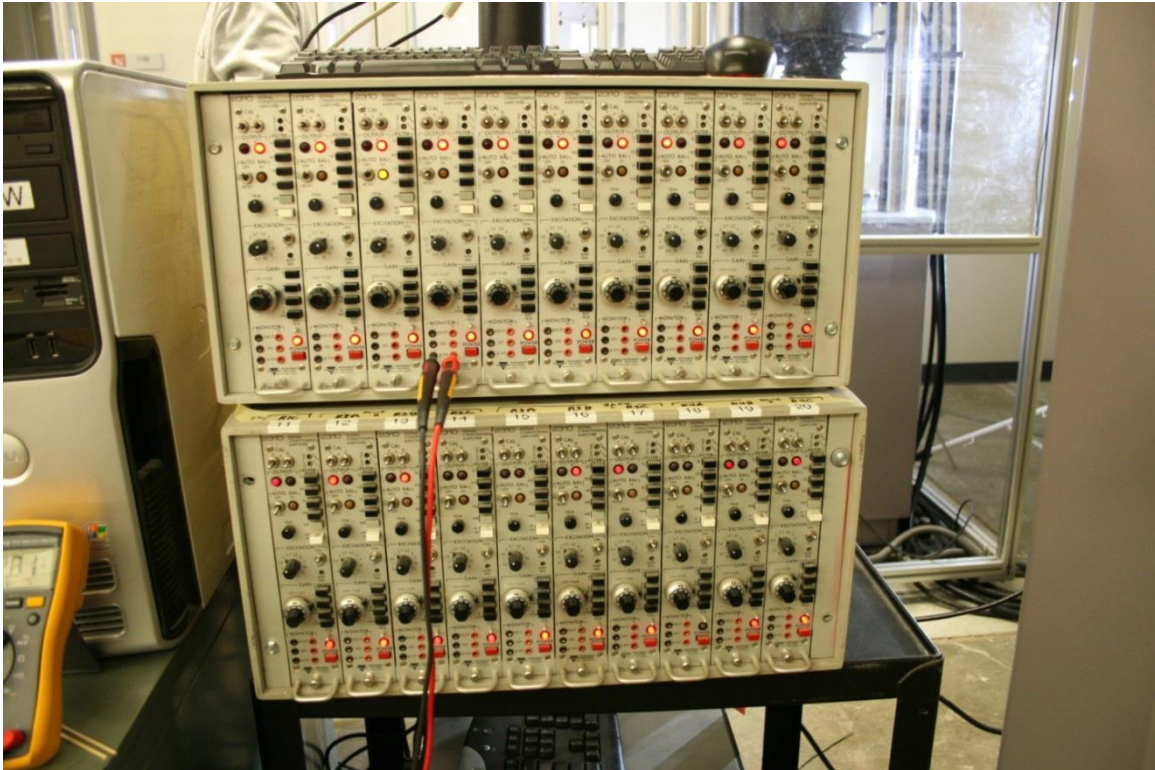


Figure 103. Data Acquisition Setup for Beam Testing

CHAPTER 10 COMPRESSION TESTING (CFC-1 THROUGH CFC-7)

Seven tests were completed for the compression load case using the test apparatus and setup that were described previously. The cylinders were placed between two fixed plates, with the actuator moving up to load each specimen in compression. All test setups were identical for test nos. CFC-1 through CFC-7. The pre-test photographs are shown in Figure 104, which are representative of all compression tests.

Test no. CFC-1 was run at a displacement rate of 0.001 in./s (0.0254 mm/s). However, this displacement rate resulted in a higher pressure rate than was allowed by the ASTM standard. All other compression tests were run at a displacement rate of 0.0005 in./s (0.0127 mm/s). The main data acquired from the tests were force, displacement, and time. Engineering stress was then calculated based on the original cross-sectional area of each part, and stress versus strain histories were developed. Strain was calculated using laser extensometer and circumferential gauge displacement readings. The laser data was used to calculate axial strain, and the circumferential gauge was used to calculate increase in area and true stress. The results of the engineering axial stress are reported in this chapter, and the true axial stress results are shown in Appendix C. The circumferential gauge was removed at approximately 75% of peak load; therefore, true stress readings were not taken through failure.

Eleven total compression cylinders were cast using the same concrete batch. Two practice tests were completed in order to become more familiar with the strain measurement devices. These tests showed an average concrete compressive strength of 9.3 ksi (64.1 MPa), much higher than the design strength. In order to confirm these numbers, two additional cylinders were sent to an external testing lab for additional

testing. After the practice test compressive strengths were confirmed with the external testing, seven additional tests were completed for the compression load case, and their results are reported herein.

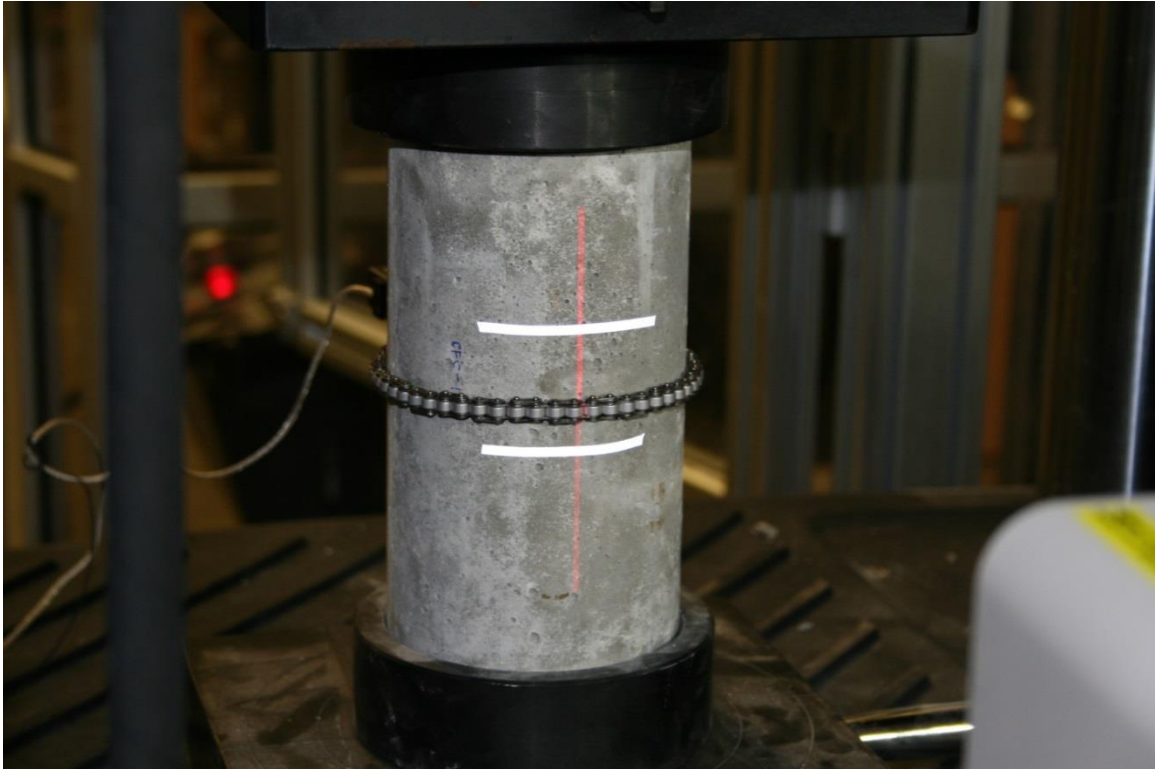


Figure 104. Pre-Test Photographs, Test Nos. CFC-1 through CFC-7

10.1 Test No. CFC-1

As the MTS Criterion machine loaded the cylinder in compression during test no. CFC-1, the specimen crushed, thus breaking into three major pieces. A diagonal shear crack formed in the upper right of the specimen and propagated to the center of the cylinder. A vertical crack propagated from the center of the cylinder down to the bottom edge. A peak load of 115.7 kip (515 kN) occurred as the specimen broke. A summary of pre- and post-test measurements is shown in Table 17. The stress versus strain plot is shown in Figure 105, and post-test photographs are shown in Figure 106.

Table 17. Test Data Sheet, Test No. CFC-1

Test ID: CFC-1

Diameter (Top):	4.034	in.
Diameter (Bottom):	3.987	in.
Average Diameter:	4.0105	in.

Cross-Sectional Area:	12.632	in. ²
-----------------------	--------	------------------

Laser Gauge Length (caliper):	1.608	in.
Laser Gauge Length (laser):	1.6028	in.

Peak Load:	115.7	kips
Peak Engineering Stress:	9.16	ksi

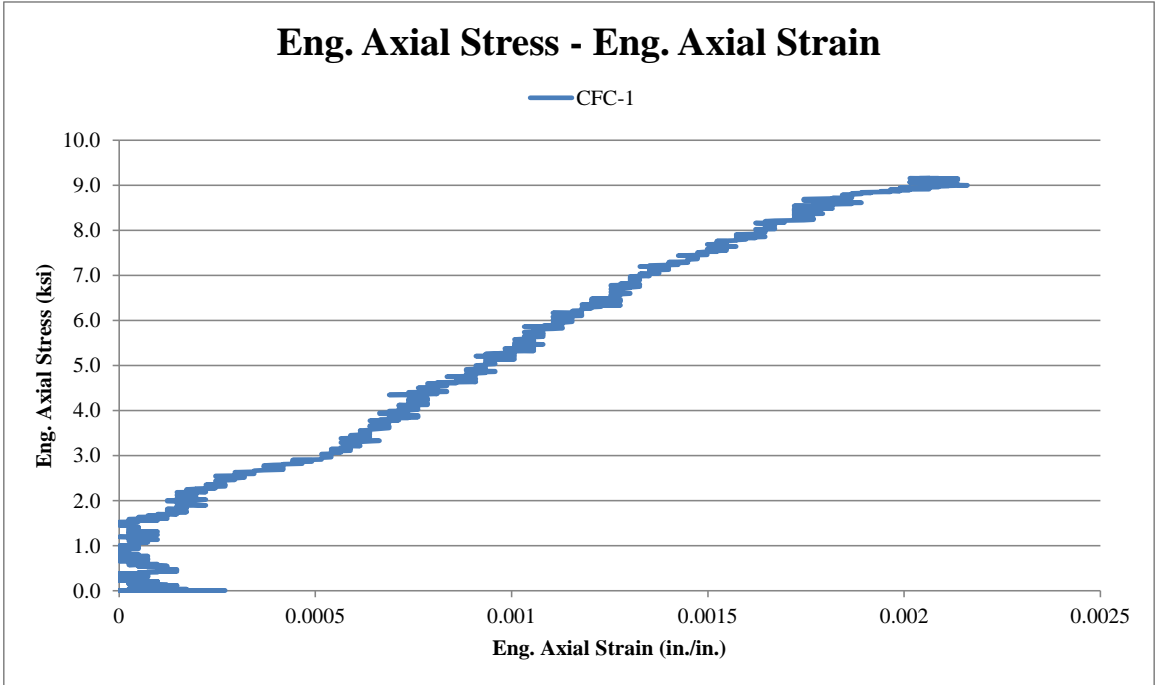


Figure 105. Stress-Strain History, Test No. CFC-1

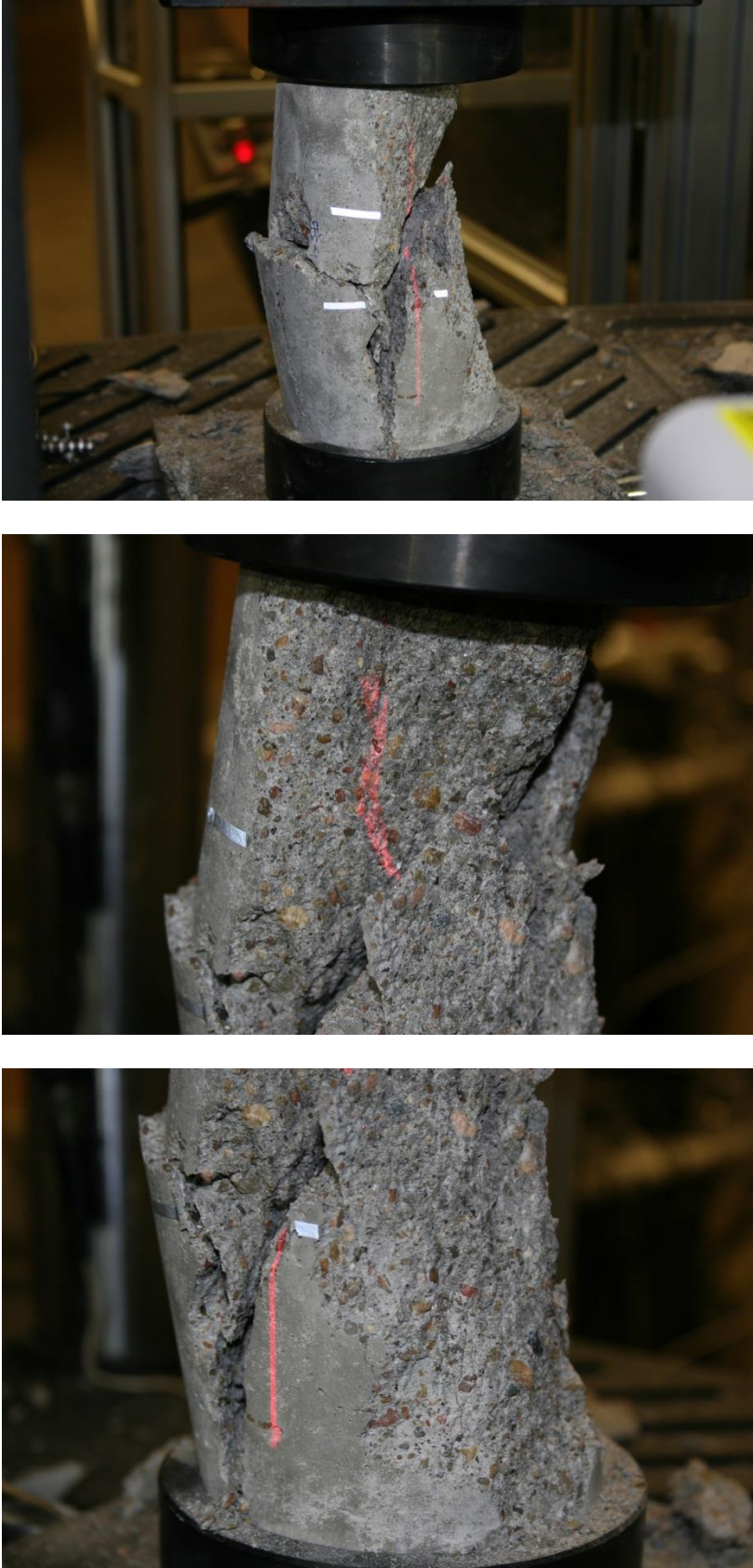


Figure 106. Post-Test Photographs, Test No. CFC-1

10.2 Test No. CFC-2

As the MTS Criterion machine loaded the cylinder in compression during test no. CFC-2, the specimen crushed with significant shearing on the right side of the cylinder. Smaller vertical cracks propagated from the bottom of the cylinder toward the middle of the cylinder. A peak load of 113.9 kip (507 kN) occurred as the specimen broke. A summary of pre- and post-test measurements is shown in Table 18. The stress versus strain plot is shown in Figure 107, and post-test photographs are shown in Figure 108.

Table 18. Test Data Sheet, Test No. CFC-2

Test ID: CFC-2

Diameter (Top):	4.088	in.
Diameter (Bottom):	3.971	in.
Average Diameter:	4.0295	in.
Cross-Sectional Area:	12.752	in. ²
Laser Gauge Length (caliper):	1.169	in.
Laser Gauge Length (laser):	1.1680	in.
Peak Load:	113.86	kips
Peak Engineering Stress:	8.93	ksi

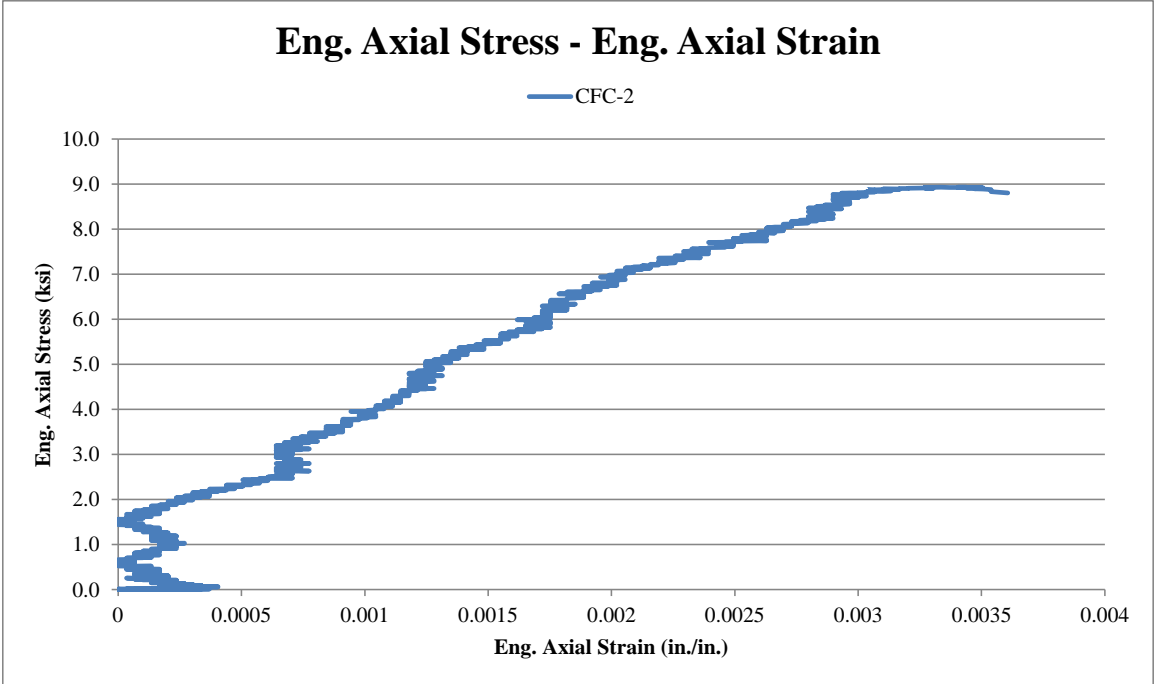


Figure 107. Stress-Strain History, Test No. CFC-2



Figure 108. Post-Test Photographs, Test No. CFC-2

10.3 Test No. CFC-3

As the MTS Criterion machine loaded the cylinder in compression during test no. CFC-3, the specimen crushed with the left side of the cylinder shearing off. Diagonal damage paths were seen from the top and bottom edges of the cylinder on the left side. A peak load of 116.8 kip (520 kN) occurred as the specimen broke. A summary of pre- and post-test measurements is shown in Table 19. The stress versus strain plot is shown in Figure 109, and post-test photographs are shown in Figure 110.

Table 19. Test Data Sheet, Test No. CFC-3

Test ID: CFC-3

Diameter (Top):	4.032	in.
Diameter (Bottom):	3.997	in.
Average Diameter:	4.0145	in.
Cross-Sectional Area:	12.658	in. ²
Laser Gauge Length (caliper):	1.247	in.
Laser Gauge Length (laser):	1.2315	in.
Peak Load:	116.83	kips
Peak Engineering Stress:	9.23	ksi

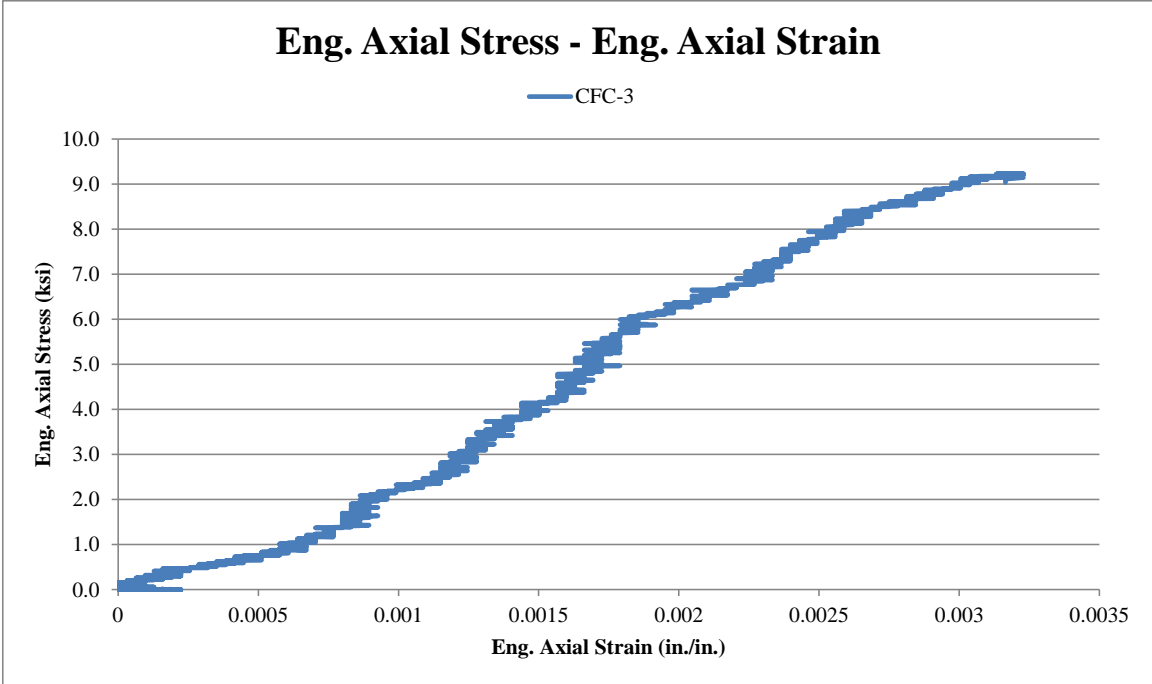


Figure 109. Stress-Strain History, Test No. CFC-3

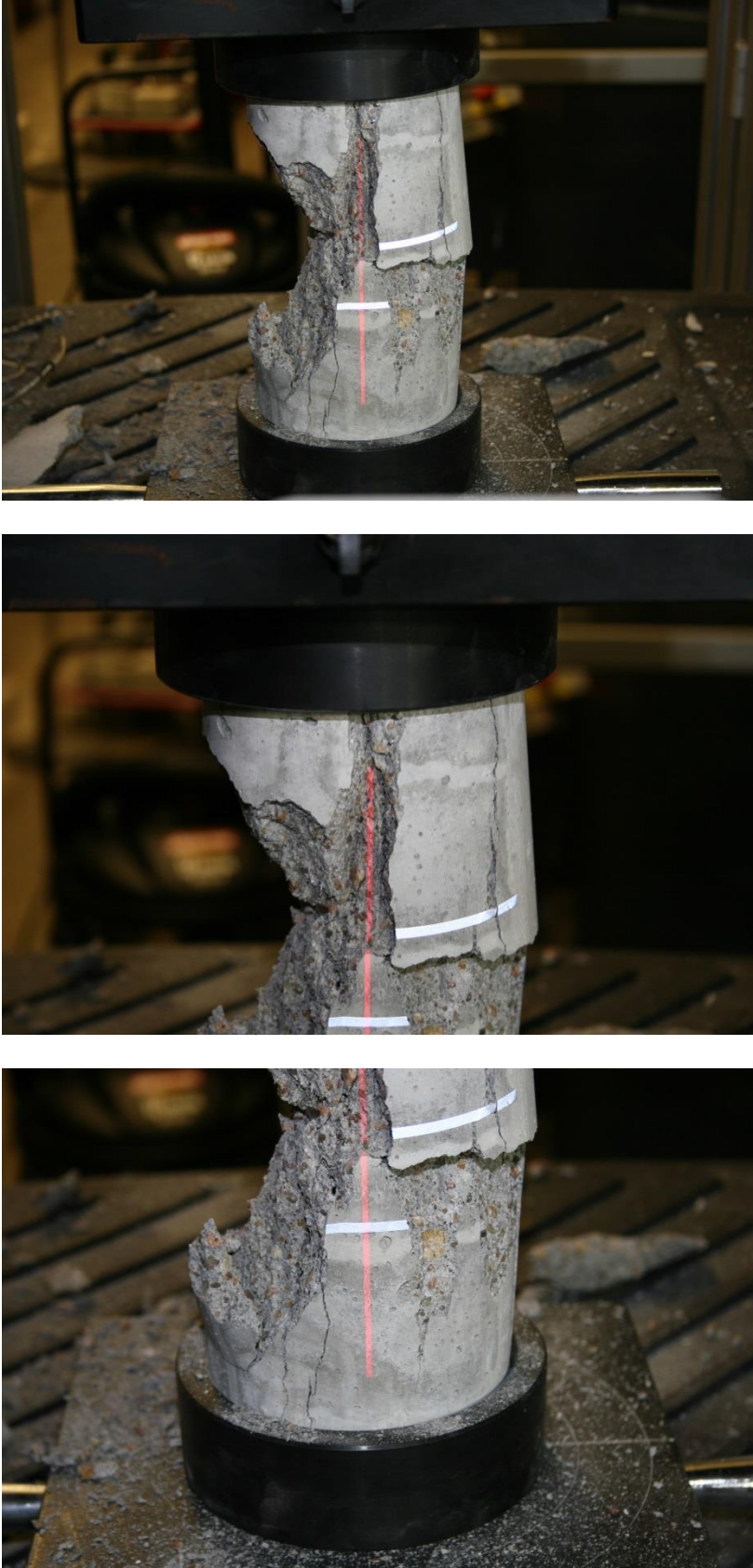


Figure 110. Post-Test Photographs, Test No. CFC-3

10.4 Test No. CFC-4

As the MTS Criterion machine loaded the cylinder in compression during test no. CFC-4, the specimen crushed with a portion of the right side being sheared off. The remainder of the cylinder was undamaged, and there were no visible cracks. A peak load of 113.6 kip (505 kN) occurred as the specimen broke. A summary of pre- and post-test measurements is shown in Table 20. The stress versus strain plot is shown in Figure 111, and post-test photographs are shown in Figure 112.

Table 20. Test Data Sheet, Test No. CFC-4

Test ID: CFC-4

Diameter (Top):	4.070	in.
Diameter (Bottom):	3.965	in.
Average Diameter:	4.0175	in.
Cross-Sectional Area:	12.677	in. ²
Laser Gauge Length (caliper):	1.169	in.
Laser Gauge Length (laser):	1.1558	in.
Peak Load:	113.55	kips
Peak Engineering Stress:	8.96	ksi

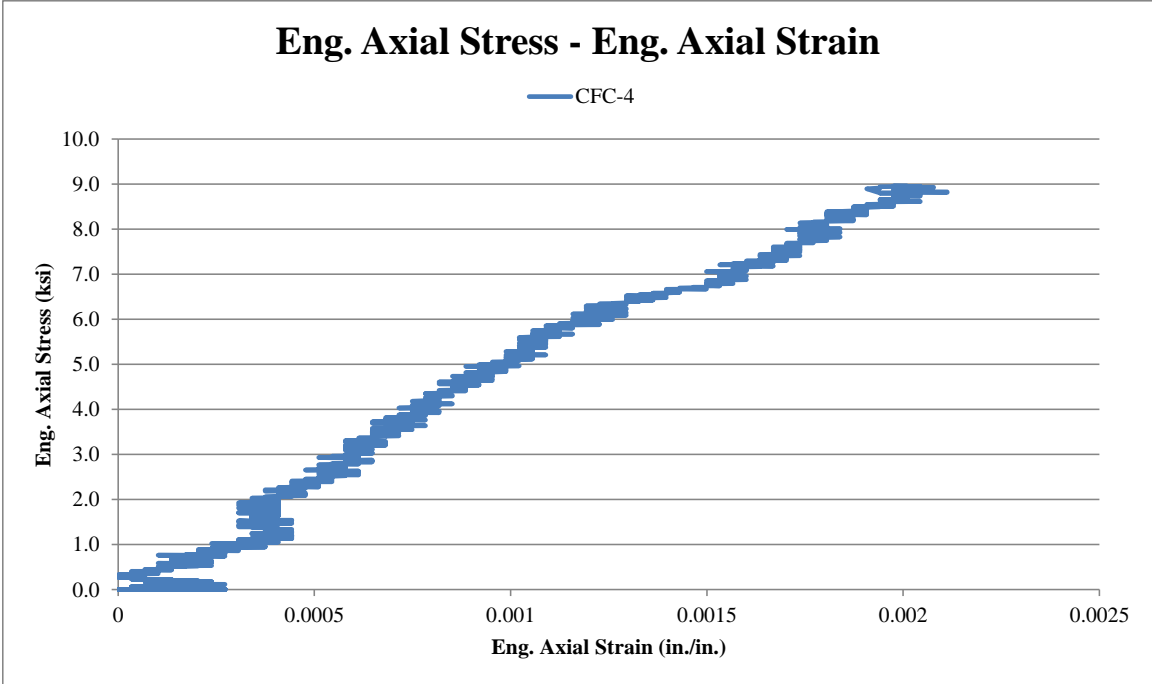


Figure 111. Stress-Strain History, Test No. CFC-4



Figure 112. Post-Test Photographs, Test No. CFC-4

10.5 Test No. CFC-5

As the MTS Criterion machine loaded the cylinder in compression during test no. CFC-5, the specimen crushed with shearing occurring across the entire front side of the cylinder. Diagonal cracks were the cause of this damage. A peak load of 115.6 kip (514 kN) occurred as the specimen broke. A summary of pre- and post-test measurements is shown in Table 21. The stress versus strain plot is shown in Figure 113, and post-test photographs are shown in Figure 114.

Table 21. Test Data Sheet, Test No. CFC-5

Test ID: CFC-5

Diameter (Top):	4.075	in.
Diameter (Bottom):	3.985	in.
Average Diameter:	4.0300	in.
Cross-Sectional Area:	12.756	in. ²
Laser Gauge Length (caliper):	1.358	in.
Laser Gauge Length (laser):	1.3552	in.
Peak Load:	115.64	kips
Peak Engineering Stress:	9.12	ksi

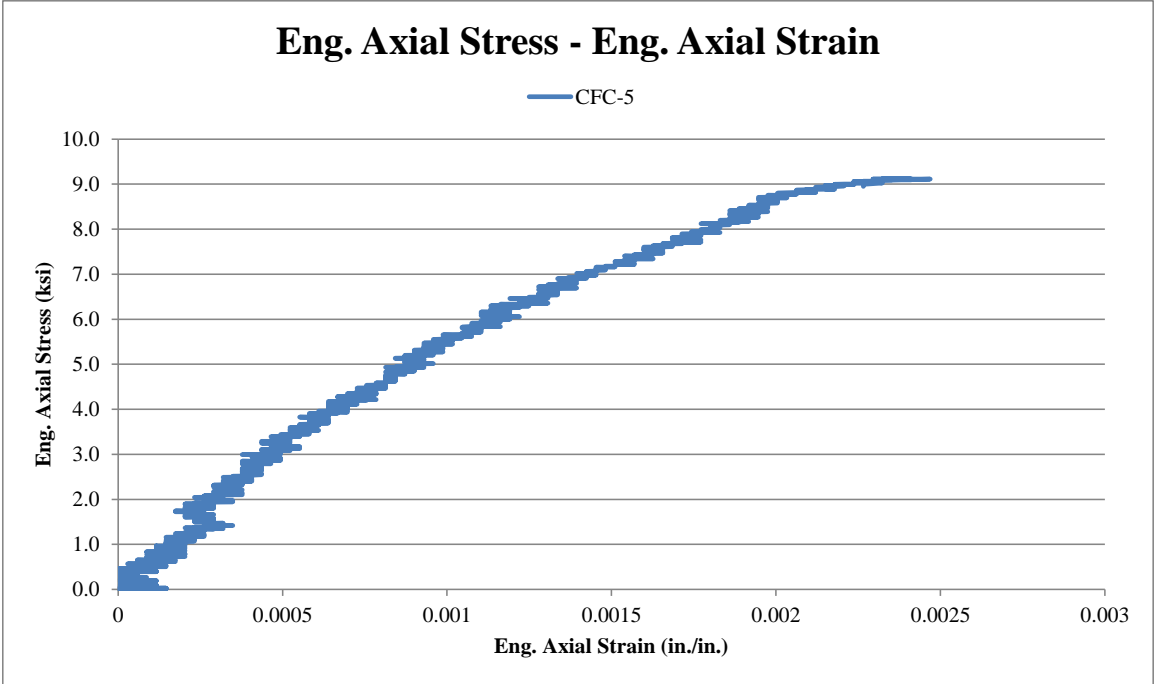


Figure 113. Stress-Strain History, Test No. CFC-5

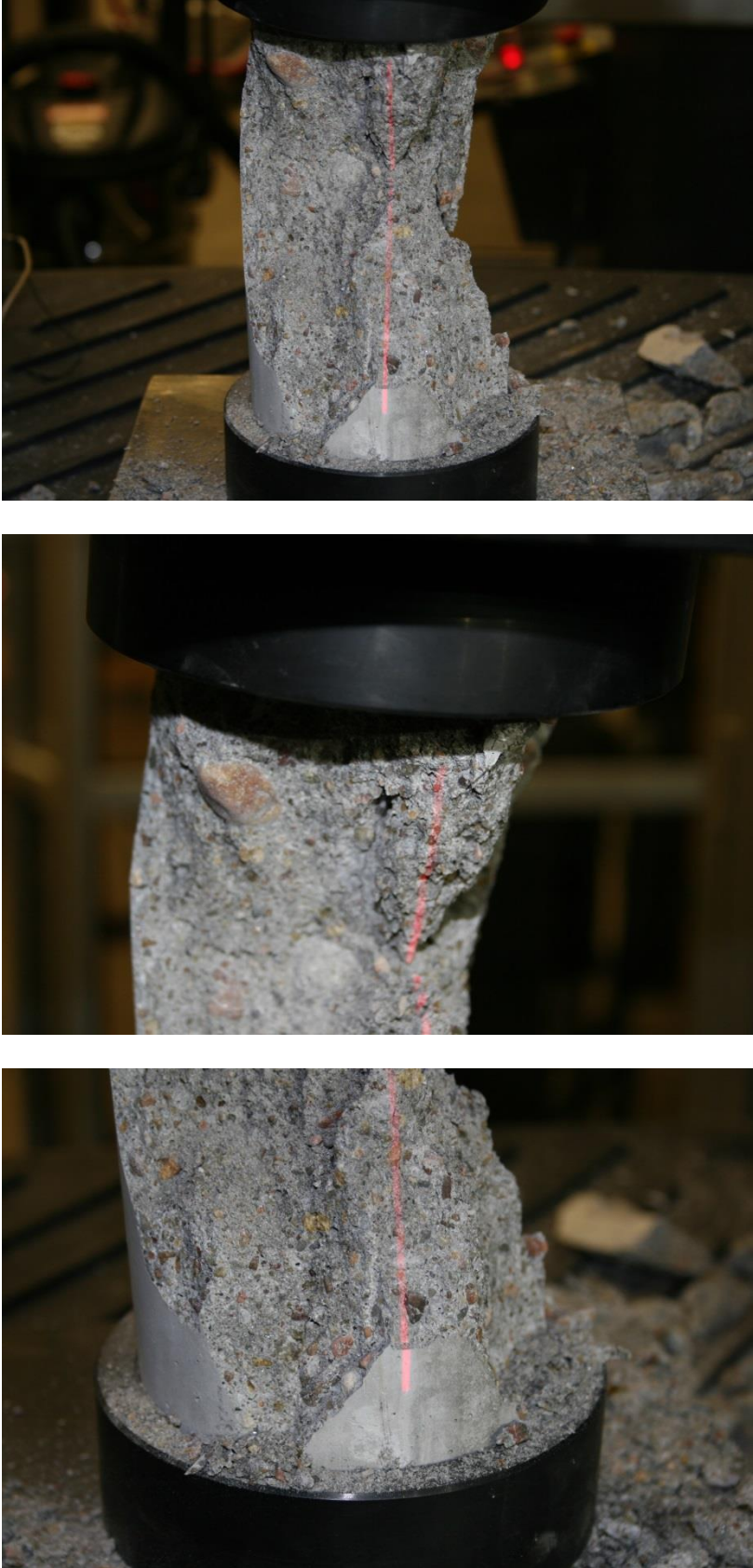


Figure 114. Post-Test Photographs, Test No. CFC-5

10.6 Test No. CFC-6

As the MTS Criterion machine loaded the cylinder in compression during test no. CFC-6, the specimen crushed, losing most of its volume. A significant amount of shearing damage occurred on the back side of the cylinder. A peak load of 110.3 kip (491 kN) occurred as the specimen broke. A summary of pre- and post-test measurements is shown in Table 22. The stress versus strain plot is shown in Figure 115, and post-test photographs are shown in Figure 116.

Table 22. Test Data Sheet, Test No. CFC-6

Test ID: CFC-6

Diameter (Top):	3.999	in.
Diameter (Bottom):	3.987	in.
Average Diameter:	3.9930	in.
Cross-Sectional Area:	12.522	in. ²
Laser Gauge Length (caliper):	1.203	in.
Laser Gauge Length (laser):	1.2001	in.
Peak Load:	110.25	kips
Peak Engineering Stress:	8.80	ksi

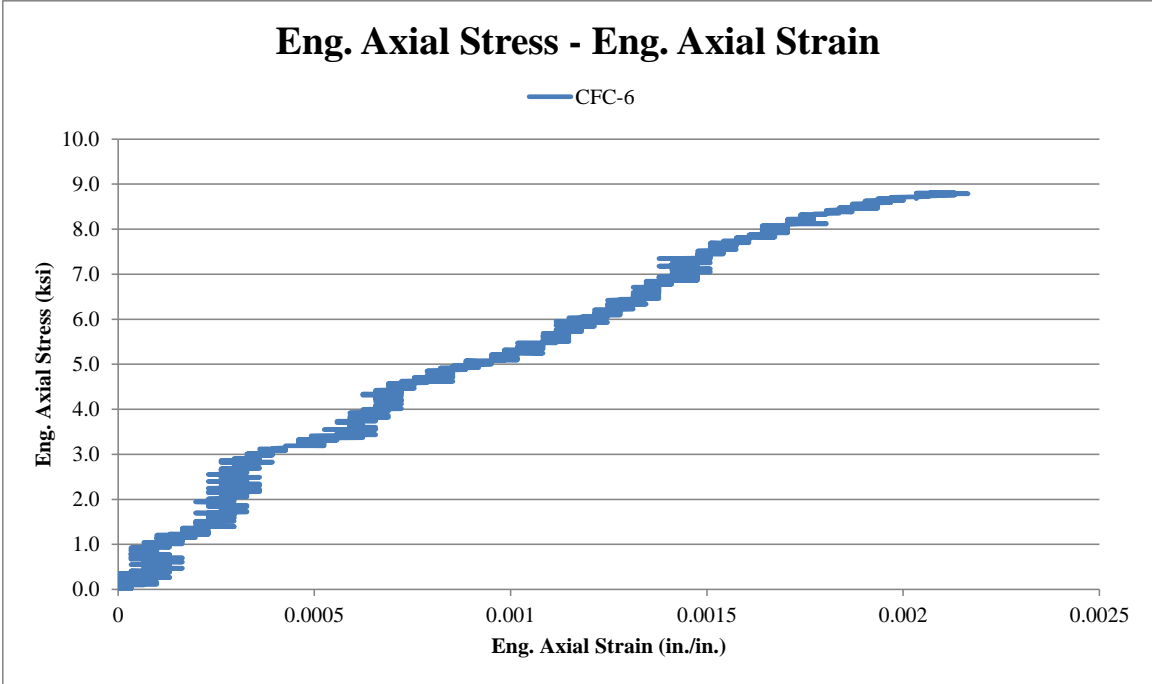


Figure 115. Stress-Strain History, Test No. CFC-6



Figure 116. Post-Test Photographs, Test No. CFC-6

10.7 Test No. CFC-7

As the MTS Criterion machine loaded the cylinder in compression during test no. CFC-7, the specimen crushed with significant deformation occurring. A majority of the right side of the cylinder was sheared away. A peak load of 115.4 kip (513 kN) occurred as the specimen broke. A summary of pre- and post-test measurements is shown in Table 23. The stress versus strain plot is shown in Figure 117, and post-test photographs are shown in Figure 118.

Table 23. Test Data Sheet, Test No. CFC-7

Test ID: CFC-7

Diameter (Top):	3.983	in.
Diameter (Bottom):	3.982	in.
Average Diameter:	3.9825	in.
Cross-Sectional Area:	12.457	in. ²
Laser Gauge Length (caliper):	1.186	in.
Laser Gauge Length (laser):	1.1835	in.
Peak Load:	115.43	kips
Peak Engineering Stress:	9.27	ksi

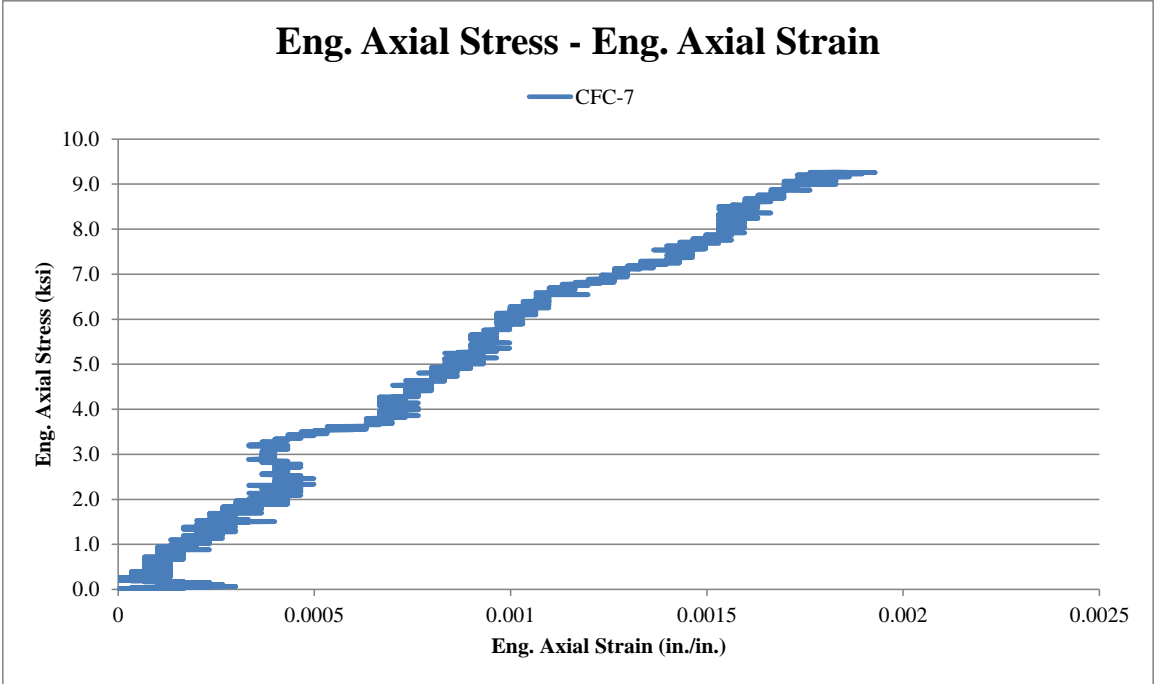


Figure 117. Stress-Strain History, Test No. CFC-7



Figure 118. Post-Test Photographs, Test No. CFC-7

10.8 Discussion

Seven static cylinder component tests were performed for the compression load case. As shown in Figure 119, the stress-strain behavior is similar for all tests. There is an excessive amount of noise in the curves due to the resolution of the laser extensometer. The resolution became an issue because such small deformations were measured. Test nos. CFC-2 and CFC-3 were outliers as the fracture occurred at higher strain values, although the peak stress values were not different from the other five tests. The average peak stress for the seven tests was 9.1 ksi (62.7 MPa), and the average failure strain was 0.0025. There was shearing behavior in all of the cylinder tests.

Based on the fact that a 6.0 ksi (41.4 MPa) mix design was batched, it is alarming that the average test strength of the cylinders was so high. This strength was confirmed via external testing on two cylinders from the same batch, as summarized in Table 24. It is common for actual concrete batches to have a higher strength than the design strength, but this degree of difference was unexpected. Nonetheless, the research study was continued with the tension and shear/flexure testing segments.

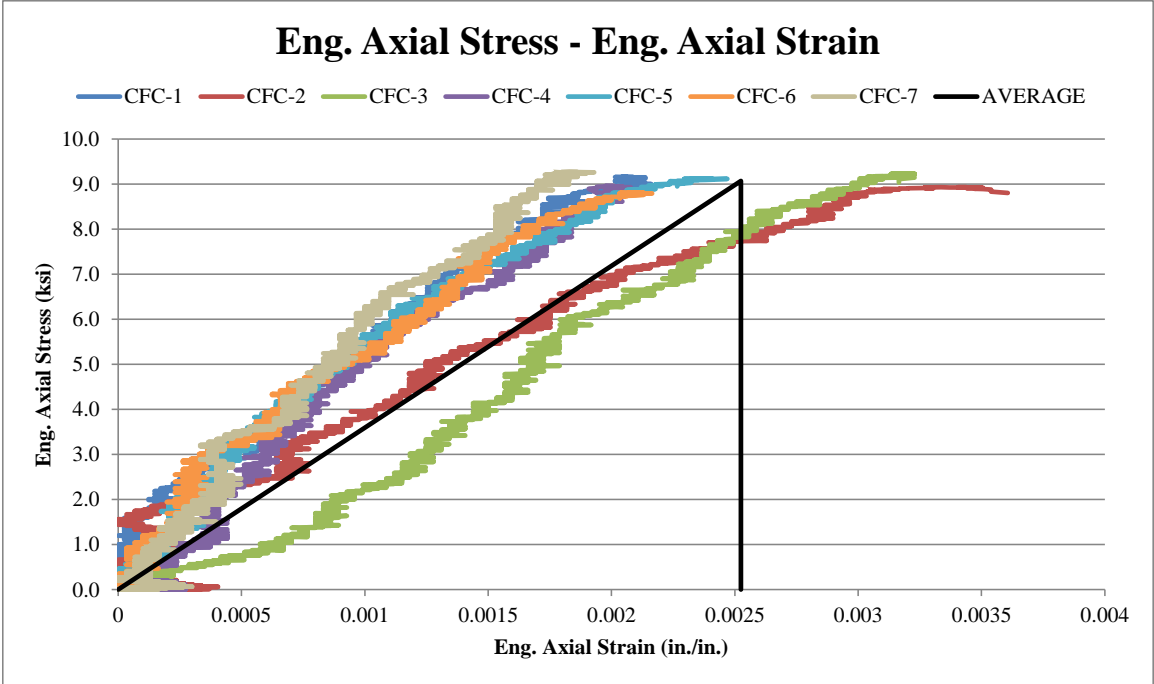


Figure 119. Stress-Strain Histories, Test Nos. CFC-1 through CFC-7

Table 24. Summary of Peak Engineering Stress for Test Nos. CFC-1 through CFC-7

Test Series	Test No.	Peak Eng. Stress
		<i>ksi</i>
Practice Tests	1	9.27
	2	9.25
Internal Tests	1	9.16
	2	8.93
	3	9.23
	4	8.96
	5	9.12
	6	8.80
	7	9.27
External Tests	1	9.12
	2	9.07

The moduli of elasticity were calculated for all seven tests as well. The results are shown in Table 25. The average modulus of elasticity was 3,768 ksi (26.0 GPa).

Table 25. Summary of Moduli of Elasticity for Test Nos. CFC-1 through CFC-7

Test No.	E
-	<i>ksi</i>
CFC-1	4,235
CFC-2	2,476
CFC-3	2,859
CFC-4	4,242
CFC-5	3,695
CFC-6	4,064
CFC-7	4,804

CHAPTER 11 TENSION TESTING (CFT-1 THROUGH CFT-6)

Six tests were completed for the tension load case using the test apparatus and setup that were described previously. The top portion of the rigging was fixed, and the actuator moved the lower rigging components, and the specimen. Test setups were identical for test nos. CFT-1 through CFT-6. Example pre-test photographs are shown in Figure 120. Additional protection was added to the test setup to prevent the fractured test specimen from contacting the controls on the front of the machine and the hydraulic lines on the back of the machine.

All tension tests were run at a displacement rate of 0.0001 in./s (0.00254 mm/s). A 0.001 in./s (0.0254 mm/s) displacement rate was applied in the beginning of the test to remove some of the slack in the rigging. The test continued to run at this elevated displacement rate until a load of 100 lb (0.4 kN) was reached, at which point the test ran at the slower load rate. The main data taken from the tests were force and time. Engineering stress was then calculated based on the original cross-sectional area of each part and stress versus time histories were developed.

Laser extensometer data was used to estimate tensile strain. The laser gauge lengths were taken before the tests began. However, there were issues with the resolution and accuracy of the extensometer and the data was not considered. These problems again were due to the small deformations that were attempted to be captured. These deformations were even smaller than those of the compression tests.



Figure 120. Pre-Test Photographs, Test Nos. CFT-1 through CFT-6

11.1 Test No. CFT-1

As the MTS Landmark machine loaded the specimen in tension during test no. CFT-1, the specimen fractured 2.6 in. (66 mm) from the bottom of the specimen, which was outside of the 4-in. (102-mm) gauge length. A peak load of 4.2 kip (18.7 kN) occurred at fracture. A summary of pre- and post-test measurements is shown in Table 26. The stress versus time plot is shown in Figure 121, and post-test photographs are shown in Figure 122.

Table 26. Test Data Sheet, Test No. CFT-1

Test ID: CFT-1

Width (critical):	3.033	in.
Thickness (critical):	4.080	in.
Cross-Sectional Area:	12.37	in. ²
Laser Gauge Length (caliper):	4.045	in.
Laser Gauge Length (laser):	4.0460	in.
Peak Load:	4.235	kips
Peak Engineering Stress:	0.342	ksi

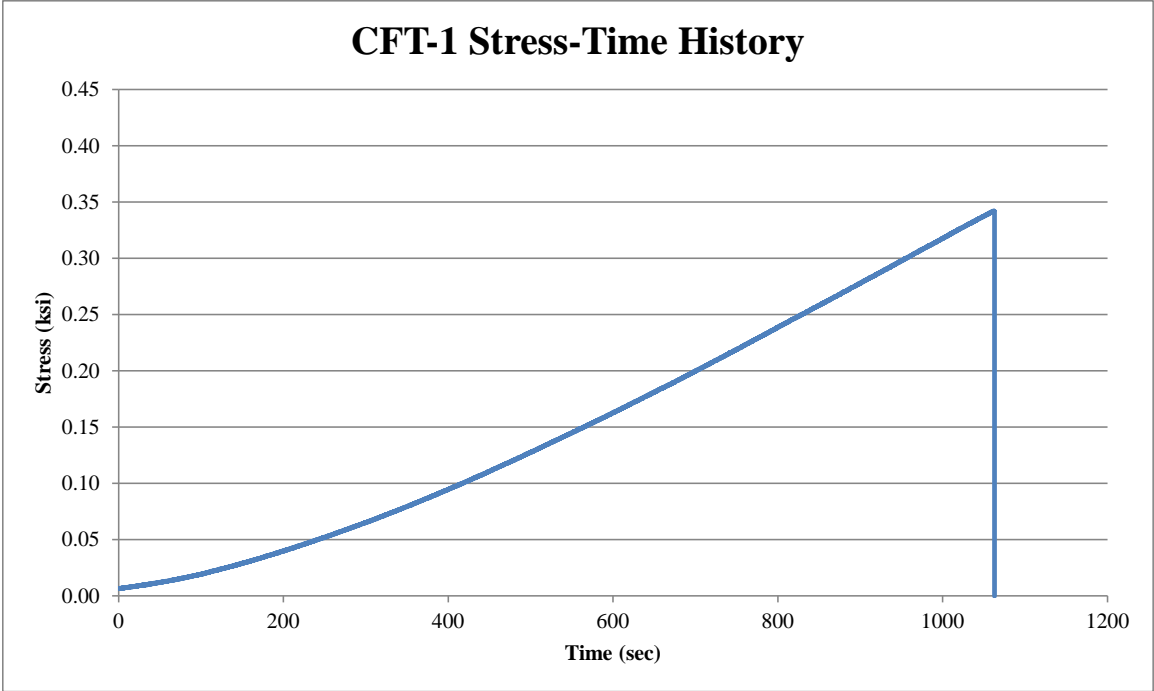


Figure 121. Stress-Time History, Test No. CFT-1

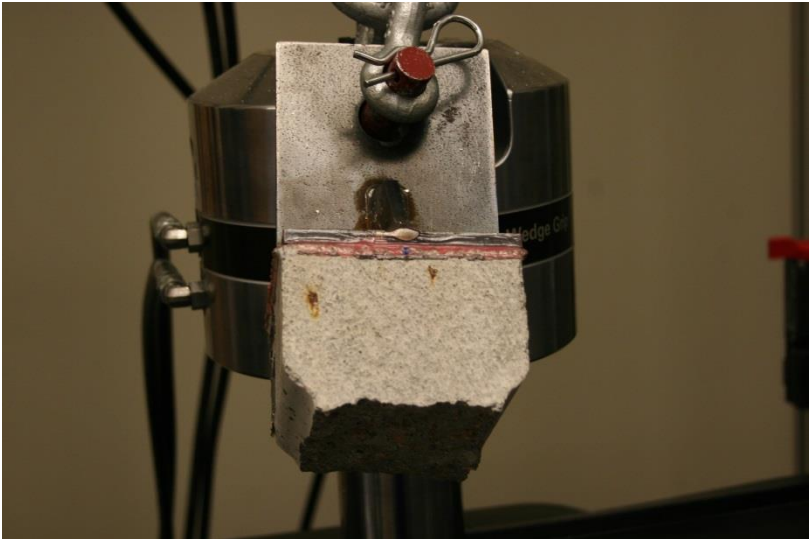
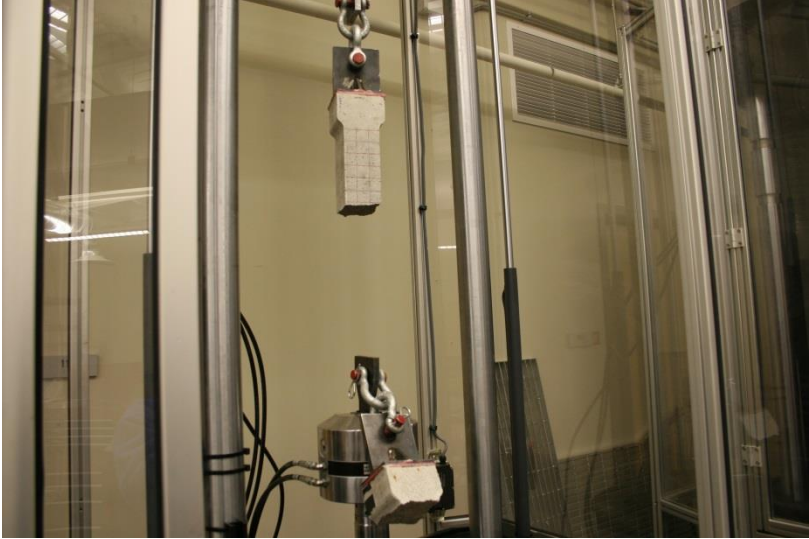


Figure 122. Post-Test Photographs, Test No. CFT-1

11.2 Test No. CFT-2

As the MTS Landmark machine loaded the specimen in tension during test no. CFT-2, the specimen fractured 5.1 in. (130 mm) from the bottom of the specimen, which was inside the 4-in. (102-mm) gauge length. A peak load of 4.4 kip (19.6 kN) occurred at fracture. A summary of pre- and post-test measurements is shown in Table 27. The stress versus time plot is shown in Figure 123, and post-test photographs are shown in Figure 124.

Table 27. Test Data Sheet, Test No. CFT-2

Test ID: CFT-2

Width (critical):	3.078	in.
Thickness (critical):	4.072	in.
Cross-Sectional Area:	12.53	in. ²
Laser Gauge Length (caliper):	3.945	in.
Laser Gauge Length (laser):	3.9404	in.
Peak Load:	4.445	kips
Peak Engineering Stress:	0.355	ksi

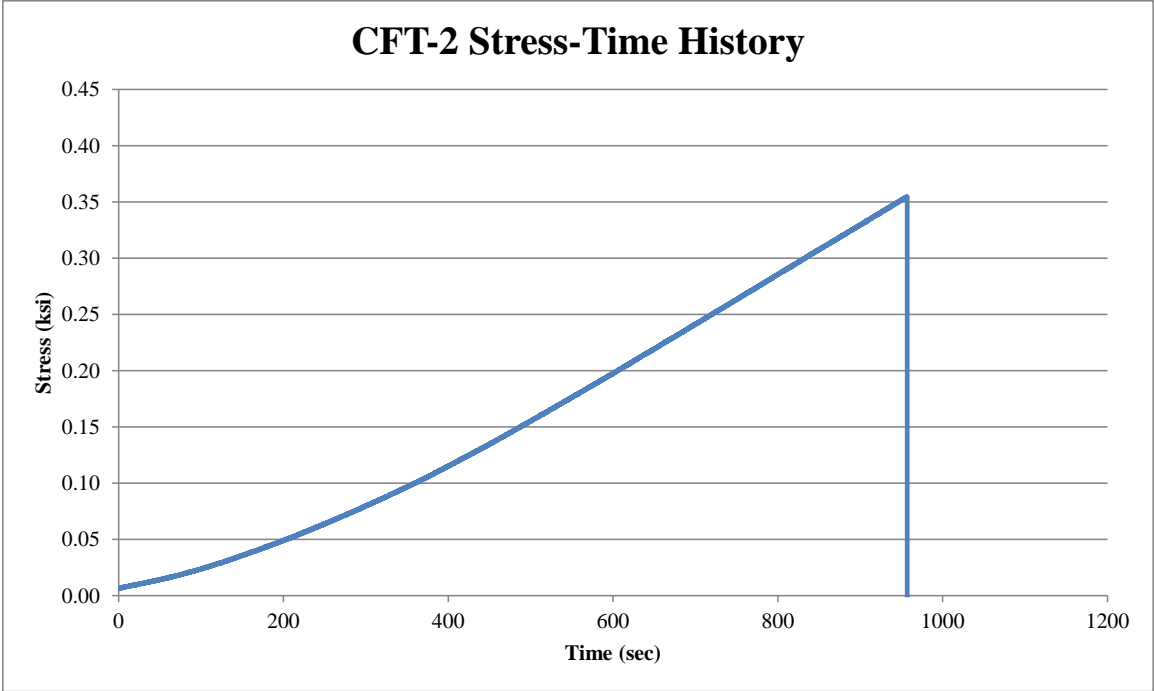


Figure 123. Stress-Time History, Test No. CFT-2

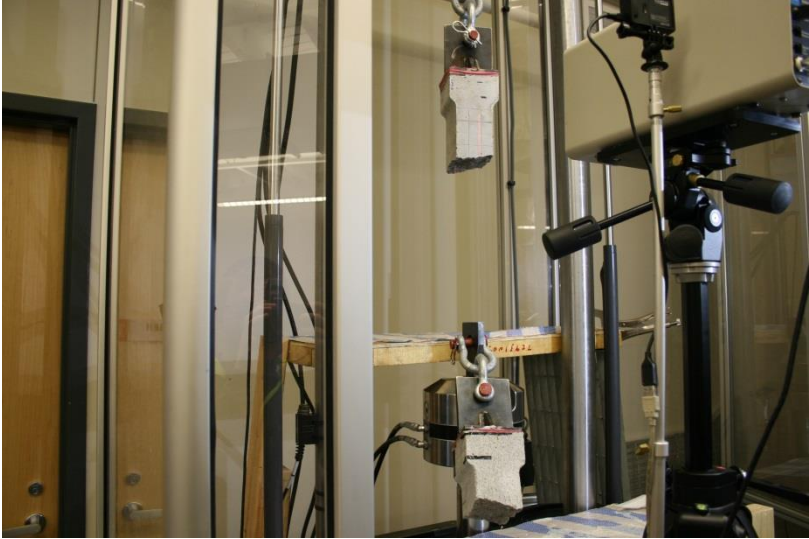


Figure 124. Post-Test Photographs, Test No. CFT-2

11.3 Test No. CFT-3

As the MTS Landmark machine loaded the specimen in tension during test no. CFT-3, the specimen fractured 2.8 in. (71 mm) from the bottom of the specimen, which was outside the 4-in. (102-mm) gauge length. A peak load of 4.4 kip (19.6 kN) occurred at fracture. A summary of pre- and post-test measurements is shown in Table 28. The stress versus time plot is shown in Figure 125, and post-test photographs are shown in Figure 126.

Table 28. Test Data Sheet, Test No. CFT-3

Test ID: CFT-3

Width (critical):	2.995	in.
Thickness (critical):	4.022	in.
Cross-Sectional Area:	12.05	in. ²
Laser Gauge Length (caliper):	3.998	in.
Laser Gauge Length (laser):	3.9877	in.
Peak Load:	4.389	kips
Peak Engineering Stress:	0.364	ksi

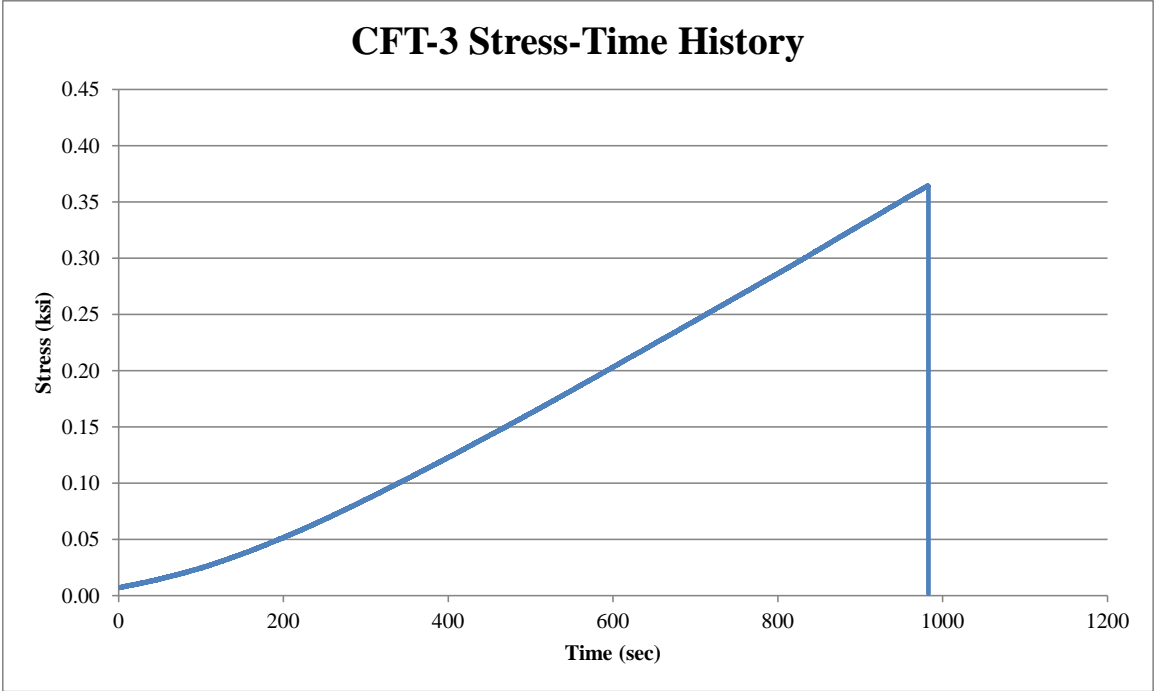


Figure 125. Stress-Time History, Test No. CFT-3

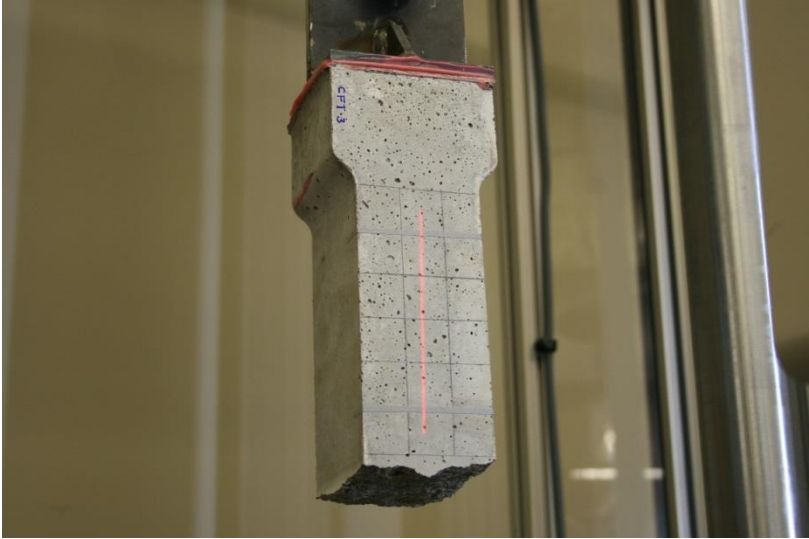


Figure 126. Post-Test Photographs, Test No. CFT-3

11.4 Test No. CFT-4

As the MTS Landmark machine loaded the specimen in tension during test no. CFT-4, the specimen fractured 4.9 in. (124 mm) from the top of the specimen, which was inside the 4-in. (102-mm) gauge length. A peak load of 4.8 kip (21.4 kN) occurred at fracture. A summary of pre- and post-test measurements is shown in Table 29. The stress versus time plot is shown in Figure 127, and post-test photographs are shown in Figure 128.

Table 29. Test Data Sheet, Test No. CFT-4

Test ID: CFT-4

Width (critical):	2.969	in.
Thickness (critical):	4.010	in.
Cross-Sectional Area:	11.91	in. ²
Laser Gauge Length (caliper):	4.027	in.
Laser Gauge Length (laser):	4.0266	in.
Peak Load:	4.846	kips
Peak Engineering Stress:	0.407	ksi

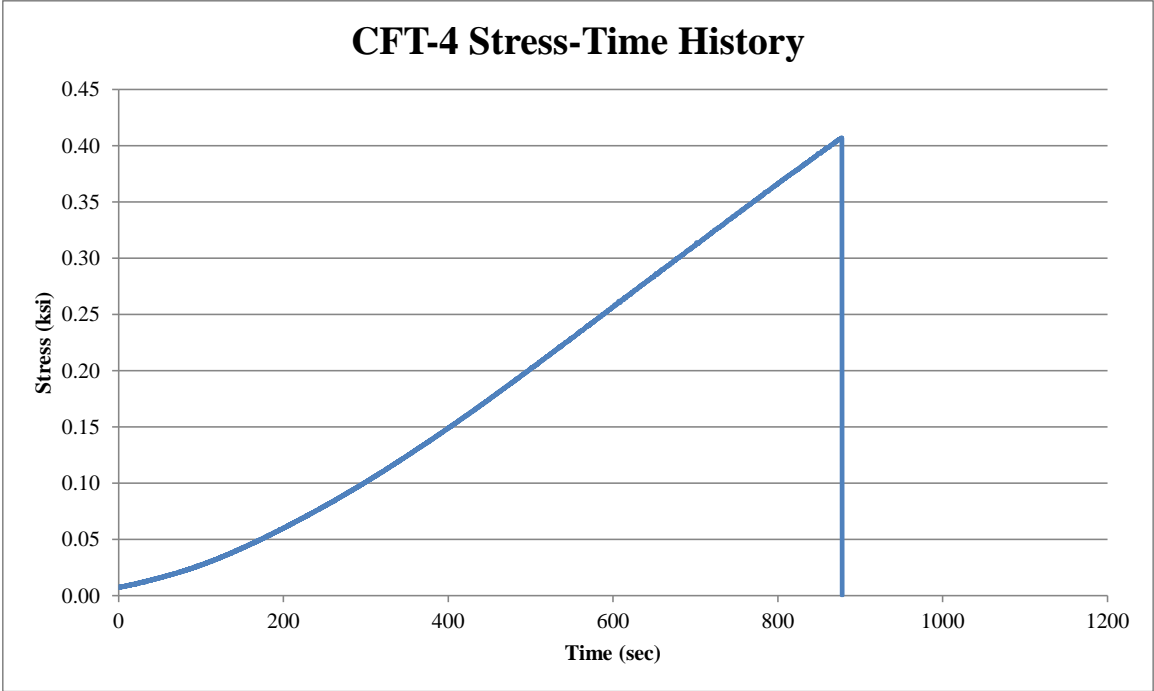


Figure 127. Stress-Time History, Test No. CFT-4



Figure 128. Post-Test Photographs, Test No. CFT-4

11.5 Test No. CFT-5

A revised test setup was used for test no. CFT-5. It was believed that the part was rotating slightly during testing, which contributed to poor laser extensometer readings. A mechanical extensometer was also used during this test, however the readings were also poor. The shackles were removed from the top loading point and the top plate was placed directly into the grips. The bottom loading point and the orientation of the specimen were rotated 90 degrees relative to other tests. As the MTS Landmark machine loaded the specimen in tension during test no. CFT-5, the specimen broke 2.3 in. (58 mm) from the top of the specimen, which was outside the 4-in. (102-mm) gauge length. A peak load of 4.3 kip (19.1 kN) occurred at fracture. A summary of pre- and post-test measurements is shown in Table 30. The stress versus time plot is shown in Figure 129, and post-test photographs are shown in Figure 130.

Table 30. Test Data Sheet, Test No. CFT-5

Test ID: CFT-5

Width (critical):	3.049	in.
Thickness (critical):	4.068	in.
Cross-Sectional Area:	12.403	in. ²
Laser Gauge Length (caliper):	3.983	in.
Laser Gauge Length (laser):	4.0071	in.
Peak Load:	4.257	kip
Peak Engineering Stress:	0.343	ksi

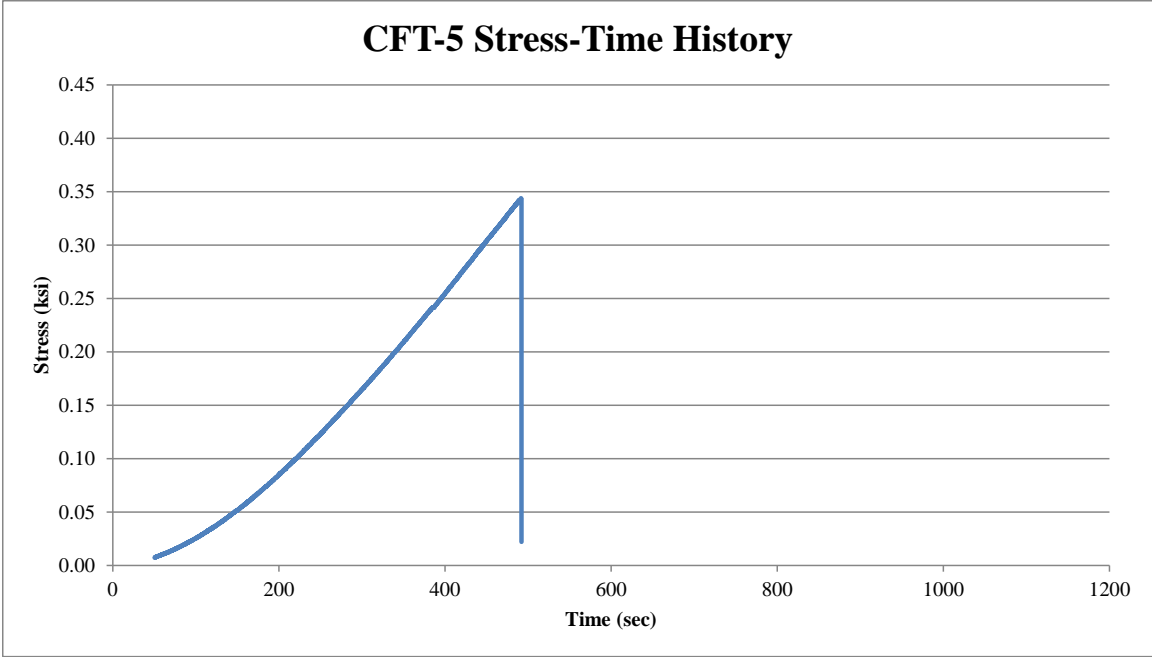


Figure 129. Stress-Time History, Test No. CFT-5



Figure 130. Post-Test Photographs, Test No. CFT-5

11.6 Test No. CFT-6

As the MTS Landmark machine loaded the specimen in tension during test no. CFT-6, the specimen broke 2.7 in. (69 mm) from the top of the specimen, which was outside the 4-in. (102-mm) gauge length. A peak load of 4.7 kip (20.9 kN) occurred at fracture. A summary of pre- and post-test measurements is shown in Table 31. The stress versus time plot is shown in Figure 131, and post-test photographs are shown in Figure 132.

Table 31. Test Data Sheet, Test No. CFT-6

Test ID: CFT-6

Width (critical):	3.095	in.
Thickness (critical):	4.091	in.
Cross-Sectional Area:	12.66	in. ²
Laser Gauge Length (caliper):	3.956	in.
Laser Gauge Length (laser):	3.9500	in.
Peak Load:	4.681	kips
Peak Engineering Stress:	0.370	ksi

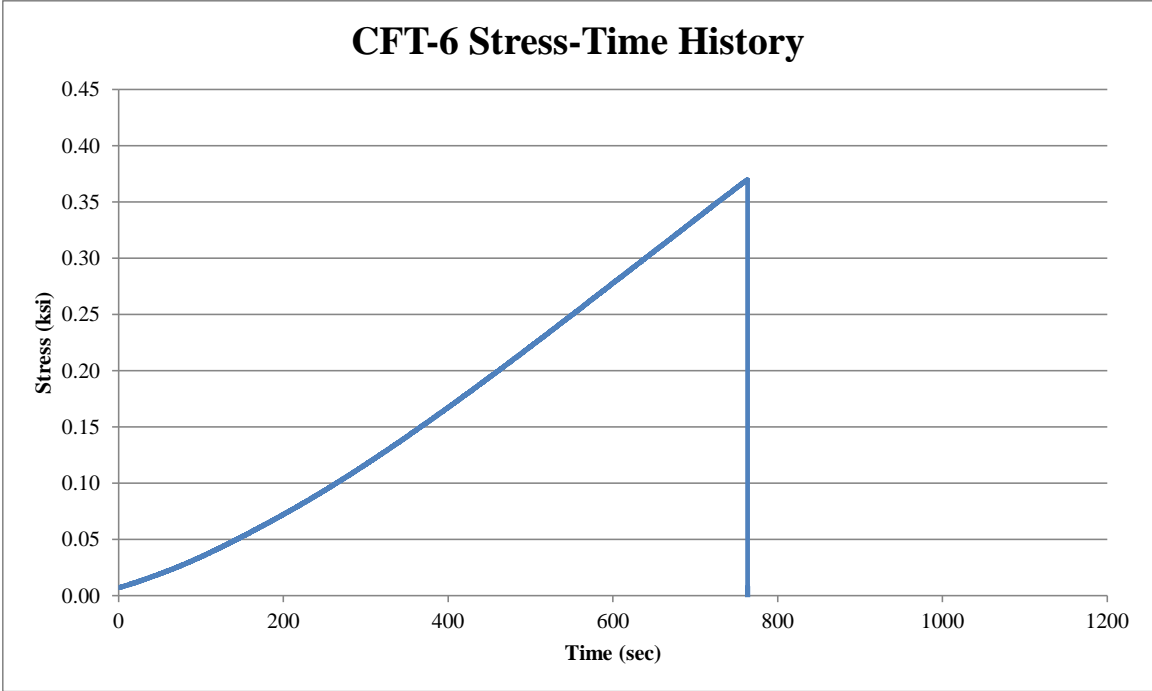


Figure 131. Stress-Time History, Test No. CFT-6

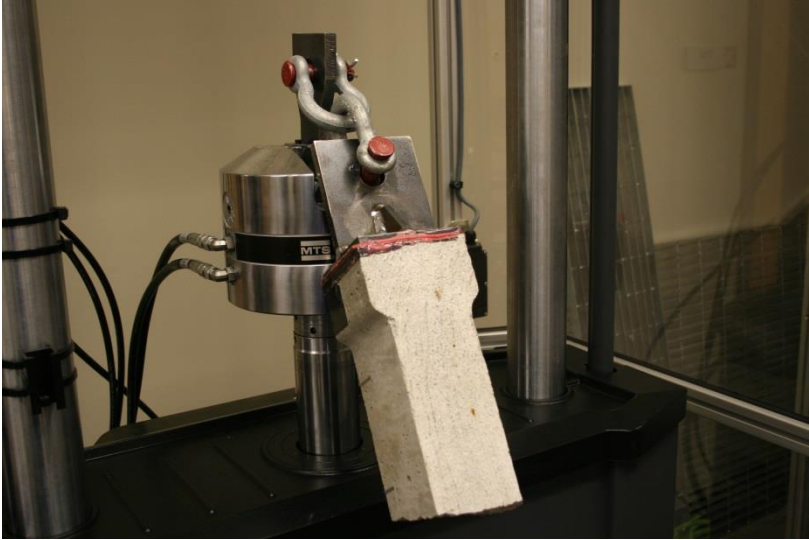
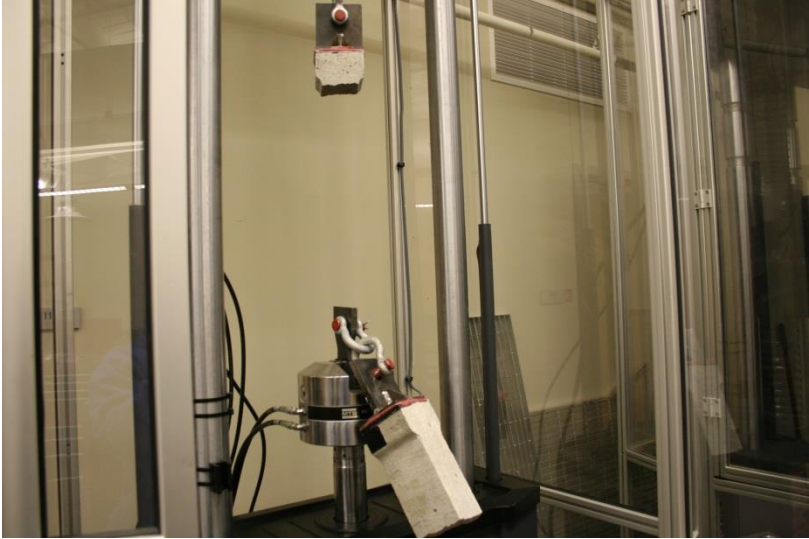


Figure 132. Post-Test Photographs, Test No. CFT-6

11.7 Discussion

Six static component tests were performed in the tension load case round of testing. Stress vs. time histories were plotted for all samples as shown in Figure 133. The epoxy layer did not debond in any of the tension tests and the peaks in the stress-time histories for all tests were similar. The average peak stress for the six tests was 0.36 ksi (2.5 MPa). Test no. CFT-5 differed from the other tests as the fracture occurred much sooner than the other tests, but the stress value was not significantly lower than the other tests. Also, the specimens all fractured in the narrowed regions of the specimens, as shown in Figure 134. Two of the specimens fractured within the 4-in. (102-mm) gauge length, and the other four fractured near the edge of the narrowed regions. The location of failure, specifically a majority of the specimens failing near the narrowed region, may indicate that the geometry affected the failure pattern.

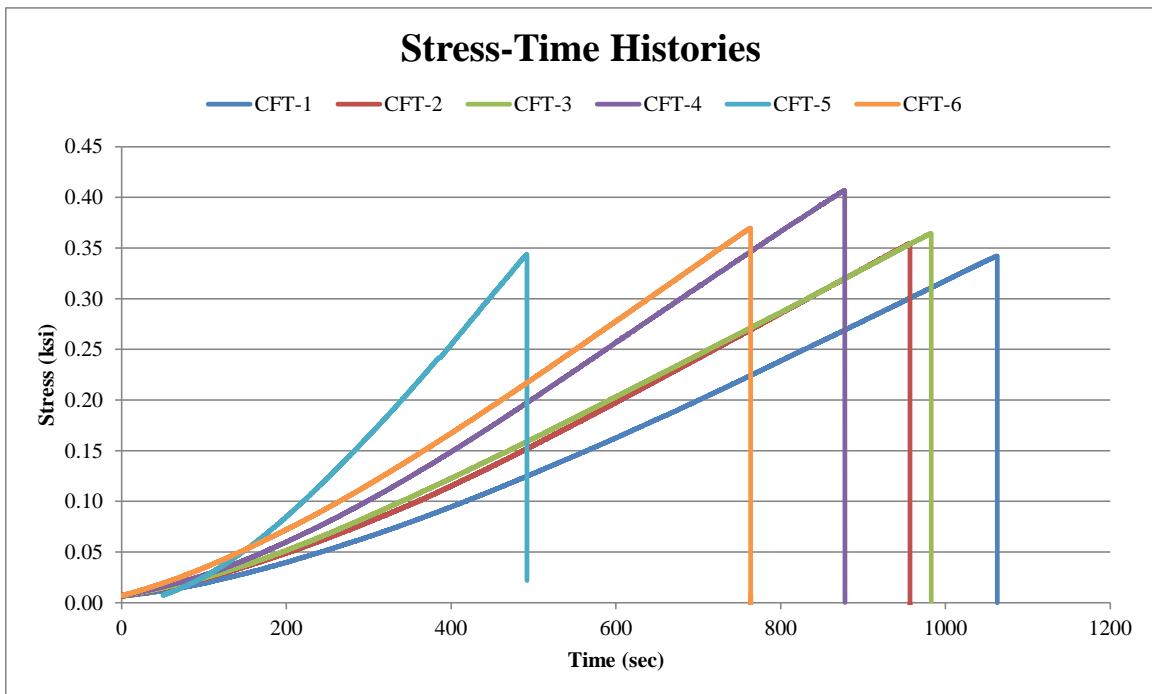


Figure 133. Stress-Time Histories, Test No. CFT-1 through CFT-6



Figure 134. Post-Test Photographs, Test Nos. CFT-1 through CFT-6

The average tensile strength was approximately 4.0% of the compressive strength. Typically a value of between 8 and 12 percent of the compressive strength is observed, and considered acceptable. Although the proportionate ratio of tensile to compression strengths is low, some studies have indicated that an acceptable range is as low as 5-10% [1].

Cubic segments of varied length from the narrower region of each dogbone were cut from the fractured specimens and were tested in compression to confirm the compression values from the compression testing segment. A summary of those results is shown in Table 32.

Table 32. Summary of Dogbone Compression Tests

Test No.	Peak Load	Peak Stress
-	<i>kip</i>	<i>ksi</i>
CFT-1	20.5	1.7
CFT-2	64.2	7.0
CFT-3	22.6	1.9
CFT-4	103.7	8.7
CFT-5	84.4	6.8
CFT-6	81.6	6.4

The highest stress that was achieved was 8.7 ksi (60.0 MPa), which is lower than the average from the compression cylinder tests. There were also significantly lower peak stress values, which may be explained by the difficulty encountered with testing a rectangular geometry in compression. The tests may have failed at lower peak loads because there was spalling along the edge of the prisms and excess pressure was placed on the specimen by the round rubber pads that were used as caps. The may have also failed early due to microcracks formed in tension tests. The size differential between the dogbones and rubber caps caused significant issues. These caps were removed for the final three tests. The 8.7 ksi (60.0 MPa) test indicated that the concrete batch was higher than the design stress. It does confirm the high compression strength seen in test nos. CFC-1 through CFC-7.

CHAPTER 12 BEAM TESTING – FLEXURE AND SHEAR (CFS-1 THROUGH CFS-6)

12.1 Introduction

Six beam bending tests were completed for the final portion of the physical testing program. The MTS Criterion machine was used to perform 4-point bending tests in accordance with ASTM C78 [28]. The top load apparatus (i.e., rollers) were configured with a constant spacing of 6 in. (152 mm) for all six tests. The test setups varied from test-to-test where the span length between lower support points changed. The varied span length allowed for investigation of both flexural and shear failure modes as well as a determination of the span length where the beam transitioned from flexure failure to shear failure. Tested span lengths ranged from 9 in. (229 mm) to 18 in. (457 mm).

Each test was conducted at a constant displacement rate throughout the event. Test nos. CFS-1 through CFS-3, and CFS-5 through CFS-6 were run at a displacement rate of 0.0003 in./s (0.00762 mm/s). A 0.0001 in./s (0.00254 mm/s) displacement rate was used in test no. CFS-4. The load was applied to each beam as the actuator base moved upward, and the top rollers provided resistance and loaded the beam. The top rollers remained stationary throughout each test. Each beam was centered on the support span rollers in both the longitudinal and transverse directions. A trigger was used to establish consistent event start times in the electronic test data; since, two different data acquisition systems were used.

Horizontal strain gauges, rosette strain gauges, and string potentiometers were used to instrument test specimens. Force from a load cell and actuator data were also acquired within the internal MTS control system. The force data was extracted in order to better align the data. Thus, the load vs. time plots were trimmed, start at 300 lb (1.3 kN),

and correspond to time zero for all six tests. Strain was measured directly from the processed horizontal and rosette gauge data. Vertical displacement was acquired using string potentiometers. Engineering stress was calculated based on the original cross-sectional area of each beam, and stress versus time histories were developed.

12.2 Test Data Evaluation Process

For all tests, the electronic test data was processed, analyzed, and evaluated to determine its adequacy. First, beam displacements were measured with the string potentiometers and compared with raw actuator displacements as well as theoretical displacements based on beams bending subjected to four-point bending and symmetrically placed, as provided in the AISC Steel Construction Manual [69] and shown in Equation 20:

Equation 20.
$$\Delta_{max} = \frac{Pa}{24E_{CFCL}}(3l^2 - 4a^2)$$

where P is one of the two point loads on the beam, or half of the total load ($2P$), a is the distance from the load to the support of the beam, E_{CFCL} is the average Young's modulus from the internal compression testing or 3768 ksi (26.0 GPa), I is the moment of inertia of the section, and l is the beam length.

The typical four-point bending setup is shown in Figure 135.

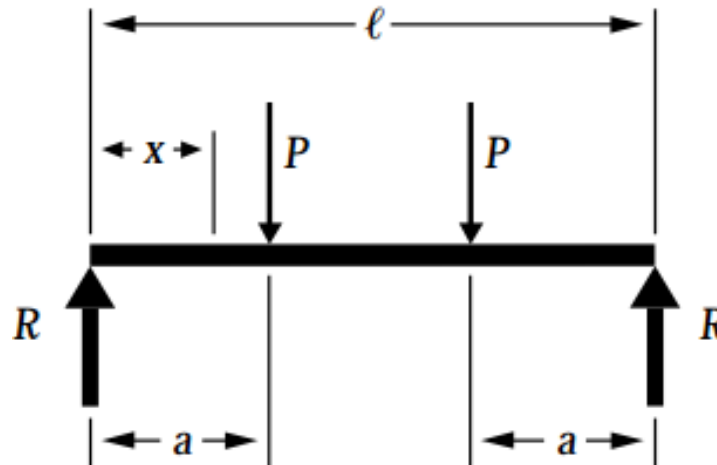


Figure 135. Four-Point Bending Test Setup

A modification proposed by Roylance [70] was also used to adjust theoretical beam displacements to include shear effects, as shown in Equation 21 below:

$$\text{Equation 21. } \delta(x) = \frac{P(L-a)}{6LE_{CF}I} \left[\frac{L}{L-a} (x-a)^3 - x^3 + (L^2 - (L-a)^2)x \right] + \frac{Pa}{6LE_{CF}I} \left[\frac{L}{a} (x - (L-a))^3 - x^3 + (L^2 - a^2)x \right]$$

where P is the point load, L is the beam length, a is the distance from the load to the support of the beam, I is the moment of inertia of the section, and x is the location where the displacement is being measured.

The horizontal strain gauge measurements (5 gauges at midsection) were subjected to simple checks to verify that results made physical sense. Test results for all five strain gauges were cross-plotted. Based on gauge placement on the beam from top to bottom, strain readings should demonstrate compression (negative) on top and tension (positive) on bottom, with reasonable strain variations between the side-mounted gauges. However, the exact strain distribution is unknown, and the beam fracture behavior may change as the span length is decreased.

For the flexural failure case, test no. CFS-1 with an 18-in. (457 mm) span, normal strains may likely vary linearly from top to bottom. For this special case, strains at the beam's centerline or neutral axis should be zero. The strain readings at end of test would likely be linearly distributed across all five gauges based on their placement. Note that the lower side gauge, E, and upper side gauge, G, were placed $\frac{3}{4}$ in. (19 mm) from bottom and top surfaces of the beam, respectively. Thus, the strain at failure for these side gauges should be somewhat close to, but less than, strains in gauges D (bottom) and H (top) for the test with an 18-in. (457-mm) span.

The second check used the horizontal strain gauge measurements for the flexural and shear failure cases to calculate the maximum normal stresses at the outer fibers between roller positions. Equation 22 is used to calculate bending stress based on a normal strain at the outer fibers – negative strain on top of beam and positive strain on bottom of beam:

Equation 22.
$$\sigma_{x,max} = \varepsilon_x E_{CFC}$$

where $\sigma_{x,max}$ is the maximum normal stress from strain gauge, ε_x is the maximum normal strain, and E_{CFC} is the average Young's modulus from the internal compression testing.

These maximum normal stresses were compared to the bending stresses obtained using the maximum force reading obtained from the MTS control system and load cell, which was calculated with the elastic bending equation provided below as Equation 23.

Equation 23.
$$\sigma_{bending,max} = \frac{Mc}{I} = \frac{Pac}{I}$$

where $\sigma_{bending,max}$ is the maximum normal stress from MTS, M is the moment caused by the loading condition (the point load or half of the total load applied multiplied by a ,

the distance from the load to the support of the beam), c is the maximum distance away from the neutral axis, and I is the moment of inertia of the section. If the bending stress is desired for another location, then c is replaced with y , where y is the vertical offset away from neutral axis. For the flexural failure case, the two bending stress calculations were compared to verify the horizontal strain gauge data.

The rosette strain gauge readings were processed, analyzed, and evaluated for principal strains, maximum shearing strain, principal stresses, maximum shearing stress, principal strain angle, and maximum shearing strain angle. The method proposed in ASTM E1561 [71] was followed to calculate principal strains and principal stresses as well as maximum shear strains and maximum shearing stresses. The principal strains, ε_1 and ε_2 were calculated based on factors, C and R . The variable C is defined as the average of two strains in the rosette using Equation 24:

Equation 24.
$$C = \frac{\varepsilon_a + \varepsilon_c}{2}$$

where ε_a is the strain in the horizontal leg of the rosette (for gauges 1 and 3 and the opposite for gauges 2 and 4) and ε_c is the strain in the vertical leg of the rosette (for gauges 1 and 3 and the opposite for gauges 2 and 4). The variable R is defined by Equation 25:

Equation 25.
$$R = \sqrt{(\varepsilon_a - C)^2 + (\varepsilon_b - C)^2}$$

where ε_b is the strain in the diagonal leg of the rosette. The principal and maximum shear strains are defined by Equation 26 through Equation 28:

Equation 26.
$$\varepsilon_1 = C + R$$

Equation 27.
$$\varepsilon_2 = C - R$$

Equation 28.
$$\gamma_{max} = 2R$$

where ε_1 is the compressive principal strain, ε_2 is the tensile principal strain, and γ_{max} is the maximum shear strain. The principal strains can be used to calculate the principal stresses using Equation 29 and Equation 30 [72]:

Equation 29.
$$\sigma_1 = \frac{E_{CFC}}{(1-\nu^2)} (\varepsilon_1 + \nu\varepsilon_2)$$

Equation 30.
$$\sigma_2 = \frac{E_{CFC}}{(1-\nu^2)} (\varepsilon_2 + \nu\varepsilon_1)$$

where σ_1 is the maximum principal stress, σ_2 is the minimum principal stress, E_{CFC} is the average Young's modulus from the internal compression testing, and ν is Poisson's ratio. An assumed Poisson's ratio, ν , of 0.19 was used for all calculations involving principal stresses and strains from the rosette data. This selection coincides with the value that was used in all five material models as part of the previous simulation efforts. From there, the maximum shearing stress, τ_{max} , was calculated using Equation 31:

Equation 31.
$$\tau_{max} = \frac{\sigma_1 - \sigma_2}{2} \text{ (in-plane)}$$

Alternatively, the maximum shearing stress could be calculated by Equation 32:

Equation 32.
$$\tau_{max} = \gamma_{max} G \text{ (in-plane)}$$

where G is the shear modulus or modulus of rigidity equal to $\frac{E}{2(1+\nu)}$, and γ_{max} is the maximum shear strain determined with the rosette data. The shear modulus, G , was calculated as 1583 ksi (10.9 GPa).

A principal stress and maximum shear stress was calculated at each time step during the loading event. The maximum shearing stress at failure was later compared to the calculated theoretical value, which is based on transverse loading on beams and discussed below.

The principal angles are used to provide an orientation for the direction in which the principal strains and stresses are acting. They are calculated using Equation 33 and Equation 34 for rosette gauges 1 and 3 on the left side of a face and adjusted by 90 degrees for rosette gauges 2 and 4 on the right side of a face [73]:

Equation 33.
$$\theta_{1p} = \frac{1}{2} \tan^{-1} \left(\frac{2\varepsilon_b - \varepsilon_a - \varepsilon_c}{\varepsilon_a - \varepsilon_c} \right)$$

Equation 34.
$$\theta_{2p} = \theta_{1p} \pm 90^\circ$$

These angles were plotted when acceptable rosette data was available. The maximum shearing plane was also determined using Equation 35 [73]:

Equation 35.
$$\theta_{1s,2s} = \theta_{1p} \pm 45^\circ$$

The theoretical maximum shear stress was also calculated based on peak load cell data acquired at failure. The modified maximum shear stress, τ_{max} can be found with Equation 36, as proposed by Timoshenko [74]:

Equation 36.
$$\tau_{max} = \frac{3}{2}(V)A(1.126)$$

where τ_{max} is the maximum shear stress, V is the vertical shear force taken as P from Figure 135, A is the area of the beam, and the magnification factor of 1.126 accounts for the beam shape having a square cross section.

A rosette strain gauge was considered to provide reasonable results when the maximum shear stress determined from the rosette gauge test data was similar to the theoretical value. This finding would somewhat be expected for the assumed flexure failure scenario, test no. CFS-1. The secondary verification for the rosette strain gauges was to review the principal stresses and determine whether any tensile stresses existed. If a principal stress in tension exceeded the maximum tension failure stress obtained from test nos. CFT-1 through CFT-6, or 407.0 psi (2.8 MPa), by 50% or more (conservative

selection), then the strain rosette data may be flagged for further investigation as it may possibly be returning erroneous data. Rosettes with non-operating channels on individual legs of the strain gauge were also not considered in the full-strain field analysis. A layout of the strain gauges and string potentiometers is shown Chapter 9, Figure 102.

12.3 Test No. CFS-1 [Support Span – 18 in. (457 mm)]

For test no. CFS-1, a span length of 18 in. (457 mm) was used, which was the largest span that could be accommodated by the test apparatus. As previously noted, a flexural beam failure was expected to occur with this configuration. The test setup is shown in Figure 136.

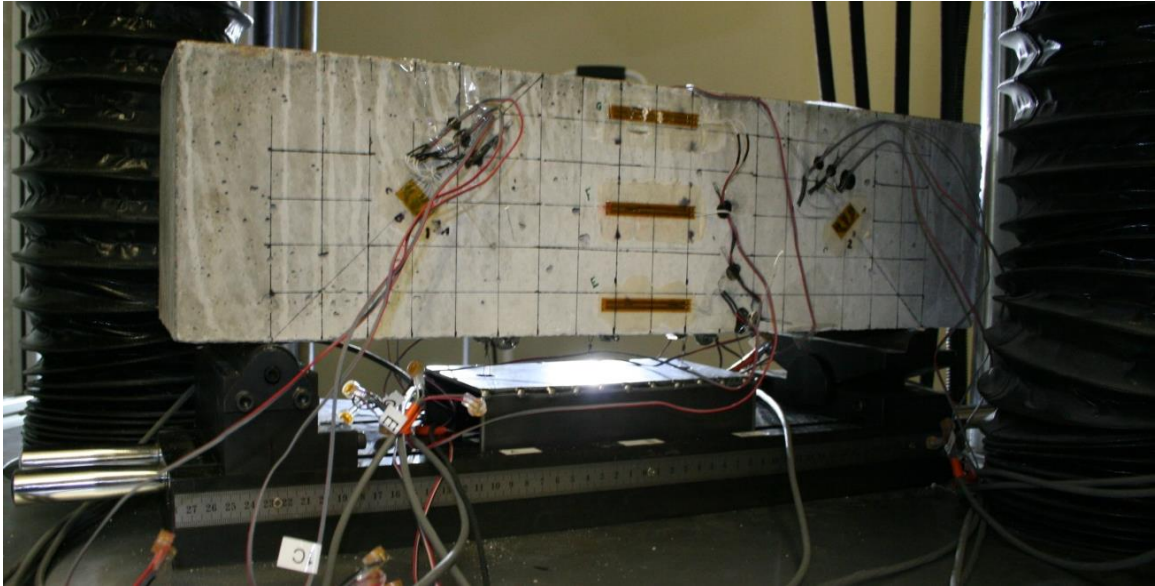


Figure 136. Test Setup for Test No. CFS-1 [18-in. (457-mm) Span]

As the MTS Criterion testing machine loaded the specimen during test no. CFS-1, the specimen failed in flexure due to excessive tensile stresses at the bottom surface and between the upper roller locations. Specifically, the vertical fracture plane occurred approximately 3 in. (76 mm) away from the centerline of the beam or near an upper roller. A peak load of 5.8 kip (25.8 kN) was measured when the specimen fractured. Thus, each upper roller was assumed to transfer a peak load equal to 2.9 kip (12.9 kN) to the top of the beam, thus resulting in a reaction at both lower supports equal to 2.9 kip (12.9 kN). The load versus time plot is shown in Figure 137, and post-test photographs are shown in Figure 138 and Figure 139.

All horizontal strain gauges that were placed at the vertical centerline of the beam appeared to perform in an acceptable manner during test no. CFS-1. In addition, no horizontal strain gauges between rollers broke as the flexural failure occurred away from the vertical centerline of the beam. The strain readings revealed maximum negative (compression) and maximum positive (tension) normal strains of -7.64×10^{-5} in./in. (top) and 7.97×10^{-5} in./in. (bottom), respectively, as shown in Table 33 and Figure 140. Horizontal normal strains appeared to be very similar in the top and bottom halves of the beam, almost creating a mirrored image and an indication of a linear strain distribution. As depicted in Figure 141, normal strains were plotted in the direction of the horizontal beam axis for each vertical gauge position [0 in. (beam centerline), $\pm 2\frac{1}{4}$ in. (57 mm) (upper and lower side gauges), and ± 3 in. (76 mm) (top and bottom gauges)]. From this comparison, it is also apparent that normal strains were linearly distributed on the transverse plane (i.e., y-z plane). Finally, the middle strain gauge revealed strains which largely oscillated around zero for the duration of the test. Overall, the horizontal strain gauge data was deemed reasonable.

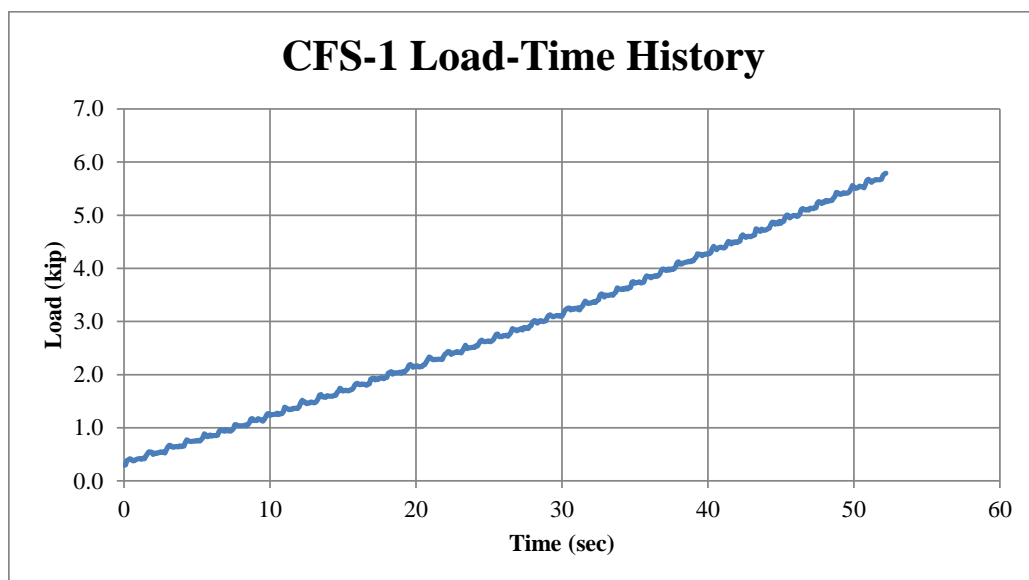


Figure 137. Load vs. Time, Test No. CFS-1 [18-in. (457-mm) Span]

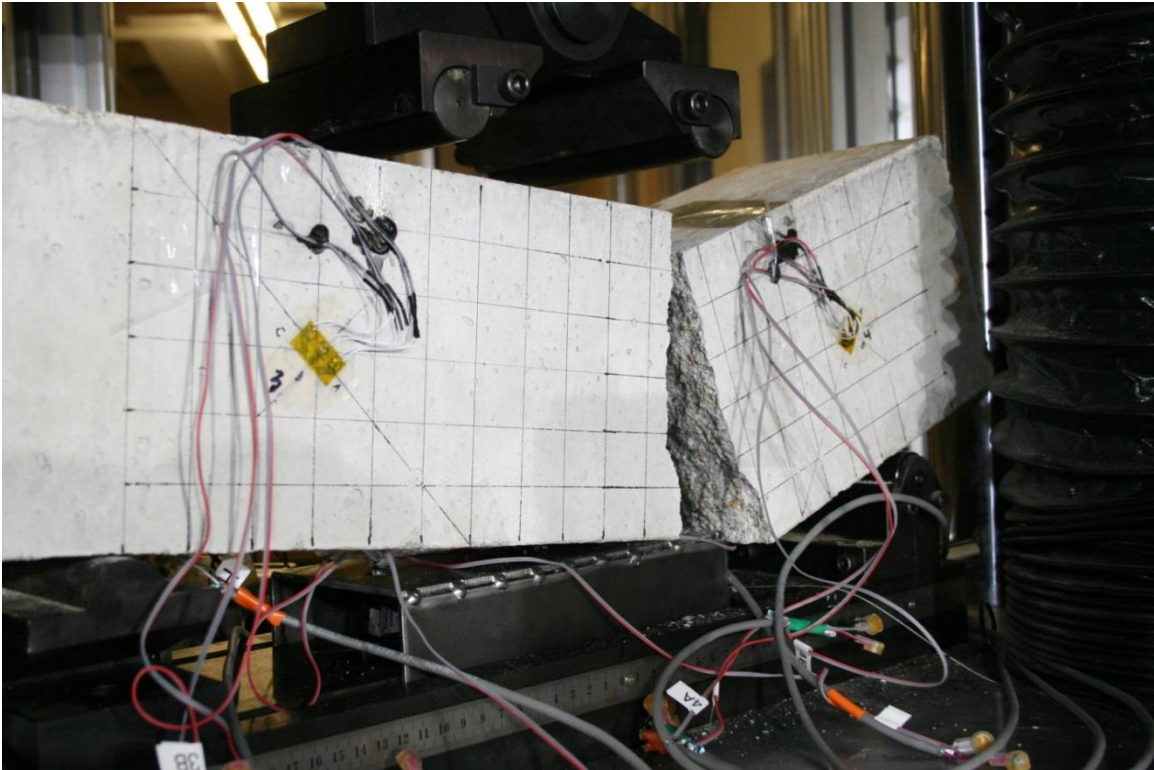
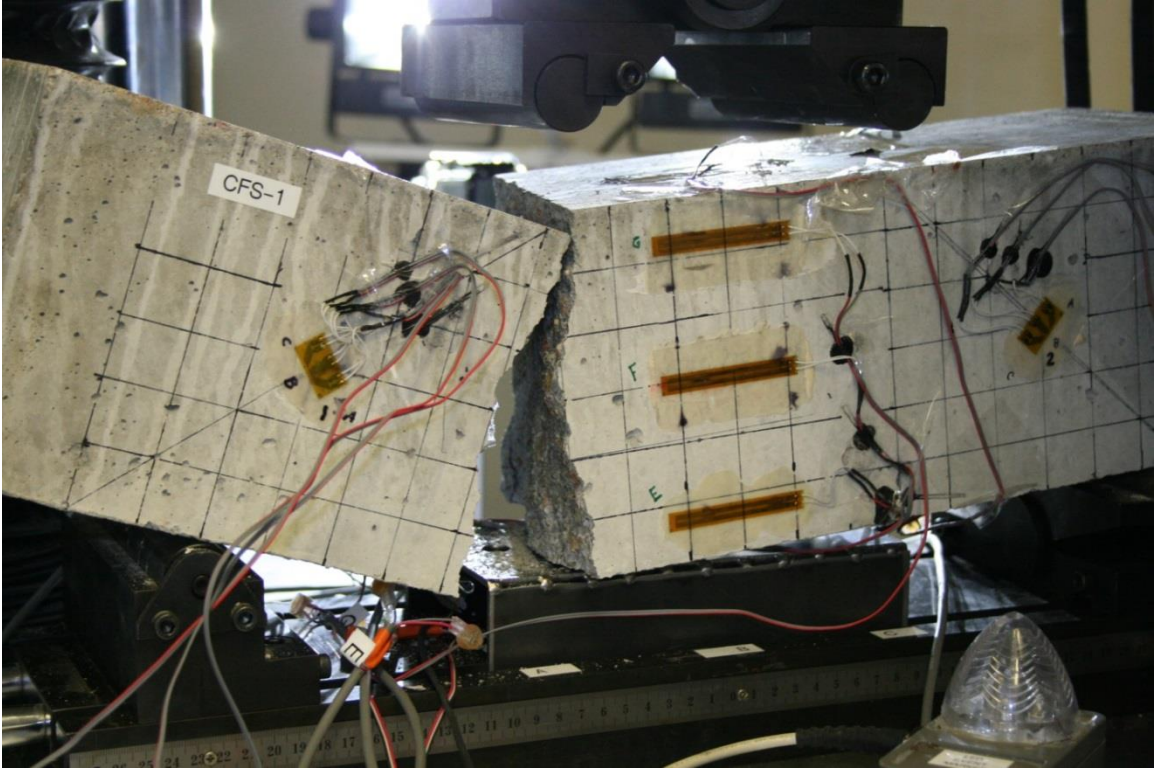


Figure 138. Post-Test Damage, Test No. CFS-1 [18-in. (457-mm) Span]

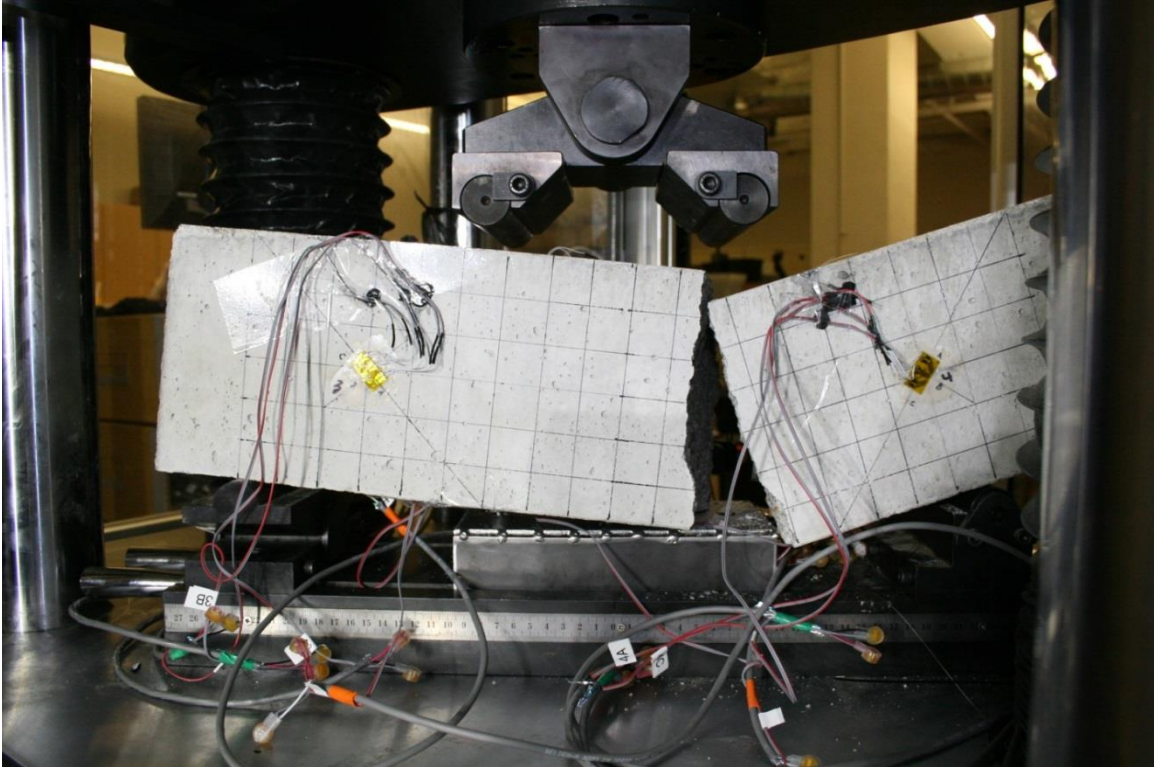


Figure 139. Additional Post-Test Damage, Test No. CFS-1 [18-in. (457-mm) Span]

Table 33. Normal Strain and Stress Distribution for Horizontal Gauges, Test No. CFS-1

Gauge Designation and Location	Normal Strain, ϵ_x, @ Failure <i>in./in.</i>	Estimated Maximum Normal Stress (Eq. 22) <i>psi</i>	Estimated Maximum Normal Stress (Eq. 23) <i>psi</i>
D (bottom)	7.97E-05	384.0	482.9
E	5.38E-05	259.0	362.1
F (middle)	2.95E-06	14.2	0.0
G	-6.12E-05	-294.5	-362.1
H (top)	-7.64E-05	-368.0	-482.9

Once the normal strains were processed, analyzed, and reviewed, an estimate was made to determine the maximum normal stress, $\sigma_{x,max}$, based on measured strains using Equation 22. The normal stress distribution was also estimated using strain readings at the upper and lower side positions. The maximum normal stress for each strain gauge is shown in Table 33, while the normal stress for four gauges as a function of time is provided in Figure 142 and Figure 143. An estimate was also made to determine the maximum normal stress, $\sigma_{bending,max}$, using the MTS load data and Equation 23. The maximum normal stress based on MTS load data and elastic bending is depicted in Table 33 for the top and bottom surfaces. Further, the normal stress corresponding to the other gauge locations was also calculated with MTS load data and provided in Table 33. The normal stress as a function of time and using MTS load data is shown graphically in Figure 142 and Figure 143. When comparing the normal stresses using the two methods, it is apparent that similar trends were predicted during the test duration. The estimated normal stress based on MTS load data exceeded the prediction using the strain readings for the outer four gauges. The maximum midspan normal stress was ± 482.9 psi (3.3 MPa) for the MTS load data and calculated moments, while the maximum midspan

normal stresses were +384.0 psi/-368.0 psi (+2.6 MPa/-2.5 MPa) using the strain data. For the noted assumptions and acquired data, the estimated normal stresses seemed to be mostly reasonable, although closer stress predictions were desired.

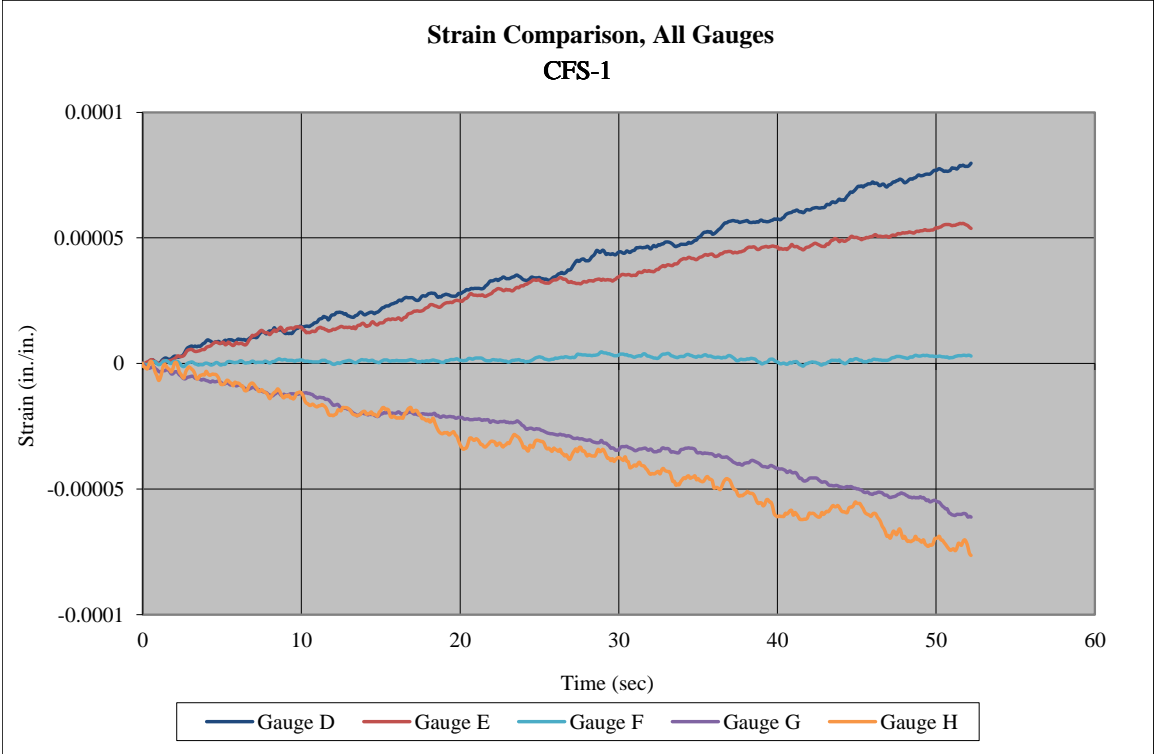


Figure 140. Normal Strains for Top, Side, and Bottom Gauges, Test No. CFS-1 [18-in. (457-mm) Span]

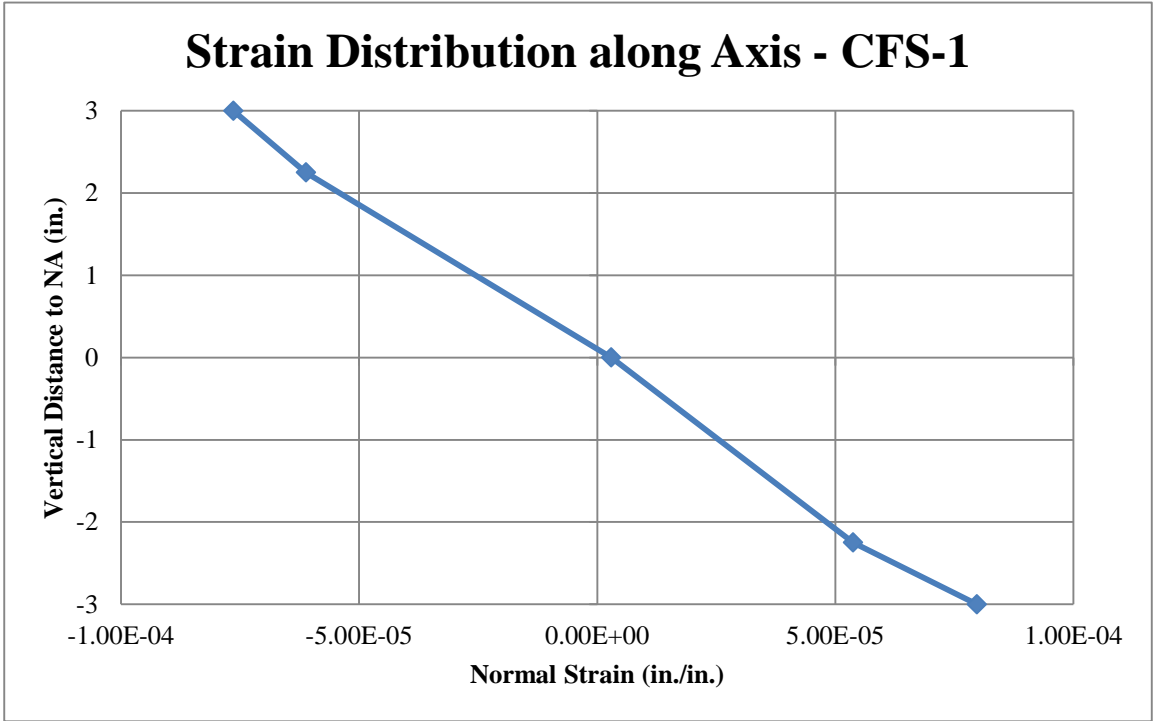


Figure 141. Vertical Distance versus Normal Strain, Test No. CFS-1 [18-in. (457-mm) Span]

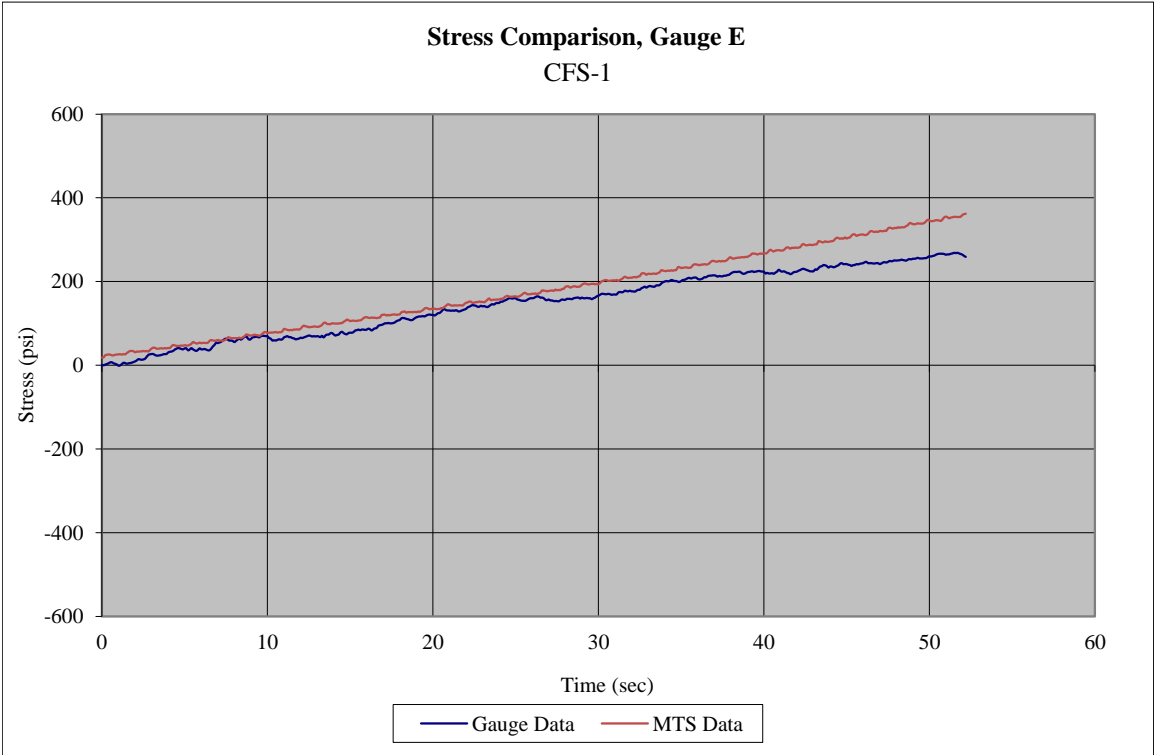
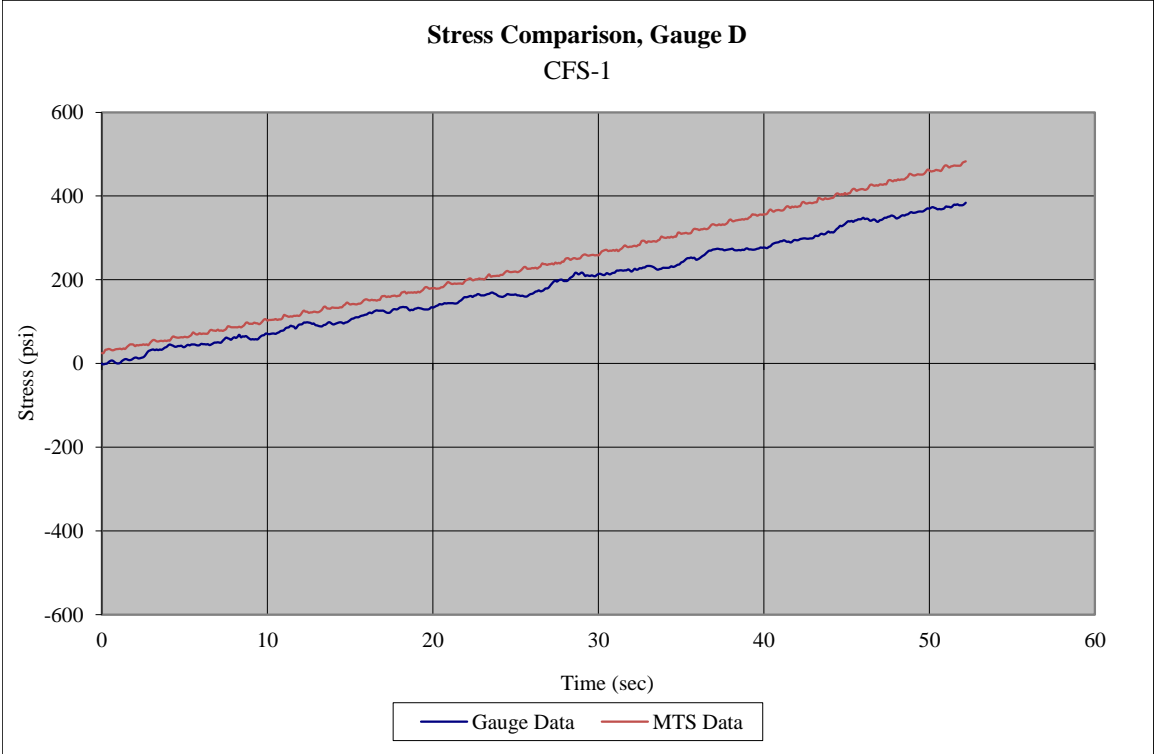


Figure 142. Estimated Midspan Normal Stresses from Bottom Strain Gauges and MTS Load Data, Test No. CFS-1 [18-in. (457-mm) Span]

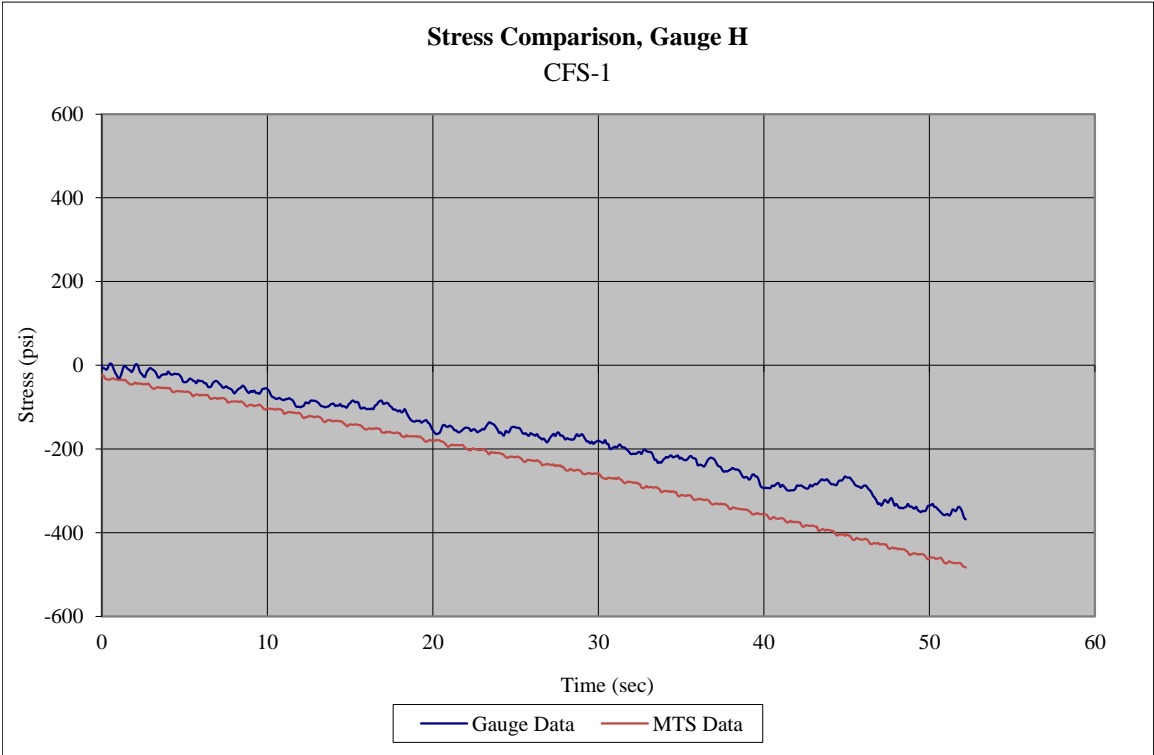
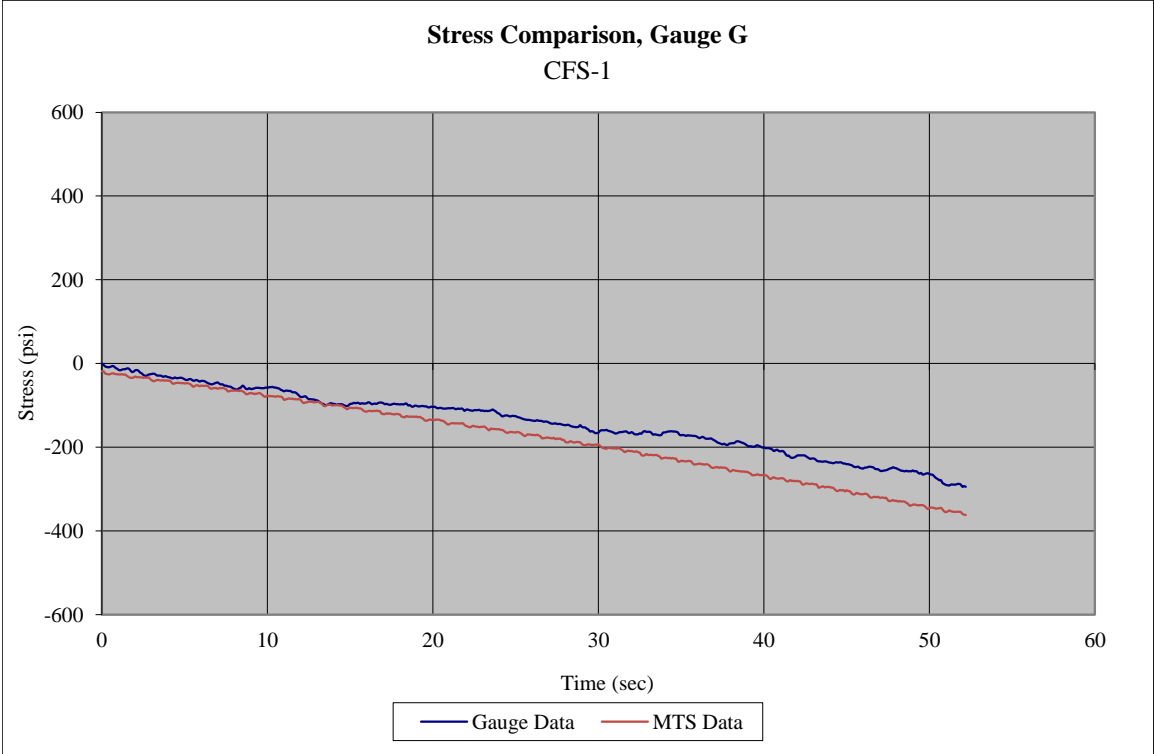


Figure 143. Estimated Midspan Normal Stresses from Top Strain Gauges and MTS Load Data, Test No. CFS-1 [18-in. (457-mm) Span]

Four rosette strain gauges were attached to the front and back faces of the beam near the horizontal centerline and midway between the upper roller and lower support. In addition, no rosette strain gauges between the lower support and upper roller broke as the flexural failure occurred away from the rosette strain gauges. Measured strains are provided in Figure 144 and Figure 145 for each rosette and each individual gauge, if acquired. Some rosette strain gauges appeared to perform in an acceptable manner during test no. CFS-1. However, some gauges provided data that may raise questions upon first glance. Based on symmetric loading and the 18-in. (457-mm) beam span, the strains would be expected to be very similar across all rosettes. However, this outcome did not appear to always be the case.

First, rosette no. 1 (left-front position facing front) provided nearly zero strain for all three gauges (A – horizontal, B – diagonal, and C – vertical). Note that the A-gauge was aligned with the positive horizontal beam axis at its geometric centerline. Second, rosette no. 2 (right-front position facing front) provided nearly zero strain for two gauges (C – horizontal and A – vertical). Note that the C-gauge was aligned with the negative horizontal axis. Further, the diagonal gauge provided negative compressive strain along the 135 degree plane rotated away from the positive x or horizontal beam axis on front face. Third, rosette no. 3 (left-back position facing back) provided data for only two gauges (A – horizontal and B – diagonal). Note that the A-gauge was aligned with the positive horizontal beam axis at its geometric centerline for the back face. The A-gauge (horizontal) provided nearly zero strain, while the B-gauge (diagonal) provided negative compressive strain along the 45-degree plane rotated away from the positive x or horizontal beam axis on back face. Finally, rosette no. 4 (right-back position facing back)

provided nearly zero strain for two gauges (C – horizontal and A – vertical). Note that the C-gauge was aligned with the negative horizontal axis. Further, the diagonal gauge provided negative compressive strain along the 135 degree plane rotated away from the positive x or horizontal beam axis on back face.

The vertical and horizontal strains, gauges A and C, should be near zero for this beam configuration with 18-in. (457-mm) span, as the horizontal gage was placed along the neutral axis of the beam. All A and C gauges were near zero. Data for gauge 3C was not obtained due to a problematic Vishay channel that was later replaced. Therefore, a full-strain field analysis was not completed for rosette no. 3. As such, a rosette strain gauge analysis using gauge 2A through 2C was expected to yield favorable results. With strain rosettes 1 and 4, some questions arose regarding validity of data. To start, all strain readings for gauge 1 were zero, which was not expected, especially for diagonal gauge 1B. Next, gauge 4B produced a very high compression strain as compared to gauges 2B and 3B. Thus, less confidence existed with results produced with gauges 1 and 4. The maximum strain readings are provided in Table 34, and strain versus time is shown graphically in Figure 144 and Figure 145.

Maximum principal and maximum shear strains are summarized in Table 34 for gauges 2 and 4 rosettes which had all three gauges acquire data that was deemed reasonable. Values ranged from 4.04×10^{-5} in./in. to 8.64×10^{-5} in./in. for the maximum principal strain, ϵ_1 . Values for the minimum principal strain, ϵ_2 , ranged from -2.70×10^{-6} in./in. to -8.94×10^{-5} in./in. The highest maximum shear strain for test no. CFS-1 was 1.76×10^{-4} in./in. Subsequently, Equation 32 and Equation 36 were used to compute the theoretical maximum shear stress and maximum shear strain of 135.9 psi (0.9 MPa) and

6.72×10^{-5} in./in., respectively. Rosette no. 2 provided a very good match, while gauge 4 did not provide a very good match. The maximum and minimum principal strains and shear strain from rosette nos. 2 and 4 are shown in Figure 146.

Principal angles are summarized in Figure 147 for rosette gauges 2 and 4. Based on the orientation described previously, it would be expected that gauges 2 and 4 would return a principal angle θ_{p1} near 135 degrees. This finding was confirmed based on the plot, as the principal angles for gauges 2 and 4 are shown as a constant value between 130 and 140 degrees. The second principal angle, θ_{p2} , was then near 45 degrees, as the values were constant between 40 and 50 degrees. Based on these angles, the associated shear angles would be 180 and 90 degrees, which would be anticipated based on a simple shear stress block located at the centerline of the beam, or neutral axis for this case.

Maximum principal stresses are summarized in Table 34 for rosettes that had all three gauges acquire data that was deemed reasonable. These values were calculated using Equation 30. Values ranged from 138.9 psi (1.0 MPa) to 271.2 psi (1.9 MPa) for the maximum principal stress, σ_1 . Subsequently, these values were compared to the known maximum tensile strength from CFT testing, 407.0 psi (2.8 MPa).

Based on the analysis provided above, it appears that only rosette nos. 2 and 4 were providing reliable data for full-strain field analysis. Rosette no. 1 had a very low maximum shear stress, and the strain in the diagonal gauge was nearly zero. Rosette no. 3 could not be analyzed because of the missing data for gauge C, although the other two channels (A and B) revealed reasonable data. However the remaining two gauges can be used for front/back comparison with Rosette no. 2.

The final piece of instrumentation was the string potentiometers. Following testing, questions arose regarding the accuracy of the resulting displacement data after comparison to displacements determined with Equation 20 and Equation 21, as well as the actuator movement over the same period. The theoretical equations tended to provide lower displacements than measured, while the actuator displacement data was generally higher than measured with the string potentiometer. It was somewhat difficult to determine which string potentiometers had results that may have inaccuracies due to instrumentation placement, data resolution, etc. could be trusted. As such, the displacement data and results are not included in this section. String potentiometer and actuator data are found in Appendix D.

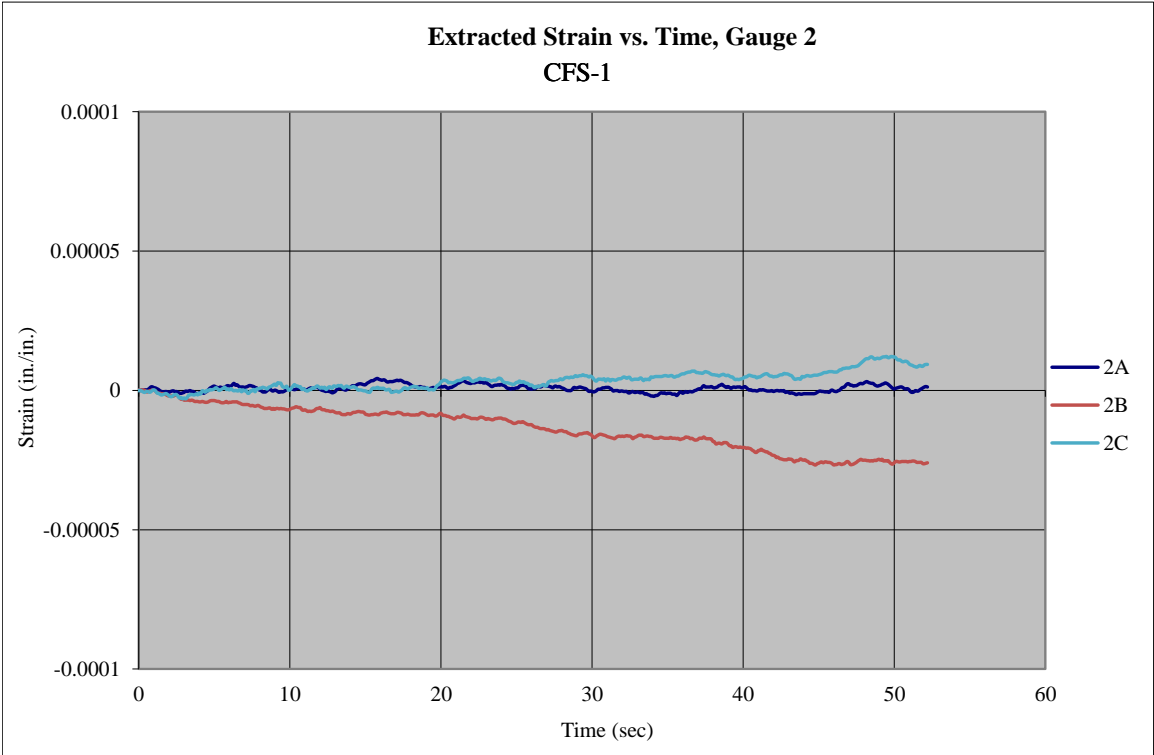
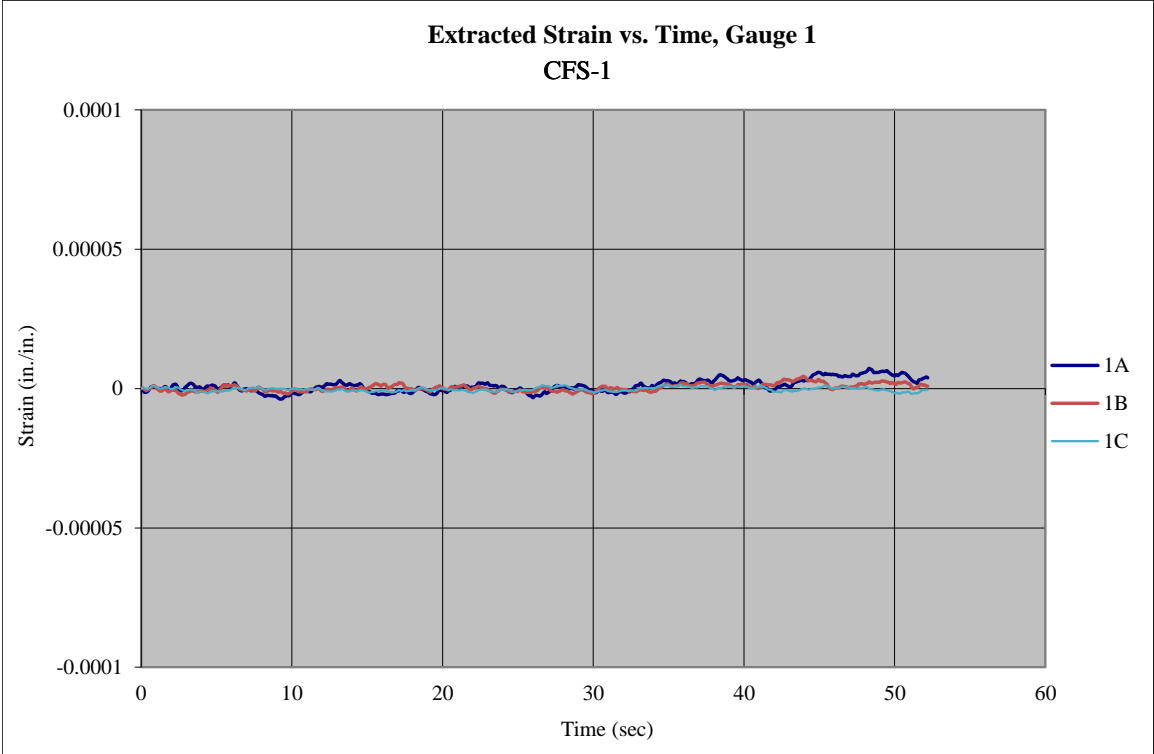


Figure 144. Extracted Strain Plots for Rosette Strain Gauges 1 and 2, Test No. CFS-1 [18-in. (457-mm) Span]

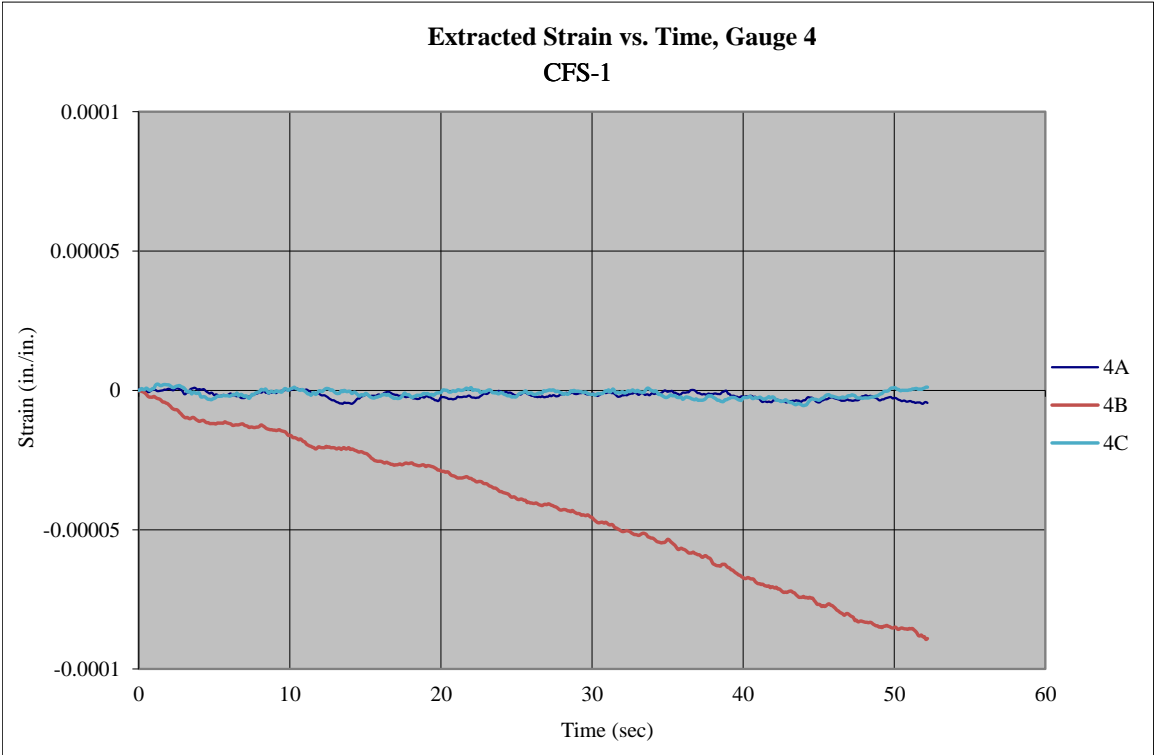
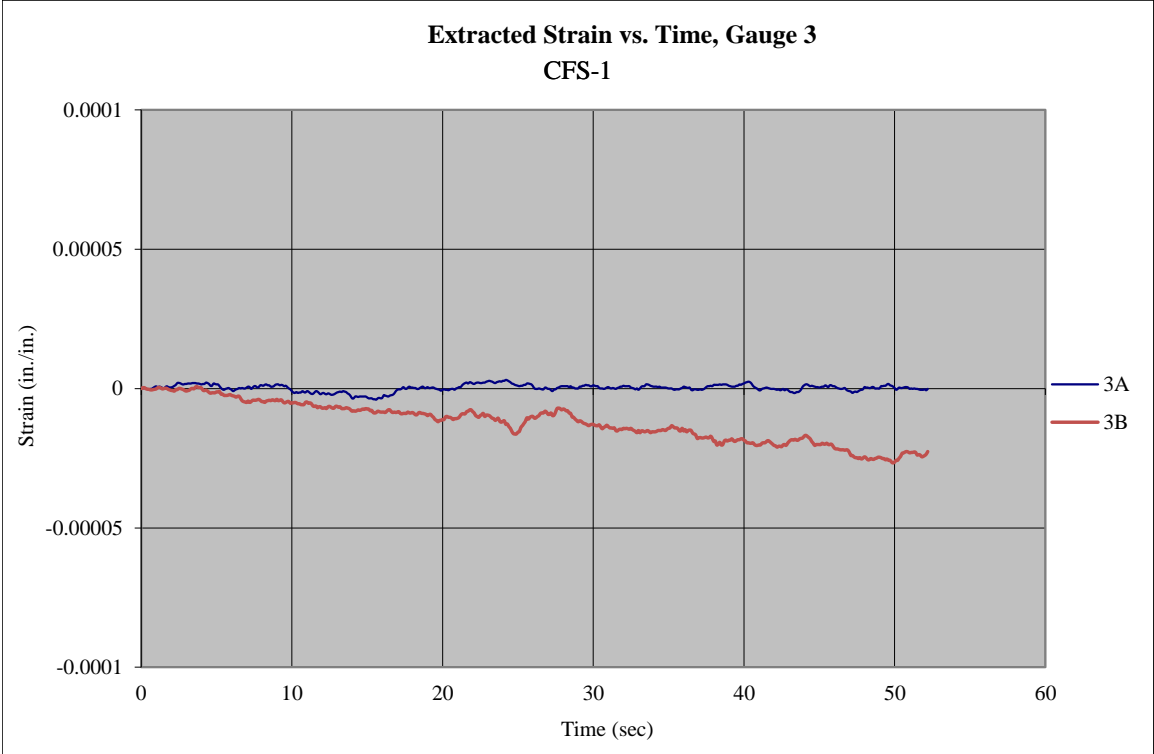


Figure 145. Extracted Strain Plots for Rosette Strain Gauges 3 and 4, Test No. CFS-1 [18-in. (457-mm) Span]

Table 34. Summary of Stress and Strains for Rosette Gauges, Test No. CFS-1

Rosette Gauge	Normal Strain, ϵ_x , @ Failure <i>in./in.</i>	Estimated Max./Min. Principal Strain (Eqs. 27 & 28)		Estimated Max./Min. Principal Stress (Eqs. 30 & 31)		Estimated γ_{max} (Eq. 29) <i>in./in.</i>	Estimated τ_{max} (Eq. 32) <i>psi</i>	Estimated τ_{max} (Eq. 37) <i>psi</i>	Estimated Principal Angles, θ_{1p} & θ_{2p} (Eq. 34 & 35) <i>degrees</i>	Estimated Shear Angles, θ_{1s} & θ_{2s} (Eq. 36) <i>degrees</i>
		ϵ_1 <i>in./in.</i>	ϵ_2 <i>in./in.</i>	σ_1 <i>psi</i>	σ_2 <i>psi</i>					
1	1A	3.85E-06	-	-	-	-	-	-	-	-
	1B	8.71E-07	-	-	-	-	-	-	-	-
	1C	-4.01E-07	-	-	-	-	-	-	-	-
2	2A	1.22E-06	-2.70E-05	138.9	-82.1	6.69E-05	106.0	135.9	135, 45	180, 90
	2B	-2.60E-05	-2.70E-05	138.9	-82.1	6.69E-05	106.0	135.9	135, 45	180, 90
	2C	9.30E-06	-2.70E-05	138.9	-82.1	6.69E-05	106.0	135.9	135, 45	180, 90
3	3A	-1.15E-07	-	-	-	-	-	-	-	-
	3B	-2.26E-05	-	-	-	-	-	-	-	-
4	4A	-4.51E-06	-8.94E-05	271.2	-285.4	1.76E-04	278.3	135.9	135, 45	180, 90
	4B	-8.91E-05	-8.94E-05	271.2	-285.4	1.76E-04	278.3	135.9	135, 45	180, 90
	4C	1.14E-06	-8.94E-05	271.2	-285.4	1.76E-04	278.3	135.9	135, 45	180, 90

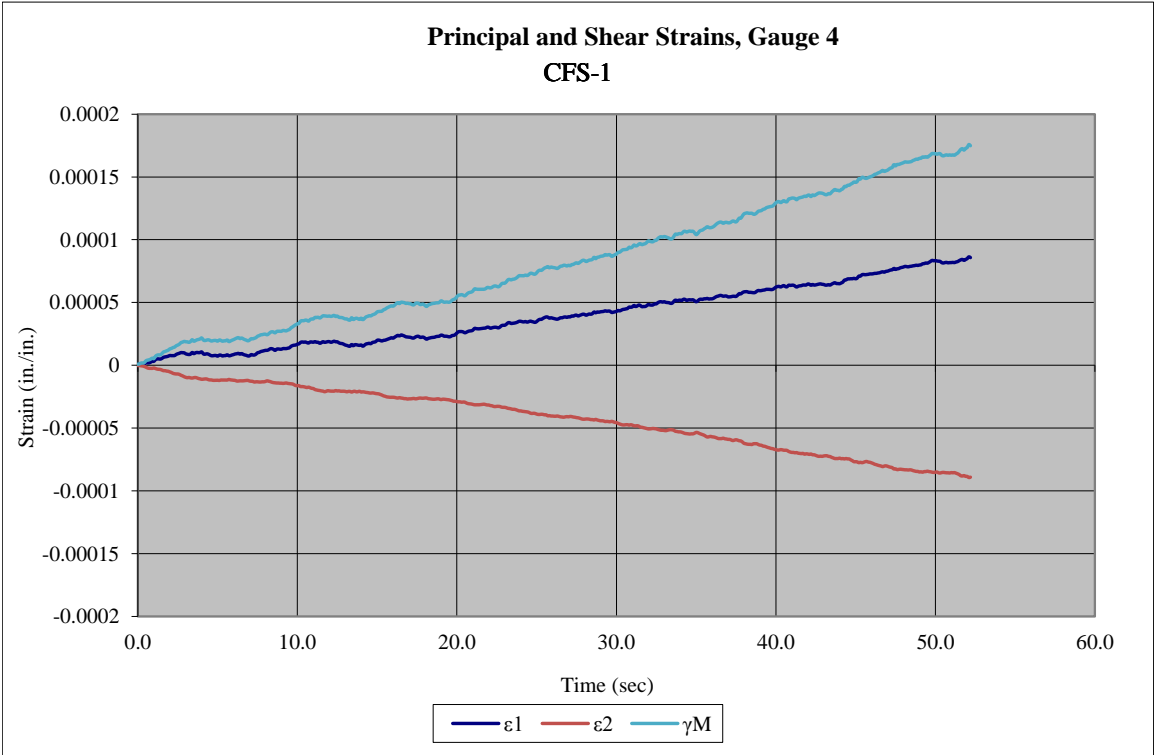
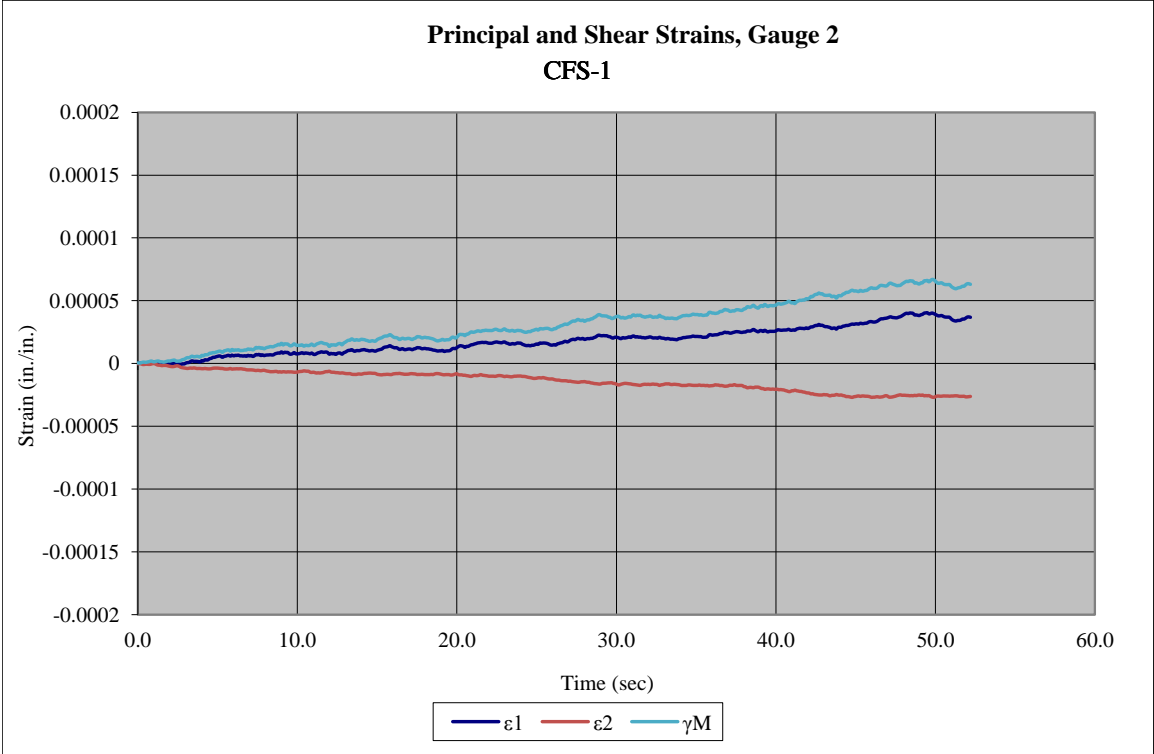


Figure 146. Principal Strains for Test No. CFS-1 [18-in. (457-mm) Span]

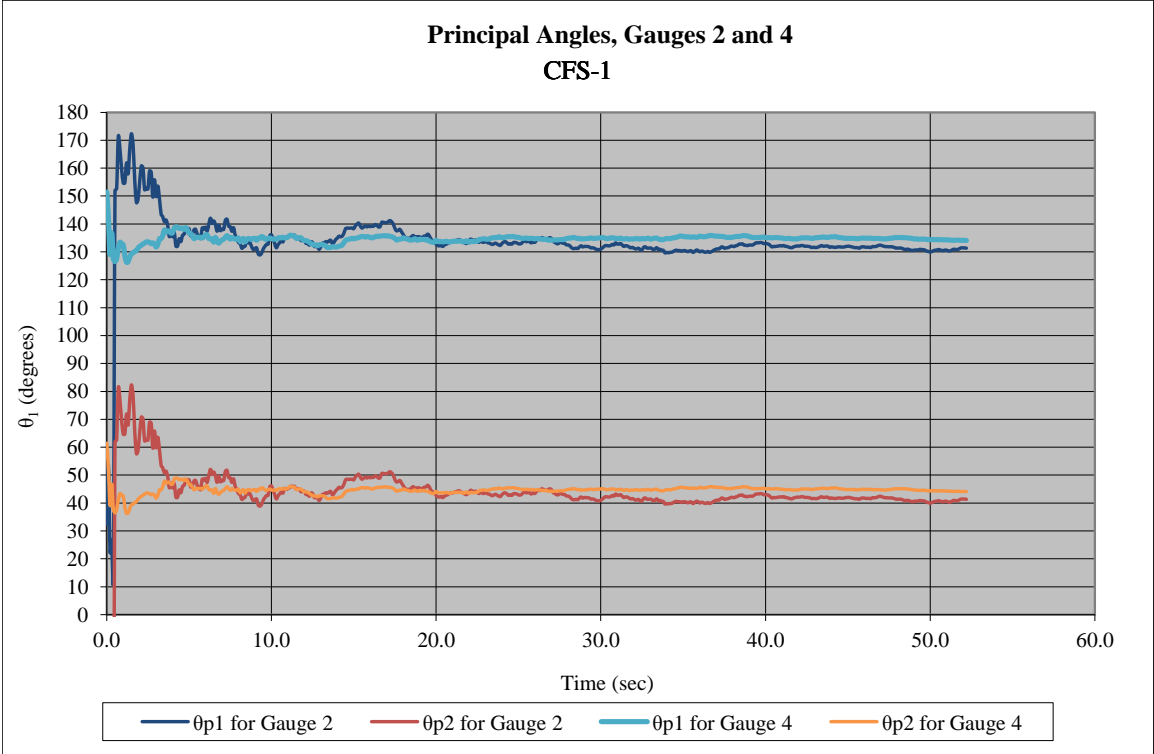


Figure 147. Principal Angles for Test No. CFS-1 [18-in. (457-mm) Span]

12.4 Test No. CFS-2 [Support Span – 12 in. (305 mm)]

For test no. CFS-2, a span length of 12 in. (305 mm) was used. It was uncertain whether a flexural or shear failure would occur with this configuration. The test setup is shown in Figure 148.

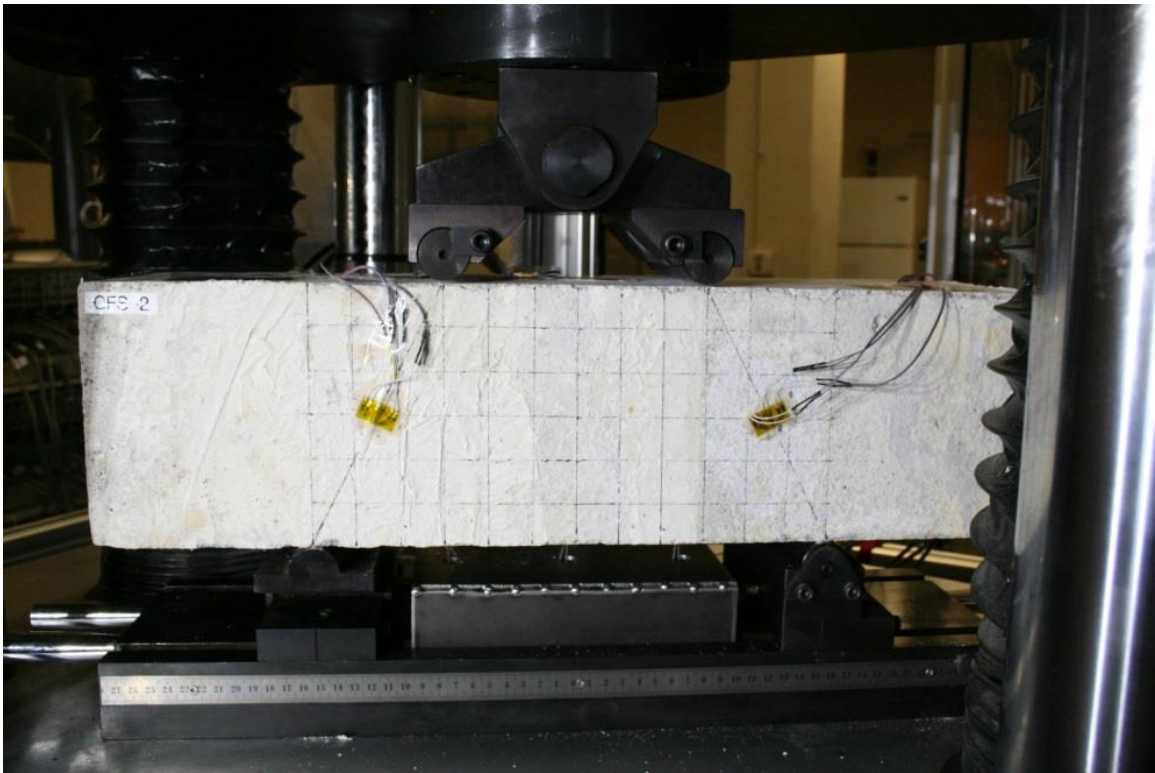


Figure 148. Test Setup for Test No. CFS-2 [12-in. (305-mm) Span]

As the MTS Criterion testing machine loaded the specimen during test no. CFS-2, the specimen failed in flexure due to excessive tensile stresses at the midspan of the bottom surface. Specifically, the vertical fracture plane occurred approximately 0.5 in. (13 mm) away from the centerline of the beam. A peak load of 14.3 kip (63.6 kN) was measured when the specimen fractured. Thus, each upper roller was assumed to transfer a peak load equal to 7.2 kip (32.0 kN) to the top of the beam, thus resulting in a reaction at

both lower supports equal to 7.2 kip (32.0 kN). The load versus time plot is shown in Figure 149, and post-test photographs are shown in Figure 150 and Figure 151.

All horizontal strain gauges that were placed at the vertical centerline of the beam appeared to have acquired data during test no. CFS-2. In addition, all horizontal strain gauges between rollers broke as the flexural failure occurred at the vertical centerline of the beam. The strain readings revealed maximum negative (compression) and maximum positive (tension) normal strains of -6.52×10^{-5} in./in. (top) and 1.35×10^{-4} in./in. (bottom), respectively, as shown in Table 35 and Figure 152. Horizontal normal strains appeared to be larger in the bottom half of the beam, creating a non-linear strain distribution. In addition, the strains at gauges D and E were nearly equal. As depicted in Figure 153, normal strains were plotted in the direction of the horizontal beam axis for each vertical gauge position [0 in. (beam centerline), $\pm 2\frac{1}{4}$ in. (57 mm) (upper and lower side gauges), and ± 3 in. (76 mm) (top and bottom gauges)]. Finally, the middle strain gauge revealed strains which largely oscillated around zero for the duration of the test. Based on the measured difference between the top and bottom gauges, the horizontal strain readings raised some concerns.

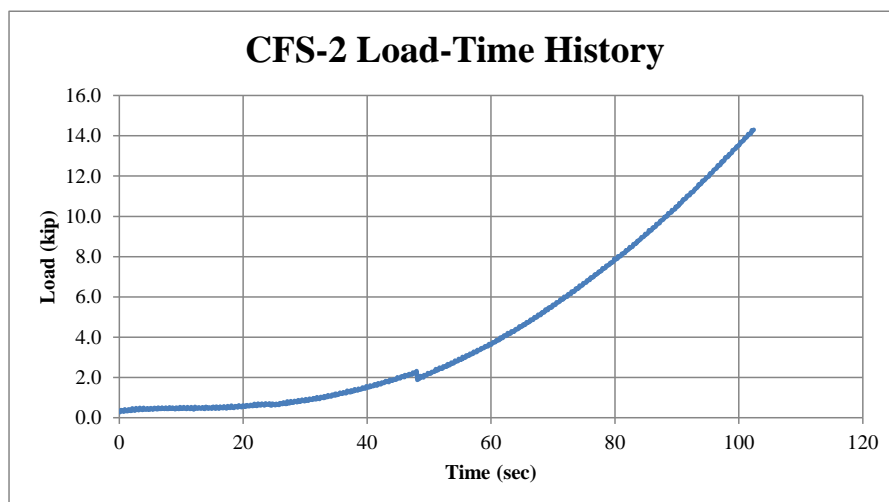


Figure 149. Load vs. Time, Test No. CFS-2 [12-in. (305-mm) Span]

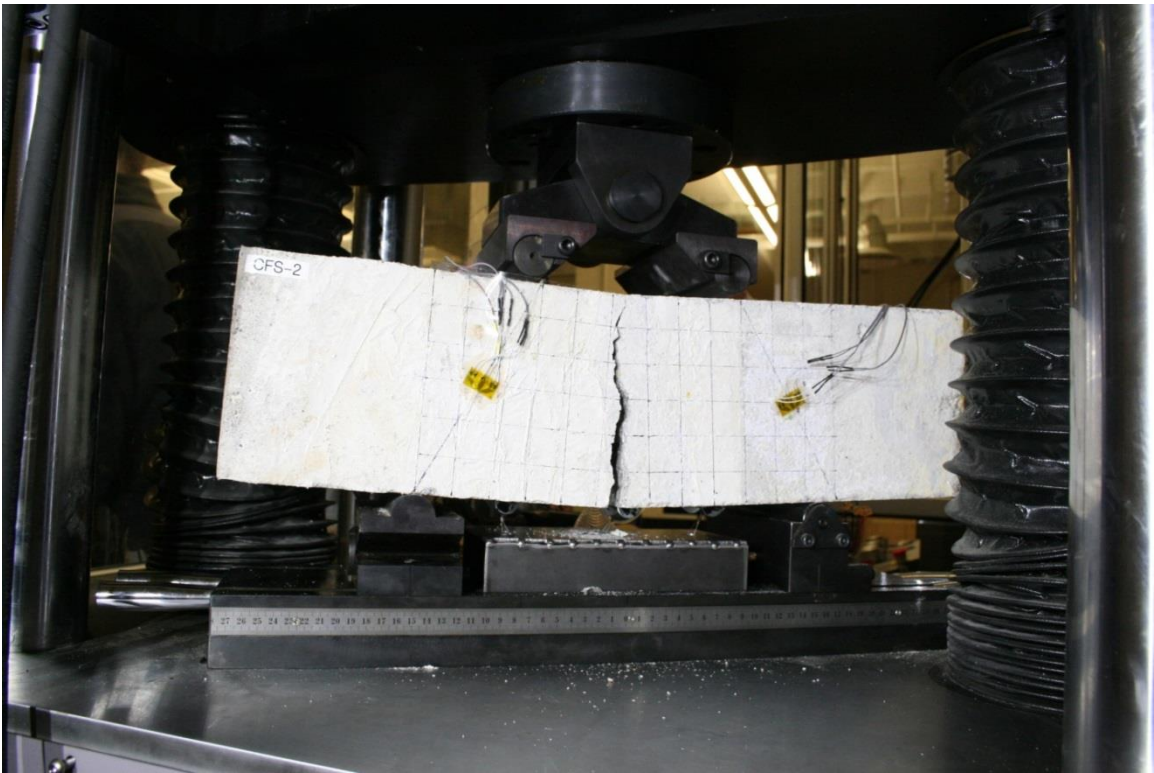
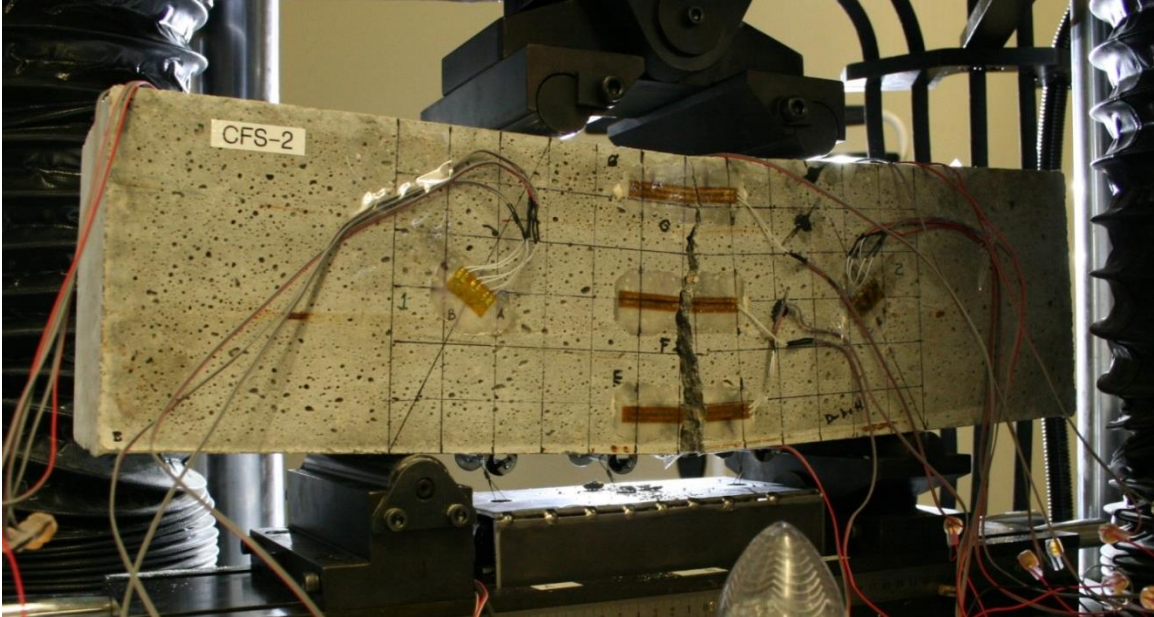


Figure 150. Post-Test Damage, Test No. CFS-2 [12-in. (305-mm) Span]

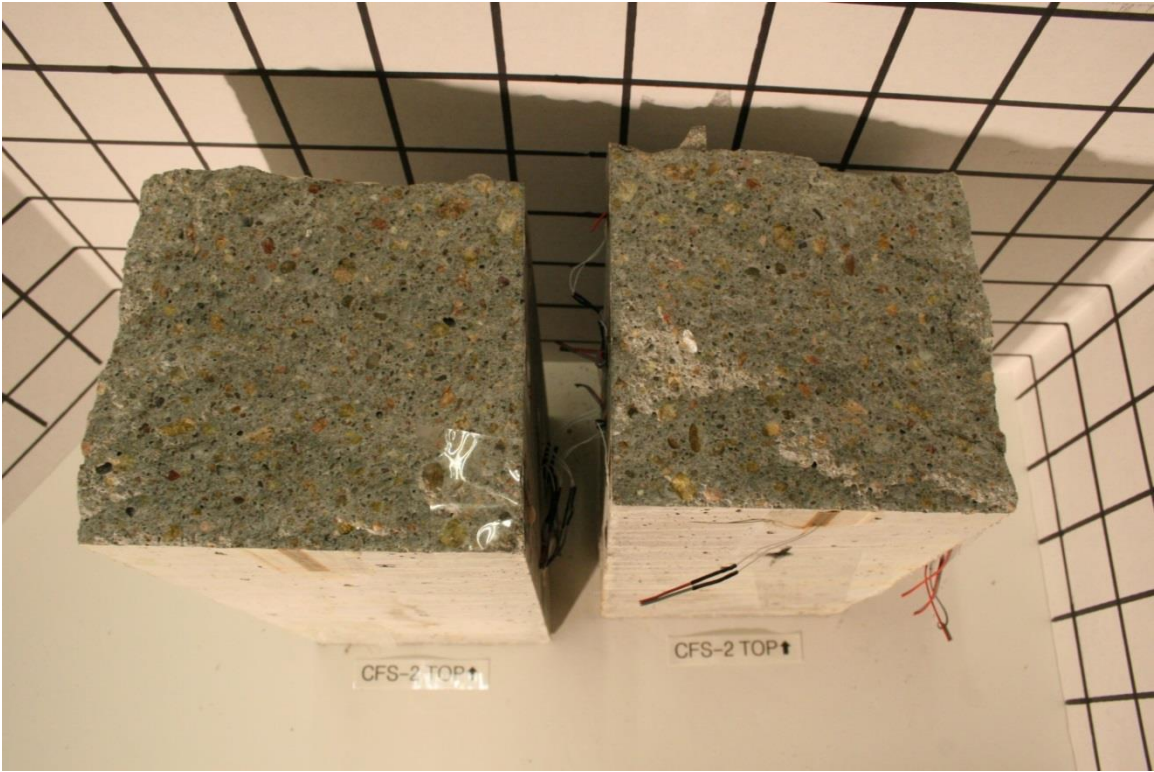
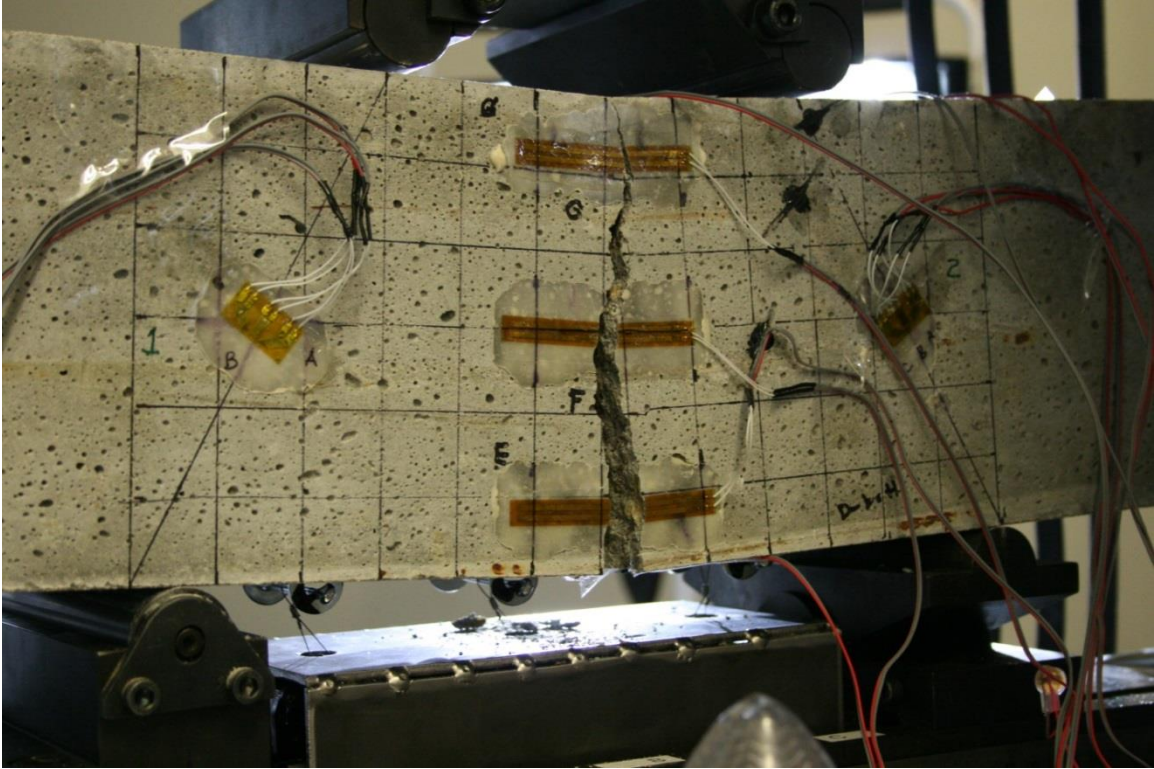


Figure 151. Additional Post-Test Damage, Test No. CFS-2 [12-in. (305-mm) Span]

Table 35. Normal Strain and Stress Distribution for Horizontal Gauges, Test No. CFS-2

Gauge Designation and Location	Normal Strain, ϵ_x, @ Failure <i>in./in.</i>	Estimated Maximum Normal Stress (Eq. 22) <i>psi</i>	Estimated Maximum Normal Stress (Eq. 23) <i>psi</i>
D (bottom)	1.35E-04	649.3	595.6
E	1.32E-04	636.9	446.7
F (middle)	8.60E-07	4.1	0.0
G	-5.68E-05	-273.7	-446.7
H (top)	-6.52E-05	-314.0	-595.6

Once the normal strains were processed, analyzed, and reviewed, an estimate was made to determine the maximum normal stress, $\sigma_{x,max}$, based on measured strains using Equation 22. The normal stress distribution was also estimated using strain readings at the upper and lower side positions. The maximum normal stress for each strain gauge is shown in Table 35, while the normal stress for four gauges as a function of time is provided in Figure 154 and Figure 155. An estimate was also made to determine the maximum normal stress, $\sigma_{bending,max}$, using the MTS load data and Equation 23. The maximum normal stress based on MTS load data and elastic bending is depicted in Table 35 for the top and bottom surfaces. Further, the normal stress corresponding to the other gauge locations was also calculated with MTS load data and provided in Table 35. The normal stress as a function of time and using MTS load data is shown graphically in Figure 154 and Figure 155. When comparing the normal stresses using the two methods, it is apparent that similar trends were not predicted during the test duration. The estimated normal stress based on MTS load data exceeded the prediction using the strain readings for the bottom two gauges but not for the top two gauges. The maximum midspan normal stress was ± 595.6 psi (4.1 MPa) for the MTS load data and calculated

moments, while the maximum midspan normal stresses were +649.3 psi/-314.0 psi (+4.5 MPa/-2.2 MPa) using the strain data. More investigation is needed to explore these differences, including any assumptions and limitations.

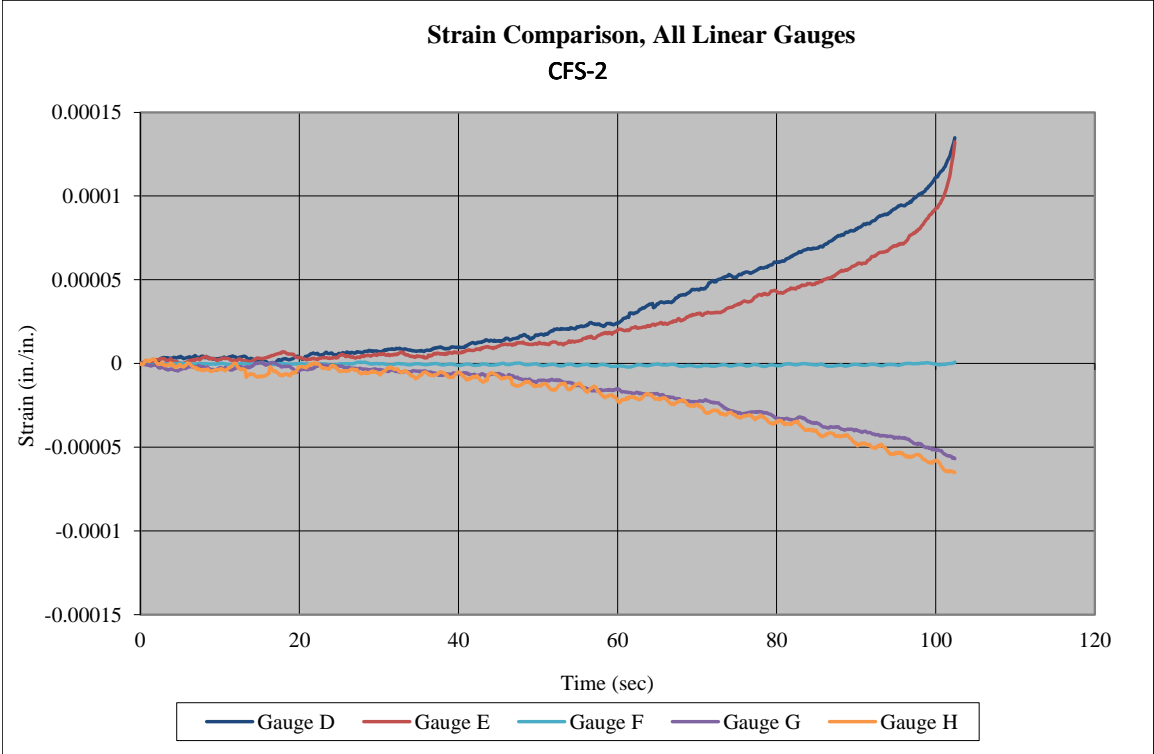


Figure 152. Normal Strains for Top, Side, and Bottom Gauges, Test No. CFS-2 [12-in. (305-mm) Span]

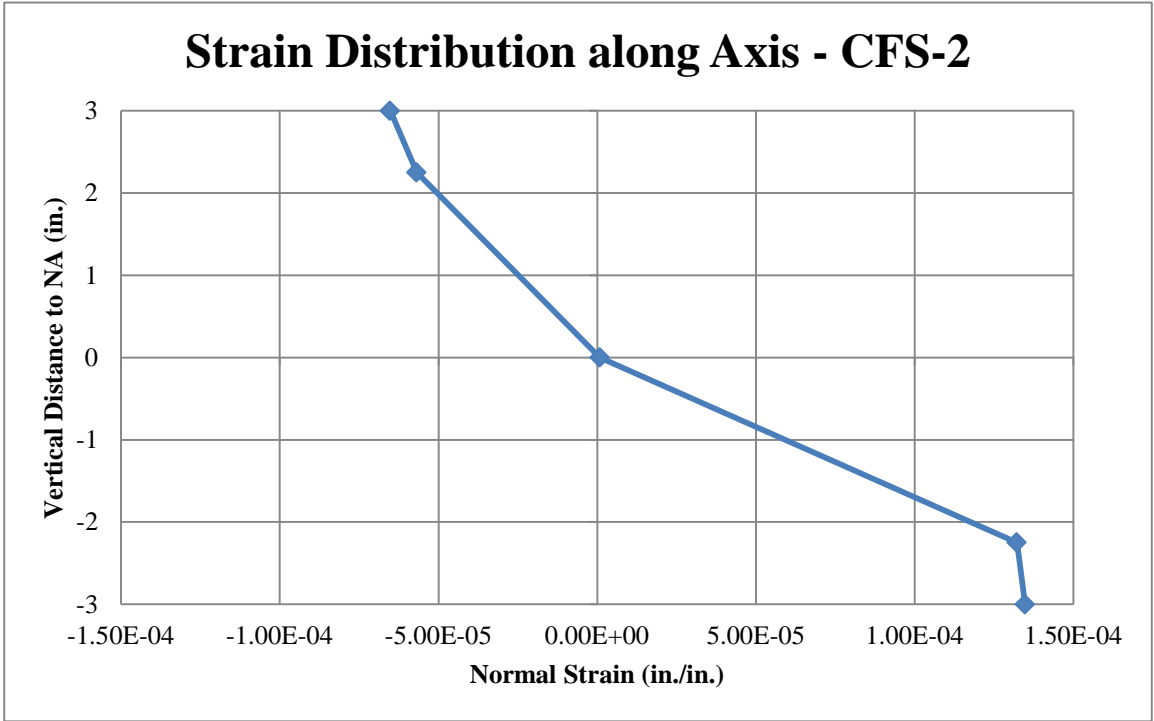


Figure 153. Vertical Distance versus Normal Strain, Test No. CFS-2 [12-in. (305-mm) Span]

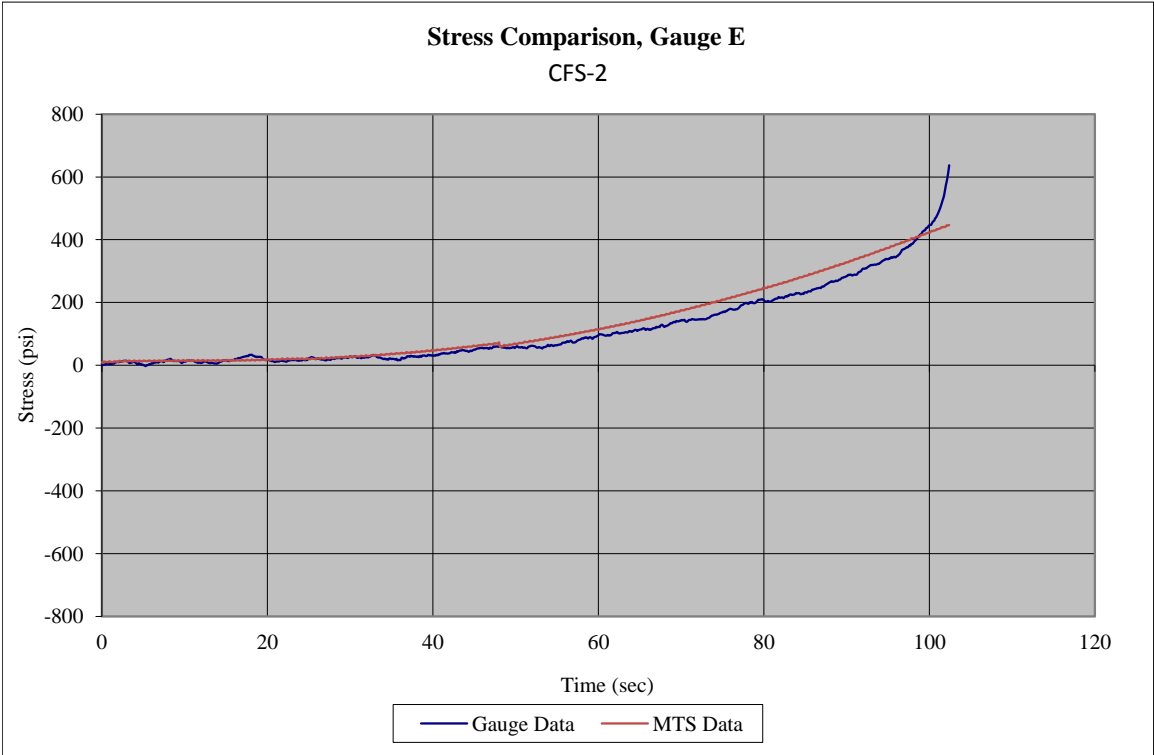
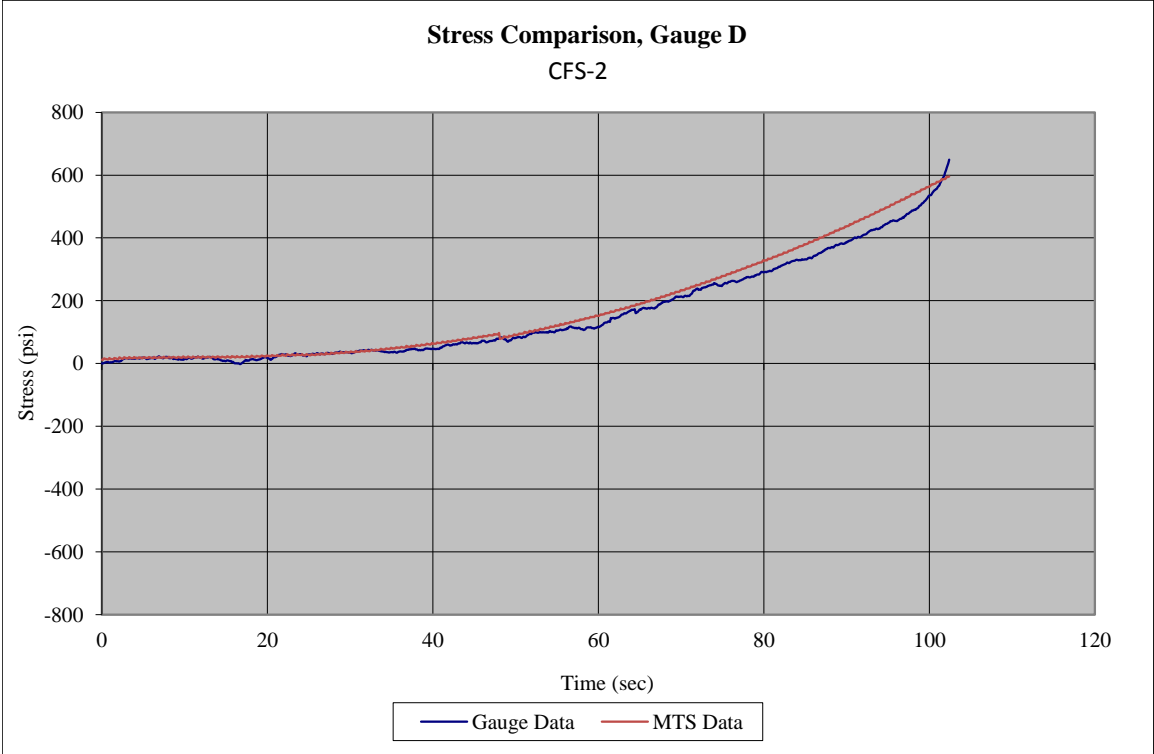


Figure 154. Estimated Midspan Normal Stresses from Bottom Strain Gauges and MTS Load Data, Test No. CFS-2 [12-in. (305-mm) Span]

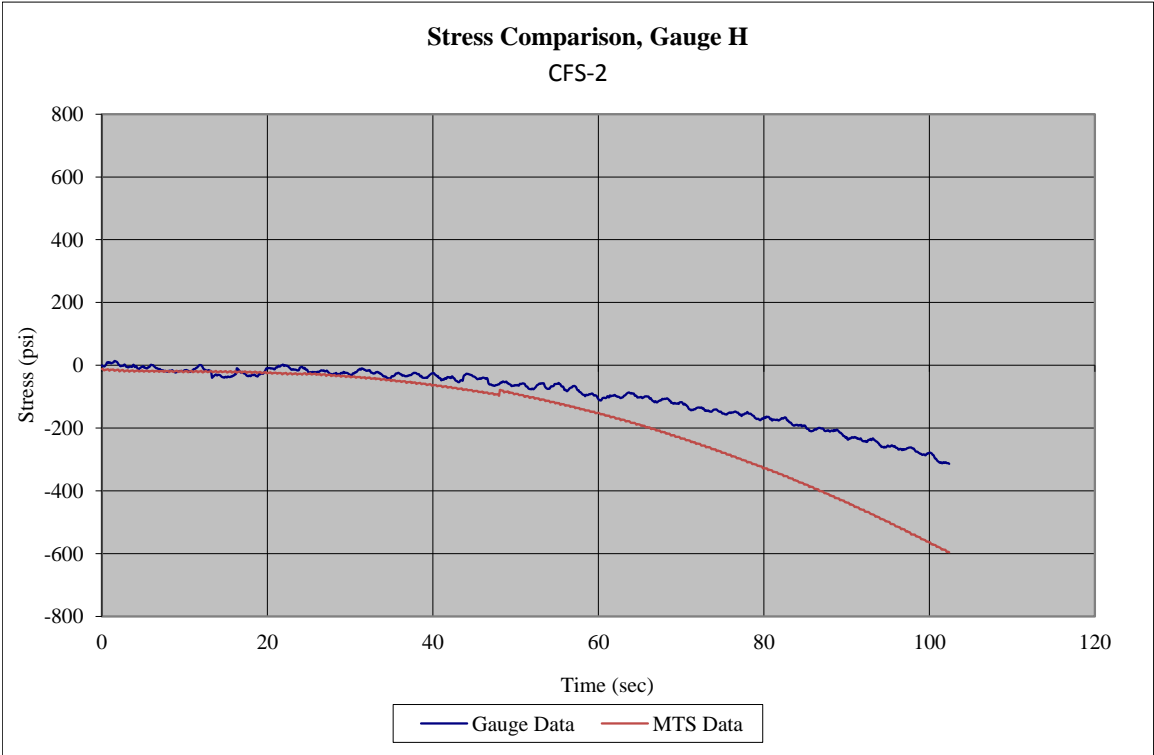
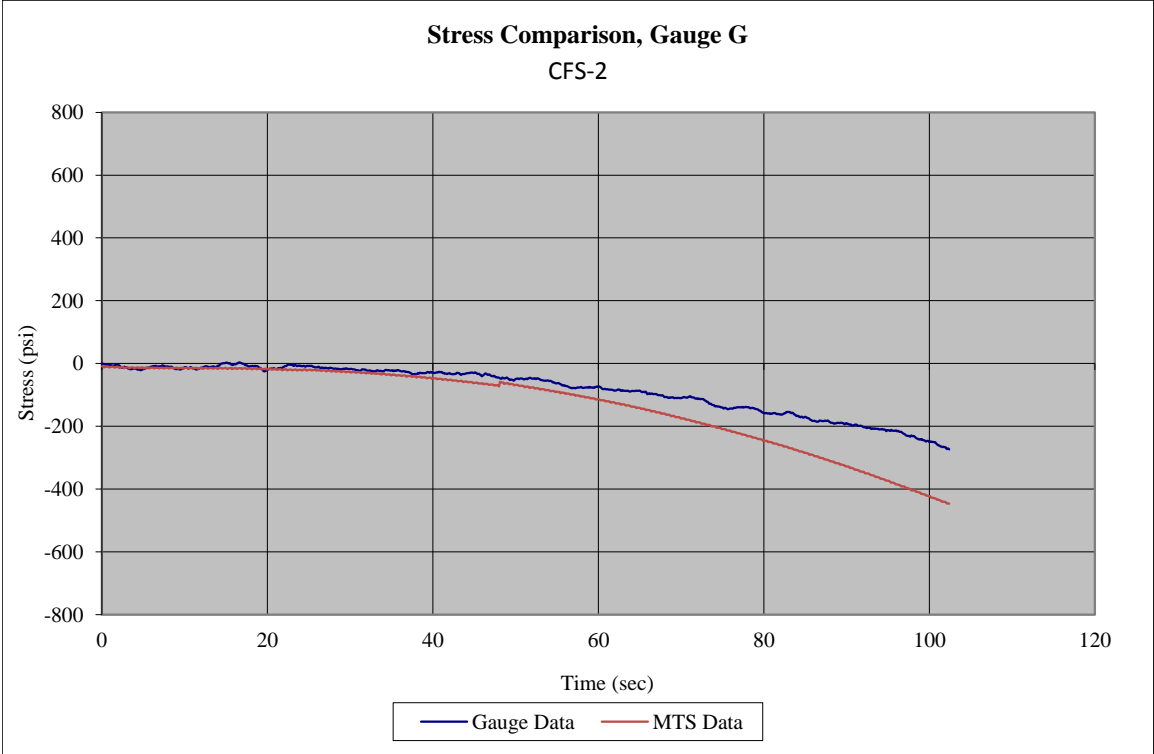


Figure 155. Estimated Midspan Normal Stresses from Top Strain Gauges and MTS Load Data, Test No. CFS-2 [12-in. (305-mm) Span]

Four rosette strain gauges were attached to the front and back faces of the beam 18 degrees counterclockwise (1 and 3) and 18 degrees clockwise (2 and 4) from the horizontal centerline due to installation error. Note that the axis in this test was different from all other flexure and shear tests. In addition, no rosette strain gauges between the lower support and upper roller broke as the flexural failure occurred away from the rosette strain gauges. Measured strains are provided in Figure 156 and Figure 157 for each rosette and each individual gauge, if acquired. Some rosette strain gauges appeared to perform in an acceptable manner during test no. CFS-2. However, some gauges provided data that may raise questions upon first glance. Based on symmetric loading, the strains may initially be expected to be very similar across all rosettes. However, this outcome did not appear to always be the case.

First, rosette no. 1 (left-front position facing front) provided nearly zero strain for only one gauge (A – 18 degrees counterclockwise from the horizontal axis). Note that the A-gauge was aligned 18 degrees counterclockwise from the positive horizontal beam axis at its geometric centerline. The remaining two gauges, B (diagonal) and C (18 degrees counterclockwise from the vertical beam axis), provided negative compressive strain. Second, rosette no. 2 (right-front position facing front) provided data for only two gauges (C – 18 degrees clockwise from the negative horizontal axis and A – 18 degrees clockwise from the positive vertical axis). Note that the C-gauge was aligned 18 degrees clockwise from the negative horizontal axis. Further, the rotated-vertical gauge provided negative compressive strain along the 117 degree plane rotated away from the adjusted positive x or 18 degrees counterclockwise from the horizontal beam axis on front face. Third, rosette no. 3 (left-back position facing back) provided data for only two gauges (A

– 18 degrees counterclockwise from the horizontal beam axis and B – diagonal). Note that the A-gauge was aligned 18 degrees counterclockwise from the positive horizontal beam axis at its geometric centerline for the back face. The B-gauge (diagonal) provided nearly zero strain, while the A-gauge (18 degrees counterclockwise from the horizontal beam axis) provided negative compressive strain along the 63 degree plane rotated away from the adjusted positive x or 18 degrees counterclockwise from the horizontal beam axis on back face. Finally, rosette no. 4 (right-back position facing back) provided nearly zero strain for two gauges (C – 18 degrees counterclockwise from the horizontal beam axis and B – diagonal). Note that the C-gauge was aligned 18 degrees counterclockwise from the negative horizontal axis. Further, the vertical gauge , A, provided negative compressive strain along the 153 degree plane rotated away from the adjusted positive x or 18 degrees counterclockwise from the horizontal beam axis on back face.

Even with the rotation of the rosette axes, none of the B gauges should provide failure strains for this beam configuration with the 12-in. (305-mm) span. However, some of the gauges were near zero. Gauges 3B and 4B produced nearly zero strain. Data for gauges 2B and 3C was not obtained due to a problematic Vishay channel that was later replaced. Therefore, a full-strain field analysis was not completed for rosette nos. 2, 3, and 4. The maximum strain readings are provided in Table 36, and strain versus time is shown graphically in Figure 156 and Figure 157.

Based on the analysis provided above, it appears that only rosette no. 1 was providing reliable data for full-strain field analysis. Rosette nos. 2, 3, and 4 could not be analyzed for full-strain field due to missing and/or inaccurate data for gauges B and/or C. Rosette no. 4 also had zero strains in selected gauges.

Maximum principal and maximum shear strains are summarized in Table 36 for rosette gauge 1 which had all three gauges acquire data. The value of 9.06×10^{-5} in./in. was found for the maximum principal strain, ϵ_1 . The value for the minimum principal strain, ϵ_2 , -1.32×10^{-4} in./in. The maximum shear strain for test no. CFS-2 was 2.22×10^{-4} in./in. Subsequently, Equation 32 and Equation 36 were used to compute the theoretical maximum shear stress and maximum shear strain of 335.3 psi (2.3 MPa) and 1.66×10^{-4} in./in., respectively.

Principal angles are summarized in Figure 158 for rosettes that had all three gauges acquire and return adequate data. Based on the orientation described previously, it would be expected that gauge 1 would return a principal angle θ_{p1} slightly larger than 45 degrees due to support changes. Based on the plot, the principal angle for gauge 1 is shown as a constant value near 50 degrees. The second principal angle, θ_{p2} , was near 140 degrees. Based on these angles, the associated shear angles would be 95 and 5 degrees.

Maximum principal stresses are summarized in Table 36 for rosettes that had all three gauges acquire data. These values were calculated using Equation 30. The value was 256.3 psi (1.8 MPa) for the maximum principal stress, σ_1 . Subsequently, the value was compared to the known maximum tensile strength from CFT testing, 407.0 psi (2.8 MPa).

The final piece of instrumentation was the string potentiometers. Similar to test no. CFS-1, questions arose regarding the accuracy of the resulting displacement data after comparison to displacements determined with Equation 20 and Equation 21, as well as the actuator movement over the same period. The theoretical equations tended to provide lower displacements than measured, while the actuator displacement data was generally

higher than measured with the string potentiometer. It was somewhat difficult to determine which string potentiometers had results that may have inaccuracies due to instrumentation placement, data resolution, etc. could be trusted. As such, the displacement data and results are not included in this section. String potentiometer and actuator data are found in Appendix D.

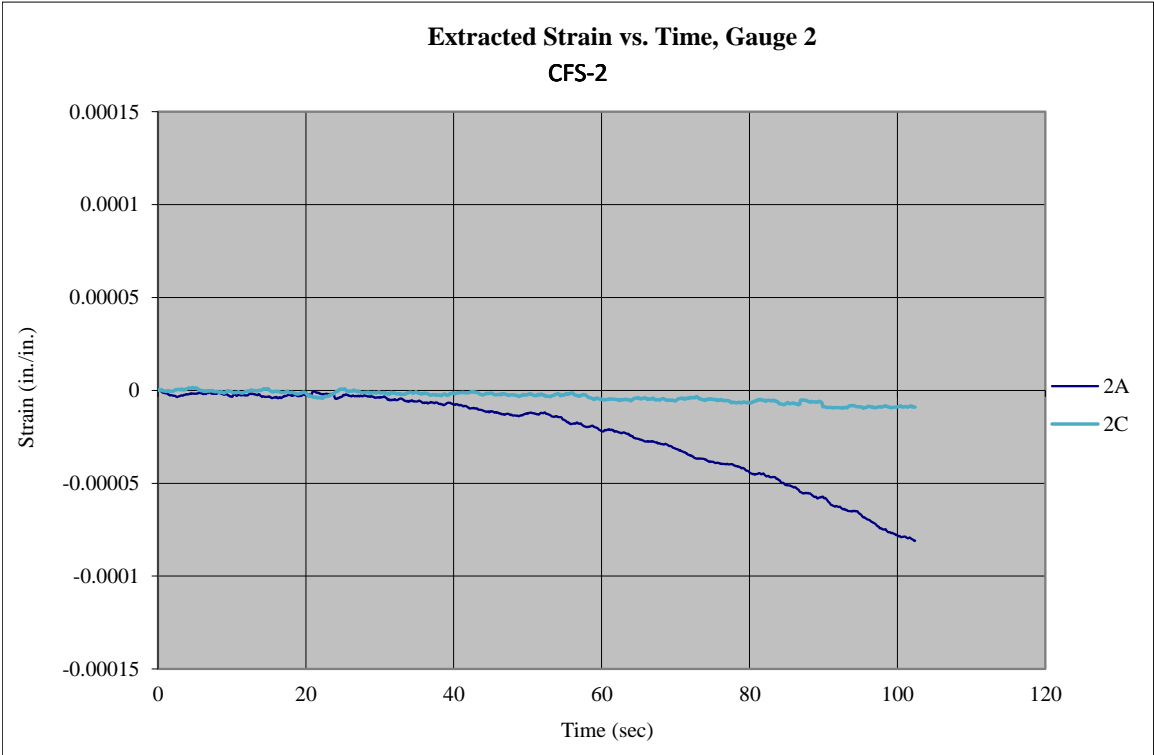
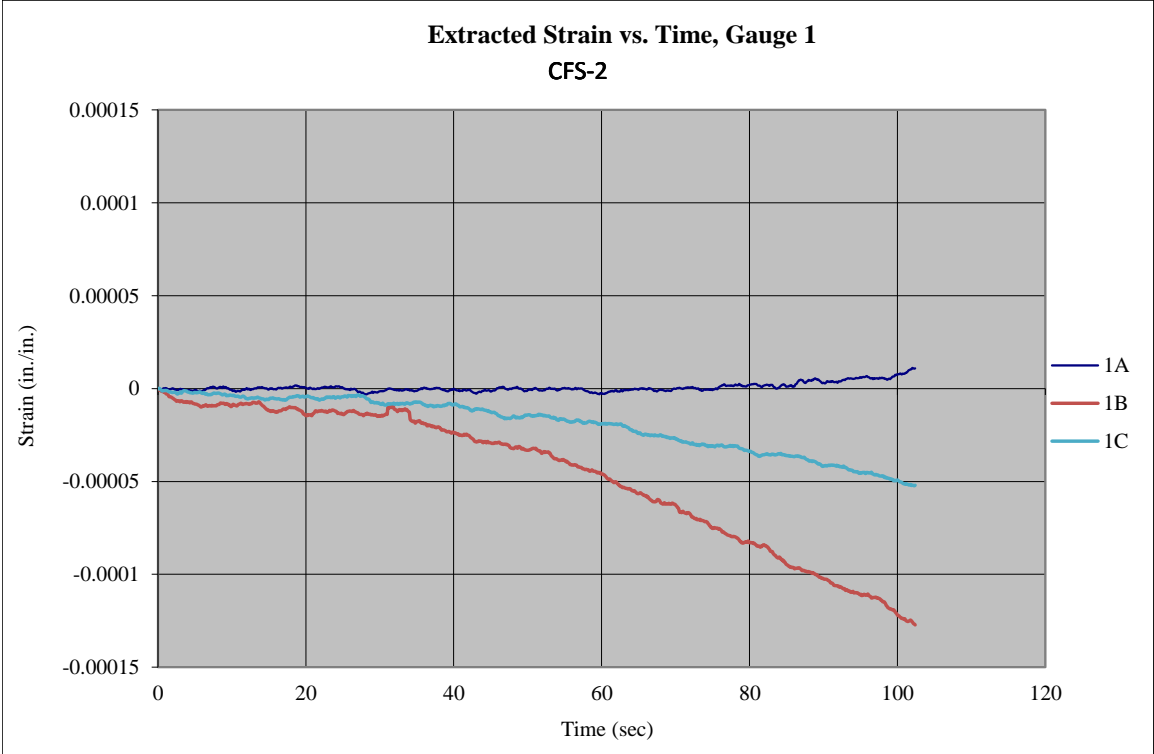


Figure 156. Extracted Strain Plots for Rosette Strain Gauges 1 and 2, Test No. CFS-2 [12-in. (305-mm) Span]

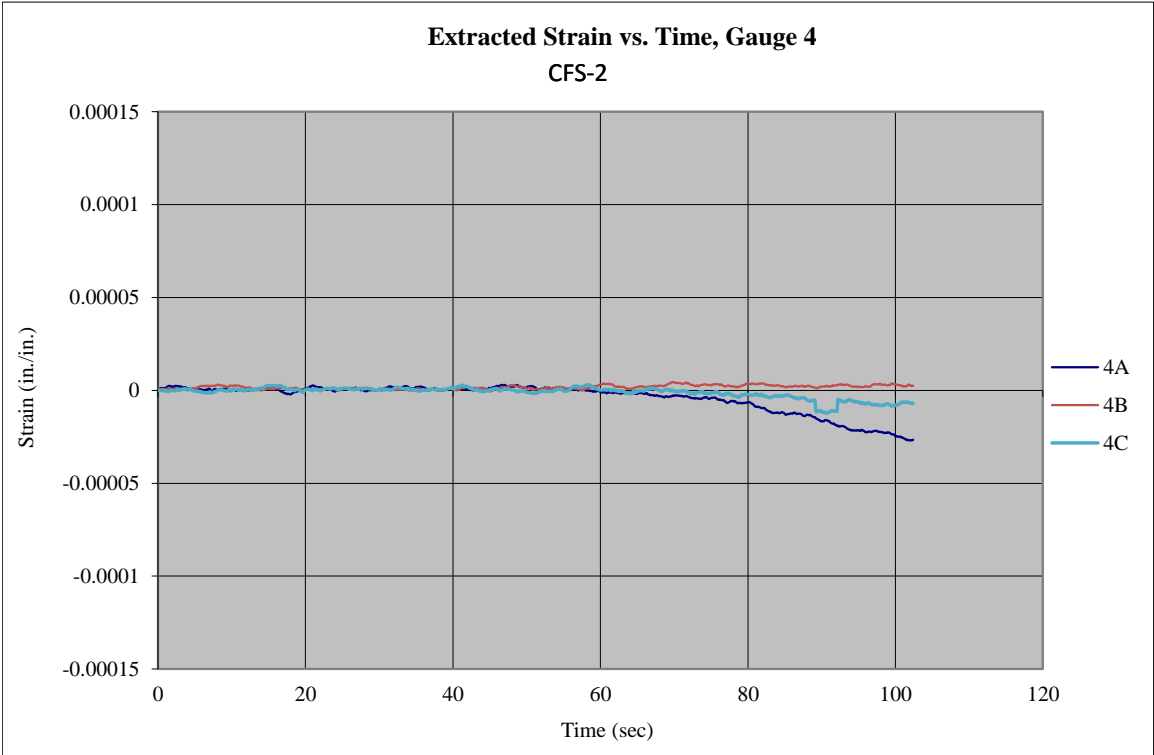
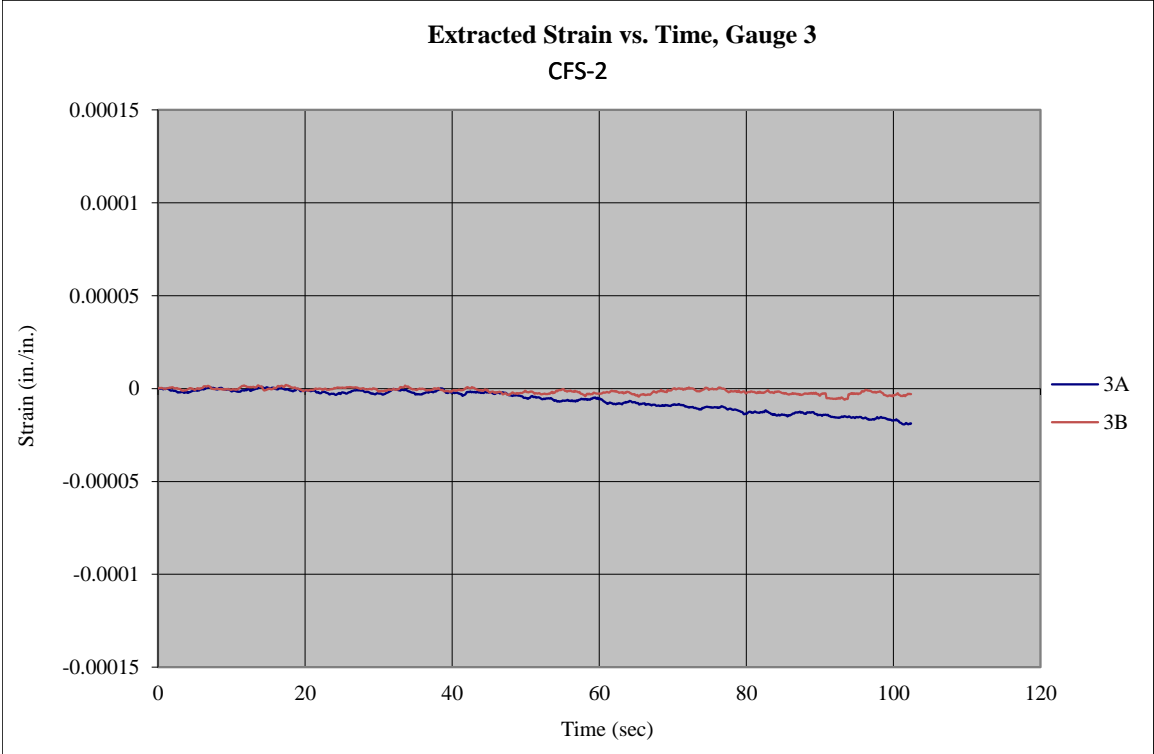


Figure 157. Extracted Strain Plots for Rosette Strain Gauges 3 and 4, Test No. CFS-2 [12-in. (305-mm) Span]

Table 36. Summary of Stress and Strains for Rosette Gauges, Test No. CFS-2

Rosette Gauge	Normal Strain, ϵ_x , @ Failure <i>in./in.</i>	Estimated Max./Min. Principal Strain (Eqs. 27 & 28)		Estimated Max./Min. Principal Stress (Eqs. 30 & 31)		Estimated γ_{max} (Eq. 29) <i>in./in.</i>	Estimated τ_{max} (Eq. 32) <i>psi</i>	Estimated τ_{max} (Eq. 37) <i>psi</i>	Estimated Principal Angles, θ_{1p} & θ_{2p} (Eq. 34 & 35) <i>degrees</i>	Estimated Shear Angles, θ_{1s} & θ_{2s} (Eq. 36) <i>degrees</i>
		ϵ_1 <i>in./in.</i>	ϵ_2 <i>in./in.</i>	σ_1 <i>psi</i>	σ_2 <i>psi</i>					
1	1A	1.09E-05								
	1B	-1.27E-04	-1.32E-04	256.3	-447.8	2.22E-04	352.0	335.3	50, 140	95, 5
	1C	-5.20E-05								
2	2A	-8.09E-05								
	2C	-9.02E-06								
3	3A	-1.87E-05								
	3B	-2.98E-06								
	4A	-2.65E-05								
4	4B	2.37E-06								
	4C	-7.06E-06								

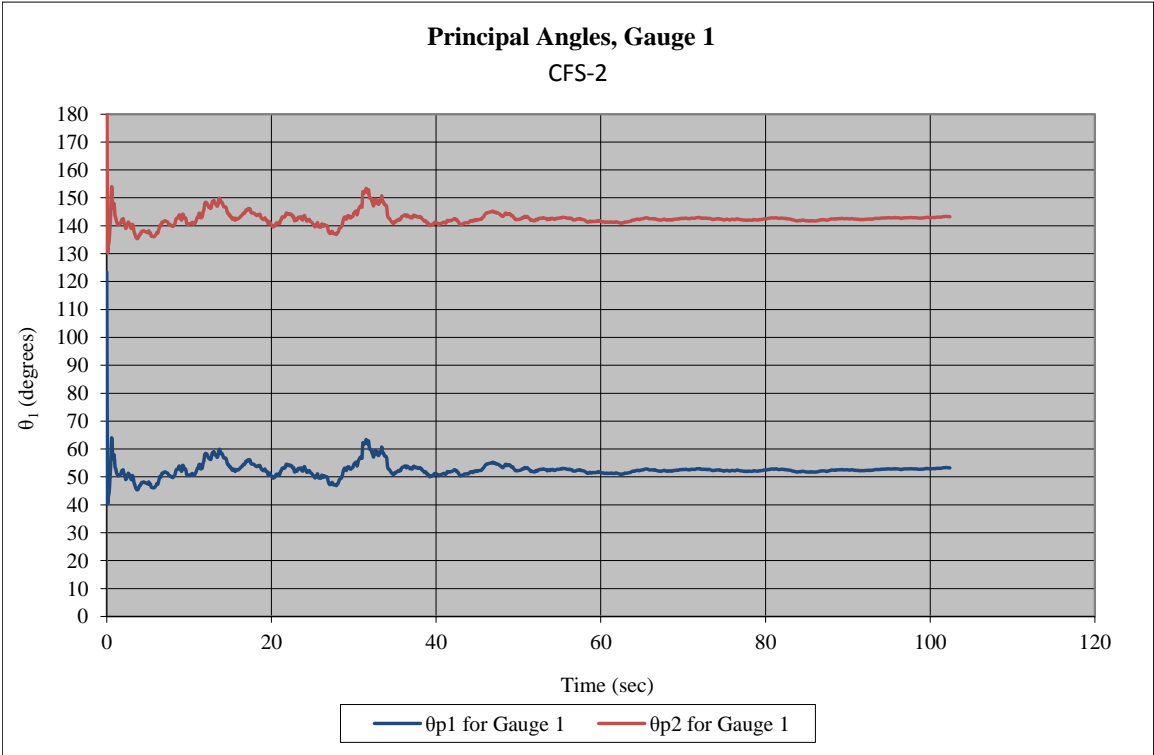
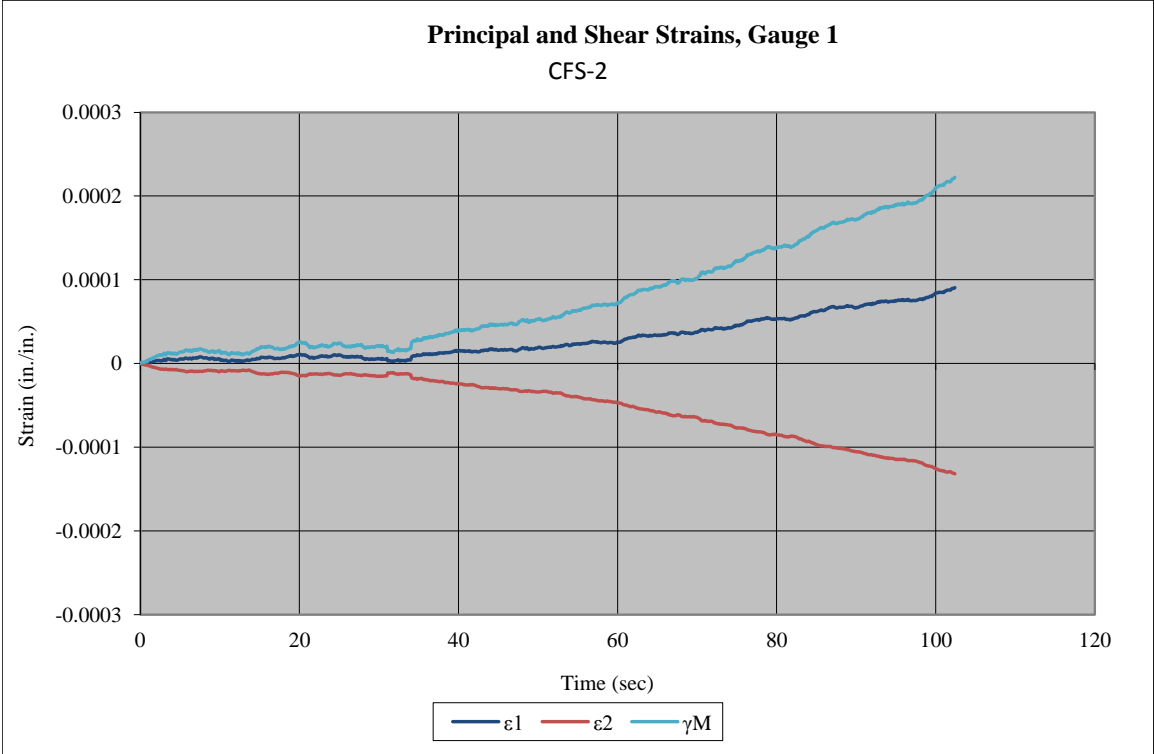


Figure 158. Principal Strains and Angles for Test No. CFS-2 [12-in. (305-mm) Span]

12.5 Test No. CFS-3 [Support Span – 10 in. (254 mm)]

For test no. CFS-3, a span length of 10 in. (254 mm) was used. A shear failure was more likely to occur with this configuration. The test setup is shown in Figure 159.

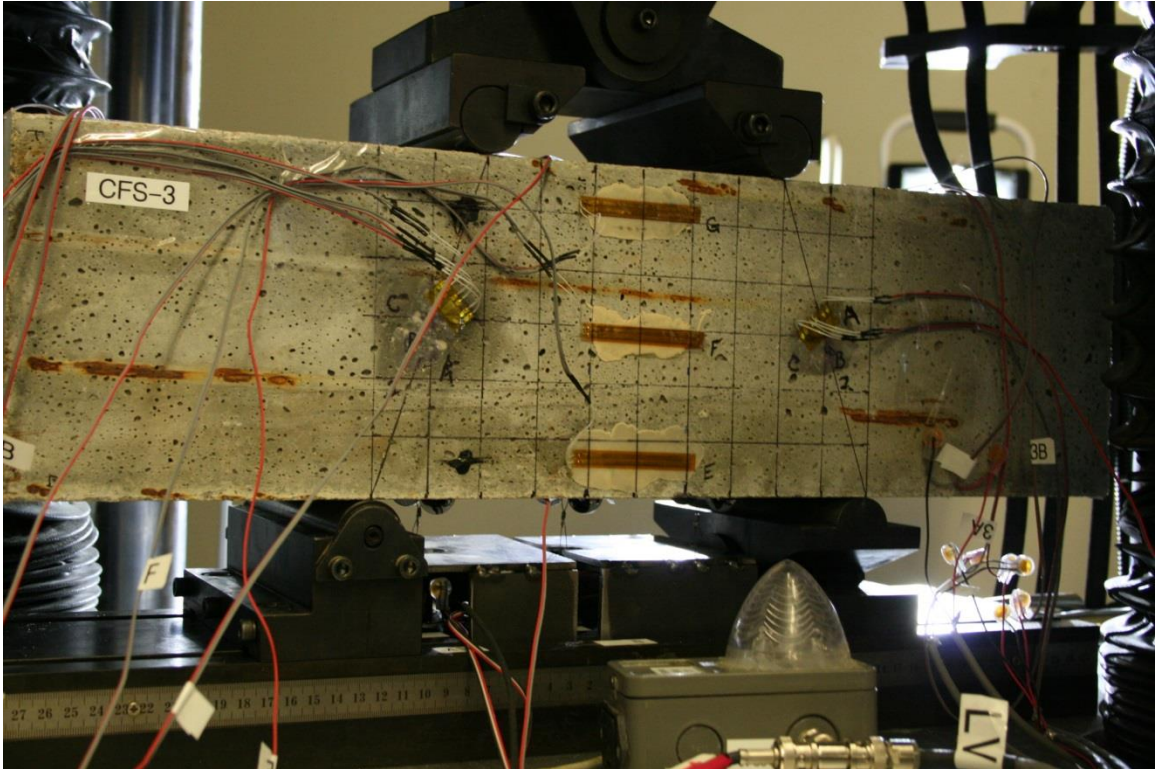


Figure 159. Test Setup for Test No. CFS-3 [10-in. (254-mm) Span]

As the MTS Criterion testing machine loaded the specimen during test no. CFS-3, the specimen failed in shear due to a diagonal crack between the upper and lower roller locations. Specifically, the diagonal fracture plane occurred on the left-front side of the beam. A peak load of 16.9 kip (75.2 kN) was measured when the specimen fractured. Thus, each upper roller was assumed to transfer a peak load equal to 8.5 kip (37.8 kN) to the top of the beam, thus resulting in a reaction at both lower supports equal to 8.5 kip (37.8 kN). The load versus time plot is shown in Figure 160, and post-test photographs are shown in Figure 161 and Figure 162.

All horizontal strain gauges that were placed at the vertical midpoint of the beam appeared to have acquired data during test no. CFS-3. In addition, none of the horizontal strain gauges between rollers broke as the shear failure occurred diagonally between the upper and lower rollers on the front, left side of the beam. The strain readings revealed maximum negative (compression) and maximum positive (tension) normal strains of -3.70×10^{-5} in./in. (top) and 8.55×10^{-5} in./in. (bottom), respectively, as shown in Table 37 and Figure 163. The strains at gauges G and H were nearly equal. As depicted in Figure 164, normal strains were plotted in the direction of the horizontal beam axis for each vertical gauge position [0 in. (beam centerline), $\pm 2\frac{1}{4}$ in. (57 mm) (upper and lower side gauges), and ± 3 in. (76 mm) (top and bottom gauges)]. Finally, the middle strain gauge revealed strains which oscillated around zero for a portion of the test but ultimately rose to -1.15×10^{-5} in./in. by the end of the physical test. Based on the measured difference between the top and bottom gauges, the horizontal strain readings raised some concerns.

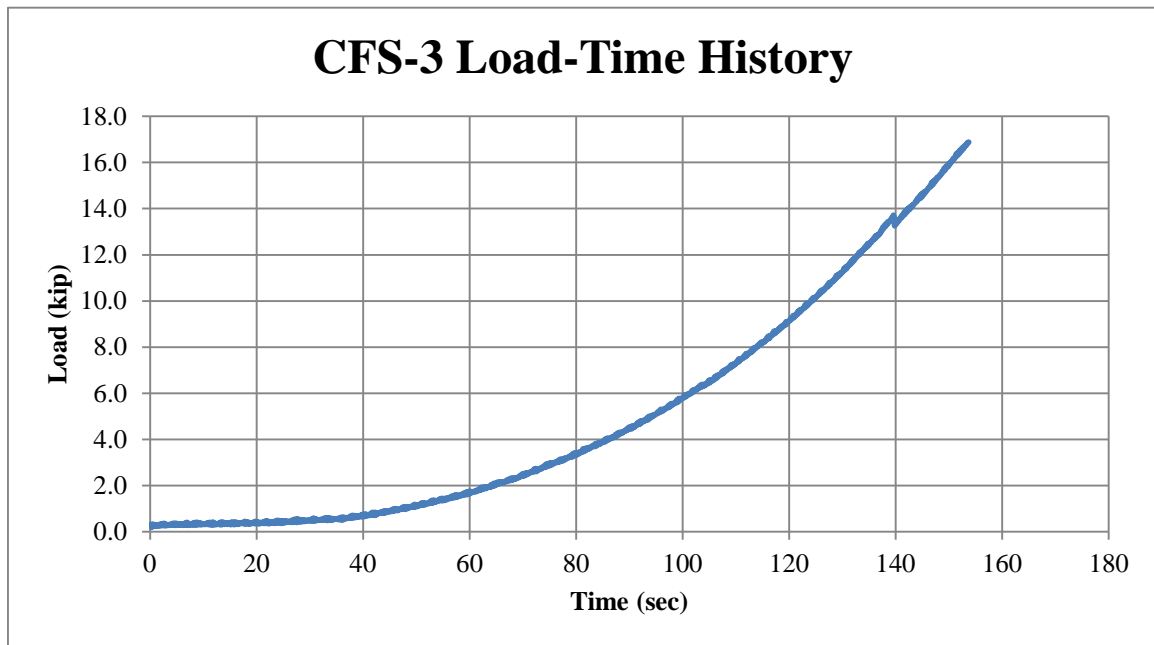


Figure 160. Load vs. Time, Test No. CFS-3 [10-in. (254-mm) Span]

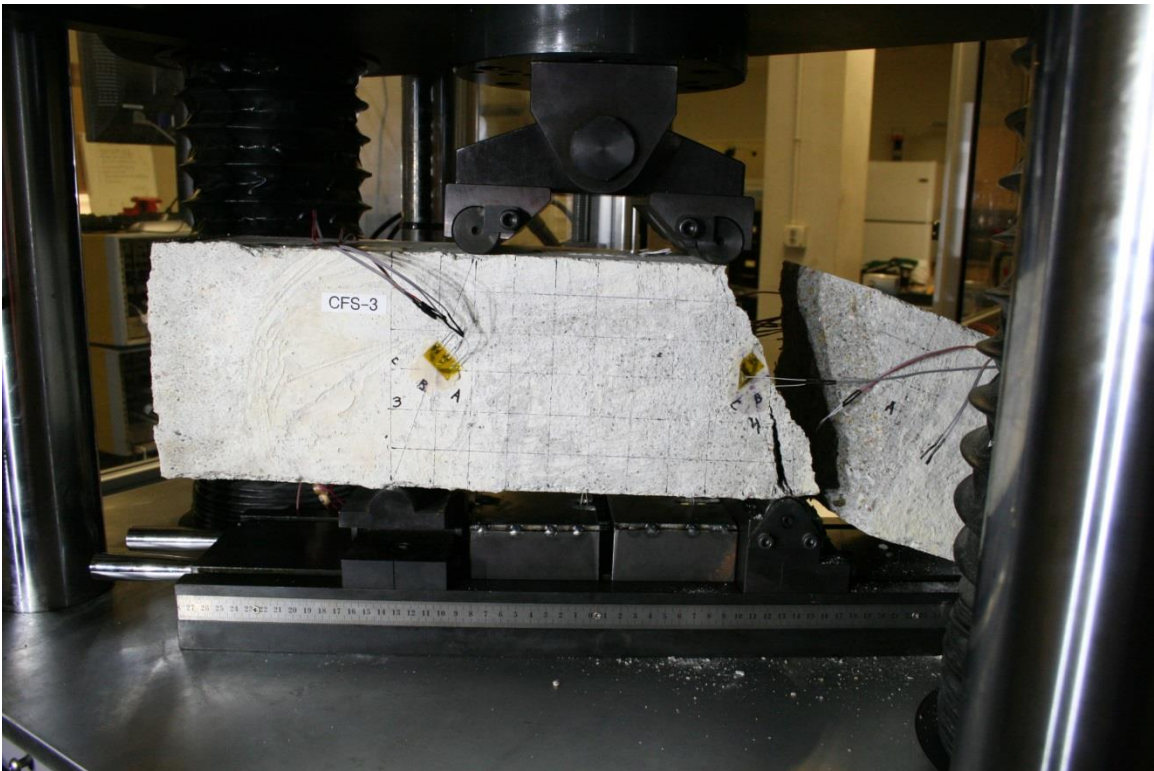
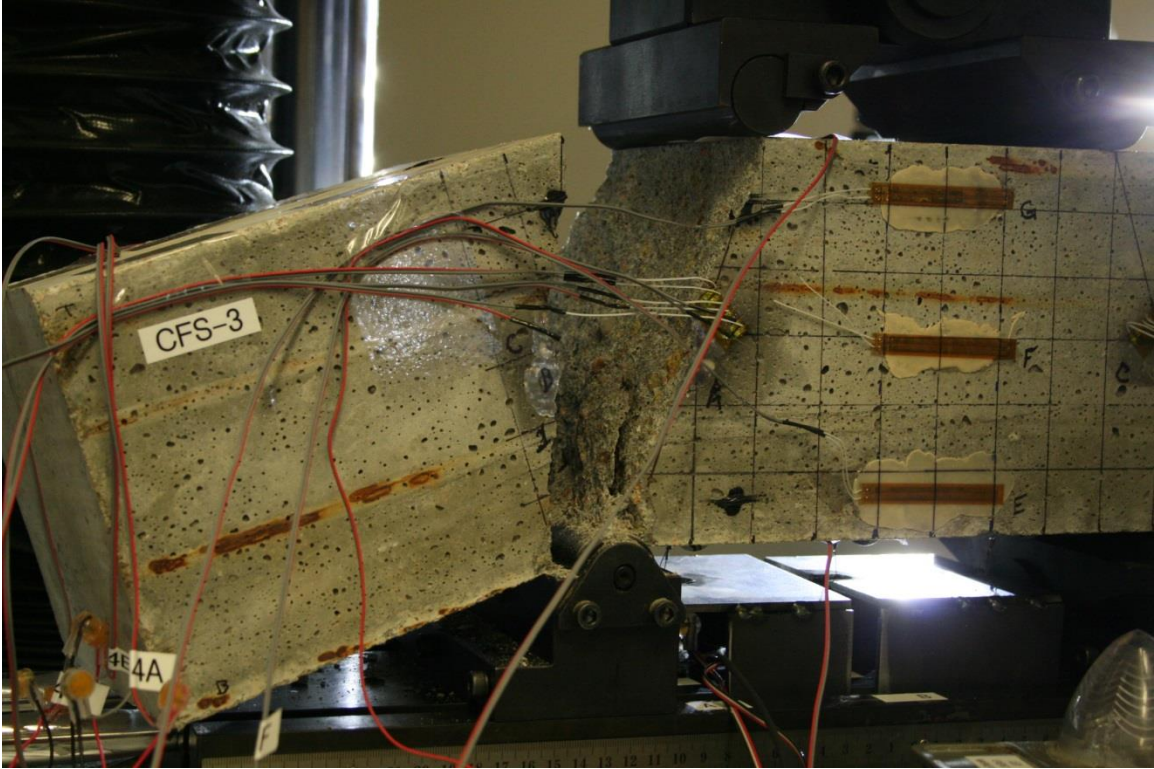


Figure 161. Post-Test Damage, Test No. CFS-3 [10-in. (254-mm) Span]

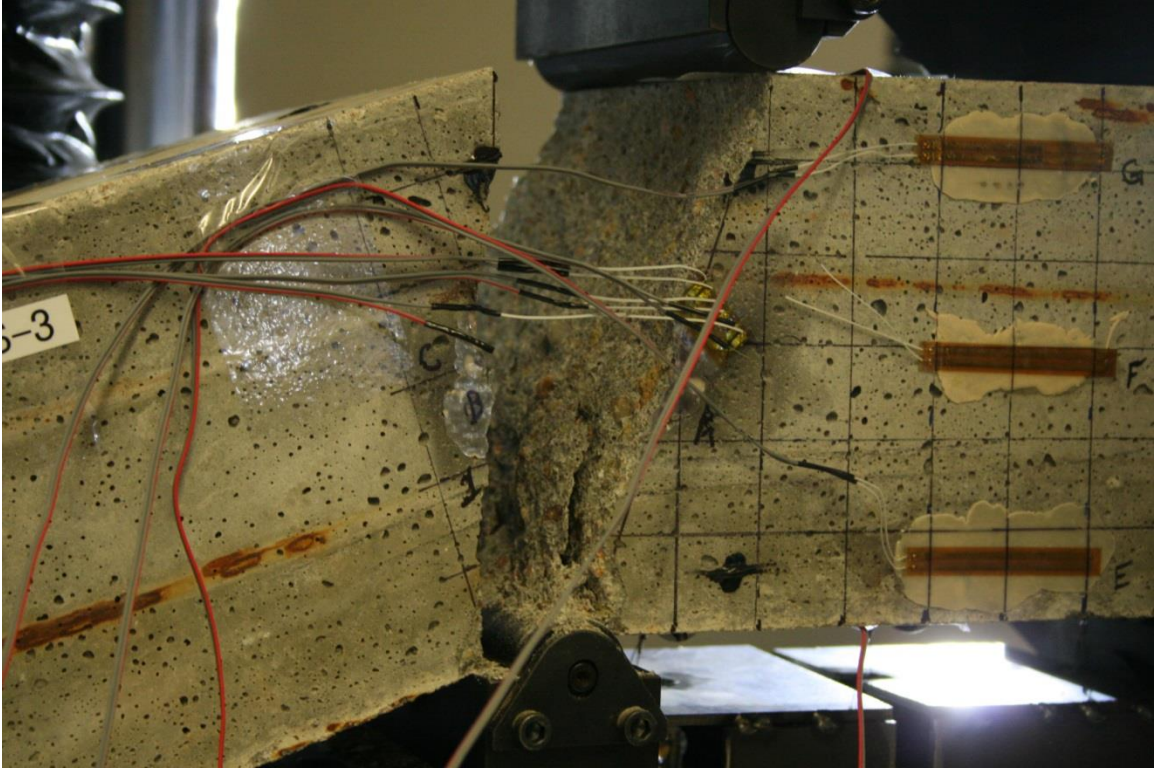


Figure 162. Additional Post-Test Damage, Test No. CFS-3 [10-in. (254-mm) Span]

Table 37. Normal Strain and Stress Distribution for Horizontal Gauges, Test No. CFS-3

Gauge Designation and Location	Normal Strain, ϵ_x, @ Failure <i>in./in.</i>	Estimated Maximum Normal Stress (Eq. 22) <i>psi</i>	Estimated Maximum Normal Stress (Eq. 23) <i>psi</i>
D (bottom)	8.55E-05	411.9	468.8
E	4.06E-05	195.4	351.6
F (middle)	-1.15E-05	-55.4	0.0
G	-3.26E-05	-156.9	-351.6
H (top)	-3.70E-05	-178.3	-468.8

Once the normal strains were processed, analyzed, and reviewed, an estimate was made to determine the maximum normal stress, $\sigma_{x,max}$, based on measured strains using Equation 22. The normal stress distribution was also estimated using strain readings at the upper and lower side positions. The maximum normal stress for each strain gauge is shown in Table 37, while the normal stress for four gauges as a function of time is provided in Figure 165 and Figure 166. An estimate was also made to determine the maximum normal stress, $\sigma_{bending,max}$, using the MTS load data and Equation 23. The maximum normal stress based on MTS load data and elastic bending is depicted in Table 37 for the top and bottom surfaces. Further, the normal stress corresponding to the other gauge locations was also calculated with MTS load data and provided in Table 37. The normal stress as a function of time and using MTS load data is shown graphically in Figure 165 and Figure 166. When comparing the normal stresses using the two methods, it is apparent that similar trends were not predicted during the test duration. The estimated normal stress based on MTS load data exceeded the prediction using the strain readings for the top and bottom gauges. The maximum midspan normal stress was \pm

468.8 psi (2.1 MPa) for the MTS load data and calculated moments, while the maximum midspan normal stresses were +411.9 psi/-178.3 psi (+1.8 MPa/-0.8 MPa) using the strain data. More investigation is needed to explore these differences, including any assumptions and limitations.

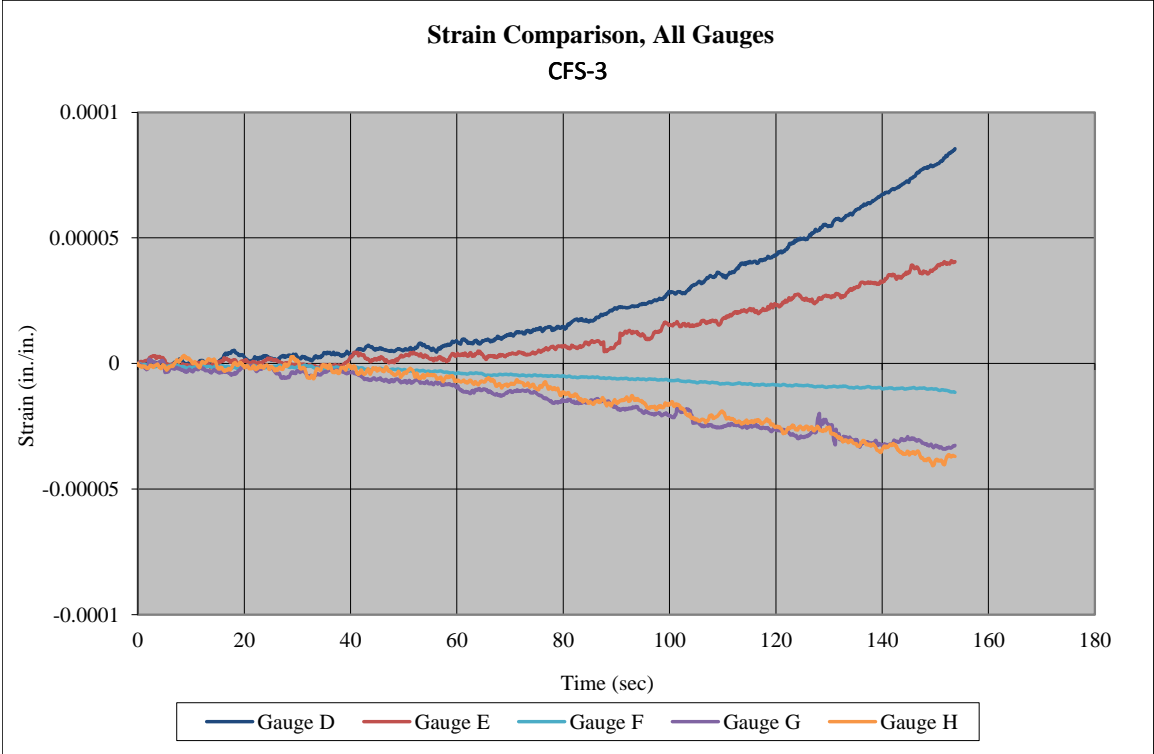


Figure 163. Normal Strains for Top, Side, and Bottom Gauges, Test No. CFS-3 [10-in. (254-mm) Span]

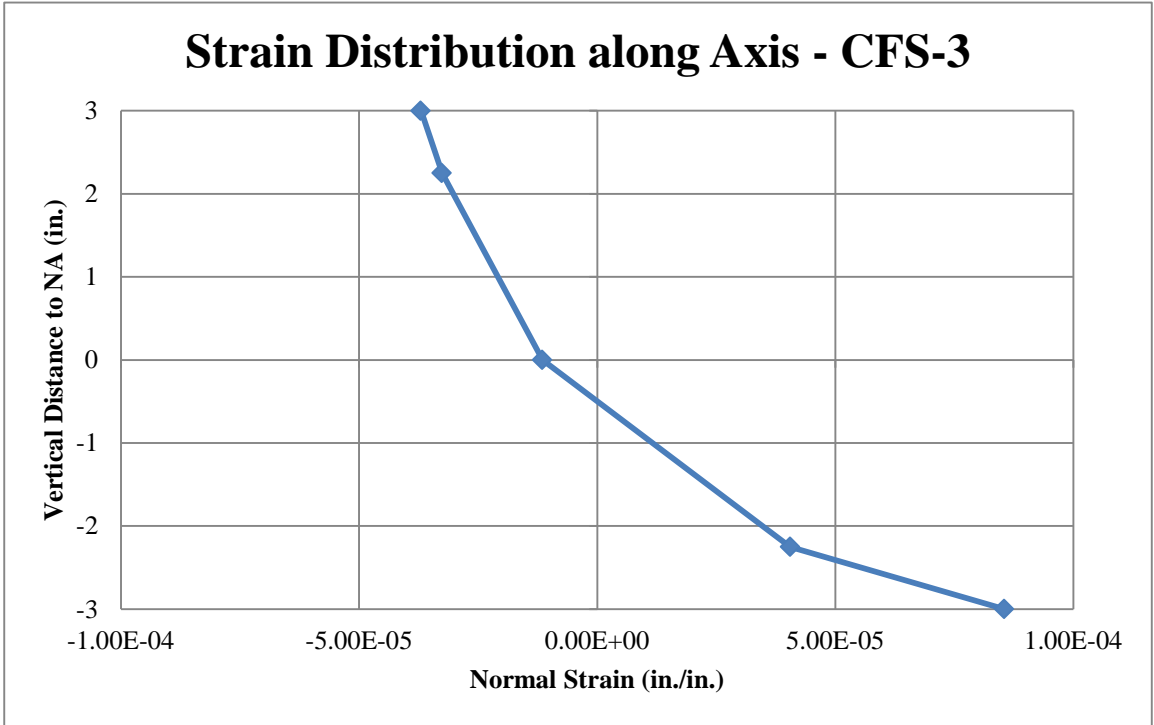


Figure 164. Vertical Distance versus Normal Strain, Test No. CFS-3 [10-in. (254-mm) Span]

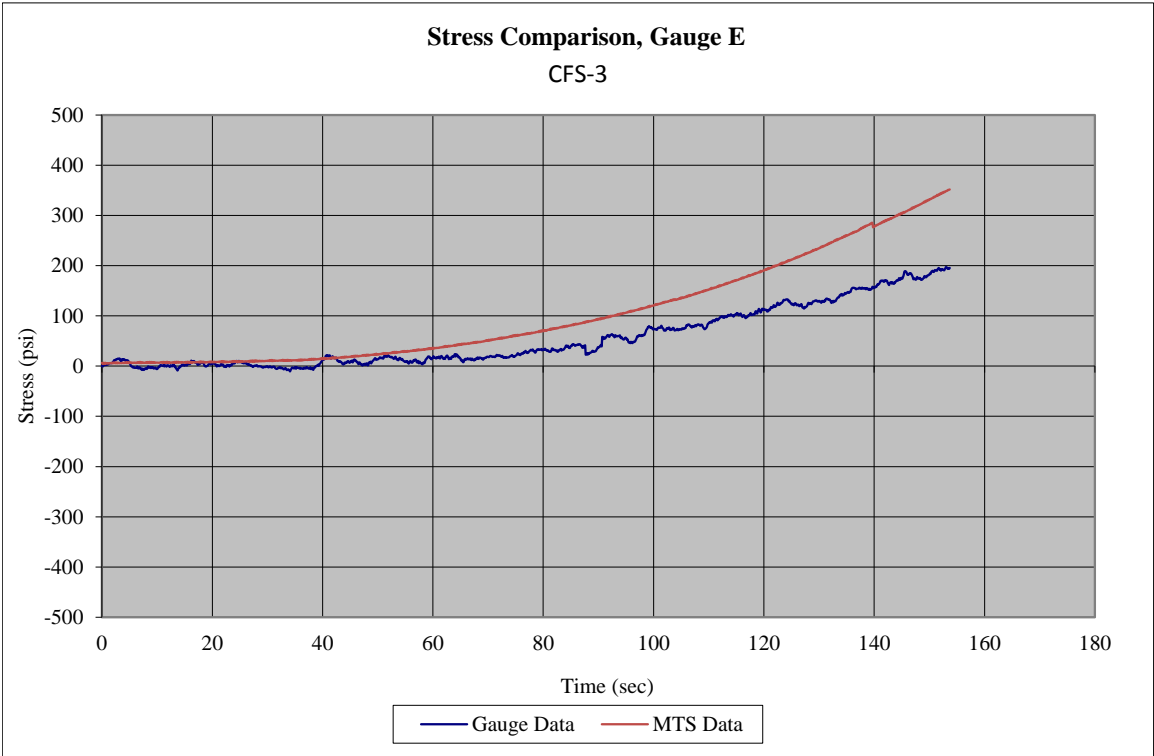
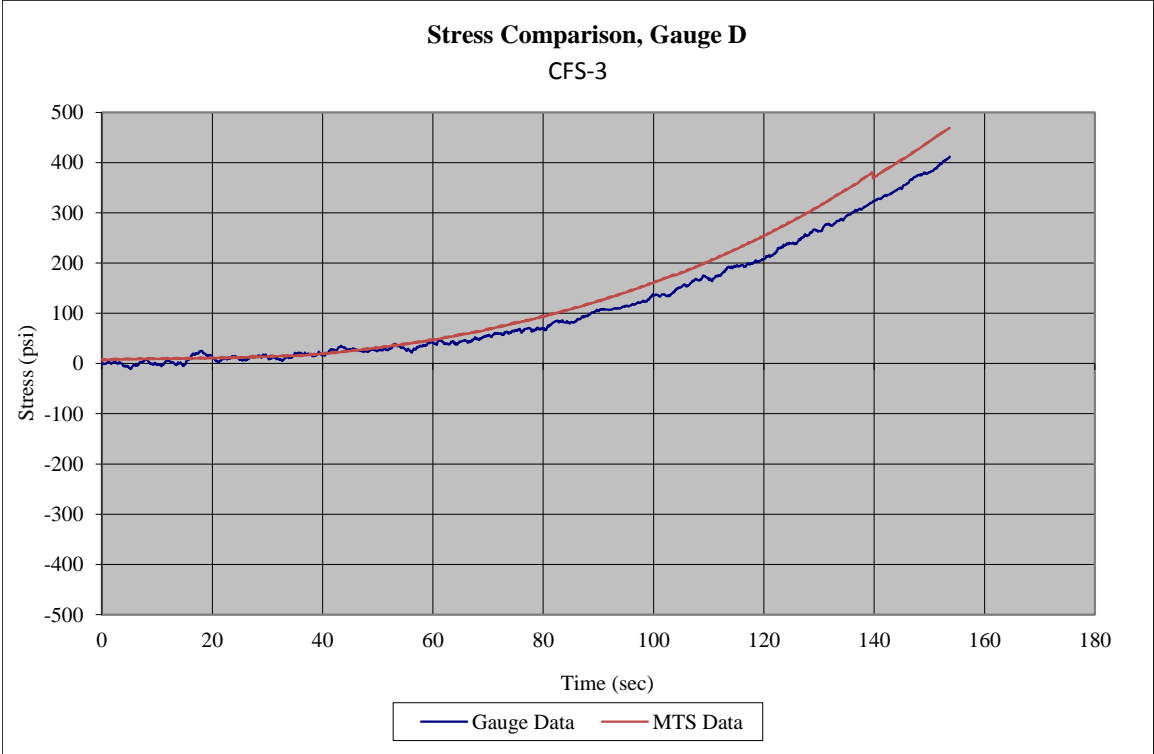


Figure 165. Estimated Midspan Normal Stresses from Bottom Strain Gauges and MTS Load Data, Test No. CFS-3 [10-in. (254-mm) Span]

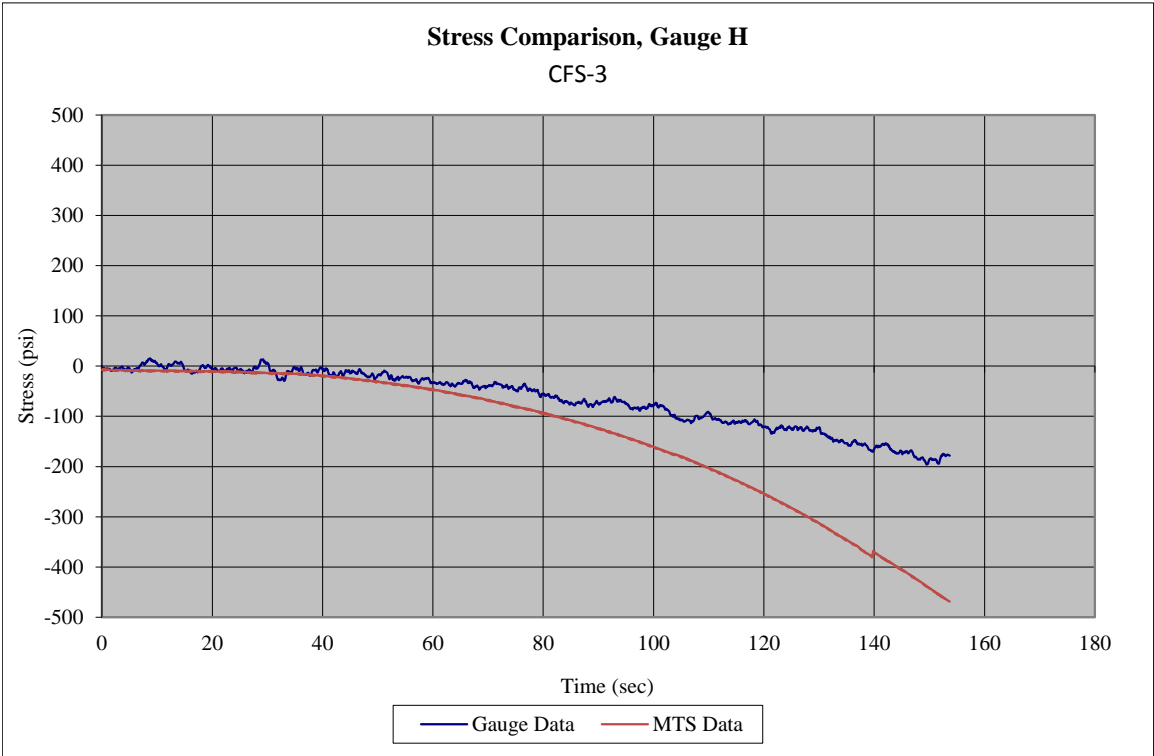
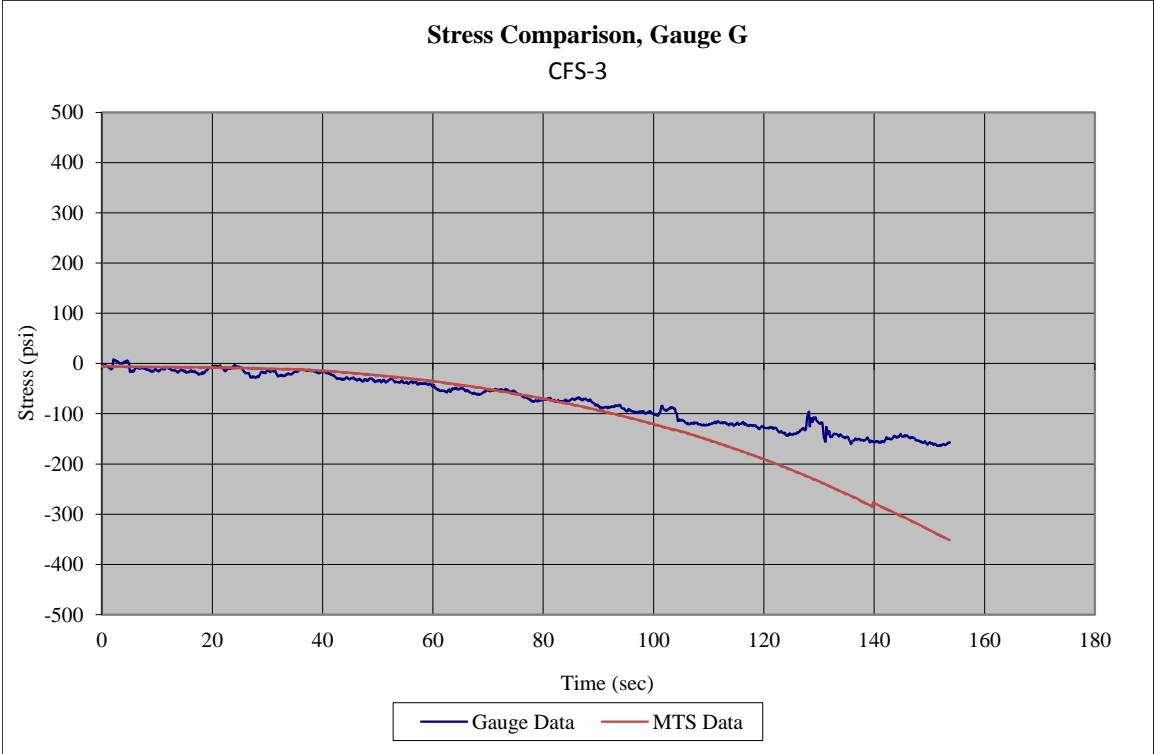


Figure 166. Estimated Midspan Normal Stresses from Top Strain Gauges and MTS Load Data, Test No. CFS-3 [10-in. (254-mm) Span]

Four rosette strain gauges were attached to the front and back faces of the beam near the horizontal centerline and midway between the upper roller and lower support. In addition, two rosette strain gauges (left-front position facing front and right-back position facing back) between the lower support and upper roller broke as the shear failure occurred directly along the path of the rosette strain gauges. Measured strains are provided in Figure 167 and Figure 168 for each rosette and each individual gauge, if acquired. Rosette gauge 1 appeared to perform in an acceptable manner during test no. CFS-3. However, the three remaining gauges provided data that may raise questions upon first glance. Based on symmetric loading, the strains would be expected to be very similar across all rosettes. However, this outcome did not appear to always be the case.

First, rosette no. 1 (left-front position facing front) provided negative compressive strain for two gauges (B – diagonal and C – vertical), but positive tensile strain for the third gauge (A – horizontal). Note that the A-gauge was aligned with the positive horizontal beam axis at its geometric centerline. Second, rosette no. 2 (right-front position facing front) provided nearly zero strain for one gauge (B – diagonal). Note that the C-gauge was aligned with the negative horizontal axis. Further, both the horizontal and vertical gauges provided positive tensile and negative compressive strains, respectively. Third, rosette no. 3 (left-back position facing back) provided nearly zero strain for all three gauges (A – horizontal, B – diagonal, and C – vertical). Note that the A-gauge was aligned with the positive horizontal beam axis at its geometric centerline for the back face. Finally, rosette no. 4 (right-back position facing back) provided positive tensile strain for two gauges (A – vertical and B – diagonal) and negative compressive

strain for the third gauge (C – horizontal). Note that the C-gauge was aligned with the negative horizontal axis.

All strains, gauges A through C, would likely be non-zero for this beam configuration with 10-in. (254-mm) span. However, some gauges did have zero strain throughout. Following a review for all four rosette gauges, it was apparent that none of the gauges had very similar strain readings for the acquired data channels. The horizontal gauges for rosette nos. 1, 2, and 4 provided a positive tensile strain, while the vertical gauges provided a negative compression. The diagonal gauge (B) provided negative compressive strain at rosette no. 1 and positive tensile strain at rosette no. 4. The strains in 3A, 3B, and 3C were close to zero strain throughout the event, which was unexpected for this scenario. With strain rosette no. 3, some questions arose regarding the validity of data. Thus, less confidence existed with results produced with gauge 3. The maximum strain readings are provided in Table 38, and strain versus time is shown graphically in Figure 167 and Figure 168.

Based on the analysis provided above, it appears that only rosette no. 1 was providing reliable data for full-strain field analysis. Rosette no. 2 had a diagonal gauge with zero strain. Rosette no. 3 had zero strains for all three gauges. Rosette no. 4 had positive strain in diagonal gauge B.

Maximum principal and maximum shear strains are summarized in Table 38 for rosette no. 1. The value for the maximum principal strain, ϵ_1 for gauge 1 was 1.17×10^{-4} in./in. The value for the minimum principal strain, ϵ_2 for gauge 1 was -1.57×10^{-4} in./in. The highest maximum shear strain for test no. CFS-3 was 2.74×10^{-4} in./in. Subsequently, Equation 32 and Equation 36 were used to compute the theoretical

maximum shear stress and maximum shear strain of 351.6 psi (1.6 MPa) and 1.74×10^{-4} in./in., respectively. A plot of the maximum and minimum principal strain and shear strain from rosette no. 1 is shown in Figure 169.

Principal angles are summarized in Figure 169 for rosettes that had all three gauges acquire and return adequate data. Based on the plot, the principal angle for gauge 1 ranges between 60 and 70 degrees. The principal angle for gauge 1 was confirmed as this value was expected to be between 0 and 90 degrees. The second principal angle, θ_{p2} , was then near 155 degrees for gauge 1. Based on these angles, the associated shear angles would be 110 and 20 degrees for gauge 1.

Maximum principal stresses are summarized in Table 38 for all rosettes that had all three gauges acquire and return adequate data. These values were calculated using Equation 30. The value 342.8 psi (2.4 MPa) for the maximum principal stress, σ_1 was slightly larger than the known maximum tensile strength from CFT testing, 407.0 psi (2.8 MPa).

The final piece of instrumentation was the string potentiometers. Similar to prior tests, questions arose regarding the accuracy of the resulting displacement data after comparison to displacements determined with Equation 20 and Equation 21, as well as the actuator movement over the same period. The theoretical equations tended to provide lower displacements than measured, while the actuator displacement data was generally higher than measured with the string potentiometer. It was somewhat difficult to determine which string potentiometers had results that may have inaccuracies due to instrumentation placement, data resolution, etc. could be trusted. As such, the

displacement data and results are not included in this section. String potentiometer and actuator data are found in Appendix D.

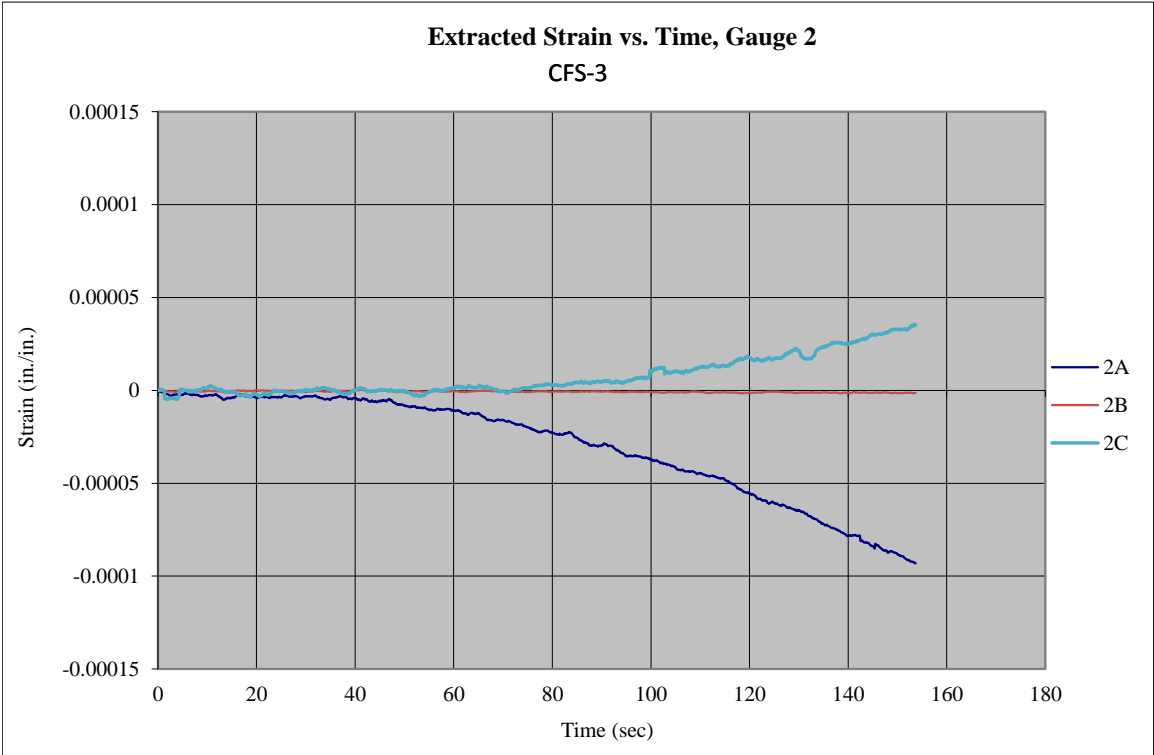
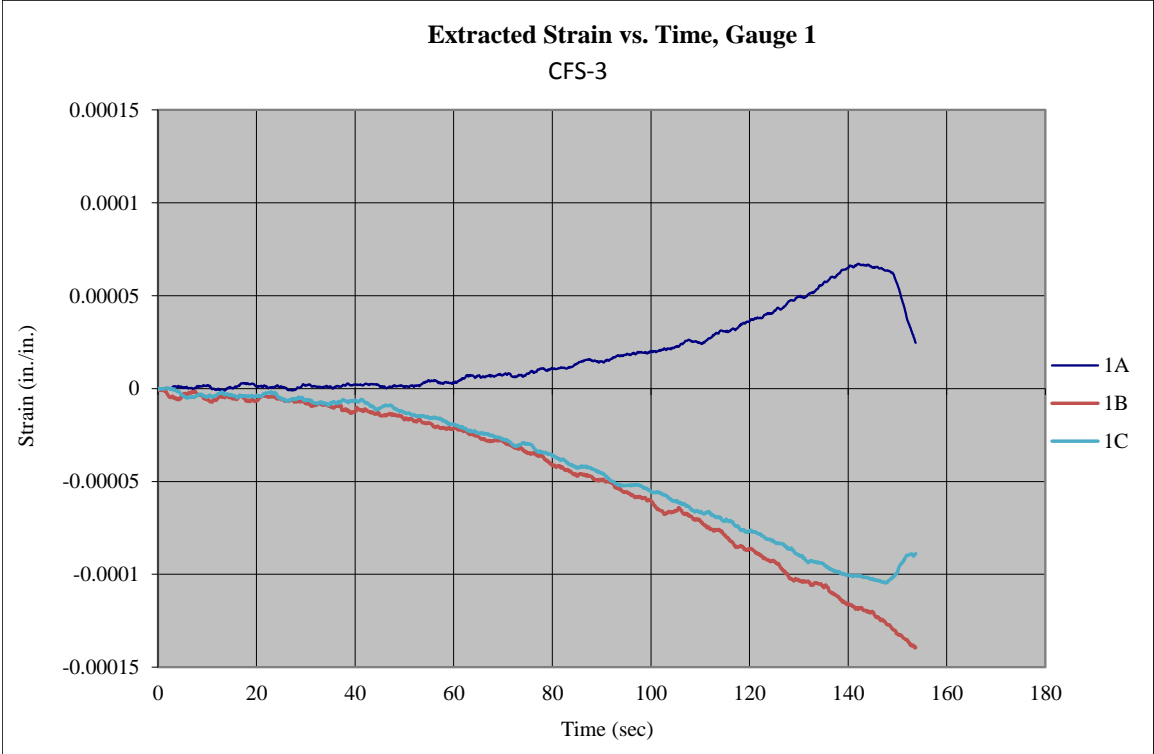


Figure 167. Extracted Strain Plots for Rosette Strain Gauges 1 and 2, Test No. CFS-3 [10-in. (254-mm) Span]

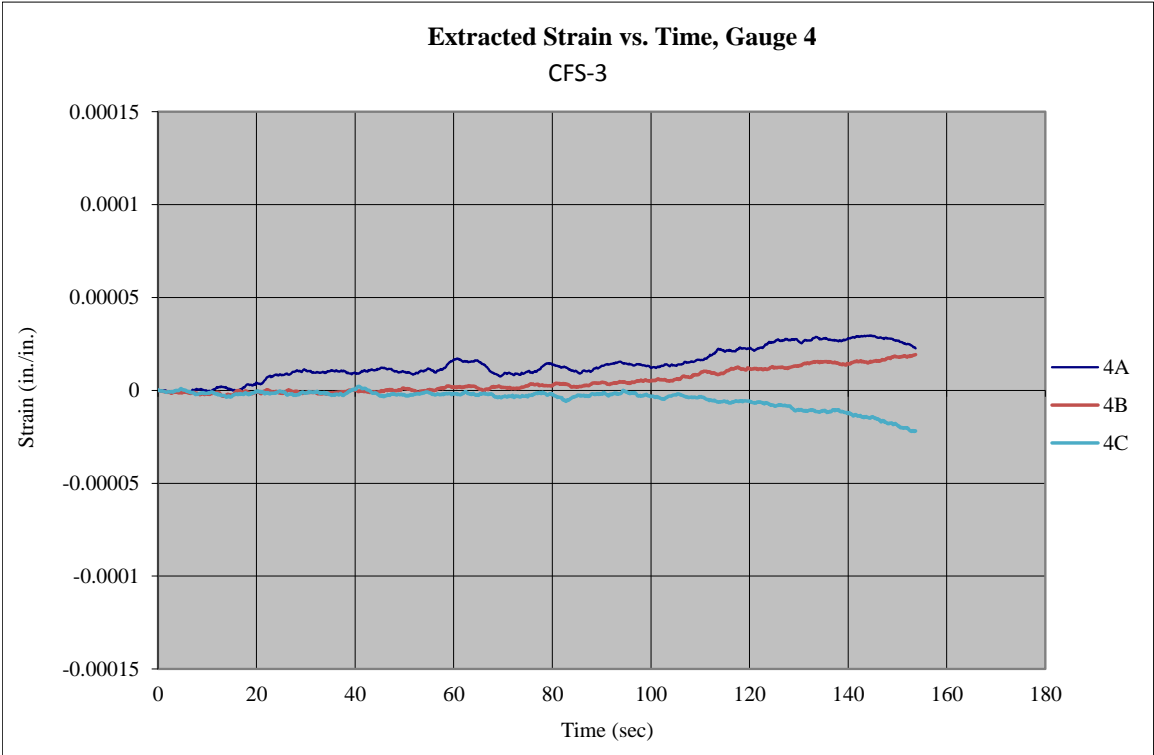
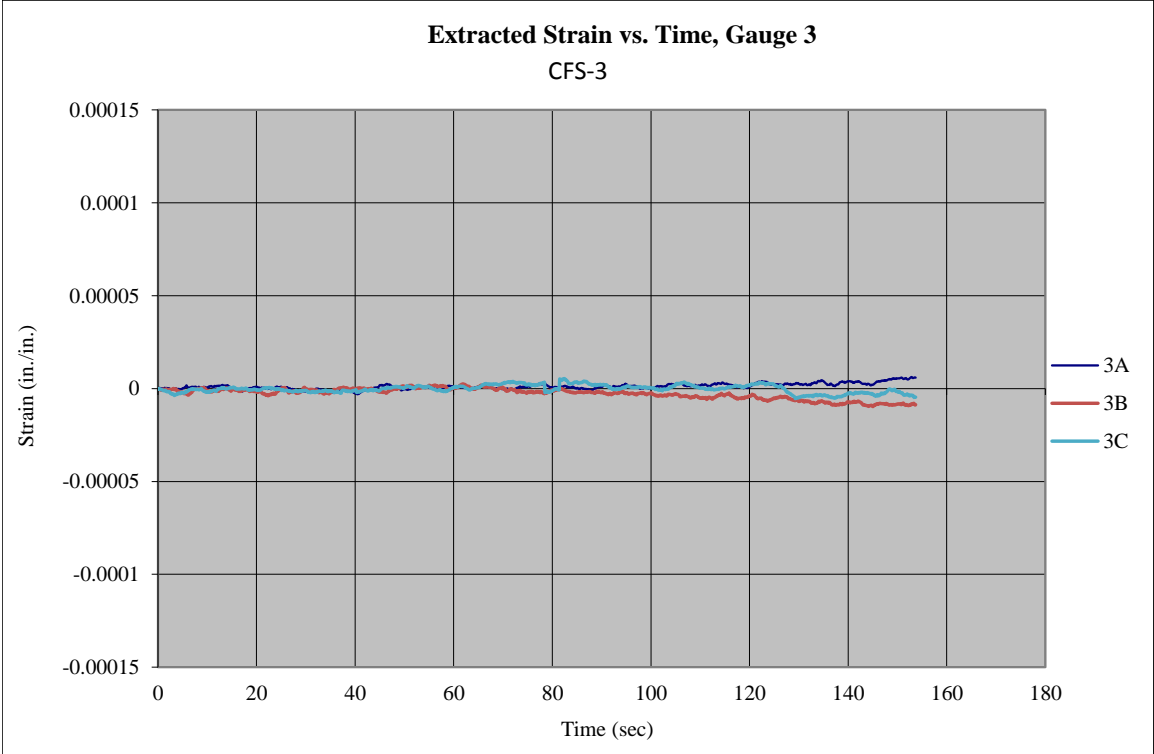


Figure 168. Extracted Strain Plots for Rosette Strain Gauges 3 and 4, Test No. CFS-3 [10-in. (254-mm) Span]

Table 38. Summary of Stress and Strains for Rosette Gauges, Test No. CFS-3

Rosette Gauge	Normal Strain, ϵ_x , @ Failure <i>in./in.</i>	Estimated Max./Min. Principal Strain (Eqs. 27 & 28)		Estimated Max./Min. Principal Stress (Eqs. 30 & 31)		Estimated γ_{max} (Eq. 29) <i>in./in.</i>	Estimated τ_{max} (Eq. 32) <i>psi</i>	Estimated τ_{max} (Eq. 37) <i>psi</i>	Estimated Principal Angles, θ_{1p} & θ_{2p} (Eq. 34 & 35) <i>degrees</i>	Estimated Shear Angles, θ_{1s} & θ_{2s} (Eq. 36) <i>degrees</i>
		ϵ_1 <i>in./in.</i>	ϵ_2 <i>in./in.</i>	σ_1 <i>psi</i>	σ_2 <i>psi</i>					
1	1A	2.46E-05								
	1B	-1.39E-04	1.17E-04	342.8	-534.7	2.74E-04	434.5	351.6	65, 155	110, 20
	1C	-8.89E-05								
2	2A	-9.30E-05								
	2B	-1.35E-06								
	2C	3.53E-05								
3	3A	5.86E-06								
	3B	-8.67E-06								
	3C	-4.61E-06								
4	4A	2.26E-05								
	4B	1.93E-05								
	4C	-2.19E-05								

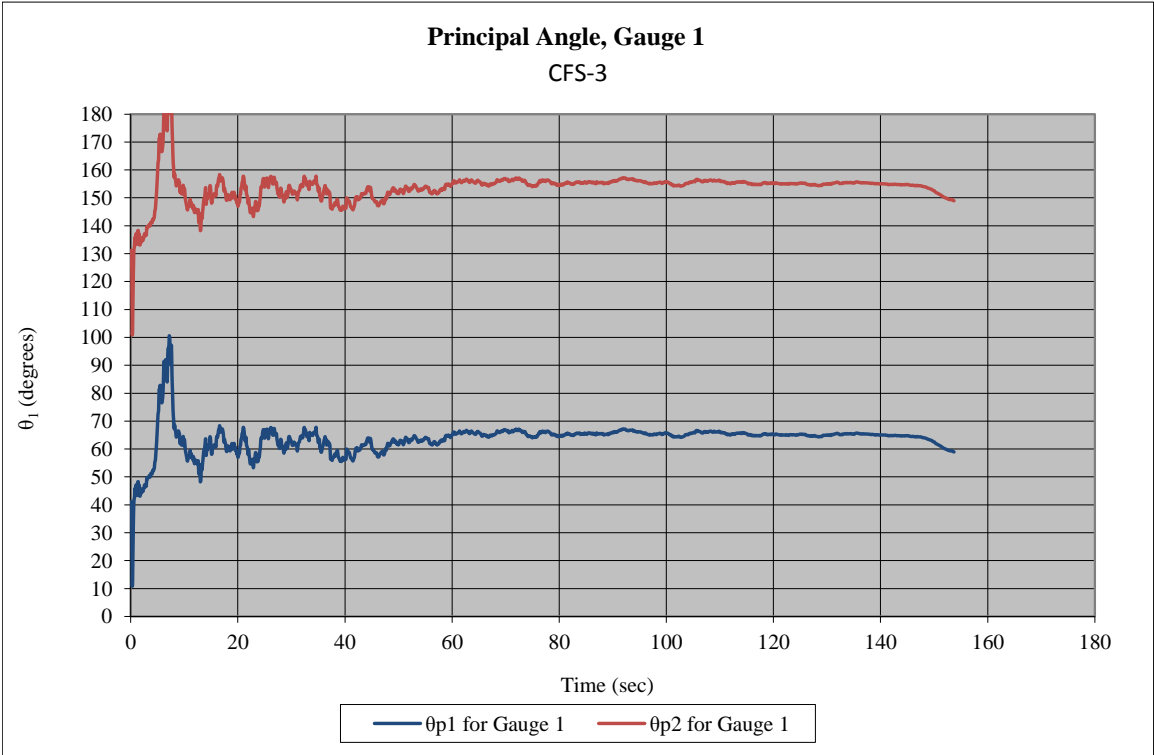
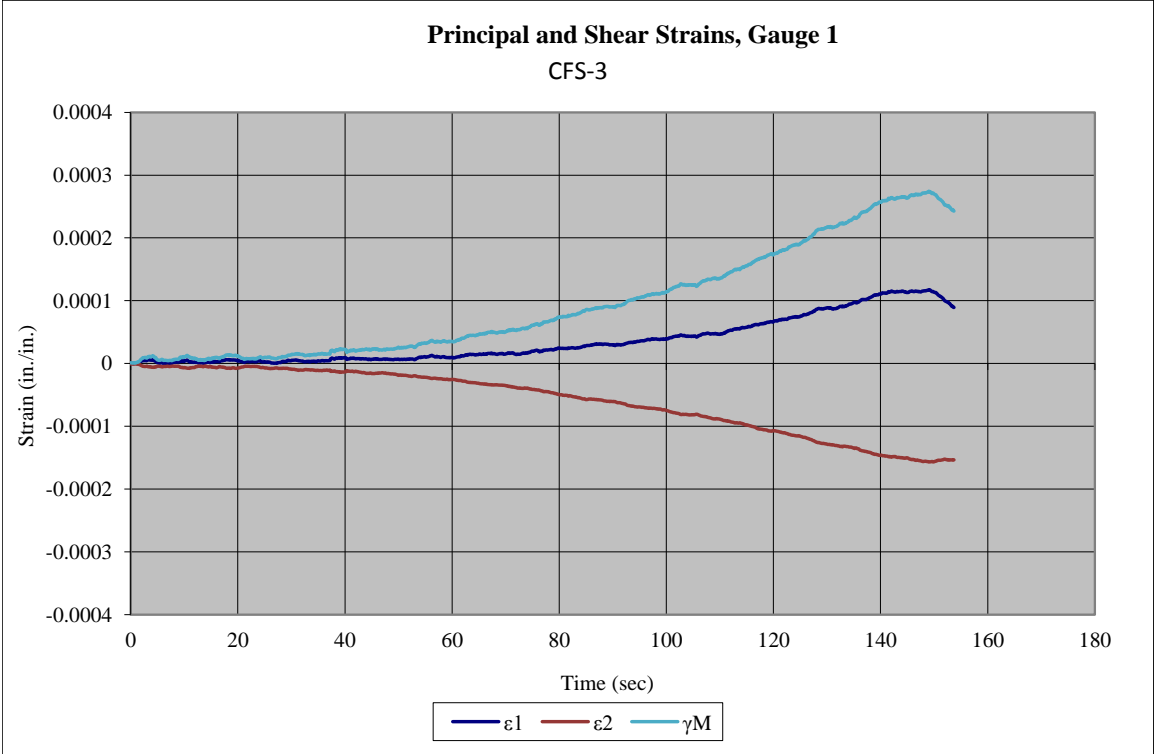


Figure 169. Principal Strains and Angles for Test No. CFS-3 [10-in. (254-mm) Span]

12.6 Test No. CFS-4 [Support Span – 11 in. (279 mm)]

For test no. CFC-4, a span length of 11 in. (279 mm) was used. The failure mode for this configuration was unknown. The test setup is shown in Figure 170.

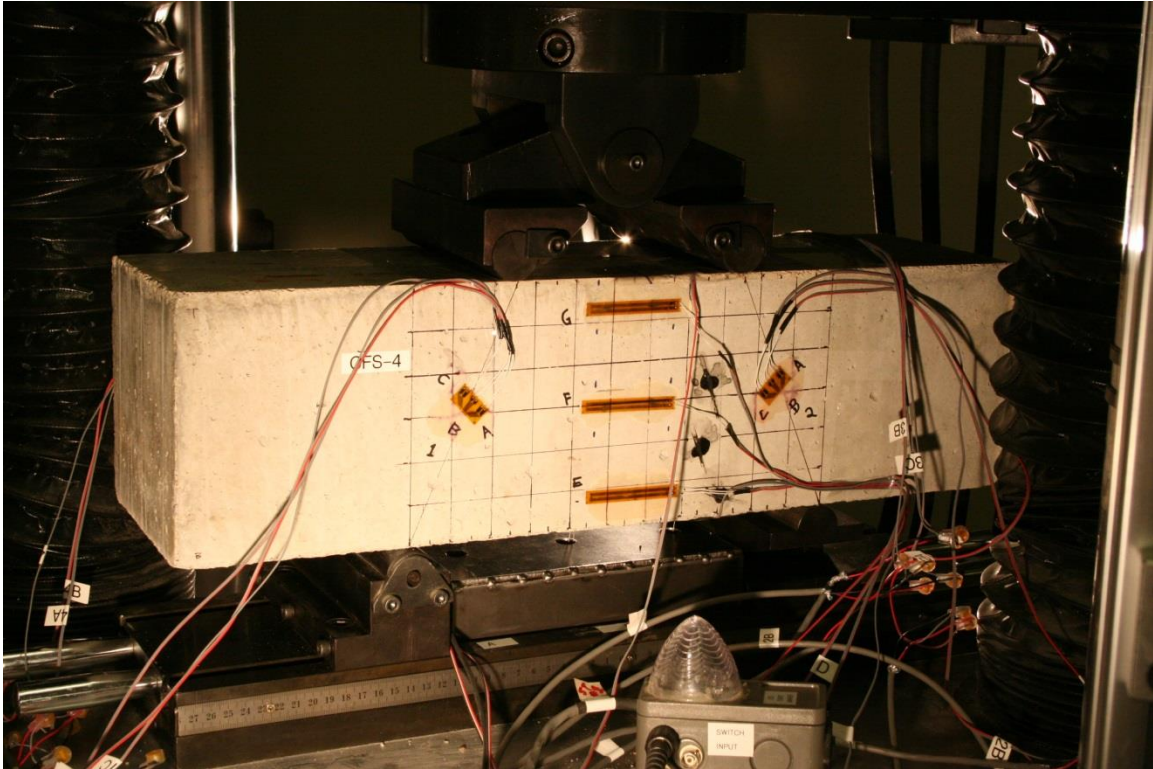


Figure 170. Test Setup for Test No. CFS-4 [11-in. (279-mm) Span]

As the MTS Criterion testing machine loaded the specimen during test no. CFS-4, the specimen failed in flexure due to excessive tensile stresses at the bottom surface and between the upper roller locations. The failure plane was not perfectly vertical, somewhat different than the failure planes in tests nos. CFS-1 and CFS-2. The vertical fracture plane occurred 0.5 in. (13 mm) left of the vertical centerline of the beam. A peak load of 16.9 kip (75.2 kN) was measured when the specimen fractured. Thus, each upper roller was assumed to transfer a peak load equal to 8.5 kip (37.8 kN) to the top of the beam, thus resulting in a reaction at both lower supports equal to 8.5 kip (37.8 kN). The load versus

time plot is shown in Figure 171, and post-test photographs are shown in Figure 172 and Figure 173.

All horizontal strain gauges that were placed at the vertical centerline of the beam appeared to have acquired data during test no. CFS-4. In addition, all of the horizontal strain gauges between rollers broke as the curved failure pattern occurred between the upper rollers. The strain readings revealed maximum negative (compression) and maximum positive (tension) normal strains of -1.06×10^{-4} in./in. (top) and 2.51×10^{-4} in./in. (bottom), respectively, as shown in Table 39 and Figure 174. Horizontal normal strain at the bottom of the beam appeared to be very large, creating a non-linear strain distribution. In addition, the strains at gauges G and H were nearly equal. As depicted in Figure 175, normal strains were plotted in the direction of the horizontal beam axis for each vertical gauge position [0 in. (beam centerline), $\pm 2\frac{1}{4}$ in. (57 mm) (upper and lower side gauges), and ± 3 in. (76 mm) (top and bottom gauges)]. Finally, the middle strain gauge revealed strains which largely oscillated around zero for the duration of the test. Based on the measured difference between the top and bottom gauges, the horizontal strain readings raised some concerns.

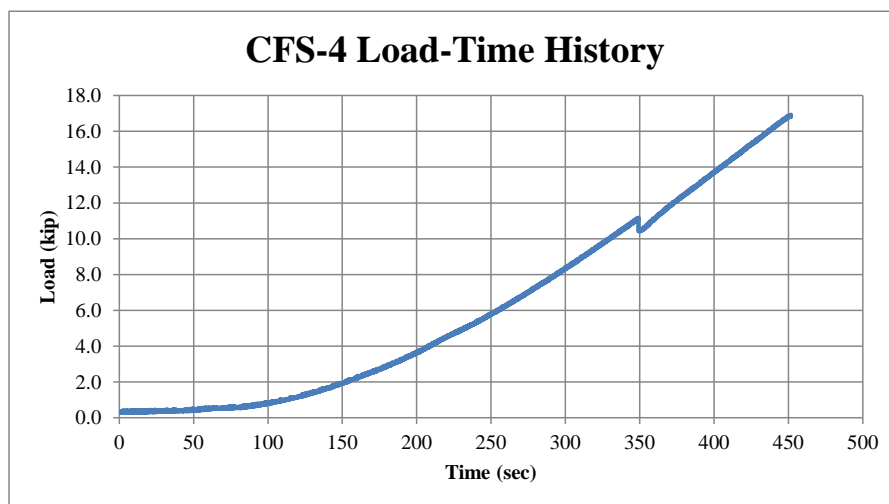


Figure 171. Load vs. Time, Test No. CFS-4 [11-in. (279-mm) Span]

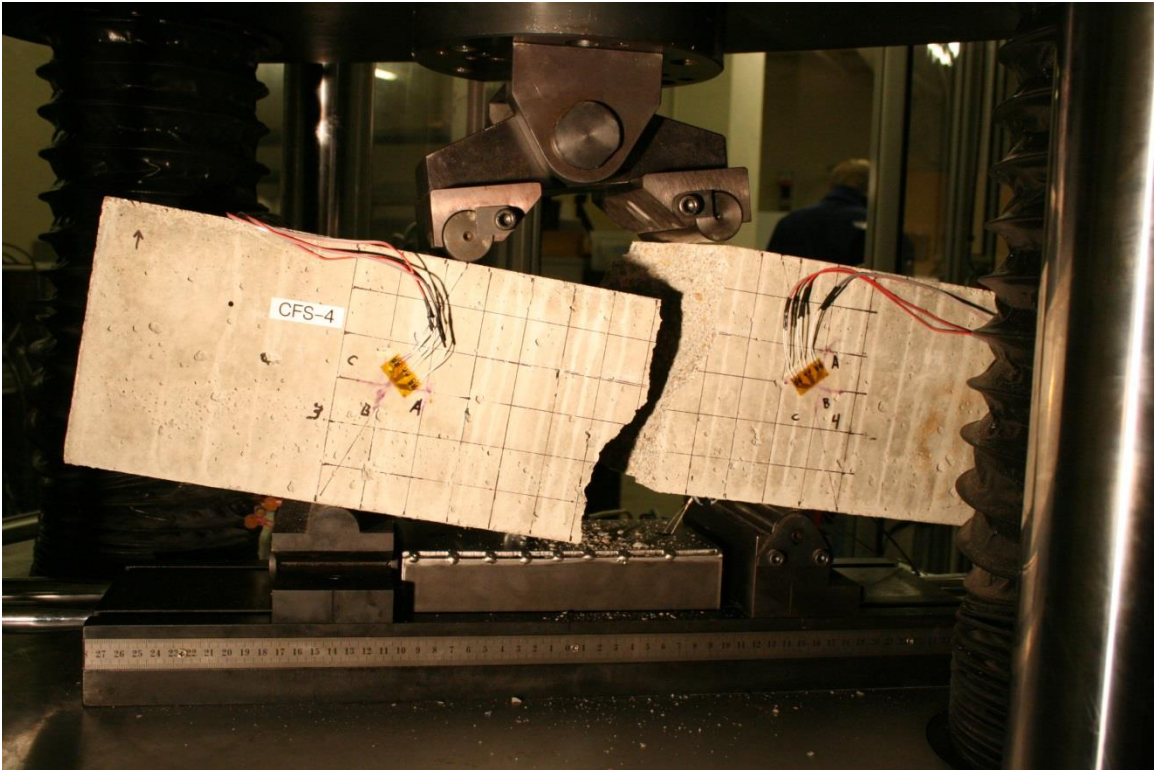
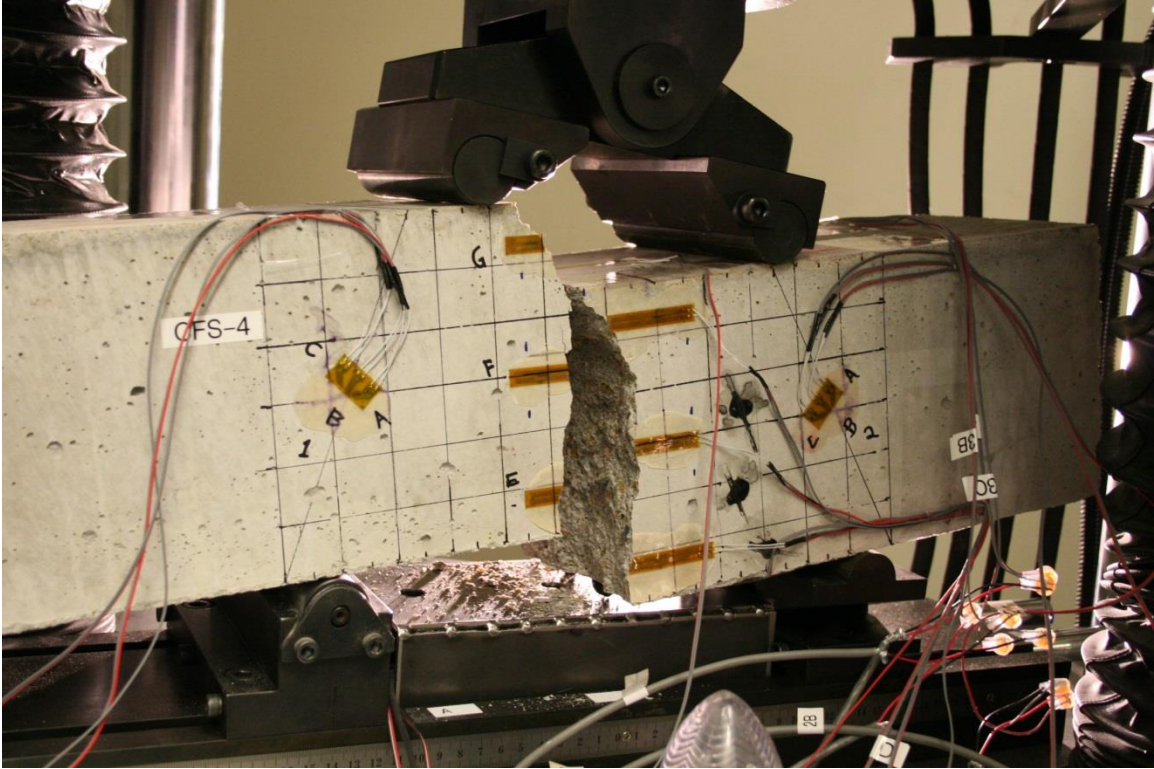


Figure 172. Post-Test Damage, Test No. CFS-4 [11-in. (279-mm) Span]

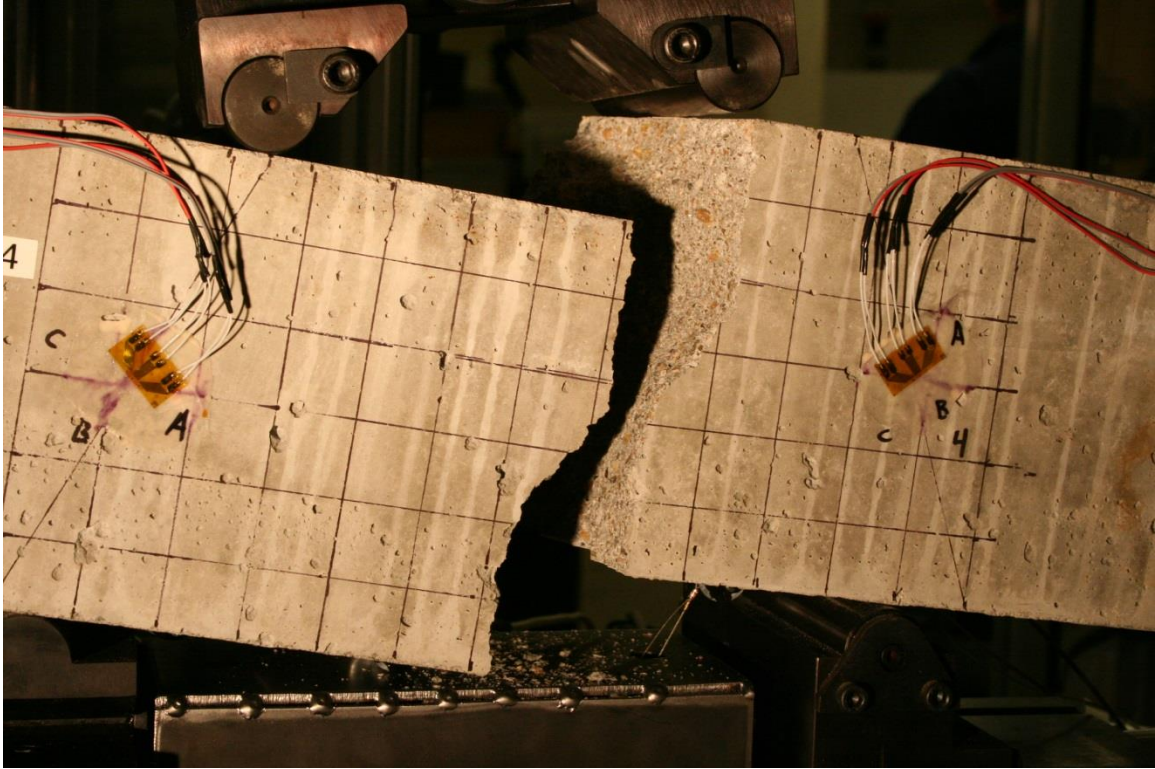


Figure 173. Additional Post-Test Damage, Test No. CFS-4 [11-in. (279-mm) Span]

Table 39. Normal Strain and Stress Distribution for Horizontal Gauges, Test No. CFS-4

Gauge Designation and Location	Normal Strain, ϵ_x, @ Failure <i>in./in.</i>	Estimated Maximum Normal Stress (Eq. 22) <i>psi</i>	Estimated Maximum Normal Stress (Eq. 23) <i>psi</i>
D (bottom)	2.51E-04	1210.9	587.4
E	7.95E-05	382.9	440.5
F (middle)	-3.08E-06	-14.8	0.0
G	-9.56E-05	-460.5	-440.5
H (top)	-1.06E-04	-510.9	-587.4

Once the normal strains were processed, analyzed, and reviewed, an estimate was made to determine the maximum normal stress, $\sigma_{x,max}$, based on measured strains using Equation 22. The normal stress distribution was also estimated using strain readings at the upper and lower side positions. The maximum normal stress for each strain gauge is shown in Table 39, while the normal stress for four gauges as a function of time is provided in Figure 176 and Figure 177. An estimate was also made to determine the maximum normal stress, $\sigma_{bending,max}$, using the MTS load data and Equation 23. The maximum normal stress based on MTS load data and elastic bending is depicted in Table 39 for the top and bottom surfaces. Further, the normal stress corresponding to the other gauge locations was also calculated with MTS load data and provided in Table 39. The normal stress as a function of time and using MTS load data is shown graphically in Figure 176 and Figure 177. When comparing the normal stresses using the two methods, it is apparent that similar trends were not predicted during the test duration. The estimated normal stress based on MTS load data exceeded the prediction using the strain readings for the top gauge but not the bottom gauge. The maximum midspan normal

stress was ± 587.4 psi (4.1 MPa) for the MTS load data and calculated moments, while the maximum midspan normal stresses were +1210.9 psi/-510.9 psi (+8.3 MPa/-3.5 MPa) using the strain data. More investigation is needed to explore these differences, including any assumptions and limitations.

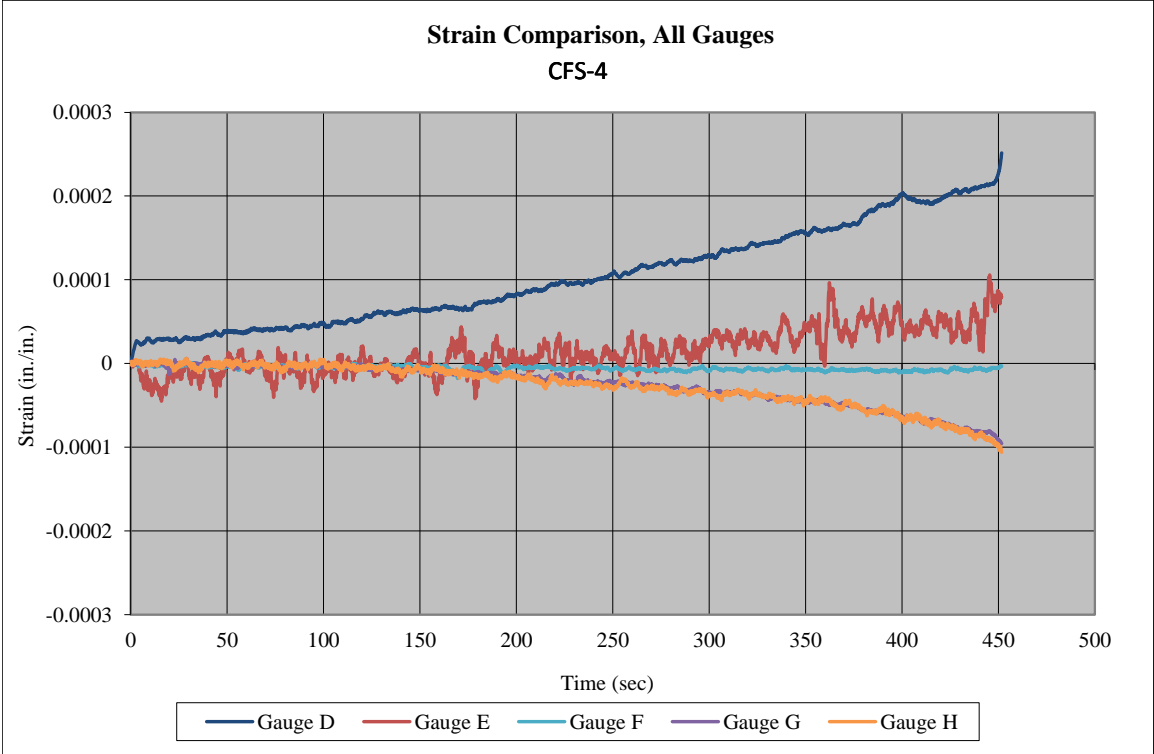


Figure 174. Normal Strains for Top, Side, and Bottom Gauges, Test No. CFS-4 [11-in. (279-mm) Span]

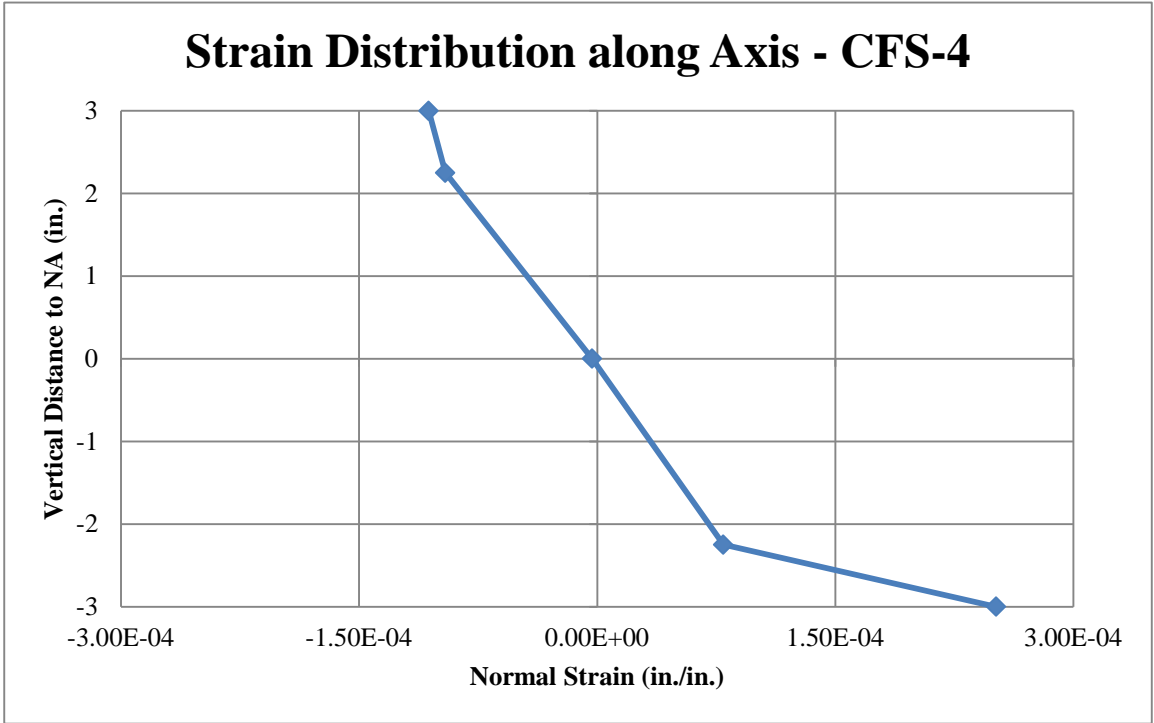


Figure 175. Vertical Distance versus Normal Strain, Test No. CFS-4 [11-in. (279-mm) Span]

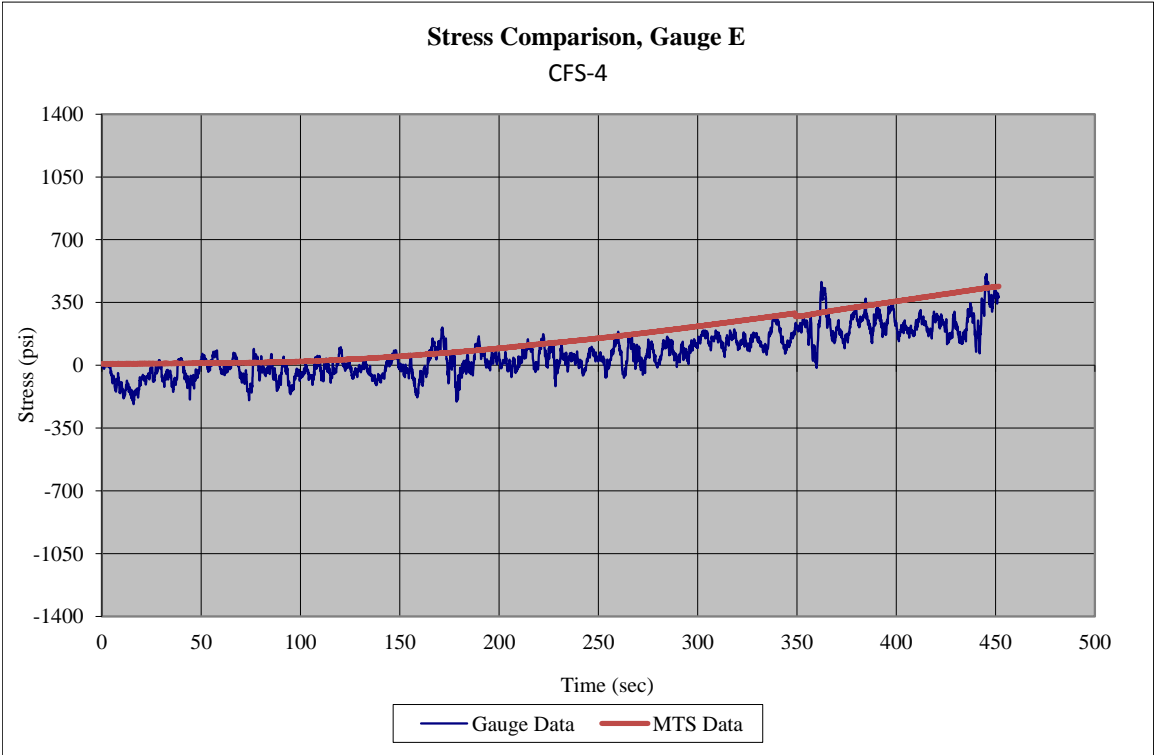
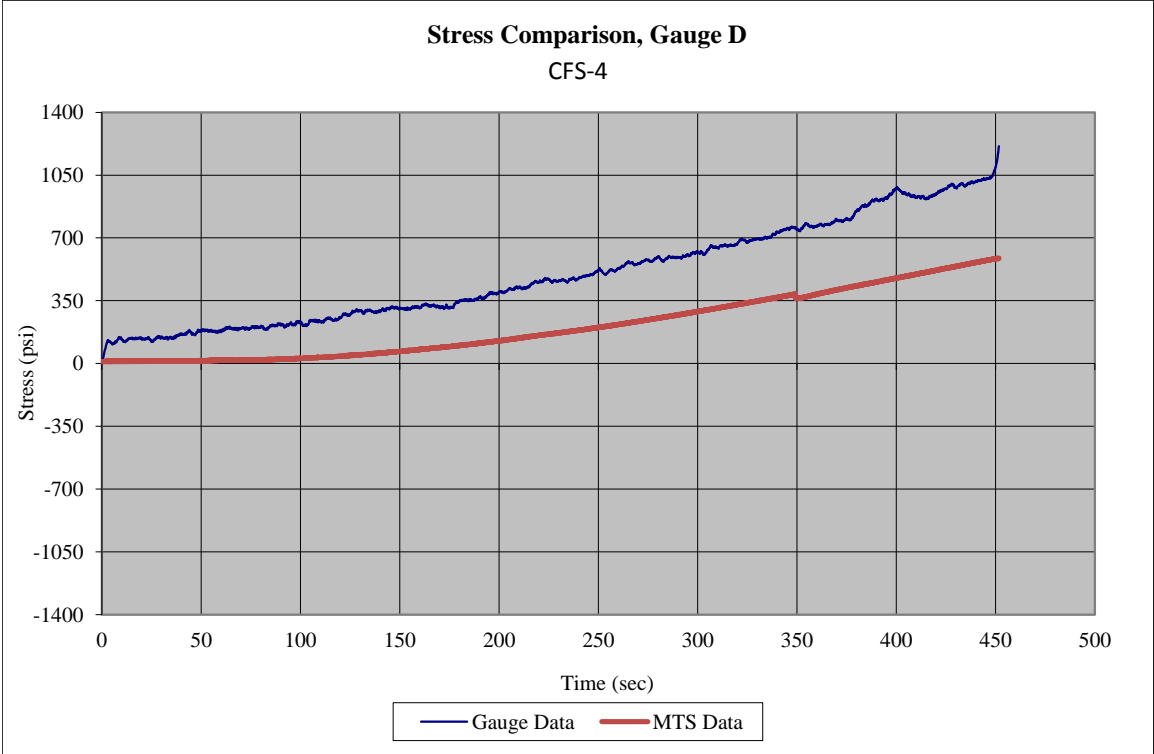


Figure 176. Estimated Midspan Normal Stresses from Bottom Strain Gauges and MTS Load Data, Test No. CFS-4 [11-in. (279-mm) Span]

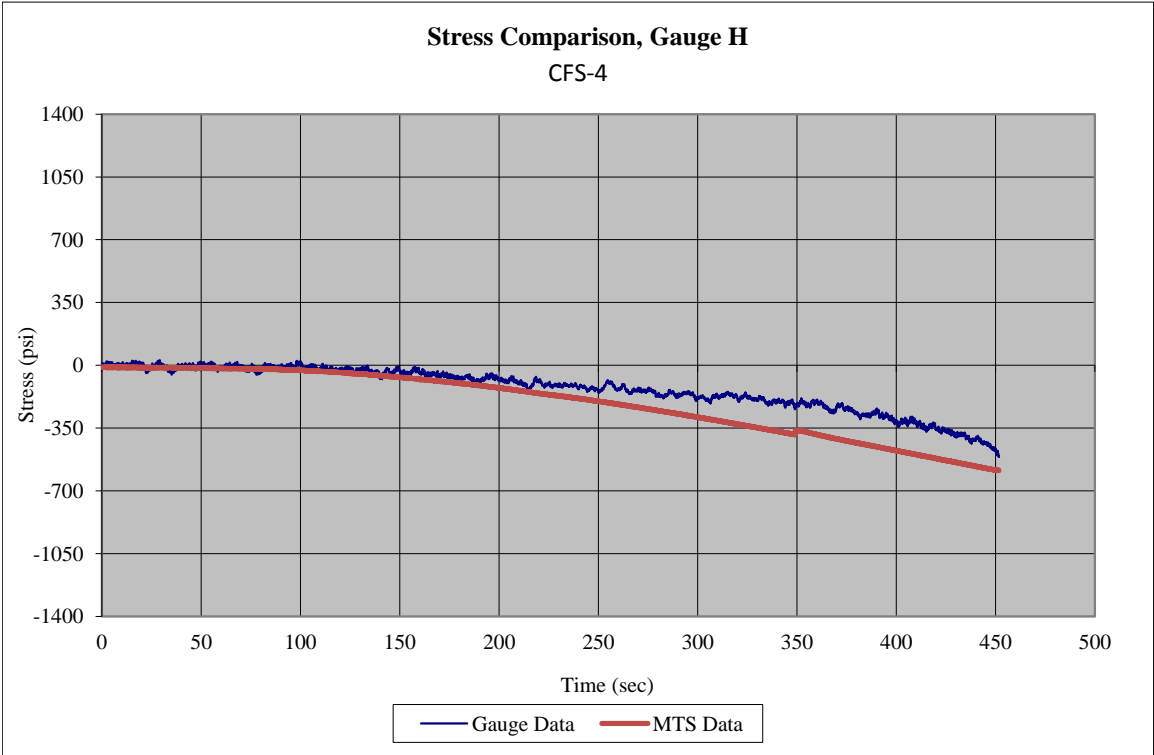
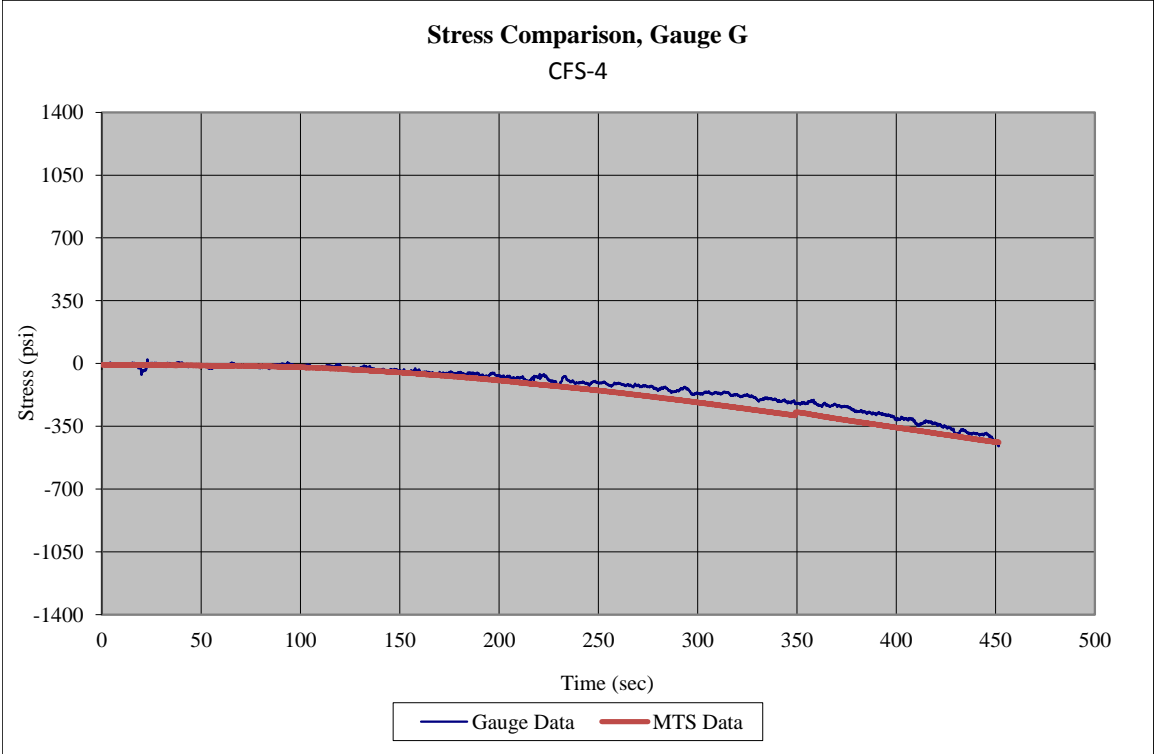


Figure 177. Estimated Midspan Normal Stresses from Top Strain Gauges and MTS Load Data, Test No. CFS-4 [11-in. (279-mm) Span]

Four rosette strain gauges were attached to the front and back faces of the beam near the horizontal centerline and midway between the upper roller and lower support. None of the rosette gauges broke as the curved failure pattern occurred between the upper rollers. Measured strains are provided in Figure 178 and Figure 179 for each rosette and each individual gauge, if acquired. Some rosette strain gauges appeared to perform in an acceptable manner during test no. CFS-4. However, some gauges provided data that may raise questions upon first glance. Based on symmetric loading, the strains would be expected to be very similar across all rosettes. However, this outcome did not appear to always be the case.

First, rosette no. 1 (left-front position facing front) provided negative compressive strain for two gauges (B – diagonal and C – vertical), but positive tensile strain for the third gauge (A – horizontal). Note that the A-gauge was aligned with the positive horizontal beam axis at its geometric centerline. Second, rosette no. 2 (right-front position facing front) provided nearly zero strain for one gauge (B – diagonal). Note that the C-gauge was aligned with the negative horizontal axis. Further, both the horizontal and vertical gauges provided positive tensile and negative compressive strains, respectively, along the 135 degree plane rotated away from the positive x or horizontal beam axis on front face. Third, rosette no. 3 (left-back position facing back) provided nearly zero strain for two gauges (A – horizontal and C – vertical). Note that the A-gauge was aligned with the positive horizontal beam axis at its geometric centerline for the back face. Finally, rosette no. 4 (right-back position facing back) provided nearly zero strain for all gauges (A – vertical, B – diagonal, and C – horizontal). Note that the C-gauge was aligned with the negative horizontal axis.

All strains, gauges A through C, would likely be non-zero for this beam configuration with 11-in. (279-mm) span. However, some gauges did have zero strain throughout. Following a review for all four rosette gauges, it was apparent that none of the strain gauges had similar strain readings for the acquired data channels. First, the horizontal gauges for rosette nos. 1 and 2 provided a positive tensile strain, while the vertical gauges provided a negative compression. The diagonal gauge (B) provided negative compressive strain at rosette nos. 1 and 3 and zero strain at rosette nos. 2 and 4. Thus, less confidence existed with results produced with gauge 2 and 4. Second, the strains in 4A, 4B, and 4C were close to zero strain throughout the event, which was unexpected for this scenario and raise questions regarding the validity of the data. The maximum strain readings are provided in Table 40, and strain versus time is shown graphically in Figure 178 and Figure 179. Plots with an alternative scale, as shown in Figure 180, indicated that there were strains near zero.

Maximum principal and maximum shear strains are summarized in Table 40 for rosette gauges 1 and 3 which had all three gauges acquire and return adequate data. Values ranged from 6.35×10^{-5} in./in. to 2.57×10^{-4} in./in. for the maximum principal strain, ϵ_1 . Values for the minimum principal strain, ϵ_2 , ranged from -9.38×10^{-5} in./in. to -3.98×10^{-4} in./in. The highest maximum shear strain for test no. CFS-4 was 6.54×10^{-4} in./in. Subsequently, Equation 32 and Equation 36 were used to compute the theoretical maximum shear stress and maximum shear strain of 352.4 psi (2.4 MPa) and 1.74×10^{-4} in./in., respectively. A plot of the maximum and minimum principal strain and shear strain from rosette nos. 1 and 3 is shown in Figure 181.

Principal angles are summarized in Figure 182 for rosette nos. 1 through 3. Based on the plot, the principal angles for gauge 1 ranged between 60 and 70 degrees and the principal angles for gauge 3 ranged between 40 and 50 degrees. Results from gauges 1 and 3 would be expected to be similar, between 0 and 90 degrees. The second principal angle, θ_{p2} , was then near 150 degrees for gauge 1 and 140 degrees for gauge 3. Based on these angles, the associated shear angles would be 105 and 15 degrees for gauge 1 and 95 and 5 degrees for gauge 3.

Maximum principal stresses are summarized in Table 40 for all rosettes that had all three gauges acquire and return adequate data. These values were calculated using Equation 30. Values ranged from 179.9 psi (1.2 MPa) to 711.0 psi (4.9 MPa) for the maximum principal stress, σ_1 . Subsequently, these values were compared to the known maximum tensile strength from CFT testing, 407.0 psi (2.8 MPa).

Based on the analysis provided above, it appears that only rosette no. 3 provided reliable data for full-strain field analysis. Rosette no. 1 had a maximum principal stress that exceeded the known maximum tensile strength from CFT testing. Rosette no. 2 had a gauge with zero strain and the principal angle was 90 degrees from the expected value. Rosette no. 4 had zero strains for all three gauges and its principal angle was not constant.

The final piece of instrumentation was the string potentiometers. As in previous tests, questions arose regarding the accuracy of the resulting displacement data after comparison to displacements determined with Equation 20 and Equation 21, as well as the actuator movement over the same period. The theoretical equations tended to provide lower displacements than measured, while the actuator displacement data was generally higher than measured with the string potentiometer. It was somewhat difficult to

determine with string potentiometers which results may have inaccuracies due to instrumentation placement, data resolution, etc. could be trusted. As such, the displacement data and results are not included in this section. String potentiometer and actuator data are found in Appendix D.

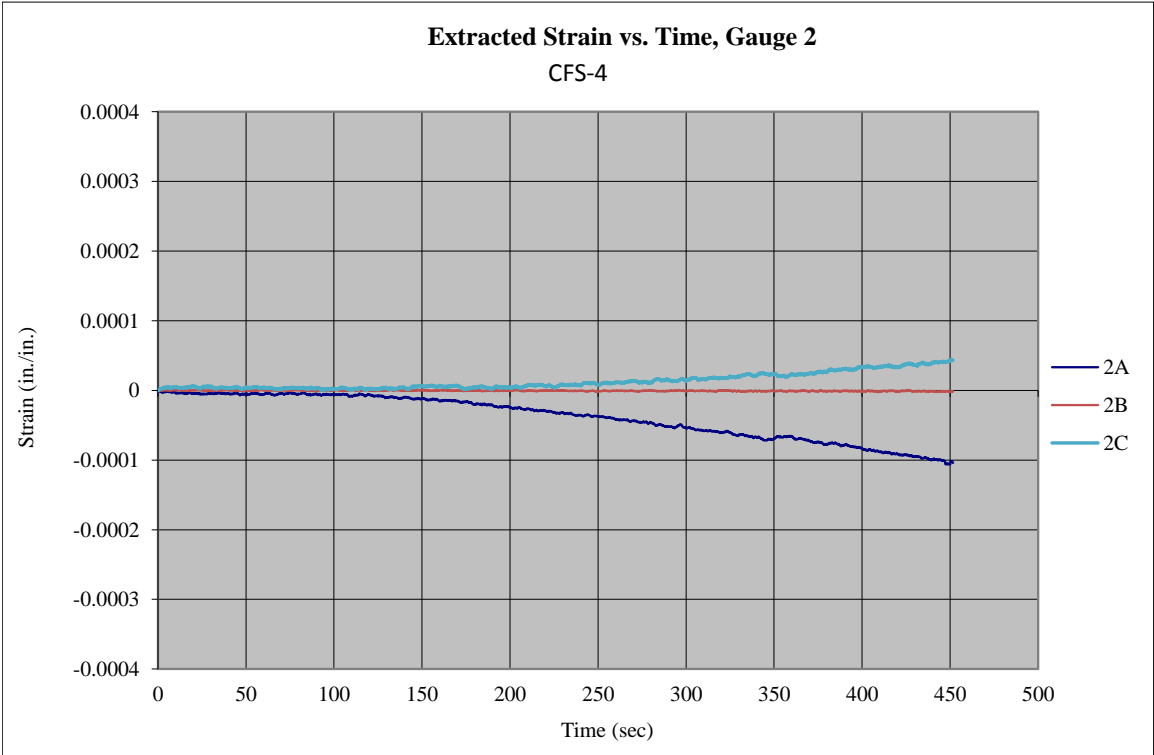
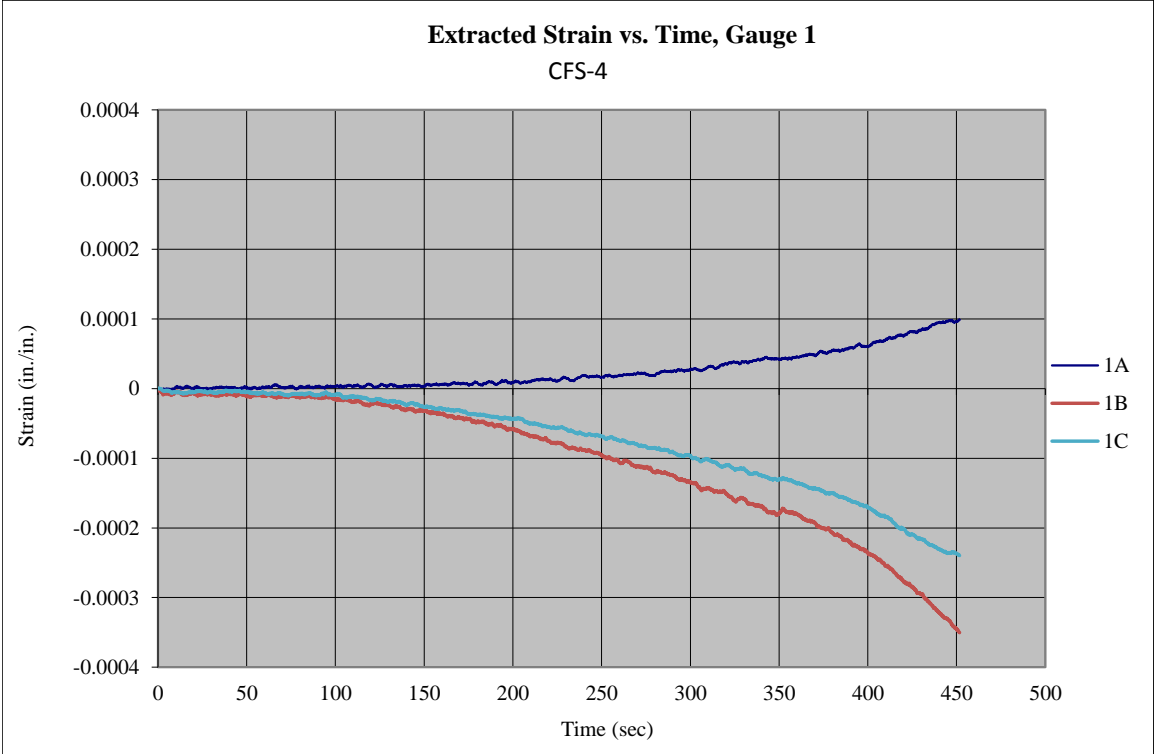


Figure 178. Extracted Strain Plots for Rosette Strain Gauges 1 and 2, Test No. CFS-4 [10-in. (254-mm) Span]

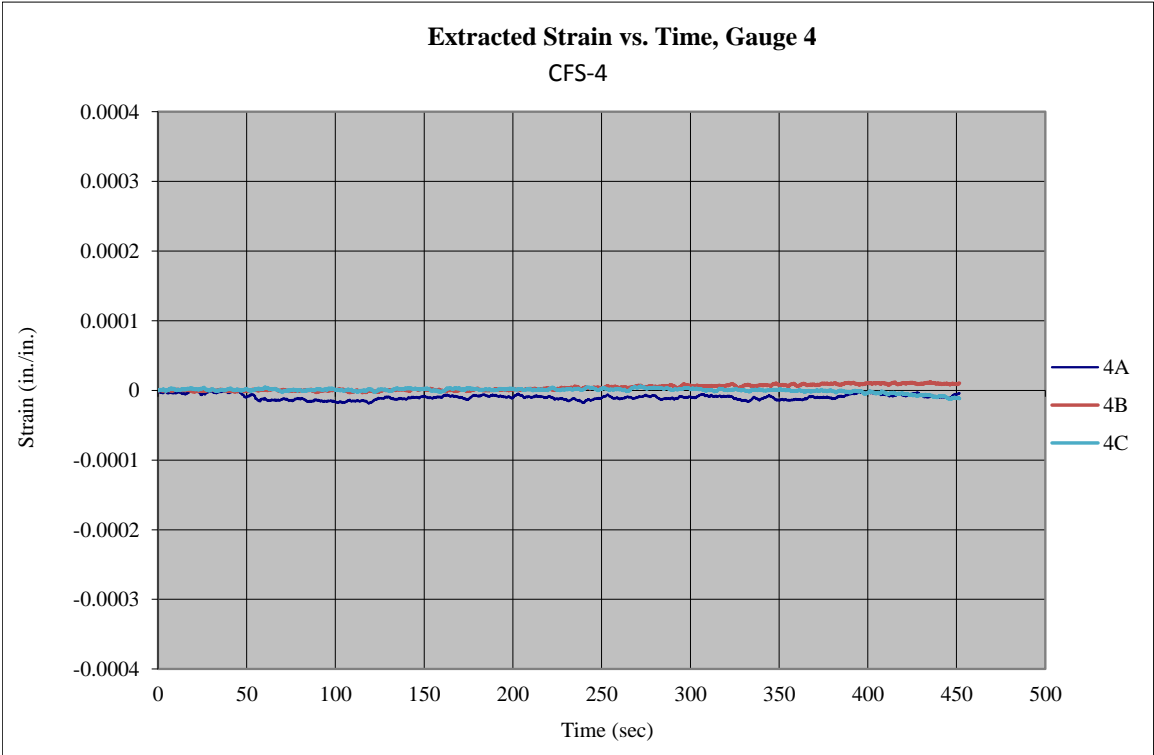
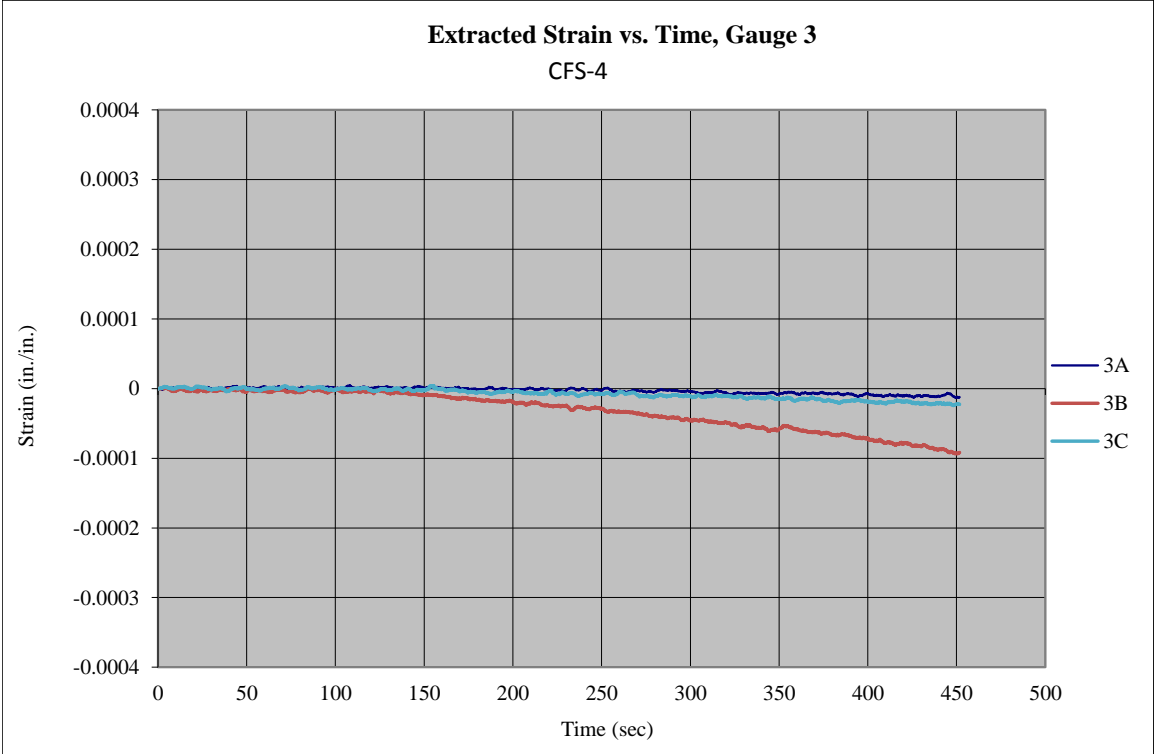


Figure 179. Extracted Strain Plots for Rosette Strain Gauges 3 and 4, Test No. CFS-4 [11-in. (279-mm) Span]

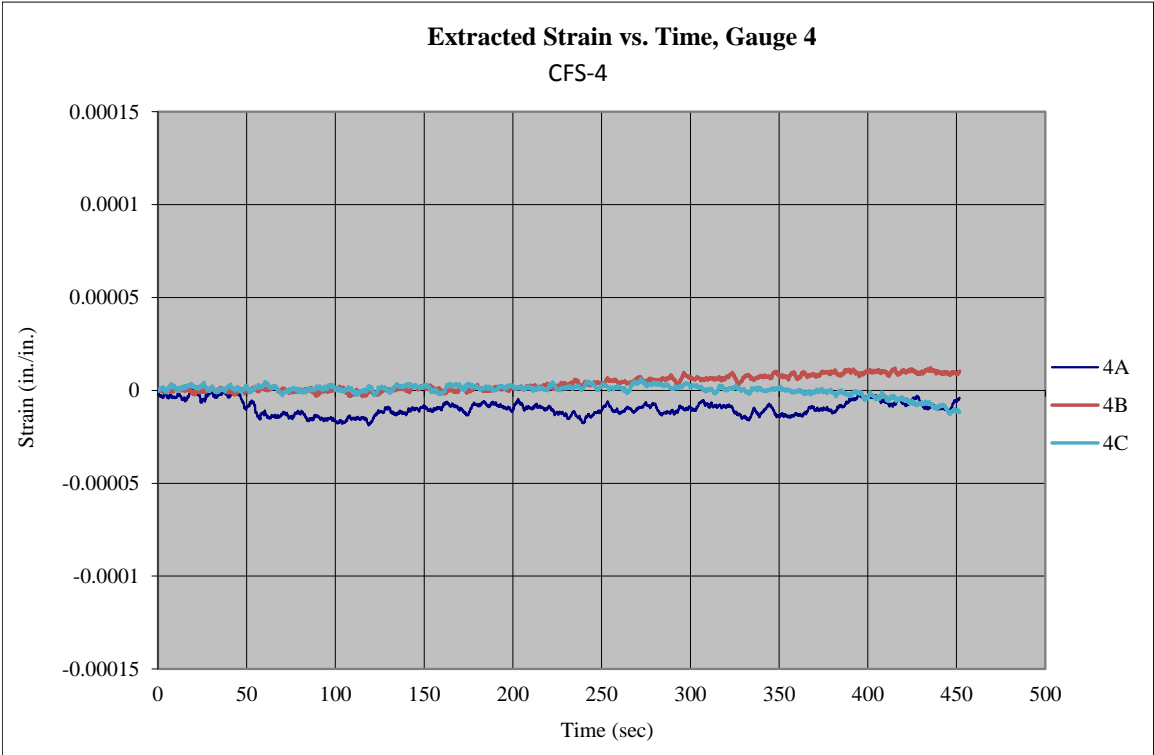
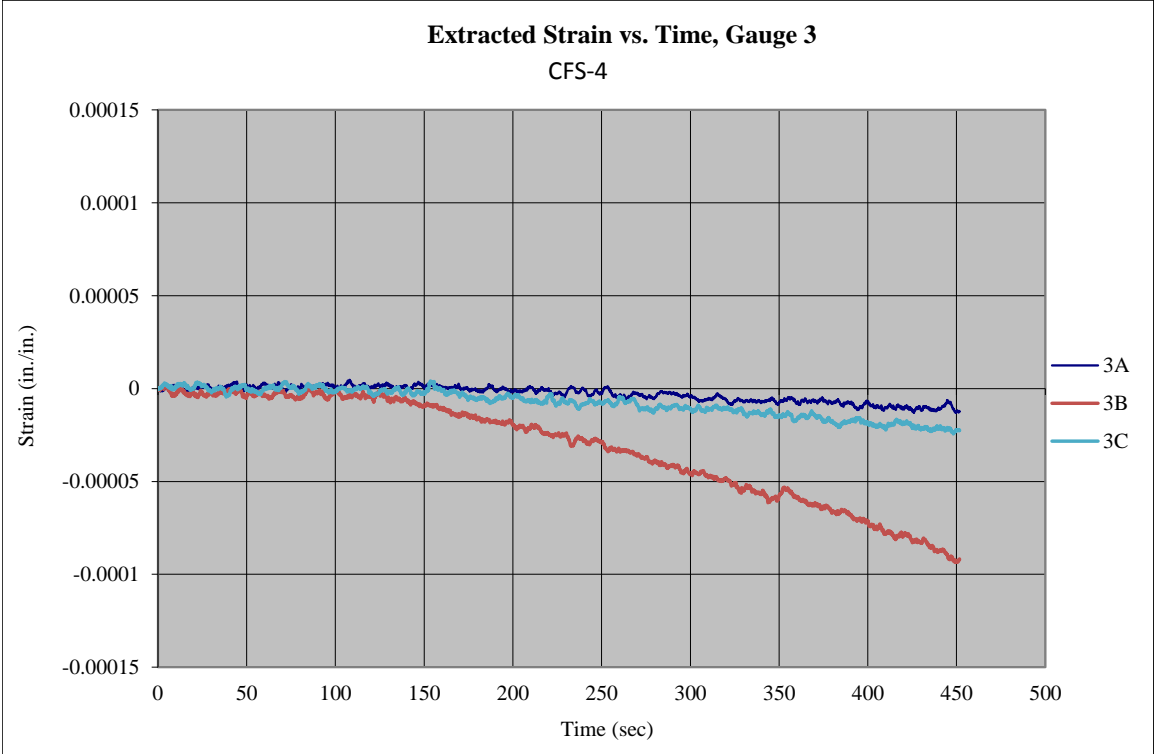


Figure 180. Extracted Strain Plots for Rosette Strain Gauges 3 and 4 with Alternative Scale, Test No. CFS-4 [11-in. (279-mm) Span]

Table 40. Summary of Stress and Strains for Rosette Gauges, Test No. CFS-4

Rosette Gauge	Normal Strain, ϵ_x , @ Failure <i>in./in.</i>	Estimated Max./Min. Principal Strain (Eqs. 27 & 28)		Estimated Max./Min. Principal Stress (Eqs. 30 & 31)		Estimated γ_{max} (Eq. 29) <i>in./in.</i>	Estimated τ_{max} (Eq. 32) <i>psi</i>	Estimated τ_{max} (Eq. 37) <i>psi</i>	Estimated Principal Angles, θ_{1p} & θ_{2p} (Eq. 34 & 35) <i>degrees</i>	Estimated Shear Angles, θ_{1s} & θ_{2s} (Eq. 36) <i>degrees</i>
		ϵ_1 <i>in./in.</i>	ϵ_2 <i>in./in.</i>	σ_1 <i>psi</i>	σ_2 <i>psi</i>					
1	1A	9.88E-05								
	1B	-3.50E-04	-3.98E-04	711.0	-1363.5	6.54E-04	1035.9	352.4	60, 150	105, 15
	1C	-2.40E-04								
2	2A	-1.04E-04								
	2B	-1.54E-06	-	-	-	-	-	-	-	-
	2C	4.33E-05								
3	3A	-1.24E-05								
	3B	-9.17E-05	-9.38E-05	179.9	-323.1	1.56E-04	246.3	352.4	50, 140	95, 5
	3C	-2.26E-05								
4	4A	-4.04E-06								
	4B	1.04E-05	-	-	-	-	-	-	-	-
	4C	-1.17E-05								

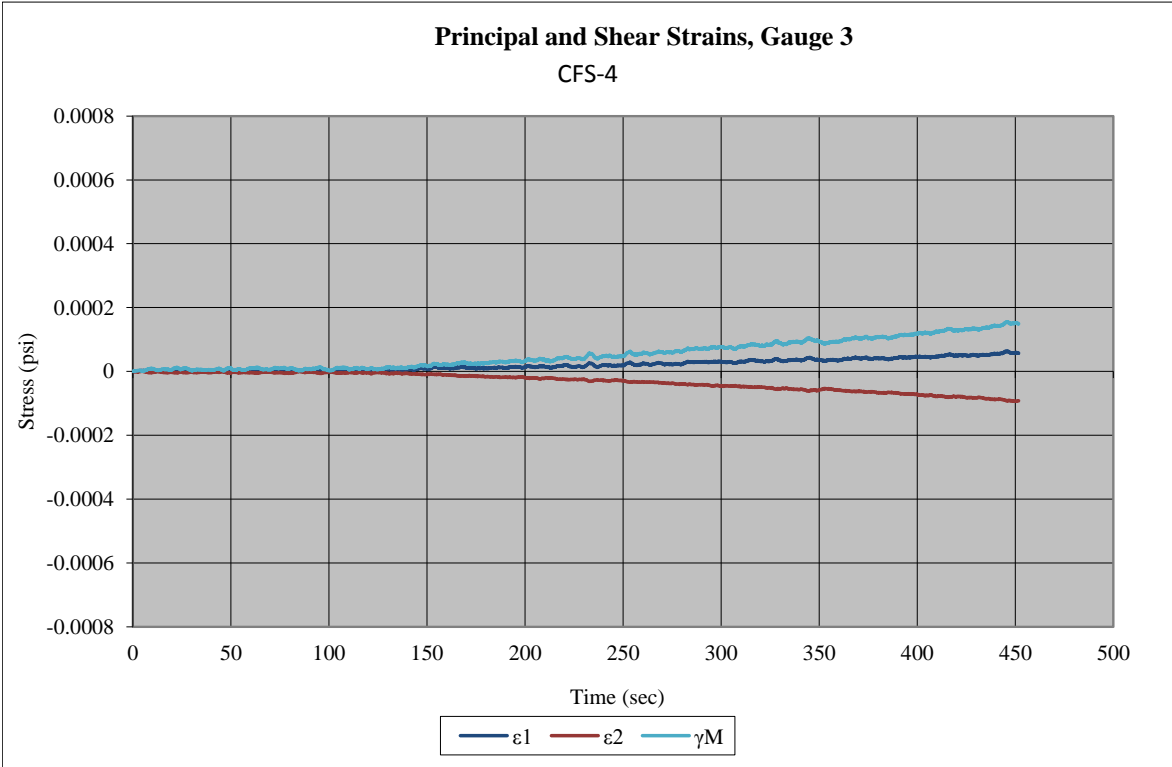
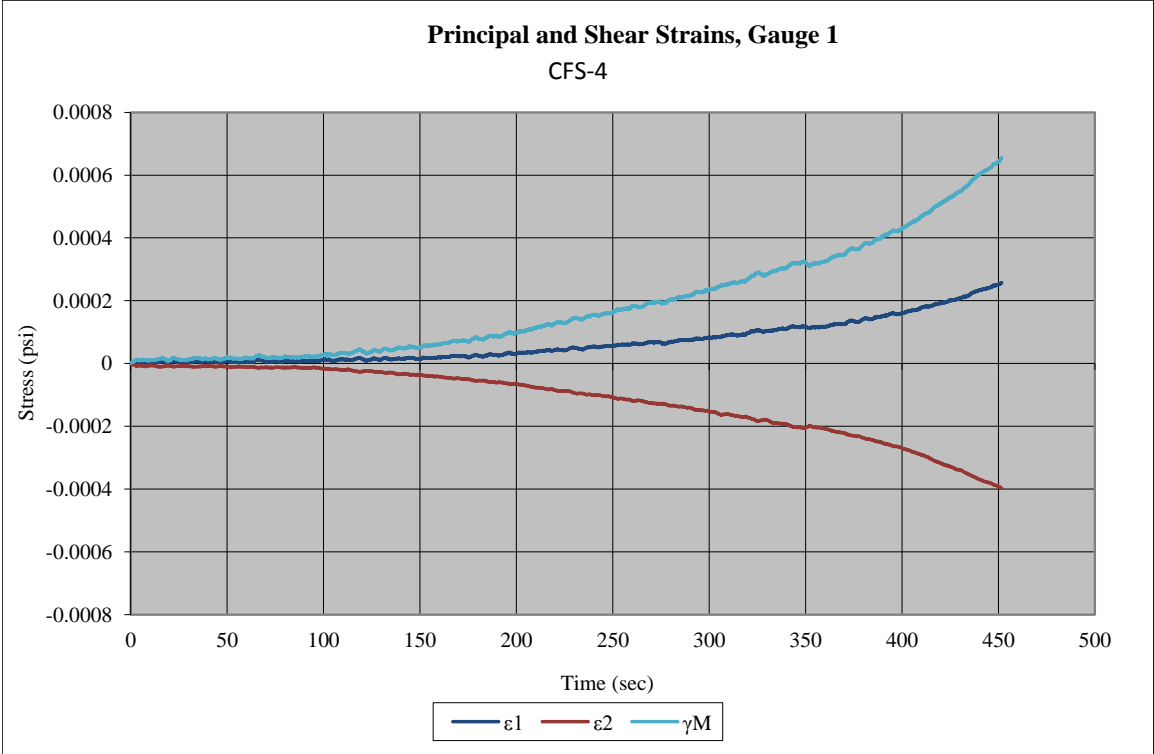


Figure 181. Principal Strains for Gauges 1 and 3, Test No. CFS-4 [10-in. (254-mm) Span]

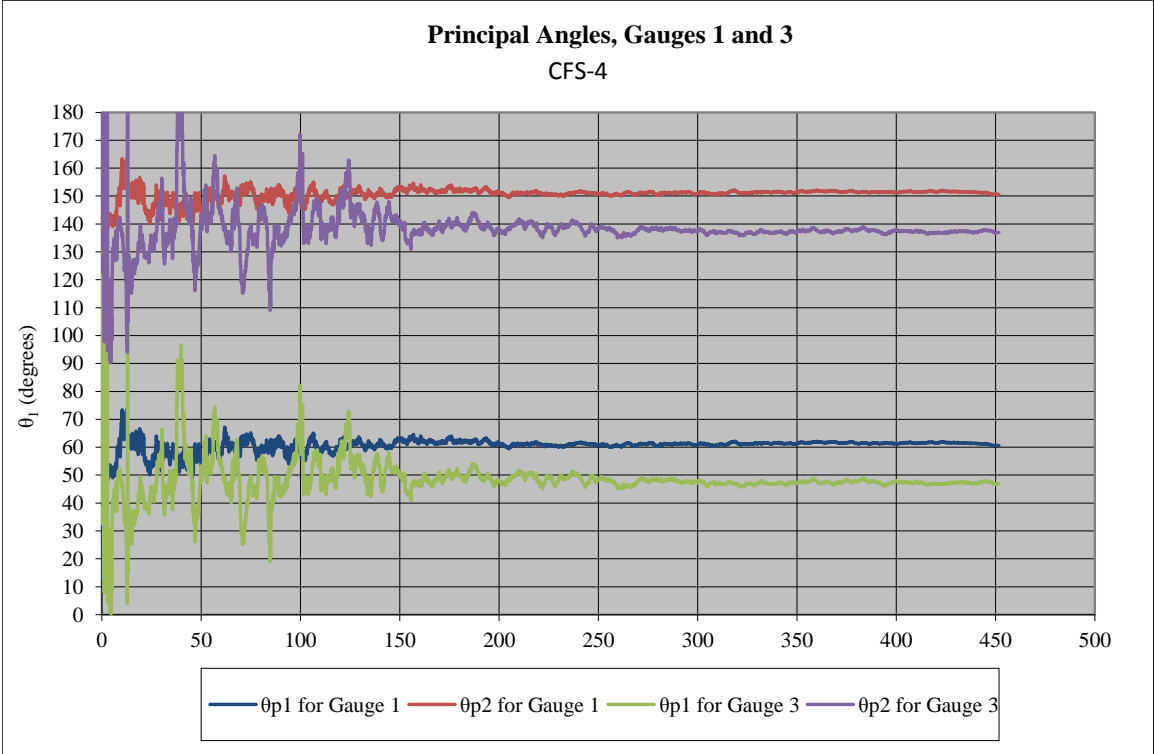


Figure 182. Principal Angles for Test No. CFS-4 [11-in. (279-mm) Span]

12.7 Test No. CFS-5 [Support Span – 10 in. (254 mm)]

For test no. CFS-5, a span length of 10 in. (254 mm) was repeated. A shear failure was expected to occur with this configuration. The test setup is shown in Figure 183.

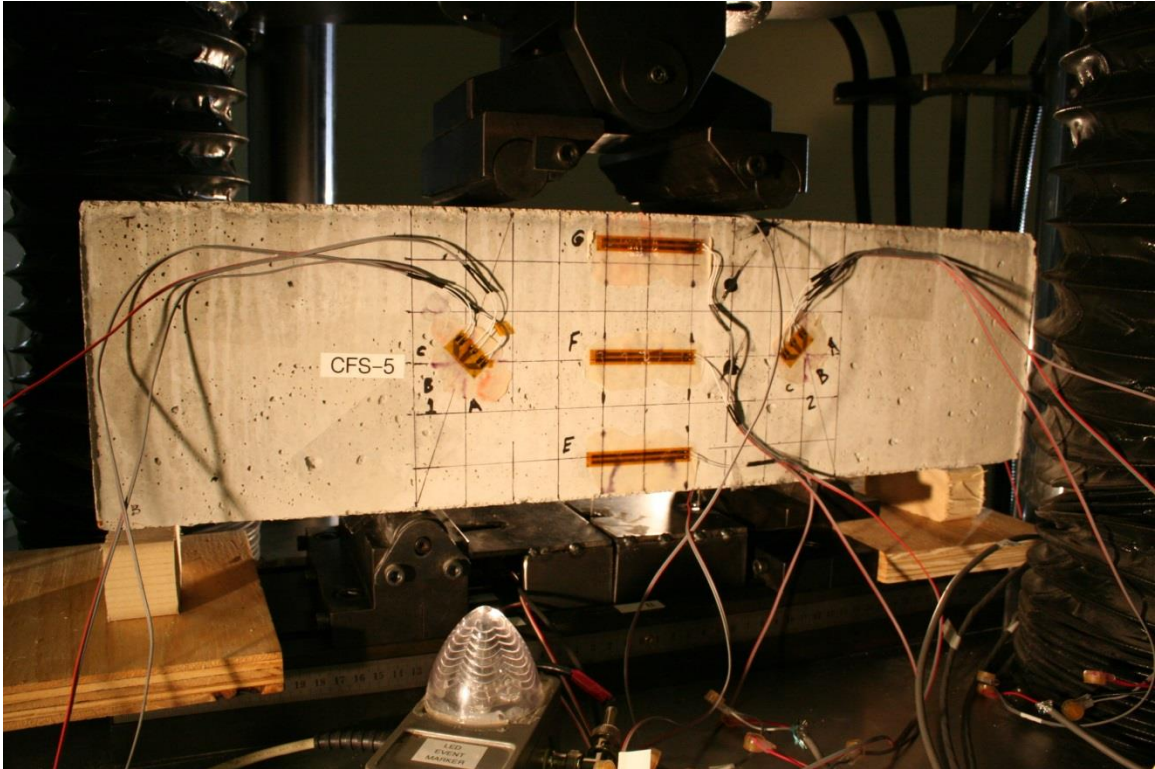


Figure 183. Test Setup for Test No. CFS-5 [10-in. (254-mm) Span]

As the MTS Criterion testing machine loaded the specimen during test no. CFS-5, the specimen failed in flexure due to excessive tensile stresses at the bottom surface and between the upper roller locations. Specifically, the vertical fracture plane occurred 1.0 in. (25 mm) right of the vertical centerline of the beam. A peak load of 19.0 kip (84.5 kN) was measured when the specimen fractured. Thus, each upper roller was assumed to transfer a peak load equal to 9.5 kip (42.3 kN) to the top of the beam, thus resulting in a reaction at both lower supports equal to 9.5 kip (42.3 kN). The load versus time plot is shown in Figure 184, and post-test photographs are shown in Figure 185 and Figure 186.

All horizontal strain gauges that were placed at the vertical centerline of the beam appeared to have acquired data during test no. CFS-5. In addition, one of the horizontal strain gauges between rollers broke as the flexural failure occurred near the vertical centerline of the beam. The strain readings revealed maximum negative (compression) and maximum positive (tension) normal strains of -5.46×10^{-5} in./in. (top) and 1.07×10^{-4} in./in. (bottom), respectively, as shown in Table 41 and Figure 187. Horizontal normal strain at the top of the beam appeared to be very small, creating a non-linear strain distribution. In addition, the strain at gauge G was larger than the strain at gauge H. As depicted in Figure 188, normal strains were plotted in the direction of the horizontal beam axis for each vertical gauge position [0 in. (beam centerline), $\pm 2\frac{1}{4}$ in. (57 mm) (upper and lower side gauges), and ± 3 in. (76 mm) (top and bottom gauges)]. Finally, the middle strain gauge revealed strains which that were larger than zero for the duration of the test, reaching a maximum of -1.61×10^{-5} in./in. Based on the measured difference between the top and bottom gauges, the horizontal strain readings raised some concerns.

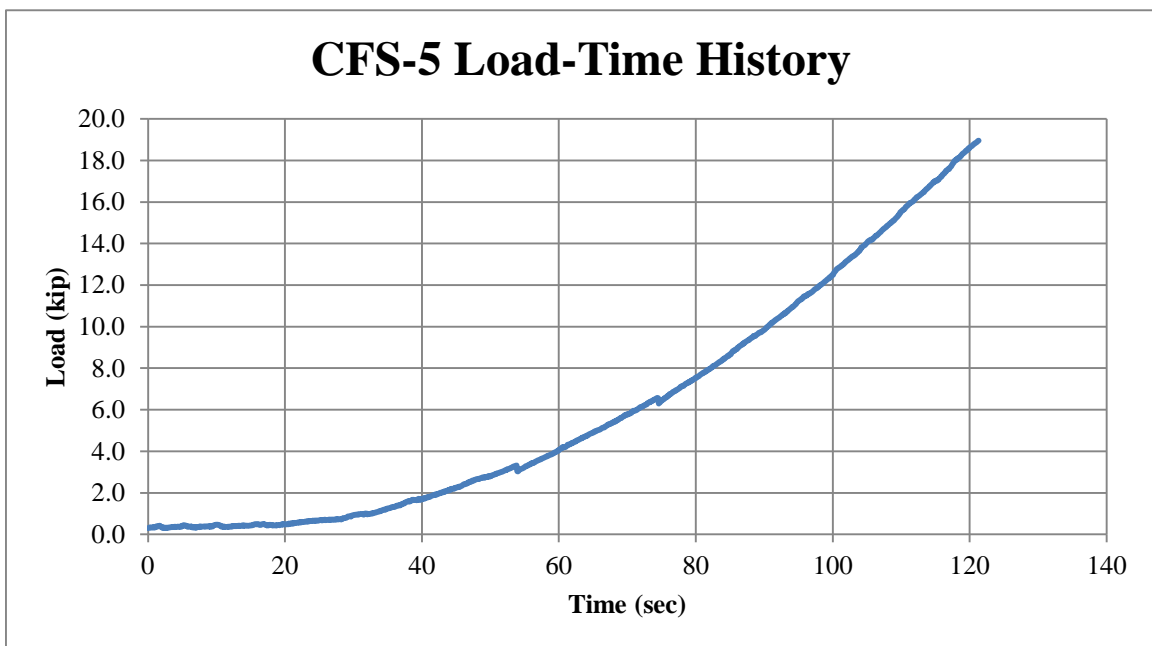


Figure 184. Load vs. Time, Test No. CFS-5 [10-in. (254-mm) Span]

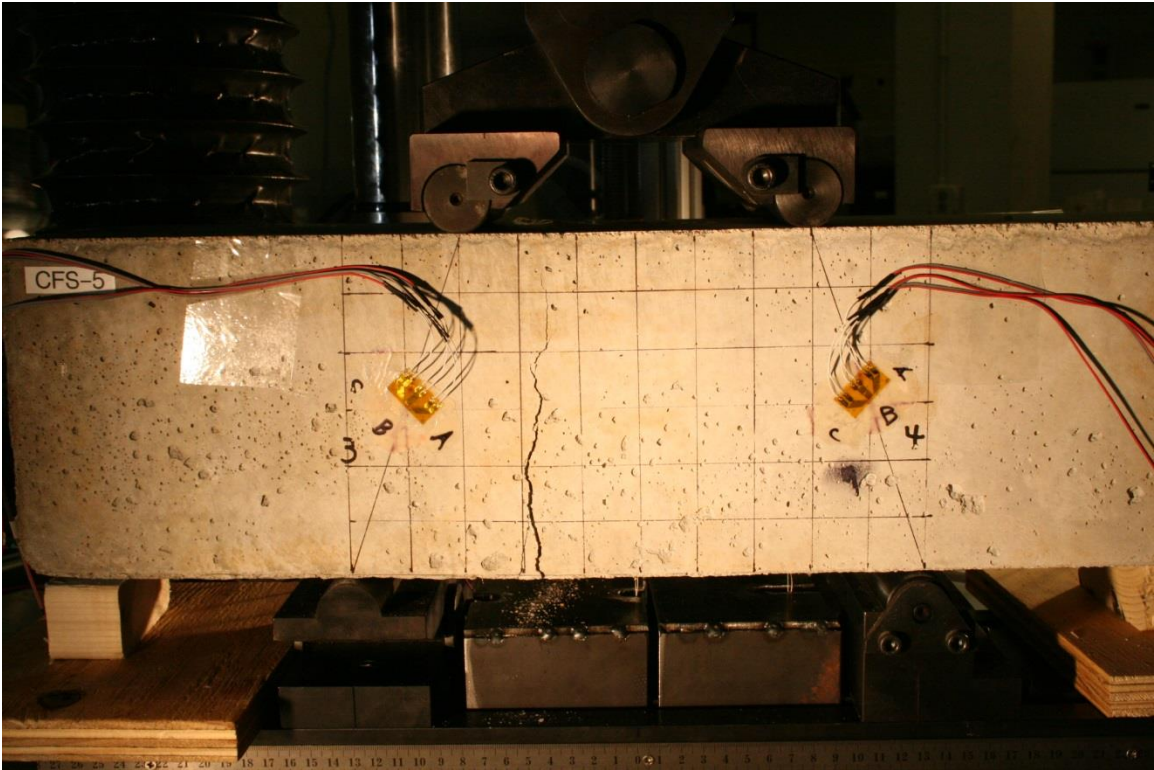
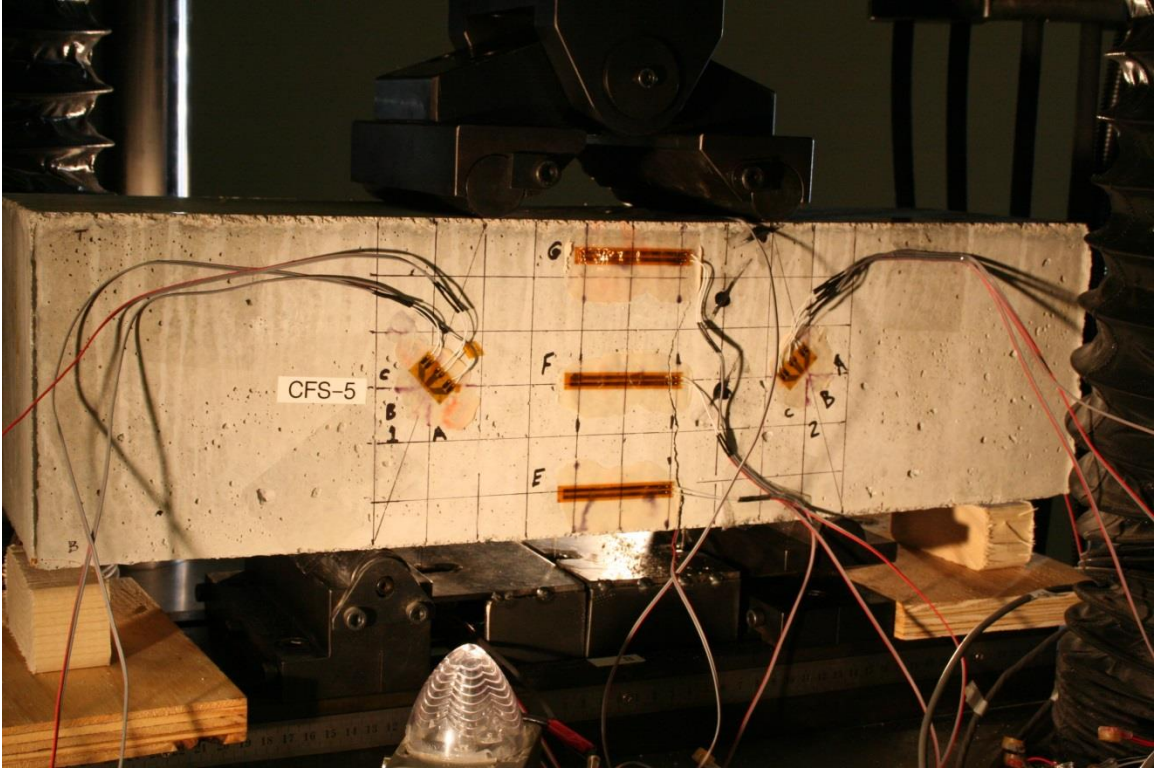


Figure 185. Post-Test Damage, Test No. CFS-5 [10-in. (254-mm) Span]

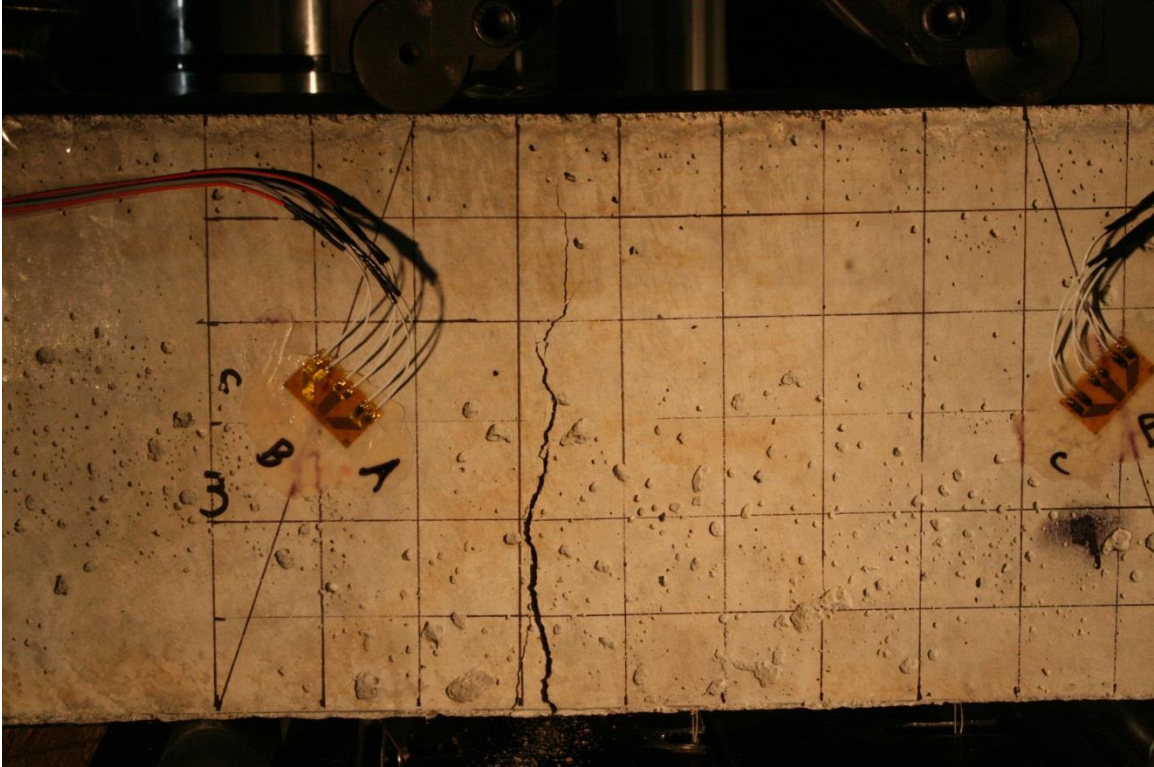


Figure 186. Additional Post-Test Damage, Test No. CFS-5 [10-in. (254-mm) Span]

Table 41. Normal Strain and Stress Distribution for Horizontal Gauges, Test No. CFS-5

Gauge Designation and Location	Normal Strain, ϵ_x, @ Failure <i>in./in.</i>	Estimated Maximum Normal Stress (Eq. 22) <i>psi</i>	Estimated Maximum Normal Stress (Eq. 23) <i>psi</i>
D (bottom)	1.07E-04	515.6	526.5
E	7.33E-05	353.2	394.9
F (middle)	-1.61E-05	-77.7	0.0
G	-5.46E-05	-262.8	-394.9
H (top)	-4.04E-05	-194.4	-526.5

Once the normal strains were processed, analyzed, and reviewed, an estimate was made to determine the maximum normal stress, $\sigma_{x,max}$, based on measured strains using Equation 22. The normal stress distribution was also estimated using strain readings at the upper and lower side positions. The maximum normal stress for each strain gauge is shown in Table 41, while the normal stress for four gauges as a function of time is provided in Figure 189 and Figure 190. An estimate was also made to determine the maximum normal stress, $\sigma_{bending,max}$, using the MTS load data and Equation 23. The maximum normal stress based on MTS load data and elastic bending is depicted in Table 41 for the top and bottom surfaces. Further, the normal stress corresponding to the other gauge locations was also calculated with MTS load data and provided in Table 41. The normal stress as a function of time and using MTS load data is shown graphically in Figure 189 and Figure 190. When comparing the normal stresses using the two methods, it is apparent that similar trends were not predicted during the test duration. The estimated normal stress based on MTS load data exceeded the prediction using the strain readings for the top and bottom gauges. The maximum midspan normal stress was \pm 526.5 psi (3.6 MPa) for the MTS load data and calculated moments, while the maximum

midspan normal stresses were +515.6 psi/-262.8 psi (+3.6 MPa/-1.8 MPa) using the strain data. More investigation is needed to explore these differences, including any assumptions and limitations.

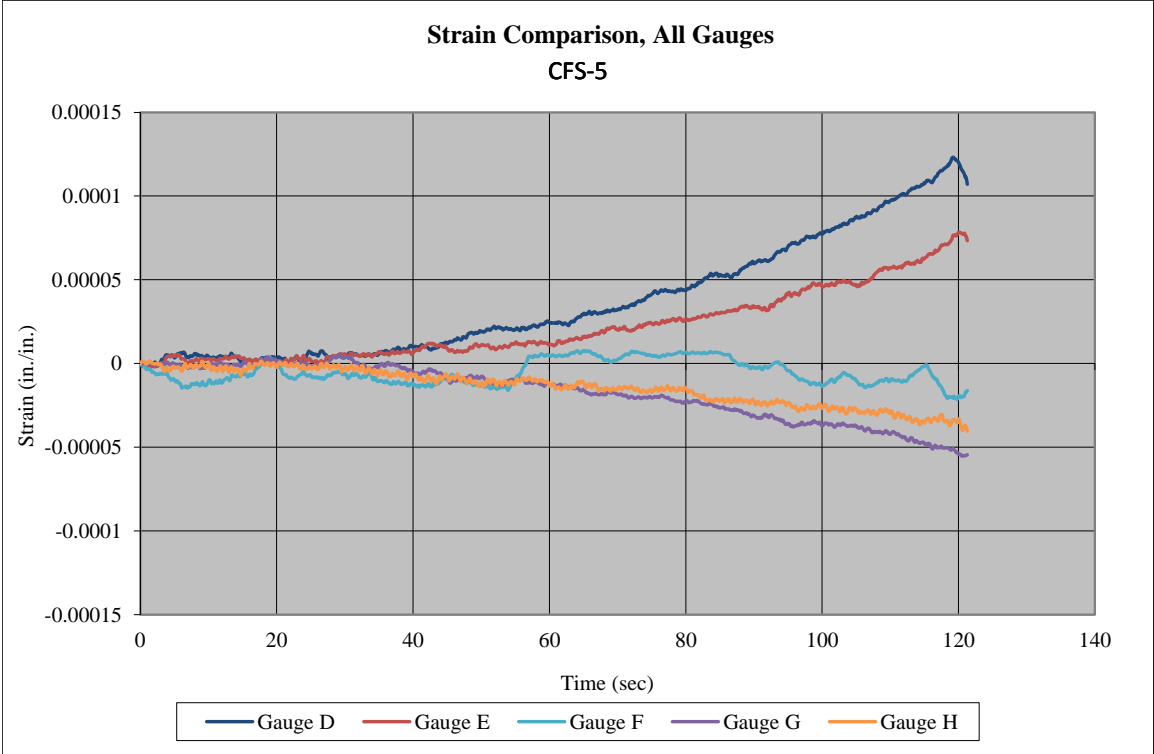


Figure 187. Normal Strains for Top, Side, and Bottom Gauges, Test No. CFS-5 [10-in. (254-mm) Span]

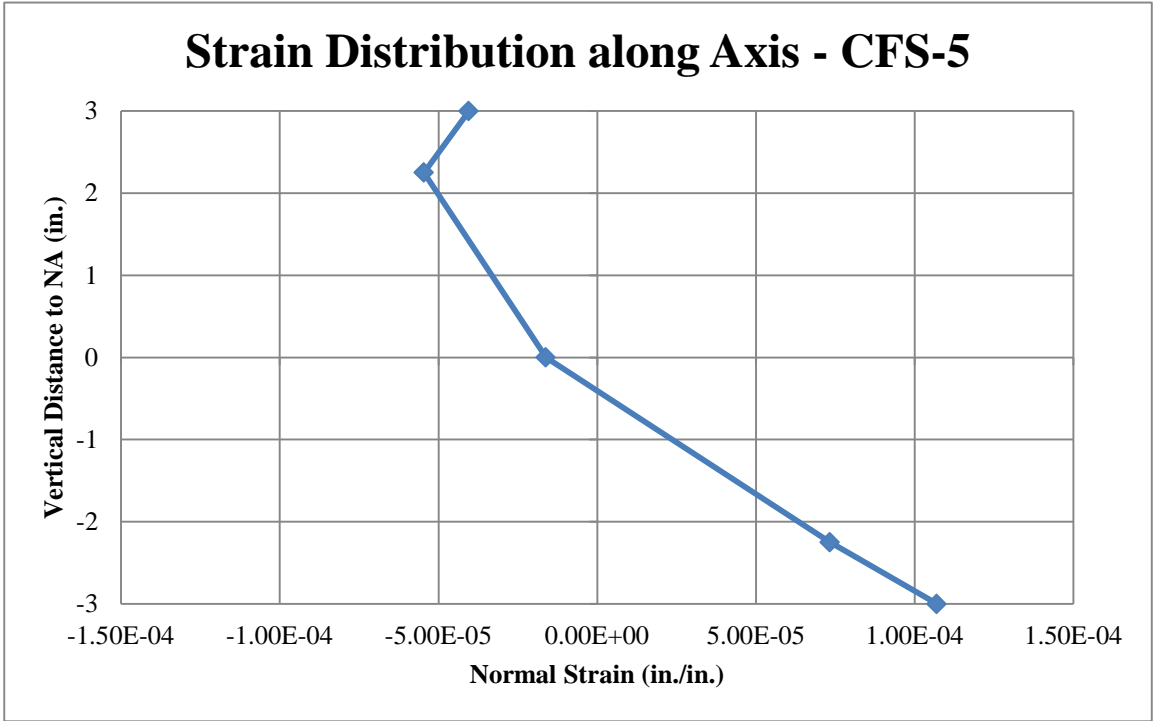


Figure 188. Vertical Distance versus Normal Strain, Test No. CFS-5 [10-in. (254-mm) Span]

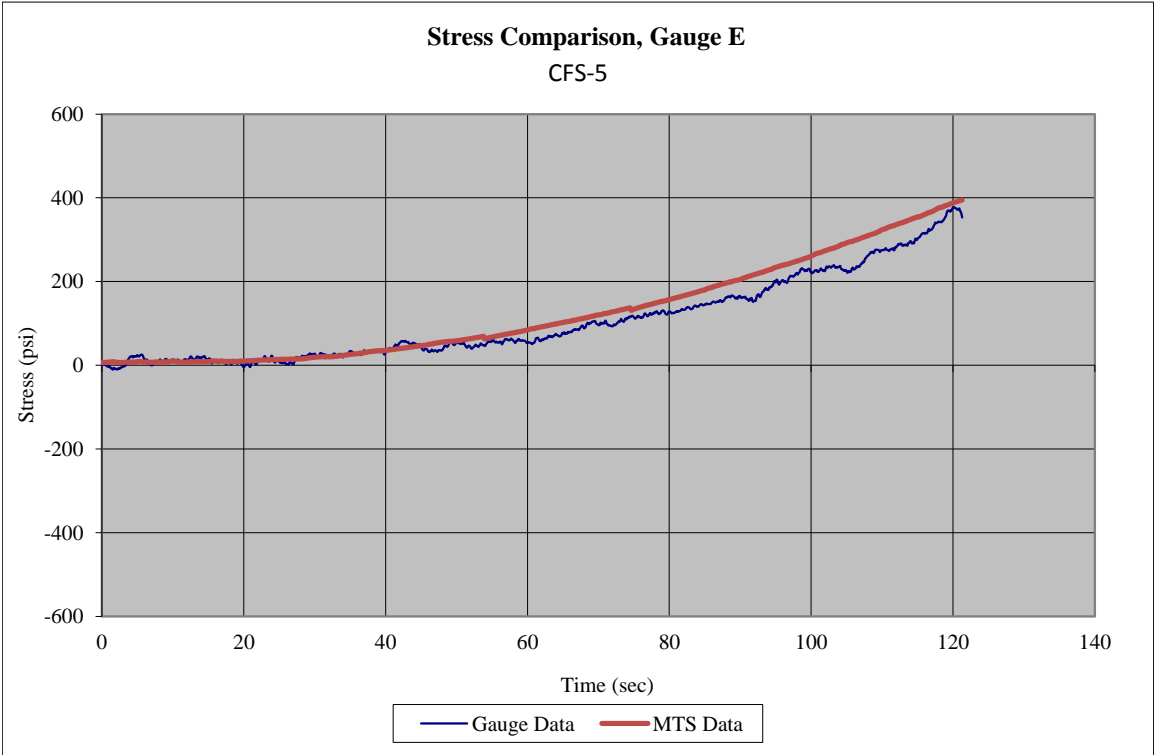
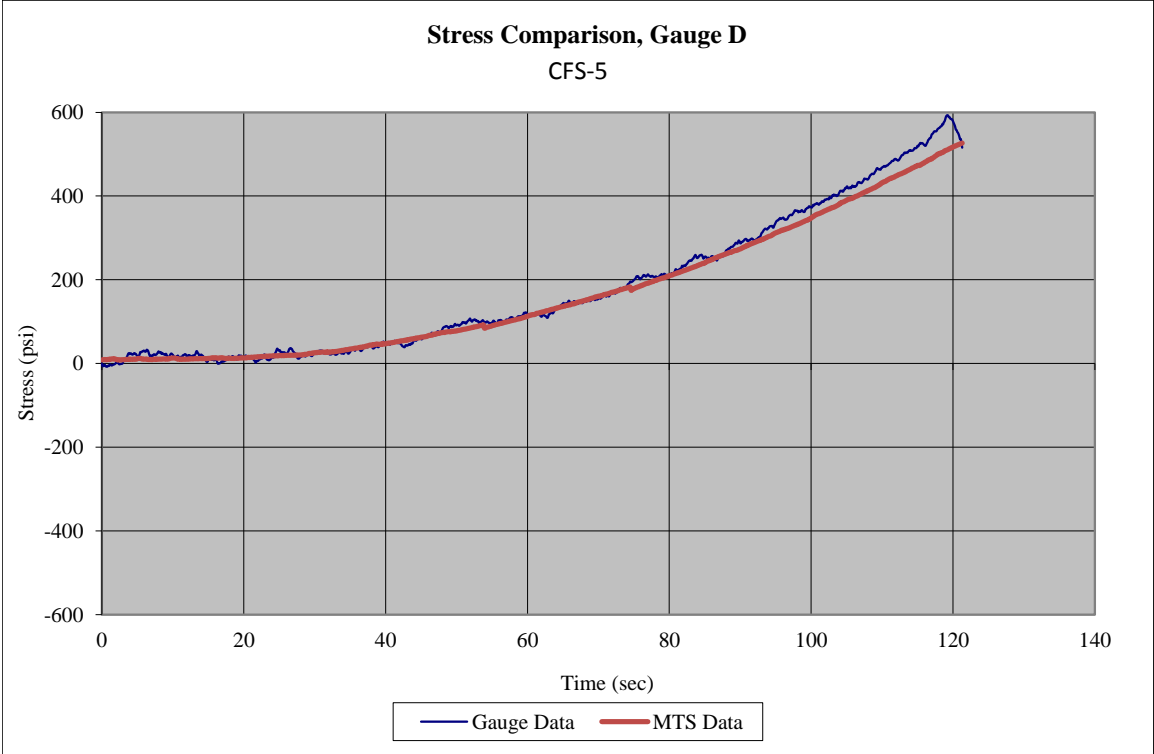


Figure 189. Estimated Midspan Normal Stresses from Bottom Strain Gauges and MTS Load Data, Test No. CFS-5 [10-in. (254-mm) Span]

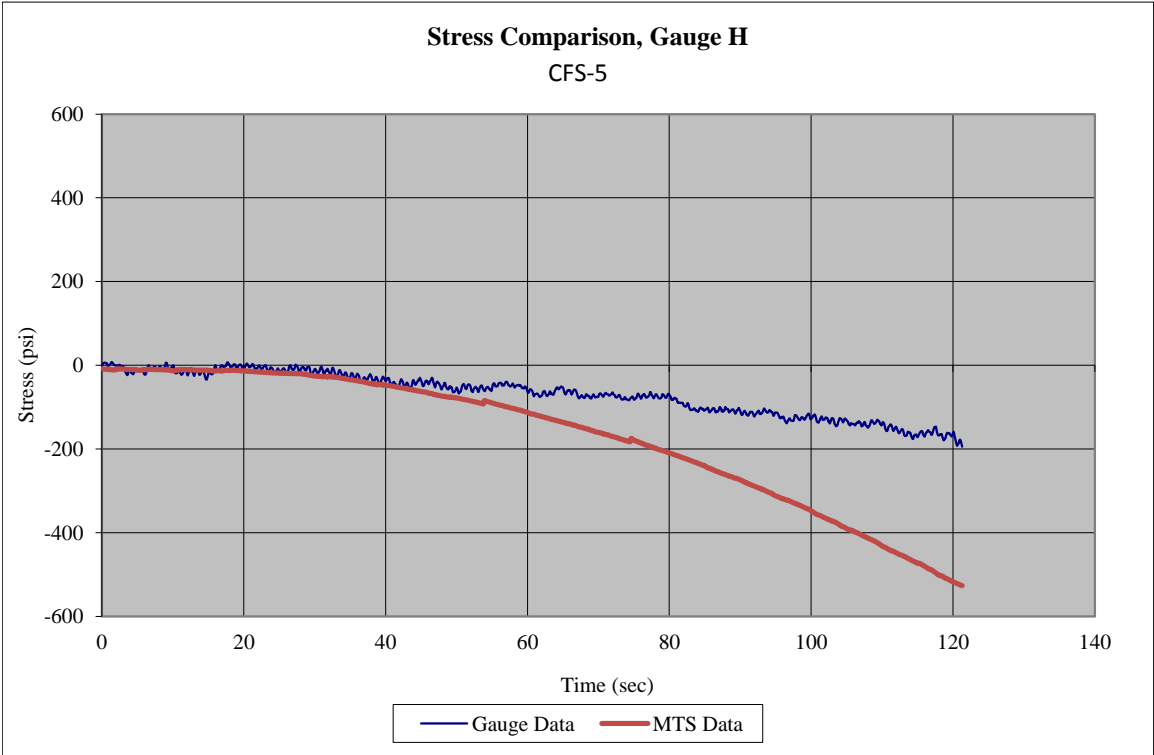
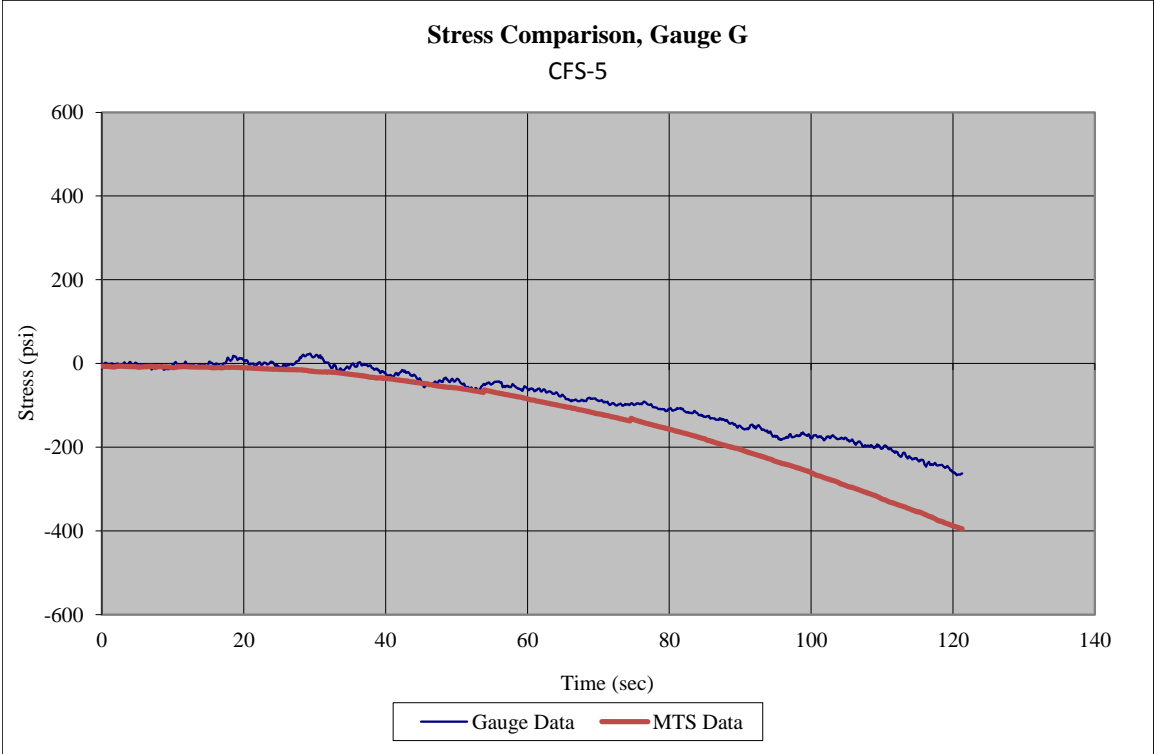


Figure 190. Estimated Midspan Normal Stresses from Top Strain Gauges and MTS Load Data, Test No. CFS-5 [10-in. (254-mm) Span]

Four rosette strain gauges were attached to the front and back faces of the beam near the horizontal centerline and midway between the upper roller and lower support. None of the rosette gauges broke as the flexural failure occurred near the vertical centerline of the beam. Measured strains are provided in Figure 191 and Figure 192 for each rosette and each individual gauge, if acquired. Some rosette strain gauges appeared to perform in an acceptable manner during test no. CFS-5. However, some gauges have provided data that may raise questions upon first glance. Based on symmetric loading, the strains would be expected to be very similar across all rosettes. However, this outcome did not appear to always be the case.

First, rosette no. 1 (left-front position facing front) provided negative compressive strain for two gauges (B – diagonal and C – vertical), but positive tensile strain for the third gauge (A – horizontal). Note that the A-gauge was aligned with the positive horizontal beam axis at its geometric centerline. Second, rosette no. 2 (right-front position facing front) provided negative compressive strain for two gauges (A – vertical and B – diagonal), but positive tensile strain for the third gauge (C – horizontal). Note that the C-gauge was aligned with the negative horizontal axis. Third, rosette no. 3 (left-back position facing back) provided nearly zero strain for one gauge (B – diagonal). Further, both the horizontal (A) and vertical (C) gauges provided positive tensile and negative compressive strains, respectively. Note that the A-gauge was aligned with the positive horizontal beam axis at its geometric centerline for the back face. Finally, rosette no. 4 (right-back position facing back) provided negative compressive strain for two gauges (A – vertical and B – diagonal) and positive tensile strain for the third gauge (C – horizontal). Note that the C-gauge was aligned with the negative horizontal axis.

All strains, gauges A through C, would likely be non-zero for this beam configuration with 10-in. (254-mm) span. However, one gauge, 3B, did have zero strain throughout. Following a review for all four rosette gauges, it was apparent that none of the strain gauges had similar strain readings for the acquired data channels. First, the horizontal gauges for all rosettes provided a positive tensile strain, while the vertical gauges provided negative compression strain. The diagonal gauge (B) provided negative compressive strain at rosette no. 1, 2, and 4 and zero strain at rosette no. 3. Thus, less confidence existed with results produced with gauge 3. The maximum strain readings are provided in Table 42, and strain versus time is shown graphically in Figure 191 and Figure 192.

Maximum principal and maximum shear strains are summarized in Table 42 for rosette gauges 2 and 4. Values ranged from 5.29×10^{-5} in./in. to 8.63×10^{-5} in./in. for the maximum principal strain, ϵ_1 . Values for the minimum principal strain, ϵ_2 , ranged from -8.84×10^{-5} in./in. to -1.56×10^{-4} in./in. The highest maximum shear strain for test no. CFS-5 was 2.42×10^{-4} in./in. Subsequently, Equation 32 and Equation 36 were used to compute the theoretical maximum shear stress and maximum shear strain of 394.9 psi (2.7 MPa) and 1.95×10^{-4} in./in., respectively. All rosettes provided a good match of strain. A plot of the maximum and minimum principal strain and shear strain from rosette gauges 2 and 4 are shown in Figure 193.

Principal angles are summarized in Figure 194 for rosette nos. 2 and 4. Based on the plot, the first principal angle for gauge 2 ranged between 110 and 120 degrees and the principal angle for gauge 4 ranged between 110 and 120 degrees. The principal angles for gauge 2 and 4 were confirmed as these values were expected to be between 90 and 180

degrees. The second principal angle, θ_{p2} , was then near 20 degrees for gauge 2 and 25 degrees for gauge 4. Based on these angles, the associated shear angles would be 155 and 65 degrees for gauge 2 and 160 and 70 degrees for gauge 4.

Maximum principal stresses are summarized in Table 42 for rosette gauges 2 and 4. These values were calculated using Equation 30. Values ranged from 141.0 psi (1.0 MPa) to 226.9 psi (1.6 MPa) for the maximum principal stress, σ_1 . Subsequently, these values were compared to the known maximum tensile strength from tension testing, 407.0 psi (2.8 MPa).

Based on the analysis provided above, it appears that only rosette nos. 2 and 4 provided reliable data for full-strain field analysis. Rosette no. 1 had bad data for the principal angle. The principal angle in rosette no. 3 was 90 degrees from the expected value.

The final piece of instrumentation was the string potentiometers. As in previous tests, questions arose regarding the accuracy of the resulting displacement data after comparison to displacements determined with Equation 20 and Equation 21, as well as the actuator movement over the same period. The theoretical equations tended to provide lower displacements than measured, while the actuator displacement data was generally higher than measured with the string potentiometer. It was somewhat difficult to determine which string potentiometers had results that may have inaccuracies due to instrumentation placement, data resolution, etc. could be trusted. As such, the displacement data and results are not included in this section. String potentiometer and actuator data are found in Appendix D.

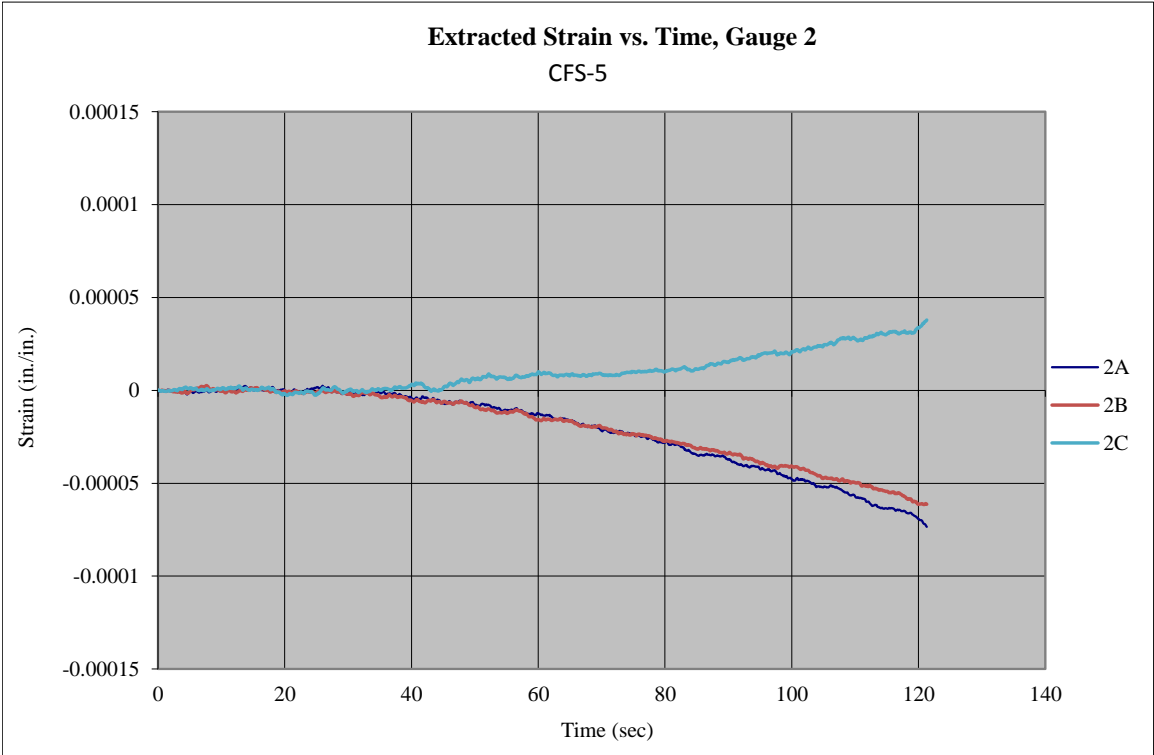
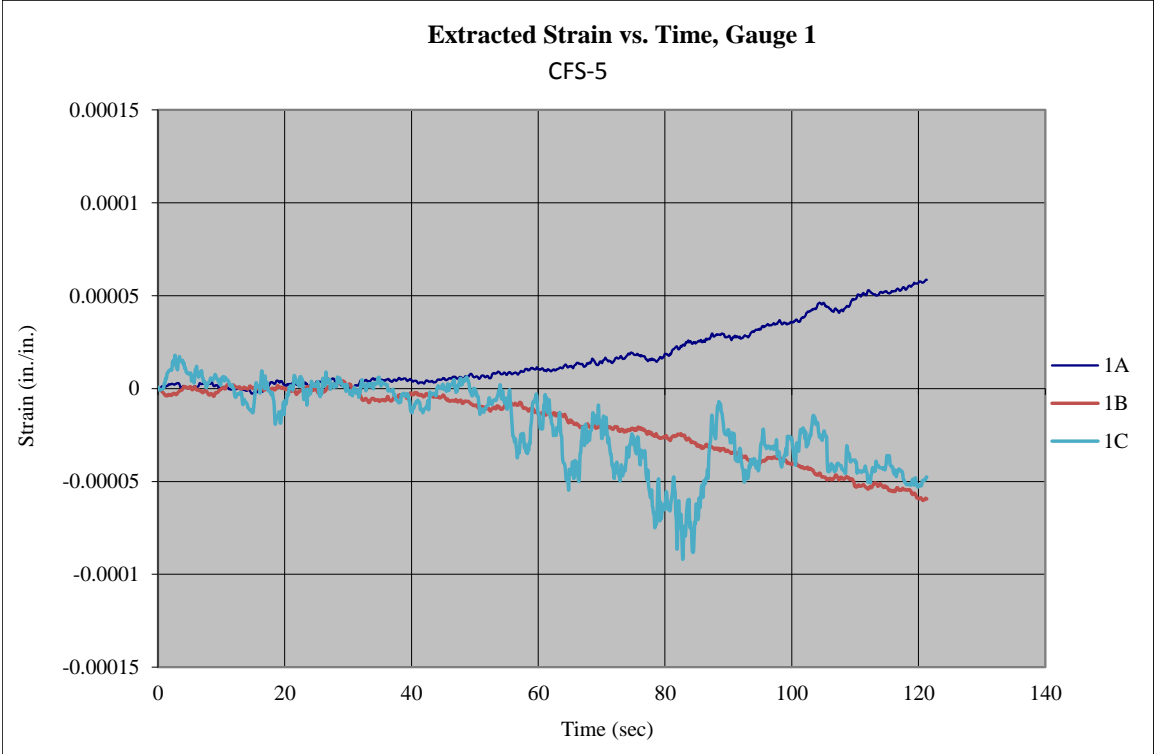


Figure 191. Extracted Strain Plots for Rosette Strain Gauges 1 and 2, Test No. CFS-5 [10-in. (254-mm) Span]

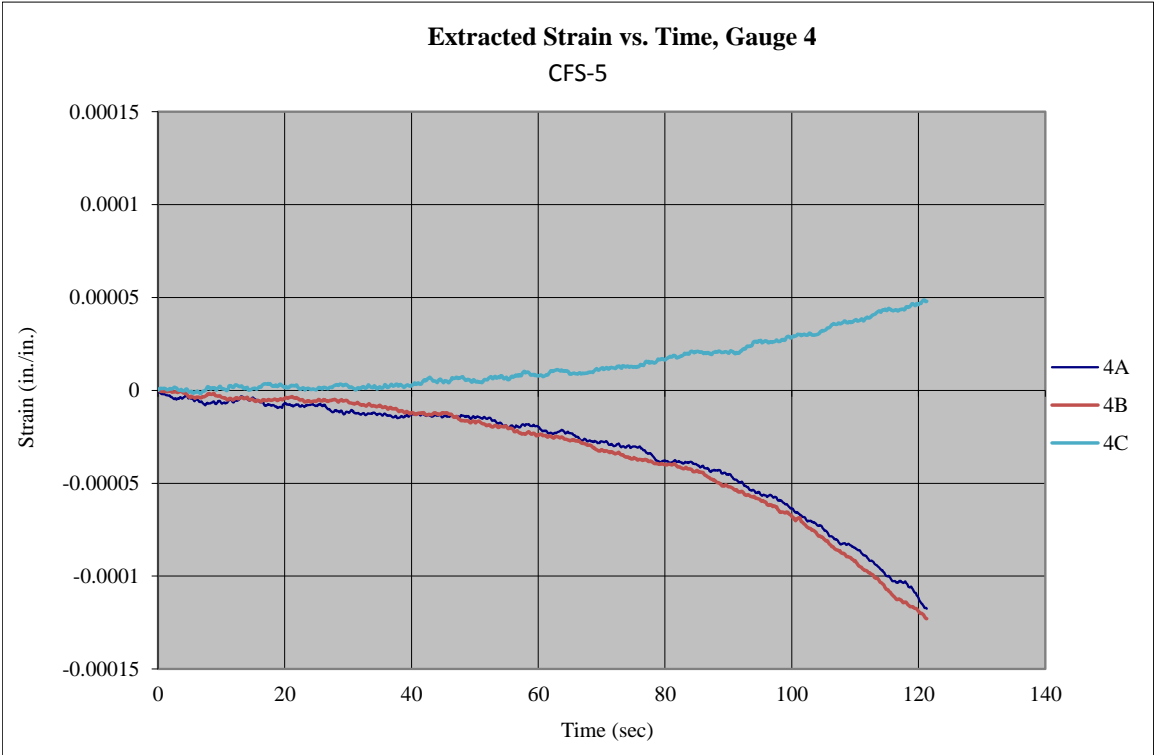
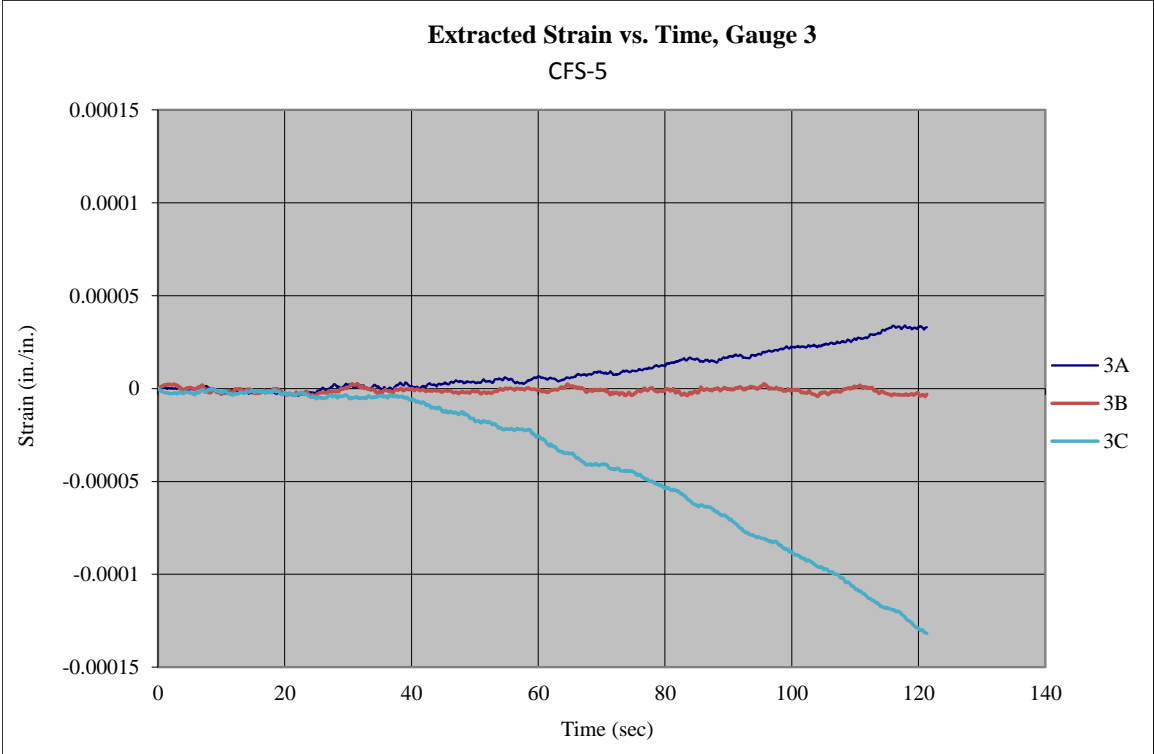


Figure 192. Extracted Strain Plots for Rosette Strain Gauges 3 and 4, Test No. CFS-5 [10-in. (254-mm) Span]

Table 42. Summary of Stress and Strains for Rosette Gauges, Test No. CFS-5

Rosette Gauge	Normal Strain, ϵ_x , @ Failure <i>in./in.</i>	Estimated Max./Min. Principal Strain (Eqs. 27 & 28)		Estimated Max./Min. Principal Stress (Eqs. 30 & 31)		Estimated γ_{max} (Eq. 29) <i>in./in.</i>	Estimated τ_{max} (Eq. 32) <i>psi</i>	Estimated τ_{max} (Eq. 37) <i>psi</i>	Estimated Principal Angles, θ_{1p} & θ_{2p} (Eq. 34 & 35) <i>degrees</i>	Estimated Shear Angles, θ_{1s} & θ_{2s} (Eq. 36) <i>degrees</i>
		ϵ_1 <i>in./in.</i>	ϵ_2 <i>in./in.</i>	σ_1 <i>psi</i>	σ_2 <i>psi</i>					
1	1A	5.85E-05	-	-	-	-	-	-	-	-
	1B	-5.94E-05	-	-	-	-	-	-	-	-
	1C	-4.76E-05	-	-	-	-	-	-	-	-
2	2A	-7.35E-05	-	-	-	-	-	-	-	-
	2B	-6.13E-05	-	-	-	-	-	-	-	-
	2C	3.79E-05	-8.84E-05	141.0	-306.5	1.41E-04	223.7	394.9	110, 20	65, 155
3	3A	3.30E-05	-	-	-	-	-	-	-	-
	3B	-3.06E-06	-	-	-	-	-	-	-	-
	3C	-1.32E-04	-	-	-	-	-	-	-	-
4	4A	-1.18E-04	-	-	-	-	-	-	-	-
	4B	-1.23E-04	-1.56E-04	226.9	-544.6	2.42E-04	382.8	394.9	115, 25	70, 160
	4C	4.80E-05	-	-	-	-	-	-	-	-

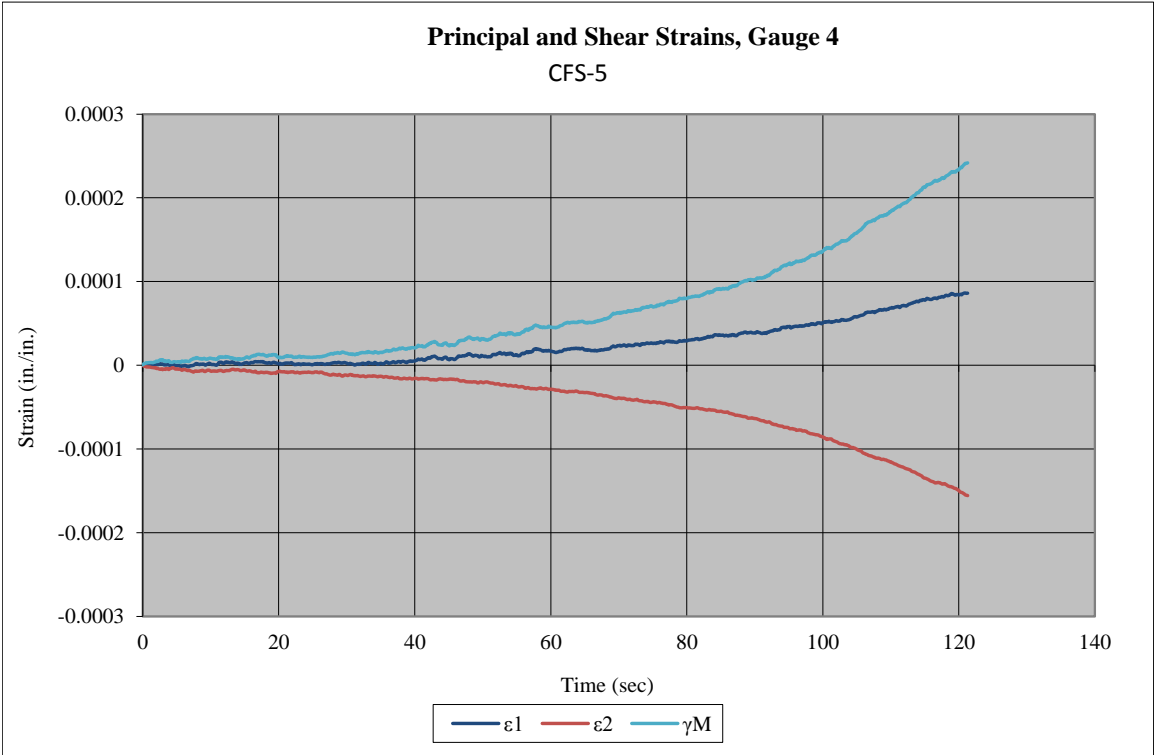
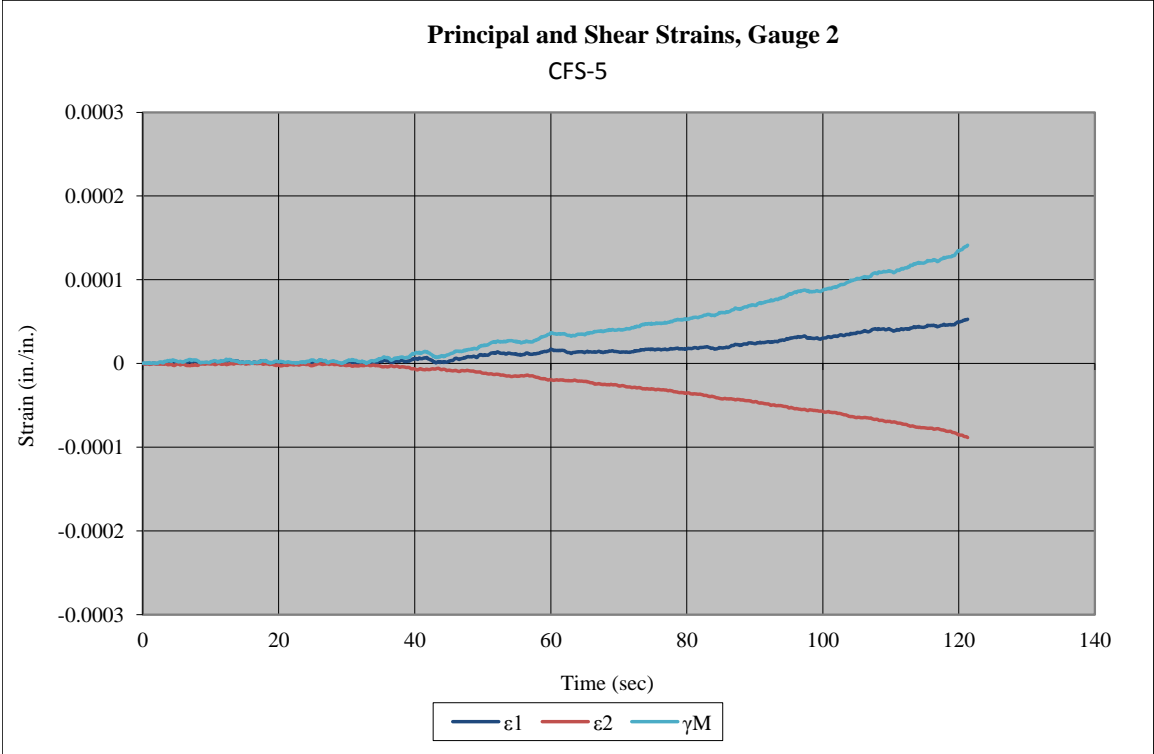


Figure 193. Principal Strains for Gauges 2 and 4, Test No. CFS-5 [10-in. (254-mm) Span]

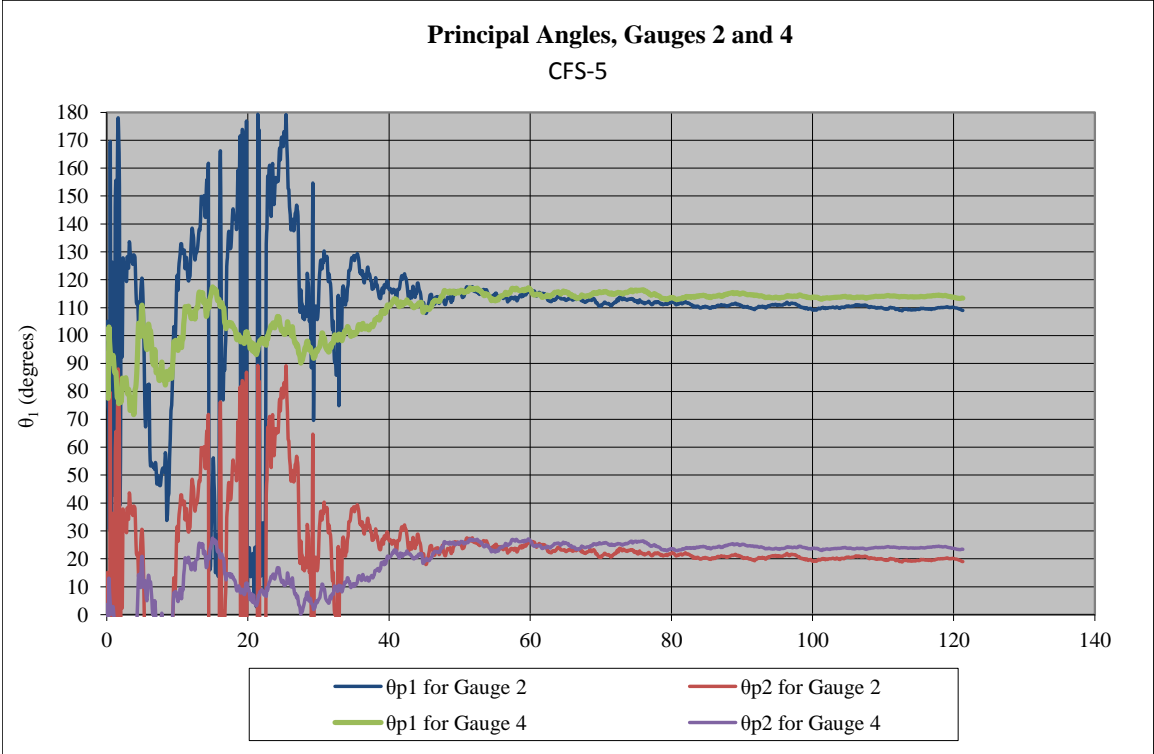


Figure 194. Principal Angles for Test No. CFS-5 [10-in. (254-mm) Span]

12.8 Test No. CFS-6 [Support Span – 9 in. (229 mm)]

For test no. CFS-6, a span length of 9 in. (229 mm) was used. A shear failure was expected to occur with this configuration. The test setup is shown in Figure 195.

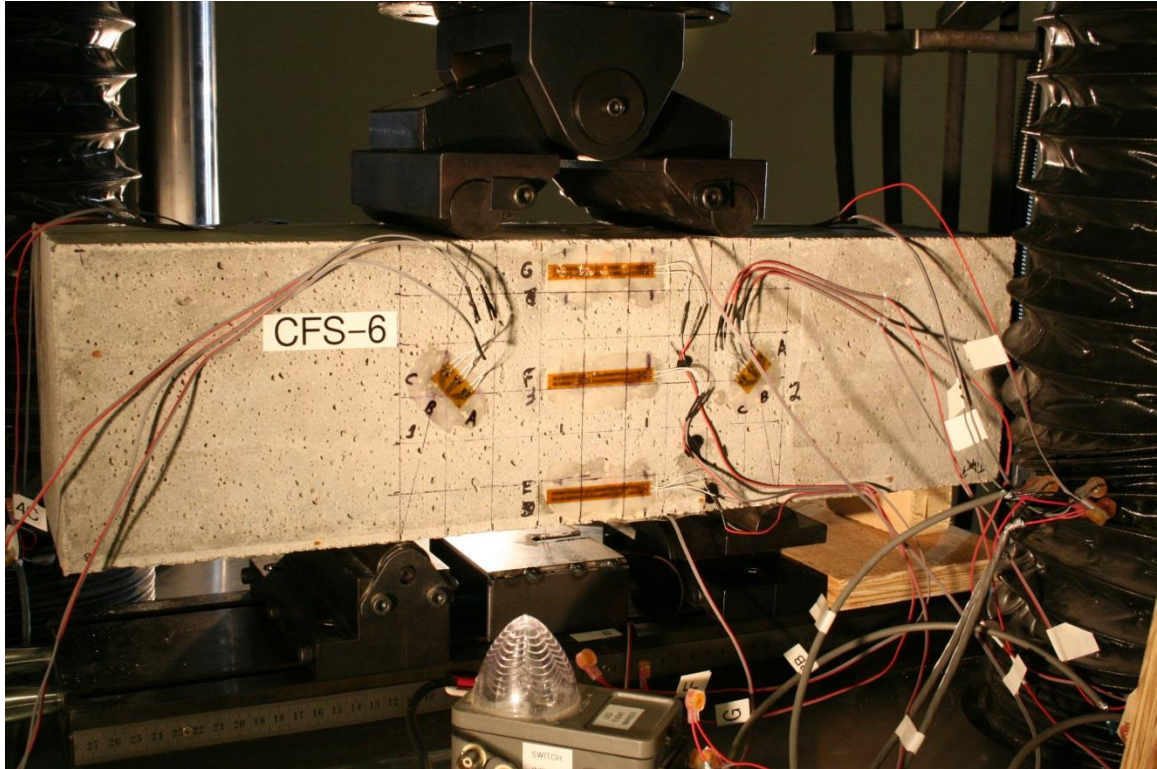


Figure 195. Test Setup for Test No. CFS-6 [9-in. (229-mm) Span]

As the MTS Criterion testing machine loaded the specimen during test no. CFS-6, the specimen failed in shear due to a diagonal crack between the upper and lower roller locations. Specifically, the diagonal fracture plane occurred on the left-front side of the beam. A peak load of 39.8 kip (177.0 kN) was measured when the specimen fractured. Thus, each upper roller was assumed to transfer a peak load equal to 19.9 kip (88.5 kN) to the top of the beam, thus resulting in a reaction at both lower supports equal to 19.9 kip (88.5 kN). The load versus time plot is shown in Figure 196, and post-test photographs are shown in Figure 197 and Figure 198.

All horizontal strain gauges that were placed at the vertical centerline of the beam appeared to have acquired data during test no. CFS-6. In addition, one of the horizontal strain gauges between rollers broke as the shear failure occurred near the vertical centerline of the beam. The strain readings revealed maximum negative (compression) and maximum positive (tension) normal strains of -7.75×10^{-5} in./in. (top) and 1.02×10^{-3} in./in. (bottom), respectively, as shown in Table 43 and Figure 199. Horizontal normal strain at the bottom of the beam appeared to be very large, creating a non-linear strain distribution. In addition, the strain at gauge G was larger than the strain at gauge H. As depicted in Figure 200, normal strains were plotted in the direction of the horizontal beam axis for each vertical gauge position [0 in. (beam centerline), $\pm 2\frac{1}{4}$ in. (57 mm) (upper and lower side gauges), and ± 3 in. (76 mm) (top and bottom gauges)]. Finally, the middle strain gauge revealed strains which that were larger than zero for the duration of the test, reaching a maximum of 1.51×10^{-4} in./in. Based on the measured difference between the top and bottom gauges, the horizontal strain readings raised some concerns.

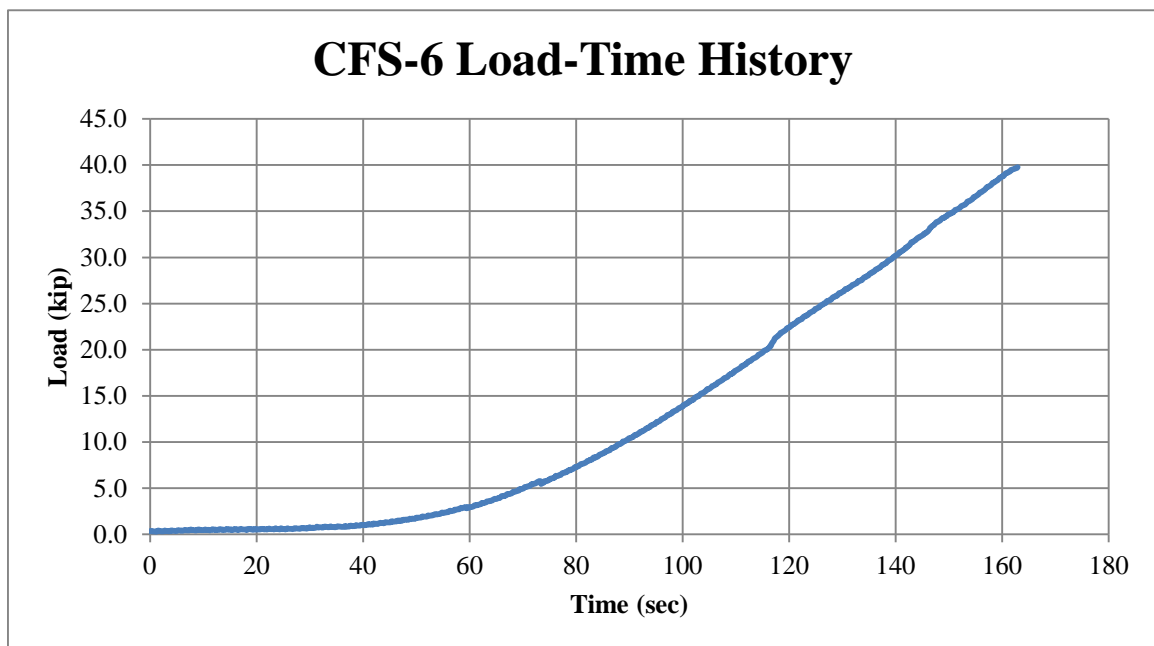


Figure 196. Load vs. Time, Test No. CFS-6 [9-in. (229-mm) Span]

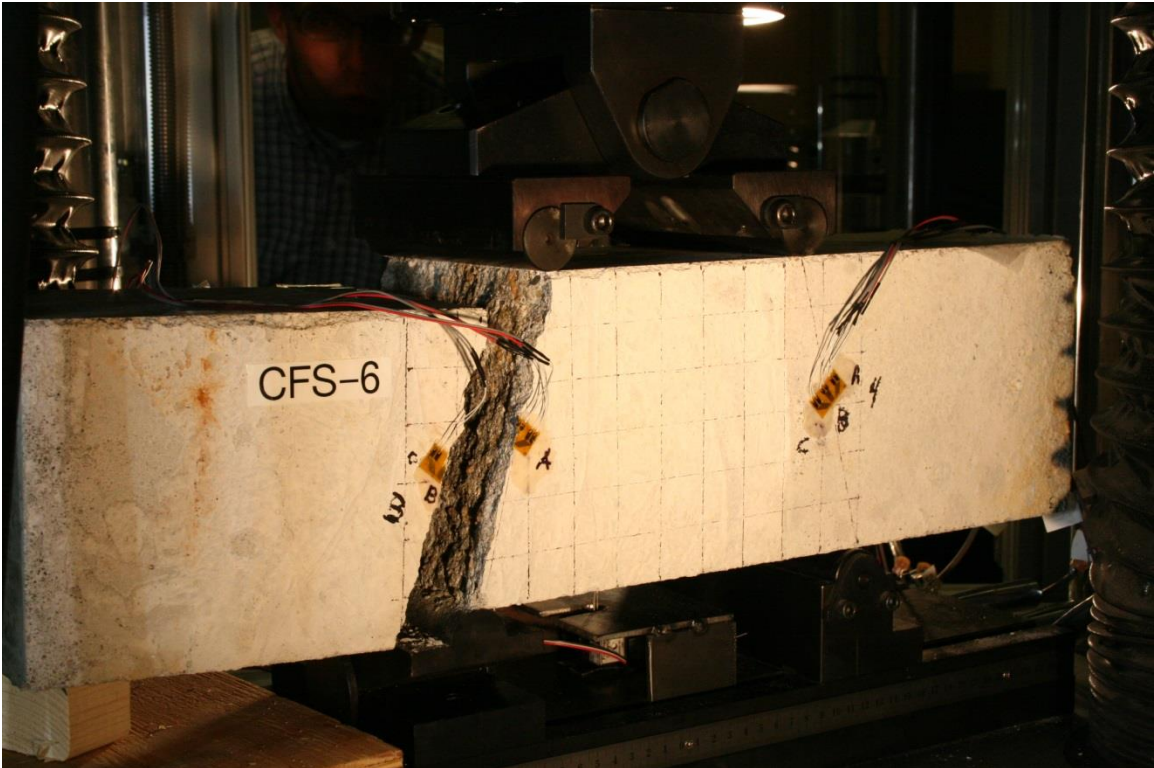
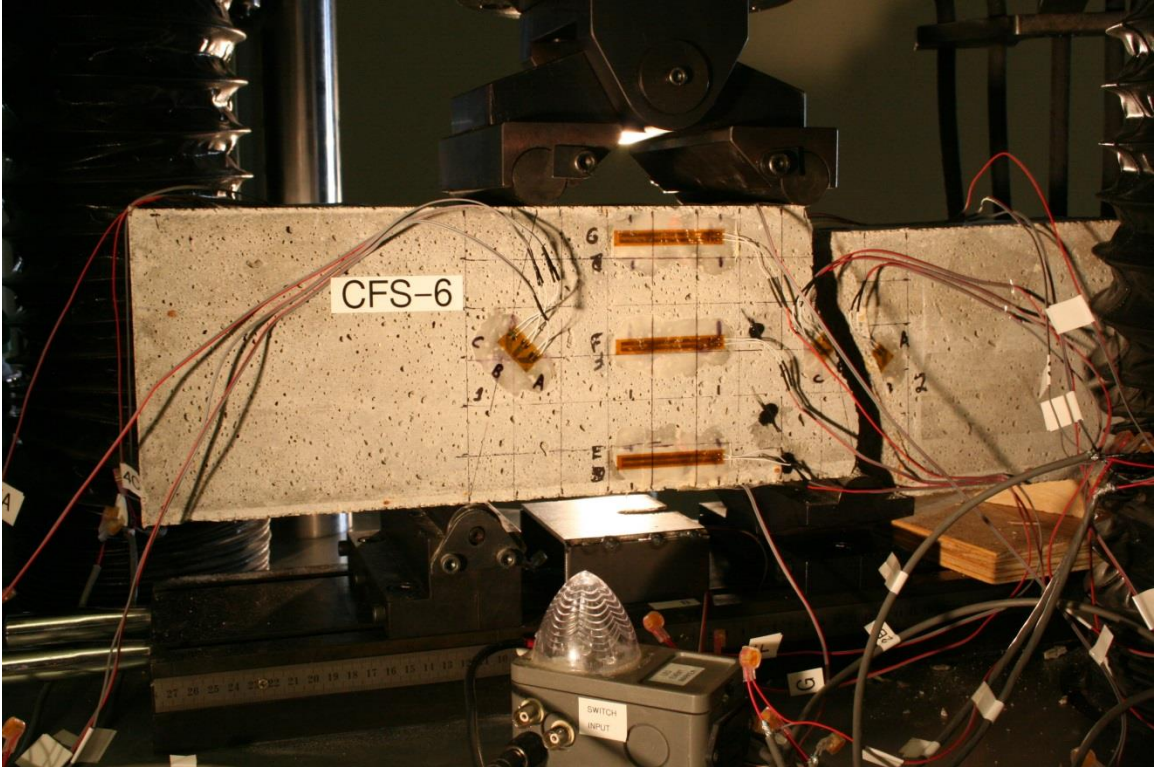


Figure 197. Post-Test Damage, Test No. CFS-6 [9-in. (229-mm) Span]

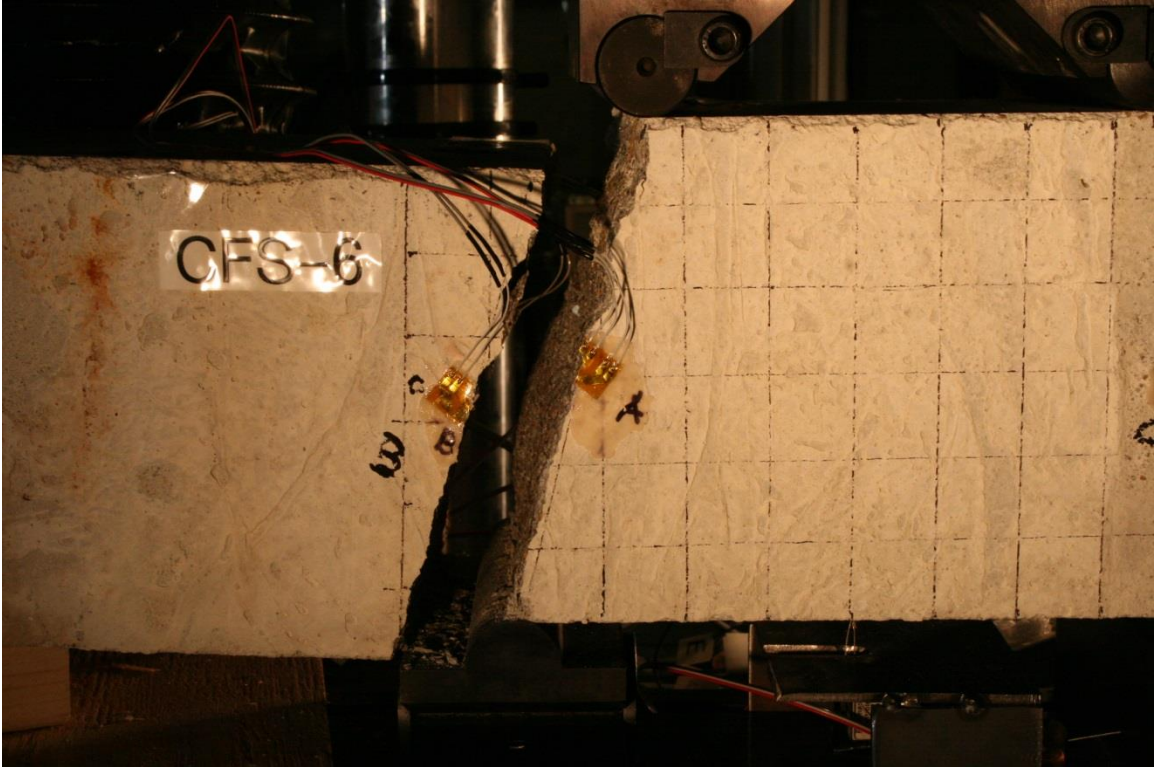


Figure 198. Additional Post-Test Damage, Test No. CFS-6 [9-in. (229-mm) Span]

Table 43. Normal Strain and Stress Distribution for Horizontal Gauges, Test No. CFS-6

Gauge Designation and Location	Normal Strain, ϵ_x, @ Failure <i>in./in.</i>	Estimated Maximum Normal Stress (Eq. 22) <i>psi</i>	Estimated Maximum Normal Stress (Eq. 23) <i>psi</i>
D (bottom)	8.52E-04	4100.7	828.6
E	1.02E-03	4910.8	621.4
F (middle)	1.51E-04	727.9	0.0
G	-9.19E-05	-442.6	-621.4
H (top)	-7.75E-05	-373.5	-828.6

Once the normal strains were processed, analyzed, and reviewed, an estimate was made to determine the maximum normal stress, $\sigma_{x,max}$, based on measured strains using Equation 22. The normal stress distribution was also estimated using strain readings at the upper and lower side positions. The maximum normal stress for each strain gauge is shown in Table 43, while the normal stress for four gauges as a function of time is provided in Figure 201 and Figure 202. An estimate was also made to determine the maximum normal stress, $\sigma_{bending,max}$, using the MTS load data and Equation 23. The maximum normal stress based on MTS load data and elastic bending is depicted in Table 41 for the top and bottom surfaces. Further, the normal stress corresponding to the other gauge locations was also calculated with MTS load data and provided in Table 43. The normal stress as a function of time and using MTS load data is shown graphically in Figure 201 and Figure 202. When comparing the normal stresses using the two methods, it is apparent that similar trends were not predicted during the test duration. The estimated normal stress based on MTS load data exceeded the prediction using the strain readings for the top gauge but not the bottom gauge. The maximum midspan normal stress was ± 828.6 psi (5.7 MPa) for the MTS load data and calculated moments, while

the maximum midspan normal stresses were +4910.8 psi/-442.6 psi (+33.9 MPa/-3.1 MPa) using the strain data. More investigation is needed to explore these differences, including any assumptions and limitations.

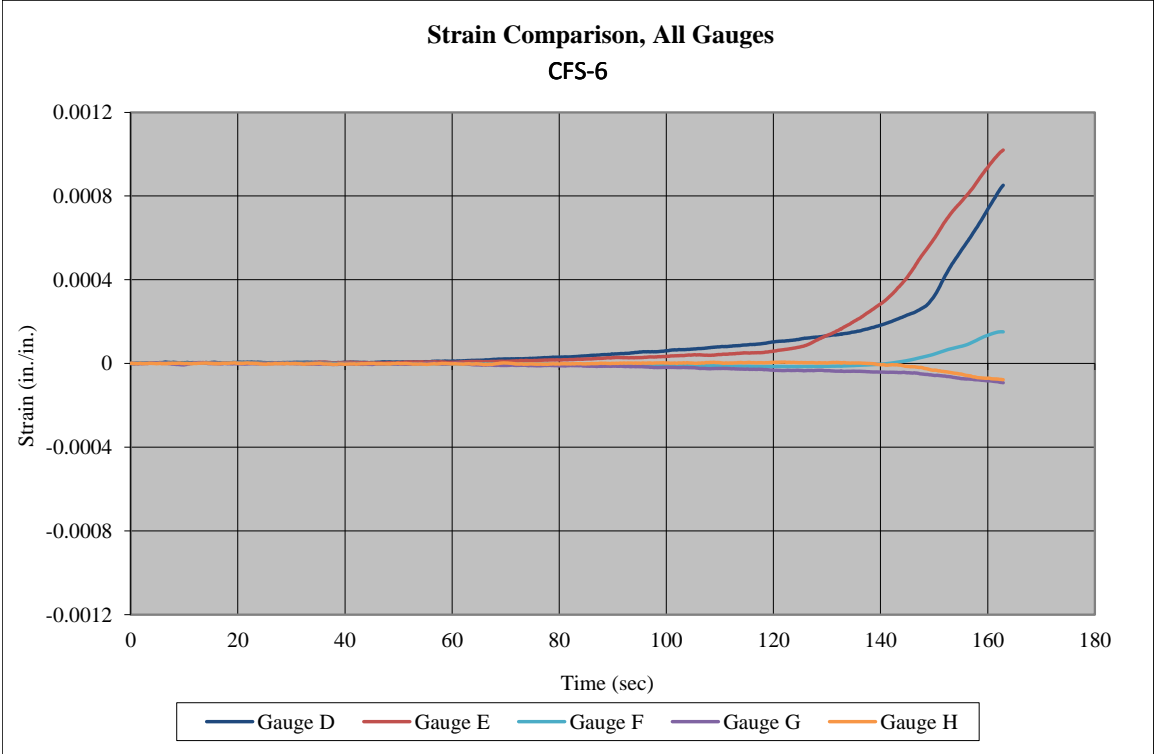


Figure 199. Normal Strains for Top, Side, and Bottom Gauges, Test No. CFS-6 [9-in. (229-mm) Span]

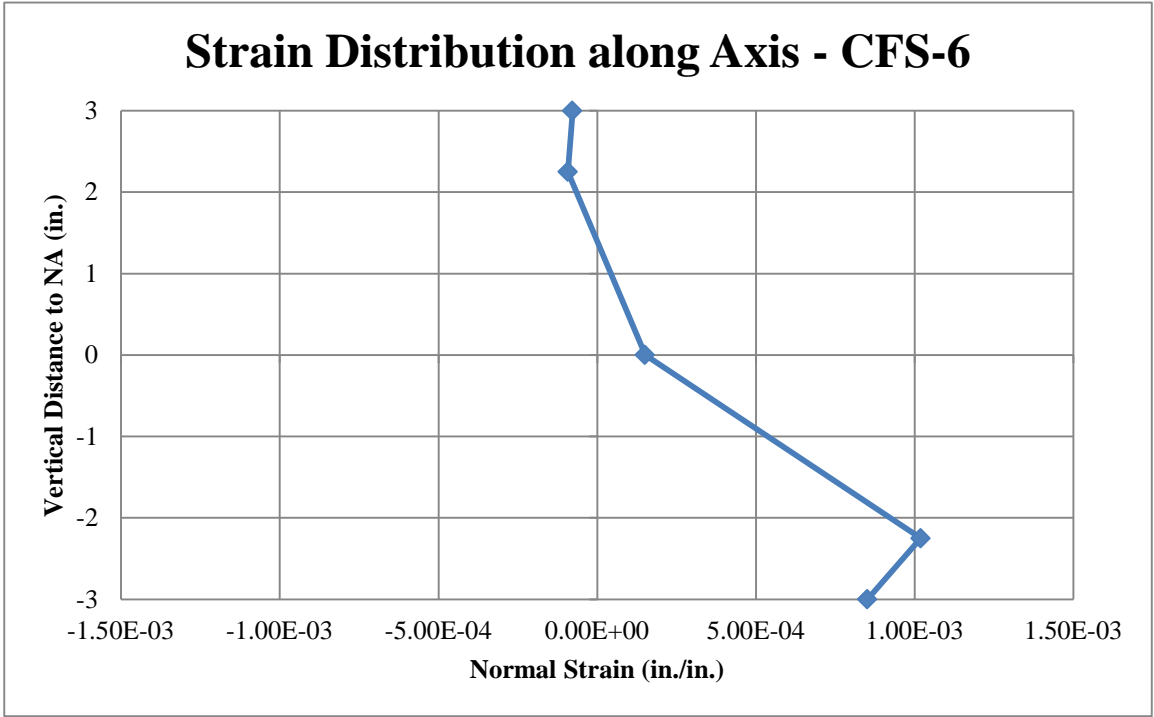


Figure 200. Vertical Distance versus Normal Strain, Test No. CFS-6 [9-in. (229-mm) Span]

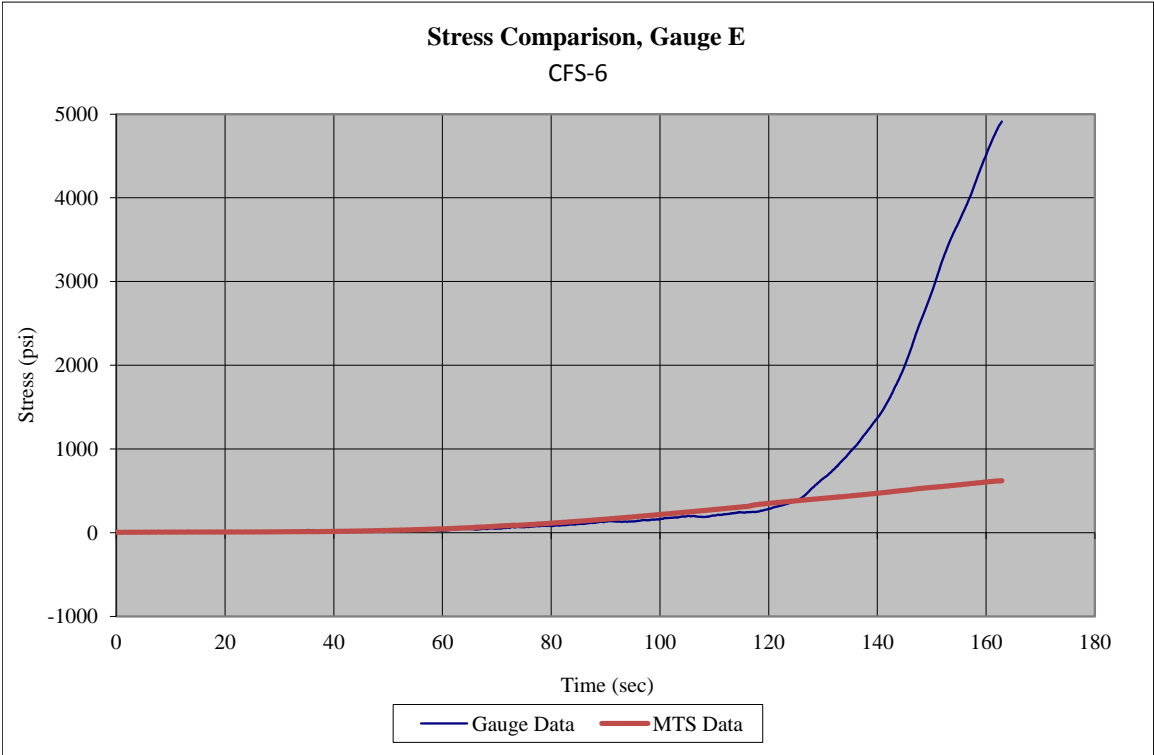
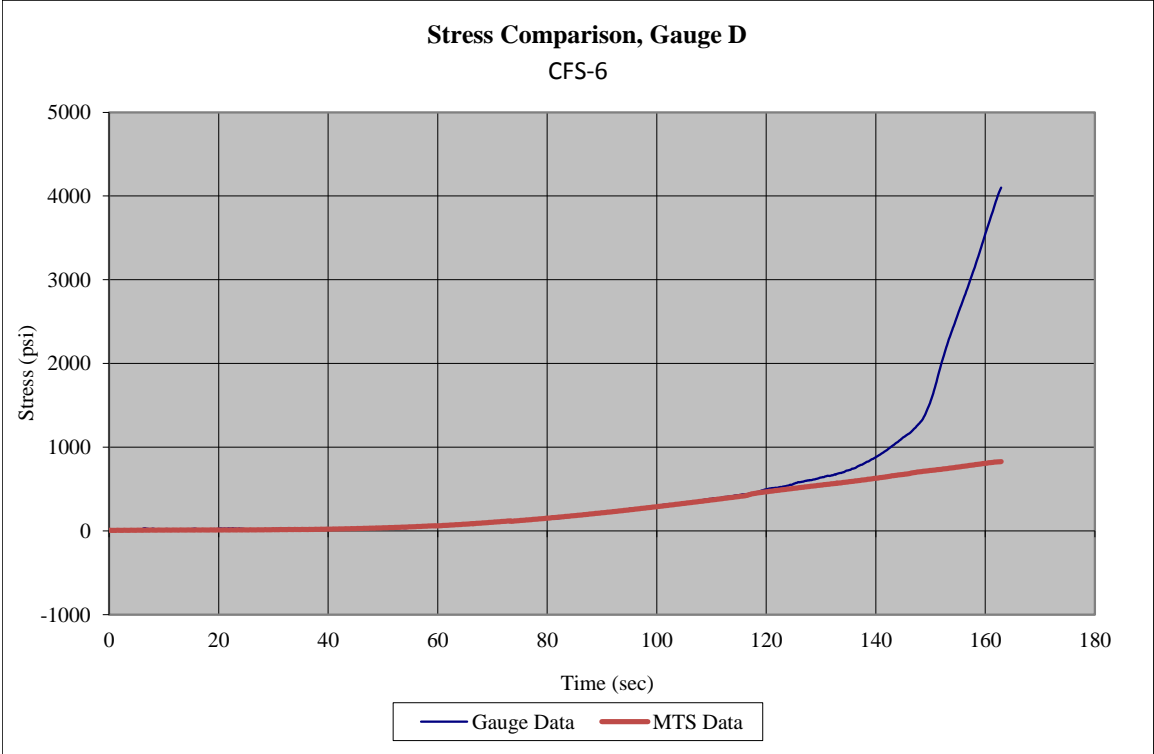


Figure 201. Estimated Midspan Normal Stresses from Bottom Strain Gauges and MTS Load Data, Test No. CFS-6 [9-in. (229-mm) Span]

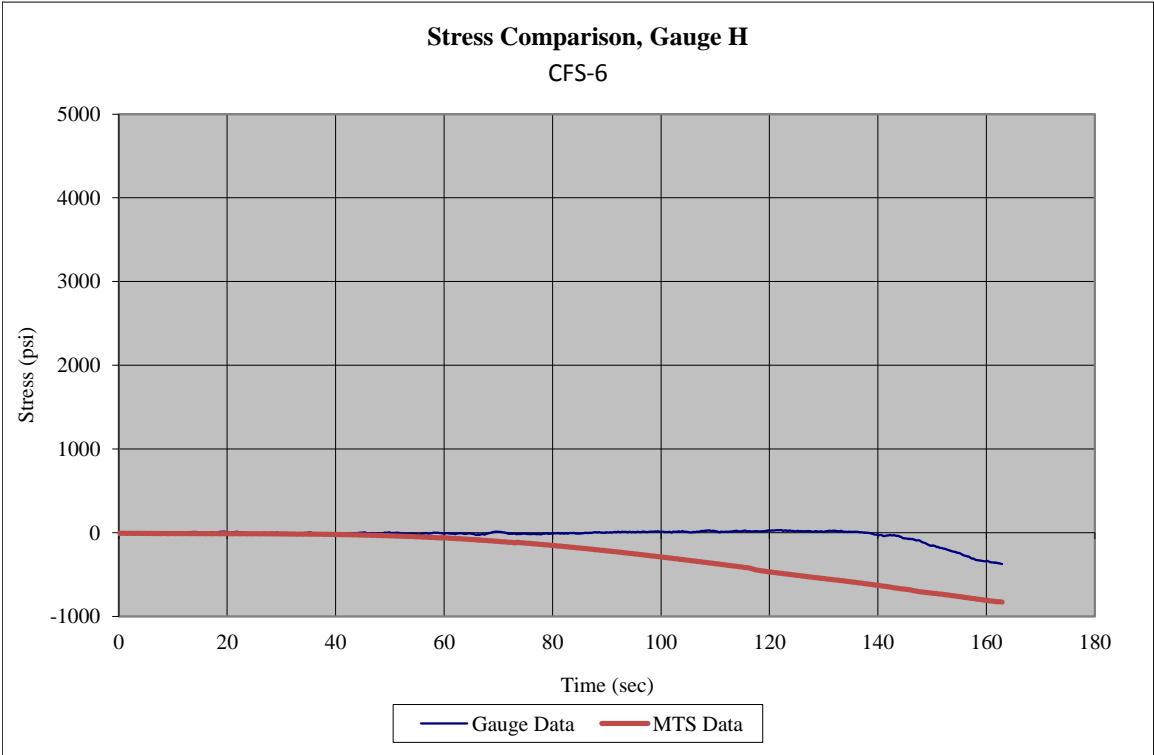
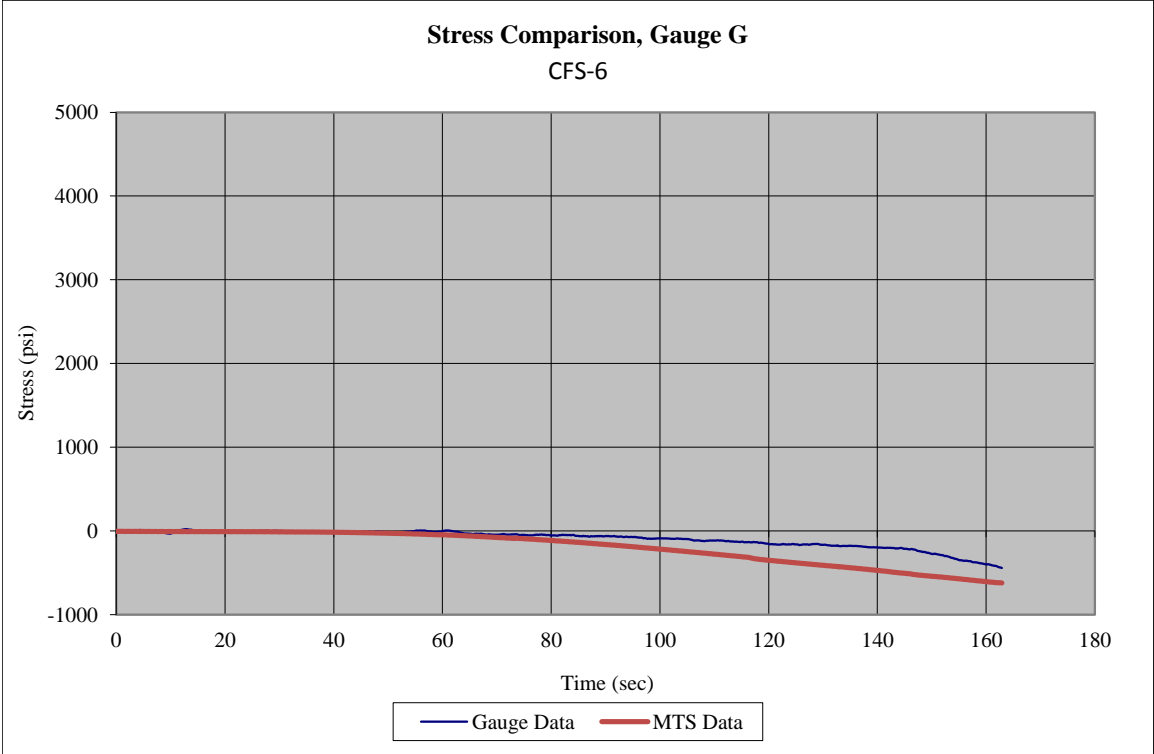


Figure 202. Estimated Midspan Normal Stresses from Top Strain Gauges and MTS Load Data, Test No. CFS-6 [9-in. (229-mm) Span]

Four rosette strain gauges were attached to the front and back faces of the beam near the horizontal centerline and midway between the upper roller and lower support. None of the rosette gauges broke as the shear failure occurred near the vertical centerline of the beam. Measured strains are provided in Figure 203 and Figure 204 for each rosette and each individual gauge, if acquired. Some rosette strain gauges appeared to perform in an acceptable manner during test no. CFS-6. However, some gauges have provided data that may raise questions upon first glance. Based on symmetric loading, the strains would be expected to be very similar across all rosettes. However, this outcome did not appear to always be the case.

First, rosette no. 1 (left-front position facing front) provided negative compressive strain for two gauges (B – diagonal and C – vertical), but positive tensile strain for the third gauge (A – horizontal). Note that the A-gauge was aligned with the positive horizontal beam axis at its geometric centerline. Second, rosette no. 2 (right-front position facing front) provided negative compressive strain for gauge A (vertical), but positive tensile strain for gauge C (horizontal). Note that the C-gauge was aligned with the negative horizontal axis. The diagonal gauge, gauge B, provided zero strain throughout. Third, rosette no. 3 (left-back position facing back) provided positive tensile strain for one gauge (A – horizontal) and negative compressive strain for the other two gauges. Note that the A-gauge was aligned with the positive horizontal beam axis at its geometric centerline for the back face. Finally, rosette no. 4 (right-back position facing back) provided negative compressive strain for two gauges (A – vertical and B – diagonal) and positive tensile strain for the third gauge (C – horizontal). Note that the C-gauge was aligned with the negative horizontal axis.

All strains, gauges A through C, would likely be non-zero for this beam configuration with 9-in. (229-mm) span. However, one gauge, 2B, did have zero strain throughout. Following a review for all four rosette gauges, it was apparent that gauges 1 and 4 had similar strain readings for the acquired data channels. First, the horizontal gauges for all rosettes provided a positive tensile strain while the vertical gauges provided negative compression strain. The diagonal gauge (B) provided negative compressive strain at rosette no. 1, 3, and 4 and zero strain at rosette no. 2. Thus, less confidence existed with results produced with gauges 1, 2, and 3. The maximum strain readings are provided in Table 44, and strain versus time is shown graphically in Figure 203 and Figure 204.

Maximum principal and maximum shear strains are summarized in Table 44 for rosette gauge 4. The value of 9.16×10^{-5} in./in. was found for the maximum principal strain, ϵ_1 . The value for the minimum principal strain, ϵ_2 , -1.51×10^{-4} in./in. The maximum shear strain for test no. CFS-6 was 2.43×10^{-4} in./in. Subsequently, Equation 32 and Equation 36 were used to compute the theoretical maximum shear stress and maximum shear strain of 828.6 psi (5.7 MPa) and 4.09×10^{-4} in./in., respectively.

Principal angles are summarized in Figure 205 for rosette no. 4. Based on the plot, the first principal angle for gauge 4 ranged between 100 and 110 degrees. Due to orientation and the angle should be between 90 and 180 degrees. The second principal angle, θ_{p2} , was then near 15 degrees for gauge 4. Based on these angles, the associated shear angles would be 150 and 60 degrees for gauge 4, which confirms what would be anticipated based on a simple shear stress block located at the centerline of the beam, or neutral axis for this case.

Maximum principal stresses are summarized in Table 44 for rosette no. 4. These values were calculated using Equation 30. The value was 247.0 psi (1.7 MPa) for the maximum principal stress, σ_1 . Subsequently, the value was compared to the known maximum tensile strength from tension testing, 407.0 psi (2.8 MPa).

The final piece of instrumentation was the string potentiometers. As in previous testing, questions arose regarding the accuracy of the resulting displacement data after comparison to displacements determined with Equation 20 and Equation 21, as well as the actuator movement over the same period. The theoretical equations tended to provide lower displacements than measured, while the actuator displacement data was generally higher than measured with the string potentiometer. It was somewhat difficult to determine which string potentiometers had results that may have inaccuracies due to instrumentation placement, data resolution, etc. could be trusted. As such, the displacement data and results are not included in this section. String potentiometer and actuator data are found in Appendix D.

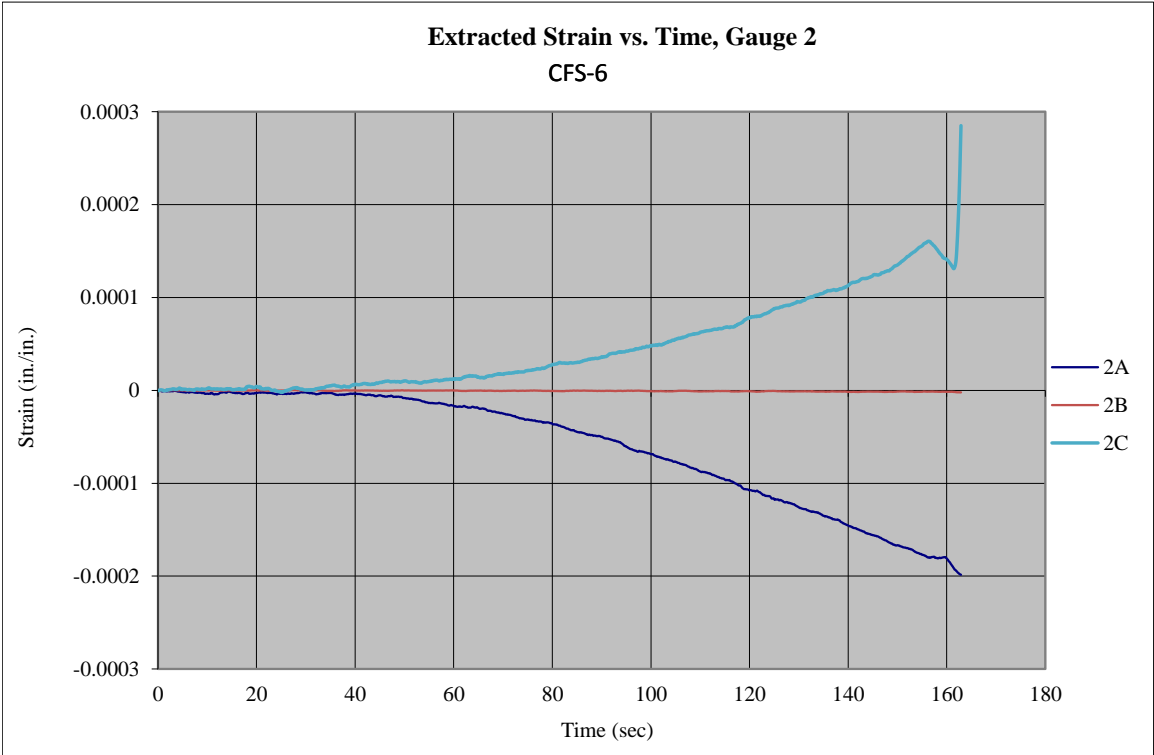
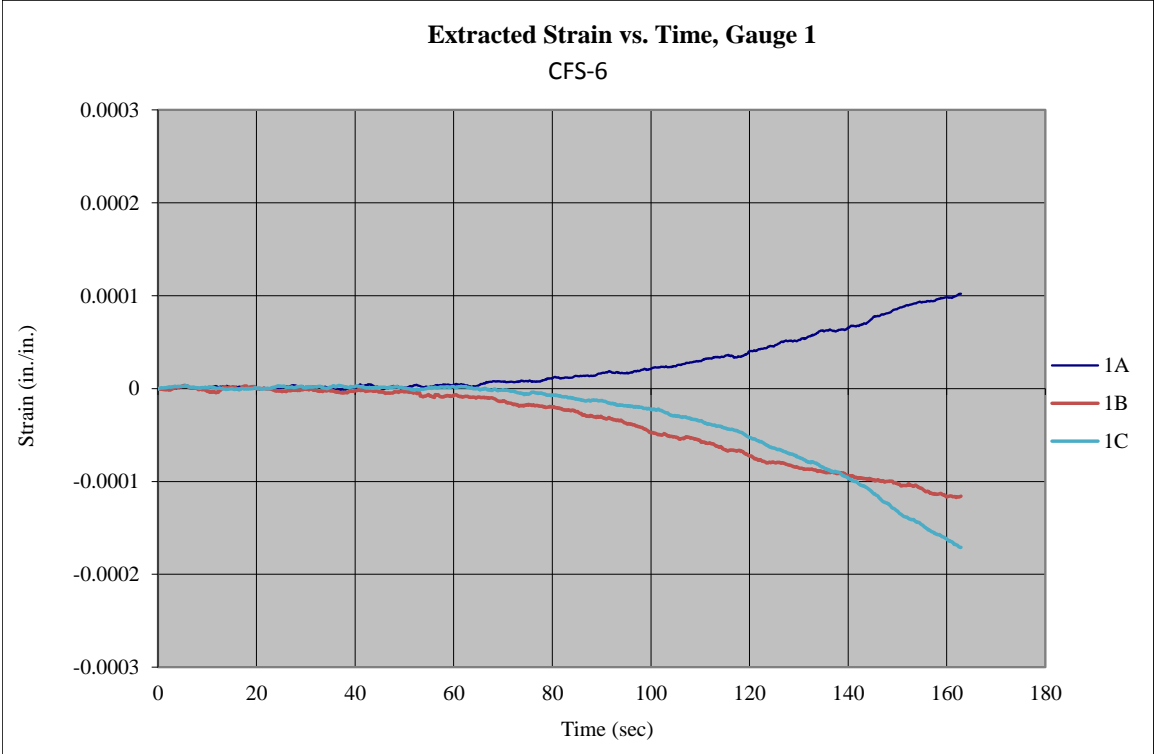


Figure 203. Extracted Strain Plots for Rosette Strain Gauges 1 and 2, Test No. CFS-6 [9-in. (229-mm) Span]

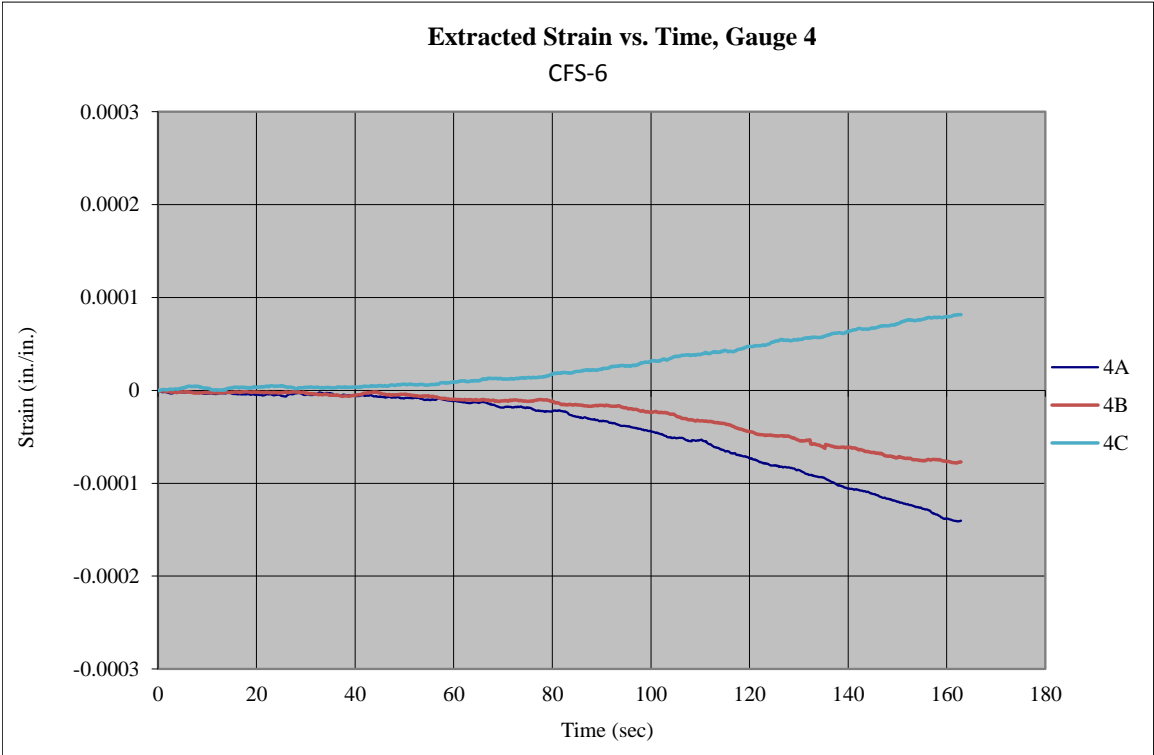
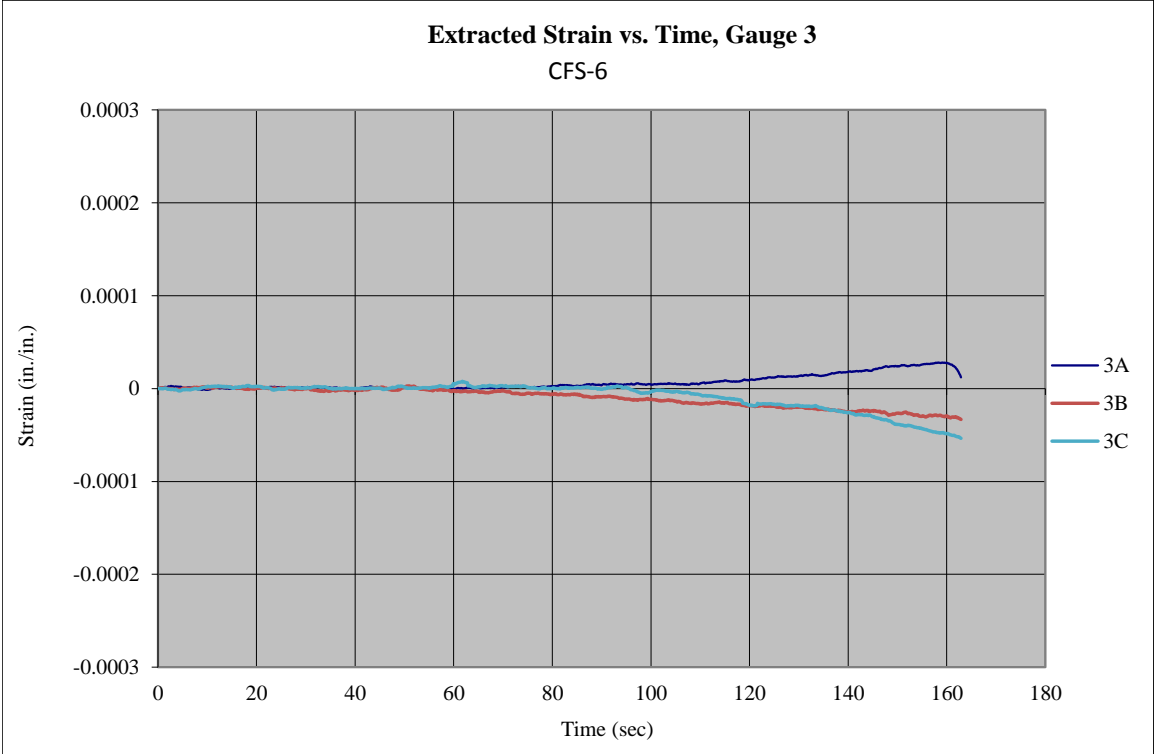


Figure 204. Extracted Strain Plots for Rosette Strain Gauges 3 and 4, Test No. CFS-6 [9-in. (229-mm) Span]

Table 44. Summary of Stress and Strains for Rosette Gauges, Test No. CFS-6

Rosette Gauge	Normal Strain, ϵ_x , @ Failure <i>in./in.</i>	Estimated Max./Min. Principal Strain (Eqs. 27 & 28)		Estimated Max./Min. Principal Stress (Eqs. 30 & 31)		Estimated γ_{max} (Eq. 29) <i>in./in.</i>	Estimated τ_{max} (Eq. 32) <i>psi</i>	Estimated τ_{max} (Eq. 37) <i>psi</i>	Estimated Principal Angles, θ_{1p} & θ_{2p} (Eq. 34 & 35) <i>degrees</i>	Estimated Shear Angles, θ_{1s} & θ_{2s} (Eq. 36) <i>degrees</i>
		ϵ_1 <i>in./in.</i>	ϵ_2 <i>in./in.</i>	σ_1 <i>psi</i>	σ_2 <i>psi</i>					
1	1A	1.02E-04	-	-	-	-	-	-	-	-
	1B	-1.16E-04	-	-	-	-	-	-	-	-
	1C	-1.71E-04	-	-	-	-	-	-	-	-
2	2A	-1.98E-04	-	-	-	-	-	-	-	-
	2B	-2.13E-06	-	-	-	-	-	-	-	-
	2C	2.85E-04	-	-	-	-	-	-	-	-
3	3A	1.21E-05	-	-	-	-	-	-	-	-
	3B	-3.32E-05	-	-	-	-	-	-	-	-
	3C	-5.35E-05	-	-	-	-	-	-	-	-
4	4A	-1.40E-04	-	-	-	-	-	-	-	-
	4B	-7.71E-05	9.16E-05	-1.51E-04	247.0	-522.4	384.0	828.6	105, 15	150, 60
	4C	8.15E-05								

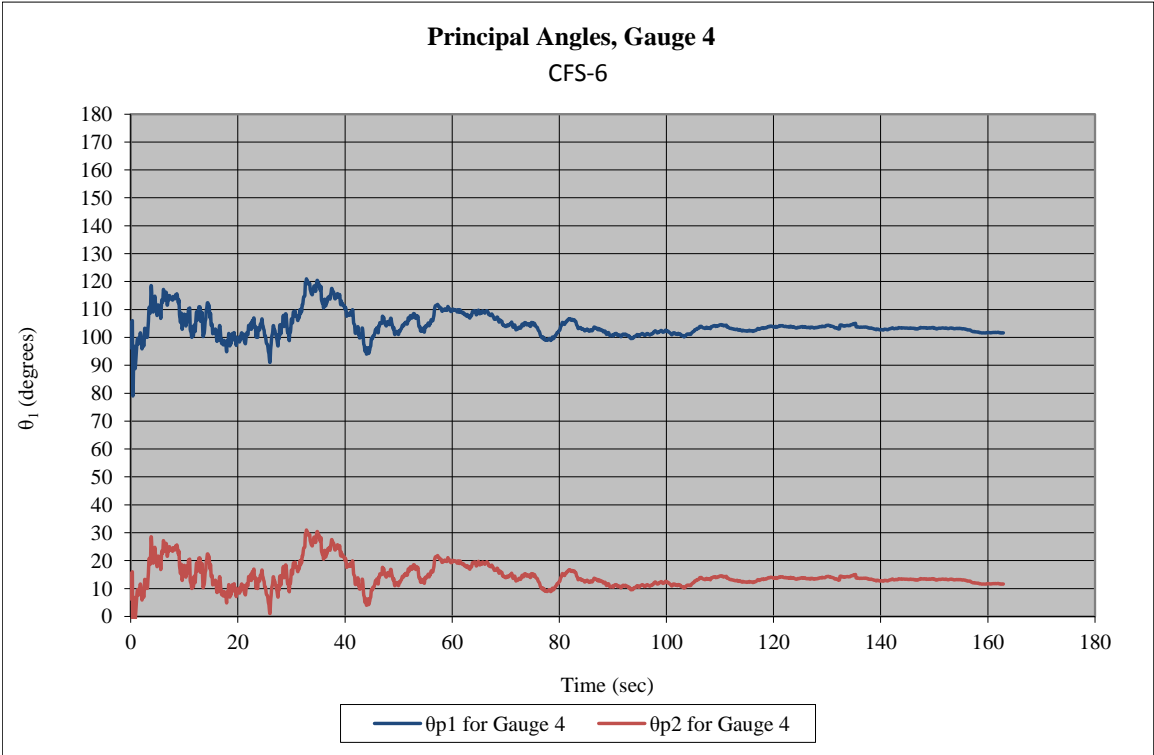
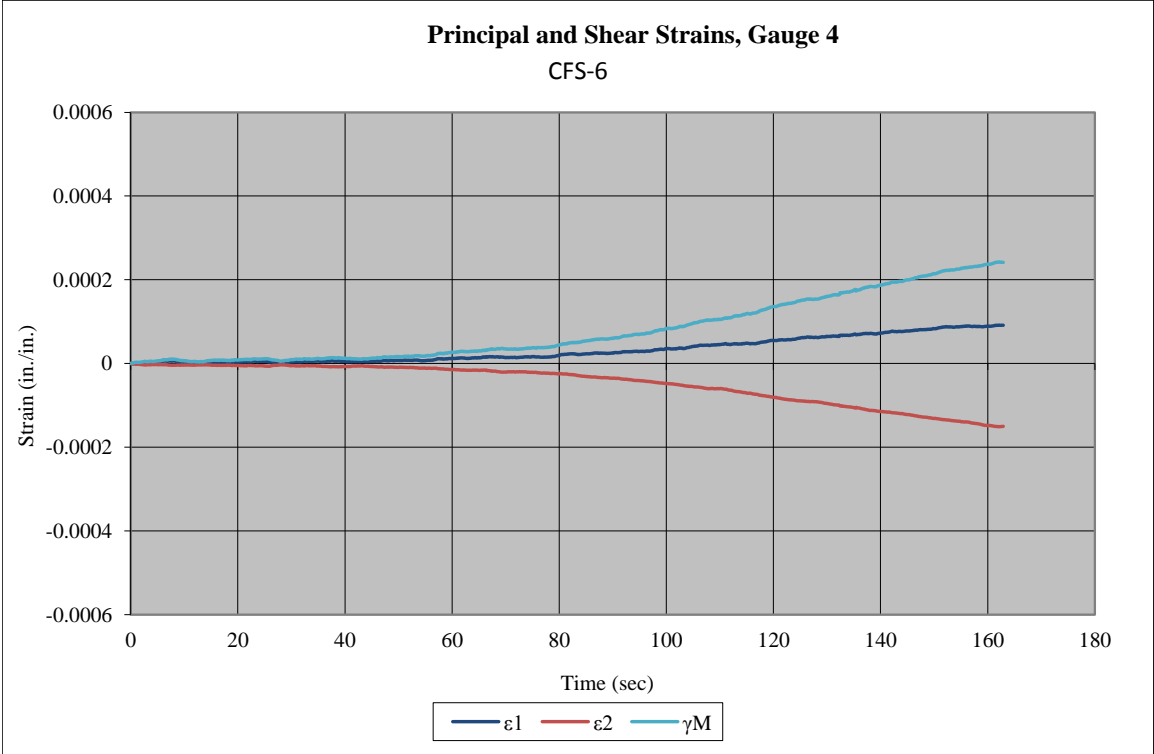


Figure 205. Principal Strains and Angles for Test No. CFS-6 [9-in. (229-mm) Span]

12.9 Discussion

Based on the results from all six tests, it is evident that more investigation is required in order to explore difference and oddities that came up over the course of the beam testing program. Concerns were raised with the data for both the horizontal and rosette strain gauges. Additionally, no reliable data was believed to be obtained from the string potentiometers in any of the tests. In the horizontal gauges, there was non-linear stress distribution among the five gauges, as shown in Figure 206. For the rosette strain gauges, some channels provided zero strain when strain would be expected. Strain rosettes occasionally provided principal stresses that were significantly higher than the tensile strength of the concrete. Based on the uncertainties in the data, it was difficult to draw significant conclusions about the tests results in terms of strains, stresses and displacements.

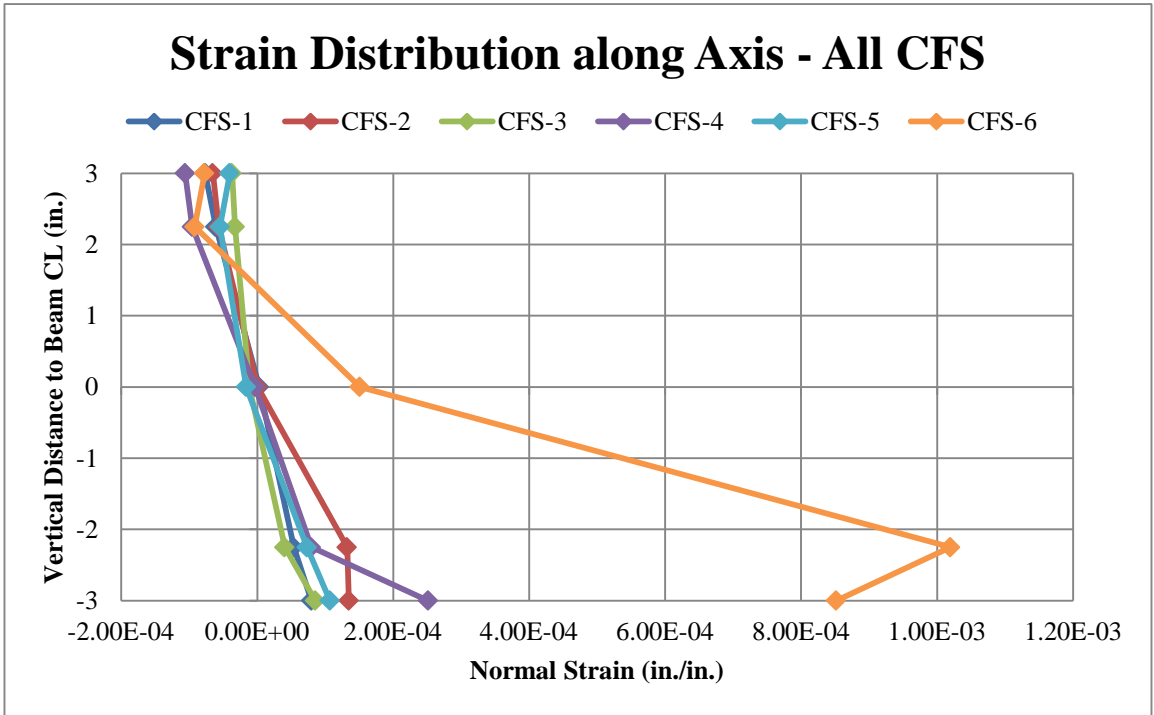


Figure 206. Vertical Distance versus Normal Strain, All CFS Tests

The peak loads for the tests varied, as would be expected for different testing setups. The peak load for test no. CFS-1 was much lower than the other five tests, at 5.8 kip (25.8 kN), and the peak load for test no. CFS-6 was much higher, at 39.8 kip (177.0 kN). The remaining four tests had peak loads between 14.3 kip (63.6 kN) and 19.0 kip (84.5 kN), as shown in Figure 207. Test no. CFS-4 was run at a different displacement rate, which explains why it failed much later on in the test than the other five tests.

However, the observed failure mode of the beams was interesting. Test no. CFS-1 started with the longest support span of 18 in. (457 mm), which was decreased in future tests. The first shear failure occurred when using a 10-in. (254-mm) support span (test no. CFS-3). When this specific support span was tested a second time (test no. CFS-5), a flexural failure occurred. This finding may signify that the 10-in. (254-mm) support span was close to the transition point between flexural and shear failure or that variability in material properties contributed to different behavior. The 9-in. (229-mm) support span provided a shear failure, and all support spans larger than 10 in. (254 mm) provided a flexural failure. This information will be used for comparison when LS-DYNA simulations are conducted on similar beam specimens and lengths.

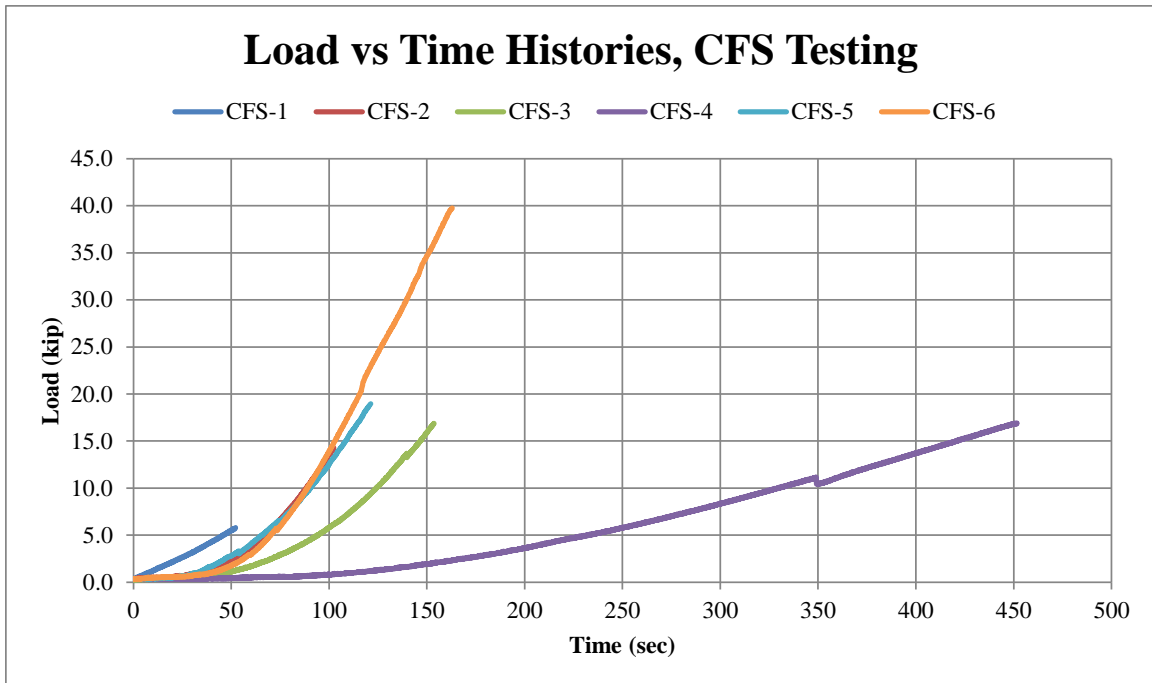


Figure 207. Shear Load-Time Histories, All CFS Tests

A comparison was also completed for the principal angles for the rosette gauges, as shown in Table 45. As the lower support span decreases, the principal angles for rosette nos. 1 and 3 should increase as the angle between supports also increases. The principal angles for rosette nos. 2 and 4 should have the opposite trend and decrease as the supports moved inward. Although some rosettes did not provide reliable data, other rosettes did provide reasonable results that followed the expected trend.

Table 45. Summary of Principal Angles, All CFS Tests

Test No.	Support Span <i>in.</i>	Geometric Angle <i>degrees</i>	Estimated Principal Angles θ_{1p} & θ_{2p} (<i>degrees</i>)			
			<i>Rosette 1</i>	<i>Rosette 2</i>	<i>Rosette 3</i>	<i>Rosette 4</i>
CFS-1	18	45.0	-	135, 45	-	135, 45
CFS-2	12	63.4	50, 140	-	-	-
CFS-4	11	67.4	60, 150	-	50, 140	-
CFS-3	10	71.6	65, 155	-	-	-
CFS-5	10	71.6	-	110, 20	-	115, 25
CFS-6	9	76.0	-	-	-	105, 15

CHAPTER 13 SIMULATION OF INTERNAL CONCRETE CYLINDER TESTS

13.1 Introduction

Three sets of simulations were completed in order to validate all tests that were performed during the CFC, CFT, and CFS testing programs. The first simulation effort on the internal component tests involved compression simulations of cylinders. For this effort, only the CSCM and K&C material models were evaluated due to previous model performance in the single element and first round of component simulations.

The intent of the cylinder simulations was to compare the simulation results from each of the five material models to the acquired test results from test nos. CFC-1 through CFC-7. The cylinders in the model had an 8-in. (203-mm) height and 4-in. (102-mm) diameter. A *RIGIDWALL_PLANAR was in place under the cylinders and fixed. A *RIGIDWALL_GEOMETRIC was displaced in the z-axis down onto the tops of the cylinders. The displacement rate was increased linearly until the end of the simulation. Cross-sections were placed through the center of the cylinders in order to measure forces for use in computing stresses. An overview of the model is shown in Figure 208.

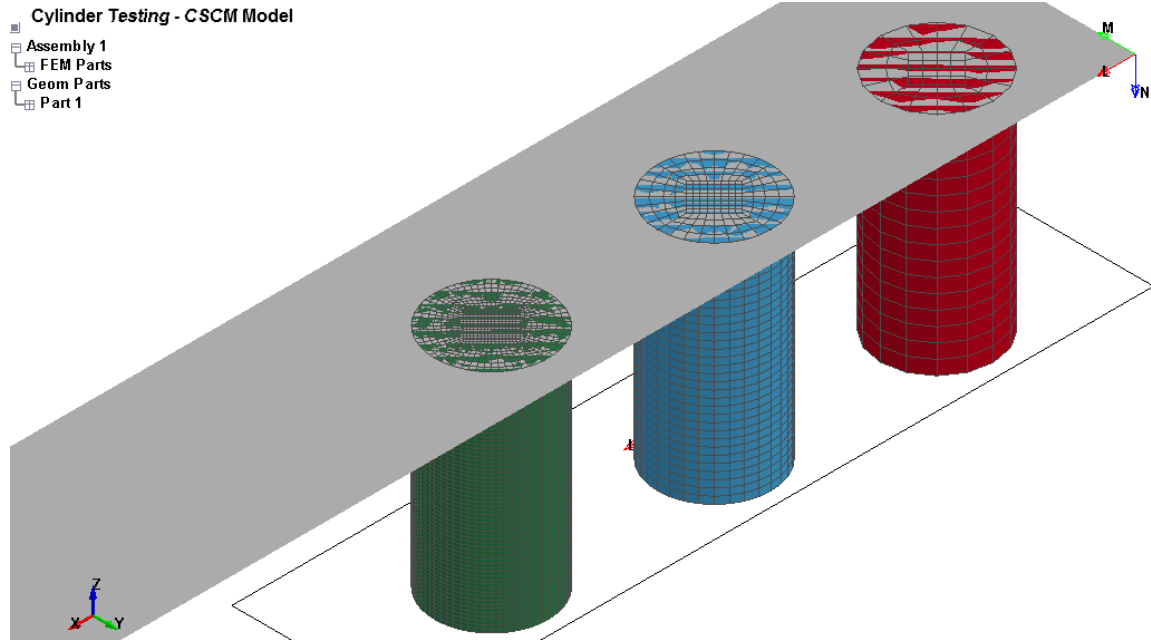


Figure 208. Overview of Internal Compression Simulation

Once in-house testing was completed, the aggregate size, compression and tensile strengths, etc., were defined in the material decks for the two models in an attempt to precisely replicate the concrete material properties. For all internal testing simulations these values included a Poisson's ratio of 0.19, a density of 150 lb/ft³ (2.4×10^{-6} kg/mm³), a maximum aggregate size of $\frac{3}{8}$ in. (10 mm), a compressive strength of 9.1 ksi (62.7 MPa), and a tensile strength of 0.36 ksi (2.5 MPa). Since all of the cylinders were within a small tolerance for diameter and length, simulation of the 4-in. dia x 8-in. tall (102-mm dia. x 203-mm tall) cylinder configuration was completed to represent all seven tests.

13.2 Simulation Data Evaluation Process

A displacement rate analysis was completed for each of the two material models to determine an appropriate simulation displacement rate. The test displacement rate of 0.0005 in./s (0.013 mm/s) could not be used in the simulation effort due to it being

disadvantageous for use in an explicit LS-DYNA analyses. A linear displacement function was assumed. Potential displacement rates ranged from 2.7 in./s (69.7 mm/s) to 0.27 in./s (6.97 mm/s), and the goal was to find convergence in the stress-strain behaviors. Once convergence was reached, this rate would be considered the optimum. For both material models, this rate was found to be 0.27 in./s (6.97 mm/s) for a total of 1000 ms.

The intent of the cylinder simulations was to compare simulation results for each of the two material models to the physical results obtained from the internal testing program. Variations were made to the configuration as well as the default material input parameters in order to find a combination that best matched the physical test results. No additional parameters were tested, unlike the previous rounds of component simulations.

Multiple cylinders were used in the same simulation to directly compare variations in the model and material input parameters. There was no friction between the cylinder and loading plates and `elform1` was used throughout, based on previous simulation results. The mesh size was changed in the model, and some parameter evaluations were repeated: `ERODE`, `recov`, and `repow` for the CSCM model and the compressive damage scaling factor, B_1 , for the K&C model. Three different mesh sizes were investigated: ½ in. (13 mm), ¼ in. (6.3 mm), and ⅛ in. (3.2 mm). These mesh sizes resulted in element totals of 768, 6144, and 49,920, respectively. The development of finer meshes also resulted in smoother edges around the circumference of the cylinder, as shown in Figure 209. This change was an improvement from the last round of simulations. No friction or element type variation simulations were completed as those

model variations were previously deemed ineffective, and the models were relatively insensitive to these parameters.

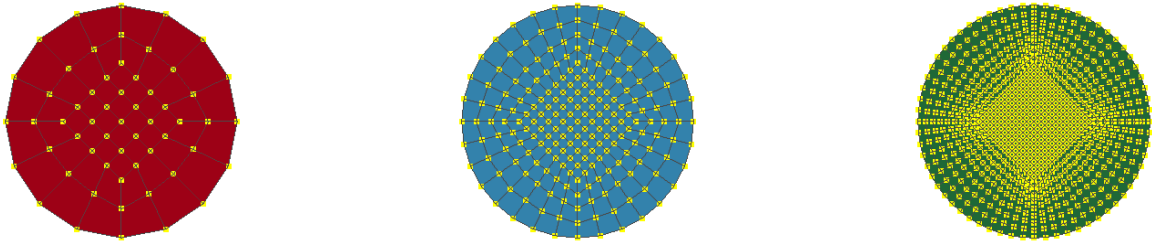


Figure 209. Mesh Sizes for Compression Cylinders

After variations were made to the model and material inputs, the simulation results were compared to the laboratory testing results, as shown in Figure 210. This physical test behavior was generated by taking the average peak stress and failure strain for the seven cylinder tests and developing a linear relationship between those coordinates and the origin. This process eliminated the noise in the test results, as seen in Figure 119. This process was required to address the noise in the strain data as well as the various peak stresses, which would have made it difficult to average the data. An assumed linear relationship was deemed appropriate as all of the tests demonstrated linear stress-strain behavior in the elastic region. Due to the poor quality of simulated deformation data, the stress-time histories were also compared with the average peak stresses obtained from the experimental tests. The simulated stress was calculated using cross-sectional force divided by the cross-sectional area of the cylinder. The simulated stresses and calculated simulation strains were plotted along with the physical test behavior. The simulation strain was calculated by dividing the displacement of selected nodes by the original length of the specimen. The second comparison for the material models included the animation of cylinder compression and crush for qualitative analysis.

This evaluation included both the element deletion pattern for the CSCM model as well as the damage profile of the cylinder for both models.

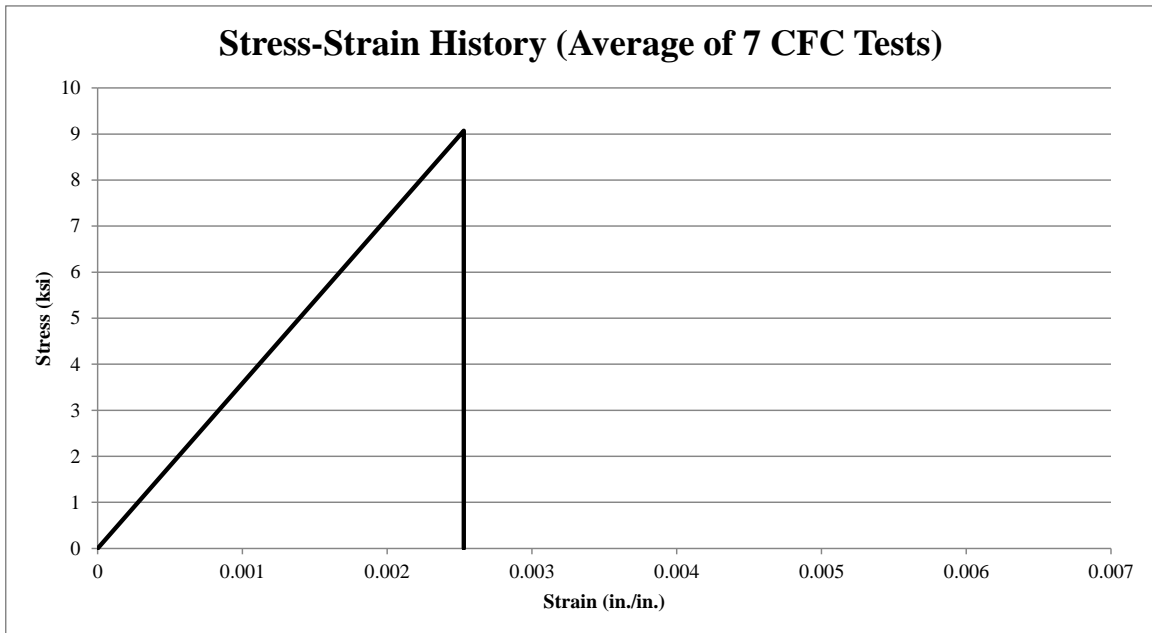


Figure 210. Compression Test Stress-Strain Behavior, Compression (Average of 7 Tests)

13.3 CSCM Model – Simulation Results

The parameters (ERODE, recov, and repow) were varied within the LS-DYNA simulations involving the CSCM model, which required between 1 to 2 hours to complete. Various mesh sizes were also simulated, which ran for over 6 hours. The following investigations were completed for the CSCM model: mesh size; ERODE; repow; and recov. No hourglass energy issues were encountered with any of the simulations involving cylinder compression with this material model.

13.3.1 Mesh

Three different mesh sizes were simulated side-by-side in the same model. Based on the animation of the loading event, the elements in the coarse mesh (1/2-in. [13-mm]) were too large, and the mesh erosion resulted in a large portion of the cylinder being

deleted, as shown in Figure 211. With so few elements through the cross-section and along the specimen height, the model was unable to predict adequate microcracking.

The peak strengths for all three mesh sizes were similar and slightly over-predicted the average peak stress for the physical testing series. Based on the plot in Figure 212, it is clear that the nodes that were chosen to track displacements for use in the strain calculation did not show a linear deformation pattern. However, other nodes selected on the cylinder yielded similar results. The element deletion pattern for all cylinders caused this inaccurate stress-strain behavior for all simulated nodes. The moduli of elasticity were different between the simulation and test results, as was seen in previous simulations; the modulus of elasticity in the simulation was 7248 ksi (50.0 GPa) and in the experimental test was 3586 ksi (24.7 GPa).

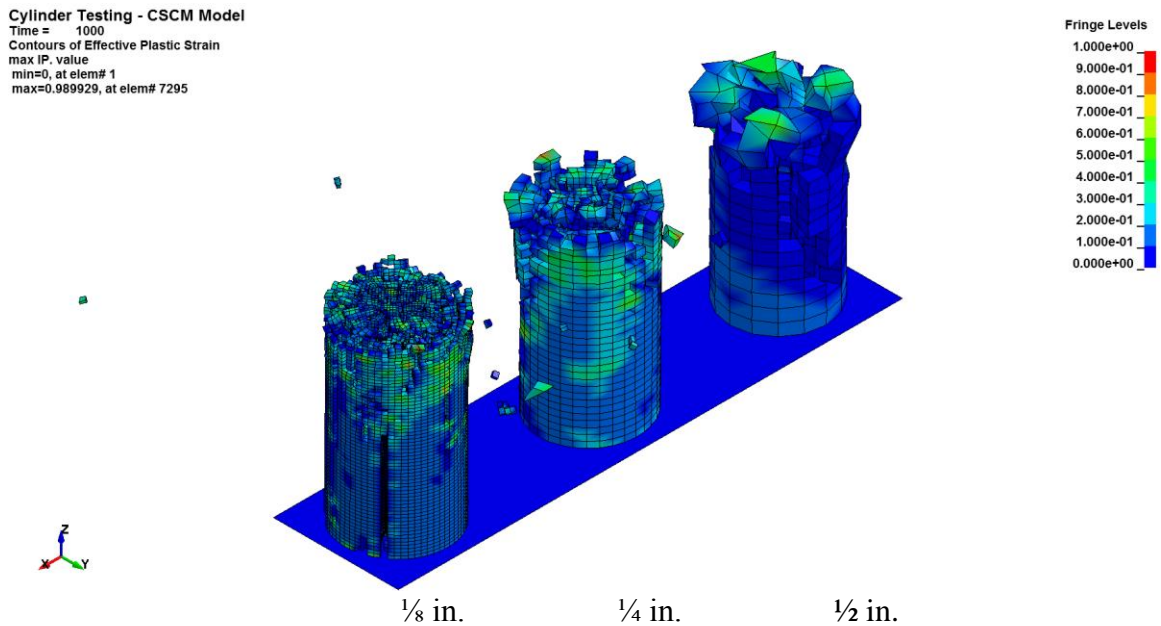


Figure 211. Compression Damage Contours for Mesh-Size Simulation, CSCM Model

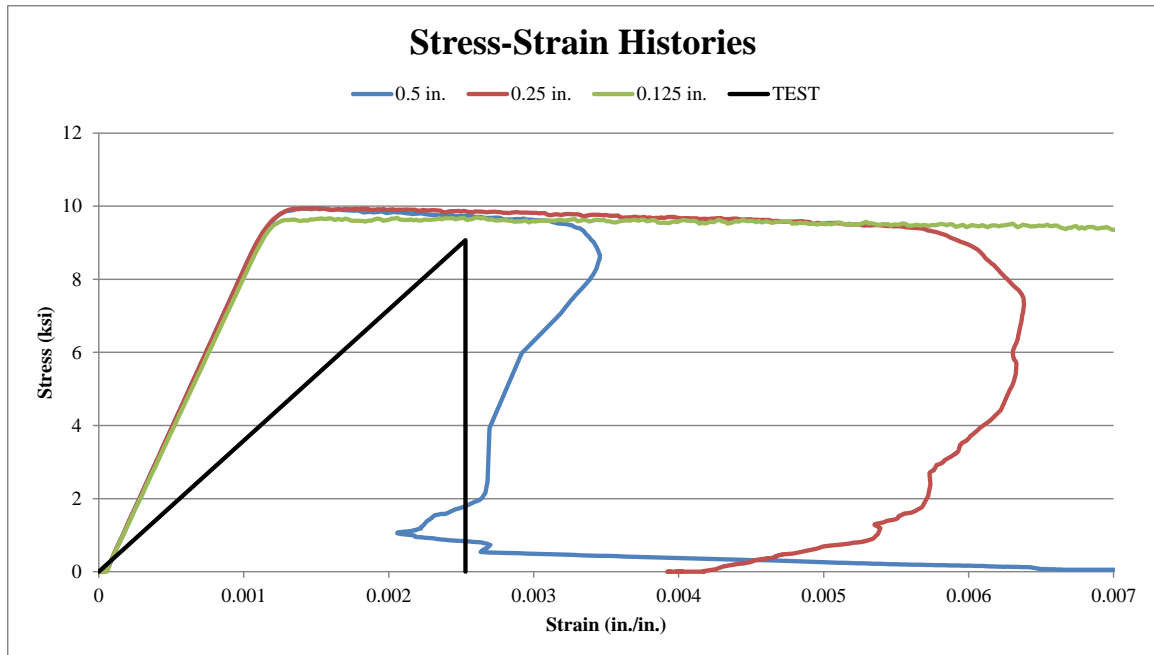


Figure 212. Compression Stress-Strain Behavior for Mesh-Size Variation, CSCM Model

The inability to accurately track displacements made it impossible to compare stress-strain plots. A direct stress-time comparison could not be made; since, the simulation and physical tests were not on the same time scale. Instead, the peak stress of the experimental tests as compared to the peak stress in the simulations, as shown in Figure 213. All peak strengths were similar for the three mesh sizes, but the softening behaviors were significantly different. The $\frac{1}{8}$ -in. (3-mm) mesh size did not soften until 500 ms, more than twice as long as the time to soften for the $\frac{1}{2}$ -in. (13-mm) mesh. Due to the coarseness of the $\frac{1}{2}$ -in. (13-mm) mesh size, the deletion behavior was not adequate. The $\frac{1}{8}$ -in. (3-mm) mesh size, however, had the closest peak load. Due to the finest mesh having delayed softening combined with the coarse mesh being too large, the $\frac{1}{4}$ -in. (6.4-mm) mesh was determined to perform the best and was selected for further analysis.

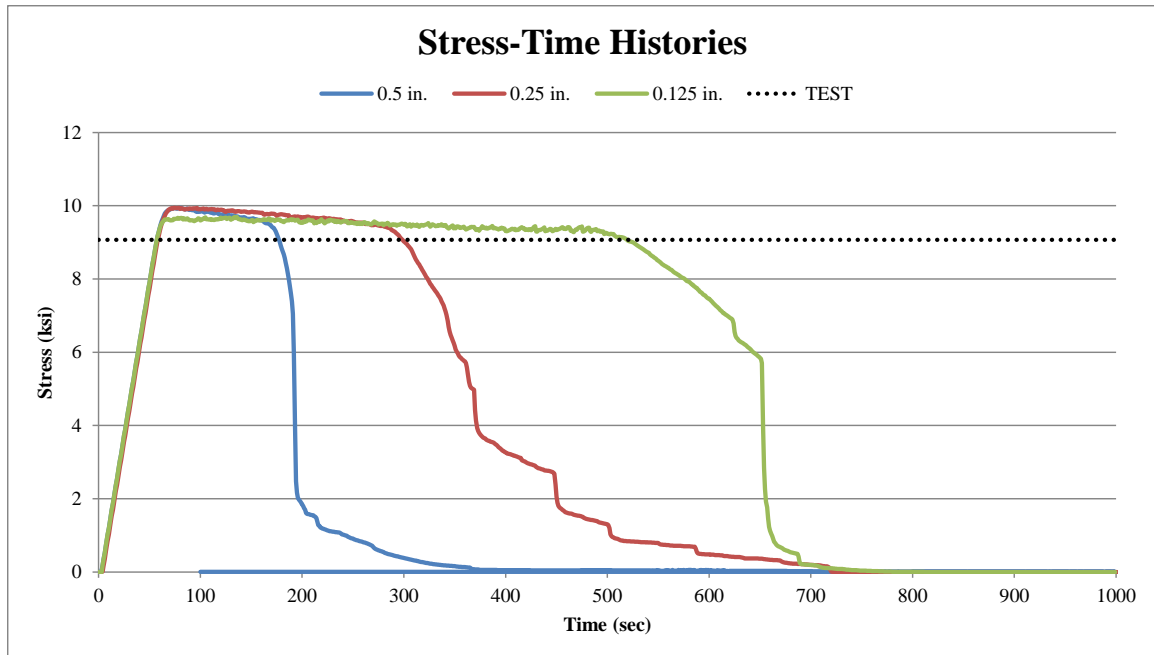


Figure 213. Compression Stress-Time Behavior for Mesh Size Variation, CSCM Model

13.3.2 ERODE, recov, and repow

These input parameters were grouped together for simulation analyses, because similar trends were found to those demonstrated in previous simulations. The ERODE parameter was varied between 1.00, 1.05, and 1.10, and the recov and repow parameters were both analyzed at 0.0, 0.5, and 1.0. Adjustments in these parameters generally did not affect the simulated stress-strain or stress-time behaviors. The peak stresses were nearly the same regardless of the ERODE, recov, or repow value, as specifically shown in Figure 214 for the three parameters. The only observed difference was the location of significant damage, as some values concentrated damage at the top of the cylinder and other values caused the majority of damage at the bottom of the cylinder. It was determined that the default values would be used: 1.00 for ERODE; 0.0 for recov; and 1.0 for repow.

A follow-up study was then completed for these three parameters as well to confirm a trend that was seen in the previous simulation effort. Three cylinders with identical meshes, as well as ERODE, recov, and repow parameters, were simulated in compression to evaluate repeatability. Despite all three cylinders having the same ERODE parameter for the damage contours shown in Figure 215, the crack locations varied widely. This finding indicated that this material model did not provide repeatable results. Note that all cylinders showed different animated behavior, thus indicating randomness in the failure behavior and/or significant instabilities in the material model.

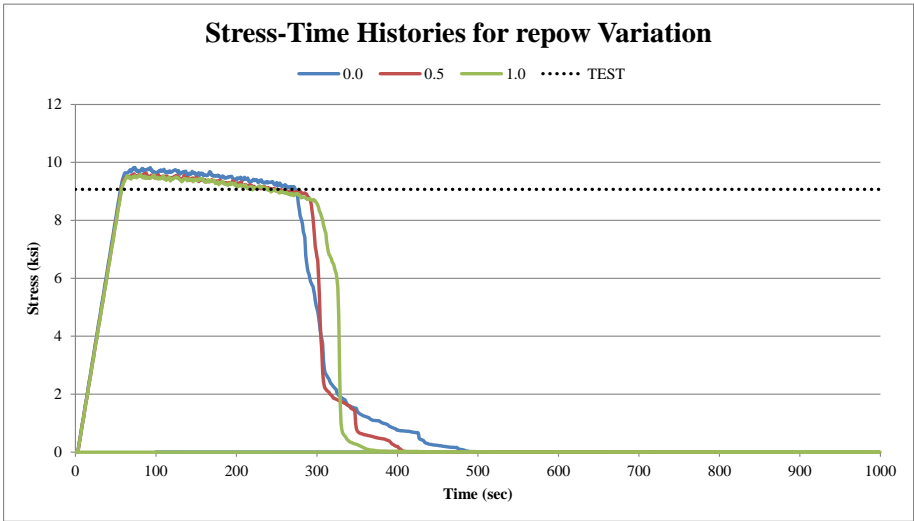
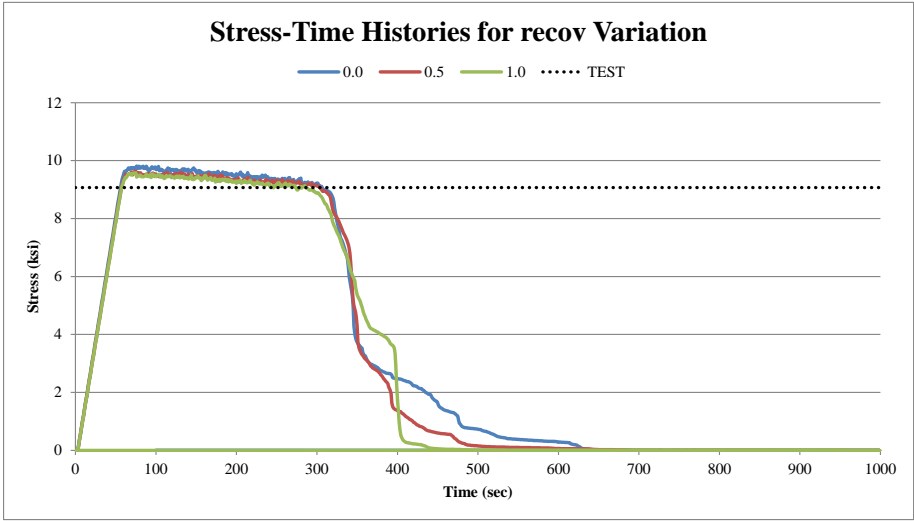
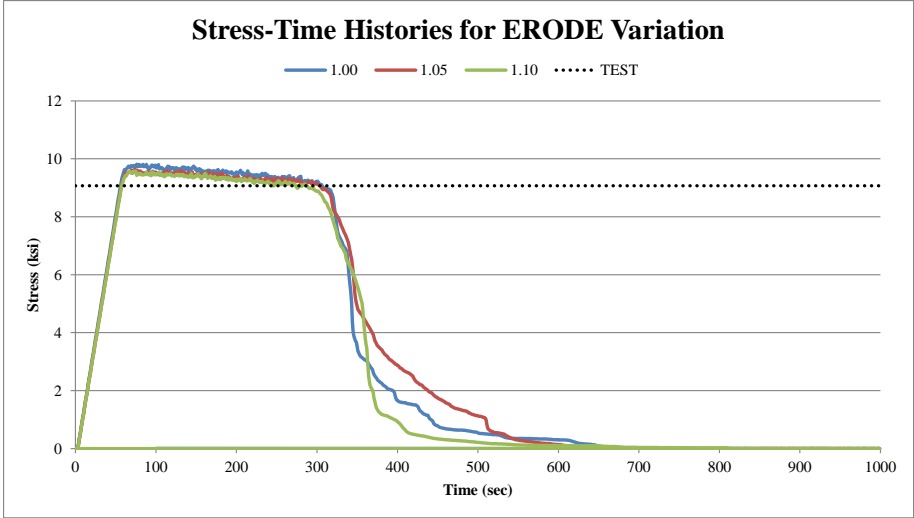


Figure 214. Compression Stress-Time Behavior for ERODE, recov, and repow Variations, CSCM Model

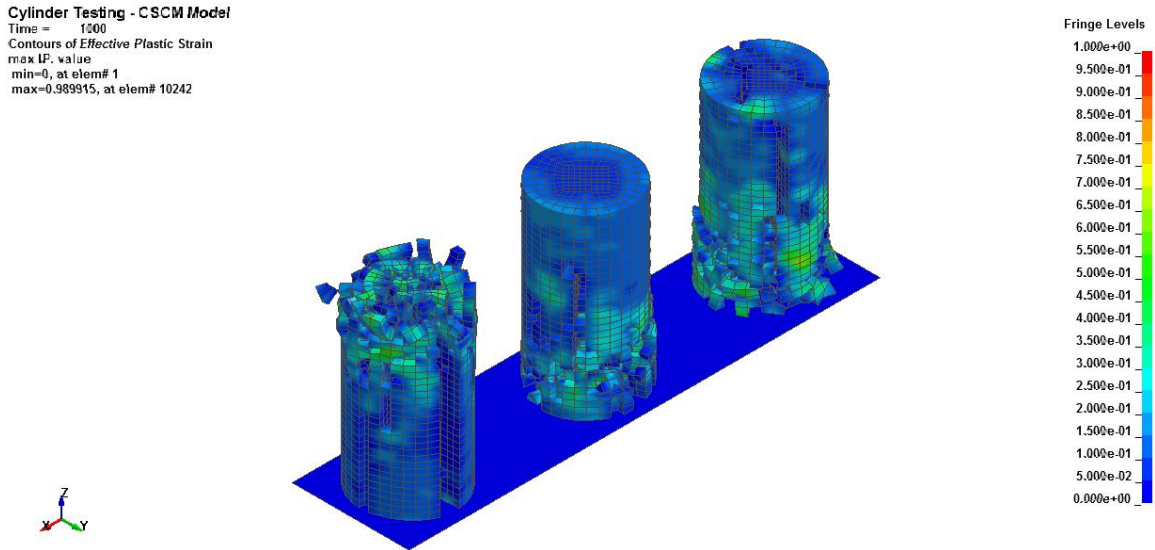


Figure 215. Compression Damage Contours for ERODE Simulation, CSCM Model

13.4 K&C Model – Simulation Results

The mesh-size simulation investigation with the K&C model required over 4 hours for runs to complete. The same B_1 parameters investigated previously (0.0-1.0; 1.0-2.0; and 2.0-3.0) were again examined in these simulations. When an attempt was made to run simulations using different B_1 parameters, the 1.0-2.0 and 2.0-3.0 ranged simulations were terminated in error. This outcome resulted in an incomplete analysis; therefore, it was determined that the default value, 1.6, was still adequate for further simulations. An analysis of the strain rate effects was not completed due to not providing accurate rate effects as defined. The DIF value was found to overestimate the increase in strength; therefore, the strain rate effects were turned off for this round of simulation. Adding element deletion capability using *MAT_ADD_EROSION into the model was considered. However, no realistic method was found, and this change would only display deletion in the animation of the simulation and not affect the forces and energies. No major hourglass energy issues were encountered with any of the simulations for

compression using this material model, although some hourglass energy (less than 5% of internal energy) was present.

13.4.1 Mesh

The simulated cylinder load cases resulted in damage throughout the cylinder, with more damage concentrated near the top of the cylinder for all three mesh sizes, where the damage reached the 2.0 maximum. There was a large amount of dilation in the elements near the top of all cylinders, as shown in Figure 216, but that dilation was expected based on the inability for this material model to delete elements. Unreasonable deformations were clearly experienced, and the damage contours are not reliable. Diagonal shear cracks were not present during this simulation.

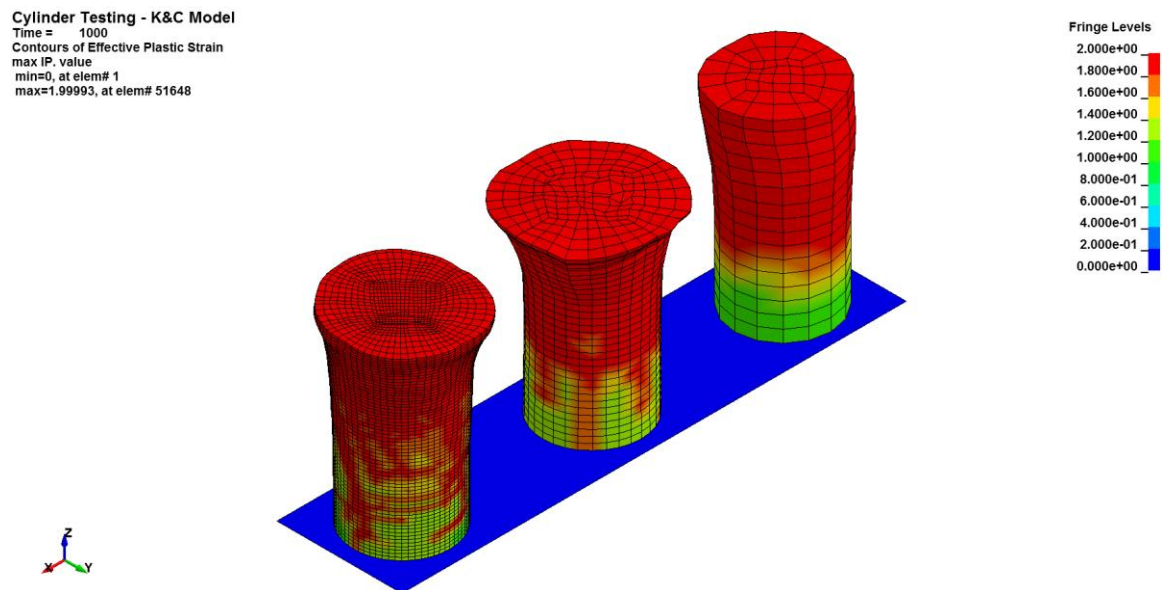


Figure 216. Compression Damage Contours for Mesh-Size Simulation, K&C Model

The stress-time cylinder behavior was very similar amongst the three mesh sizes. The simulation results with the 1/2-in. (12.7-mm) and 1/4-in. (6.4 mm) mesh sizes overlapped each other, whereas the results with the 1/8-in. (3.2-mm) mesh size returned to zero faster, as shown in Figure 217. The peak stresses for the three mesh sizes almost

matched perfectly with the averaged peak stress of 9.0 ksi (62.1 MPa) representing the physical tests of 9.1 ksi (62.7 MPa). The hourglass energy for the finest mesh (1/8-in. [3-mm]) was 4% of the internal energy and was minutely higher than observed for the other two mesh sizes, which was the only true differentiation between the three mesh sizes. Due to limited differences between the three mesh sizes, all were equivalent. This finding indicated that the mesh size selections did not significantly affect model performance for this particular component configuration.

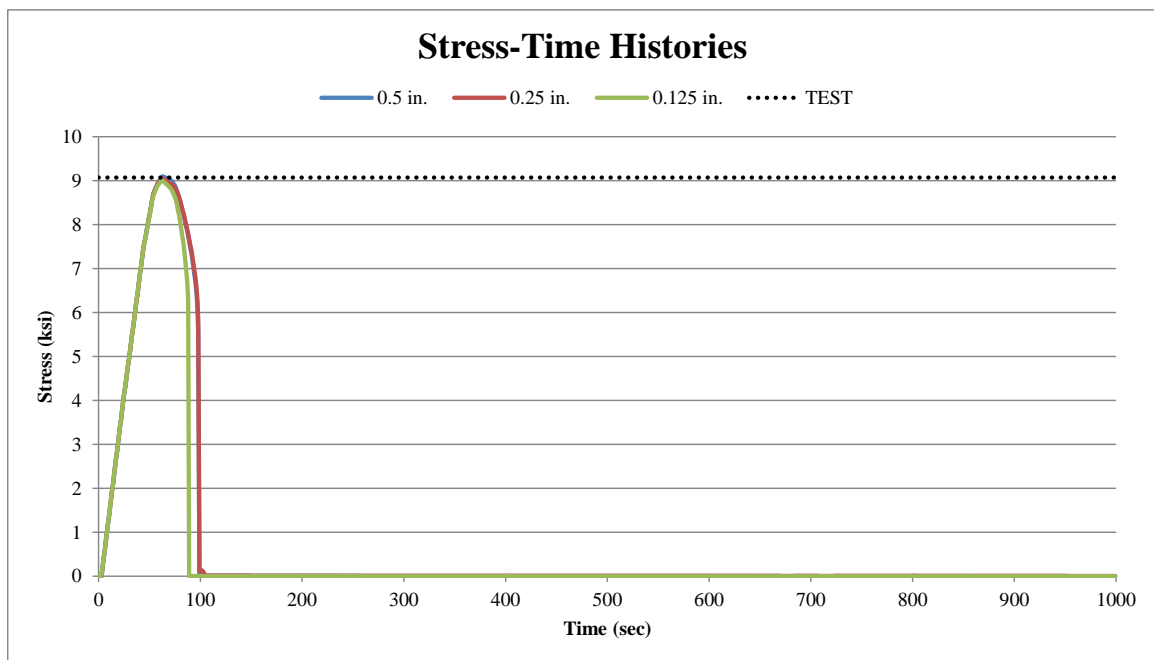


Figure 217. Compression Stress-Time Behavior for Mesh-Size Simulation, K&C Model

13.5 Discussion

In the compression simulations, both models matched the peak strength reasonably well as compared to the experimental testing. The CSCM model overestimated peak stress (by 10%), while the K&C model provided nearly an identical peak stress. The animation of the failures for both models were less impressive, but still demonstrated that the specimen was failing. There were even some diagonal failure

planes predicted by the CSCM model that agreed with the failure patterns in test nos. CFC-1 through CFC-7. Animations did not reveal actual damage appearance, but numerical performance was still acceptable.

There was less post-peak retention of strength in the K&C model, which was consistent with previous simulations. It was still concerning that some parameter adjustments in the CSCM model did not cause much varied behavior. Parameter changes did not have a noticeable effect, but modeling cylinders with identical parameters within the same model set did provide inconsistent results. This finding indicates that the material model results are not very repeatable, likely indicating a fair amount of randomness in the coding of the constitutive equations. Input parameter evaluations were not completed for the K&C model; since, the simulations with the compressive damage scaling factor simulations were terminating with errors, and the strain rate effects were ignored based on prior knowledge.

CHAPTER 14 SIMULATION OF INTERNAL CONCRETE DOGBONE TESTS

14.1 Introduction

The second set of simulations corresponded to the CFT tension testing program. Again, only the CSCM and K&C models were evaluated. The setup of test nos. CFT-1 through CFT-6 was easily replicated in the simulations. A dogbone-shaped specimen was created in the pre-processing software (LS-PrePost) using the dimensions of the specimen mold. One simulation geometry was deemed sufficient, because each sample had approximately the same dimensions. The aggregate size, concrete compression and tensile strengths, etc., were implemented into the two models to represent the specimen material properties.

The intent of the dogbone simulations was to compare the simulation results from each of the five material models to the acquired test results from test nos. CFT-1 through CFT-6. The dogbone in the model had a 4-in. x 4-in. (102-mm x 102-mm) end cross-section and a 3-in. x 4-in. (76-mm x 102-mm) critical cross-section along its 12-in. (305-mm) length. A *BOUNDARY_PRESCRIBED_MOTION was applied to the bottom nodes of the dogbone to allow for movement in the z-axis. A *BOUNDARY_SPC definition was given to the top nodes in order to hold them in place. The displacement rate was increased linearly until the end of the simulation. Cross-sections were placed through the center of the dogbones in order to measure forces for use in computing stresses. An overview of the model is shown in Figure 218.

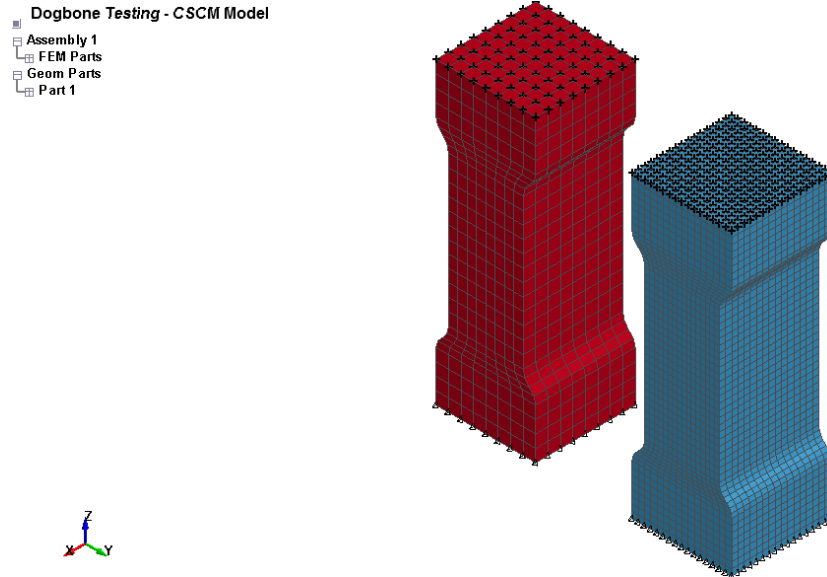


Figure 218. Overview of Internal Tension Simulation

14.2 Simulation Data Evaluation Process

A displacement rate analysis was completed for each of the two material models to determine an appropriate simulation displacement rate. The test displacement rate of 0.0001 in./s (0.0025 mm/s) could not be used in the simulation, since it was disadvantageous for use in explicit LS-DYNA analyses. A linear displacement function was assumed. Potential displacement rates ranged from 0.95 in./s (24.1 mm/s) to 9.5×10^{-3} in./s (0.24 mm/s), and the goal was to find convergence in the stress-strain behaviors. Once convergence was reached, this rate would be considered optimum. For both material models, this rate was found to be 0.019 in./s (0.48 mm/s) for a total simulation time of 5000 ms.

The intent of the dogbone simulations was to compare the simulation results for each of the two material models to the peak stresses from the internal testing program. The stress-strain behavior could not be directly compared due to difficulties associated with recording strain with the laser extensometer. Variations were made to the model

configuration as well as the default material input parameters in order to find a combination that best matched the physical test peak stresses. No additional parameters were investigated, unlike the previous round of tension simulations.

Multiple dogbone specimens were used in the same simulation to directly compare variations in the model and material input parameters. The mesh size was changed in the model, and some parameter evaluations were repeated: ERODE; recov; and repow for the CSCM model as well as the compressive damage scaling factor, $B_{1,}$ for the K&C model. Two different mesh sizes were tested: ½-in. (13-mm) and ¼-in. (6.3-mm), as shown in Figure 219. A finer band of mesh was used where the part began to narrow to ensure the curved portion was modeled accurately.

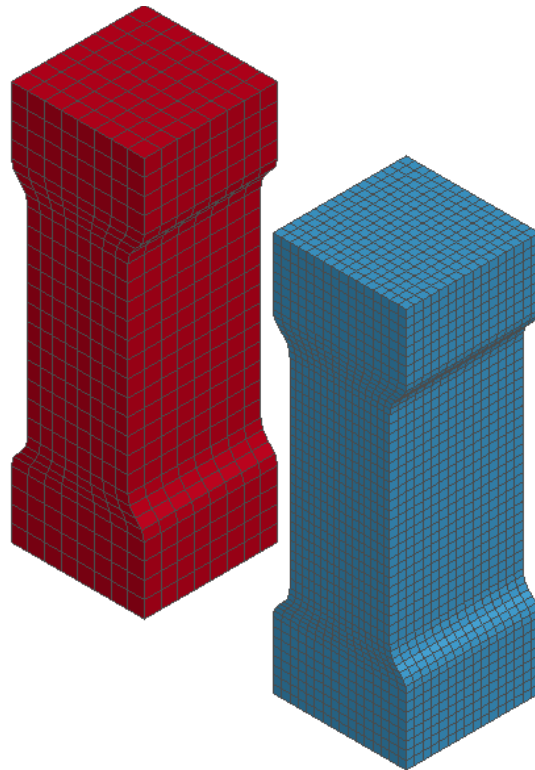


Figure 219. Mesh Sizes for Tension Dogbones

Once the different variations were made to the model and material input parameters, the simulated stress-strain results were compared to the physical test peak stress of 0.36 ksi (2.5 MPa). A stress-time or force-time relation could not be displayed, because the physical test and simulation were on different time scales. The second comparison for material models involved the dogbone animations, including element deletion pattern for the CSCM model and damage profile for both models.

14.3 CSCM Model – Simulation Results

Several parameters were varied within LS-DYNA simulations involving the CSCM model, which required between 1 to 2 hours each to complete. The mesh-size variations were also simulated and ran for over 3 hours. The following parameter investigations were completed for this model: mesh; ERODE; repow; and recov. Hourglass energy issues were addressed after the initial simulations were completed.

An initial simulation was completed using the default hourglass energy. There were high hourglass energies in the model, so an effort was made to control these energies using hourglass control types 3 through 9. It was determined that hourglass control type HG4 using *HOURLASS was the best control method for this specific model. It was used for the remaining simulations.

14.3.1 Mesh

Two different mesh sizes were compared for the CSCM model: ½-in. (12.7-mm) and ¼-in. (6.4-mm). High hourglass energies that could not be controlled were encountered with the ⅛-in. (3.2-mm) mesh size, therefore it was not considered. In the specimen animations, two major bands of damage formed on the parts near both locations where the parts began to neck, as shown in Figure 220. The higher damage occurred near

the top of the dogbone for the finer mesh, and lower damage occurred near the bottom of the dogbone for the more coarse mesh. The parts eventually fractured at these locations.

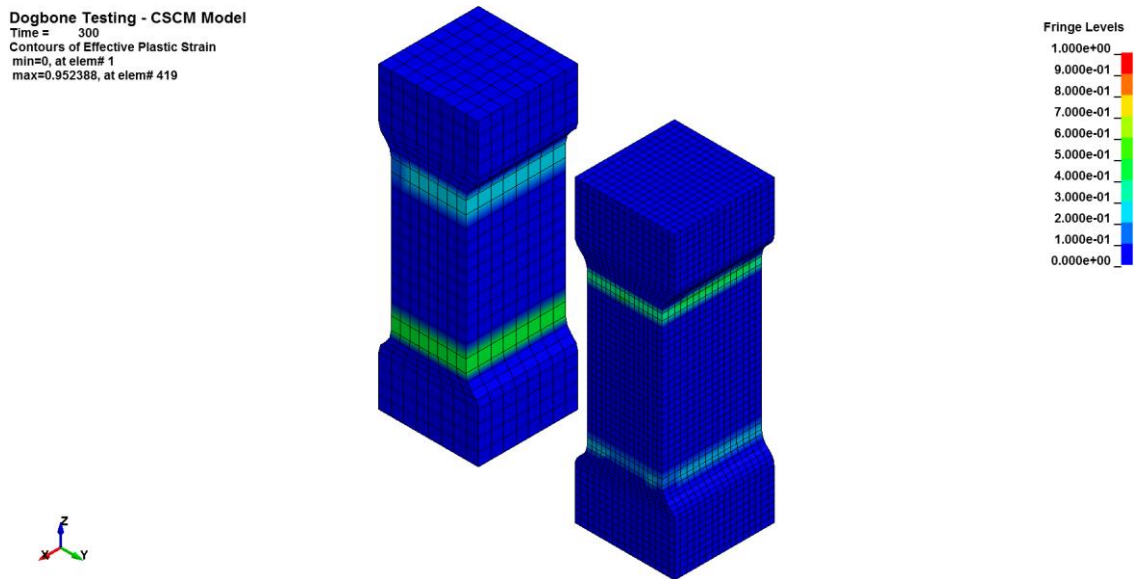


Figure 220. Tension Damage Contours of Mesh-Size Simulation, CSCM Model

When comparing the stress-strain behaviors from the simulations with the experimental testing peak stress, both mesh sizes resulted in a peak stress of 0.43 ksi (2.7 MPa) over-estimated the physical test peak stress of 0.36 ksi (2.5 MPa), as shown in Figure 221. The only difference between the two mesh sizes was the post-peak response. Again, the major comparison between the simulation and laboratory test results for tension was the peak stress. Since both mesh sizes had nearly the same peak stress, another indicator was used to evaluate mesh size. The softening behavior with the coarser mesh ($\frac{1}{2}$ in. [12.7-mm]) occurred more quickly, with the curve falling off faster. This behavior was somewhat preferred in tension, as there was little to no softening expected. Softening behavior was difficult to compare without any physical test strain results, but knowing little softening was expected, the mesh size with the least softening would be

preferred. Therefore, the 1/2-in. (13-mm) mesh was used in the remainder of the simulations.

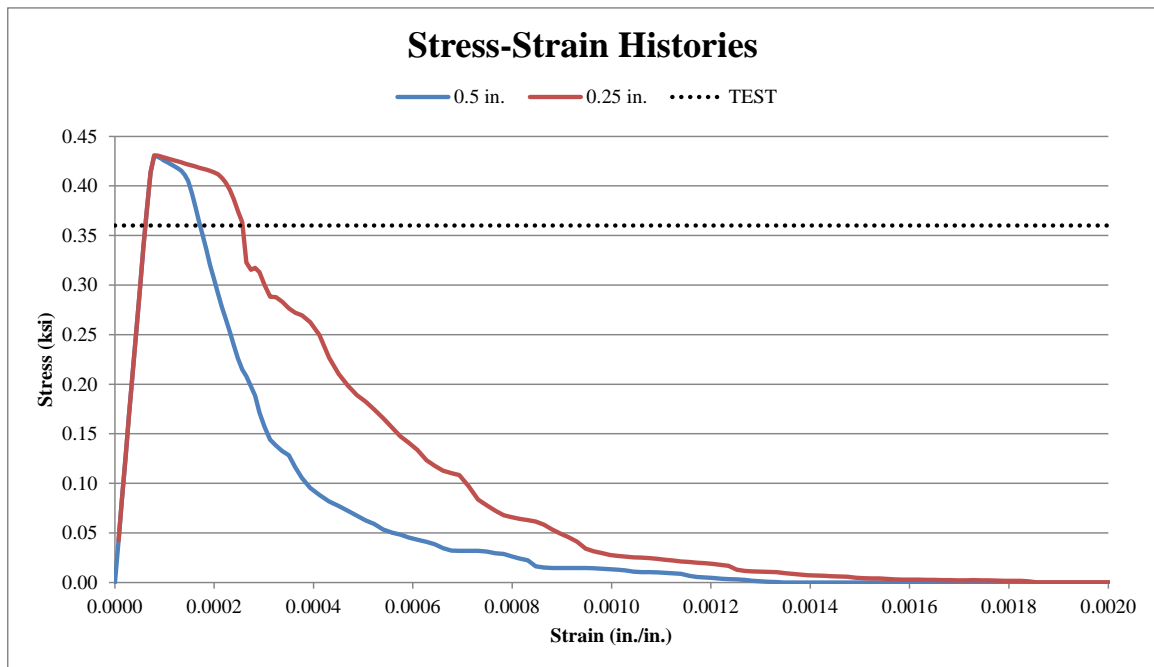


Figure 221. Tension Stress-Strain Behavior for Mesh-Size Variation, CSCM Model

14.3.2 ERODE, recov, and repow

Parameters were evaluated to determine model sensitivity. Again, the default values were found to be the best for the ERODE, recov, and repow parameters. The following values were checked for ERODE: 1.00; 1.05; and 1.10. The following values were investigated for both recov and repow: 0.0; 0.5; and 1.0. There was some varied behavior for parameter changes in the tension simulations as shown in Figure 222.

In the ERODE simulation effort, the 1.10 value was associated with high hourglass energies for this part, and it did not fail. Its stress-strain behavior was different from the other two values that were tested. The best performance was associated with the 1.00 value was again preferred for ERODE. The only observed difference with the recov parameter was the location of failure, either at the top or bottom necking region on the

part. For the repow parameter of 0.5, the entire part deleted mid-way through the simulation and resulted in high hourglass energies. Additionally, the stress-strain behavior for this parameter was far different than observed for the other parameters. Therefore the default parameters were recommended for the three parameters. For all parameters, the peak stress was overestimated, as was the case in previous simulations.

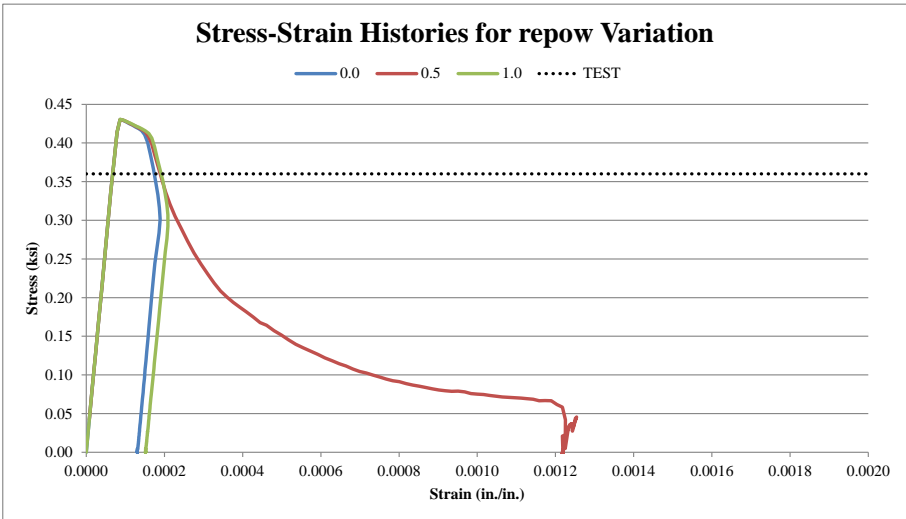
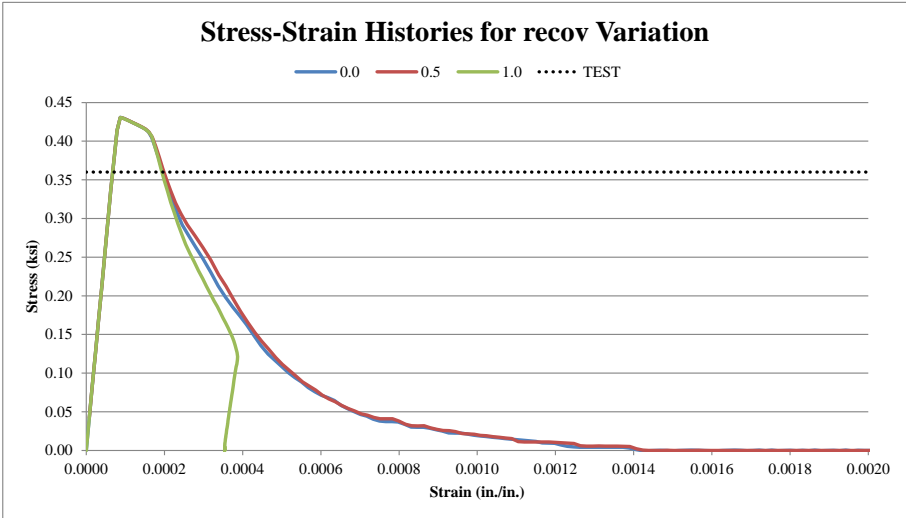
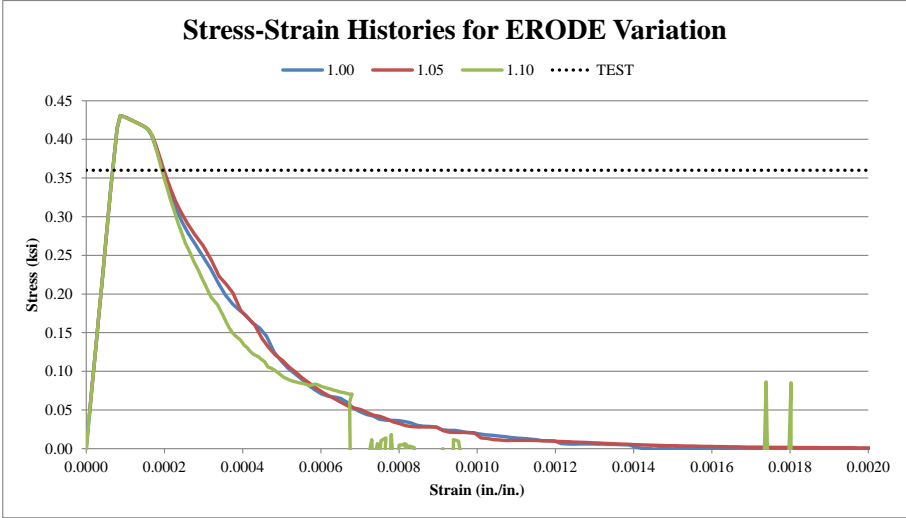


Figure 222. Tension Stress-Strain Behavior for ERODE, recov, and repow Variations, CSCM Model

14.4 K&C Model – Simulation Results

The compressive damage scaling factor, B_1 , was varied for the tension load case. A mesh-size comparison was also completed for this material model evaluation. The strain rate effects were again not considered; as they did not behave as defined in prior simulations. Hourglass energy issues were addressed after an initial simulation effort was completed.

14.4.1 Mesh

The initial simulation effort resulted in high hourglass energies, thus additional hourglass energy control methods were implemented. The same hourglass control types were tested for this material model, and it was determined that the same control type, HG4, worked best for this simulation due to its ability to limit the hourglass energies. This hourglass control was implemented for all remaining simulations.

In the simulation animations, there were again two major damage bands where the part necked down to the slimmer cross-section. Unlike the CSCM model, there were intermediate areas of damage accumulation between these two bands, as shown in Figure 223. The damage accumulated at higher levels near the top of the part and failure likely would have occurred at this location if a feature of the material model. On the surface of the part, the damage parameter only reached 1.4, but elements within the part reached the 2.0 failure threshold.

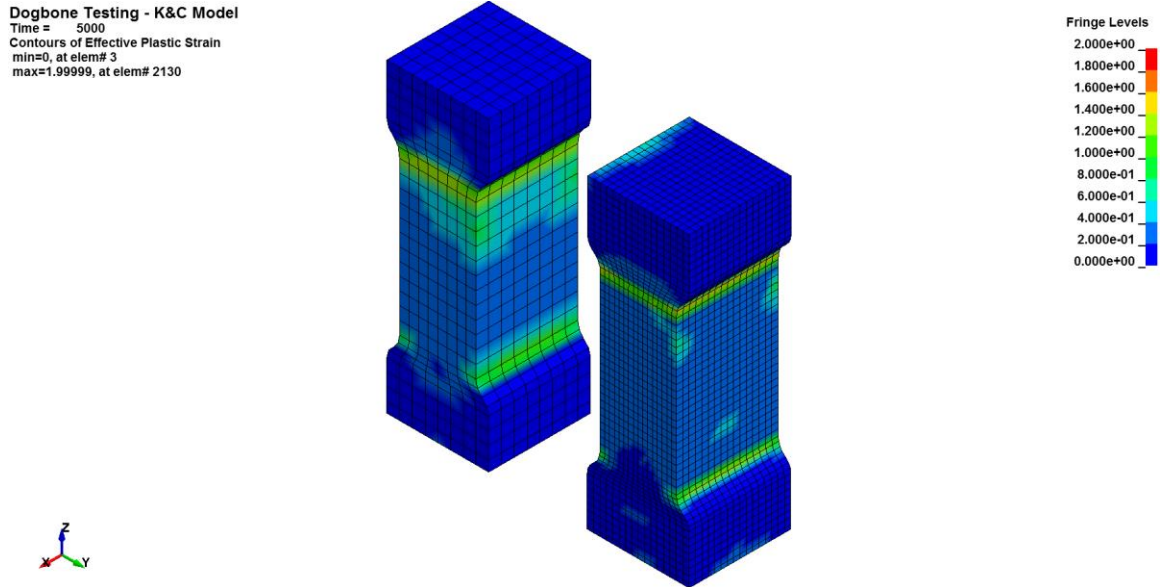


Figure 223. Tension Damage Contours for Mesh-Size Simulation, K&C Model

The stress-strain behavior for the K&C model was improved relative to that observed for the CSCM model. The peak stresses were of 0.34 ksi (2.3 MPa) and 0.30 ksi (2.1 MPa) slightly underestimated for the ½ in. (12.7 mm) and ¼ in. (6.4 mm) mesh sizes, respectively, as shown in Figure 224. The coarser mesh was closer to the physical test peak stress of 0.36 ksi (2.5 MPa). There was little softening after peak stress was reached. This behavior was preferred and expected for the tension load case as a more brittle failure was believed to be more likely to occur. Again with a limited study and no point of comparison, the conclusions on softening were based on the expectation that no softening should be occurring. The coarser mesh, ½ in. (12.7 mm), was preferred as it more accurately predicted peak stress.

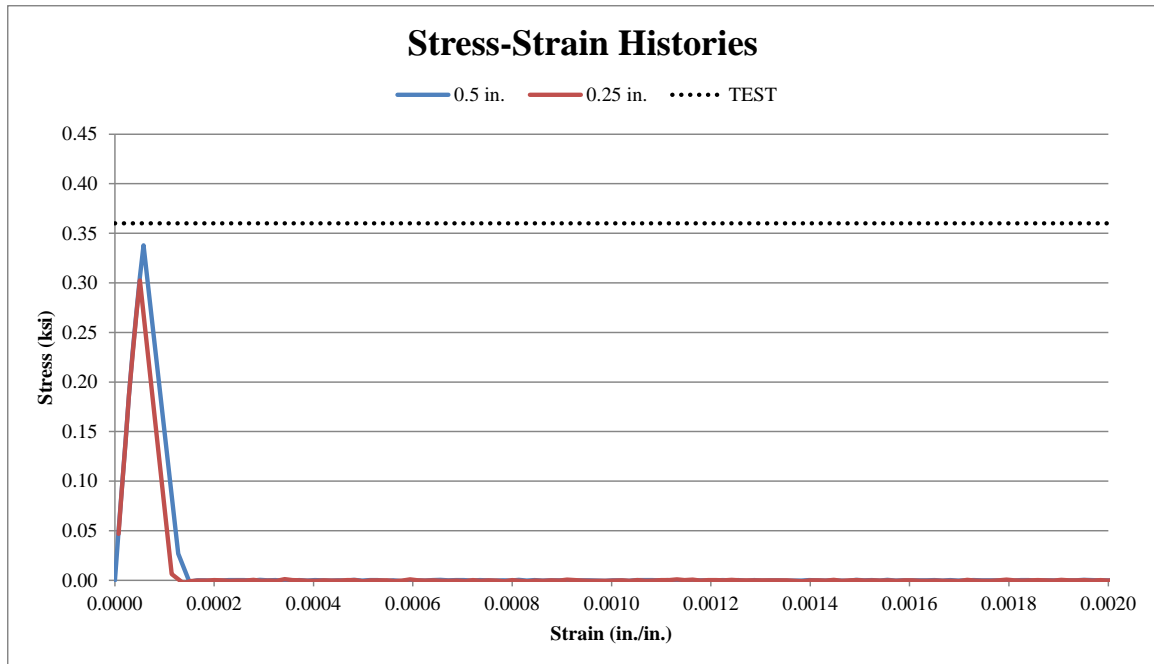
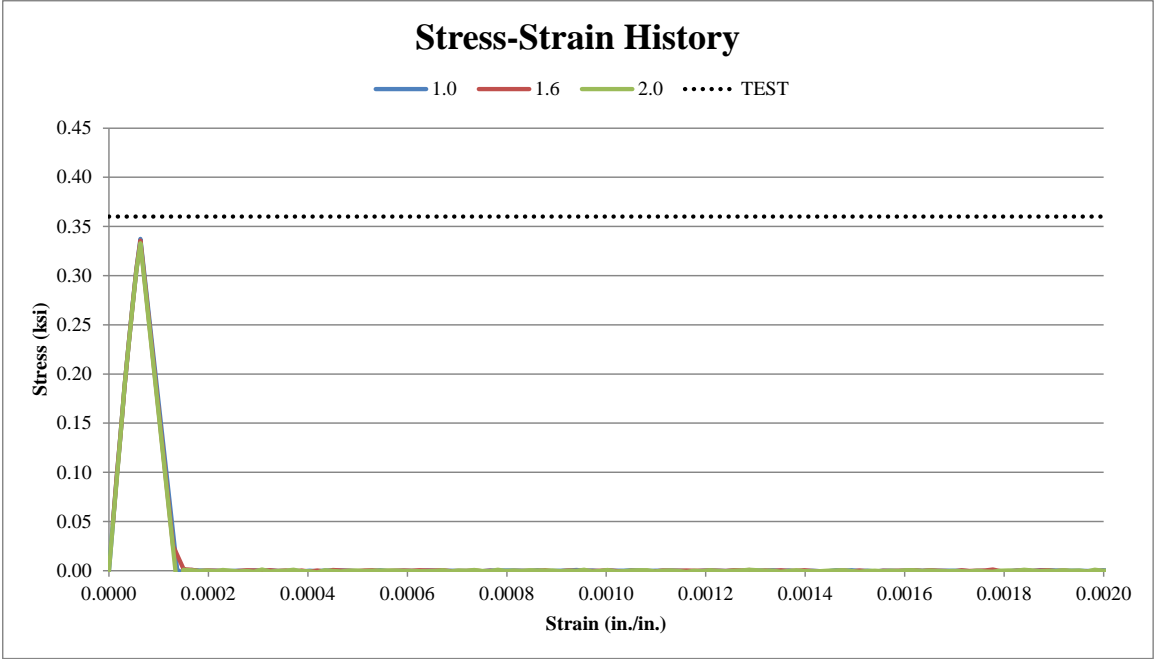


Figure 224. Tension Stress-Strain Behavior for Mesh-Size Simulation, K&C Model

14.4.2 Compressive Damage Scaling Factor

Three different ranges of the compressive damage scaling factor were simulated with the coarser mesh. The following values for B_1 were simulated across three separate models: 0.0, 0.6, and 1.0; 1.0, 1.6, and 2.0; and 2.0, 2.6, and 3.0. There were minimal differences in simulation results for these ranges, both in the stress-strain behavior and the damage profiles, as shown in Figure 225 for the 1.0 to 2.0 range. This behavior was true for all the ranges tested. Therefore, it was assumed that the default value of 1.6 was acceptable.



Dogbone Testing - K&C Model
Time = 5000
Contours of Effective Plastic Strain
min=0, at elem# 3
max=1.99998, at elem# 5154

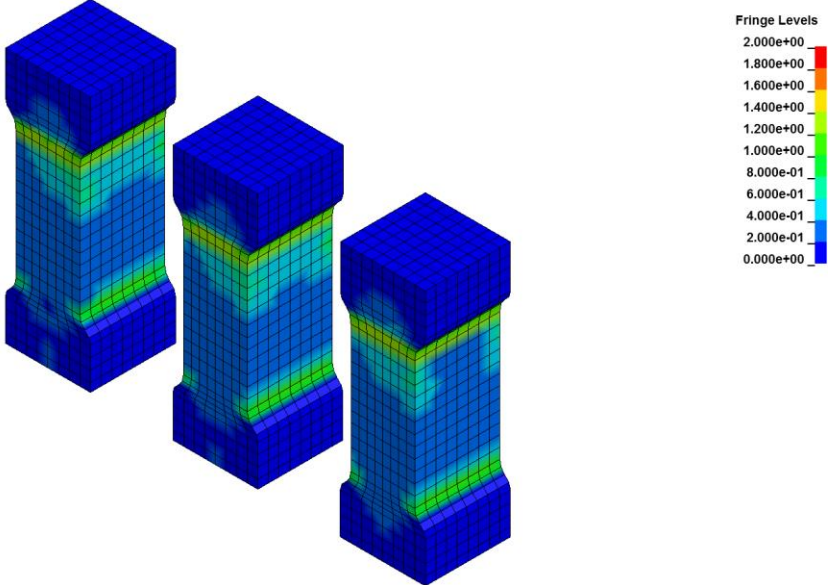


Figure 225. Tension Stress-Strain Behavior and Damage Contours for B₁ Simulation, K&C Model

14.5 Discussion

In the tension simulations, the results reasonably represented the experimental testing results for both CSCM and K&C models, as based on limited comparison. The major comparison was the peak stress of the physical tests versus that of the simulations.

For both material models, the prediction of peak stress was reasonable and within 19.4% overestimated and 6.2% underestimated for the CSCM and K&C models, respectively. Both material models revealed the same basic damage trends. Much of the damage was centered around the transition regions in the specimens or between the square ends and necked center cross-section. In the experimental dogbone tests, this damage was often located in this area. The K&C model had significantly less post-peak behavior as the tensile stresses dropped quickly to zero, while there was more softening in the CSCM model. Therefore, both models performed reasonably well in the tension load case and predicted the experimental data accurately. For tension modeling of unreinforced concrete, a ½-in. (13-mm) mesh was recommended with the default parameters.

CHAPTER 15 SIMULATIONS OF INTERNAL CONCRETE BEAM TESTS

15.1 Introduction

The final set of simulations correspond to the CFS beam testing program. Only the CSCM and K&C material models were evaluated; since, they performed the best out of the material models previously considered. The setup for test nos. CFS-1 through CFS-6 was replicated in the simulations. A 6 in. x 6 in. x 22 in. (152 mm x 152 mm x 559 mm) unreinforced concrete beam was created using the LS PrePost software. Each test specimen was approximately the same shape and size. Thus, there was no need to exactly replicate each beam geometry. The aggregate size, concrete compression and tensile strengths, etc., were implemented as parameters into the two material models to represent the specimen material properties.

To simulate the experimental conditions, rollers were meshed with shell elements and placed at both the load points and the support points, as shown in Figure 226 for the coarsest mesh in the 9-in. (229-mm) support span simulation. Both sets of rollers were rigid and finely meshed to minimize contact issues. A *BOUNDARY_PRESCRIBED_MOTION was applied to the bottom rollers to allow for movement in the z-axis. A *BOUNDARY_SPC definition was given to the top rollers in order to hold them in place. The displacement rate was increased linearly until the end of the simulation. Cross-sections were placed through the center of the beams and rigid contact forces were acquired to determine peak forces. Six physical load tests were used to evaluate five span lengths. Thus, bending simulations were performed on spans of 9, 10, 11, 12, and 18 in. (229, 254, 279, 305, and 457 mm).

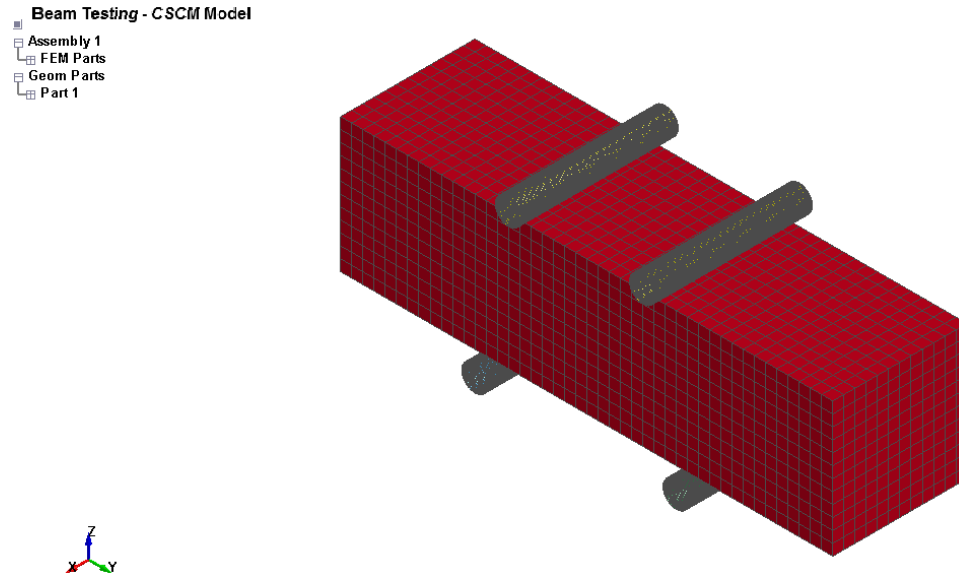


Figure 226. Overview of Internal Flexure and Shear Simulation

15.2 Simulation Data Evaluation Process

A displacement rate of 0.17 in./s (4.3 mm/s) was used for all simulations. The actual test displacement rate of 0.0003 in./s (0.0076 mm/s) could not be used in the simulation, because it was disadvantageous for use in explicit LS-DYNA analyses.

The experimental test data was used to evaluate simulation results from each of the two material models. Vertical cross-sections were placed in the model to record cross-sectional forces and displacements at the middle of the beam, the two fixed upper supports, and the two lower load locations. Contact forces were also recorded at the top and bottom supports. The failure pattern and location were also compared between simulation and physical test results. Force and strain curves were not over-plotted with test data, because the simulation and experimental tests were on different time scales.

Material property parameters were fixed based on results from previous tests associated with each material model. Non-default hourglass controls were used to limit non-physical hourglass distortions. Higher levels of hourglass energy were tolerated for

these models due to the complexity of the loading conditions. Hourglass energies were controlled using HG control type 6 for both material models. Additionally, repow was set to 0.5 for the CSCM model, as this parameter change lowered hourglass energies.

An alternate study was completed with varied parameters for the CSCM model recommended in a joint study by TTI and MwRSF [51] to attempt to further decrease hourglass energies. The results of this study are displayed in Appendix E.

The first models were evaluated with three mesh variations to investigate sensitivity to element size. Note that no material model variations were made during this round of simulations. Three different mesh sizes were initially investigated: ½ in. (13 mm), ¼ in. (6 mm), and ⅛ in. (3 mm). All three mesh sizes were compared throughout the beam simulations, since they yielded similar results.

15.3 CSCM Model Investigation and Evaluation

A simulation investigation for each of the five support spans was completed for the CSCM material model.

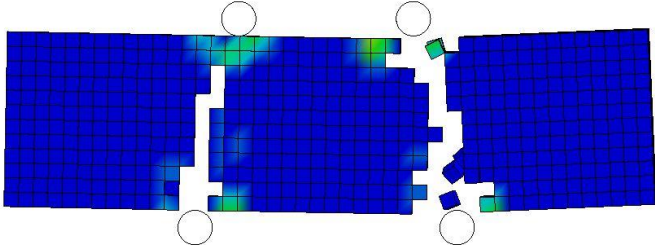
15.3.1 9-in. (229-mm) Support Span

The first support span distance correlated with test no. CFS-6, which was 9 in. (229 mm). In the experimental testing, this setup resulted in shear failure. Therefore, this failure was expected to be replicated in the simulations. This behavior was achieved for the ½-in. (13-mm) mesh, as the failure occurred along a diagonal plane on each end of the beam between the upper and lower supports, as shown in Figure 227 for time equal to 130 ms. However, flexural failure occurred in the ¼-in. (6-mm) and ⅛-in. (3-mm) meshes.

Simulation results indicated a peak load of 43.9 kip (195 kN) occurred when summing forces at rollers was near the peak load of 39.8 kip (177 kN) observed in test no. CFS-6 for the ½-in. (13-mm) mesh only, as shown in Figure 228. However, the ¼-in. (6-mm) and ⅛-in. (3-mm) mesh sizes had higher peak loads, at 50.0 kip (222.4 kN) and 56.5 kip (251.3 kN), respectively. Given the complex loading, it appears that the CSCM model accurately predicted the maximum force for the 9-in. (229-mm) support span in only the ½-in. (12.7-mm) mesh size.

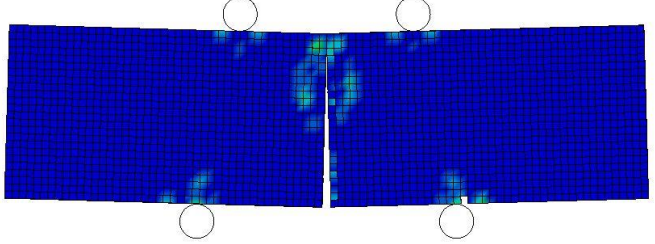
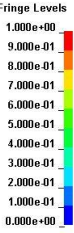
The energy plots showed similar trends. The hourglass energy was limited, but it was up to 17% of the internal energy for the ¼ in. (6 mm) mesh size. These hourglass energies are tolerated due to the complex load case and are shown in Figure 229. Based on the force and energy comparison for the three mesh sizes, the simulated behavior with the ½-in. (13-mm) mesh provided the best comparison to the experimental testing results using the selected parameters, especially in terms of peak load and failure pattern. This peak load was over-estimated by 10.3 percent.

Beam Testing - CSCM Model
Time = 130
Contours of Effective Plastic Strain
max IP. value
min=0, at elem# 195601
max=0.98915, at elem# 199691



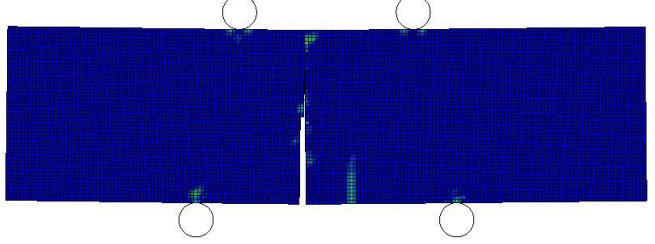
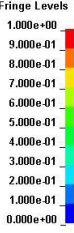
1/2 in. (13 mm)

Beam Testing - CSCM Model
Time = 130
Contours of Effective Plastic Strain
max IP. value
min=0, at elem# 201937
max=0.989721, at elem# 227977



1/4 in. (6 mm)

Beam Testing - CSCM Model
Time = 130
Contours of Effective Plastic Strain
max IP. value
min=0, at elem# 310801
max=0.989541, at elem# 526067



1/8 in. (3 mm)

Figure 227. Damage Pattern for 9-in. (229-mm) Span at 130 ms, CSCM Model

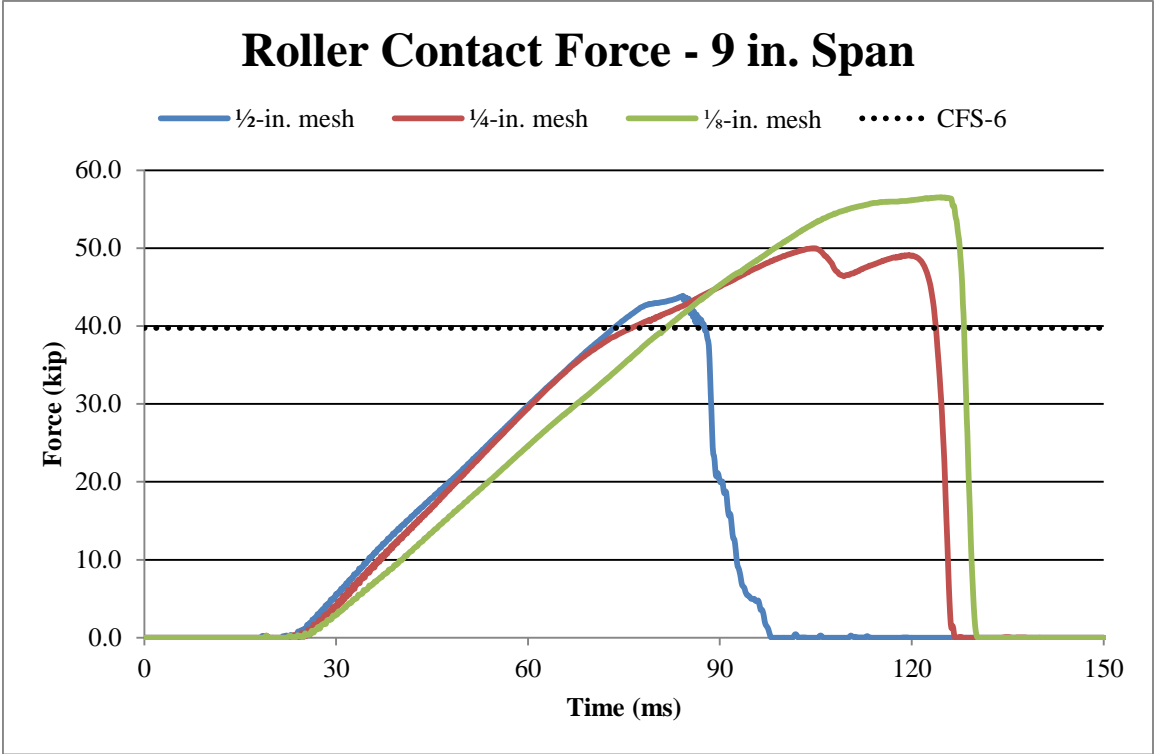


Figure 228. Force Comparison for 9-in. (229-mm) Span, CSCM Model

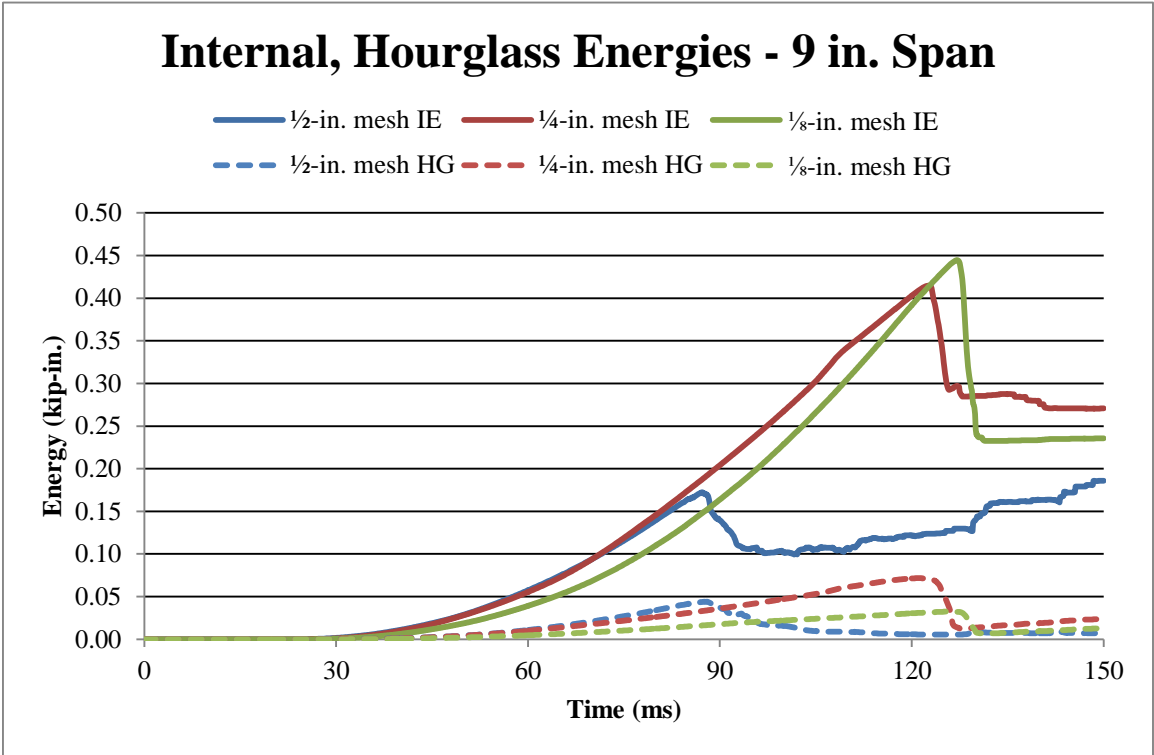


Figure 229. Energy Comparison for 9-in. (229-mm) Span, CSCM Model

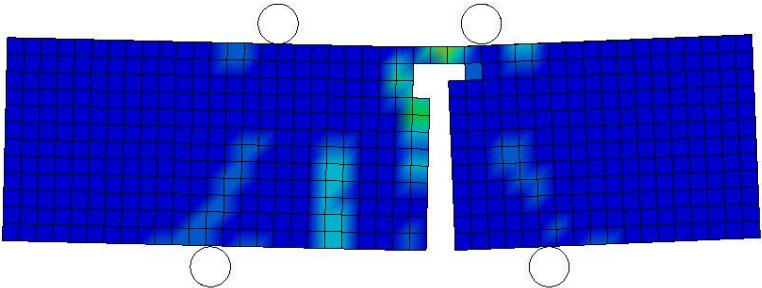
15.3.2 10-in. (254-mm) Support Span

The 10-in. (254-mm) support span distance correlated with test nos. CFS-3 and CFS-5. In the experimental testing, this setup resulted in shear failure in test no. CFS-3 and flexural failure in test no. CFS-5. Therefore, no particular failure was expected in the simulations. All of the mesh sizes failed in a vertical plane at varying locations between the roller supports, as shown in Figure 230 for time equal to 100 ms. Therefore, the simulations resulted in a flexural failure for the 10-in. (254-mm) support span.

Simulation results indicated a peak load of 36.7 kip (163 kN) occurred when summing forces at rollers was near the average peak load of 18.0 kip (80 kN) observed in test nos. CFS-3 and CFS-5 for the ½-in. (13-mm) mesh only, as shown in Figure 231. However, the ¼-in. (6-mm) and ⅛-in. (3-mm) mesh sizes had higher peak loads, at 41.7 kip (186 kN) and 43.5 kip (194 kN), respectively. The simulated behavior for the ½-in. (13-mm) mesh provided the closest prediction for peak load to the physical test, although no mesh seemed to accurately predict peak load.

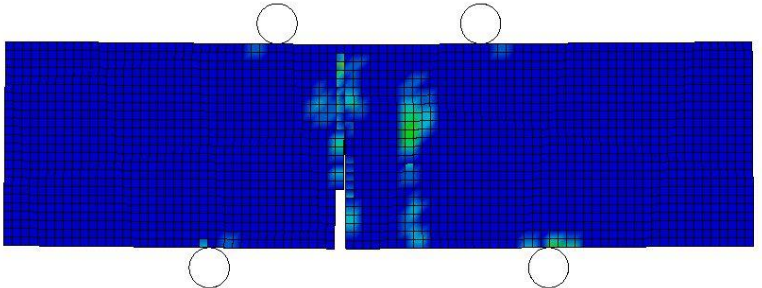
The energy plots showed similar trends. The hourglass energy was limited, but it was up to 22% of the internal energy for the ½-in. (12.7-mm) mesh size. These hourglass energies are tolerated and are shown in Figure 232. Based on the force and energy comparison for the three mesh sizes, the simulated behavior with the ½-in. (13-mm) mesh appeared to provide the closest comparison to the experimental testing results in terms for peak load. However, no mesh size provided peak forces that were very close to the physical test results using the selected parameters. The smallest error for simulated peak load was observed with the ½-in. (13-mm) mesh at 117.2 percent. Again, all three mesh sizes predicted a flexural failure.

Beam Testing - CSCM Model
Time = 99.999
Contours of Effective Plastic Strain
max IP. value
min=0, at elem# 195601
max=0.988386, at elem# 198500



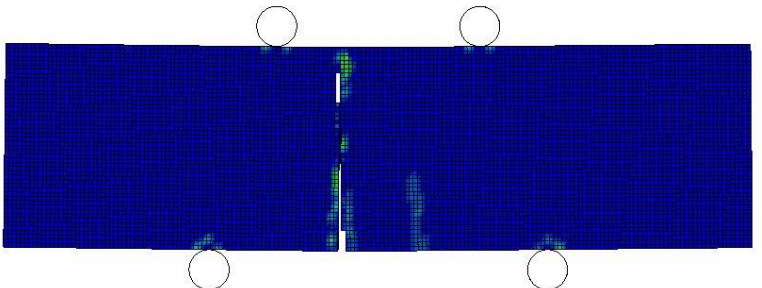
1/2 in. (13 mm)

Beam Testing - CSCM Model
Time = 99.999
Contours of Effective Plastic Strain
max IP. value
min=0, at elem# 201937
max=0.988976, at elem# 532601



1/4 in. (6 mm)

Beam Testing - CSCM Model
Time = 99.999
Contours of Effective Plastic Strain
max IP. value
min=0, at elem# 310801
max=0.989842, at elem# 532632



1/8 in. (3 mm)

Figure 230. Damage Pattern for 10-in. (254-mm) Span at 100 ms, CSCM Model

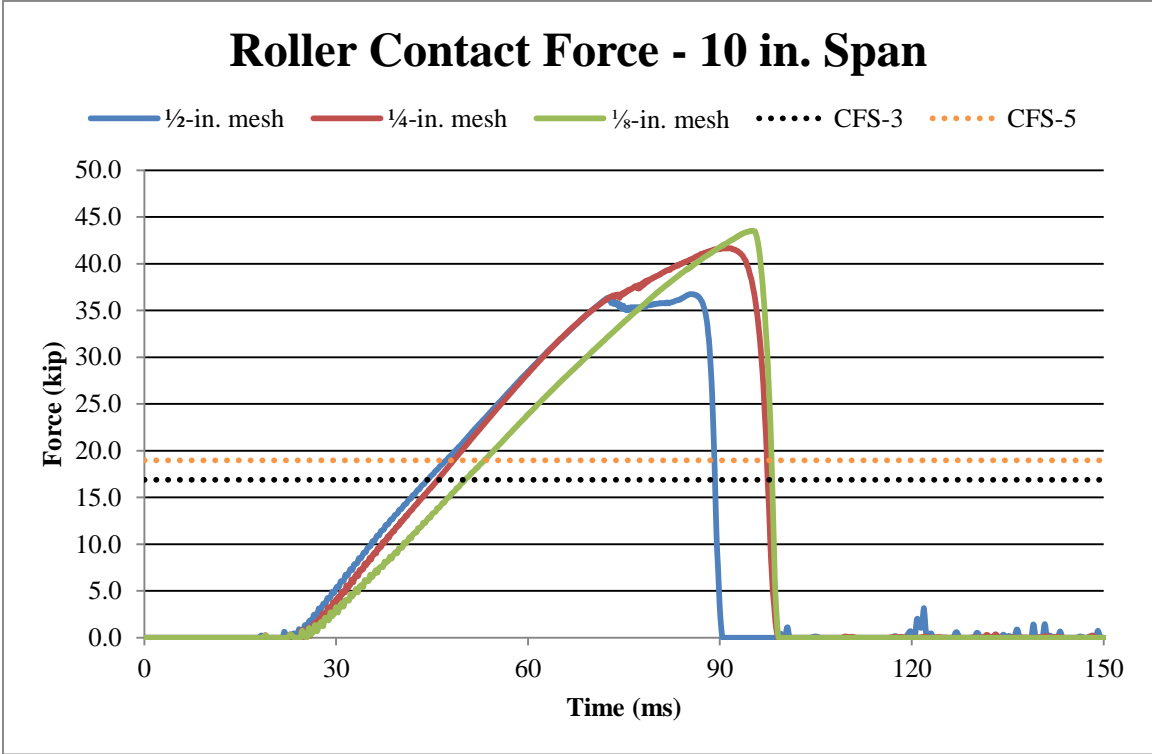


Figure 231. Force Comparison for 10-in. (254-mm) Span, CSCM Model

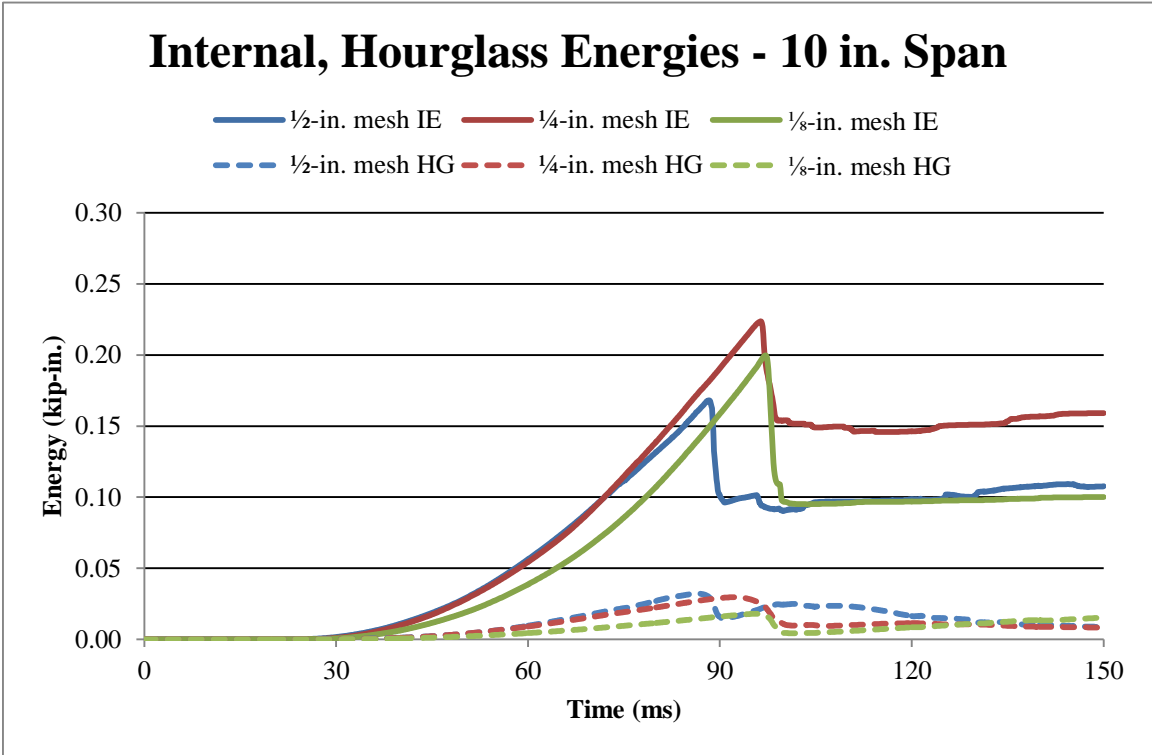


Figure 232. Energy Comparison for 10-in. (254-mm) Span, CSCM Model

15.3.3 11-in. (279-mm) Support Span

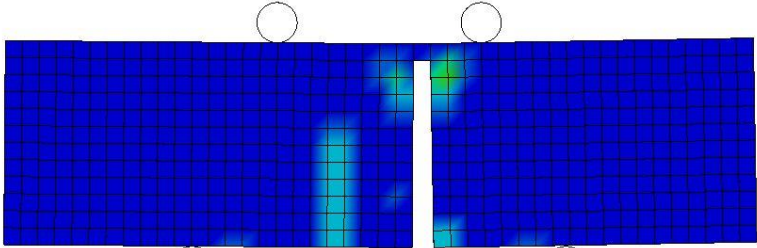
The 11-in. (279-mm) support span distance correlated with test no. CFS-4. In the experimental testing, this setup resulted in flexural failure. Therefore, this failure was expected to be replicated in the simulations. This behavior was achieved for all three mesh-size models which failed in a vertical plane at some distance away from the centerline of the beam, as shown in Figure 233 for time equal to 100 ms. There was some damage accruing near the bottom rollers, but no further indications of shear failure occurred for the 11-in. (279-mm) support span.

Simulation results indicated a peak load of 30.2 kip (134 kN) occurred when summing forces at rollers was near the peak load of 16.9 kip (75 kN) observed in test no. CFS-4 for the ½-in. (13-mm) mesh only, as shown in Figure 234. However, the ¼-in. (6-mm) and ⅛-in. (3-mm) mesh sizes had higher peak loads, at 34.6 kip (154 kN) for both mesh sizes. The simulated behavior for the ½-in. (13-mm) mesh provided the closest prediction for peak load to the physical test, although no mesh seemed to accurately predict peak load.

The energy plots showed similar trends. The hourglass energy was limited, but it was up to 14% of the internal energy for the ½-in. (12.7-mm) mesh size. These hourglass energies are tolerated and are shown in Figure 235. Based on the force and energy comparison for the three mesh sizes, the simulated behavior with the ½-in. (13-mm) mesh appeared to provide the closest comparison to the experimental testing results in terms of peak load. However, no mesh size provided peak forces that were very close to the physical test results using the selected parameters. The smallest error for simulated peak

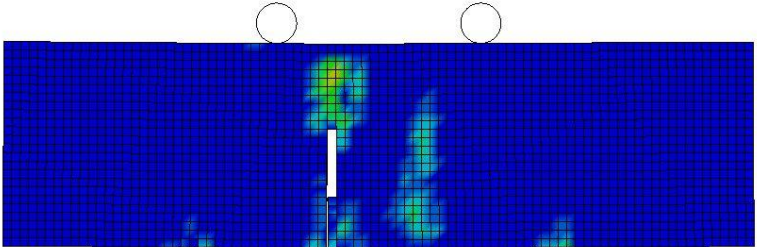
load was observed with the ½-in. (13-mm) mesh at 78.7 percent. Again, all three mesh sizes predicted a flexural failure.

Beam Testing - CSCM Model
Time = 100
Contours of Effective Plastic Strain
max IP. value
min=0, at elem# 195601
max=0.978255, at elem# 198499



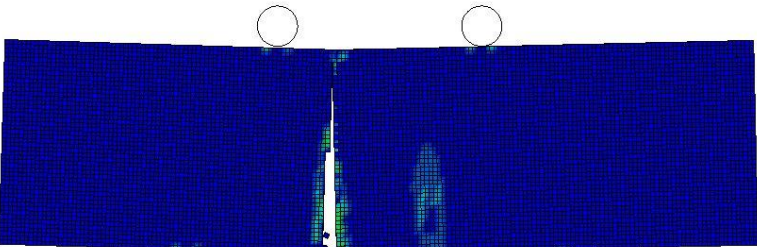
1/2 in. (13 mm)

Beam Testing - CSCM Model
Time = 100
Contours of Effective Plastic Strain
max IP. value
min=0, at elem# 201937
max=0.989633, at elem# 230848



1/4 in. (6 mm)

Beam Testing - CSCM Model
Time = 100
Contours of Effective Plastic Strain
max IP. value
min=0, at elem# 310801
max=0.989928, at elem# 536596



1/8 in. (3 mm)

Figure 233. Damage Pattern for 11-in. (279-mm) Span at 100 ms, CSCM Model

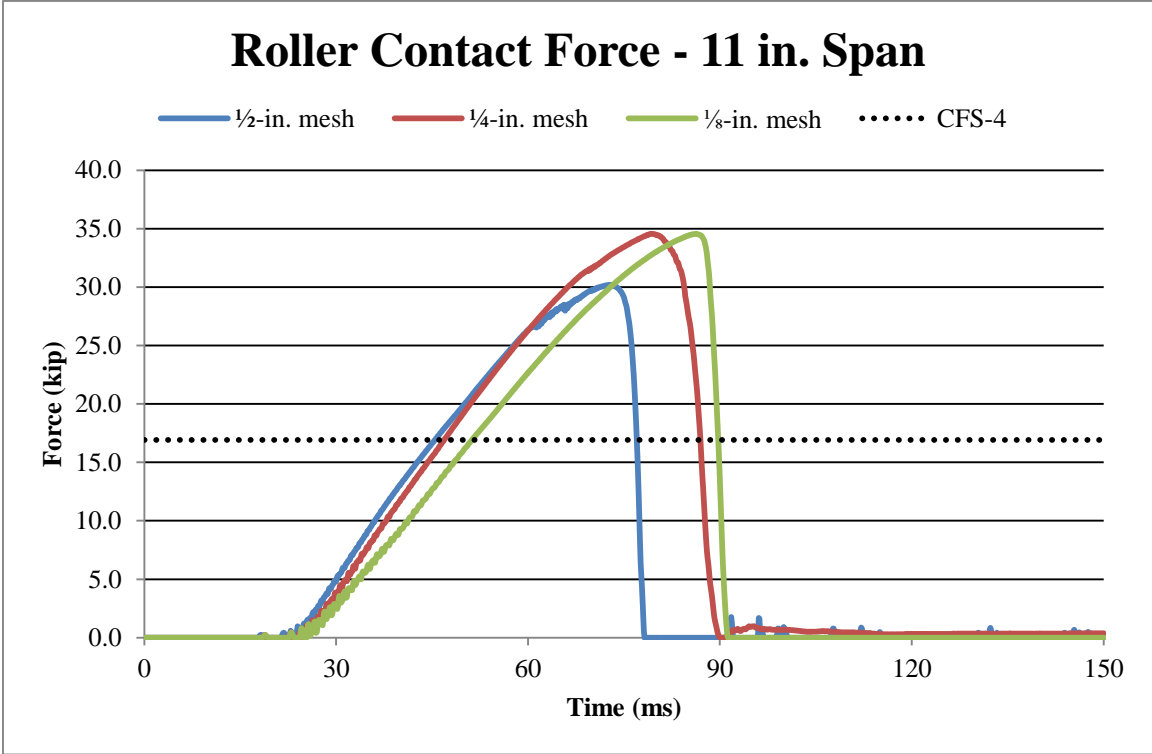


Figure 234. Force Comparison for 11-in. (279-mm) Span, CSCM Model

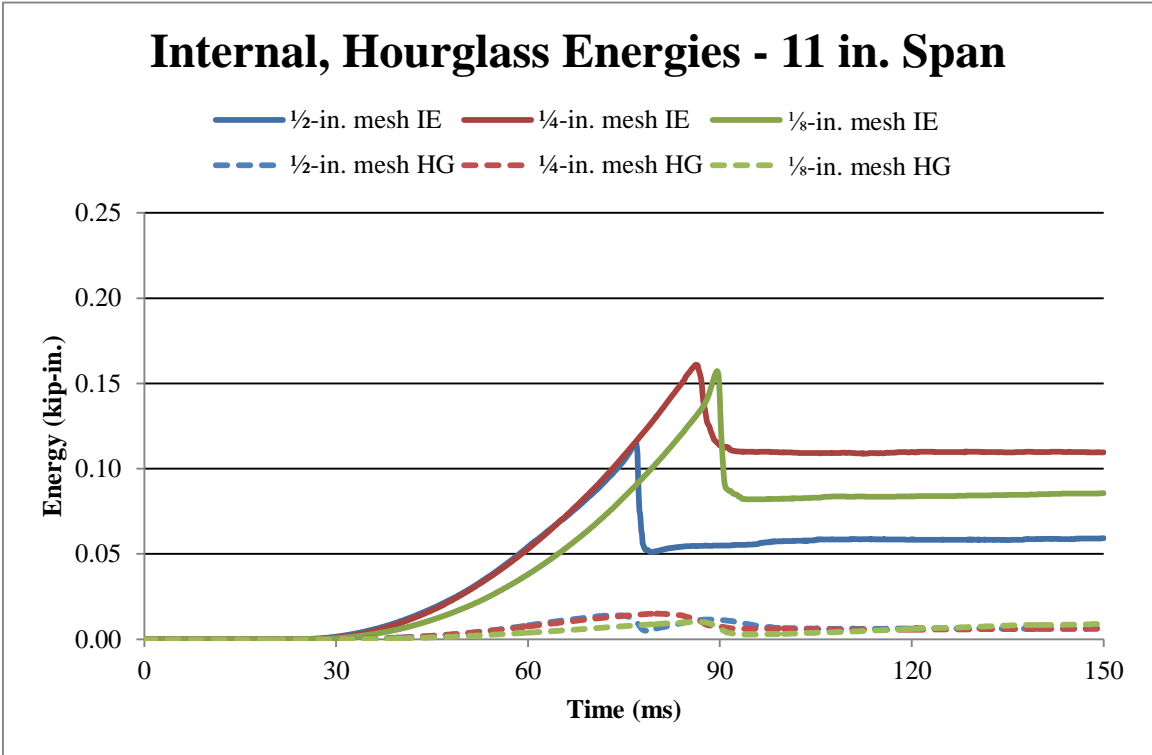


Figure 235. Energy Comparison for 11-in. (279-mm) Span, CSCM Model

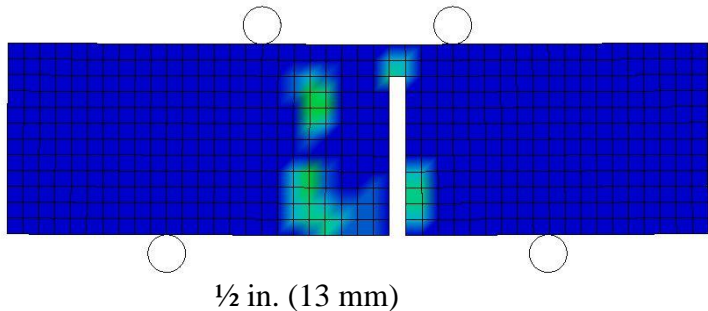
15.3.4 12-in. (305-mm) Support Span

The 12-in. (305-mm) support span distance correlated with test no. CFS-2. In the experimental testing, this setup resulted in flexural failure. Therefore, this failure was expected to be replicated in the simulations. This behavior was achieved for all three mesh-size models which failed in a vertical plane at some distance away from the centerline of the beam, as shown in Figure 236 for time equal to 100 ms. There was some damage accruing near the bottom rollers, but no further indications of shear failure occurred for the 12-in. (305-mm) support span.

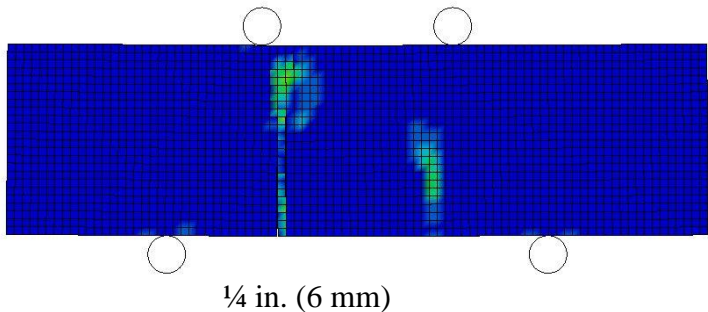
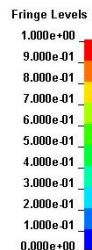
Simulation results indicated a peak load of 25.2 kip (112 kN) occurred when summing forces at rollers was near the peak load of 14.3 kip (64 kN) observed in test no. CFS-2 for the ½-in. (13-mm) mesh only, as shown in Figure 237. However, the ¼-in. (6-mm) and ⅛-in. (3-mm) mesh sizes had higher peak loads, at 26.9 kip (120 kN) and 28.1 kip (125 kN), respectively. The simulated behavior for the ½-in. (13-mm) mesh provided the closest prediction for peak load to the physical test, although no mesh seemed to accurately predict peak load.

The energy plots showed similar trends. The hourglass energy was negligible, as shown in Figure 238. Based on the force and energy comparison for the three mesh sizes, the simulated behavior with the ½-in. (13-mm) mesh appeared to provide the closest comparison to the experimental testing results in terms of peak load. However, no mesh size provided peak forces that were very close to the physical test results using the selected parameters. The smallest error for simulated peak load was observed with the ½-in. (13-mm) mesh at 76.2 percent. Again, all three mesh sizes predicated a flexural failure.

Beam Testing - CSCM Model
Time = 99.999
Contours of Effective Plastic Strain
max IP. value
min=0, at elem# 195601
max=0.985685, at elem# 198404



Beam Testing - CSCM Model
Time = 99.999
Contours of Effective Plastic Strain
max IP. value
min=0, at elem# 201937
max=0.989151, at elem# 232093



Beam Testing - CSCM Model
Time = 99.999
Contours of Effective Plastic Strain
max IP. value
min=0, at elem# 310801
max=0.98939, at elem# 480674

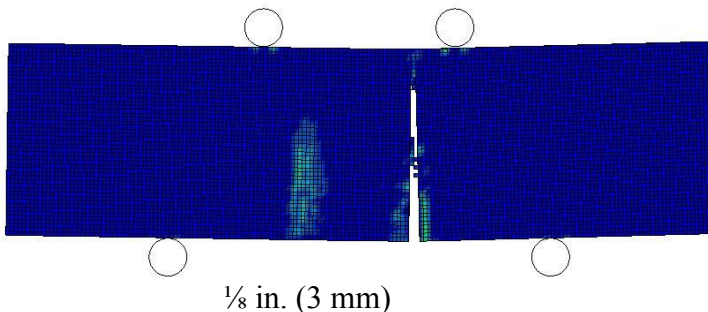
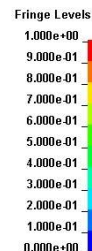


Figure 236. Damage Pattern for 12-in. (305-mm) Span at 100 ms, CSCM Model

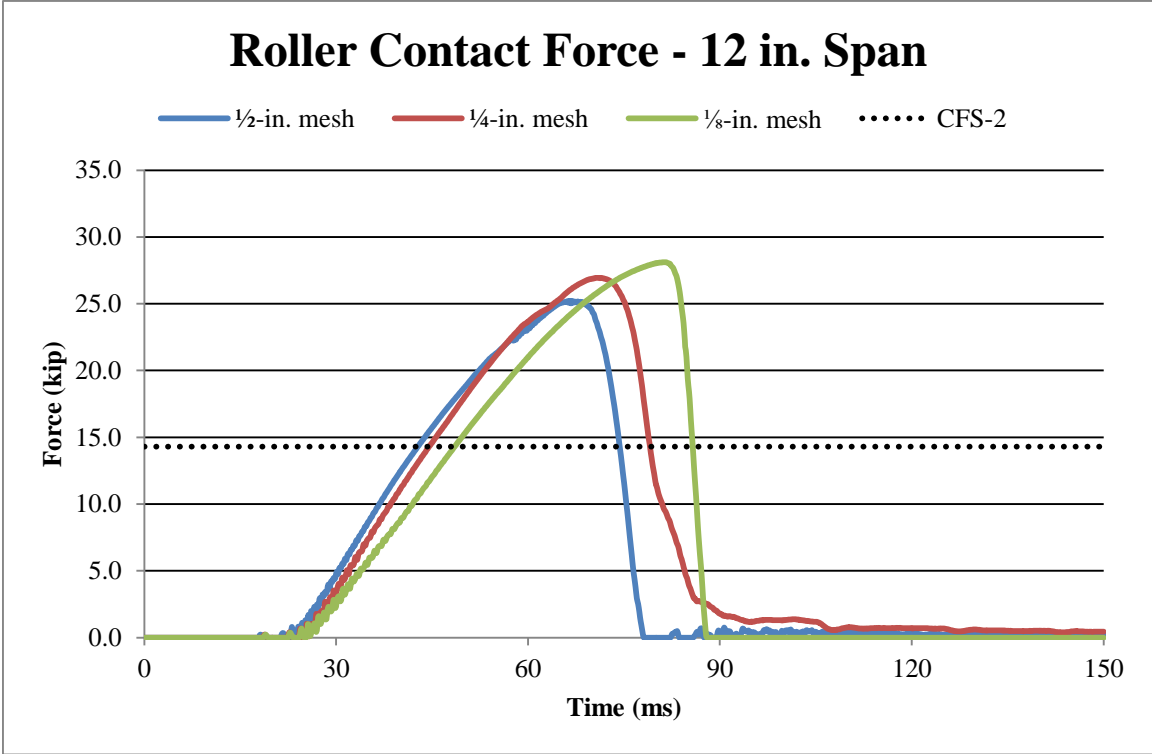


Figure 237. Force Comparison for 12-in. (305-mm) Span, CSCM Model

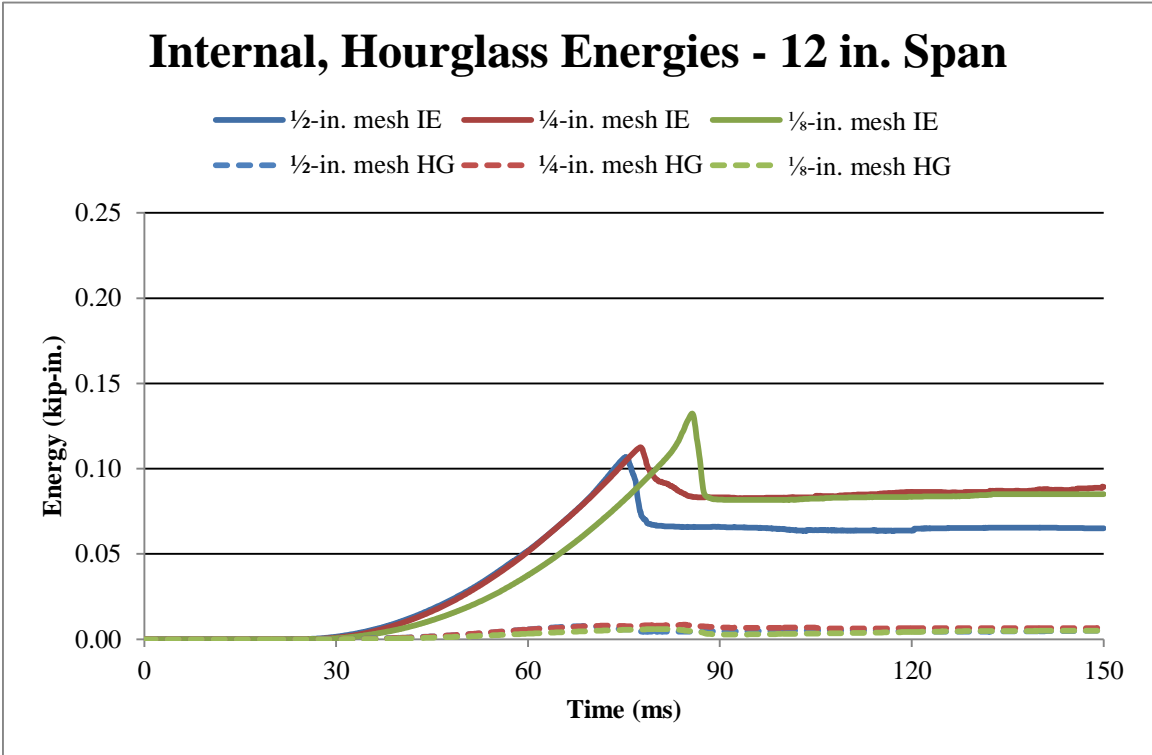


Figure 238. Energy Comparison for 12-in. (305-mm) Span, CSCM Model

15.3.5 18-in. (457-mm) Support Span

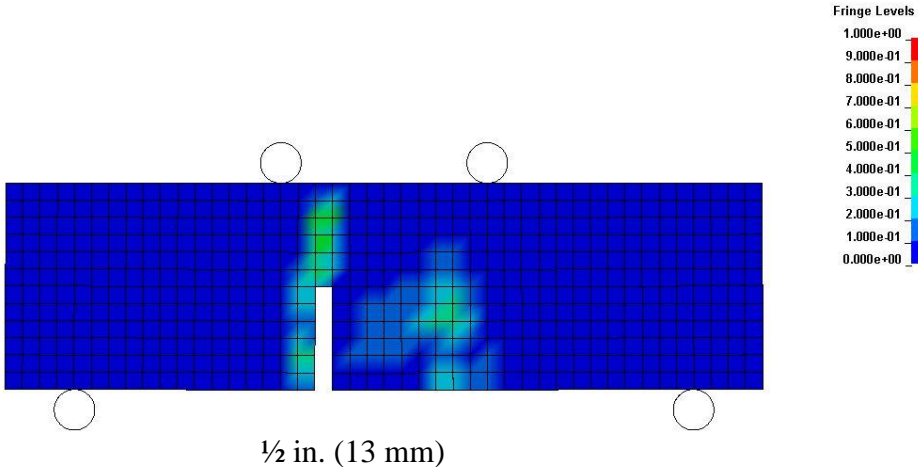
The 18-in. (457-mm) support span distance correlated with test no. CFS-1. In the experimental testing, this setup resulted in flexural failure. Therefore, this failure was expected to be replicated in the simulations. This behavior was achieved for all three mesh-size models which failed in a vertical plane at some distance away from the centerline of the beam, as shown in Figure 239 for time equal to 100 ms. Element deletion only occurred in the model using a ½-in. (13-mm) mesh. There was no damage accruing near the bottom rollers, nor indications of shear damage for the 18-in. (457-mm) support span.

Simulation results indicated a peak load of 11.9 kip (53 kN) occurred when summing forces at rollers was near the peak load of 5.8 kip (26 kN) observed in test no. CFS-2 for the ½-in. (13-mm) mesh only, as shown in Figure 237. However, the ¼-in. (6-mm) and ⅛-in. (3-mm) mesh sizes had higher peak loads, at 12.5 kip (56 kN) and 12.8 kip (57 kN), respectively. The simulated behavior for the ½-in. (13-mm) mesh provided the closest prediction for peak load to the physical test, although no mesh seemed to accurately predict peak load.

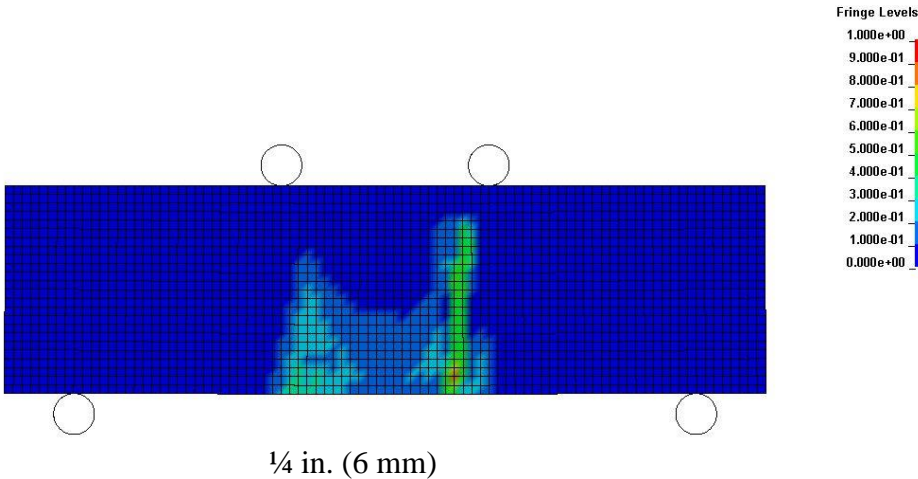
The energy plots showed similar trends. The hourglass energy was negligible, as shown in Figure 241. Based on the force and energy comparison for the three mesh sizes, the simulated behavior with the ½-in. (13-mm) mesh appeared to provide the closest comparison to the experimental testing results in terms of peak load. However, no mesh size provided peak forces that were very close to the physical test results using the selected parameters. The smallest error for simulated peak load was observed with the ½-

in. (13-mm) mesh at 103.4 percent. Again, all three mesh sizes predicted a more traditional flexural failure.

Beam Testing - CSCM Model
Time = 100
Contours of Effective Plastic Strain
max IP. value
min=0, at elem# 195601
max=0.988205, at elem# 199253



Beam Testing - CSCM Model
Time = 100
Contours of Effective Plastic Strain
max IP. value
min=0, at elem# 201937
max=0.985761, at elem# 222477



Beam Testing - CSCM Model
Time = 100
Contours of Effective Plastic Strain
max IP. value
min=0, at elem# 310801
max=0.815016, at elem# 553270

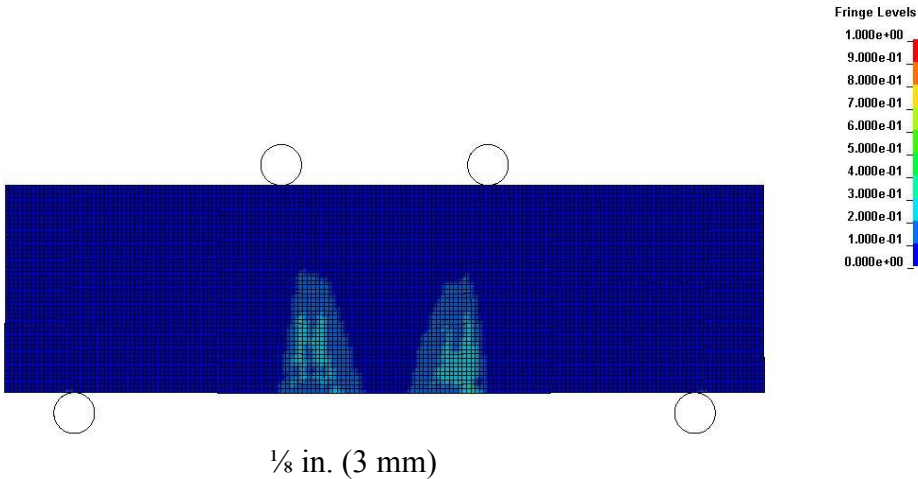


Figure 239. Damage Pattern for 18-in. (457-mm) Span at 100 ms, CSCM Model

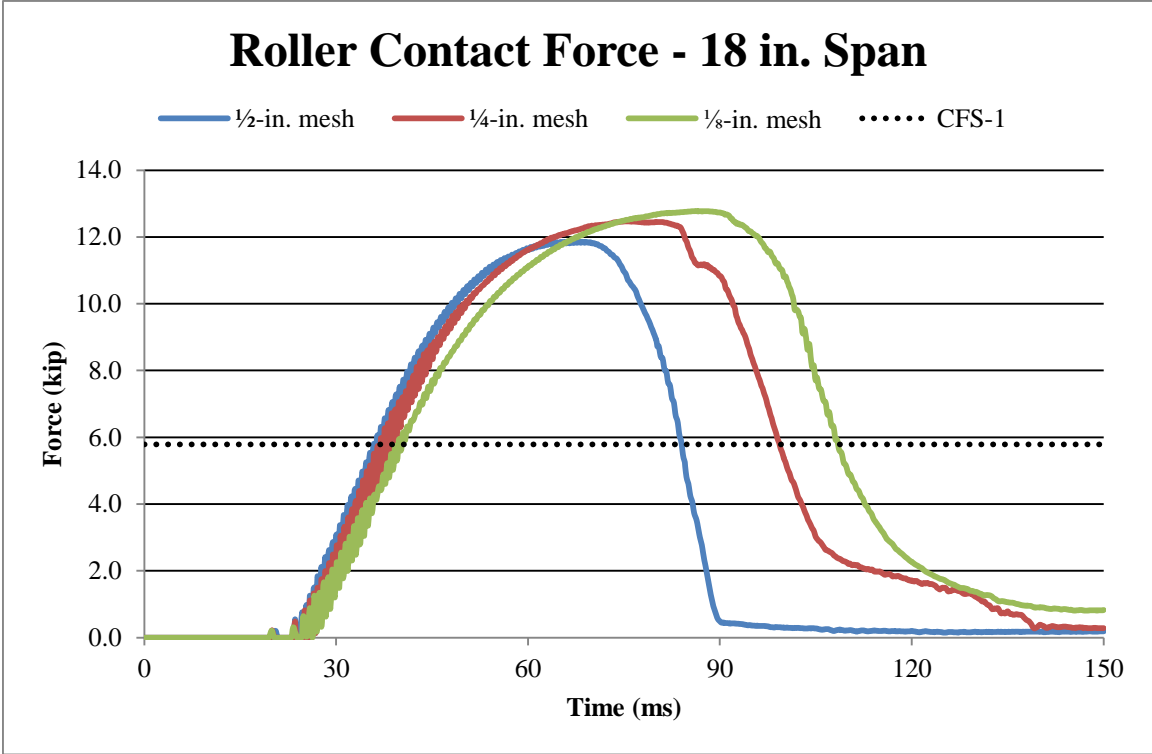


Figure 240. Force Comparison for 18-in. (457-mm) Span, CSCM Model

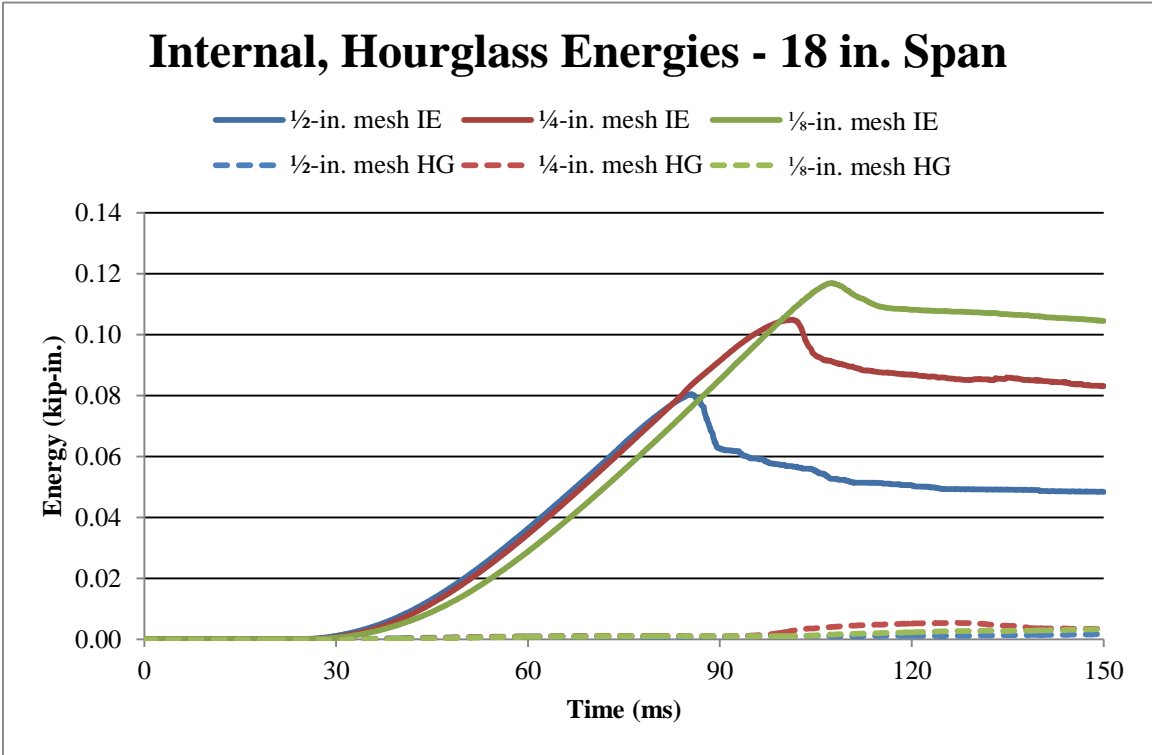


Figure 241. Energy Comparison for 18-in. (457-mm) Span, CSCM Model

15.4 K&C Model Investigation and Evaluation

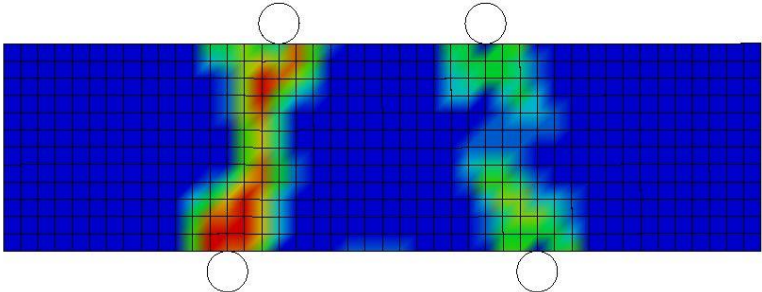
An evaluation for each of the five support spans was completed for the K&C material model. All three mesh sizes were evaluated using hourglass control type 6. All material parameters were the default parameters. This determination was made based on knowledge gained from other simulations with this material model. Force and strain curves were not over-plotted with test data, because the simulation and experimental tests were on different time scales.

15.4.1 9-in. (229-mm) Support Span

The first support span distance correlated with test no. CFS-6, which was 9 in. (229 mm). In the experimental testing, this setup resulted in shear failure. Therefore, this failure was expected to be replicated in the simulations. This behavior was achieved for all three mesh sizes, as the failure occurred were along a diagonal plane between the upper and lower supports, as shown in Figure 242 for the time equal to 50 ms.

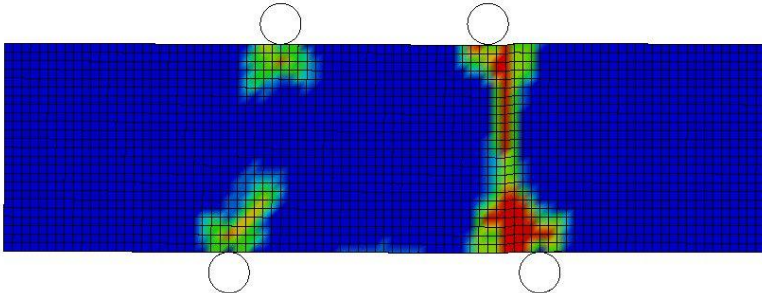
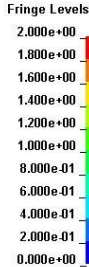
Simulation results indicated a peak load of 19.6 kip (87 kN) occurred when summing forces at rollers was near the peak load of 39.8 kip (177 kN) observed in test no. CFS-6 for the ¼-in. (6-mm) mesh only, as shown in Figure 243. However, the ½-in. (13-mm) and ⅛-in. (3-mm) mesh sizes had lower peak loads, at 19.3 kip (89 kN) and 17.1 kip (76 kN), respectively. The simulated behavior for the ¼-in. (6-mm) mesh provided the closest prediction for peak load to the physical test, although no mesh seemed to accurately predict peak load.

Beam Testing - K&C Model
Time = 50
Contours of Effective Plastic Strain
max IP. value
min=0, at elem# 195601
max=1.99635, at elem# 199864



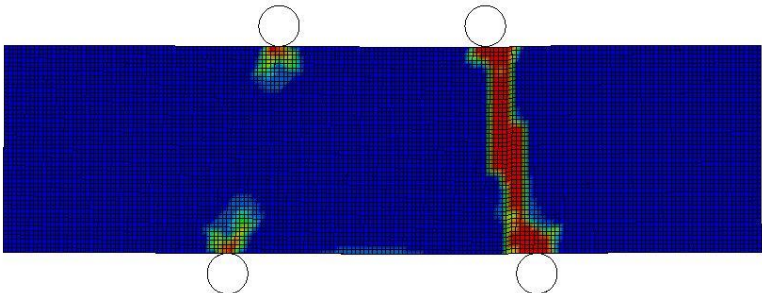
1/2 in. (13 mm)

Beam Testing - K&C Model
Time = 50
Contours of Effective Plastic Strain
max IP. value
min=0, at elem# 201937
max=1.99988, at elem# 218959



1/4 in. (6 mm)

Beam Testing - K&C Model
Time = 50
Contours of Effective Plastic Strain
max IP. value
min=0, at elem# 310801
max=2, at elem# 458961



1/8 in. (3 mm)

Figure 242. Damage Pattern for 9-in. (229-mm) Span at 50 ms, K&C Model

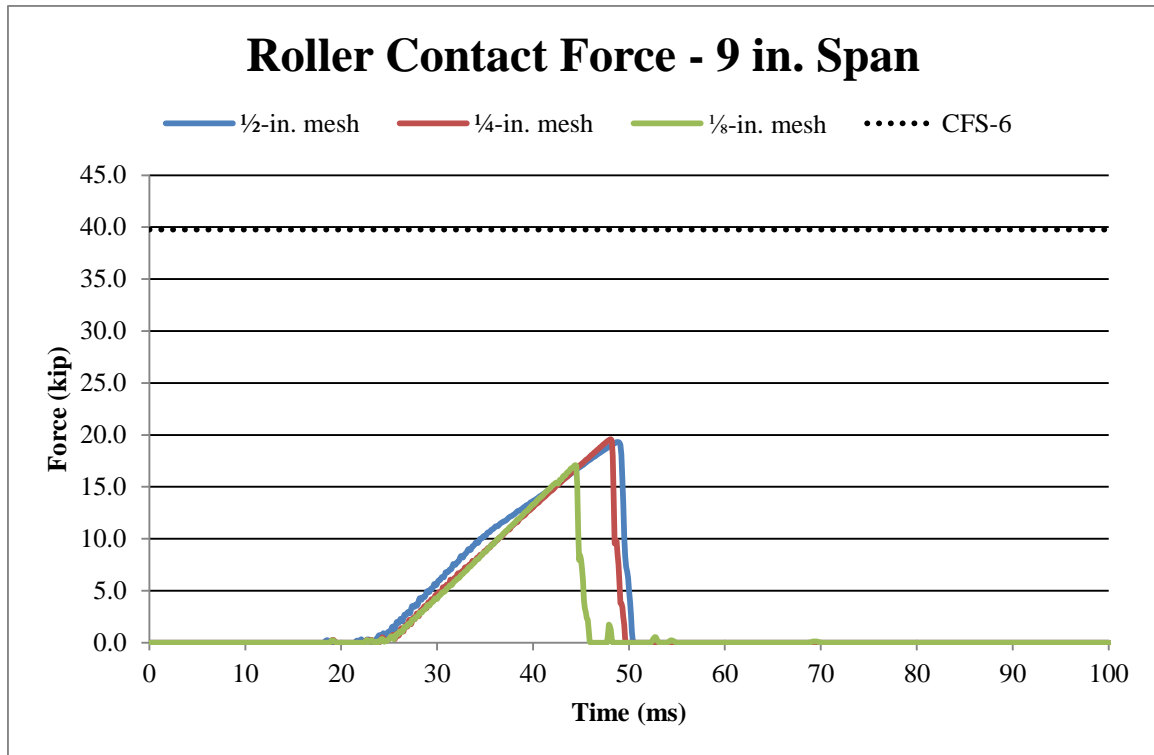


Figure 243. Force Comparison for 9-in. (229-mm) Span, K&C Model

The energy plots showed similar trends. The hourglass energy was limited, but it was up to 29% of the internal energy for the 1/8-in. (3-mm) mesh size. These hourglass energies are tolerated and are shown in Figure 244. Based on the force and energy comparison for the three mesh sizes, the simulated behavior with the 1/4-in. (6-mm) mesh provided the closest comparison to the experimental testing results using the selected parameters. However, all three meshes poorly predicted peak force. The smallest error for simulated peak load was observed with the 1/4-in. (6-mm) mesh at 50.8 percent. But, all three mesh sizes accurately predicted shear failure.

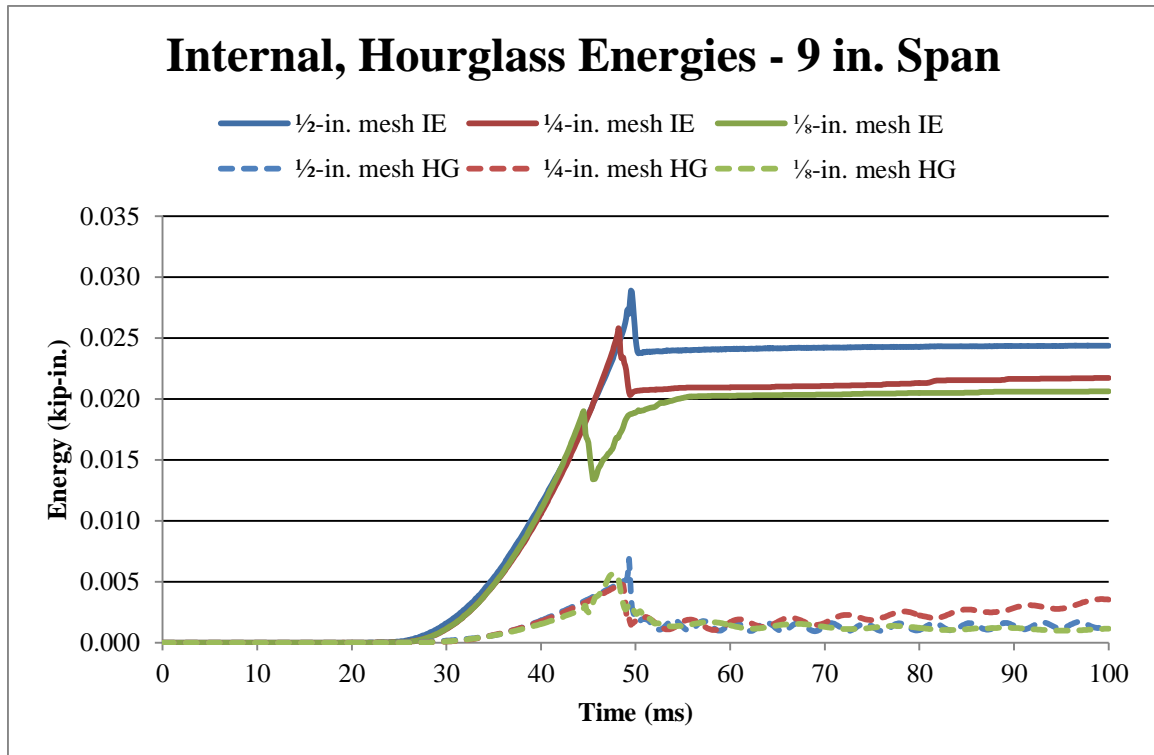
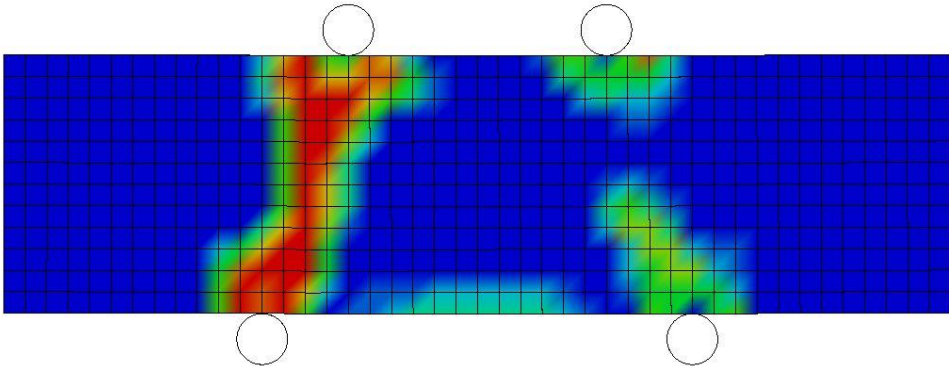


Figure 244. Energy Comparison for 9-in. (229-mm) Span, K&C Model

15.4.2 10-in. (254-mm) Support Span

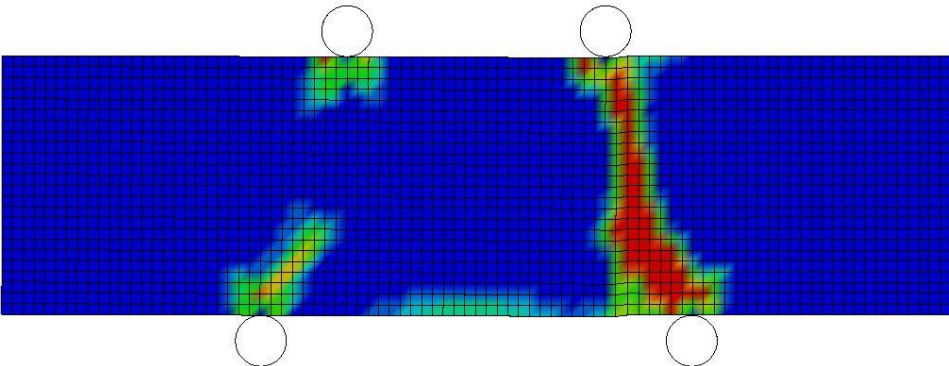
The 10-in. (254-mm) support span distance correlated with test nos. CFS-3 and CFS-5. In the experimental testing, this setup resulted in shear failure in test no. CFS-3 and flexural failure in test no. CFS-5. Therefore, no particular failure was expected in the simulations. All of the mesh sizes failed in a diagonal plane between the upper and lower rollers, as shown in Figure 245 for the time equal to 50 ms. Therefore, the simulations resulted in a shear failure for the 10-in. (254-mm) support span.

Beam Testing - K&C Model
Time = 50
Contours of Effective Plastic Strain
max IP. value
min=0, at elem# 195601
max=1.99721, at elem# 200057



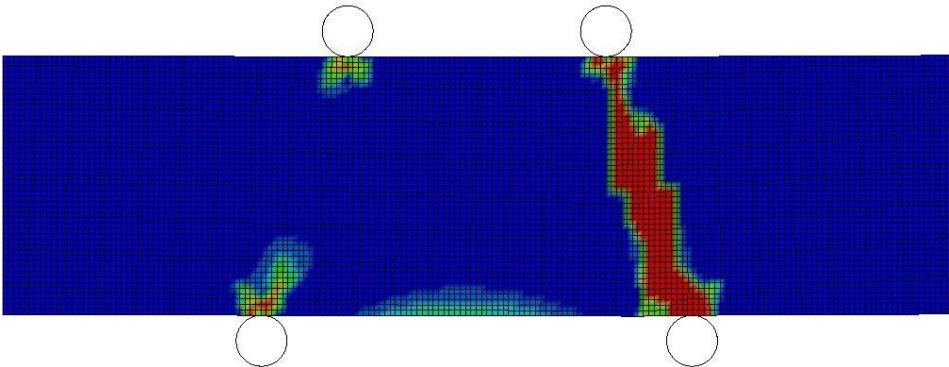
1/2 in. (13 mm)

Beam Testing - K&C Model
Time = 50
Contours of Effective Plastic Strain
max IP. value
min=0, at elem# 201937
max=1.99926, at elem# 219252



1/4 in. (6 mm)

Beam Testing - K&C Model
Time = 50
Contours of Effective Plastic Strain
max IP. value
min=0, at elem# 310801
max=1.9997, at elem# 441326



1/8 in. (3 mm)

Figure 245. Damage Pattern for 10-in. (254-mm) Span at 50 ms, K&C Model

Simulation results indicated a peak load of 18.0 kip (80 kN) occurred when summing forces at rollers was exactly that of the average peak load of 18.0 kip (80 kN) observed in test nos. CFS-3 and CFS-5 for the 1/2-in. (13-mm) and 1/4-in. (6-mm) mesh sizes, as shown in Figure 246. However, the 1/8-in. (3-mm) mesh size had a lower peak load, at 16.3 kip (73 kN). Given the complex loading, it appears that the K&C model accurately predicted the maximum force for all three mesh sizes.

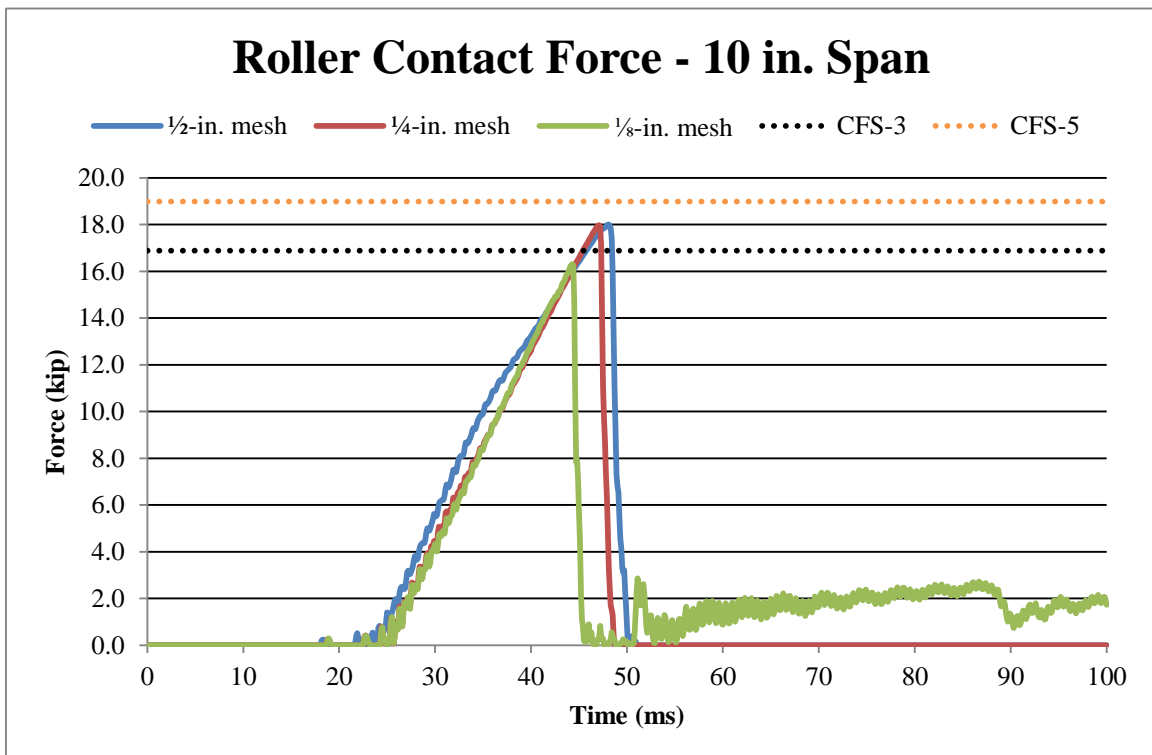


Figure 246. Force Comparison for 10-in. (254-mm) Span, K&C Model

The energy plots showed similar trends. The hourglass energy was limited, but it was up to 30% of the internal energy for the 1/2-in. (13-mm) mesh size. These hourglass energies are tolerated and are shown in Figure 247. Based on the force and energy comparison for all three mesh sizes, the simulated behavior with the 1/2-in. (13-mm) mesh and 1/4-in. (6-mm) mesh provided the better comparisons to the experimental testing results for peak load using the selected parameters. The smallest error for simulated peak

load, computed using the average peak load of test nos. CFS-3 and CFS-5, was observed with the 1/2-in. (13-mm) mesh and 1/4-in. (6-mm) meshes at 0.6 percent. Again, all three mesh sizes predicted shear failure.

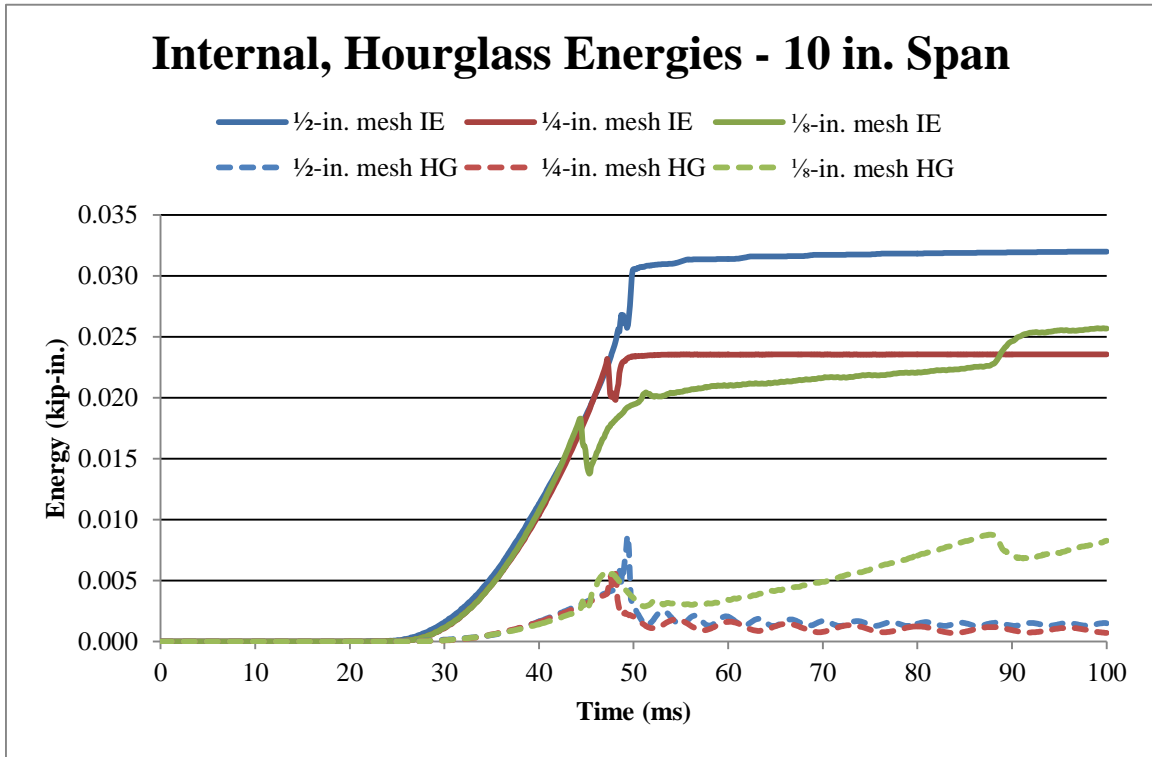


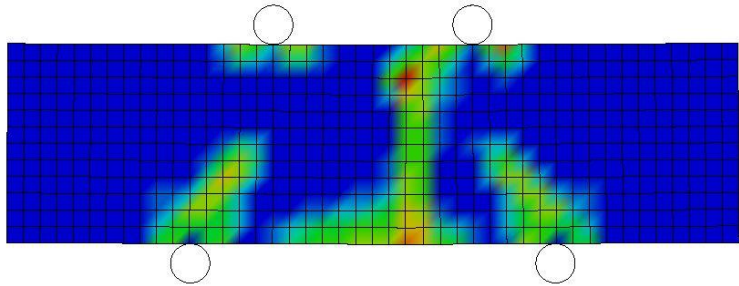
Figure 247. Energy Comparison for 10-in. (254-mm) Span, K&C Model

15.4.3 11-in. (279-mm) Support Span

The 11-in. (279-mm) support span distance correlated with test no. CFS-4. In the experimental testing, this setup resulted in flexural failure. Therefore, this failure was expected to be replicated in the simulations. This behavior was achieved for the 1/2-in. (13-mm) and 1/4-in. (6-mm) mesh sizes; these two mesh sizes had a majority of the beam damage accrue in a vertical plane, as shown in Figure 248 for the time equal to 50 ms. There was still some damage occurring along a diagonal plane with these two mesh sizes. The 1/8-in. (3-mm) mesh size model primarily failed in shear for the 11-in. (279-mm)

support span. The fringe or damage level for the shear failure was much more distinct with the 1/8-in. (3-mm) mesh than observed for the other two meshes.

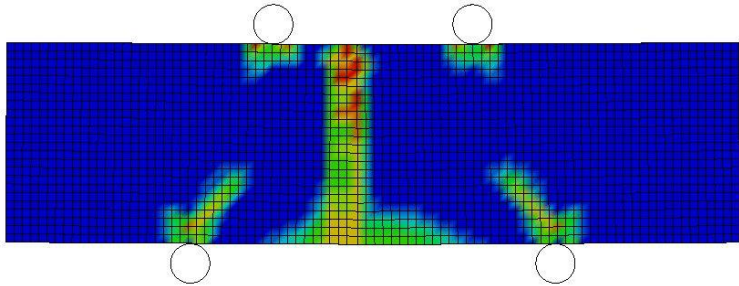
Beam Testing - K&C Model
Time = 49.999
Contours of Effective Plastic Strain
max IP. value
min=0, at elem# 195601
max=1.99842, at elem# 198409



1/2 in. (13 mm)



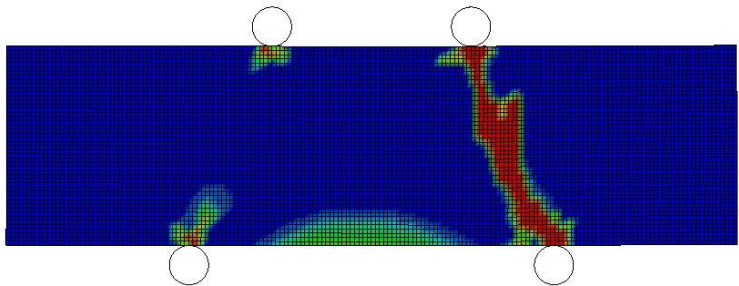
Beam Testing - K&C Model
Time = 49.999
Contours of Effective Plastic Strain
max IP. value
min=0, at elem# 201937
max=1.99948, at elem# 228738



1/4 in. (6 mm)



Beam Testing - K&C Model
Time = 49.999
Contours of Effective Plastic Strain
max IP. value
min=0, at elem# 310801
max=2, at elem# 405531



1/8 in. (3 mm)

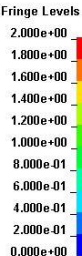


Figure 248. Damage Pattern for 11-in. (279-mm) Span at 50 ms, K&C Model

Simulation results indicated a peak load of 16.9 kip (75 kN) occurred when summing forces at rollers was exactly that of the peak load of 16.9 kip (75 kN) observed in test no. CFS-4 for the 1/2-in. (13-mm) mesh size, as shown in Figure 249. However, the 1/4-in. (6-mm) and 1/8-in. (3-mm) mesh sizes had lower peak loads, at 16.4 kip (73 kN) and 15.7 kip (70 kN), respectively. Given the complex loading, it appears that the K&C model accurately predicted the maximum force for all three mesh sizes.

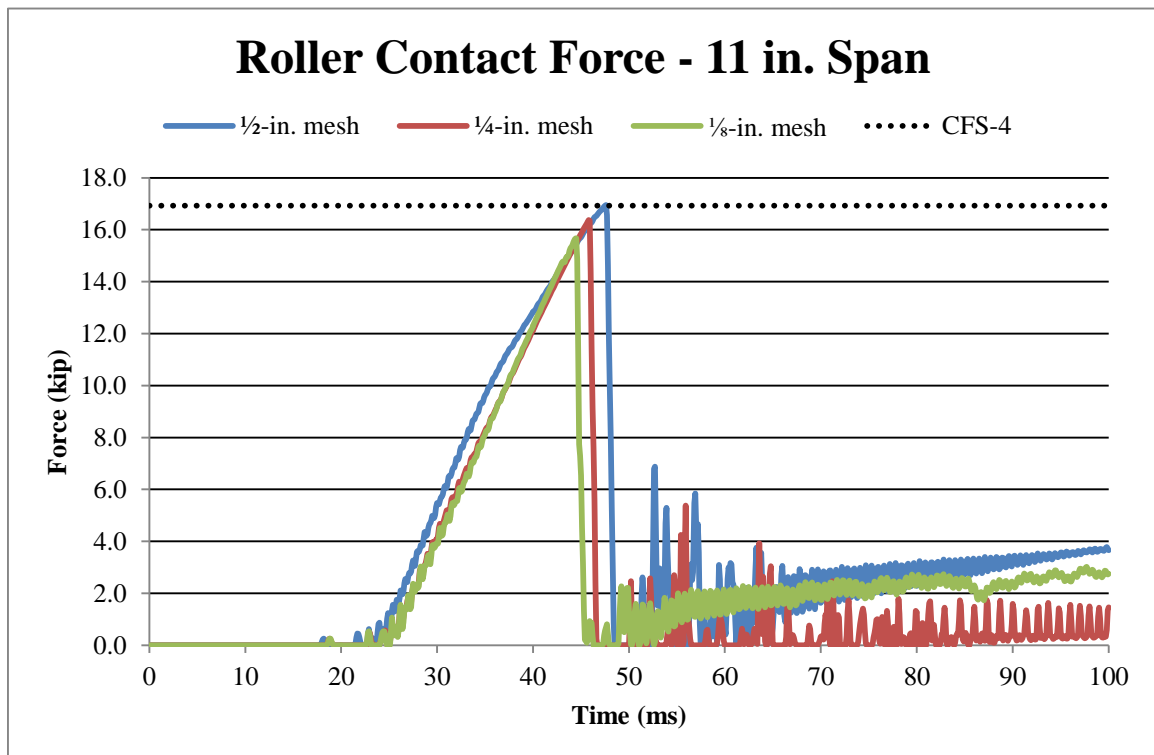


Figure 249. Force Comparison for 11-in. (279-mm) Span, K&C Model

The energy plots showed similar trends. The hourglass energy was limited, but it was up to 30% of the internal energy for the 1/2-in. (13-mm) mesh size at failure. These hourglass energies are tolerated and are shown in Figure 250. The highest hourglass energies occurred after the peak force was reached. Based on the force and energy comparison for all three mesh sizes, the simulated behavior with the 1/2-in. (13-mm) mesh-size model arguably provided the best comparison to the experimental testing

results for peak load, damage, and energy evaluation, using the selected parameters. The smallest error for simulated peak load was observed with the 1/2-in. (13-mm) mesh at 0.0 percent. Two mesh sizes, 1/2 in. (13 mm) and 1/4 (6 mm), predicted flexural failure, while the smallest mesh size, 1/8 in. (3 mm) predicted shear failure.

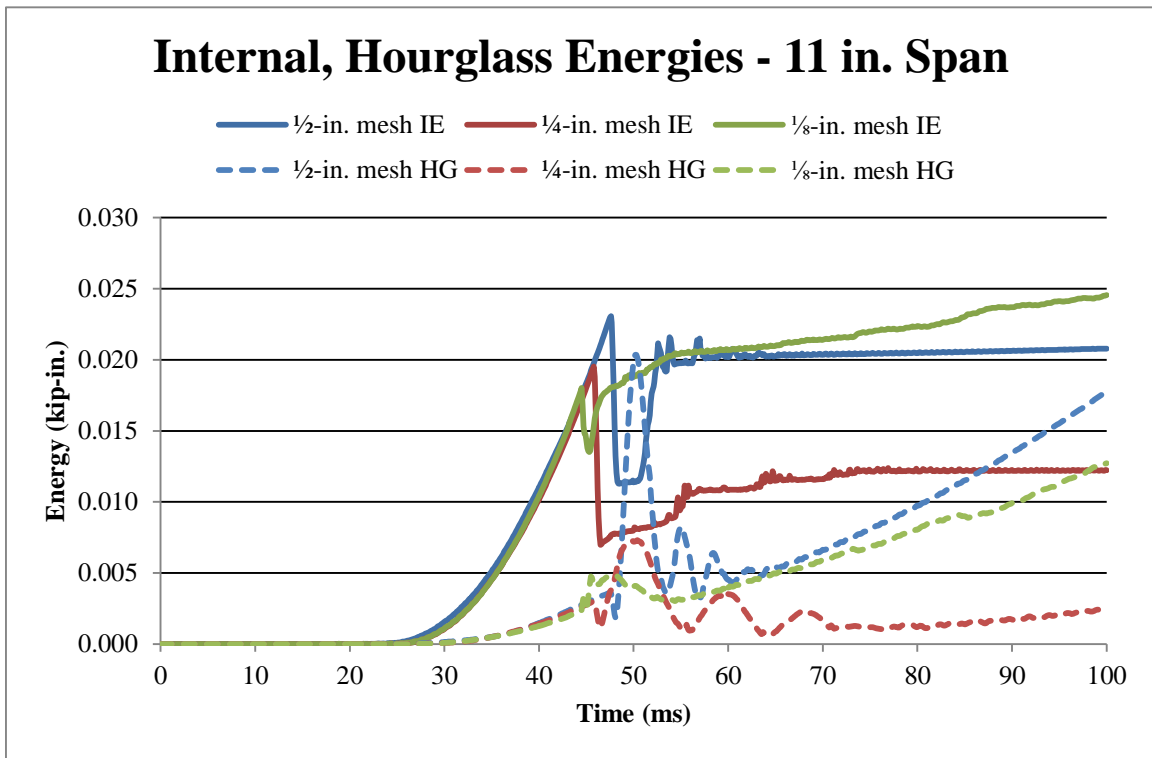
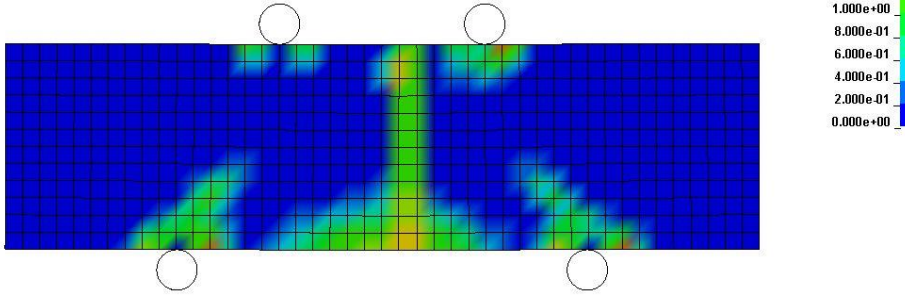


Figure 250. Energy Comparison for 11-in. (279-mm) Span, K&C Model

15.4.4 12-in. (305-mm) Support Span

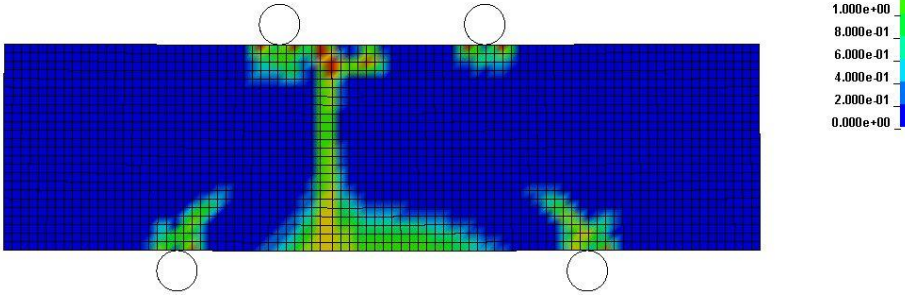
The 12-in. (305-mm) support span distance correlated with test no. CFS-2. In the experimental testing, this setup resulted in flexural failure. Therefore, this failure was expected to be replicated in the simulations. This behavior was achieved for all three mesh sizes which failed in a vertical plane at some distance away from the centerline of the beam, as shown in Figure 251 for the time equal to 50 ms. There was some damage accruing along the diagonal plane between the upper and lower rollers, but the flexural damage was the most prominent damage for the 12-in. (305-mm) support span.

Beam Testing - K&C Model
Time = 50
Contours of Effective Plastic Strain
max IP. value
min=0, at elem# 195601
max=2, at elem# 198529



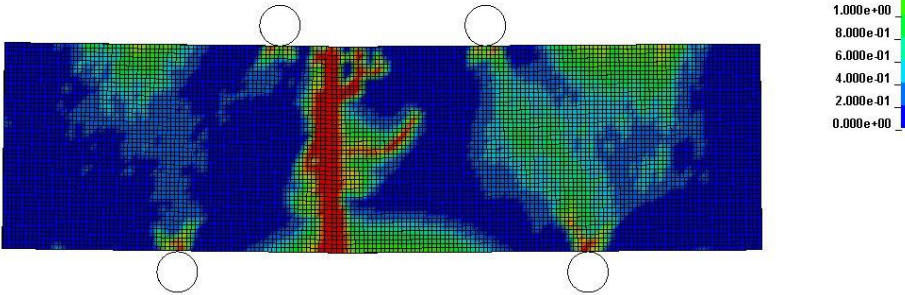
1/2 in. (13 mm)

Beam Testing - K&C Model
Time = 50
Contours of Effective Plastic Strain
max IP. value
min=0, at elem# 201937
max=1.9996, at elem# 231042



1/4 in. (6 mm)

Beam Testing - K&C Model
Time = 50
Contours of Effective Plastic Strain
max IP. value
min=0, at elem# 310801
max=2, at elem# 486992



1/8 in. (3 mm)

Figure 251. Damage Pattern for 12-in. (305-mm) Span at 50 ms, K&C Model

Simulation results indicated a peak load of 14.0 kip (62 kN) occurred when summing forces at rollers was exactly that of the peak load of 14.3 kip (64 kN) observed

in test no. CFS-2 for the 1/2-in. (13-mm) mesh size, as shown in Figure 252. However, the 1/4-in. (6-mm) and 1/8-in. (3-mm) mesh sizes had lower peak loads, at 13.4 kip (60 kN) for both mesh sizes. Given the complex loading, it appears that the K&C model accurately predicted the maximum force for all three mesh sizes.

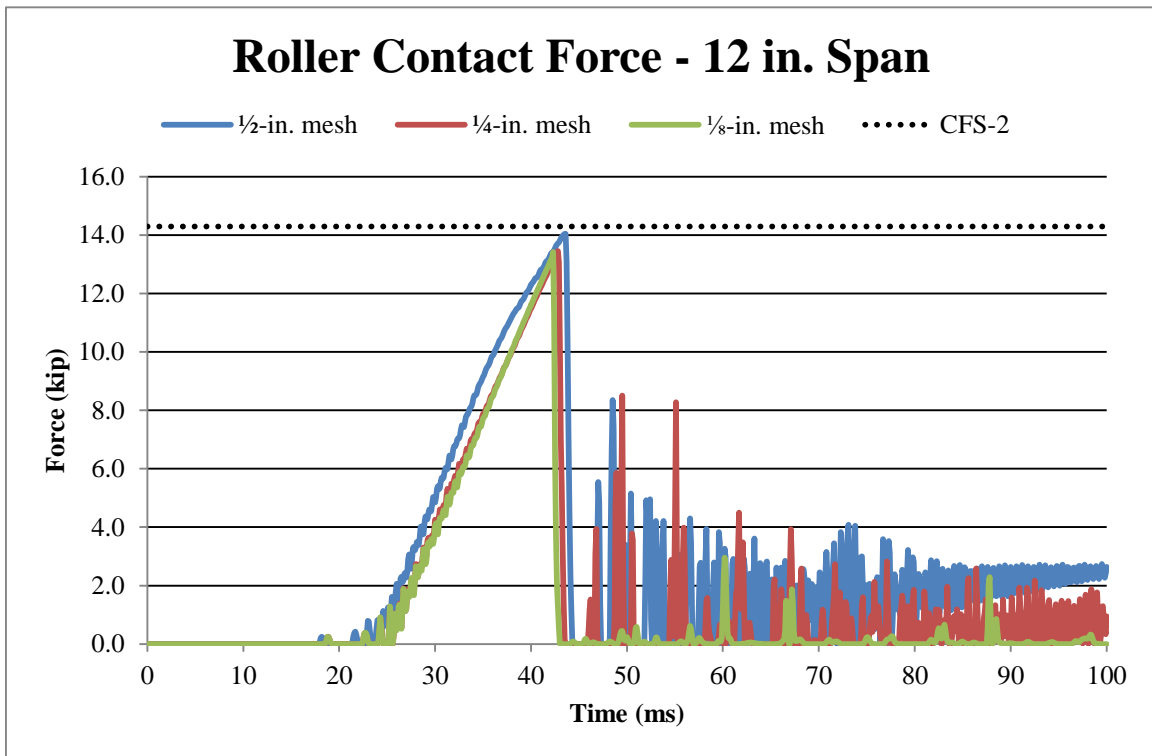


Figure 252. Force Comparison for 12-in. (305-mm) Span, K&C Model

The energy plots showed similar trends. The hourglass energy was limited, but it was up to 25% of the internal energy for the 1/8-in. (3-mm) mesh size at failure. These hourglass energies are tolerated and are shown in Figure 253. The high hourglass energies occurred after the peak stress was reached. Based on the force and energy comparison for all three mesh sizes, the simulated behavior with the 1/2-in. (13-mm) mesh-size arguably provided the better overall comparison to the experimental testing results for peak load, damage, and energy evaluation using the selected parameters. The smallest error for simulated peak load was observed with the 1/2-in. (13-mm) mesh at 2.1

percent. Again, all three mesh sizes predicted flexural failure, although some shear behavior was observed as well.

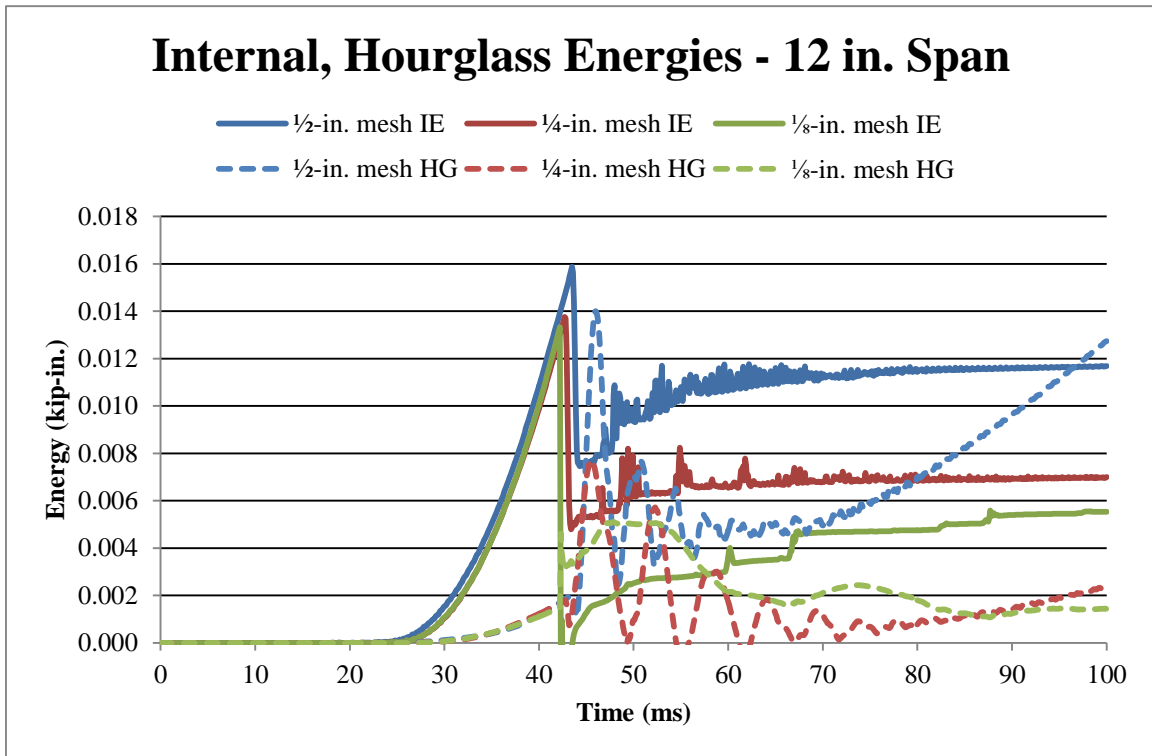
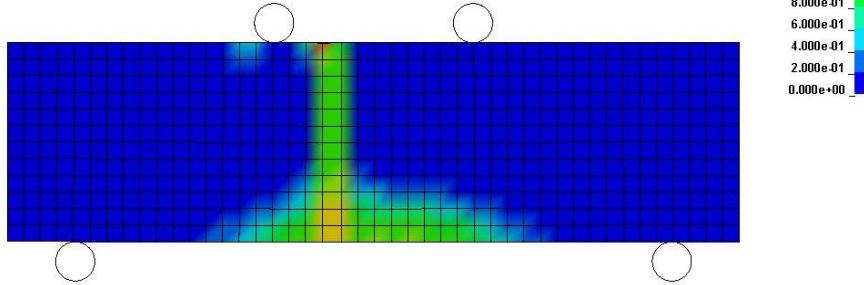


Figure 253. Energy Comparison for 12-in. (305-mm) Span, K&C Model

15.4.5 18-in. (457-mm) Support Span

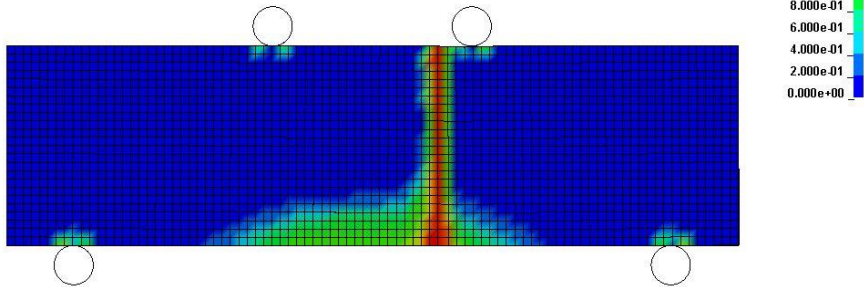
The 18-in. (457-mm) support span distance correlated with test no. CFS-1. In the experimental testing, this setup resulted in flexural failure. Therefore, this failure was expected to be replicated in the simulations. This behavior was achieved for all three mesh-size models which failed in a vertical plane at some distance away from the centerline of the beam, as shown in Figure 254 for the time equal to 50 ms. There was minor damage accruing near the bottom rollers, and no further indications of shear damage occurred for the 18-in. (457-mm) support span.

Beam Testing - K&C Model
Time = 50
Contours of Effective Plastic Strain
max IP. value
min=0, at elem# 195601
max=1.99918, at elem# 199173



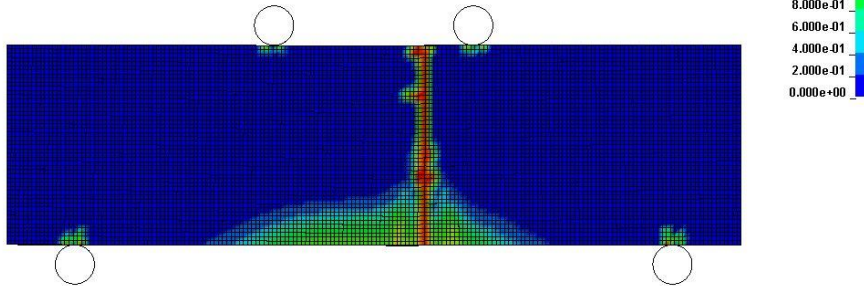
1/2 in. (13 mm)

Beam Testing - K&C Model
Time = 50
Contours of Effective Plastic Strain
max IP. value
min=0, at elem# 201937
max=1.99957, at elem# 222402



1/4 in. (6 mm)

Beam Testing - K&C Model
Time = 50
Contours of Effective Plastic Strain
max IP. value
min=0, at elem# 310801
max=2, at elem# 475485



1/8 in. (3 mm)

Figure 254. Damage Pattern for 18-in. (457-mm) Span at 50 ms, K&C Model

Simulation results indicated a peak load of 6.7 kip (30 kN) occurred when summing forces at rollers was exactly that of the peak load of 5.8 kip (26 kN) observed in test no. CFS-1 for the 1/8-in. (3-mm) mesh size, as shown in Figure 255. However, the 1/2-in. (13-mm) and 1/4-in. (6-mm) mesh sizes had higher peak loads, at 7.1 kip (32 kN) and 6.8 kip (30 kN), respectively. Given the complex loading, it appears that the K&C model accurately predicted the maximum force for all three mesh sizes.

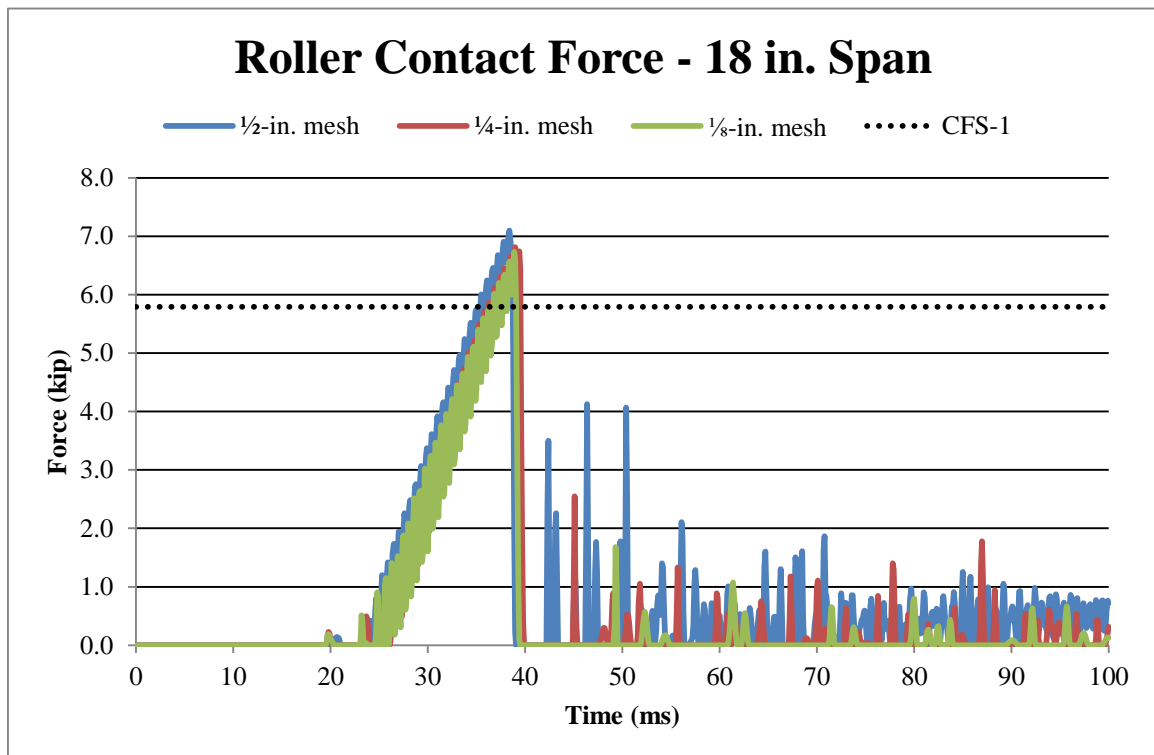


Figure 255. Force Comparison for 18-in. (457-mm) Span, K&C Model

The energy plots showed similar trends. The hourglass energy was limited, but it was up to 16% of the internal energy for the 1/8-in. (3-mm) mesh size at failure. These hourglass energies are tolerated and are shown in Figure 256. The high hourglass energies occurred after peak load was reached. Based on the force and energy comparison for all three mesh sizes, the simulated behavior with the 1/8-in. (3-mm) mesh-size model appeared to provide the better comparison to the experimental testing results for peak

load, damage, and energy evaluation, using the selected parameters. However, the other two mesh sizes also provided very reasonable results. The smallest error for simulated peak load was observed with the 1/8-in. (3-mm) mesh at 15.5 percent. Again, all three mesh sizes predicted flexural failure.

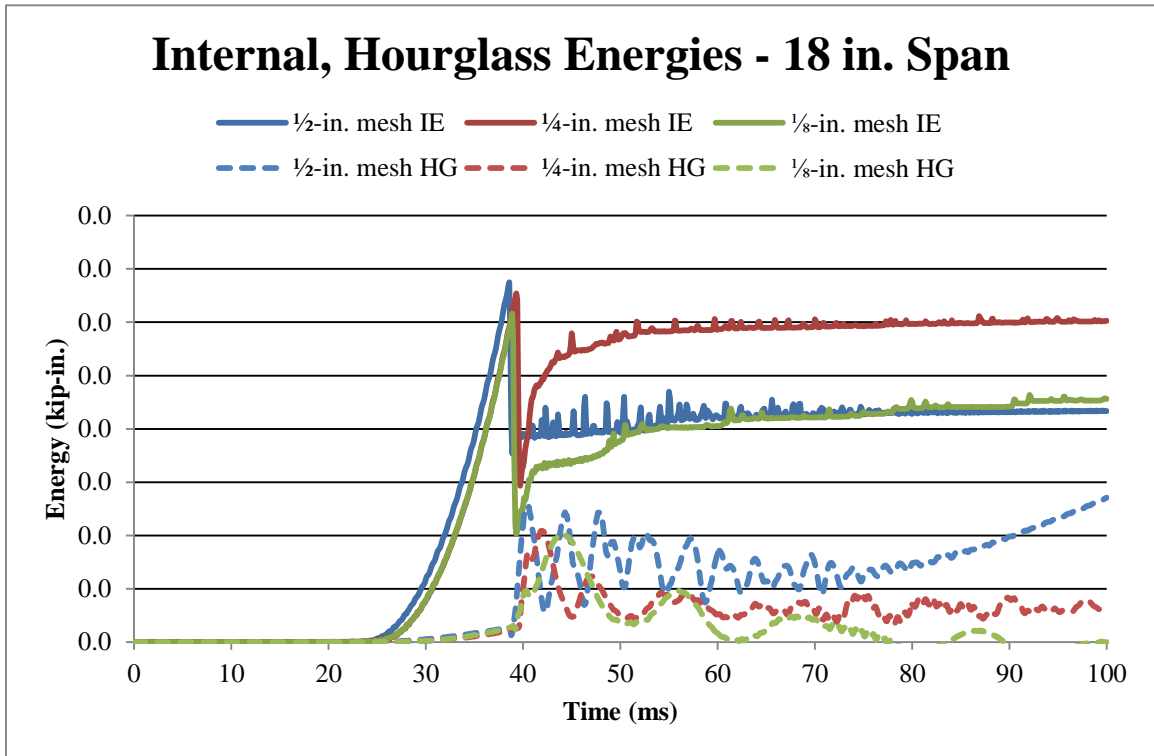


Figure 256. Energy Comparison for 18-in. (457-mm) Span, K&C Model

15.5 Discussion

The beam simulation effort investigated the capability of two selected material models to handle complex behaviors, including shear and flexural failures. All of the support spans from the experimental testing program were simulated using three different mesh sizes - 1/2 in. (13 mm), 1/4 in. (6 mm), and 1/8 mm (3 mm). Moderate to high hourglass energies were observed throughout most simulations. The performance of both material models is summarized in Table 46. The ability to change failure modes while only changing the support span by 1 in. (25 mm) is considered a rather significant

achievement. Overall, it appeared that the 1/2-in. (13-mm) mesh size performed better for the CSCM model, although peak load was only closely predicted in one out of the five load cases. The 1/2-in. (13-mm), 1/4-in. (6-mm), and 1/8-in. (3-mm) mesh sizes all performed reasonably well for the K&C model, with the 1/2-in. (13-mm) mesh size showing improved performance.

Table 46. Summary of CSCM and K&C Material Model Behavior

Material Model	Support Span	Failure Mode			Peak Load (kip)			Percent Error (%)		
		1/2-in.	1/4-in.	1/8-in.	1/2-in.	1/4-in.	1/8-in.	1/2-in.	1/4-in.	1/8-in.
CSCM	9 in.	Shear	Flexure	Flexure	43.9	50.0	56.5	10.3	25.6	42.0
	10 in.	Flexure	Flexure	Flexure	36.7	41.7	43.5	105.0	133.0	143.0
	11 in.	Flexure	Flexure	Flexure	30.2	34.6	34.6	78.7	104.7	104.7
	12 in.	Flexure	Flexure	Flexure	25.2	26.9	28.1	76.2	88.1	96.5
	18 in.	Flexure	Flexure	Flexure	11.9	12.5	12.8	105.2	115.5	120.7
K&C	9 in.	Shear	Shear	Shear	19.3	19.6	17.1	51.5	50.8	57.0
	10 in.	Shear	Shear	Shear	18.0	18.0	16.3	0.6	0.6	8.9
	11 in.	Flexure	Flexure	Shear	16.9	16.4	15.7	0.0	3.0	7.1
	12 in.	Flexure	Flexure	Flexure	14.0	13.4	13.4	2.1	6.3	6.3
	18 in.	Flexure	Flexure	Flexure	7.1	6.8	6.7	22.4	17.2	15.5

 - Smallest percent error

For the CSCM model, only the 9-in. (229-mm) support span did not result in the correct failure mode for all three mesh sizes. In this simulation, the 1/4-in. (6-mm) and 1/8-in. (3-mm) mesh sizes both showed flexural failure when shear failure was expected. The force-time curve for each of the two mesh sizes failed after all other simulations, at 130 ms. For simulations on the 10-in. (254-mm) support span, all three mesh sizes demonstrated flexural failure. In the experimental testing, this span was considered the transition point, as one test failed in shear and the other test failed in flexure. Overall, the

physical behavior observed with the CSCM model often matched the behavior observed in the experimental testing program.

Despite those comparisons, the CSCM material model simulations generally resulted in peak loads that were much larger than observed in the experimental testing. In many instances, the simulated peak load was twice that observed in the experimental testing program, with errors as high as 143.0 percent. The only support span that resulted in a close prediction for peak load was at 9 in. (229 mm), or as low as 10.3 percent error.

The K&C material model also largely predicted physical behavior correctly. The only instance when the correct failure mechanism was not well predicted was for the $\frac{1}{8}$ -in. (3-mm) mesh size with the 11-in. (279-mm) support span. The simulation resulted in a shear failure when a flexure failure was expected. For the 10-in. (254-mm) support span, which was considered the transition point, simulations with the K&C material model failed in shear. Even though element erosion did not exist for the material model, the damage profile for the beams still matched the experimental tests very well.

Unlike the CSCM model, the K&C model accurately predicted peak loads for four out of the five support spans. In fact, the simulated peak load was nearly identical to experimental test result in three out of the five simulations, 10-in. (254-mm) through 12-in. (305-mm) spans. The simulated peak load was within 15.5 percent for the 18-in. (457-mm) support span. However, the 9-in. (229-mm) support span resulted in simulated peak loads that reached 57.0 percent error. It is interesting to note that the 9-in. (229-mm) span was the only case that was correctly predicted for the CSCM material model. Overall, the K&C material model mostly predicted both physical and computational behavior observed in the experimental testing program. Further investigation into hourglass

controls is necessary in order to limit hourglass energies and use the model more confidently.

It was expected that this load case would be more difficult to replicate with simulation. The ability for both material models to transition between shear and flexural failure by changing the support span by just 1 in. (25 mm) was somewhat significant. This observation was a positive sign that these material models can possibly accommodate varied loading conditions that are commonly observed in many engineering applications, including roadside safety structures. It is rare that compression, tension, or shear act independently on a component. These material models show some promise in positively representing physical behavior under load. However, further investigation of the material models is deemed necessary when steel reinforcement is added.

CHAPTER 16 SUMMARY, CONCLUSIONS, AND RECOMMENDATIONS

16.1 Summary and Conclusions

The objective of this study was to investigate and evaluate several current concrete material models that are available in LS-DYNA. Over the course of many rounds of simulations, the models' adequacies were analyzed. Different loading conditions and failure modes were used for plain concrete simulations and testing different material model input parameters. Data from experimental testing performed by other researchers as well as those performed in the MwRSF structures laboratory was compared to that of corresponding simulations. Single-element and component-level simulations were completed to understand model behavior and provide guidance for future study.

Due to the heterogeneity of concrete, material failure was very challenging to predict. The mechanical behavior of concrete can be affected by many different properties. Concrete behavior will also vary based on the loading condition. Constitutive models have been developed to help predict this behavior. Many different mathematical models exist, including linear-elastic, plastic, and continuum damage models. Each model has its own unique definitions and special considerations. These mathematical models have been used to create material models for use in FEA concrete modeling to create material models. These FEA concrete material models can be verified by comparing simulation results with experimental results obtained from standard concrete laboratory tests.

For this study, the FEA software that was used to generate the simulations was LS-DYNA. In this program, there are many available concrete material models. Five

material models were selected for this investigative effort due to minimal material input, rate-dependent behavior, or the ability to track concrete damage, including: CSCM; K&C; RHT; Winfrith; and CDPM. Only the CSCM model had the ability to delete elements. These material models were used over the course of three different rounds of simulations: single-element models; simulation of external component testing; and simulation of internal component testing.

During the single-element simulations on unreinforced concrete in Chapter 4, three basic load cases were considered: compression; tension; and shear. These simulations were helpful in understanding the basic behavior of the material models using simple geometry and loading. Two different constraint conditions were also included to represent both unconfined and confined elements for compression and tension. The default material model inputs were used for all single-element simulations. The following major results were evaluated: stress-strain relationships for true stresses and strains; true stress in the z-direction; change in volume at the peak stress; change in the total volume; force in the z-direction; the maximum damage value for the element; and whether or not the element failed and/or eroded. Varying results were found for each of the loading cases and each of the material models. The compression and tension simulations were successful in that some of the models provided maximum stresses that matched the input values of the simulation. However, the shear case was not perfected and may not provide results representative of the pure shear case. This information was used going forward for the external component testing simulations.

Despite the knowledge gained, component modeling of external laboratory tests was deemed necessary. In Chapters 5 through 7, three major laboratory setups were

replicated in simulation, and results of the physical test and simulation were compared. In Chapter 5, the first loading case, compression, was covered. A stress-strain test curve was obtained from a study [42] that focused on the pre- and post-peak response phenomena when concrete cylinders were loaded, unloaded, and reloaded in uniaxial compression. A component cylinder was created in LS PrePost and run in LS-DYNA using the five different material models. The stress-strain behavior of the simulation was then compared to that of the experimental test. Variations were made to the model and input deck in order to fully understand the models' performance. Two element types (elform 1 and elform 2) were simulated, along with three mesh sizes: $\frac{3}{4}$ in. (19 mm); $\frac{3}{8}$ in. (10 mm); and $\frac{3}{16}$ in. (5 mm). Changing the fracture energy value in the CSCM model affected the softening behavior of the model. In the K&C model, it was found that the strain rate enhancement factors were not working properly and were overpredicting the peak stresses. A few parameters were varied in the Winfrith model, but their effect was inconclusive as changing input parameters did not affect the stress-strain behavior. It was determined that none of the models were perfect, but three of the models (CSCM, K&C, and Winfrith) performed adequately. Excessive simulation run time was required for the RHT and CDPM models, making them undesirable. Specifically, there was an issue with the plastic solver in the CDPM model that prevented it from completing simulations. Elform 1 and a $\frac{3}{8}$ -in. (10-mm) mesh size were recommended. Overall, the CSCM model provided the most similar behavior to the experimental compression test.

The second loading case, covered in Chapter 6, was tension. An axial stress-displacement plot was used from this study for comparison with the simulation results [67]. A concrete flat plate specimen was created in LS PrePost and loaded in direct

tension. Similar adjustments were made to the model and input decks for each of the material models. Two element types (elform 1 and elform 2) were simulated, along with three mesh sizes: $\frac{3}{4}$ in. (19 mm); $\frac{3}{8}$ in. (10 mm); and $\frac{3}{16}$ in. (5 mm). The stress-deformation behavior of the simulation was then compared to the experimental testing. Some of the same issues from the compression simulations were found again. In the CSCM simulations, it was found that the results were not repeatable. Multiple simulations with identical input parameters for ERODE, recov, and repow were not providing the same stress-deformation behavior. The same issues with the strain rate effects of the K&C model arose in the tension simulations. The predictions of the RHT model again overpredicted the peak stress from the experimental testing. There were shooting nodes in the Winfrith model, and the plastic solver in the CDPM model was again an issue. Elform 1 and the $\frac{3}{16}$ -in. (5-mm) mesh size were recommended for this study. Only the CSCM and K&C material models performed adequately for tension, with the K&C model performing better.

In Chapter 7, the final load case, shear, was simulated. Shear testing of unreinforced concrete is not very common, and limited research studies were available for use in this study. One particular study involved a rectangular specimen placed in a shear box [68]. A more complex model was created in LS PrePost to create the shear box, and the top and bottom portions of the box were displaced horizontally to imitate shear loading. The stress-deformation behavior of the simulations was compared against that obtained in the experimental testing program. It was determined that inadequate deformation data was present; therefore, limited analysis was conducted on the five material models besides peak stresses. Two element types (elform 1 and elform 2) were

simulated, along with three mesh sizes: $\frac{3}{4}$ in. (19 mm); $\frac{3}{8}$ in. (10 mm); and $\frac{3}{16}$ in. (5 mm). The same issues with the ERODE, recov, and repow parameters in the CSCM model again surfaced during these simulations. In the K&C model, it was found that as the compressive damage scaling factor decreased, the peak stresses decreased as well. No other input parameters were investigated for the RHT, Winfrith, or CDPM models. Elform 1 and the $\frac{3}{8}$ -in. (10-mm) mesh size were preferred. The CSCM, K&C, and RHT models performed better than others in this load case, with the K&C model performing best overall.

In Chapter 8, three (RHT, Winfrith, and CDPM) of the five material models were eliminated from consideration after the simulation effort performed on external laboratory component tests. These models had poor performance in both the single-element and external-component testing simulation phases. The RHT was inconsistent throughout the investigation. It generally over-predicted peak stresses, and its stress-strain or stress-displacement behavior greatly differed from physical test data. The Winfrith model performed well in the compression load case, but it failed to provide any useable data in the tension and shear simulations. There were, in fact, situations in which the Winfrith model did not provide any results and erred out. Finally, the CDPM model performed poorly in the single-element simulations and did not perform well in the external component simulations. The plastic solver of the model was prohibiting simulations from completing, indicating its inability to be used for simulations involving more than one element.

The two concrete models that were considered for all simulations were the CSCM and K&C models. The CSCM model performed consistently in the first two rounds of

simulation. The peak stresses were similar to the peak stresses in the single-element models and performed the best in all compression simulations. The model also has capabilities, such as automatic parameter generation and element erosion, which are highly desired. Despite its sterling performance and these benefits, it was discovered in the external component test simulations that the model was not always repeatable and mesh results did not conform to expectations. When input parameters were identical and multiple simulations were run, the results were often different. Randomness was expected in concrete itself due to its heterogeneous and variability in testing, but this behavioral tendency was concerning in numerical simulations. Different simulation results were also obtained when the mesh size was varied, which should not have been the case. Despite these facts, the CSCM model generally provided fair results and was used in the internal component testing simulations.

The K&C model also performed consistently through the first two rounds of simulation. In the single-element modeling, this material model provided the closest matches for peak stresses in the compression and tension load cases. The model also performed similarly well in the external component simulations, oftentimes better than the CSCM model. However, minimal softening occurred in this model. Additionally, the lack of an element deletion capability for the material model makes failure planes and material damage slightly more difficult to show. The strain rate effects in the model also were not working properly, typically overestimating the calculated dynamic increase factor. Despite these shortcomings, the K&C model performed reasonably well in the first two rounds of simulation.

The final stage of simulations involved replicating in-house experimental testing. Compression, tension, and flexure/shear loading tests were developed, and specimens were cast to be used in these physical tests. The MTS equipment in the MwRSF laboratory was used to complete all physical testing. These machines provided force, time, and displacement readings. Additional instrumentation was used to track strain in four-point beam bending tests. In Chapter 10, concrete cylinders were tested in compression, resulting in an average compressive strength of 9.1 ksi (62.7 MPa) among the seven tests. In Chapter 11, concrete dogbone specimens were tested in tension, resulting in an average tensile strength of 0.36 ksi (2.5 MPa) among the six tests.

In Chapter 11, concrete beam specimens were tested in four-point bend tests. The span supports on the bottom face of the beam were varied in order to cause shear or flexure failure patterns. In the beam testing program, two (9 and 10 in. [229 and 254 mm]) of the six test span lengths resulted in shear failure. Four (10, 11, 12, and 18 in. [254, 279, 305, and 457 mm]) of the six test span lengths resulted in flexural failure. After five different support spans were tested, it was determined that the 10-in. (254-mm) support span was likely the transition point between shear and flexural failure modes. The ability to demonstrate a likely transition point was an impressive achievement, and the goal was to identify this transition in the associated simulations.

In Chapter 13, two material models were created to replicate the geometry and material properties from the seven in-house compression tests. A cylinder was created in LS-DYNA and loaded in pure compression. Input parameters were only varied for the CSCM model, only to confirm that the repeatability issues with the ERODE, recov, and repow parameters were still occurring. Adjustments in these parameters generally did not

affect the simulated stress-strain or stress-time behaviors. In the in-house compression and tension simulations, the default input parameters were used for both material models. In the compression simulations, the CSCM model overestimated the peak stress and showed some diagonal failure planes that were present in the experimental testing. The K&C material model, however, had a nearly identical match with the physical test peak stress. There was little post-peak behavior with this load case, which was consistent with previous simulations. Overall, both material models performed reasonably well under compression.

In Chapter 14, the dogbone specimen geometry and material properties were replicated in LS-DYNA simulations and loaded in direct tension. The peak stress was overestimated by the CSCM model, and there was more softening in the model than would be expected for direct tension. Fewer parameter variations were made to the model based on previous knowledge gained, but the repeatability issue discovered in the single-element and external-component test simulations was again present. For the K&C model, the peak stress was slightly underestimated. There was again little softening behavior in the material model, but this observation was expected for a direct tension test. Both material models also performed adequately for this load case.

In Chapter 15, four-point bend specimens were simulated at different support spans for the CFS testing program. Both models resulted in high hourglass energies, despite efforts to limit it. A repow input parameter of 0.5 decreased some of the hourglass energies in the CSCM model, making it the only non-default parameter used for either material model. The CSCM model generally overpredicted the peak load, with error as high as 143.0 percent. The correct failure pattern was predicted in all but one of the

simulations, the 9-in. (229-mm) support span. In the simulation, the ¼-in. (6-mm) and ⅛-in. (3-mm) mesh sizes resulted in flexural failure, when shear failure was seen in the experimental testing program. Despite the adequate behavior in predicting physical behavior, the peak load predictions were expected to be closer. The K&C model, however, showed adequate physical behavior, as well as excellent peak load predictions for four of the five simulations. The simulated peak load was nearly identical to experimental test result in three out of the five simulations, with the largest error at 57.0 percent amongst all simulations. The error in peak load predictions for span lengths of 10 in. (254 mm), 11 in. (279 mm), and 12 in. (305 mm) were 0.6%, 0.0%, and 2.1%, respectively. Both models adequately showed the transition between flexural and shear failure, with CSCM predicted shear failure at a 10-in. (254-mm) span, and K&C predicting flexure at a 10-in. (254-mm) span.

16.2 Recommendations

It was clear that the CSCM and K&C material models performed adequately in some cases and inadequately in other cases. There are obvious benefits to both that allow for a reasonable prediction of concrete fracture. Again, this process is difficult because of the typically unpredictable nature of concrete. When considering an improved model, there are parts of each model that should be considered. The CSCM model has the major benefits of element erosion, automatic parameter generation, and simple damage tracking. Although the model does have the capability of adjusting specific model input parameters, these parameters are neither reliable nor repeatable. Due to the mesh sensitivity feature of the model, a change in mesh size should not result in different behavior because the fracture energy should remain constant despite element size, yet this

occurred. Additionally, more studies should be performed using the CSCM model in complex loading conditions, similar to the four-point bending tests.

The K&C model has its own benefits, such as automatic parameter generation and the ability for the user to input the tensile strength directly and damage tracking. However, it is not flawless either. Despite its accuracy in predicting peak stresses and showing better performance in the four-point bending simulations, the model has some deficiencies. The damage in the material model is handled separately for compression and tension. It would be preferred for damage to be shown as an average of the two independent damage values. The damage parameters are thus at maximum when damage levels reach 2.0. Additionally, more investigation should be conducted into strain rate effects and why those are overpredicting concrete strength. Throughout all simulations in this study, strain rate effects were turned off. This selection may become more of an issue under dynamic loading conditions. The biggest drawback of the model is its inability to erode elements. This fact oftentimes caused excessive dilation in the specimen and may lead the user to believe that more deformation is occurring than should be expected.

It is clear from this investigation that there is still work to be performed in the area of concrete modeling using LS-DYNA software. There are many different ways to model concrete for roadside safety applications, but it appears that the specialized concrete models could benefit from enhancement that would allow for improved prediction of material failure. There are parts of the analyzed models that can be used going forward, but improvements definitely are required. If these improvements are made, concrete modeling could be more accurate and allow for progress in roadside safety design using finite element simulation.

Specifically for this study, more effort could be focused on complex loading conditions. The success of modeling flexural and shear failure in the beam simulations was an impressive accomplishment. Yet, much is still to be learned about how these material models perform when combined loading is occurring, as it often occurs in roadside safety applications. Thus, additional work, such as multi-axial and dynamic loading, is recommended to continue this Phase I study.

More effort should also be invested in properly instrumenting test specimens. In the tension testing, strain data could not be gathered due to the inadequacy for the laser extensometer at such low strain resolution. Having this strain data would have allowed for better comparisons with simulated data. In the beam testing, a more accurate or reliable method for obtaining displacement and strain readings would have provided better results for verification. Improved data in the string potentiometers would have been especially helpful when trying to understand beam displacements. Due to this lack of accurate and reliable data, more physical test data is required for enhanced comparisons for these two cases.

More work needs to be completed for the beam testing and associated simulations. There were issues with accurately predicting peak loads for both models. The hourglass energies in the two material models were moderate to high, and significant efforts to decrease hourglass energies fell short. These material models need to be refined in order to perform better across many loading conditions.

Finally, more focus can be placed on the material models themselves. Limited model input parameters were investigated due to limited published information regarding alternative input parameters. Additionally, the ranges for the input parameters were

chosen based on other researcher recommendations and closeness to the default value. An expanded investigation into all material model input parameters would be helpful. Issues, such as the strain rate effects not working for the K&C model and some of the CSCM model parameters not showing repeatable behavior, could also be addressed. These changes would drastically improve upon the work that was completed in this research study.

Once more clarity is provided with unreinforced concrete, investigation of reinforced concrete should occur; since, it is common in roadside safety structures. Material models would need to be re-evaluated to determine if they are compatible with internal reinforcement and/or to determine how reinforcement would be added. At this time, additional material models could be considered as well. A full understanding of how unreinforced concrete behaves with LS-DYNA material models would create a basis for the reinforced concrete study.

CHAPTER 17 REFERENCES

1. Nguyen, G.D., "A Thermodynamic Approach to Constitutive Modelling of Concrete using Damage Mechanics and Plasticity Theory," Doctoral Thesis submitted to the University of Oxford, 2005.
2. Ortiz, M., "A constitutive theory for the inelastic behavior of concrete," *Mechanics of Materials*, Vol. 4, 1985, pp. 67-93.
3. Hearing, B., "Fracture behavior of Mortar-Aggregate Interfaces in Concrete," Master's Thesis submitted to the Massachusetts Institute of Technology, January 1997.
4. Ruiz, G., Zhang, X.X., Poveda, E., Porras, R., and Del Viso, J.R., "Fracture behavior of high-strength concrete at different loading rates," *Fracture Mechanics of Concrete and Concrete Structures*, 2010.
5. Montoya, E., Vecchio, F.J., and Sheikh, S.A., "Compression field Modeling of Confined Concrete: Constitutive Models," *Journal of Materials in Civil Engineering*, Vol. 18, No. 4, July/August 2006, pp. 510-517.
6. Song, H.-W., Bang, C.-S., Nam, J.-W., and Byun, K.-J., "Homogenized Crack Model for Finite Element Analysis of Concrete Fracture," *Fracture Mechanics of Concrete Structures*, Vol. 1, April 2014, pp. 213-220.
7. "Concrete material model," pp. 23-101.
8. Liu, C.-C., Lu, H.-X., and Guan P., "Coupled viscoplasticity damage constitutive model for concrete materials," *Applied Mathematics and Mechanics*, Vol. 28, No. 9, 2007, pp. 1145-1152.
9. Jacobsen, J.S., Poulsen, P.N., Olesen, J.F., and Krabbenhoft, K., "Constitutive mixed mode model for cracks in concrete," *Engineering Fracture Mechanics*, Vol. 99, 2013, pp. 30-47.
10. Suaris, W. and Shah, S.P., "Constitutive model for Dynamic Loading of Concrete," *Journal of Structural Engineering*, Vol. 111, No. 3, March 1985, pp. 563-576.
11. Caggiano, A., "Application of some classic constitutive theories to the numerical simulation of the behavior of plain concrete," Doctoral Thesis submitted to the University of Salerno, 2008.
12. Gettu, R., Bazant, Z.P., and Karr, M.E., "Fracture Properties and Brittleness of High-Strength Concrete," *ACI Materials Journal*, Vol. 87, No. 6, November-December 1990, pp. 608-618.

13. Pivonka, P., Ozbolt, J., Lackner, R., and Mang H.A., "Comparative studies of 3D-constitutive models for concrete: application of mixed-mode fracture," *International Journal for Numerical Methods in Engineering*, Vol. 60, 2004, pp. 549-570.
14. Abu Al-rub, R.K. and Kim, S.M., "Computational applications of a coupled plasticity-damage constitutive model for simulating plain concrete fracture," *Engineering Fracture Mechanics*, Vol. 77, 2010, pp. 1577-1603.
15. Buyukozturk, O. and Shareef, S.S., "Constitutive Modeling of Concrete in Finite Element Analysis," *Computers & Structures*, Vol. 21, No. 3, 1985, pp. 581-610.
16. Tenchev, R. and Purnell, P., "An application of a damage constitutive model to concrete at high temperature and prediction of spalling," *International Journal of Solids and Structures*, Vol. 42, 2005, pp. 6550-6595.
17. Yupu, S. and Huailiang, W., "Endochronic damage constitutive model for fully-graded aggregate mass concrete," *Frontiers of Architectural and Civil Engineering*, Vol. 1, No. 3, 2007, pp. 274-280.
18. Graffe, R. and Linero, D., "Numerical modeling of the fracture process of mode I of concrete beams with known cracking path by means of a discrete model of cohesive crack," *Numerical modeling of the fracture process*, Vol. 25, No. 3, December 2010, pp. 399-418.
19. Lade, P.V. and Kim, M.K., "Single Hardening Constitutive Model for Soil, Rock and Concrete," *International Journal of Solids and Structures*, Vol. 32, No. 14, 1995, pp. 1963-1978.
20. Marzec, I. and Tejchman, J., "Computational modelling of concrete behavior under static and dynamic conditions," *Bulletin of the Polish Academy of Sciences*, Vol. 61, No. 1, 2013, pp. 85-96.
21. Nguyen, G.D. and Houlsby, G.T., "Nonlocal damage modelling of concrete: a procedure for the determination of model parameters," Report No. OUEL 2287/05, University of Oxford, 2005.
22. Shiyun, X., Hongnan, L., and Gao, L., "3-D consistency dynamic constitutive model of concrete," *Earthquake Engineering and Engineering Vibration*, Vol. 9, 2010, pp. 233-246.
23. Jankowiak, T. and Lodygowski, T., "Identification of Parameters of Concrete Damage Plasticity Constitutive Model," *Foundations of Civil and Environmental Engineering*, No. 6, 2005, pp. 53-69.
24. Oliver Martin "Comparison of different Constitutive Models for Concrete in ABAQUS/Explicit for Missile Impact Analyses," *JRC Scientific and Technical Reports*, 2010.

25. Brozovsky, J., Mynarz, M., and Sucharda, O., "Constitutive Modelling of Concrete in 2D Using Smeared Crack Model," June 2008.
26. ASTM C39, "Standard Test Method for Compressive Strength of Cylindrical Concrete Specimens," ASTM International.
27. ASTM D2936, "Standard Test Method for Direct Tensile Strength of Intact Rock Specimens," ASTM International.
28. ASTM C78, "Standard Test Method for Flexural Strength of Concrete (Using Simple Beam with Third-Point Loading)," ASTM International.
29. Zhang, Y., Abraham, O., Grondin, F., Loukili, A., Tournat, V., Le Duff, A., Lascoup, B., and Durand, O., "Study of stress-induced velocity variation in concrete under direct tensile force and monitoring of the damage level by using thermally-compensated Coda Wave Interferometry," *Ultrasonics*, Vol. 52, 2012, pp. 1038-1045.
30. Kim, J.J. and Taha, M.R., "Experimental and Numerical Evaluation of Direct Tension Test for Cylindrical Concrete Specimens," *Advances in Civil Engineering*, 2014.
31. Yan, D. and Lin, G., "Dynamic properties of concrete in direct tension," *Journal of Cement and Concrete Research*, Vol. 36, 2006, pp. 1371-1378.
32. Graybeal, B.A. and Baby, F., "Development of Direct Tension Test Method for Ultra-High-Performance Fiber-Reinforced Concrete," *ACI Materials Journal*, Vol. 110, No. 2, March-April 2013, pp. 177-186.
33. Kim, D.J., El-Tawil, S. and Naaman, A.E., "Rate-dependent tensile behavior of high performance fiber reinforced cementitious composites," *Materials and Structures*, Vol. 42, 2009, pp. 399-414.
34. Zhen-hai, G. and Xiu-qin, Z., "Investigation of Complete Stress-Deformation Curves for Concrete in Tension," *ACI Materials Journal*, July-August 1987, pp. 278-285.
35. Perdikaris, P.C. and Romeo, A., "Size Effect on Fracture Energy of Concrete and Stability Issues in Three-Point Bending Fracture Toughness Testing," *ACI Materials Journal*, Vol. 92, No. 5, September-October 1995, pp. 483-496.
36. Gustafsson, P.J. and Hillerborg, A., "Sensitivity in Shear Strength of Longitudinally Reinforced Concrete Beams to Fracture Energy of Concrete," *ACI Structural Journal*, May-June 1988, pp. 286-294.
37. Bazant, Z.P. and Prat, P.C., "Effect of Temperature and Humidity on Fracture Energy of Concrete," *ACI Materials Journal*, July-August 1988, pp. 262-271.

38. Navalurkar, R.K., Hsu, C-T. T., Kim, S.K., and Wecharatana, M., "True Fracture Energy of Concrete," *ACI Materials Journal*, Vol. 96, No. 2, March-April 1999, pp. 213-225.
39. Martin, J., Stanton, J., Mitra, N., and Lowes, L.N., "Experimental Testing to Determine Concrete Fracture Energy Using Simple Laboratory Test Setup," *ACI Materials Journal*, Vol. 104, No. 6, November-December 2007, pp. 575-584.
40. Park, K., Paulino, G.H., and Roesler, J.R., "Prediction of Concrete Fracture Mechanics Behavior and Size Effect using Cohesive Zone Modeling,"
41. Roseler, J. Bordelon, A., Gaedicke, C., Park, K., and Paulino, G., "Fracture Behavior and Properties of Functionally Graded Fiber-Reinforced Concrete," *Multiscale and Functionally Graded Materials*, 2006, pp. 513-518.
42. Lee, Y.H. and Willam, K., "Mechanical Properties of Concrete in Uniaxial Compression," *ACI Materials Journal*, V. 94, No. 6, November-December 1997, pp. 457-471.
43. Rosa, A.L., Yu, R.C., Ruiz, G., Saucedo, L., and Sousa, J.L.A.O., "A loading rate dependent cohesive model for concrete fracture," *Journal of Engineering Fracture Mechanics*, Vol. 82, 2012, pp. 195-208.
44. Darwin, D., Barham, S., Kozul, R., and Luan, S., "Fracture Energy of High-Strength Concrete," *ACI Materials Journal*, Vol. 98, No. 5, September-October 2001, pp. 410-417.
45. Coughlin, A., "Contact Charge Blast Performance of Fiber Reinforced and Polyurea Coated Concrete Vehicle Barriers," Master's Thesis submitted to Pennsylvania State University, August 2008.
46. Zhou, X.Q. and Hao, H. "Modelling of compressive behavior of concrete-like materials at high strain rate," *International Journal of Solids and Structures*, Vol. 45, 2008, pp. 4648-4661.
47. Musselman, E., "Characterizing Blast and Impact Resistance of Long Carbon Fiber Reinforced Concrete," Doctoral Thesis submitted to Pennsylvania State University, August 2007.
48. Li, Q.M. and Meng, H., "About the Dynamic Strength Enhancement of Concrete-Like Materials in a Split Hopkinson Pressure Bar Test," *International Journal of Solids and Structures*, Vol. 40, 2003, pp. 343-360.
49. Wu, Y., Crawford, J.E., and Magallanes, J.M., "Performance of LS-DYNA Concrete Constitutive Models," *Constitutive Modeling*, 12th International LS-DYNA Users Conference.

50. Livermore Software Technology Corporation (LSTC), LS-DYNA Keyword User's Manual (Material Models), Version R7.0, Volume II, February 2013.
51. Murray, Y.D., "Theory and Evaluation of Concrete Material Model 159," *Material Technology*, 8th International LS-DYNA Users Conference, pp. 25-35.
52. "Comité Euro-International du Béton," *CEB-FIP Model Code 1990*, Redwood Books, Trowbridge, Wiltshire, UK, 1993.
53. Brannon, R.M. and Leelavanichkul, S., "Survey of Four Damage Models for Concrete," Sandia National Laboratories, August 2009.
54. Malvar, L.J. and Ross, C.A., "Review of Strain Rate Effects for Concrete in Tension," *ACI Materials Journal*, V. 95, No. 6, November-December 1998, pp. 735-739.
55. Borrvall, T., and Riedel, W., "The RHT Concrete Model in LS-DYNA," 8th European LS-DYNA Users Conference, May 2011.
56. Schwer, L.E., "The Winfrith Concrete Model: Beauty or Beast? Insights into the Winfrith Concrete Model," 8th European LS-DYNA Users Conference, May 2011.
57. Ottosen, N.S., "A Failure Criterion for Concrete," *Journal of the Engineering Mechanics Division*, Vol. 103, No. 4, July/August 1977, pp. 527-535.
58. Grassl, P. and Jirasek, M., "Damage-plastic model for concrete failure," *International Journal of Solids and Structures*, V. 43, 2006, pp. 7166-7196.
59. Abu-Odeh, A., "Application of New Concrete Model to Roadside Safety Barriers," *Crash/Safety (1)*, 9th International LS-DYNA Users Conference, 2006.
60. Schwer, L.E. and Malvar, L.J., "Simplified Concrete Modeling with *MAT_CONCRET_DAMAGE_REL3," *Material*, LS-DYNA Anwenderforum, 2005, pp. 49-60.
61. Crawford, J.E., Wu, Y., Choi, H.-J., Magallanes, J.M., and Lan, S., *Use and Validation of the Release III K&C Concrete Material Model in LS-DYNA*, Report No. TR-11-36.6, Karagozian & Case, 2011.
62. Schwer, L.E., "Modeling Rebar, the Forgotten Sister in Reinforced Concrete Modeling," *Constitutive Modeling*, 13th International LS-DYNA Users Conference.
63. Mindess, S. and Young, F.J., 'Concrete', Prentice-Hall, Inc., Englewood Cliffs, NJ (1981) 671.
64. Shah, S.P. and Sankar, R., "Internal Cracking and Strain-Softening Response of Concrete under Uniaxial Compression," *ACI Materials Journal*, V. 84, No. 3, March-April 1988, pp. 200-212.

65. Murray, Y.D., et al., *User's Manual for LS-DYNA Concrete Material Model 159*, FHWA-HRT-05-062, US Department of Transportation, 2007.
66. Murray, Y.D., et al., *Evaluation of LS-DYNA Concrete Material Model 159*, FHWA-HRT-05-063, US Department of Transportation, 2007.
67. Gopalaratnam, V.S. and Shah, S.P., "Softening Response of Plain Concrete in Direct Tension," *ACI Materials Journal*, V. 82, No. 3, May-June 1985, pp. 310-323.
68. Wong, R.C.K., Ma, S.K.Y., Wong, R.H.C., and Chau, K.T., "Shear Strength Components of Concrete Under Direct Shearing," *Cement and Concrete Research*, V. 37, 2007, pp. 1248-1256.
69. Steel Construction Manual, *American Institute of Steel Construction*, Edition 14; AISC Standard Number 325-11.
70. Roylance, D., "Beam Displacements," *Massachusetts Institute of Technology*, November 2000.
71. ASTM E1561, "Standard Practice for Analysis of Strain Gauge Rosette Data," ASTM International.
72. "Strain Transformation and Rosette Gage Theory," *AE3145 Strain Transformation and Rosette Gage Theory*, pp. 1-7.
73. "Strain Gage Rosettes: Selection, Application, and Data Reduction," *Micro-Measurements*, Tech Note TN-515, August 2014.
74. Timoshenko, S., *Theory of Elasticity*, McGraw-Hill, New York, 1st edition, 1934.

CHAPTER 18 APPENDICES

Appendix A. Material Model Card Inputs


```

*MAT_CSCM
$ mid ro nplot incre irate erode recov itretrc
$ pred
$
$ g k alpha theta lamda beta nh ch
$
$ alpha1 theta1 lamda1 beta1 alpha2 theta2 lamda2 beta2
$
$ r x0 w d1 d2
$
$ b gfc d gft gfs pwrc pwrt pmod
$
$ eta0c nc eta0t nt overc overt srate repow
$
$

```

Figure A-1. Material Model Input Card for CSCM Model

```

*MAT_CONCRETE_DAMAGE_REL3
$ mid ro pr
$
$ ft a0 a1 a2 b1 omega a1f
$
$ slambda nout edrop rsize ucf lcrate locwid npts
$
$ 101 102 103 104 105 106 107 108
$
$ 109 110 111 112 113 b3 a0y a1y
$
$ e01 e02 e03 e04 e05 e06 e07 e08
$
$ e09 e10 e11 e12 e13 b2 a2f a2y
$
$

```

Figure A-2. Material Model Input Card for K&C Model

```

*MAT_RHT
$ mid ro shear onempa epsf b0 b1 t1
$
$ a n fc fs* ft* q0 b t2
$
$ e0c e0t ec et betac betat ptf
$
$ gc* gt* xi d1 d2 epm af nf
$
$ gamma a1 a2 a3 pel pco np alpha0
$
$

```

Figure A-3. Material Model Input Card for RHT Model

```
*MAT_WINFRITH_CONCRETE|
$   mid      ro      tm      pr      ucs      uts      fe      asize
$
$   e        ys      eh      uelong  rate      conm     conl     cont
$
$   eps1     eps2     eps3     eps4     eps5     eps6     eps7     eps8
$
$   p1       p2       p3       p4       p5       p6       p7       p8
$
```

Figure A-4. Material Model Input Card for Winfrith Model

```
*MAT_CDPM
$   mid      ro      e      pr      ecc      qh0      ft      fc
$
$   hp       ah      bh      ch      dh      as      df      fc0
$
$   type     bs      wf      wf1     ft1     strflg   failflg
$
```

Figure A-5. Material Model Input Card for CDPM Model

Appendix B. Instrumentation Specification Sheets



Dehnungsmessstreifen
Strain gages
Jauges d'extensométrie

Widerstand
Resistance
Resistance **120 Ω ±0.35 %**

k-Faktor
Gage factor
Facteur k **2.09 ±1.0 %**

Querempfindlichkeit
Transverse sensitivity
Sensibilité transversale **-0.2 %**

Temperaturkompensation: Ferritstahl mit
Temperature compensation: steel with
Compensation de température: acier avec **α = 10.8 [10⁻⁶ / K]**

Bestellnummer
Order No.
No. de référence

K-LY4-1-13-120-2-25

Typ
Type
Type

50/120 LY41-2L-0.5M

Stückzahl
Contents
Quantité

10

Temperaturkoeffizient
des k-Faktors
Température coefficient
of gage factor
Coefficient de température
du facteur k

93 ±10 [10⁻⁶ / K]

(-10°C ... +45°C)

Fertigenis
Foil lot
Lot de la feuille

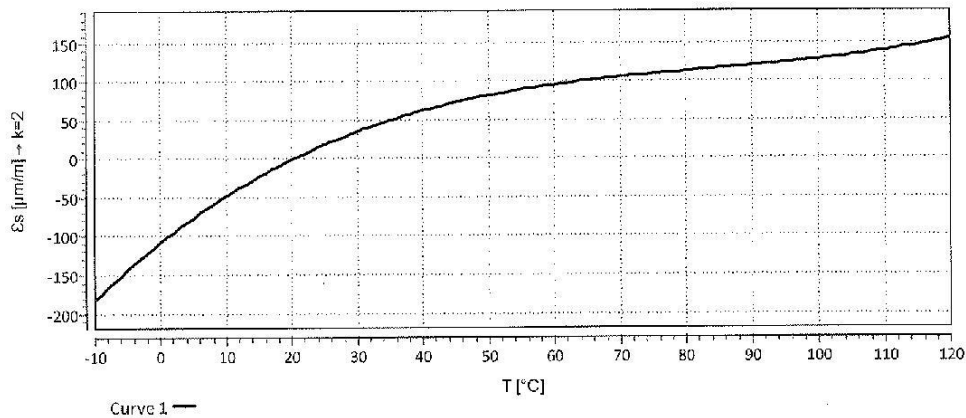
A417/22

Herstellungslös
Production batch
Lot de fabrication

812067311

Maximale Brückenпиттenspannung
maximal bridge excitation voltage
tension d'alimentation de pont maxi

12.5 V



$$\epsilon_s(T) = -26.12 + 2.56 * T - 7.19E-02 * T^2 + 2.88E-04 * T^3 \pm (T-20) * 0.30 [\mu\text{m/m}] + 4.115 * (T-20) [\mu\text{m/m}]$$

Alle technischen Daten nach VDI/VDE 2635. Geben Sie bei Rückfragen bitte Bezeichnung und Herstellungslos an.

All specifications in accordance with VDI/VDE 2635. In case of further inquiries please indicate order no. and production batch number.

Toutes les caractéristiques techniques selon la norme VDI/VDE 2635. Dans toutes communications, prière d'indiquer le numéro de commande et le numéro du lot de production.

Reponse an température des jauges d'extensométrie appliquées sur des matériaux dont les coefficients de dilatation thermique α sont indiqués. Mesurée à variation continue de la température.

Curve 1: Jauges avec câble en PVC.
T = température en °C
(sans dimension)

Temperaturgang der Dehnungsmessstreifen bei Applikationen mit oben angegebenen Wärmeausdehnungskoeffizienten n. Gemessen bei kontinuierlicher Temperaturänderung.

Kennlinie 1: DMS mit PVC Kabel.
T = Temperatur in °C
(dimensionlos)

The temperature response refers to strain gages bonded to materials with specified coefficients of thermal expansion α. Values are measured with continuous temperature variation.

Curve 1: Strain gages with PVC cable.
T = temperature in °C
(dimensionless)

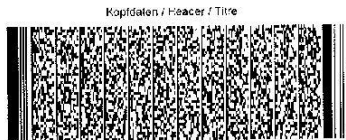


Figure B-1. Specifications for Linear Strain Gauges



**Dehnungsmessstreifen
Strain gages
Jauges d'extensométrie**

Bestellnummer
Order No.
No. de référence **K-RY8-1-47-120-2-25**

Typ
Type
type **6/120 RY81-2L-0.5M**

Stückzahl
Contents
Quantité **5**

Temperaturkoeffizient
des k-Faktors
Temperature coefficient
of gage factor
Coefficient de température
du facteur k **93 ± 10 [10⁻⁶ / K]
(-10°C ... +45°C)**

Folienlos
Foil lot
Lot de la feuille **A417/36**

Herstellungslösung
Production batch
Lot de fabrication **812067313**

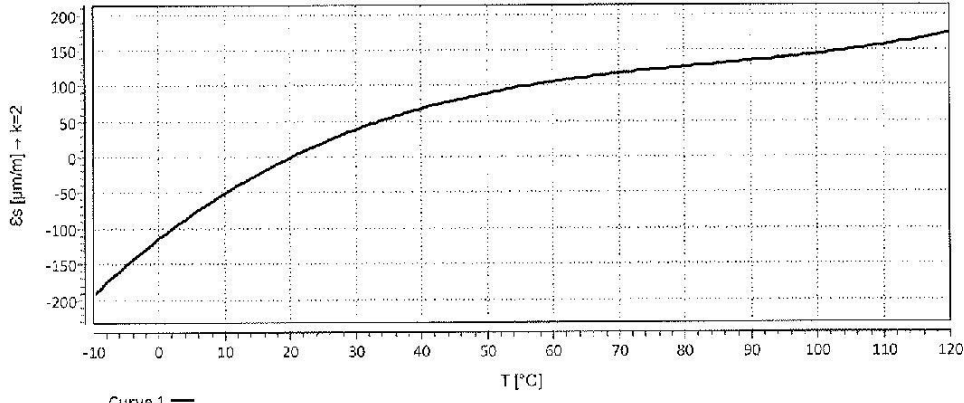
Widerstand
Resistance
Résistance **120 Ω ± 0.35 %**

k-Faktor
Gage factor
Facteur k
**a: 2.02 ± 1.0 %
b: 2.06 ± 1.0 %
c: 2.02 ± 1.0 %**

Quersensitivität
Transverse sensitivity
Sensibilité transverse
**a: 0.4 %
b: 0.2 %
c: 0.4 %**

Temperaturkompensation: Ferritischer Stahl mit
Temperature compensation: steel with
Compensation de température: acier avec **α = 10.8 [10⁻⁶ / K]**

Maximale Brückenspannung
max: max bridge excitation voltage
tension d'alimentation de pont maxi **7.5 V**



$$\epsilon_s(T) = -32.32 + 2.94 * T - 7.43E-02 * T^2 + 2.96E-04 * T^3 \pm (T-20) * 0.30 [\mu\text{m/m}] + 4.115 * (T-20) [\mu\text{m/m}]$$

All technical data in accordance with VDI/VDE 2635. In case of further inquiries please indicate order no. and production batch number.
Toutes les caractéristiques techniques selon la norme VDI/VDE 2635. Dans toutes les communications, s'il y a lieu, indiquer le numéro de commande et le numéro ou lot de production.

Temperaturgang der Dehnungsmessstreifen bei Applikationen mit oben angegebenen Wärmeausdehnungskoeffizienten: α. Gemessen bei kontinuierlicher Temperaturänderung.
Kennlinie 1: DMS mit PVC Kabel, T = Temperatur in °C (dimensionslos)

Réponse en température des jauges d'extensométrie appliquées sur des matériaux dont les coefficients de dilatation thermique α sont indiqués. Mesurée à variation continue de la température.
Courbe 1: Jauges avec câble en PVC, T = température en °C (sans dimension)

The temperature response refers to strain gages bonded to materials with specified coefficients of thermal expansion α. Values are measured with continuous temperature variation.
Curve 1: Strain gages with PVC cable, T = temperature in °C (dimensionless)

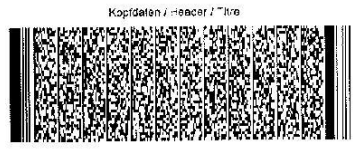



Figure B-2. Specifications for Rosette Strain Gauges

Firstmark **Final Inspection Data Sheet**

Test ID Test Date Customer Customer ID
 Pur. Order Sales Order Job Order
 Part Number Serial Number
 Design Travel (inches(mm)) DC Input (V)
 Max Acceptable Error (%): Line Slope (mV/inch (mV/mm))
 Actual Error (%): Sensitivity (inch/mV (mm/mV))

Acceptance Criteria				
Revision	Description	Instrument	Acceptance Value	Recorded Value
1.2	Inspect per WI TIS		OK	OK

Notes

Accepted By  Printed On

The instrument resolution used to perform this test is ± 0.3 mV. The mechanical travel exceeds or is equivalent to the electrical travel. This product tested on equipment traceable to NIST standards.

Firstmark Controls 866-912-6232 * 919-682-3786 (fax)
 1176 Telecom Drive * Creedmoor, NC 27522 USA info@firstmarkcontrols.com * http://www.firstmarkcontrols.com/

Figure B-3. Specification for String Potentiometer, ID #43445

Firstmark **Final Inspection Data Sheet**

Test ID: 43446 Test Date: 09-Apr-15 Customer: UNIVERSITY OF NEBRASKA Customer ID: C032615
 Pur. Order: NA Sales Order: 31939 Job Order: 48918
 Part Number: 150-0121-R2B Serial Number: 15042490

Design Travel (inches/mm): 1.50 (38.1) DC Input (V): 5.00
 Max Acceptable Error (%): 1.000 Line Slope (mV/inch (mV/mm)): 3057.355 (120.37)
 Actual Error (%): 0.155 Sensitivity (inch/mV (mm/mV)): 0.000327 (0.00831)

Acceptance Criteria				
Revision	Description	Instrument	Acceptance Value	Recorded Value
1.2	Inspect per WI TIS		OK	OK

Notes

Accepted By: F1 Printed On: 2015-04-09 11:24:27

The instrument resolution used to perform this test is ± 0.3 mV. The mechanical travel exceeds or is equivalent to the electrical travel. This product tested on equipment traceable to NIST standards.

Firstmark Controls 866-912-6232 * 919-682-3786 (fax)
 1176 Telecom Drive * Creedmoor, NC 27522 USA info@firstmarkcontrols.com * <http://www.firstmarkcontrols.com/>

Figure B-4. Specification for String Potentiometer, ID #43446

Firstmark **Final Inspection Data Sheet**

Test ID: Test Date: Customer: Customer ID:
 Pur. Order: Sales Order: Job Order:
 Part Number: Serial Number:
 Design Travel (inches(mm)): DC Input (V):
 Max Acceptable Error (%): Line Slope (mV/inch (mV/mm)):
 Actual Error (%): Sensitivity (inch/mV (mm/mV)):

Acceptance Criteria			
Revision	Description	Instrument	Recorded Value
1.2	Inspect per WI TIS		OK

Notes

Accepted By: Printed On:

The instrument resolution used to perform this test is ± 0.3 mV. The mechanical travel exceeds or is equivalent to the electrical travel. This product tested on equipment traceable to NIST standards.

Firstmark Controls 866-912-6232 * 919-682-3786 (fax)
 1176 Telecom Drive * Creedmoor, NC 27522 USA info@firstmarkcontrols.com * http://www.firstmarkcontrols.com/

Figure B-5. Specification for String Potentiometer, ID #43447

**Appendix C. True Axial Stress-Engineering Axial Strain for Test Nos. CFC-1
through CFC-7**

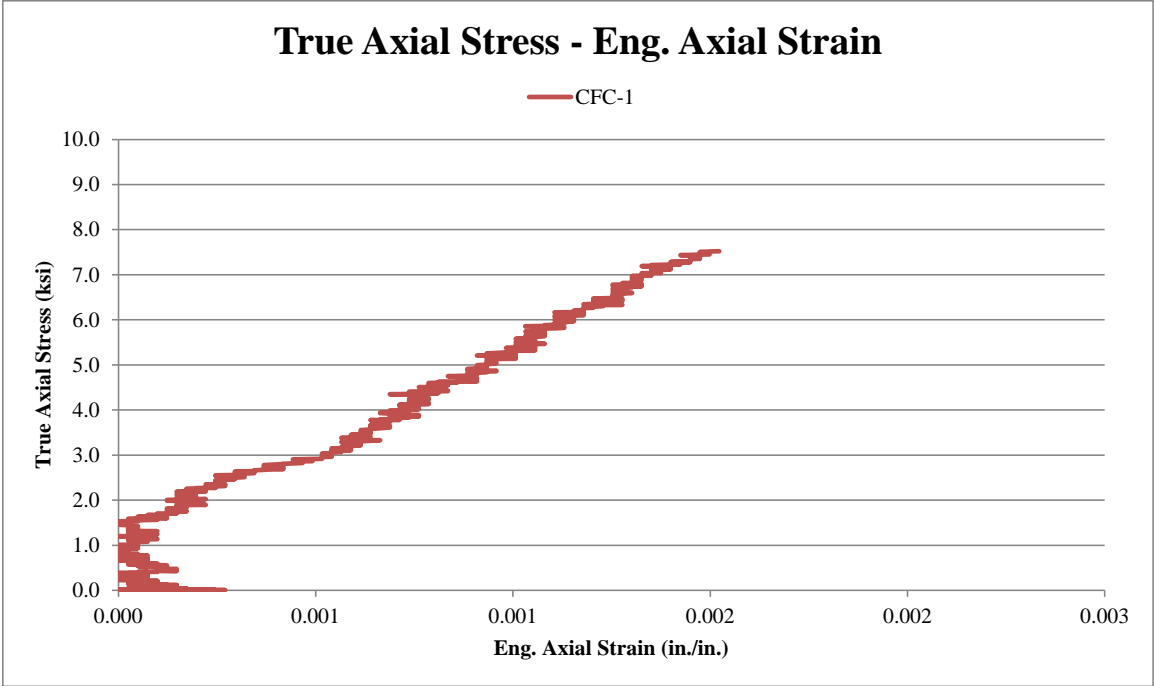


Figure C-1. Stress-Strain History, Test No. CFC-1

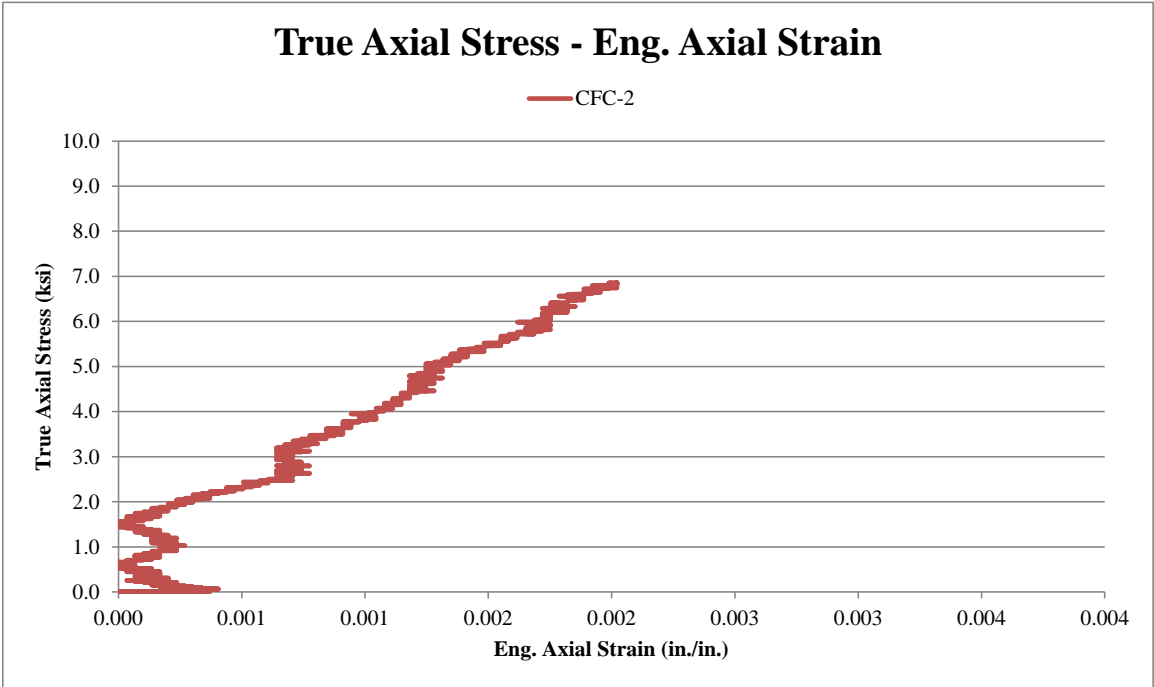


Figure C-2. Stress-Strain History, Test No. CFC-2

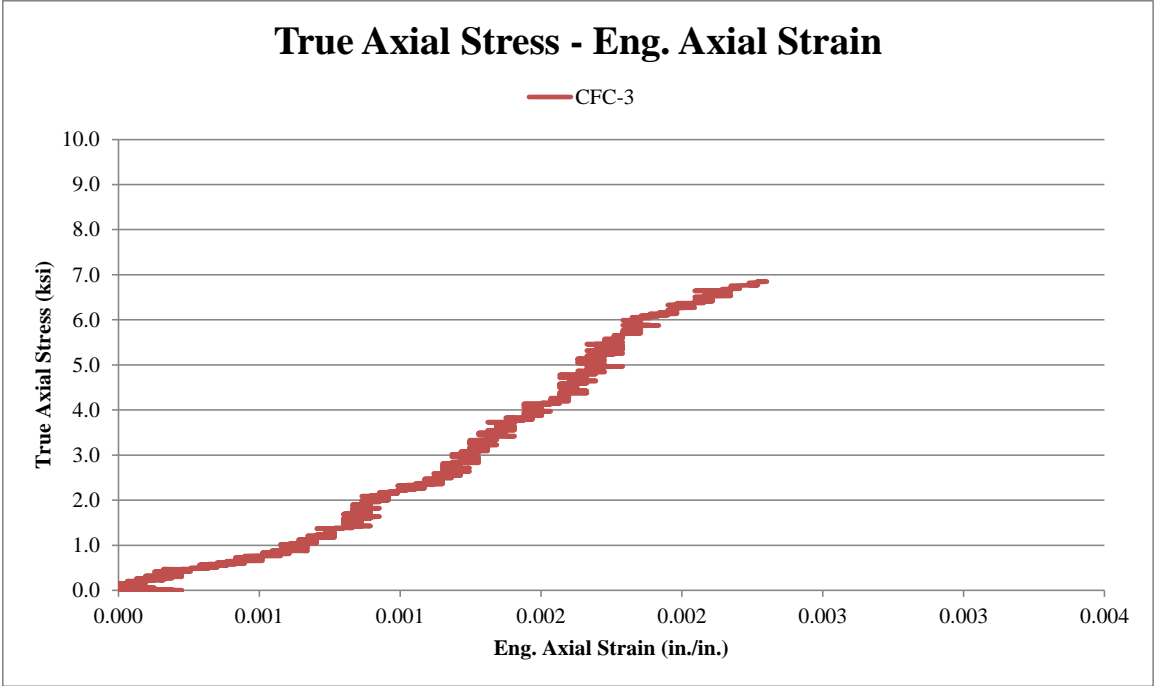


Figure C-3. Stress-Strain History, Test No. CFC-3

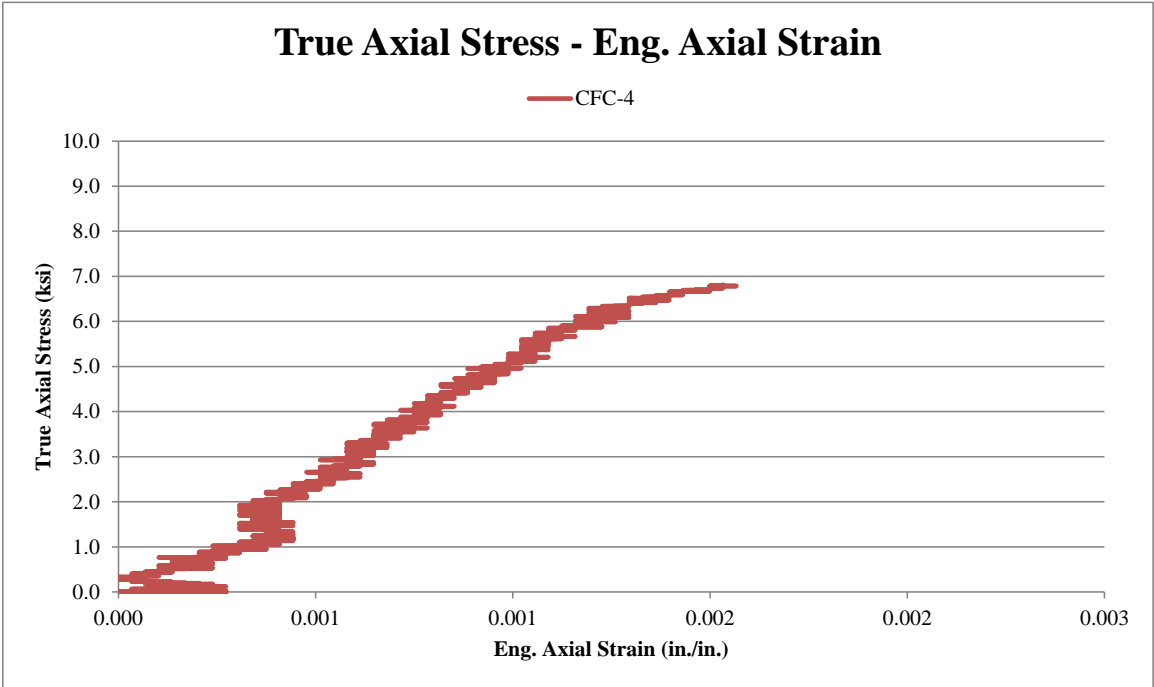


Figure C-4. Stress-Strain History, Test No. CFC-4

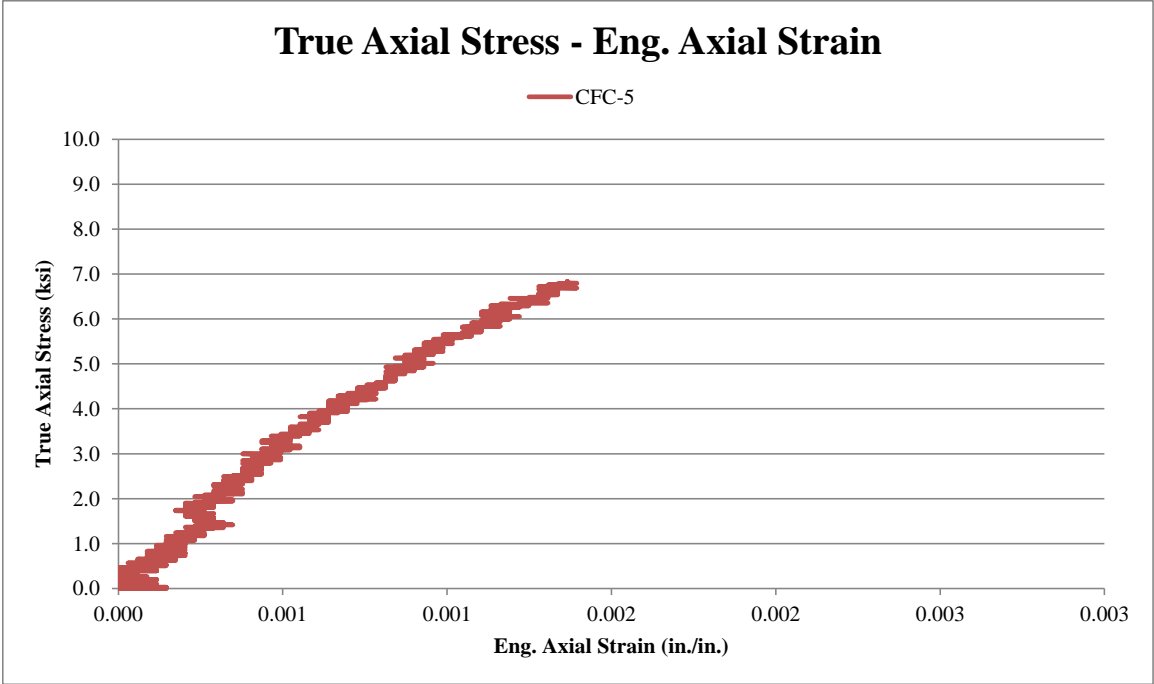


Figure C-5. Stress-Strain History, Test No. CFC-5

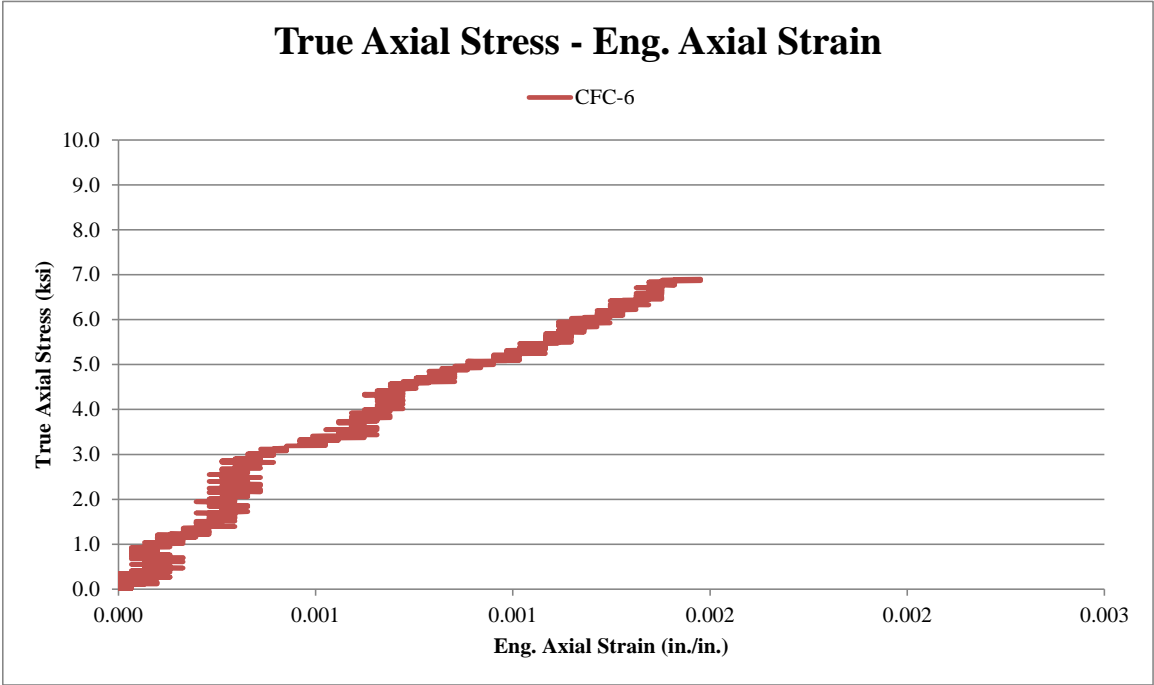


Figure C-6. Stress-Strain History, Test No. CFC-6

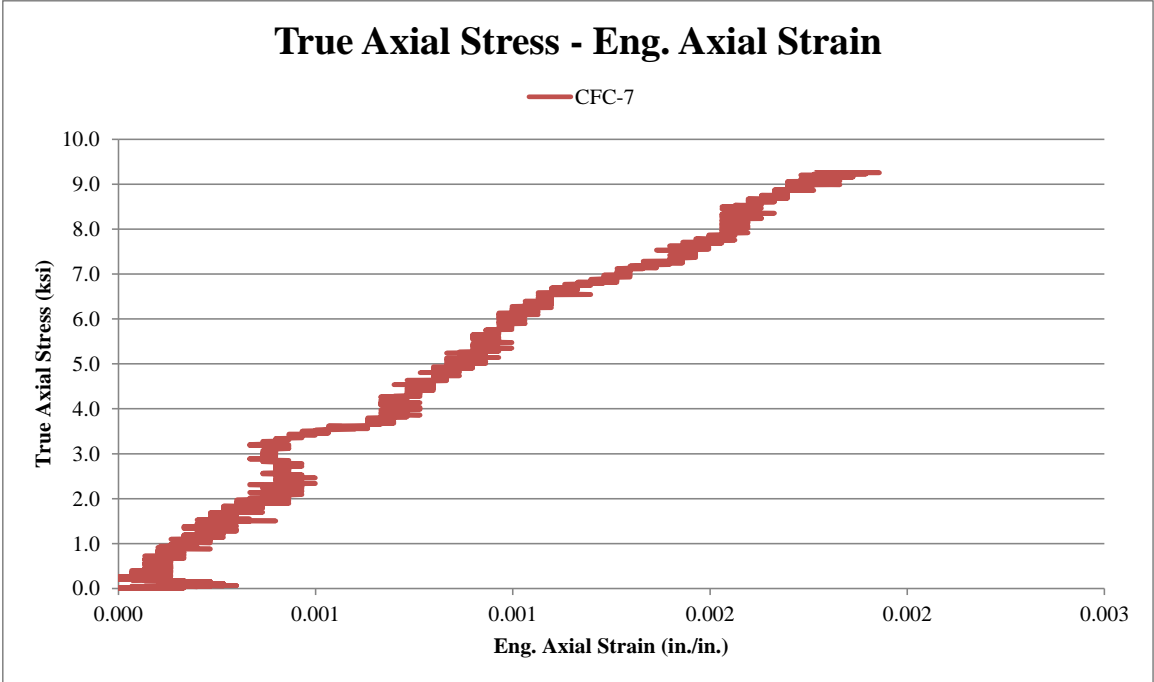


Figure C-7. Stress-Strain History, Test No. CFC-7

Appendix D. String Potentiometer Data for CFS Testing

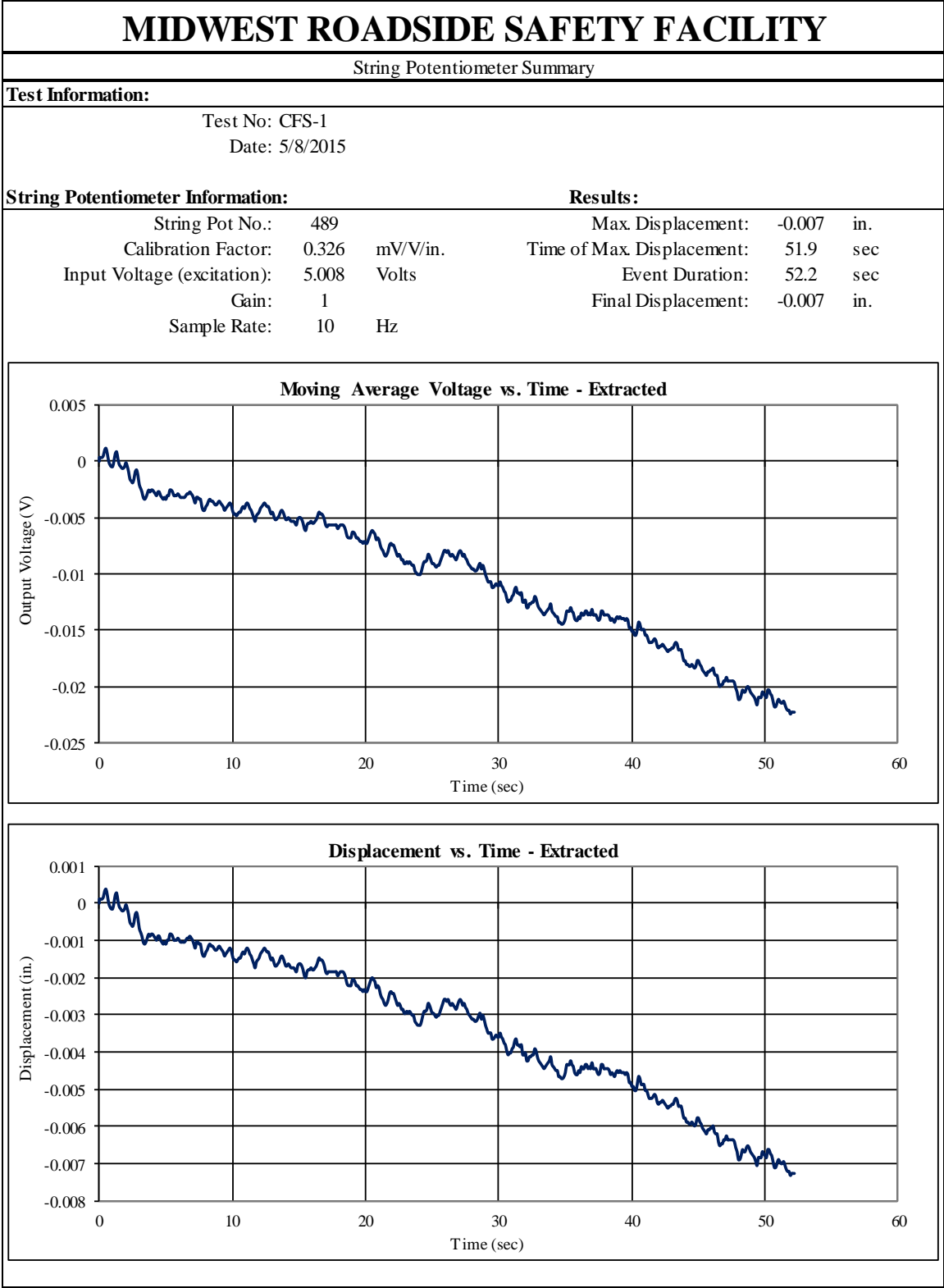


Figure D-1. String Potentiometer Summary for Gauge A, Test No. CFS-1

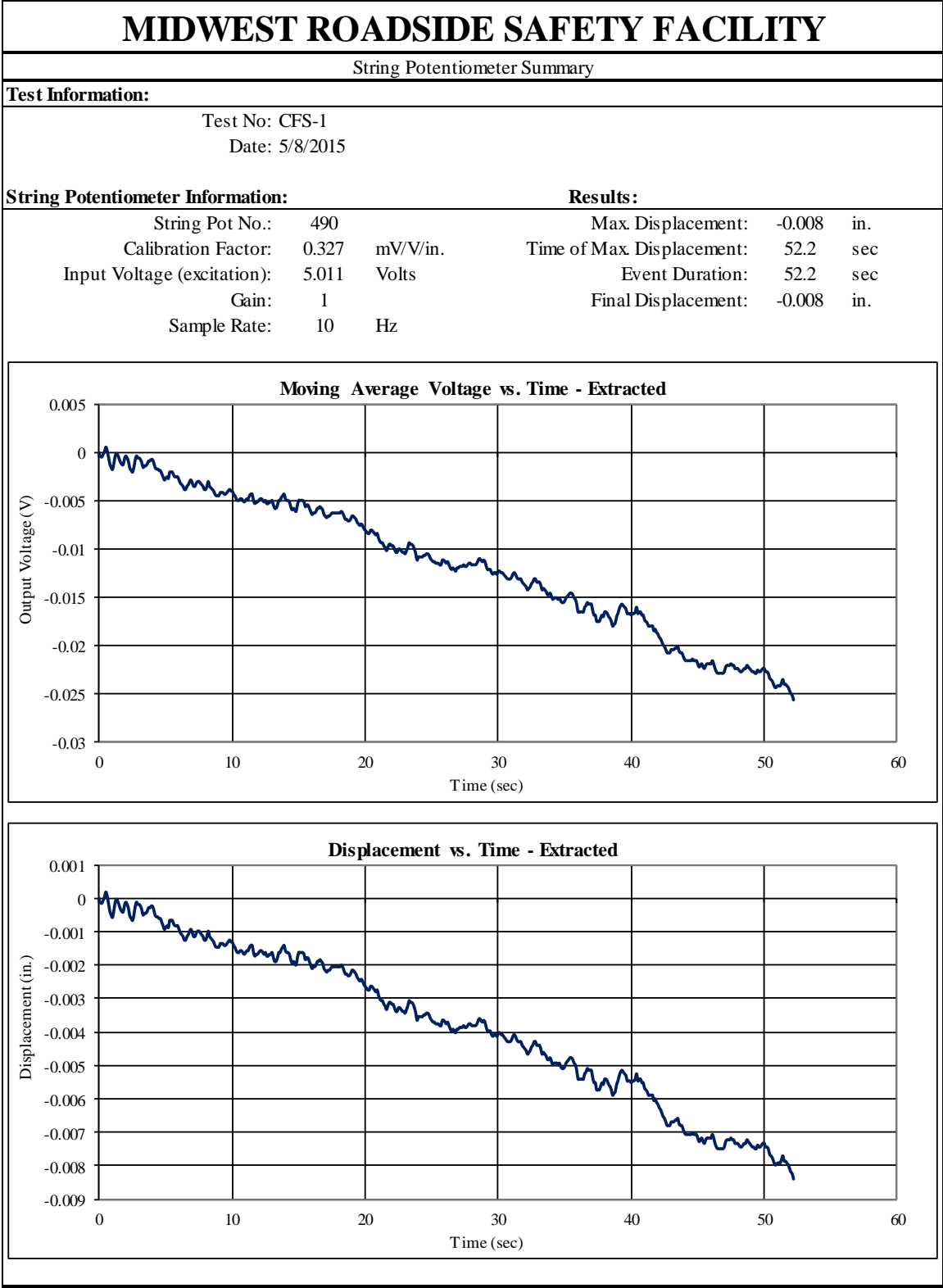


Figure D-2. String Potentiometer Summary for Gauge B, Test No. CFS-1

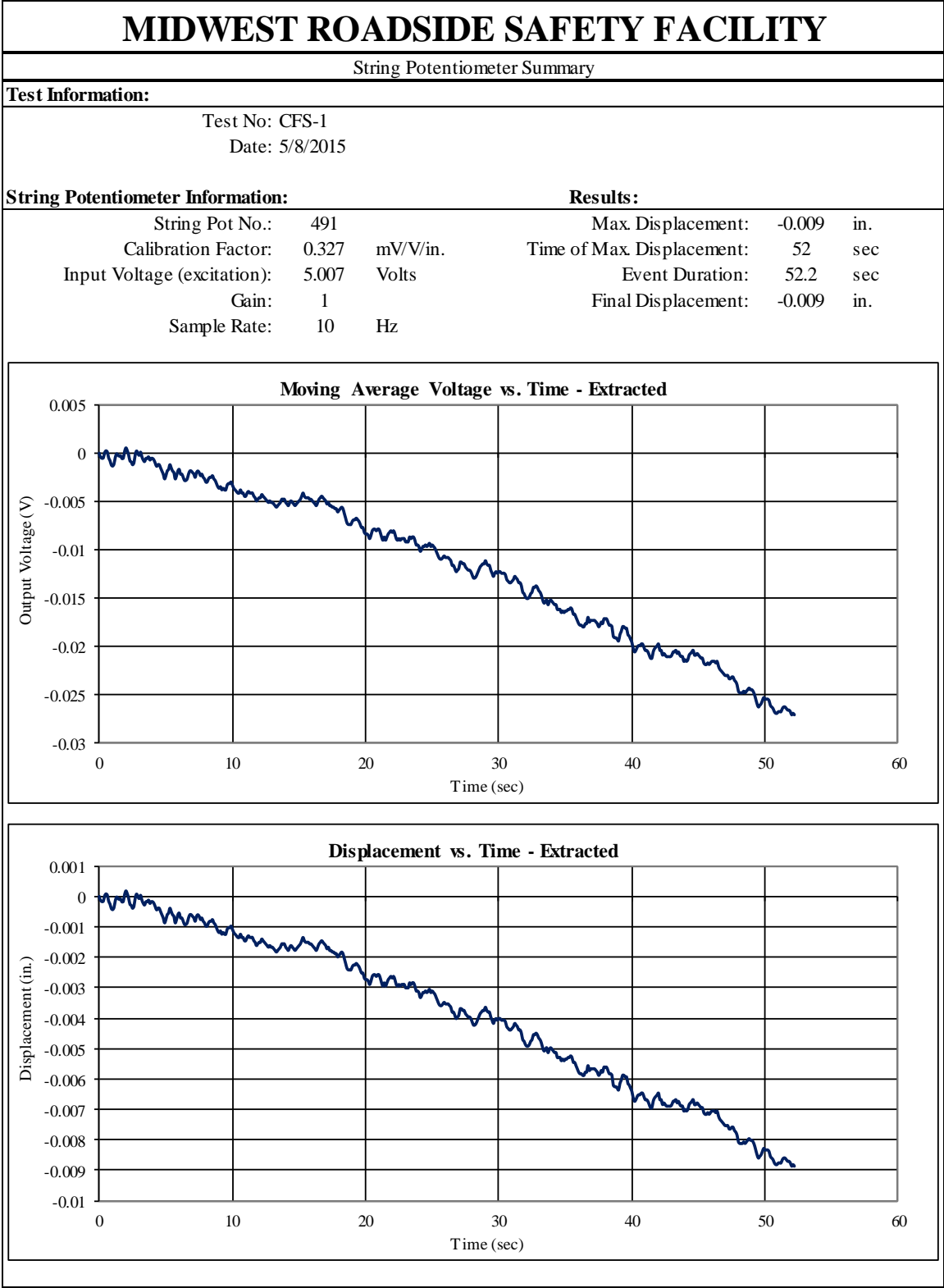


Figure D-3. String Potentiometer Summary for Gauge C, Test No. CFS-1

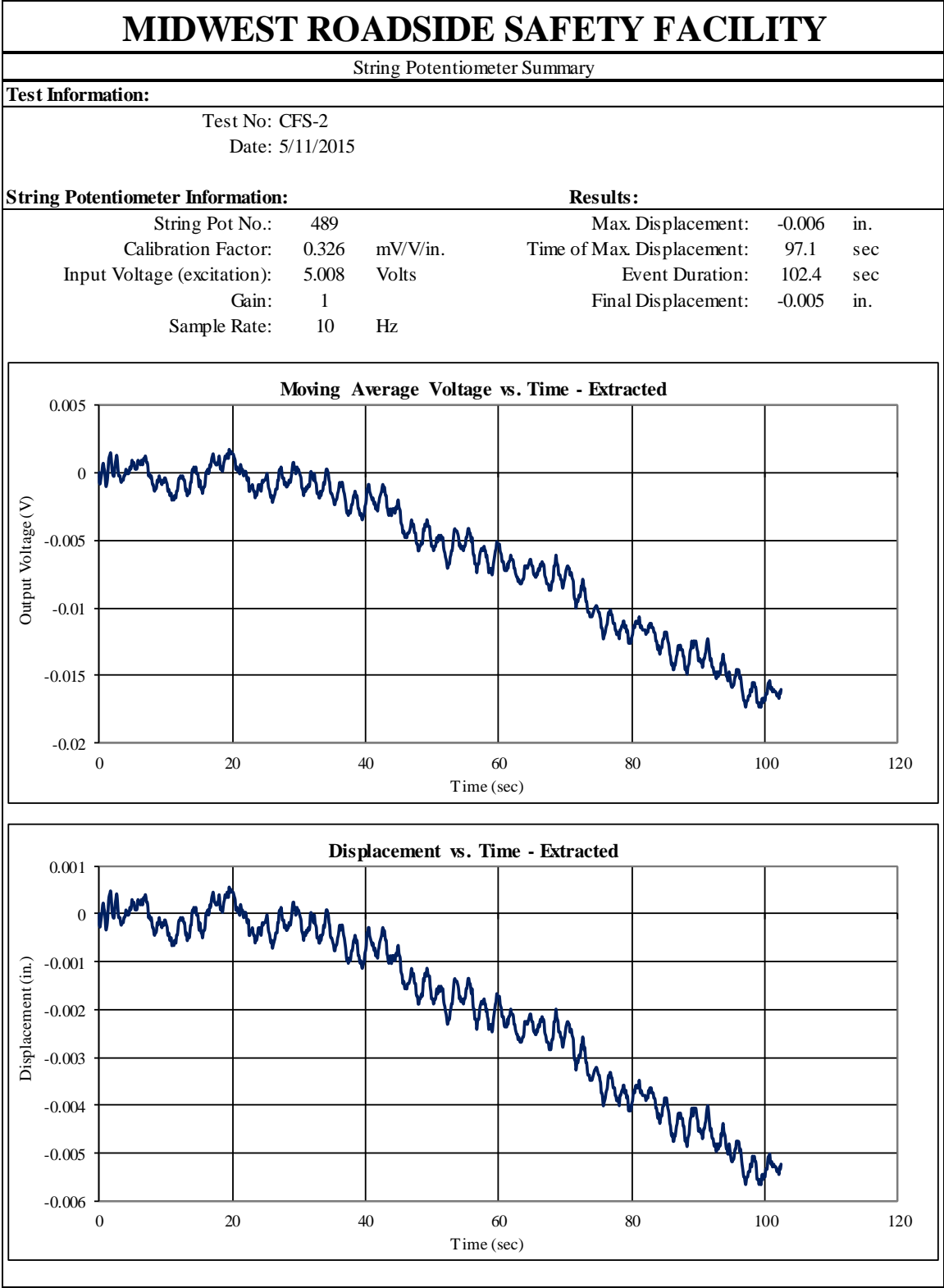


Figure D-4. String Potentiometer Summary for Gauge A, Test No. CFS-2

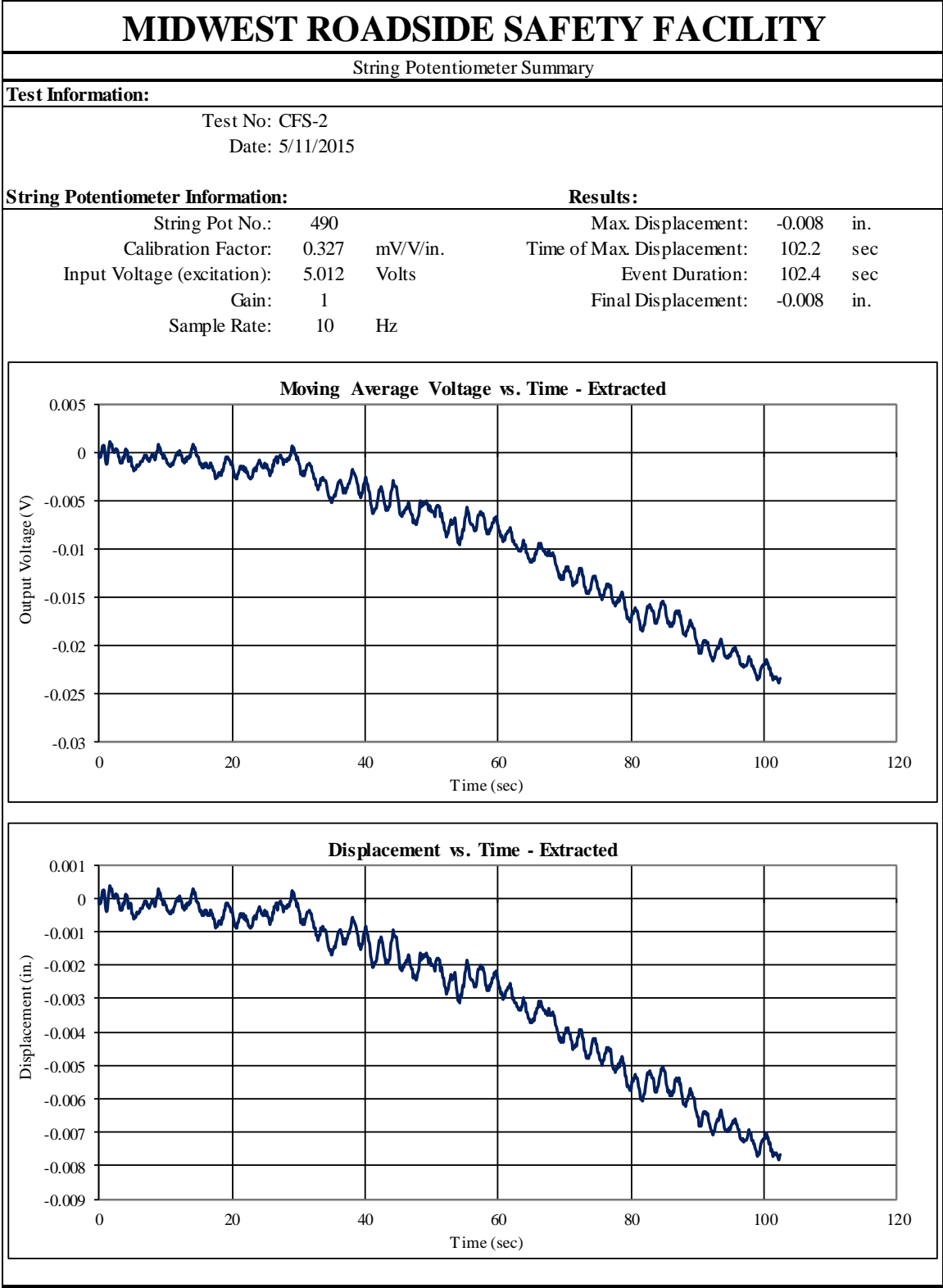


Figure D-5. String Potentiometer Summary for Gauge B, Test No. CFS-2

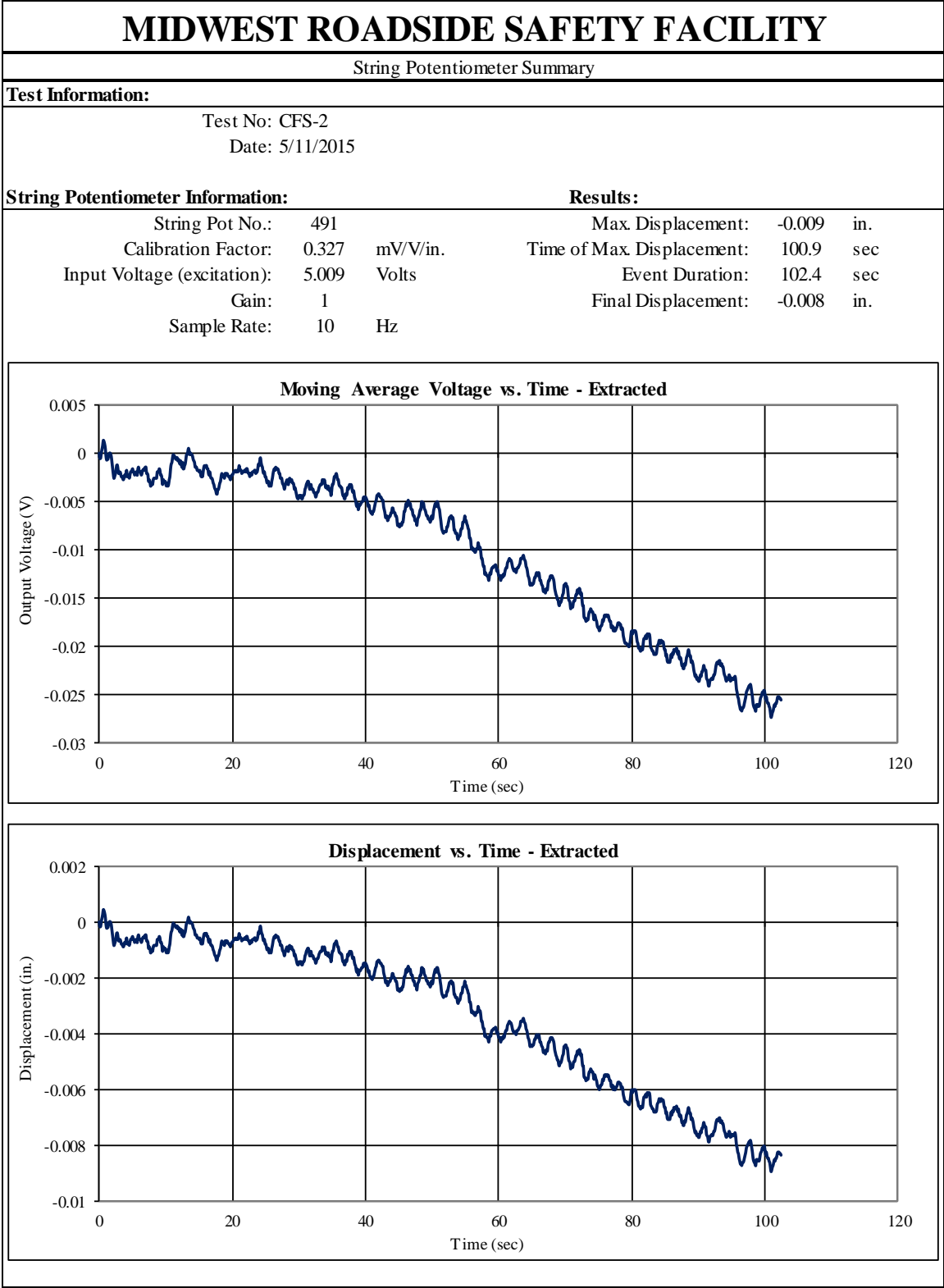


Figure D-6. String Potentiometer Summary for Gauge C, Test No. CFS-2

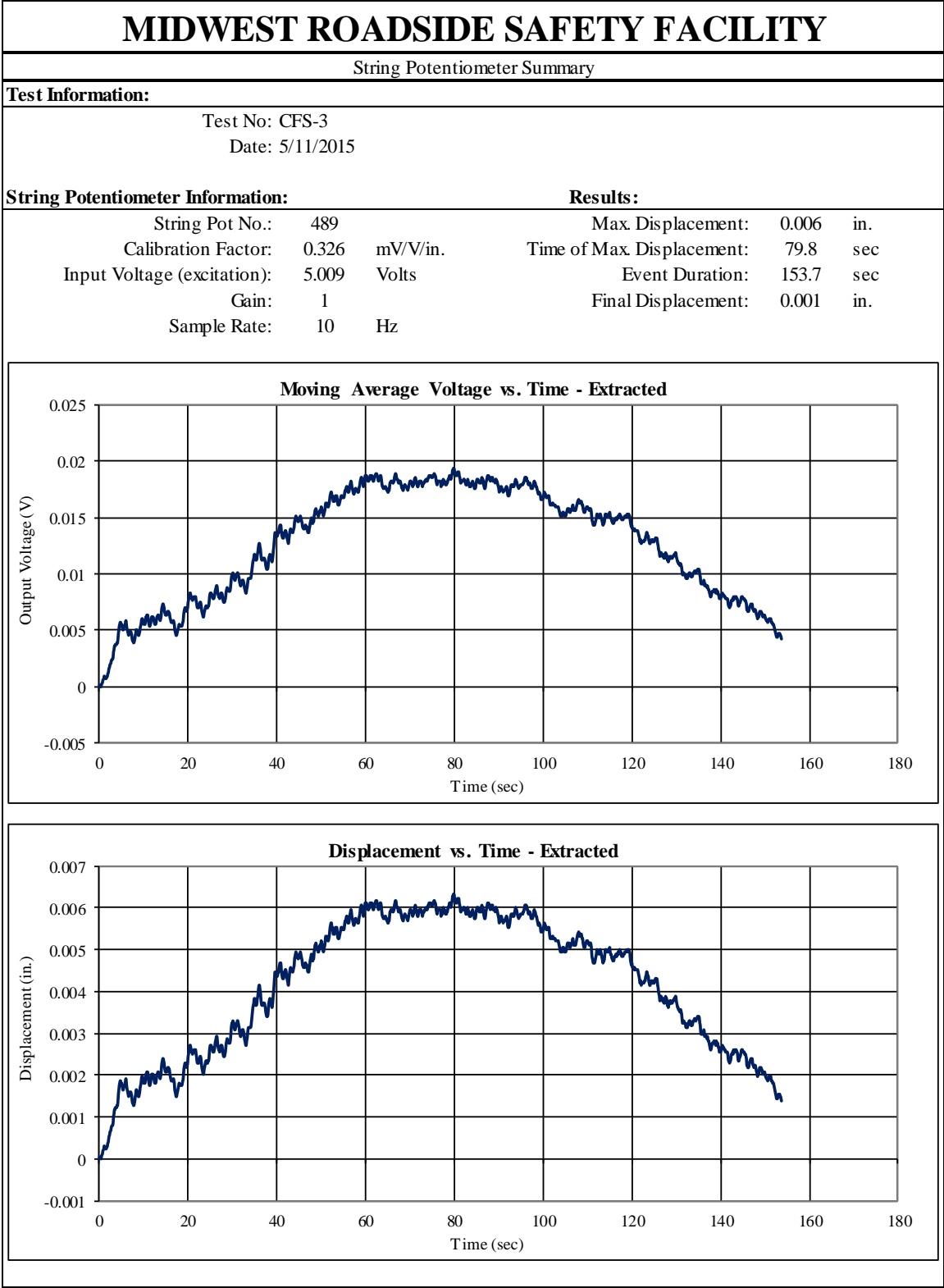


Figure D-7. String Potentiometer Summary for Gauge A, Test No. CFS-3

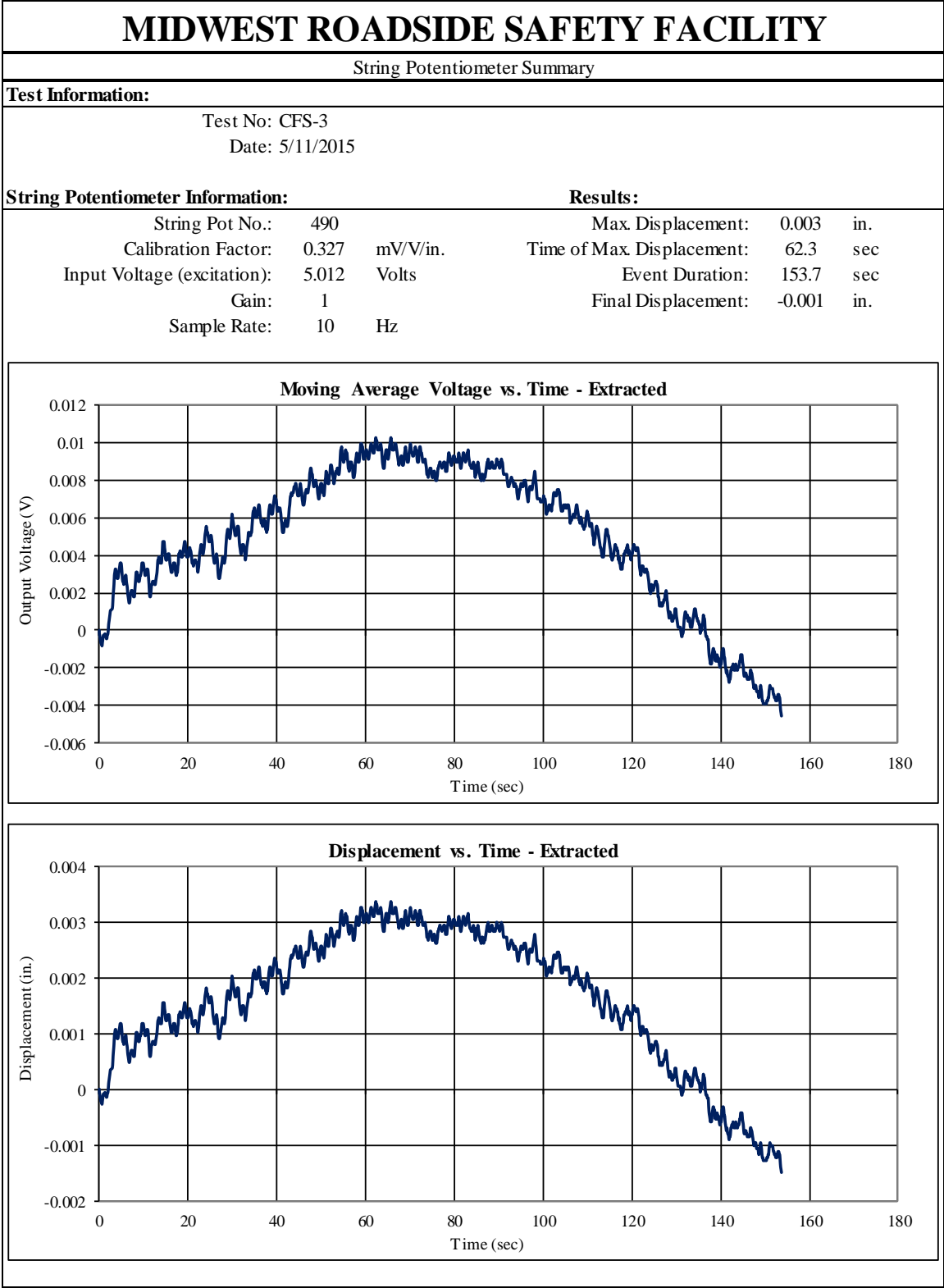


Figure D-8. String Potentiometer Summary for Gauge B, Test No. CFS-3

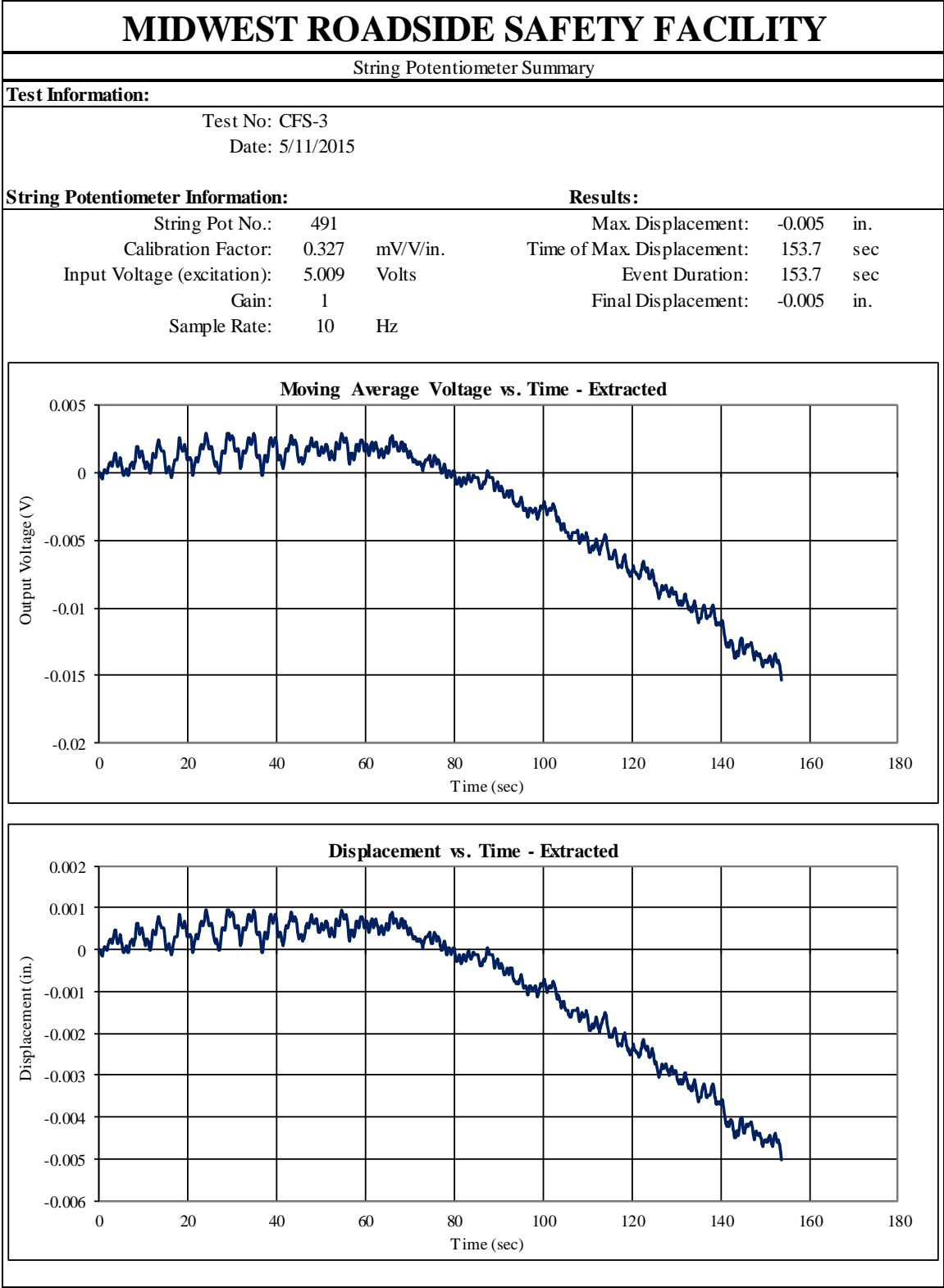


Figure D-9. String Potentiometer Summary for Gauge C, Test No. CFS-3

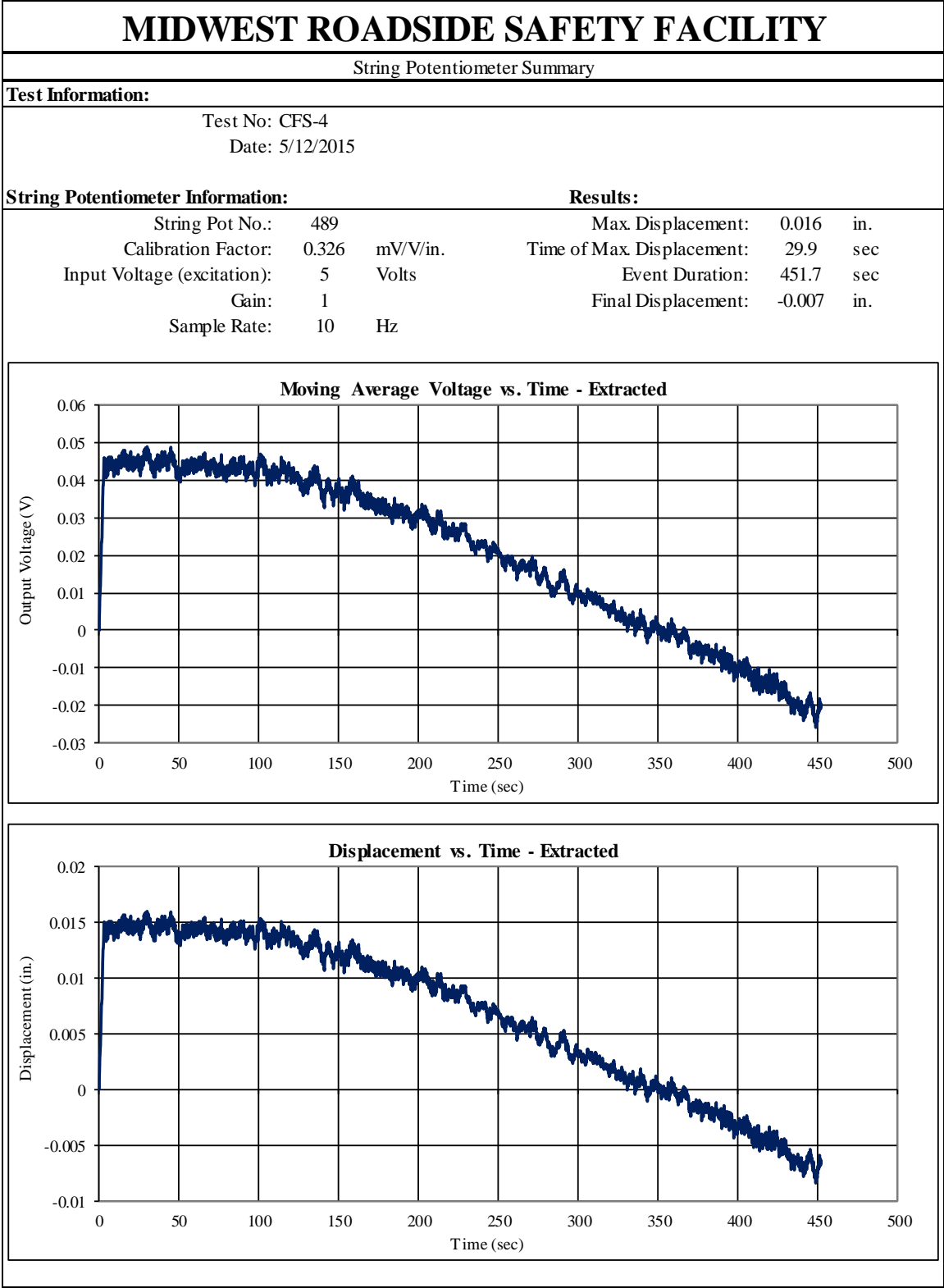


Figure D-10. String Potentiometer Summary for Gauge A, Test No. CFS-4

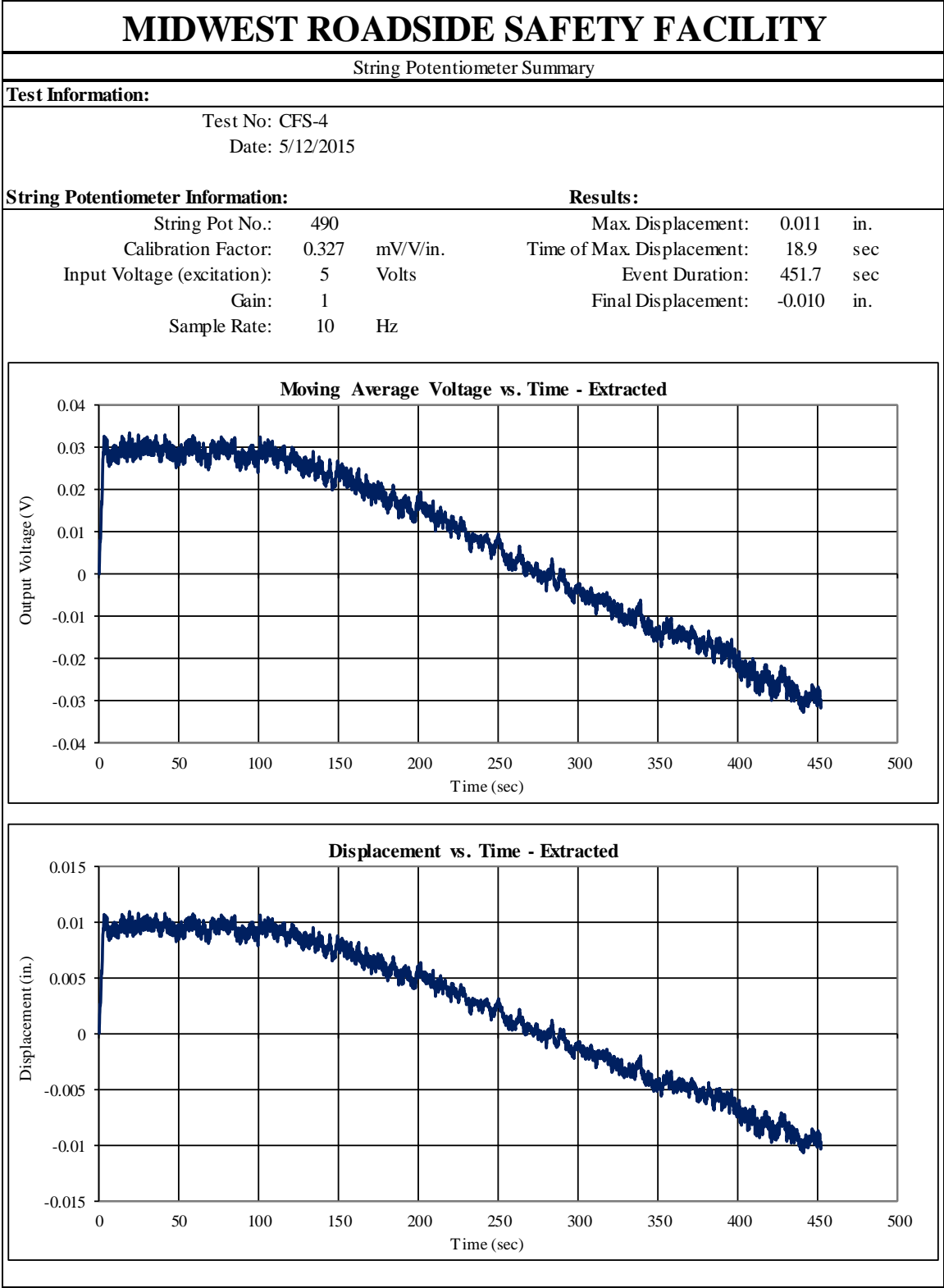


Figure D-11. String Potentiometer Summary for Gauge B, Test No. CFS-4

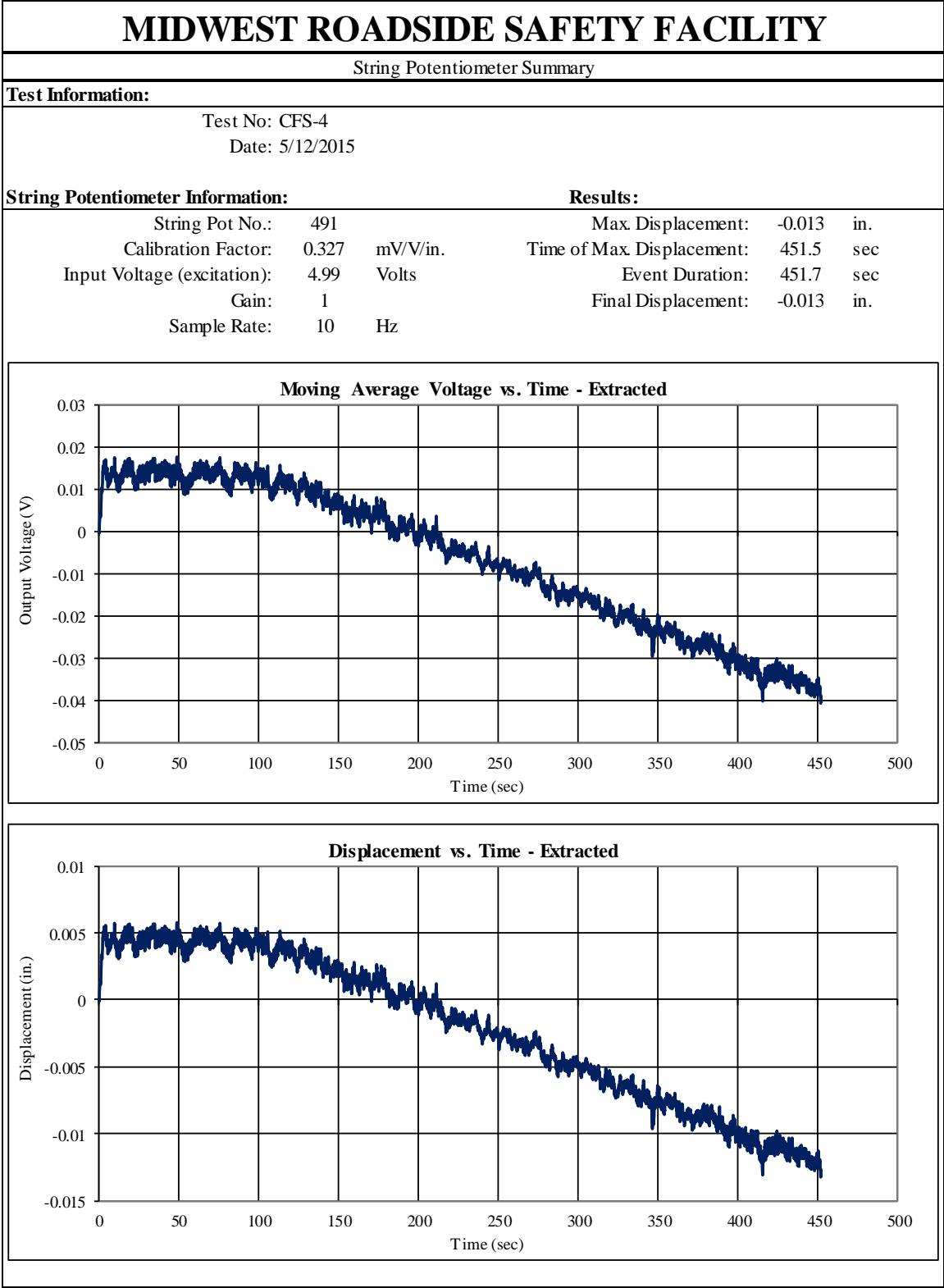


Figure D-12. String Potentiometer Summary for Gauge C, Test No. CFS-4

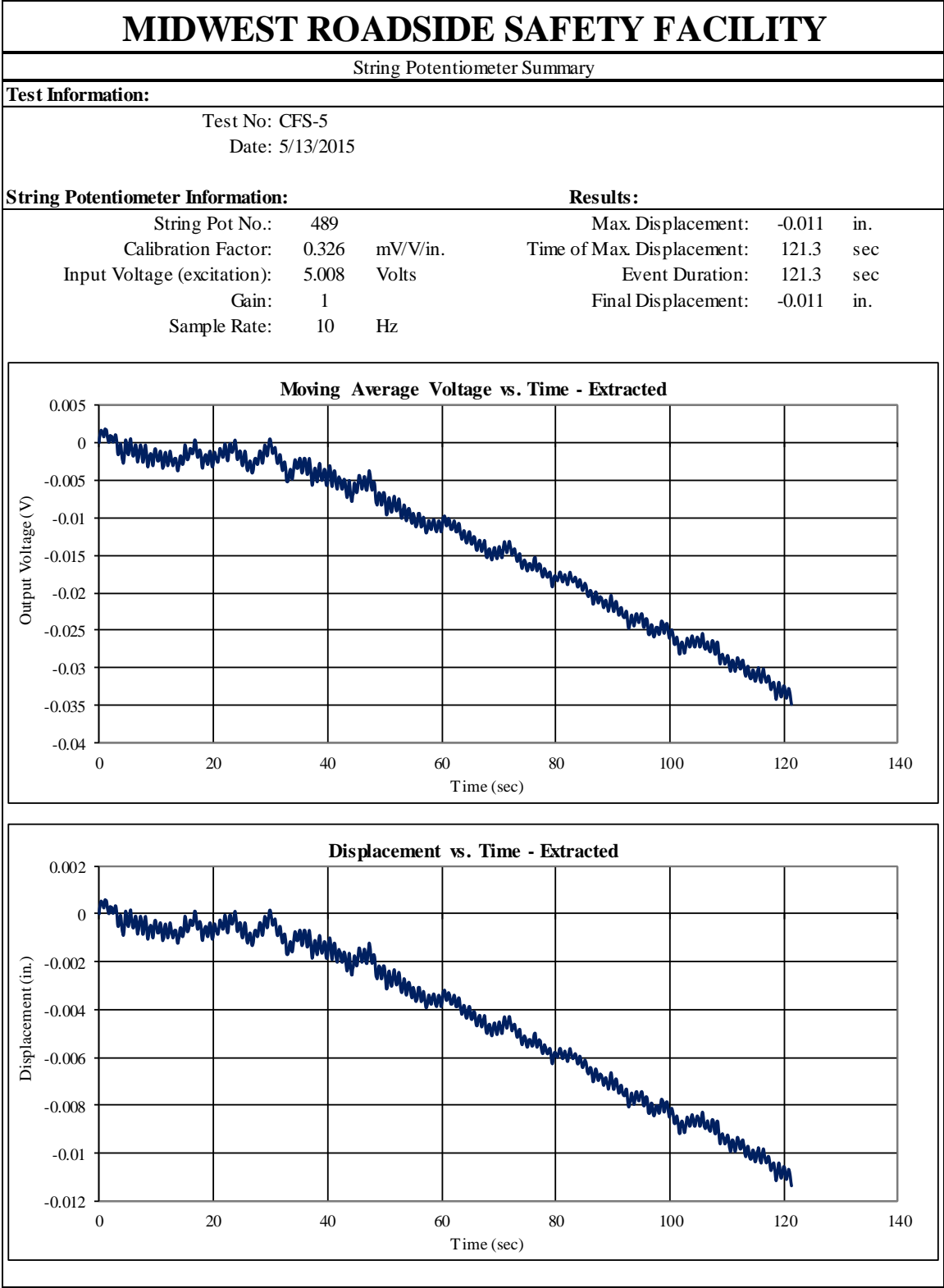


Figure D-13. String Potentiometer Summary for Gauge A, Test No. CFS-5

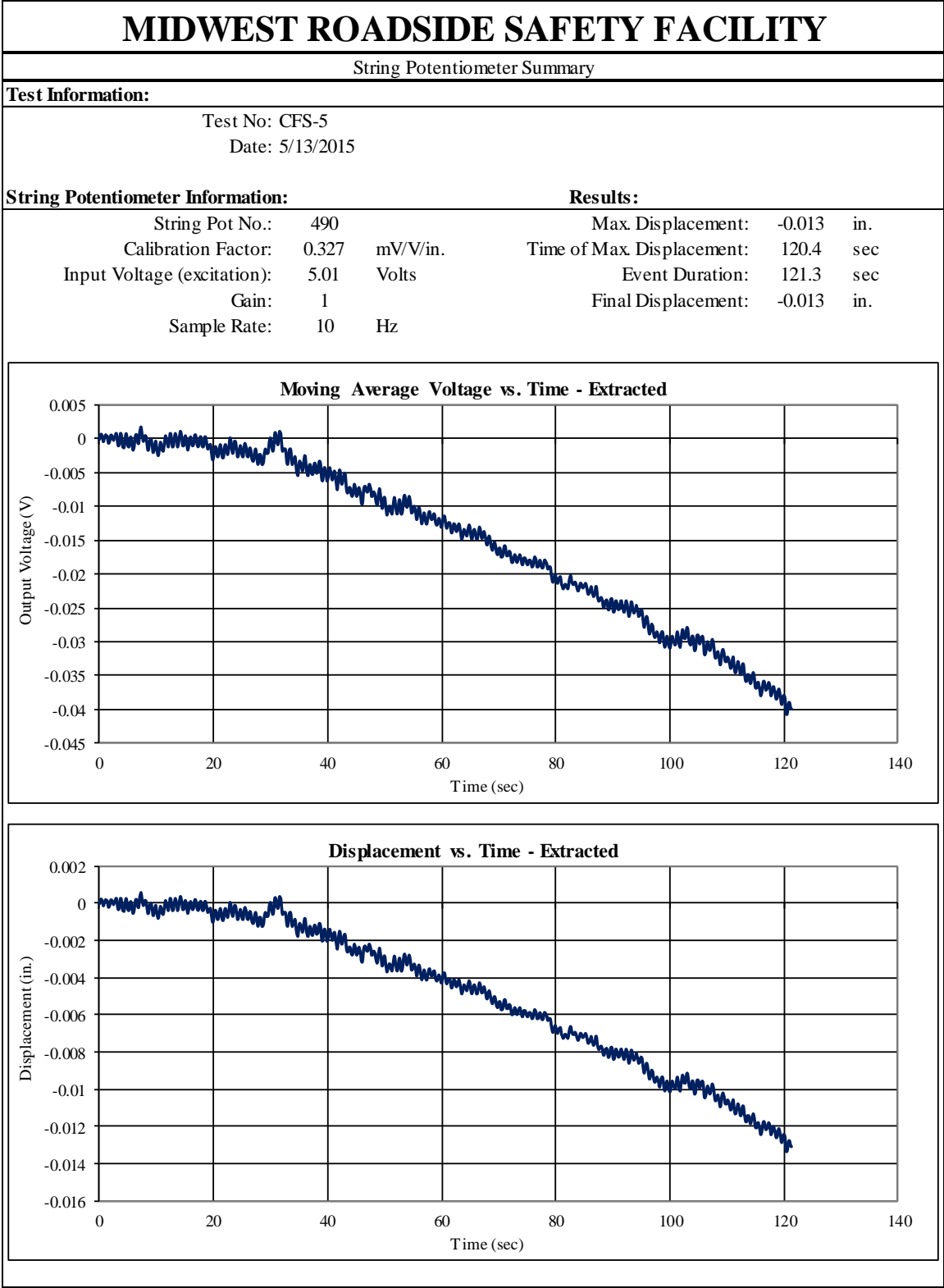


Figure D-14. String Potentiometer Summary for Gauge B, Test No. CFS-5

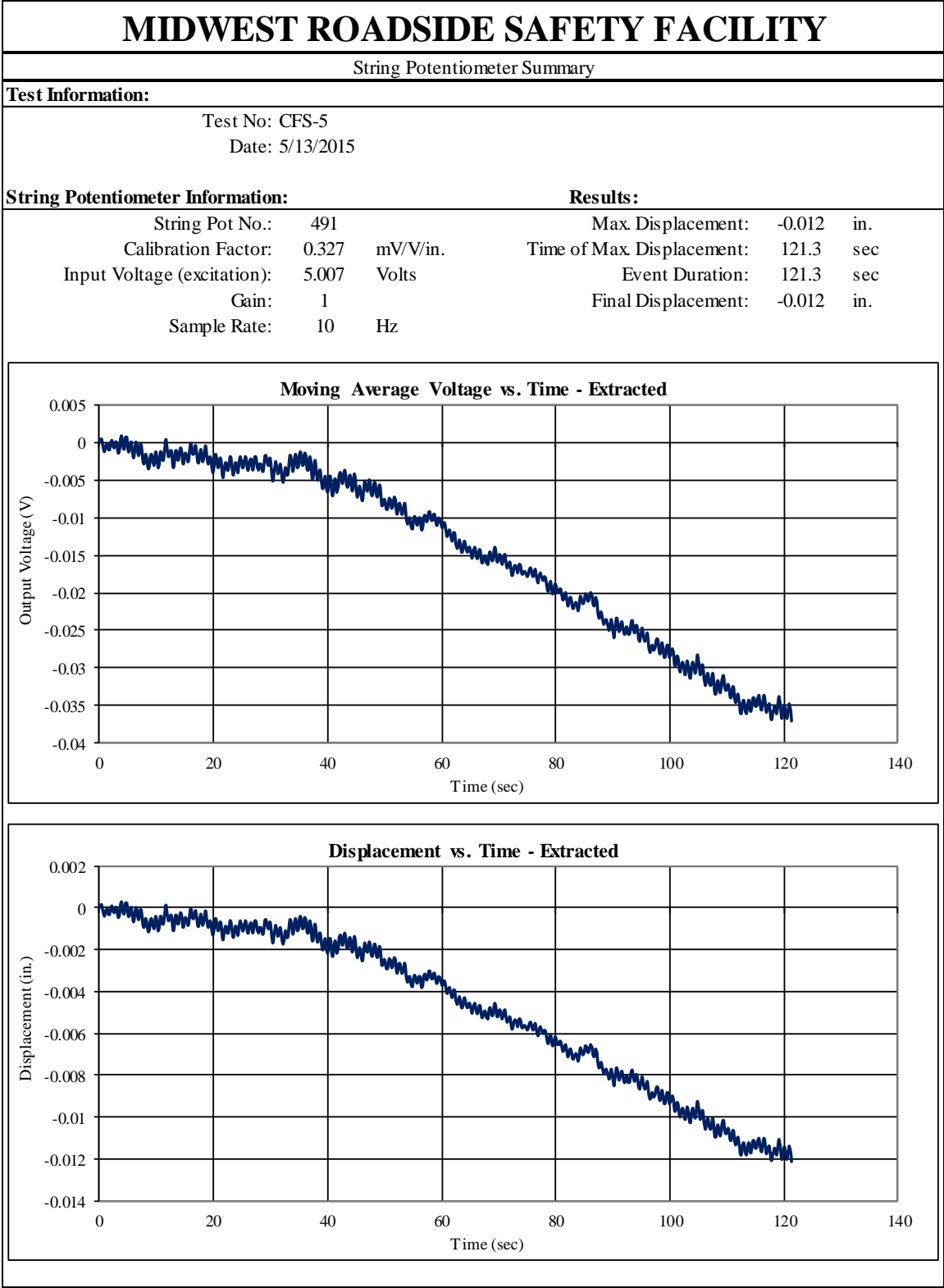


Figure D-15. String Potentiometer Summary for Gauge C, Test No. CFS-5

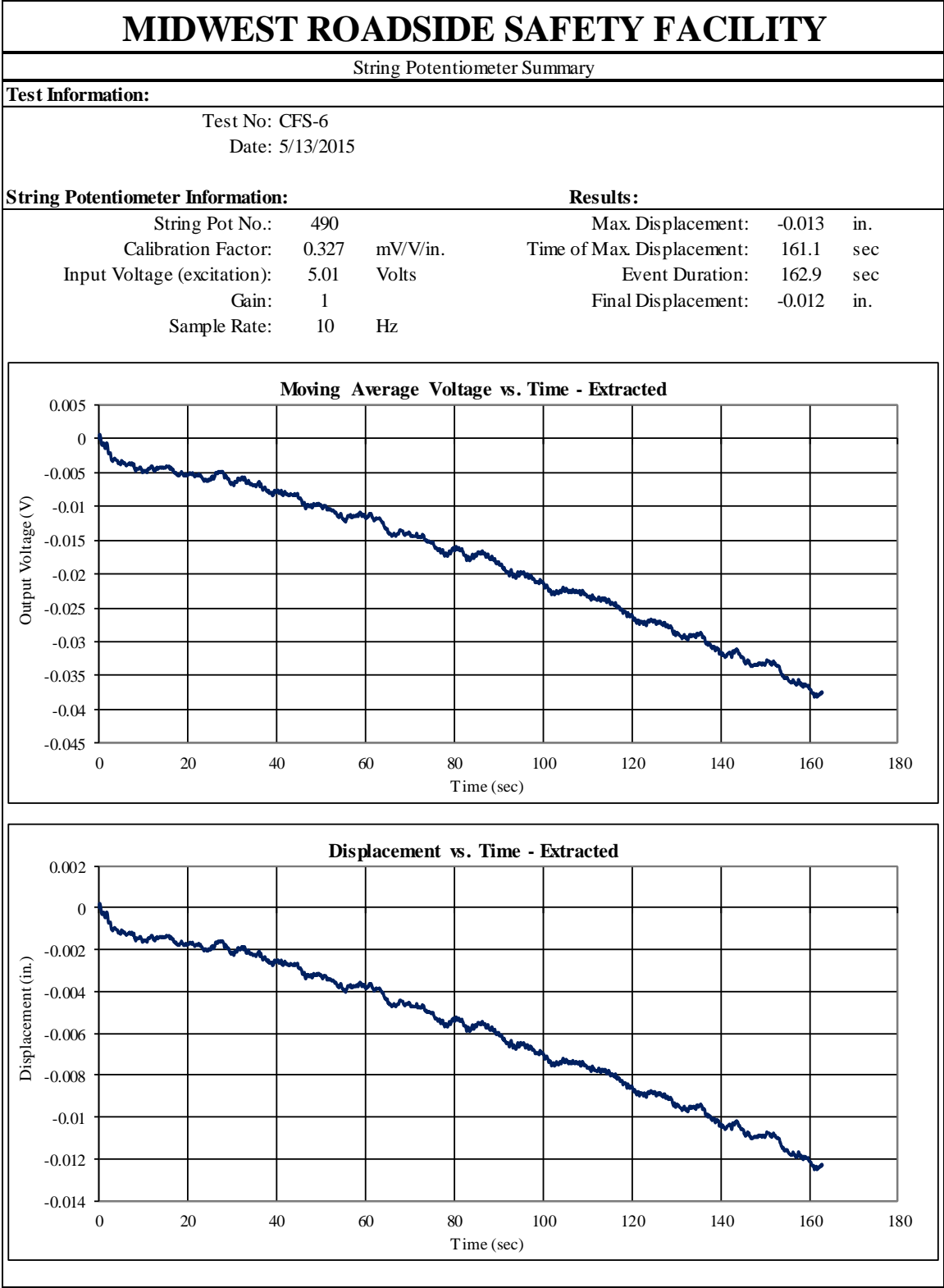
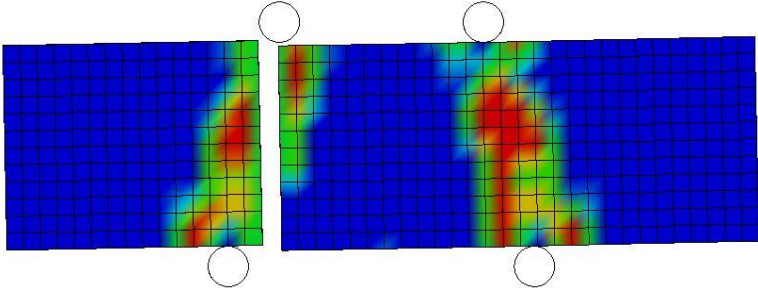


Figure D-16. String Potentiometer Summary for Gauge B, Test No. CFS-6

Appendix E. Results from Alternate Beam Simulations for CSCM Model

An alternate study was performed with input parameters recommended by a joint study by TTI and MwRSF. Fringe damage plots, force-time plots, and energy-time plots are included in this appendix. It was determined that this combination of input parameters did not yield an improvement over the results seen in Chapter 15. The parameters for this alternate study included: $\text{recov} = 1.0$; $\text{ERODE} = 1.10$; $\text{repow} = 0.5$; and $G_{fs}/G_{ft} = 0.5$.

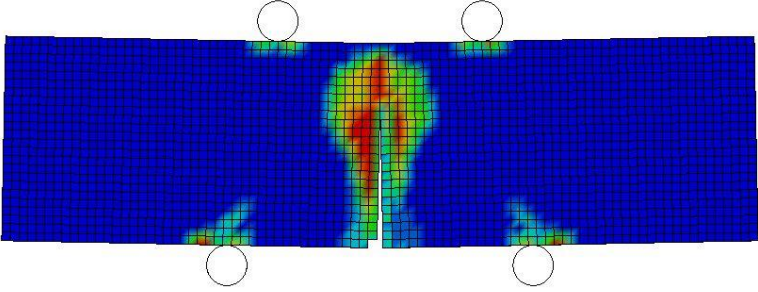
Beam Testing - CSCM Model
Time = 140
Contours of Effective Plastic Strain
max IP. value
min=0, at elem# 195601
max=0.999001, at elem# 197698



1/2 in. (13 mm)

z

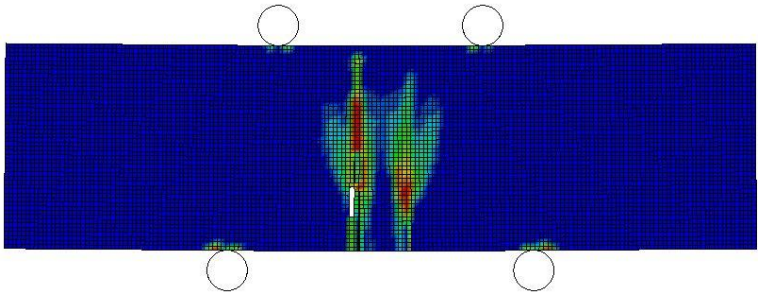
Beam Testing - CSCM Model
Time = 140
Contours of Effective Plastic Strain
max IP. value
min=0, at elem# 201937
max=0.999001, at elem# 226862



1/4 in. (6 mm)

z

Beam Testing - CSCM Model
Time = 140
Contours of Effective Plastic Strain
max IP. value
min=0, at elem# 310801
max=0.999, at elem# 495265



1/8 in. (3 mm)

z

Figure E-1. Damage Pattern for 9-in. (229-mm) Span at 140 ms, CSCM Model (Alternate)

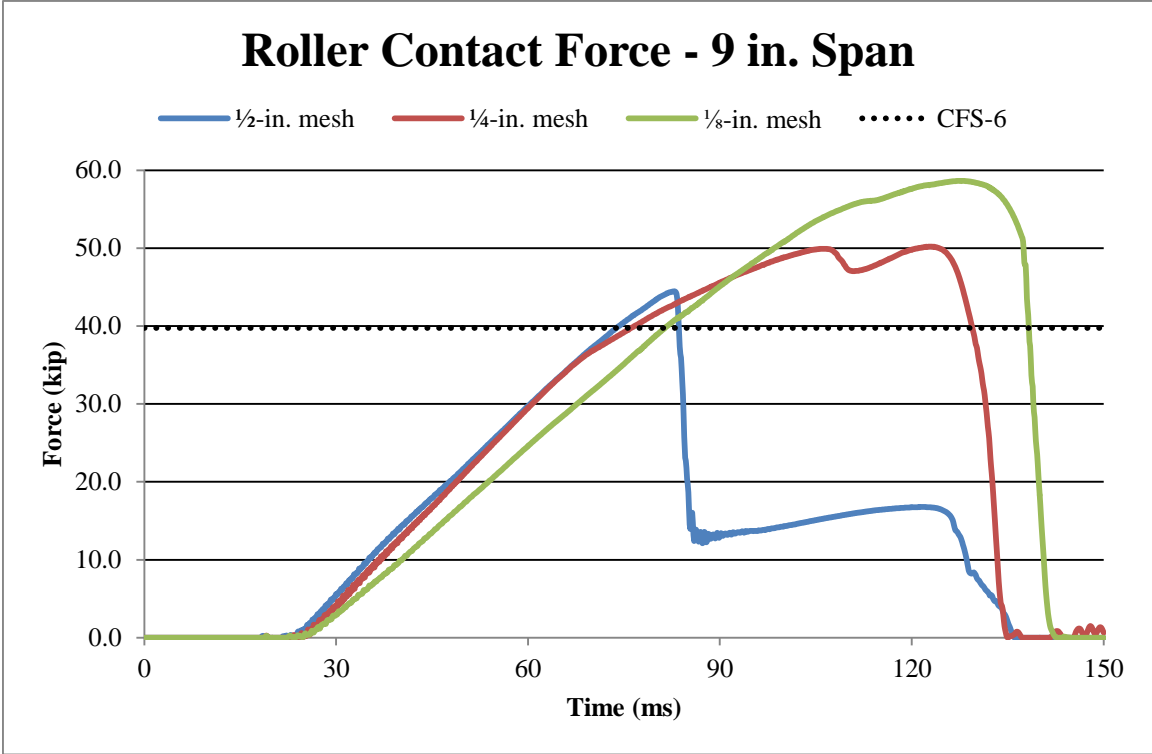


Figure E-2. Force Comparison for 9-in. (229-mm) Span, CSCM Model (Alternate)

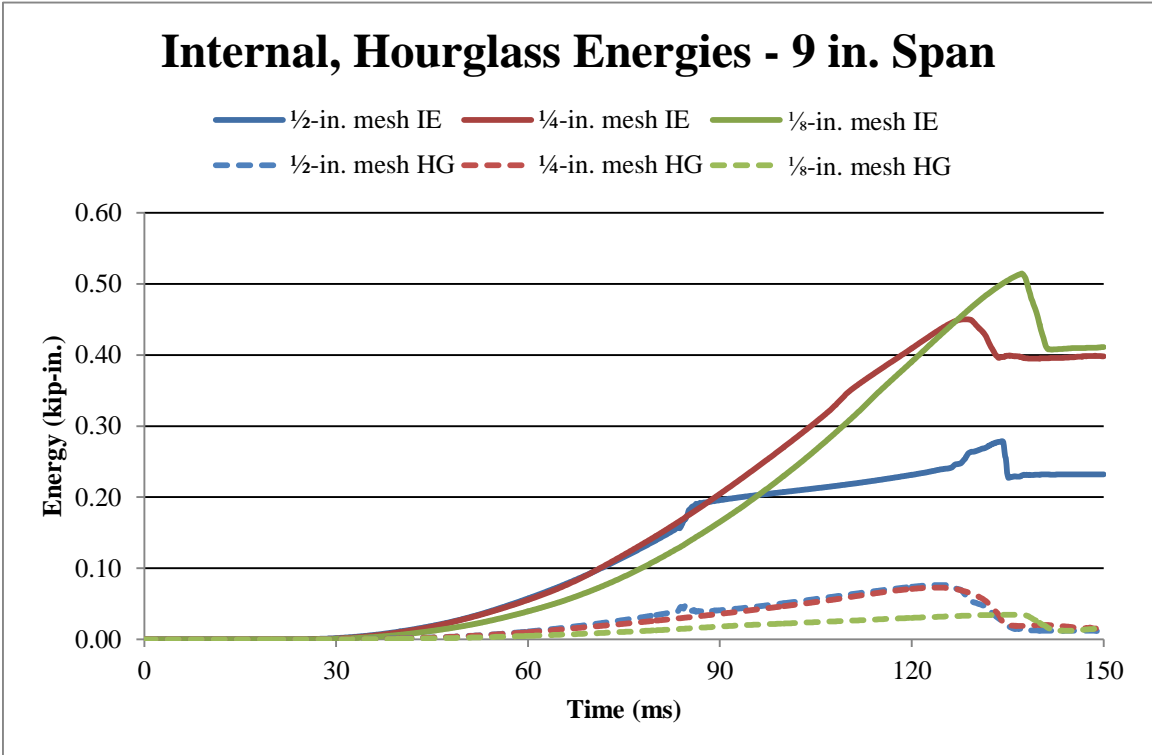
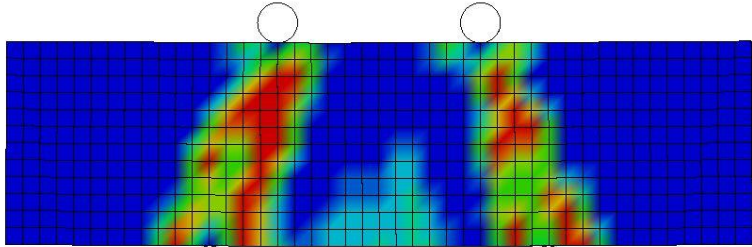


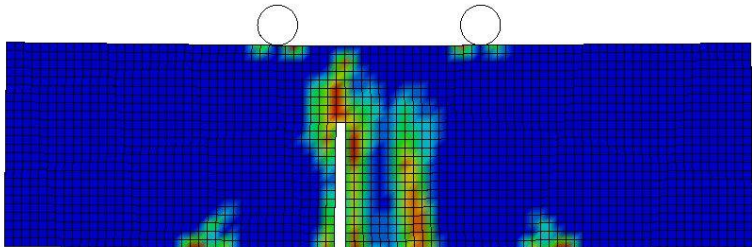
Figure E-3. Energy Comparison for 9-in. (229-mm) Span, CSCM Model (Alternate)

Beam Testing - CSCM Model
Time = 120
Contours of Effective Plastic Strain
max IP. value
min=0, at elem# 195601
max=0.999001, at elem# 199864



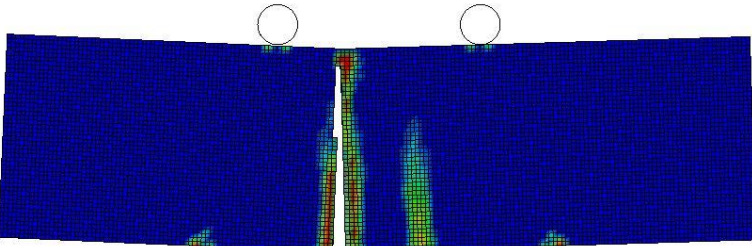
1/2 in. (13 mm)

Beam Testing - CSCM Model
Time = 120
Contours of Effective Plastic Strain
max IP. value
min=0, at elem# 201937
max=0.999001, at elem# 229587



1/4 in. (6 mm)

Beam Testing - CSCM Model
Time = 120
Contours of Effective Plastic Strain
max IP. value
min=0, at elem# 310801
max=0.999001, at elem# 531858



1/8 in. (3 mm)

Figure E-4. Damage Pattern for 10-in. (254-mm) Span at 120 ms, CSCM Model (Alternate)

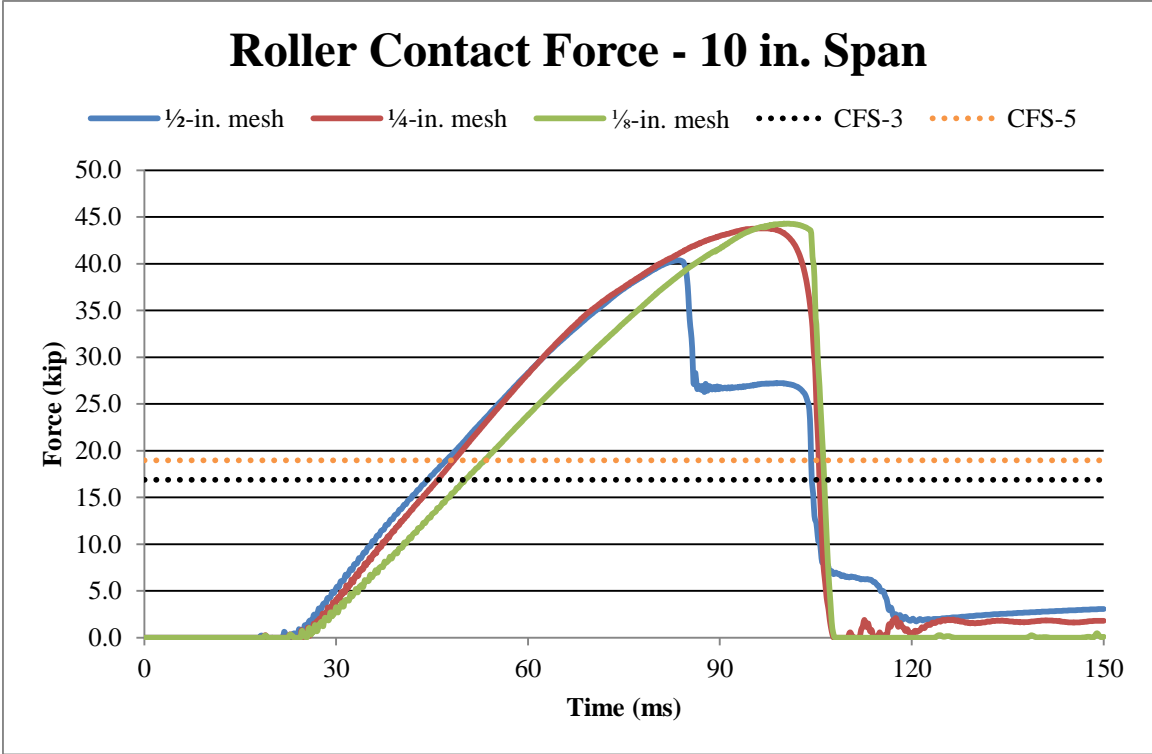


Figure E-5. Force Comparison for 10-in. (254-mm) Span, CSCM Model (Alternate)

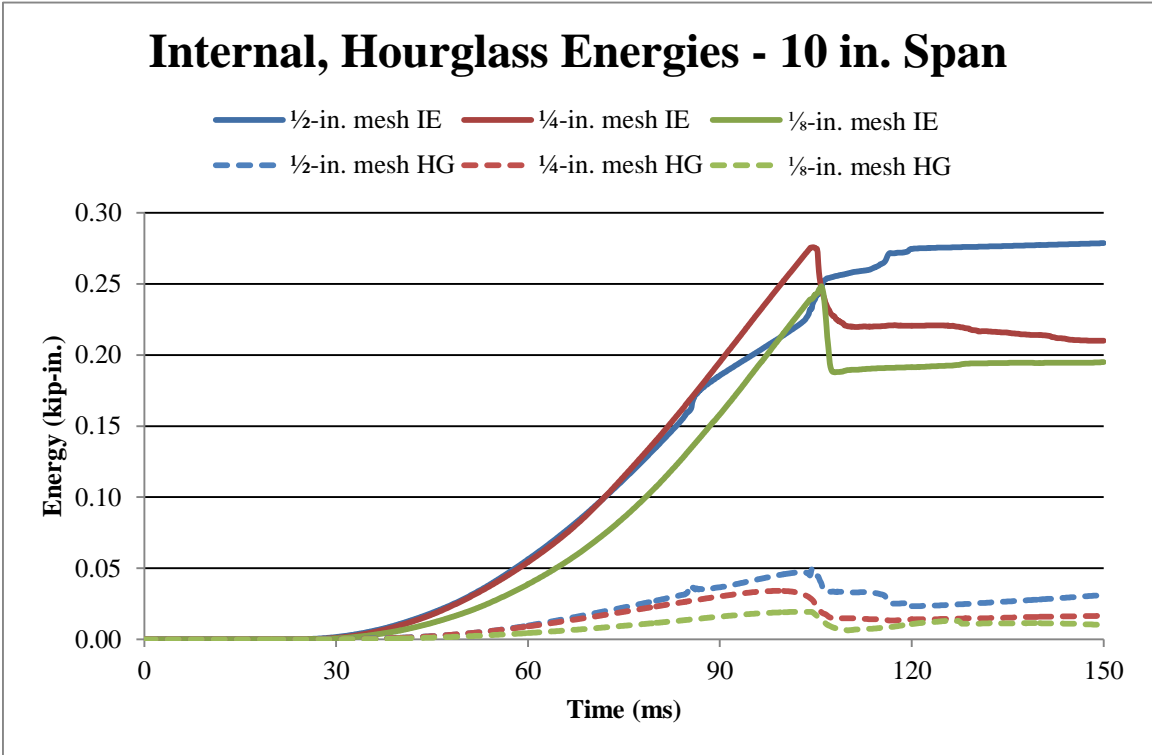
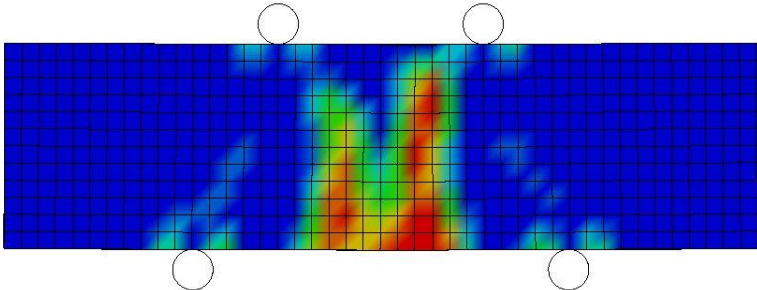


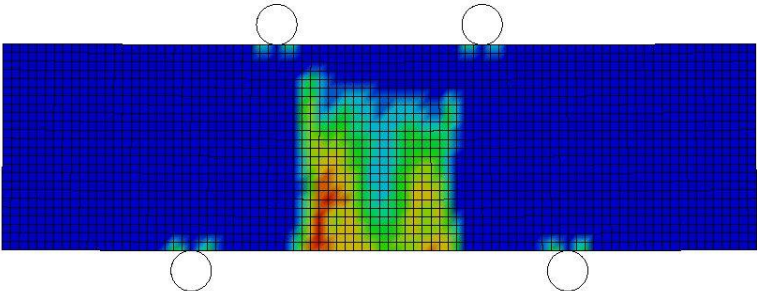
Figure E-6. Energy Comparison for 10-in. (254-mm) Span, CSCM Model (Alternate)

Beam Testing - CSCM Model
Time = 100
Contours of Effective Plastic Strain
max IP. value
min=0, at elem# 195601
max=0.999, at elem# 537881



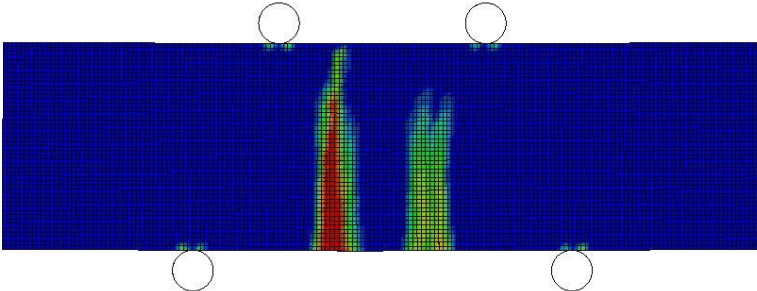
1/2 in. (13 mm)

Beam Testing - CSCM Model
Time = 100
Contours of Effective Plastic Strain
max IP. value
min=0, at elem# 201937
max=0.998998, at elem# 231763



1/4 in. (6 mm)

Beam Testing - CSCM Model
Time = 100
Contours of Effective Plastic Strain
max IP. value
min=0, at elem# 310801
max=0.999, at elem# 537881



1/8 in. (3 mm)

Figure E-7. Damage Pattern for 11-in. (279-mm) Span at 100 ms, CSCM Model (Alternate)

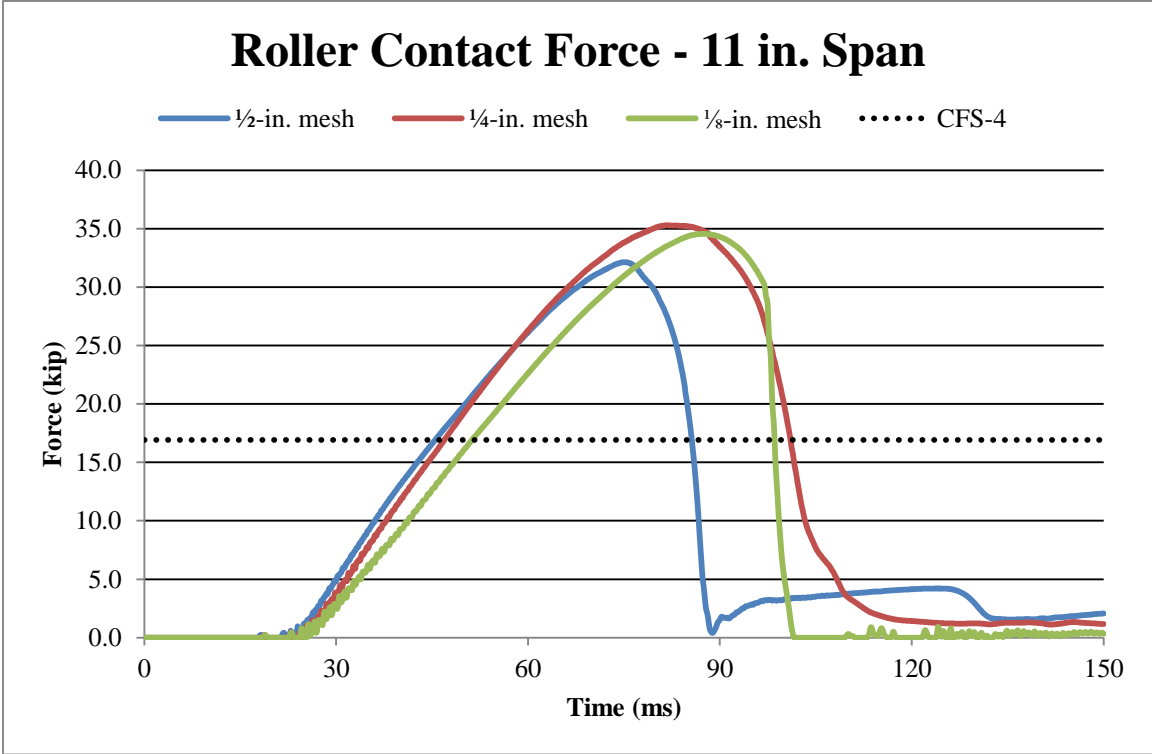


Figure E-8. Force Comparison for 11-in. (279-mm) Span, CSCM Model (Alternate)

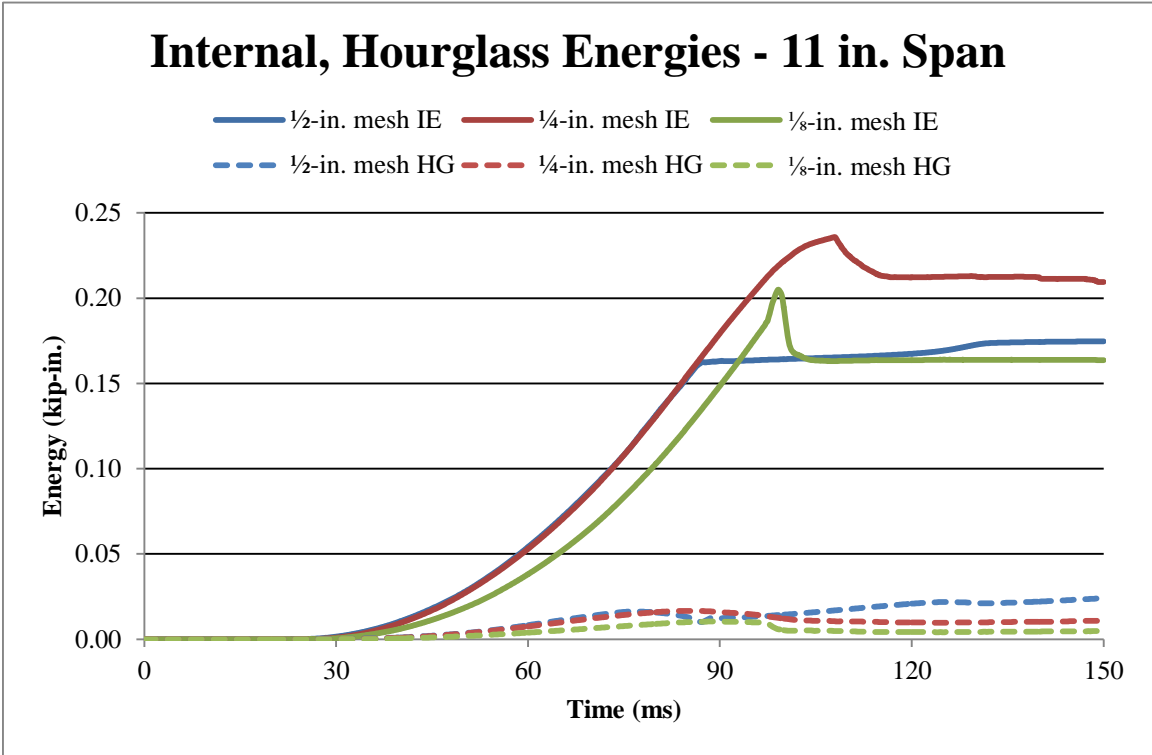
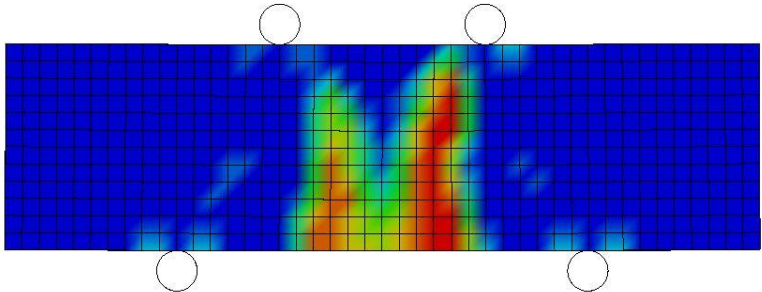


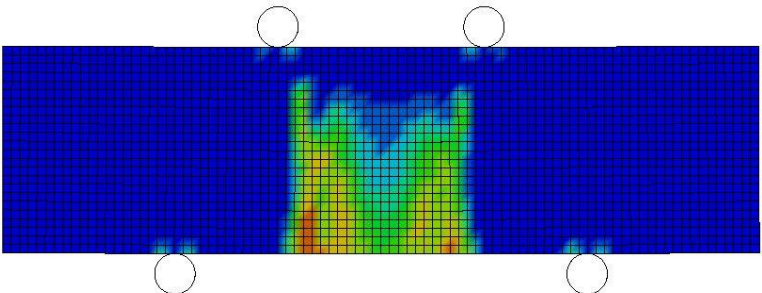
Figure E-9. Energy Comparison for 11-in. (279-mm) Span, CSCM Model (Alternate)

Beam Testing - CSCM Model
Time = 100
Contours of Effective Plastic Strain
max IP. value
min=0, at elem# 195601
max=0.999, at elem# 198082



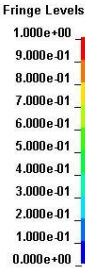
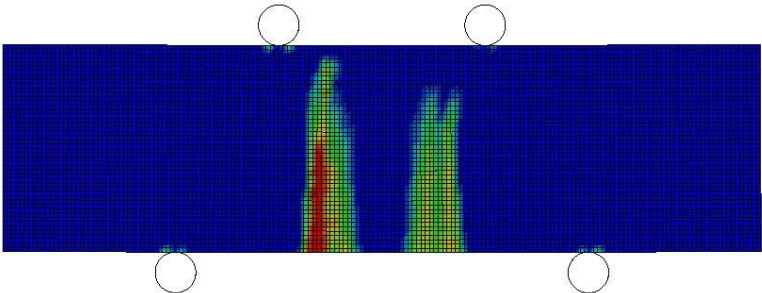
1/2 in. (13 mm)

Beam Testing - CSCM Model
Time = 100
Contours of Effective Plastic Strain
max IP. value
min=0, at elem# 201937
max=0.998917, at elem# 231764



1/4 in. (6 mm)

Beam Testing - CSCM Model
Time = 100
Contours of Effective Plastic Strain
max IP. value
min=0, at elem# 310801
max=0.998999, at elem# 546106



1/8 in. (3 mm)

Figure E-10. Damage Pattern for 12-in. (305-mm) Span at 100 ms, CSCM Model (Alternate)

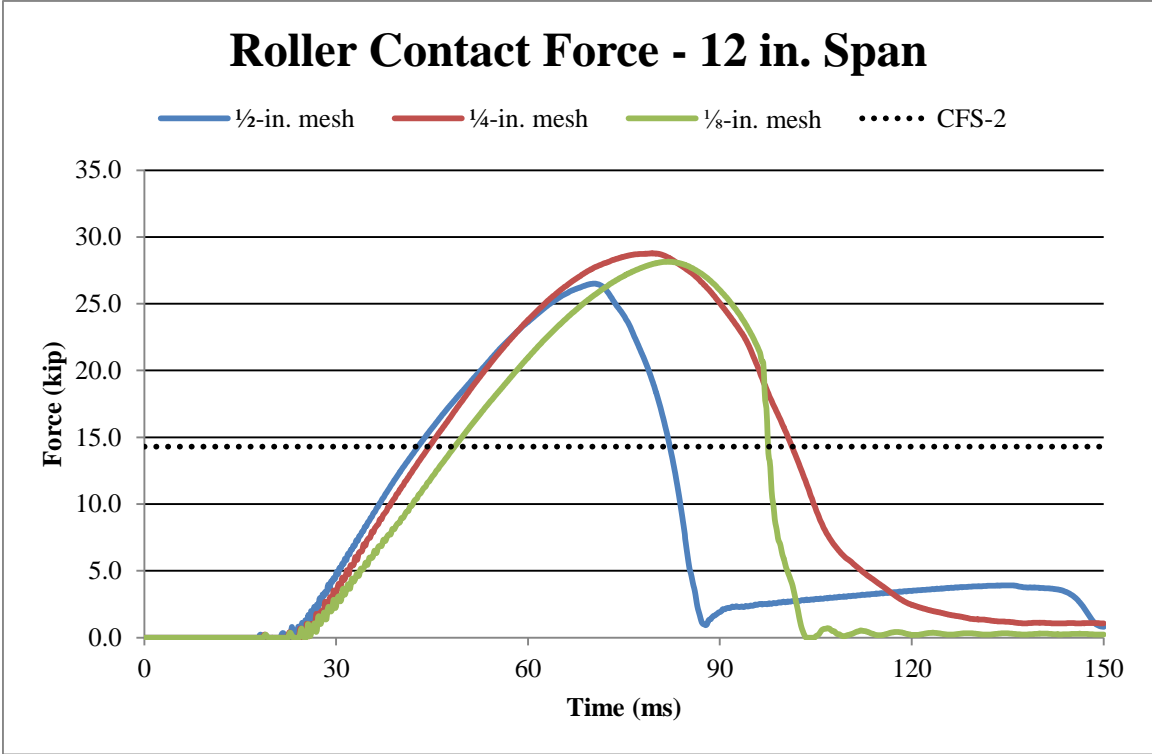


Figure E-11. Force Comparison for 12-in. (305-mm) Span, CSCM Model (Alternate)

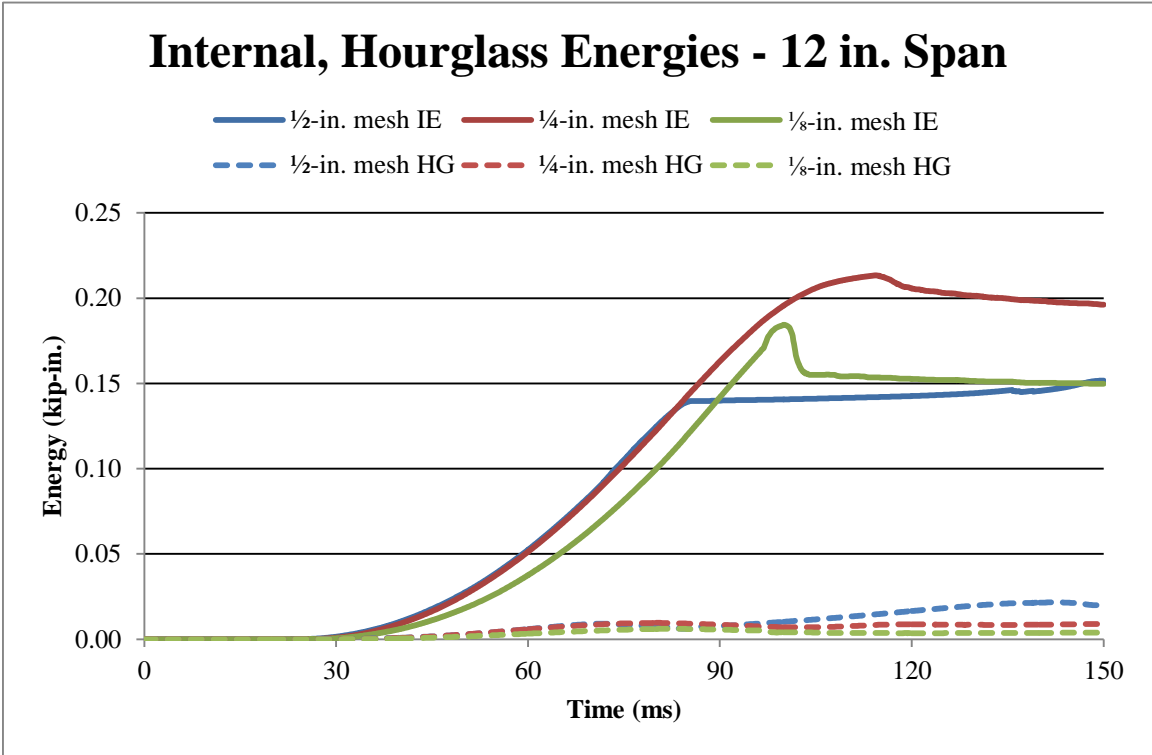
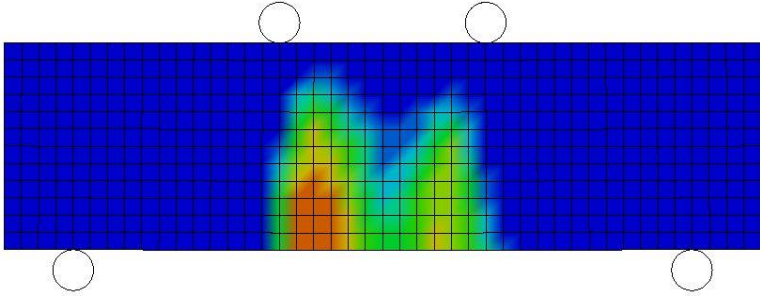


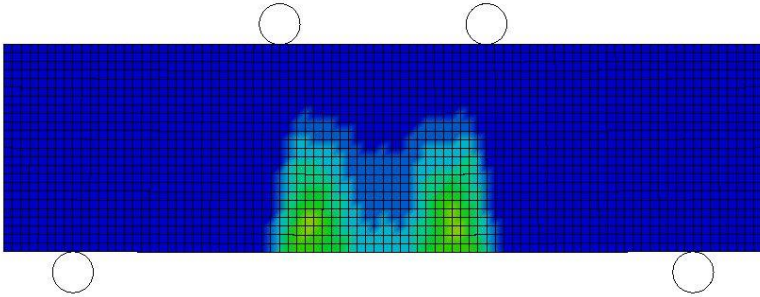
Figure E-12. Energy Comparison for 12-in. (305-mm) Span, CSCM Model (Alternate)

Beam Testing - CSCM Model
Time = 100
Contours of Effective Plastic Strain
max IP. value
min=0, at elem# 195601
max=0.985442, at elem# 199282



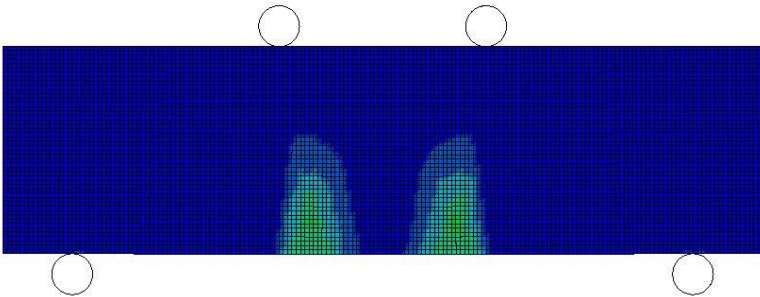
1/2 in. (13 mm)

Beam Testing - CSCM Model
Time = 100
Contours of Effective Plastic Strain
max IP. value
min=0, at elem# 201937
max=0.781417, at elem# 223163



1/4 in. (6 mm)

Beam Testing - CSCM Model
Time = 100
Contours of Effective Plastic Strain
max IP. value
min=0, at elem# 310801
max=0.611978, at elem# 550573



1/8 in. (3 mm)

Figure E-13. Damage Pattern for 18-in. (457-mm) Span at 100 ms, CSCM Model (Alternate)

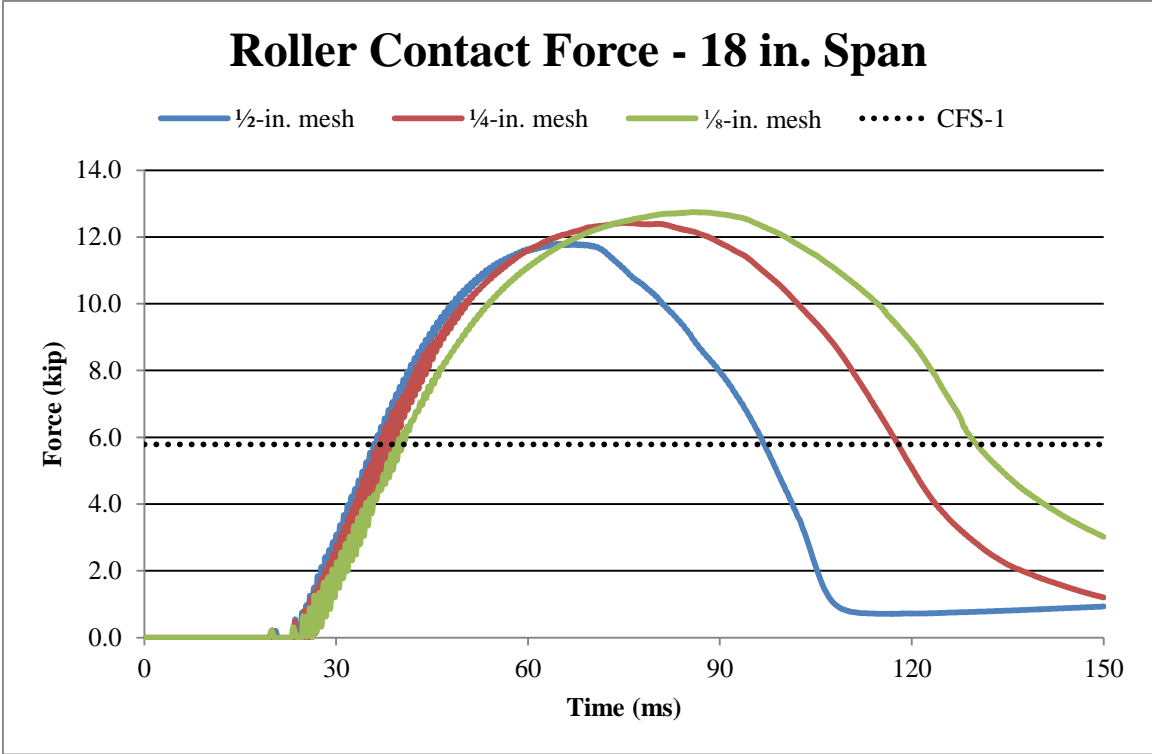


Figure E-14. Force Comparison for 18-in. (457-mm) Span, CSCM Model (Alternate)

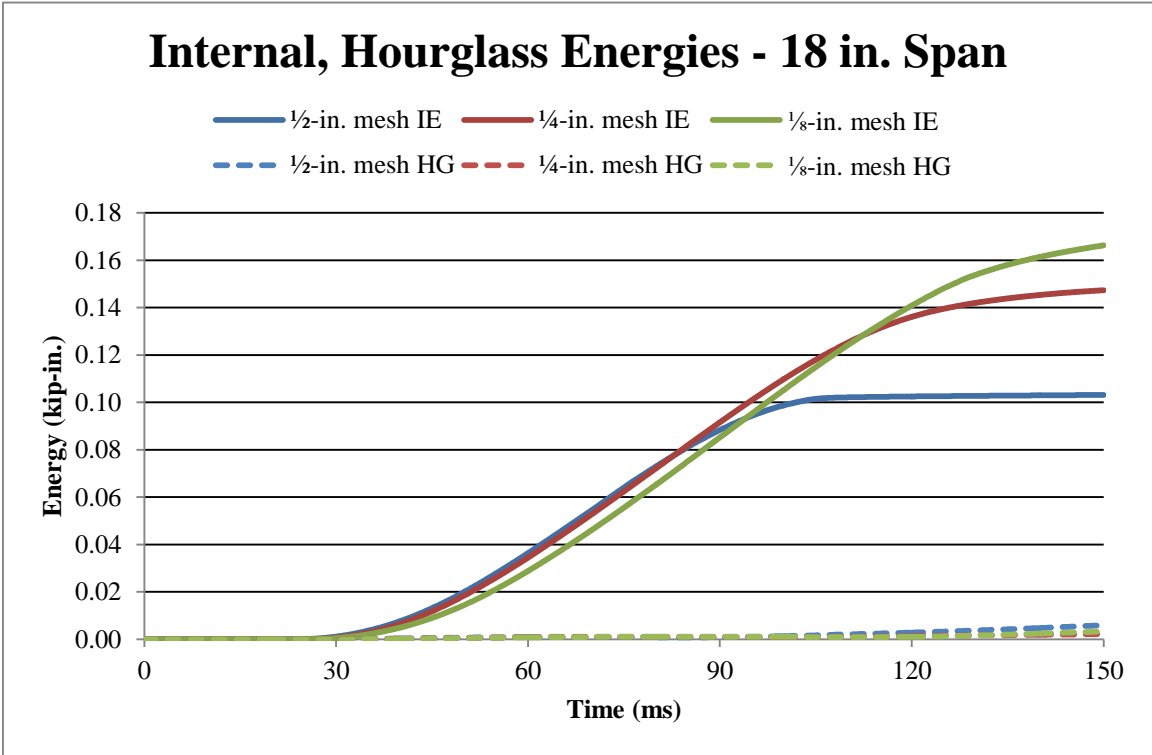


Figure E-15. Energy Comparison for 18-in. (457-mm) Span, CSCM Model (Alternate)

END OF DOCUMENT